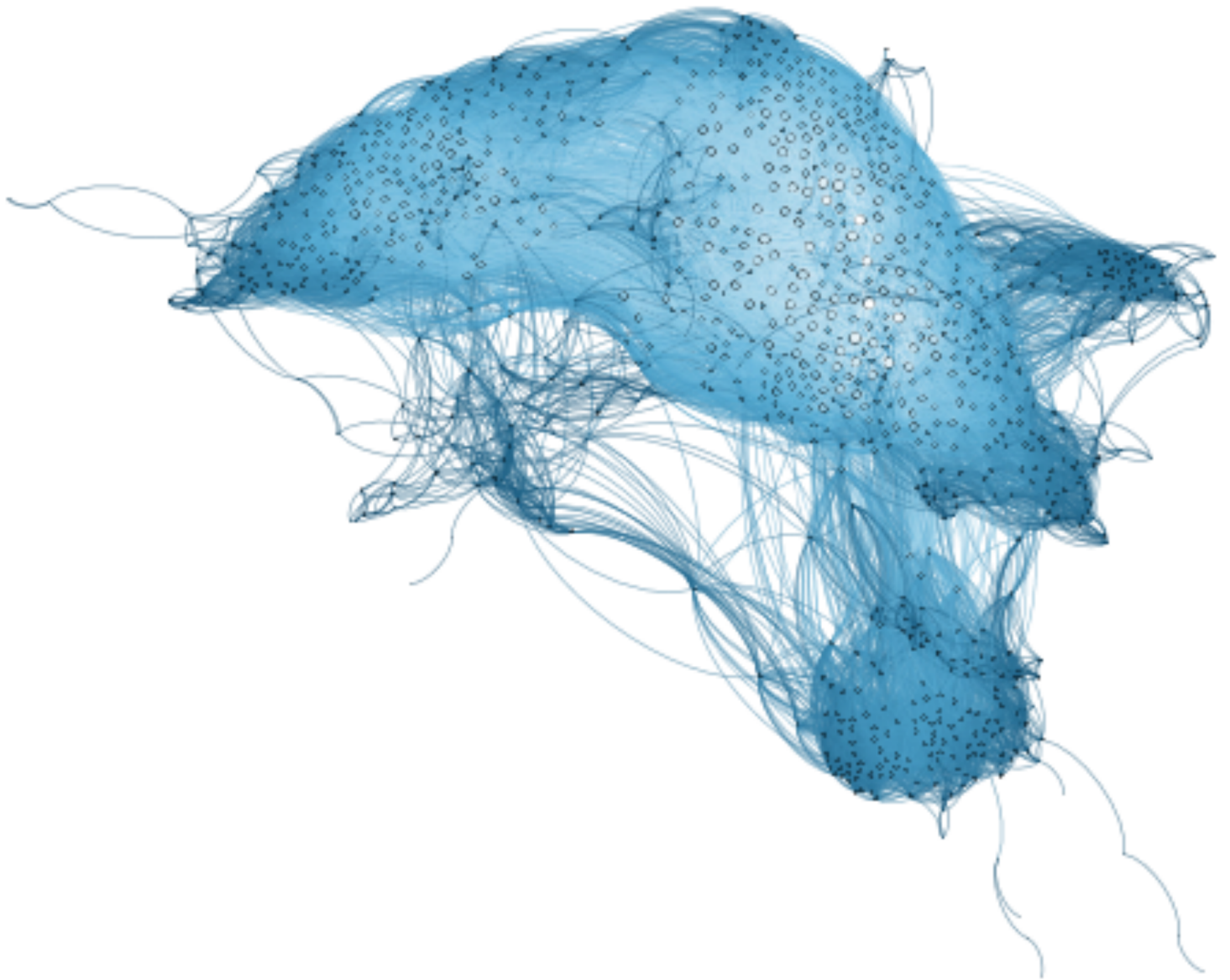


Matching of Avalanche Photodiodes and Light Injection Into Scintillation Crystals

Benjamin Wohlfahrt



Matching of Avalanche Photodiodes and Light Injection Into Scintillation Crystals

Inaugural-Dissertation

zur Erlangung des Doktorgrades der Naturwissenschaften (Dr. rer. nat.)

der Justus-Liebig-Universität Gießen

im Fachbereich 07

(Mathematik und Informatik, Physik, Geographie)

Benjamin Wohlfahrt

Justus-Liebig-Universität Gießen

II. Physikalisches Institut

Heinrich-Buff-Ring 16

35392 Gießen

Deutschland

Dekan:
Prodekan:

Prof. Dr. Kai-Thomas Brinkmann
Prof. Dr. Ludger Overbeck

1. Gutachter und Betreuer:
2. Gutachter:
1. Prüfer:
2. Prüfer:

Prof. Dr. Kai-Thomas Brinkmann
PD Dr. Jens Sören Lange
Prof. Dr. Martin Buhmann
Prof. Dr. Sangam Chatterjee

Contents

Zusammenfassung	1
Abstract	2
1 Fundamentals	4
1 Motivation	4
2 FAIR	4
3 Antiproton production	7
3.1 Collector Ring	8
3.2 High Energy Storage Ring	9
4 $\bar{\text{P}}\text{ANDA}$ -experiment	9
4.1 Physics at $\bar{\text{P}}\text{ANDA}$	12
4.1.1 Charmonium spectroscopy	13
4.1.2 Gluons	14
4.1.3 Hadrons in nuclear matter	15
4.1.4 Hypernuclear physics	15
4.2 $\bar{\text{P}}\text{ANDA}$ -Detector	16
4.2.1 Target	18
4.2.2 Micro Vertex Detector	19
4.2.3 Central Straw Tube Tracker	20
4.2.4 Time-Of-Flight Detector	21
4.2.5 DIRC	21
4.2.6 Electromagnetic Calorimeter	22
4.2.7 Muon Detection	22
4.2.8 Tracking and Particle Identification	22
5 Electromagnetic Calorimeter	24
5.1 Interactions of radiation with matter	24
5.1.1 Photon interactions	26
5.1.1.1 The photoelectric effect	26
5.1.1.2 Compton effect	26
5.1.1.3 Pair production	27
5.1.2 Charged particle interactions	28
5.1.2.1 Bremsstrahlung	29
5.1.2.2 Cherenkov radiation	30
5.1.2.3 Transition radiation	30
5.1.3 Electromagnetic shower	30
5.1.4 Scintillation	32
5.2 $\bar{\text{P}}\text{ANDA}$ Electromagnetic Calorimeter	34
5.2.1 Design concept	36
5.2.2 PWO-II	39
5.2.3 Avalanche Photodiode	41
5.2.4 Preamplifier	49
5.2.5 Readout	51

2	Matching	53
6	APD Parameters	53
6.1	APD screening	54
6.1.1	Cluster analysis	54
6.2	Parameter extraction	58
6.2.1	Diode regression modelling	58
6.2.1.1	Estimation methods and coefficients of determination	59
6.2.1.2	Empirical relationship	62
6.2.1.3	Polynomial	66
6.3	Results	69
6.3.1	Polynomial degree	69
6.3.2	Numerical convergence	75
6.3.3	Diagnostics	76
6.3.4	Q-point	78
6.3.5	Slope	82
6.3.6	Breakdown voltage	82
6.3.7	Data pool	84
6.4	Conclusions	97
7	Assignment & Matching	99
7.1	Similarity measure	100
7.1.1	Metric	102
7.2	Greedy algorithm	107
7.3	Hungarian algorithm	108
7.3.1	Adjustment to a single set	109
7.4	Edmond's algorithm	109
7.4.1	Implementation	110
7.5	Sequence	112
7.6	Results	113
7.6.1	Basic network	113
7.6.1.1	Blossom algorithm	113
7.6.1.2	Greedy algorithm	115
7.6.1.3	Pool influence on the similarity measurement	116
7.6.1.4	Metric	117
7.6.1.5	Parameter deviations	118
7.6.1.5.1	Voltages	118
7.6.1.5.2	Slopes	121
7.6.2	Modified network	123
7.6.2.1	Distance limit	125
7.6.2.1.1	Optimal distance threshold	131
7.6.2.2	Slope limit	138
7.6.2.2.1	Optimal slope threshold	142
7.6.2.3	Voltage limit	144
7.6.2.3.1	Optimal voltage threshold:	150
7.6.2.4	Comparison between all optima	153
7.6.2.5	Group APD pairings to a cluster of four pairings	153
7.6.2.5.1	Assigning the APD groupings via Mahalanobis	154
7.6.2.5.2	Assigning the APD pairings via voltage limits	156
7.6.3	Conclusion and outlook	158

3	Light coupling for the monitoring system of the Electromagnetic calorimeter	161
8	Experimental setup	163
8.1	Stability test	164
8.2	Material analysis for coating	165
8.3	Position study	168
8.4	Energy injection at various positions	169
8.5	Absolute light yield	171
8.6	Polishing dependency	173
9	Simulation & Implementation	174
9.1	SLitrani	174
9.2	Birefringence	174
9.3	Geometrical and optical parameters of the components	175
9.4	Results	177
9.4.1	Setup	179
9.4.2	Angle study at origin	179
9.4.3	Angle study at specific coordinates	181
9.4.4	Efficiency map	182
9.4.5	Elapsed time	183
9.4.6	Elapsed distance	184
9.4.7	Interaction study	185
9.4.8	Correlations between the propagation quantities	187
9.4.9	APD ratio during rotation	188
9.4.10	APD ratio during x translation	189
9.4.11	Type scan	190
9.4.12	Position impact	191
10	Conclusion and outlook	194
4	Appendix	195
11	Background	196
11.1	Crystal geometries	196
12	Matching	197
12.1	APD Parameters	197
12.1.1	Share of wafers in data points	197
12.1.2	APD 711006317	198
12.1.3	Linear mixed model	199
12.1.4	Influence of single APDs	200
12.1.5	Residual plot of the lots	201
12.1.6	Q-point	203
12.1.7	Breakdown voltage	205
12.1.8	Parameters against lots	208
12.1.9	Temperature	212
12.2	Assignment & Matching	214
12.2.1	Similarity measure	214
12.2.2	Influence of irradiation	215
12.3	Graph theory	216
12.4	Adjustment to a single set	218
12.5	Results	220

12.5.1	Distance scan	220
12.5.2	Voltage scan	224
12.5.3	Reduced graph	227
12.6	List of APDs	229
13	Beam time with Proto120 in Main	232
13.1	Mainzer Mikrotron	232
13.1.1	A2	234
13.1.2	Readout	235
13.1.3	Setup	238
13.2	Results	238
13.2.1	Data acquisition	239
13.2.2	Feature Extraction	239
13.2.3	Constraints	240
13.2.4	Cosmic single calibration	244
13.2.5	Noise	244
13.2.6	Linearity	245
13.2.7	Readout cable	247
13.2.8	Light pulser fiber coupling	247
14	Light coupling	248
14.1	Filters	248
14.2	Experimental settings	248
14.3	Slitrani settings	250
14.3.1	Geometrical and optical properties	250
14.3.2	Fiber	250
14.3.3	Cap	251
14.3.4	Crystal	253
14.3.5	Wrapping	255
14.3.6	Glue	256
14.3.7	Silicon	257
14.3.8	APD	258
14.3.9	Best angles	
15	Data sheets	
References		
15.1	Figures	

Zusammenfassung

Das zur Zeit im Bau befindliche \bar{P} ANDA-Experiment an der FAIR-Einrichtung in Darmstadt, Deutschland, erfordert ein elektromagnetisches Kalorimeter mit einem sehr niedrigen Schwellenwert von 3 MeV pro Kristall und 10 MeV pro Cluster. Dieses Kalorimeter hat die Form eines Fasses und wird drei Einheiten umfassen: Zwei Endkappen und das Fass selbst. Insgesamt werden 15552 Kristalle verwendet, wobei das Fass den Hauptteil mit 11360 Kristallen darstellt. Die Szintillationskristalle werden aus einer zweiten Generation von Blei-Wolframat ($\text{PbWO}_4\text{-II}$) hergestellt, die eine sehr schnelle Abklingzeit von etwa $\tau = 15$ ns bieten. Das erzeugte Licht wird anschliessend von zwei Lawinenphotodektoren, APDs, ausgelesen, die auf der Rückseite der Kristalle angebracht sind. Diese Photodioden werden von Hamamatsu hergestellt und ähneln den APDs, die bereits im CMS-Experiment am CERN zum Einsatz kommen, besitzen aber eine größere aktive Fläche und eine leicht modifizierte innere Struktur. Ein den APDs nachfolgender Vorverstärker, der APFEL ASIC, basierend auf 350 nm CMOS-Technologie, formt das Signal mit Hilfe eines Pulsformers dritter Ordnung und wird von 14-bit SADCs ausgelesen.

Um ein bestmögliches Auslesesignal zu erhalten, ist ein bestimmter Arbeitspunkt der Lawinenphotodektoren bei einer Verstärkung von $M = 150$ vorgesehen. Die APDs werden von dem Photosensor-Laboratory in Darmstadt vermessen, im Strahlencentrum in Gießen mit Photonen bei einer Dosis von 30 Gy bestrahlt und in Darmstadt erneut vermessen. Dabei wird je eine Kennlinienkurve Verstärkung M gegen Spannung U gemessen. Der Arbeitspunkt ist durch eine individuelle Betriebsspannung vorgegeben und weist einen bestimmten Anstieg an diesem Punkt auf. Um diesen Arbeitspunkt so genau wie möglich zu bestimmen, werden im Rahmen dieser Arbeit mehrere Interpolationsmethoden mit Hilfe statistischer Mittel untersucht, da das in der Standardliteratur üblicherweise verwendete Modell, der sogenannte Miller-Fit, bei hohen Verstärkungsspannungen (ab etwa $M = 50$) keine präzisen Vorhersagen mehr liefert. Ausgangspunkt ist daher ein polynomiales Regressionsmodell, dessen Ordnung, Anzahl verwendeter Datenpunkte und konkrete Implementierung, beispielsweise als gemischtes Modell als Referenz, analysiert werden. Ein einfaches Polynom dritten Grades bei einer Anzahl von insgesamt sechs verwendeten Datenpunkte (je drei Datenpunkte über- und unterhalb der anvisierten Verstärkung von $M = 150$) erweist sich letztlich am effizientesten. Darüber hinaus zeigt sich, dass sich eine Transformation des Datenbereiches in eine doppelt-logarithmische Skala als nützlich erweist.

Da zwei APDs pro Kristall zum Einsatz kommen werden, um das selbe Signal zu detektieren, ist es wichtig, jedem Kristall die beiden gemäß ihrer Betriebsparameter ähnlichsten APDs aus dem verfügbaren Pool so zuzuordnen, dass die Summe der zuweisbaren APDs so hoch wie möglich ist. Dazu ist zunächst ein geeignetes Werkzeug erforderlich, um die Ähnlichkeit der Parameter bestimmen zu können. Dafür wird die Mahalanobis-Distanz verwendet, die sich für kontinuierliche, multivariate Räume eignet. Solch eines wird hier durch vier Dimensionen aufgespannt, die jeweils einen Betriebsparameter einer APD repräsentieren. Diese lässt sich auch verwenden, um festzustellen, wie sehr sich die APDs als Kollektiv ähneln. Dazu zählen beispielsweise Korrelationen zwischen den Detektoren und deren Parametern, das Temperaturverhalten, die Bestimmung der Durchbruchspannung oder Parameteränderungen durch Bestrahlung.

Die Zuordnung der APDs erfolgt mittels einer Implementierung des Blossom V-Algorithmus, der ein perfektes minimal-gewichtetes Matching erzeugt. Die Beeinflussung dieses durch das Einfügen von Limits bezüglich etwaiger Parameterunterschiede innerhalb der 2er-Gruppierungen wird mit Auswirkung auf die resultierende Gesamtanzahl der Gruppierungen ausführlich untersucht.

Die Hochspannungsversorgung der APDs erfolgt über eine Platine, die insgesamt acht APDs zu regulieren vermag. Für solch ein Multi-Matching existiert bislang kein Ansatz, daher erfolgt das Gruppieren von vier 2er-Paaren zu einem 8er-Paar über sogenannte virtuelle APDs, womit sich der schon zuvor verwendete Blossom V-Algorithmus wieder verwenden lässt. Eine virtuelle APD repräsentiert dabei ein 2er-Paar über deren Mittelwerte in den Betriebsparametern. Die Spannungsaufösung der Versorgungsplatine beträgt gemäß des verwendeten 10-bit DACs 100 mV und weist einen Spannungsbereich von voraussichtlich etwa 50 V auf. Die Quartetts und auch schlussendlich die Oktetts müssen ebenfalls entsprechend zugeordnet werden, dass sie den entsprechenden Spannungsbereich erfüllen. Nutzt man für diese jeweils nur die Spannungswerte als Distanzfunktion, reduziert sich der maximale Spannungsunterschied innerhalb einer Hochspannungsplatine auf weniger als 5 Volt.

Um eine Online-Überwachung der APDs zu ermöglichen, wird ein Lichtpuls verwendet, der Licht in die Kristalle einkoppelt. Dieses wird von den APDs in entsprechende Signale umgewandelt. Aufgrund des geringen freien Volumens im mechanischen Träger des Kalorimeters ist es nicht möglich, diesen dort direkt zu installieren. Deshalb wird das Licht über eine Lichtfaser vom Lichtpuls zum jeweiligen Kristall geleitet. Dort ist wiederum eine spezielle Befestigung für die Faser erforderlich, die Einfluß auf die eingekoppelte Lichtmenge hat. Aktuell werden mehrere Designvorschläge untersucht, von denen in dieser Arbeit der erste Prototyp analysiert wurde. Dieser stellt eine kuppelartige Kappe aus Polyamid 12 dar und wird an der Vorderseite des Kristalls angebracht. Diese Methode bietet einige Freiheitsgrade wie unter anderem den Kopplungswinkel und die -tiefe der Faser. Der Einfluß dieser Parameter auf die eingekoppelte Lichtmenge wird experimentell mithilfe eines $\bar{\text{P}}\text{ANDA}$ -Szintillationskristalls und eines Photomultipliers als Detektor untersucht. Um die reflektiven Eigenschaften zu verbessern, wurde die Kappe mit Bariumsulfat beschichtet und dessen Strahlenhärte und Auftragsart untersucht. Darüber hinaus wurde die Lichteinkopplung mithilfe einer Simulation in SLitran für zwei APDs als Detektoren analysiert.

Abstract

The $\bar{\text{P}}\text{ANDA}$ -experiment currently under construction at the FAIR facility in Darmstadt, Germany, requires an electromagnetic calorimeter with a very low threshold of 3 MeV per crystal and 10 MeV per cluster. This calorimeter has a shape of a barrel and will comprise three units: Two end caps and the barrel itself. A total of 15552 crystals will be used, with the barrel representing the main part with 11360 crystals. The scintillation crystals are made from a second generation of lead tungstate ($\text{PbWO}_4\text{-II}$), which have a very fast decay time of about $\tau = 15$ ns. The generated light will be read out by two Avalanche Photodiodes, APDs, which are attached to the back of the crystals. These photodiodes are manufactured by Hamamatsu and are similar to the APDs already used in the CMS experiment at CERN, but provide a larger active area and a slightly modified inner structure. A preamplifier following the APDs, the APFEL ASIC based on 350 nm CMOS technology, forms the signal with the help of a third-order pulse shaper and is read out by 14-bit SADCs.

In order to obtain the best possible readout signal, an operating point of the avalanche photodiodes with a gain of $M = 150$ is foreseen. The APDs will be measured by the Photosensor Laboratory in Darmstadt, irradiated with photons at a dose of 30 Gy at the Strahlencentrum in Giessen and measured again in Darmstadt. Each time, a characteristic curve with gain M is measured against voltage V . The operating point is defined by an individual operating voltage and shows a certain increase at this point. In order to determine this operating point as accurately as possible, several interpolation methods are investigated in this work with the aid of statistical means, since the model commonly used in standard literature, the so-called Miller-Fit, used at high amplification gains (from about $M = 50$) does not longer provide accurate predictions. The starting point is a polynomial regression model whose order, number of data points used and concrete implementation, for example a mixed model as a reference model, are analyzed. A simple third-degree polynomial with a total of six data points (three data points each above and below the targeted gain of $M = 150$) ultimately proves to be the most efficient. Since two APDs per crystal will be used to detect the same signal, it is important to assign to each crystal the two most similar APDs from the available pool according to their operating parameters so that the sum of the assignable APDs is as high as possible. This requires a suitable tool to determine the similarity of the parameters. For this reason, the Mahalanobis distance is used, which is suitable for continuous multivariate spaces. This is spanned by four dimensions, each representing one operating parameter of an APD. This distance function can also be used to determine how similar the APDs behave as a collective. This includes, for example, correlations between the detectors and their parameters, the temperature behavior, the determination of the breakdown voltage or parameter changes due to irradiation.

The APDs are assigned using an implementation of the Blossom V algorithm, which produces a perfect minimum-weighted matching. The influence of it through the introduction of limits regarding possible parameter differences within the 2-groupings is examined in detail with effects on the resulting total number of pairings.

The high-voltage supply of the APDs is provided by a circuit board which is capable of regulating a total of eight APDs. For such a multi-matching no approach exists as of this writing. Therefore, the grouping of four

2-pairings to an 8-pair is performed via so-called virtual APDs, which allow the previously used Blossom V algorithm to be reused. A virtual APD represents the APDs of a pairing via their mean values of their operating parameters.. The voltage resolution of the supply board is according to the used 10-bit DACs 100 mV and provides a voltage range of presumably about 50 V. The quartets and finally the octets must also be assigned accordingly so that they fulfill the corresponding voltage range. If only the voltage values are used as a distance function for the octets, the maximum voltage difference within a high voltage board is less than 5 Volt.

In order to enable an online monitoring of the APDs, a light pulser is used to couple light into the crystals. This light will be converted by the APDs into corresponding signals. Due to the small free volume in the mechanical carrier of the calorimeter, it is not possible to install it directly there. Therefore, the light is guided via a light fiber from the light pulser to the respective crystal. There is a special attachment for the fiber necessary, which has an influence on the coupled light quantity. Several design proposals are currently being investigated, of which the first prototype is analyzed in this work. The prototype is a dome-shaped cap made of polyamide 12 and is mounted at the front of the crystal. This method provides some degrees of freedom such as the coupling angle and the depth of the fiber. The influence of these parameters on the amount of coupled light is experimentally investigated using a \bar{P} ANDA-scintillation crystal and a photomultiplier as a detector. In order to improve the reflective properties, the cap is coated with barium sulfate and its radiation tolerance and application method are investigated. In addition, the light injection is simulated in SLitrani with two APDs as detectors.

Part 1

Fundamentals

„The Standard Model is working too well“

Richard P. Feynman

1 Motivation

Pursuing the principle of simplification, the foundation of physics nowadays is based on four fundamental forces. The Standard Model unifies three of them and is, at the present, the most complete theory to describe nature. It is an effective field theory built upon major gauge theories and is, in return, a gauge quantum field theory itself.

The Standard Model provides a deep insight into interactions as well as the structure of matter. Especially the former is subject of interest since all incidents in nature are understood as interactions: Among particles, forces, fields or other things, depending on the point of view. Unfortunately, at this stage, the Standard Model falls short of explaining “everything” successfully. A few violations and contradictions have been noticed and some questions still remain open, for example:

Why are there exactly three families of particles?

The elementary particles can be divided into three families which differ almost only in mass

Why is there an imbalance in the mass scale of subatomic particles?

Particles gain mass through the Higgs mechanism but why do they couple in different ways?

Why is the matter-antimatter ratio unequal?

Beginning with the Big Bang, there should be a symmetric matter-antimatter ratio

Why does the potential of the strong force include a repulsive part?

Models of the effective nuclear force including short-range repulsion tend to fit experimental data better compared to those which are purely attractive

How did the universe evolve (horizon problem)?

There are two possibilities: Expansion inflationary or cyclic

In order to help answer some of these questions, a new international science facility is currently being constructed: The FAIR¹ research center.

2 FAIR

FAIR will be a new accelerator complex, located at the **GSI**² in Darmstadt, Hessen, Germany. Contributing crucial discoveries to physics, the GSI became a significant part of the national and international research landscape. Up to the present day, this research facility plays a major role in a vast range of scientific areas, for example, from nuclear physics over space research to cancer treatment. To drive forth the progress in numerous open research fields, the GSI will be extended by creating the adjoining FAIR³ facility. The resulting complex will harbor a lot of new experiments under the aegis of major ones like CBM⁴, PANDA⁵, NuStar⁶

¹Facility for Antiproton and Ion Research

²Gesellschaft für Schwerionenphysik mbH

³Facility for Antiproton and Ion Research

⁴Compressed Baryonic Matter

⁵antiProton ANnihilation at DArmstadt

⁶Nuclear Structure, Astrophysics and Reactions

and APPA⁷. A detailed summary of the research projects can be found in [73]. Physics at FAIR is related to antiprotons together with ions of all kinds over a large energy spectrum. The key component of FAIR is the accelerator **SIS100**⁸. In case of ions, it uses the GSI ion accelerator Unilac⁹ as one of two pre-stages which will be modernized to fulfill the requirements for FAIR. Subsequently to the Unilac, **ions** will be injected into the second pre-accelerator, the SIS18, with an energy of 11 MeV/u at a pulsed current of 15 mA [69].

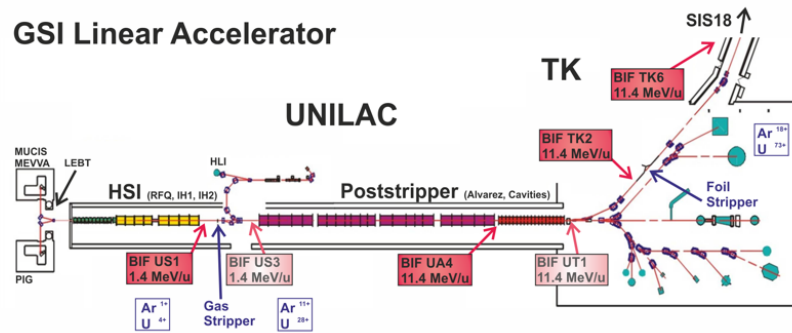


Figure 1: *The modernized universal ion linear accelerator (Unilac)* [71]. It will provide an energy of 11.4 MeV/u for or $^{238}\text{U}^{28+}$ -ions at a current of 15 mA. Ions, mostly $^{238}\text{U}^{4+}$, can be produced by a range of ion sources based on different mechanisms like electron-cyclotron-resonance, Penning ionization gauge and multi cusp ion source [61]. Along a 9 m radiofrequency quadrupole, the bunches will achieve an energy of 120 keV/u at a frequency of 36 MHz. Afterwards, the ions will pass two IH-cavities and enter an Alvarez with an energy of 1.4 MeV/u. A gaseous stripper will then remove all Uranium isotopes different from $^{238}\text{U}^{28+}$. After leaving the subsequent post stripper, a current of 15 mA is achieved at an energy of 11.4 MeV/u. The transfer line (TK) to the SIS18 consists of a foil stripper and a further charge state separator system (e.g. 73+ for Uranium).

In addition, a dedicated accelerator will be built for protons only, the so-called p-linac.

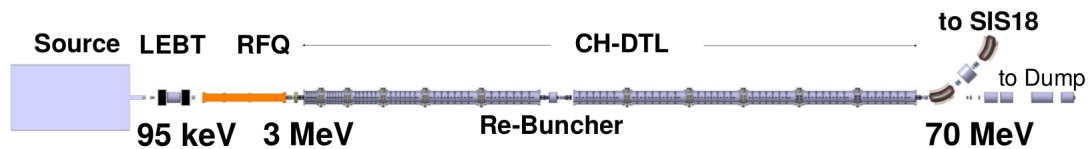


Figure 2: *The new proton linear accelerator (p-linac)* [70]. It comprises a proton source, a radiofrequency-quadrupole and a Cross-bar H-Type Drift Tube (CH-DTL) linac. The ion source provides a current of 100 mA together with an extraction energy of 95 keV. After the radiofrequency quadrupole, the particles achieve an energy of 3 MeV before they accelerate up to 70 MeV by the drift tube. Afterwards, they are injected into the SIS18 at a current of 70 mA.

It will be capable of injecting **protons** up to 70 MeV in pulses of 70 mA at 4 Hz into the subsequent synchrotron SIS18 [69]. The SIS18 will extract protons up to 4.5 GeV and ions with an energy of 200 MeV/u and into the SIS100 (see fig. 4), each at a repetition rate of 2.7 Hz [68, 69]. With a magnetic rigidity of 100 Tm, it brings up the protons to an energy of nearly 30 GeV and ions up to 1.5 GeV/u.

In contrast to other large particle accelerators which focus on high beam energies, FAIR is designed for high

⁷Atomic, Plasma Physics and Application

⁸Schwerionensynchrotron

⁹Universal Linear Accelerator

beam intensities: In case of ions $4 \cdot 10^{11}/s$ and in case of protons $2 \cdot 10^{13}/s$. The figure below depicts the global parameters of the PANDA accelerators:

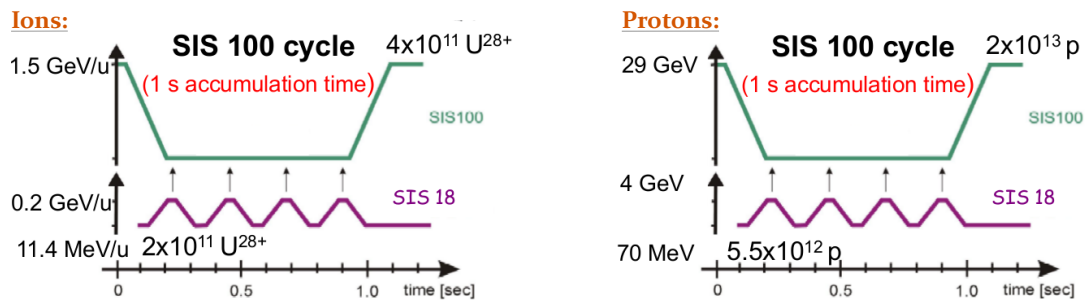


Figure 3: **Extraction parameters of the main accelerator SIS100 [118]:** Ions like $^{238}U^{28+}$ will be produced by the Unilac and extracted with 11.4 MeV/u into the SIS18. There, ions will be accelerated up to 200 MeV/u and injected into the SIS100. In the main accelerator ring, the ions will be accumulated and extracted with an intensity of $4 \cdot 10^{11}/s$ at 1.5 GeV/u. Protons will be prepared by the p-Linac. Injected into the SIS18 with an energy of 70 MeV, they will afterwards be pulled out into the SIS100 at an energy of 4 GeV. Finally, leaving the SIS100 with an intensity of $2 \cdot 10^{13}/s$, they will have achieved an energy of nearly 30 GeV.

For lower beam momenta, the particles with their quantities received from the SIS18, can bypass the main accelerator SIS100 and be guided directly to the experimental halls, storage and cooler rings.

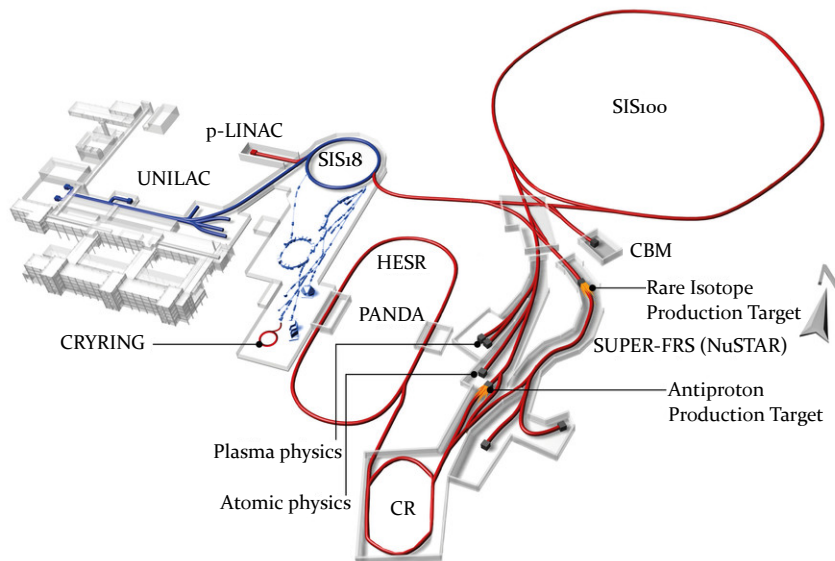


Figure 4: **Sketch of the existing GSI facility (blue) and of the planned FAIR facility (red) [17].** Ions will be produced by the upgraded Unilac and protons will be generated by the new p-Linac. Then, both pre-accelerators extract into the next pre-accelerator, the SIS18, before the particles will receive their maximum energy in the main accelerator SIS100. From there on, the particles can be guided to various experimental areas. Some of the experiments require a preceding preparation of the particles to obtain their final properties.

The research at FAIR will cover a wide spectrum and can be divided into three general topics: A deeper investigation of matter, an advanced research of the evolution of the universe as well as the utilization of ions in technology and applied research. These studies will be represented mainly by four major experiments [114, 158]:

- APPA: Research at FAIR will study plasma at unknown states. Heavy ions will be used to analyze the possible influence of cosmic radiation on crew and components for upcoming inter-planetary flights. Obtained information can be used for space flight- as well as for QED-experiments.
- CBM: At extreme energy densities, confinement¹⁰ is assumed to vanish resulting in quarks and gluons moving freely. The required conditions for such a state can be achieved through heating and compressing occurring in high-energy nucleus-nucleus collisions. On this basis, it is foreseen to explore an unobserved part of the phase diagram of nuclear matter.
- NUSTAR: Primary heavy ions will break into fragments when hitting a target. Afterwards, these fragments will be separated magnetically to be extracted in secondary beams. Such particles can be tailored for all kinds of experiments to investigate the nuclear configuration of various isotopes together with heavy elements and their processes.
- $\bar{\text{P}}\text{ANDA}$: See the dedicated section $\bar{\text{P}}\text{ANDA}$ -experiment on page 9.

With respect to the $\bar{\text{P}}\text{ANDA}$ -experiment, the production of antiprotons will now be described in detail.

3 Antiproton production

The p-linac is designed to produce **antiprotons** out of protons after leaving the accelerator chain. It is feasible to produce antiprotons by the Unilac too, but resulting in plenty of fission fragments at a lower luminosity. At FAIR, protons from the accelerators SIS18 and SIS100 will be available in a range of 1.5 – 29 GeV/c. At these momenta, the protons will hit the antiproton production target in bunches of 50 ns to generate antiprotons of up to 3 GeV in a flux of $10^7/s$ [158].

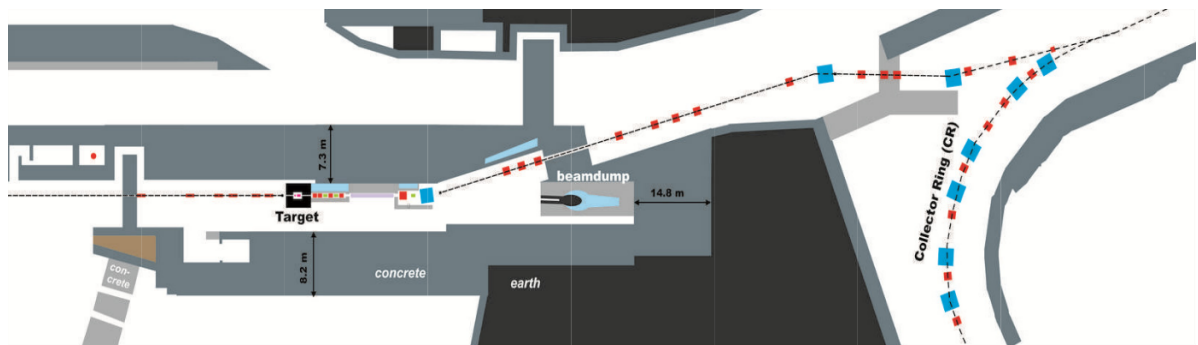


Figure 5: **Production of antiprotons** [42]. Protons extracted from SIS18 or SIS100 will hit a metal target and result in the preparation of a secondary beam that contains antiprotons of 3 GeV/c. With the help of a separator, all other kinds of particles will be removed. About 98 % of the produced antiprotons will be discarded due to a large bending angle θ or momentum p .

Afterwards, they will pass a magnetic horn which focuses the beam. An antiproton separator, a beamline of 100 m length with a very high acceptance, will isolate antiprotons above all from protons as well as from all other kinds of particles. Next to the separator, the antiprotons will be ejected and cooled by the CR.

When using a primary proton beam, antiprotons can only be produced via inelastic reactions due to baryon

¹⁰Phenomenon that quarks and gluons cannot be observed singularly

number conservation: $p + A + E_{kin} \mapsto X + \bar{p}$, where A is the target and X represents all particles in any allowed final **quantum state**. The kinetic threshold energy for an antiproton production is $6 \cdot m_p c^2 \approx 5.63$ GeV. The cross section for the production of antiprotons varies from about 50 to 100 mb, according to the related momentum range.

3.1 Collector Ring

The purpose of a collector ring is to improve and to ensure the quality properties of a beam, viz by minimizing the momentum spread and emittance. This will be done in two different ways: **Bunch rotation** and **stochastic cooling**. Antiprotons in bunches of 10^8 will be injected into the CR and caught by 1.3 MHz radiofrequency-quadrupoles. Applying a bunch rotation in the longitudinal phase space will reduce the momentum spread by a factor of 3. During stochastic cooling, bunch rotation will be disabled but it will also reduce the momentum spread. It is noteworthy that such a process is not following the Liouville's theorem. The principle of stochastic cooling works in such a way that the orbit of the beam is measured and compared to its ideal orbit. In case of a deviation it will be "kicked back" according to a phase shift of $\pi(n + 1/2)$ between the signal pick up and the kicker, an electromagnetic device. The cooling time for antiprotons will be about 10 s and in case of ions 1.5 s. The bandwidth will start at 1 – 2 GHz but will be extended later to 2 – 4 GHz [115].

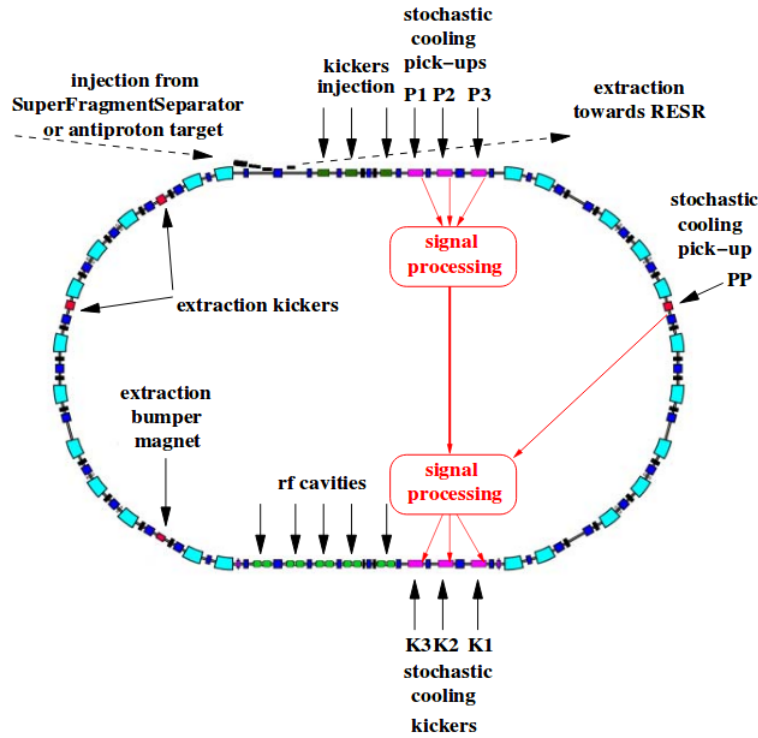


Figure 6: **Collector ring** [115]. The CR is the first stage after the production of antiprotons. It aims at cooling and fixing them at 3 GeV by the use of stochastic cooling and will reduce the relative momentum spread of antiprotons by a factor of about 10.

The CR has to prepare the particles for a further extraction to the HESR. Above all, the antiprotons have to be fixed at a velocity of 0.97 c corresponding to $p = 3$ GeV/c, whereas isotopes will be fixed at 0.83 c corresponding to 740 MeV/u. Antiprotons will enter the CR with a momentum spread of $\Delta p/p = 3\%$ and leave at $\Delta p/p = 0.2\%$, ions will be injected into the CR with $\Delta p/p = 1.5\%$ and ejected with $\Delta p/p = 0.1\%$ [41]. Finally, the antiprotons enter the HESR to be prepared for the \bar{P} ANDA-experiment.

3.2 High Energy Storage Ring

Storage rings improve the quality of the beams by providing **energy sharpness** and **focusing**. Within the HESR, this will be achieved through electron cooling and stochastic cooling, longitudinally as well as transversally. Electron cooling works via superposition of cold intense electron beams which interfere with the antiprotons at the same velocity. The injected beam will be de- or accelerated by about 0.1 GeV/cs and the momentum will be transferred via Coulomb collisions. The HESR has to ensure the cooling of antiprotons in a momentum range from 1.5 to 15 GeV/c. Two technical modes can be chosen: A **high luminosity mode** with luminosities up to $L=10^{32} \text{ cm}^{-2} \text{ s}^{-1}$ and a **high resolution mode** with a relative momentum resolution up to $\frac{\Delta p}{p} \leq 10^{-5}$.

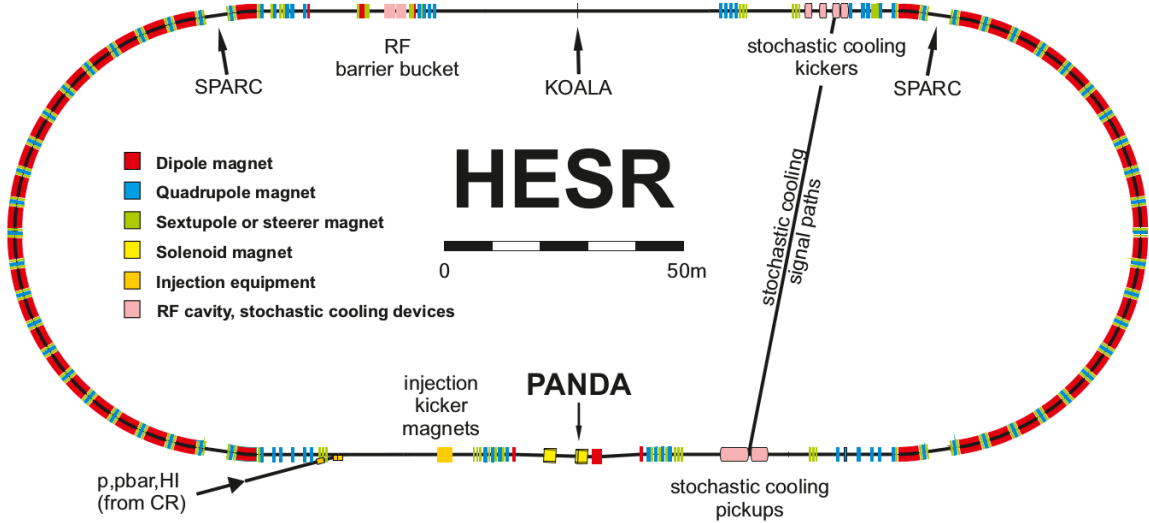


Figure 7: **High energy storage ring** [98]. Antiprotons of 3.8 GeV/c from the CR will be cooled and accelerated up to 15 GeV/c at the HESR. Cooling will be realized by a combination of electron and stochastic cooling.

Cooled antiprotons at 3.8 GeV/c from the CR will be transferred adiabatically in bunches to the HESR which is capable of accepting antiprotons with twice a momentum spread and emittance of the CR extraction parameters. Cooling already causes a loss of 30% of antiprotons but with the help of stochastic cooling and a barrier bucket system, this amount can be reduced. Finally, the antiprotons will be accumulated until a number of 10^8 antiprotons is available. Antiprotons traversing the target, respectively not impinging the target material, are recirculated in the storage ring for about 500,000 times. Meanwhile, the particles will be cooled by electron cooling to ensure a compensation of any energy loss. HESR will provide a high reaction rate and a high resolution of 30 keV to enable the study of rare production processes at $\bar{\text{P}}\text{ANDA}$ -experiment.

4 $\bar{\text{P}}\text{ANDA}$ -experiment

The $\bar{\text{P}}\text{ANDA}$ -experiment is located at the HESR and represents the main pillar of **hadron physics** at FAIR. Hadrons are compounds of quarks, elementary particles which are subject to the strong force. Its mediators are gluons and, up to the present, neither the interaction of quarks or gluons is fully understood nor in which all combination quarks and gluons can occur. $\bar{\text{P}}\text{ANDA}$ will help to deepen the knowledge about the strong force by its particular **kinematical region**. Especially the charm region is of high interest to investigate confinement and the origin of hadron masses.

Antiprotons will annihilate with target protons to produce a variety of composite particles. HESR utilizes antiprotons for its physics program because of several reasons [1, 83]:

High angular momenta directly accessible

e^+e^- -processes lead to charmonium states limited by the quantum number of the virtual photon, $J^{PC}=1^{--}$. Unfortunately, even in this indirect case, different vector spin-parity states remain unobtainable due to the angular-momentum barrier. In contrast, $\bar{p}p$ -reactions enable direct formation of all quantum states:

$$\begin{array}{l} e^+e^- \rightarrow \Psi' \\ \quad \hookrightarrow \gamma\chi_{1,2} \\ \quad \quad \hookrightarrow \gamma\gamma J/\psi \\ \quad \quad \quad \hookrightarrow \gamma\gamma e^+e^- \end{array} \qquad \begin{array}{l} \bar{p}p \rightarrow \chi_{1,2} \\ \quad \hookrightarrow \gamma J/\psi \\ \quad \quad \hookrightarrow \gamma e^+e^- \end{array}$$

Unlike formation processes as e^+e^- , a direct production provides a distinct background to identify charmonium states. While formation processes will produce charm as well as non-charm hybrids with high cross sections, production processes will generate charm-hybrids plus a different particle, e.g. π and η [95].

Antiproton-reactions are rich of gluons

The investigation of gluonic excitations is much easier when a lot of gluons are present. This happens easily in antiproton-proton reactions. Heavy glueballs could also be observed but are hard to identify due to their mixing (see Gluons on page 14).

Furthermore, the \bar{P} ANDA-detector provides additional useful aspects:

Very high resolution in formation reactions

The advantage of resonance scans through beam stepping is given by their much better resolution compared to an invariant mass reconstruction which depends on the detector resolution. \bar{P} ANDA makes it possible to discover the mass width of very narrow states through energy scans with a precision better than 100 keV.

Large mass-scale coverage

The \bar{P} ANDA-experiment provides CM-energies from 2 to 5.5 GeV/ c which enable studies of hadronic states consisting of light, strange and charm quarks.

High hadronic production rates

By taking advantage of large production cross sections in case of antiproton-proton reactions compared with electromagnetic probes, \bar{P} ANDA will provide a high statistic accuracy.

These aspects allow advanced investigations with respect to baryon and meson spectroscopy, reaction dynamics with possible CP violation as well as deeper insight into the hadron structure and more.

FAIR will provide very similar operation parameters to the previous AAC (LEAR Experiment, see table 1) but with the support of on-hand theories and investigation targets which were not available in the AAC's uptime. The CERN Antiproton accumulator has already been shutdown in the early 90's, whereas Fermilab's Tevatron stopped in 2011. For that reason, \bar{P} ANDA will come into play and aim at specific objects of investigation, depicted in fig. 8:

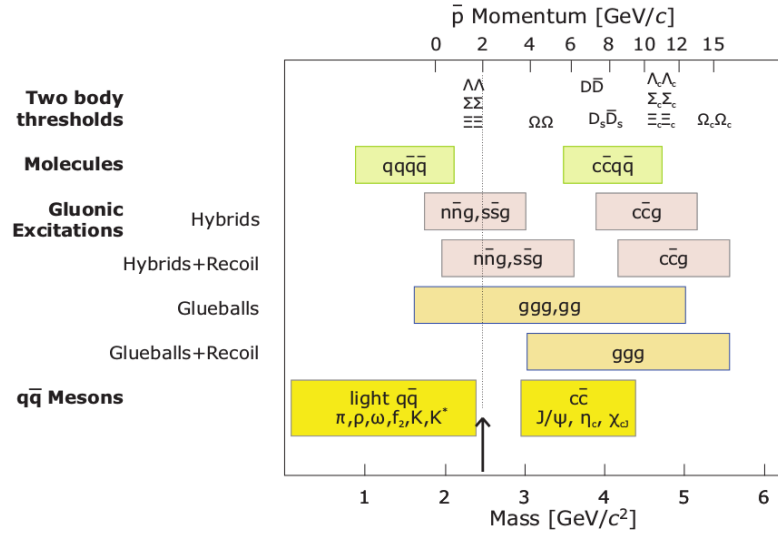


Figure 8: *Observable hadrons at HESR* [73]. The figure depicts the accessible hadrons as a function of the antiproton momentum provided by the HESR. The arrow indicates the energy range studied within LEAR at CERN, the successor of the AAC.

The following table holds a comparison of accelerators using antiprotons:

Proton beam	CERN (AAC)	Fermilab	FAIR
Kinetic energy / [GeV]	25	120	29
Maximum number of protons per cycle	1.45×10^{13}	8×10^{12}	2×10^{13}
Transverse beam emittance h/v / [$\pi \cdot \text{mm/mrad}$]	-	-	3 / 1
Cycle time / [s]	4.8	2.2	10
Pulse length of one bunch / [ns]	400	1600	50
Antiproton beam			
Kinetic energy / [GeV]	2.7	8	3
Momentum spread / [%]	6	4.5	6
Transverse emittance $h=v$	210	35	240
Yield per proton	5.4×10^{-6}	2.8×10^{-5}	5×10^{-6}
Maximum yield per cycle	7×10^7	2.6×10^8	1×10^8
Maximum possible stacking rate / [1/h]	5.3×10^{10}	2.1×10^{11}	3.5×10^{10}

Table 1: *Comparison of antiproton accelerators according to different facilities* [42]. FAIR is able to deliver the highest number of protons per cycle and also the most intense beam.

4.1 Physics at $\bar{\text{P}}\text{ANDA}$

Most of all, $\bar{\text{P}}\text{ANDA}$ embodies the hadron physics program at FAIR. The single subjects are in the first instance **charmonium spectroscopy, hybrids and glueballs**. The rules that dictate the quarks how to freeze out into hadrons are determined by the QCD¹¹. Present fundamental models of the strong interaction reproduce physics phenomena only at distances much shorter than the size of a nucleon. In this region, perturbation theory can be applied and yields high precision results and predictions but these are not applicable in the hadron region. The program of $\bar{\text{P}}\text{ANDA}$ addresses specific aspects of non-perturbative QCD by making use of the interaction potential of $c\bar{c}$ which can be computed with the help of effective field theories and LQCD¹². Due to the charm quark's heavy mass, in contrast to up, down and strange quarks, a non-relativistic treatment is more feasible and its corresponding kinematical region is crucial for a better understanding of quark confinement and mass generation.

After all, the physics at $\bar{\text{P}}\text{ANDA}$ is on the whole linked to QCD. Its **coupling constant** g_{QCD} determines the particle's interaction strength via the running coupling $\alpha_s = g^2/4\pi$. This constant is not completely constant and depends on the characteristic energy scale of the underlying process. Noteworthy it goes logarithmically:

$$\alpha_s(q^2) = \frac{12\pi}{(33 - 2n_f) \log(q^2/\Lambda^2)} \quad (1.1)$$

with Λ as the scaling parameter, n_f for the number of quark flavors to take part in self-loops and q^2 as the four-momentum transfer

This constant $\alpha_s(q^2)$ behaves very differently for q^2 than other coupling constants do since $\alpha_s(q^2)$ increases with q^2 and results in powerful interaction processes - in case of large distances. The scaling parameter Λ describes the region in which q^2 becomes ineffective, respectively, this happens when Λ^2 is greater than q^2 inducing quarks and gluons to participate only in weak processes (related to "asymptotic freedom"). The other way around, it is difficult to study this special situation because $\alpha_s(q^2)$ will oblige quarks and gluons to form hadrons. Therefore, up to now, it is not possible to observe free quarks. This attributes the scaling parameter Λ the capability to set a boundary between a world of quasi-free quarks and gluons on the one hand and a world of hadrons on the other hand. Important to emphasize: Λ is a free parameter and, thus, not predictable by theory. Thus, it has to be determined by experiments [49].

Overall, α_s describes how much a particle participates in strong interaction processes and occurs in the **phenomenological potential** of the strong force:

$$V(r) = -\frac{4}{3} \frac{\alpha_s}{r} + kr \quad (1.2)$$

with r representing the $q\bar{q}$ gap

α_s has been determined experimentally as $\alpha_s=0.1185$ at $\sqrt{s} = 91$ GeV, the mass of the Z boson. The strong potential does not decrease with the distance like other forces do, instead it increases at a rate of about 1 GeV/fm. Further researches on the Quantum Chromodynamics promise to yield a better understanding of the generation of hadronic masses which is connected to the confinement of quarks and to the spontaneous breaking of chiral symmetry. Additional general questions are the fundamental degrees of freedom of a baryon and gluonic excitations.

¹¹Quantum chromodynamics

¹²Lattice Quantum Chromodynamics

4.1.1 Charmonium spectroscopy

Charmonium¹³ is the bound state of a charm together with an anticharm quark. Its charm flavors compensate each other resulting in a so-called “**hidden-charm**”. Charmonium is somewhat special because of its spectrum. One of these states is J/ψ which is the most prominent state as it is the proof for the fourth quark (c), back in the 1970s.

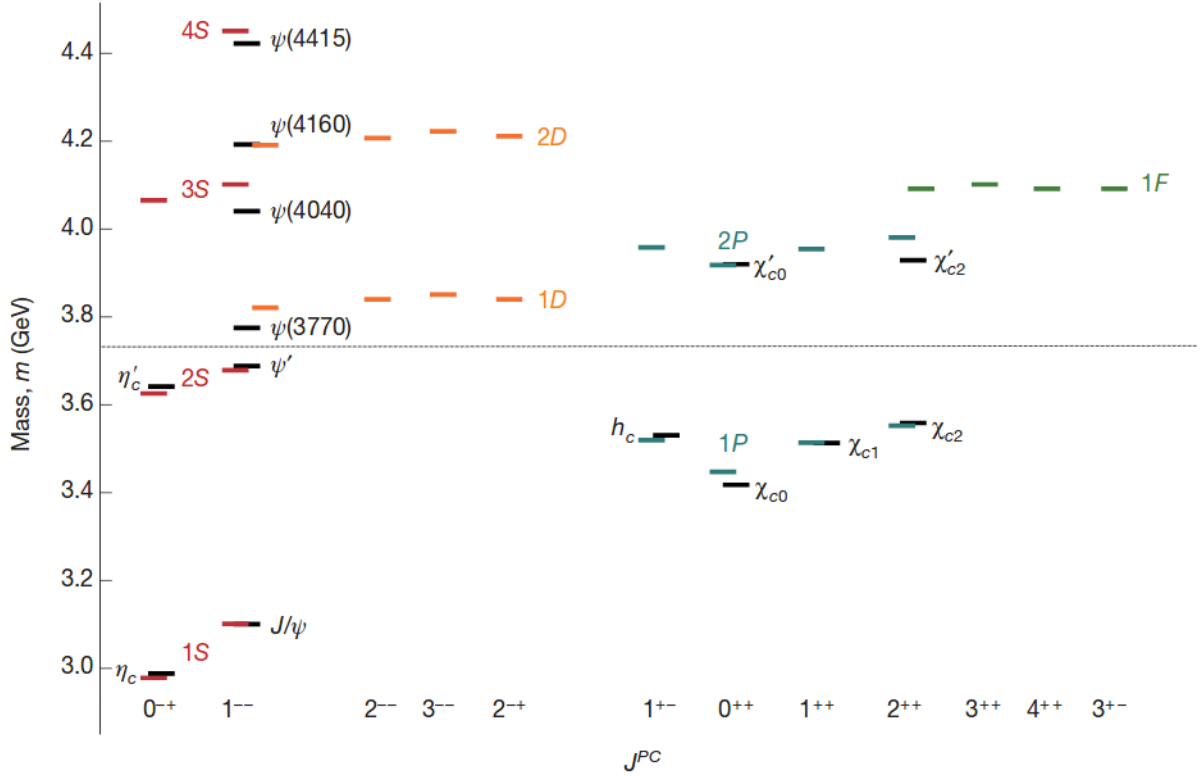


Figure 9: **Charmonium states** [106]. The spectrum highlights experimentally observed states in black and theoretically predicted ones in colours (distinguished by their angular momenta J^{PC}). The open charm threshold ($\bar{D}D$) is at about $3750 \text{ MeV}/c^2$ and sets a boundary between the upper and lower region, each with a different density. All eight states below the open charm threshold are experimentally well studied. The η_c denotes the ground state of charmonium.

Furthermore, the spectra of charmonium (below the open charm threshold) and positronium resemble each other. This promotes the assumption that the model of the strong interaction is similar to the electroweak theory which provides the subtle difference of a $1/r$ Coulomb-potential to replace the linear confinement part in the strong potential. This property of separated energy scales makes the $\bar{c}c$ -spectrum an ideal probe for confinement researches.

While the masses below the $\bar{D}D$ -threshold¹⁴ have been quite accurately measured, the region above is well unknown up to now, except of the ψ -states, especially $\psi(3770)$, which have already been observed by e^+e^- -colliders. Nevertheless, its excited states 4040, 4160 and 4415 require further investigation. h_c has also already been observed by E835 ($pp \rightarrow h_c \rightarrow J/\psi\pi^0$) and CLEO ($h_c \rightarrow \eta_c\gamma$) [12] but further observations have a very high priority because the data is inconsistent up to now.

Besides, former experiments studied the lower region only in large energy steps. In contrast to the states above the open charm threshold, strong decay modes are suppressed which result in long life times and very narrow

¹³ $\bar{c}c$

¹⁴D mesons contain exactly one charm quark as the heaviest one

widths. At the moment, the low-lying states are already well described theoretically but current models fail at higher levels. Being located below the open charm-threshold (e.g. the **D-mesons**, the so-called “*hydrogen-QCD analogue*”), they cause the charmonium region to be a vital opportunity for QCD-tests and the region above this threshold will extend the knowledge of the strong interaction in general.

4.1.2 Gluons

In the naive quark model, the nucleons are made up of three quarks and the mesons are built of a quark and an antiquark. These models do not display the real world but they have the merit of giving an image of it though neglecting the admixture of gluons as well as of sea quarks. However, reality is more complex, for example, such that the gluons, force carrier of the strong force, are in principle allowed to build up hadrons too.

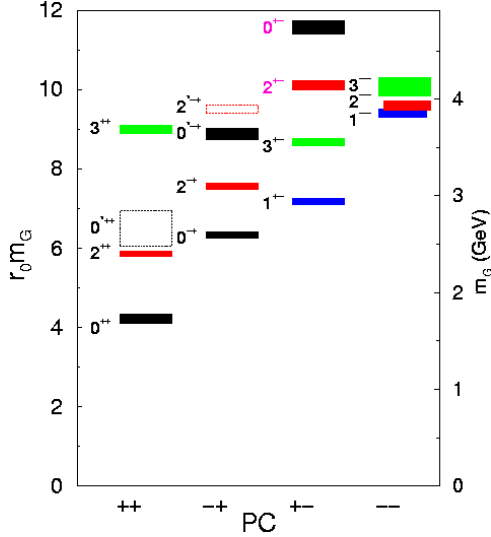


Figure 10: **Glueball spectrum** [30]. The colours indicate the spin quantum number. One of the most promising candidate is $f_0(1500)$, which has a flavor-blind decay width of $\Gamma = 110$ MeV.

Hybrids: Beside a quark and an antiquark, hybrids contain excited gluons too ($q\bar{q}g$).

Glueballs: Gluons are subject to their own force and confinement requires that particles must not exist which are not color-neutral. Thus, because gluons carry color charge, they should be able to create compounds which are colorless.

An important aspect of the research of gluonic matter is that glueballs and hybrids are allowed to have **exotic quantum numbers** (called “*oddballs*”), for example $J^{PC} = 0^{--}, 0^{+-}, \dots$. These states are promising opportunities to distinguish between pure quark-states and those with a gluonic part. Glueballs have characteristic decays such that the decay width is quite narrow and that they are flavor blind since valence quarks do not occur. Below $3.6 \text{ GeV}/c^2$, the dominant channels will likely be $\phi\phi$ and $\phi\eta$. The decays $J/\psi\phi$ and $J/\psi\eta$ are the best candidates to observe heavy glueballs [12]. The f_0 state at about $1500 \text{ MeV}/c^2$ represents the supposed glueball groundstate, while the lowest glueball with exotic quantum numbers (2^{++}) is assumed to be at about $2.4 \text{ GeV}/c^2$. In formation processes, $\bar{p}p$ hadronic systems only allow non-exotic quantum

numbers whereas in production processes even exotic quantum numbers can be generated, typically with a π or a η as a recoil particle. Experiments at LEAR hint that $\bar{p}p$ -reactions produce numerous particles with gluonic degrees of freedom in a direct way. The charmonium mass range provides a field where gluonic matter is expected to be less mixed with regular mesons since $\bar{c}c$ requires its quark content to annihilate with each other.

4.1.3 Hadrons in nuclear matter

The QCD expectation value of hadrons is assumed to be different in hadronic environment compared to vacuum. By transitioning, a **mass-shift** of hadrons can occur, in some cases larger than their natural width. However, Fermi motion will already cause broadenings up to 250 MeV which will make it rather difficult to measure modifications below 100 MeV. Mass shifts of states with a charm flavour can induce decays of neighbouring states and, therefore, facilitate mass changes to be observed. Hayashigaki supposed that the shifts of D and \bar{D} could decrease the $\bar{D}D$ -threshold enabling charmonium decays into $\bar{D}D$ [21].

The investigation of medium modifications can be bridged to the origin of masses in the context of spontaneous chiral symmetry breaking in QCD. In this context, the Goldstone theorem plays a major role by determining that, at any time a continuous symmetry is spontaneously broken, a massless scalar appears. This spontaneous breaking of the chiral symmetry is a good method to investigate the low-energy phenomena of the strong interaction and is well defined for the light quarks in the QCD.

Up to now, experiments have only studied the light quark region. Thanks to its high intensity \bar{p} -beam at the HESR, it will be possible to augment this section by the contribution of the charm region.

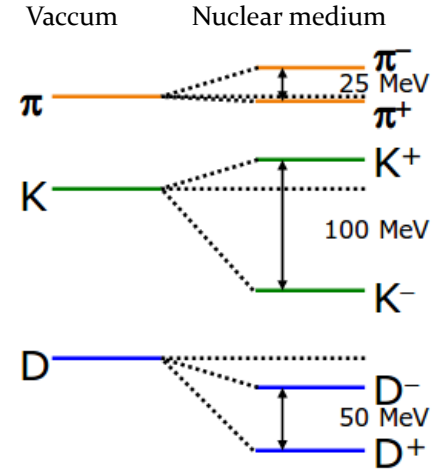
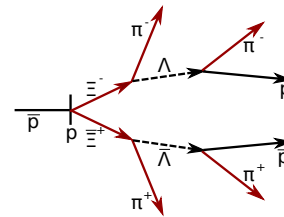
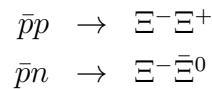


Figure 11: **Hadrons in nuclear matter** [74]. While hadron mass shifts in case of the non-charmed pseudoscalar and vector mesons will be studied at HADES and CBM, the mass shifts of charm mesons will be investigated at \bar{P} ANDA.

4.1.4 Hypernuclear physics

Nucleons are solely built of light quarks and are regularly only fragile towards the weak force which enables the generation of strong bonds among each other and results in a comparatively very long lifetime. On this basis, hypernuclei are nuclei with at least one nucleon being a hyperon Λ ¹⁵. Such nuclei have barely been sufficiently measured up to now. The investigation of hadrons including a **strange** part is essential to understand the low-energy regime of QCD due to the additional degree of freedom because it is yet unknown how the nuclear force emerges from QCD [80]. In comparison to hadrons without strangeness, hyperons are not limited in the population of nuclear states as they avoid Pauli blocking due to their quantum number strangeness. When a strange quark takes a light quark's place within a nucleus, the nuclear structure will change by producing a system of a hyperon together with the core of the remaining nucleons. Hypernuclei offer the possibility to study the structure of nuclei as well as its properties. With the help of a stored antiproton beam, Ξ -hyperons¹⁶ will be copiously produced in the \bar{P} ANDA-experiment via:



At first, the antiprotons will hit primary nuclear targets and then produce double hypernuclei in formation processes because secondary targets will catch the Ξ -particles. Among all hyperons, Λ are the only “convenient” systems to investigate the strong nuclear interaction. Λ are produced at a secondary target through

¹⁵Baryon with at least one strange quark but without a heavy quark

¹⁶Hyperons comprising two strange quark and one light quarks

e.g. $\Xi^- p \rightarrow \Lambda \Lambda$. This channel will likely decay into $p\pi^-$ and then finally emit γ . Therefore, **high-precision γ -spectroscopy** of double strange systems will be enabled by the Electromagnetic Calorimeter (see Electromagnetic Calorimeter on page 24).

4.2 $\bar{\text{P}}\text{ANDA}$ -Detector

As previously described in section 4.1, Physics at $\bar{\text{P}}\text{ANDA}$, the $\bar{\text{P}}\text{ANDA}$ -experiment is foreseen to perform high-precision tests of the hadron structure as well as of the nature of the strong interaction. The detector has to meet some demanding requirements[95][83]:

- The detection of low energy photons plays an important role (see Electromagnetic Calorimeter on page 24)
- A momentum resolution of 1 % to reconstruct invariant masses
- An excellent vertex resolution in the order of 100 μm is relevant to reconstruct open-charm states, e.g. D -mesons
- High interaction count rates up to 20 MHz have to be handled, connected with an efficient event selection
- Radiation tolerance is mandatory due to the presence of intense radiation fields
- Since $\bar{\text{P}}\text{ANDA}$ is a fixed target-experiment, it has to manage the detection of the resulting forward boost together with a 4π -scope for reactions with large opening angles due to their high transverse momenta like charmed hadron decays
- Studies of hidden-charm and of exotics require the reliable and simultaneous detection of dilepton pairs as well as a good kaon identification
- In case of e.g. hyperon studies, a good detection of antihyperons and low momentum K^+ in the forward region is mandatory together with a solid state tracker to track hyperons at large angles

The detector of the $\bar{\text{P}}\text{ANDA}$ -experiment will be placed within the HESR. It comprises an extensive symmetric **target spectrometer** and a large acceptance dipole spectrometer to cover the forward region. On basis of stochastic cooling, the HESR will ensure the beam quality and provide excellent parameters such as a high luminosity of $L = 10^{32} \text{ cm}^{-2}\text{s}^{-1}$ at a maximum momentum spread of $\delta p/p = 10^{-4}$. In case of high-precision spectroscopy, electron cooling will enable a high resolution mode for momenta up to 8 GeV/ c at a momentum spread of $\delta p/p = 10^{-5}$.

However, the required precision of the measurement of resonance masses and widths depends on the precision of the beam energy, respectively, the resolution of the line shape depends on the phase space cooled momentum distribution and not on the detector resolution. Therefore, an excellent resonance mass resolution of 30 keV is feasible. A telling example to show the capability of $\bar{\text{P}}\text{ANDA}$ is the measurement of X(3872) which has already been confirmed by BELLE and several other experiments. Its natural width is less than 1.2 MeV and simulations predict for $\bar{\text{P}}\text{ANDA}$ a Breit-Wigner response of 100 keV at a precision of 20 % [83]. And in case of Y(3940) $\bar{\text{P}}\text{ANDA}$ is expected to observe thousands events per day, whereas e.g. BELLE and BaBar needed several years for a lower statistic [161].

Since $\bar{\text{P}}\text{ANDA}$ is designed as a beam-target experiment (see fig. 12), many particles will go into the forward direction. Therefore, the Forward Spectrometer contains a dipole magnet that bends the antiproton beam to allow a positioning of the subdetectors in a 0° -direction. Overall, the forward angles will be covered by Drift Chambers located in both Spectrometers. Additionally, this will be supported by a DIRC¹⁷ in the Target Spectrometer together with a muon detector.

¹⁷Detection of Internally Reflected Cherenkov Light

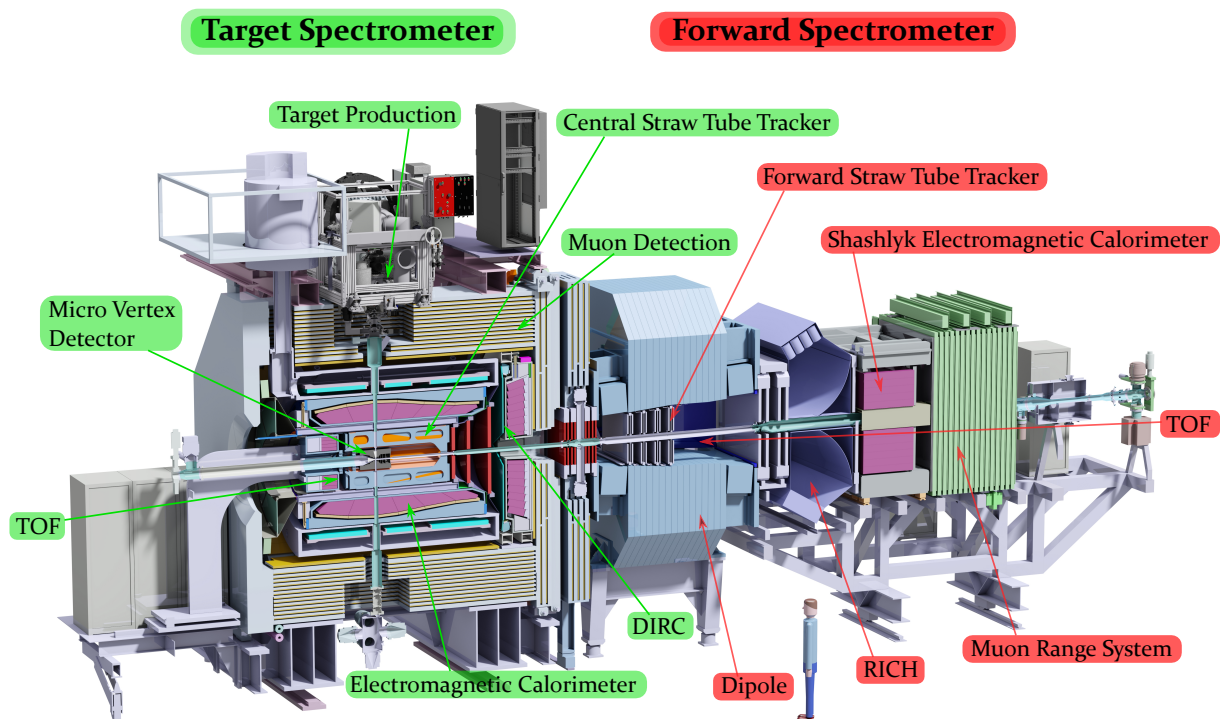


Figure 12: *PANDA-Detector* [65]. The envisaged physics program requires a 4π coverage of the solid angle together with a good particle identification. Hence, a high angular and energy resolution for photons and charged particles is mandatory. The detector contains two spectrometers: The Target Spectrometer which covers the interaction point and the Forward Spectrometer that analyzes the momentum of the forward-going particles. Both contain several subdetectors with arrangements that follow the onion principle.

In the following, the subdetectors of the Target Spectrometer will be explained in detail.

Target Spectrometer

The innermost detector is the Micro Vertex Detector which is of great importance in reconstructing vertices and providing tracking and momentum information together with the Straw Tube Tracker and the Gas Electron Multiplier Detector. The DIRC detector provides particle identification and the Electromagnetic Calorimeter delivers energy information. The complete Target Spectrometer is surrounded by a solenoid magnet and perpendicular to each other, both the beam pipe and the target pipe cross all subdetectors.

The Target Spectrometer covers the interaction point and provides a 4π **acceptance**. Thus, it is particularly designed for the detection of **transverse reaction processes**. It contains a superconducting solenoid magnet with a field homogeneity of better than 2% to measure high transverse momentum tracks of charged particles. Overall, the Target Spectrometer is designed modularly to ensure different setup possibilities without the need of a full assembly. Moreover, the detector will be arranged in three sections:

- the forward part covers vertical angles down to 5° and horizontal angles down to 10° ,
- the barrel part spans the angles between 22° and 140° and
- the backward part detects signals between 145° and 170° .

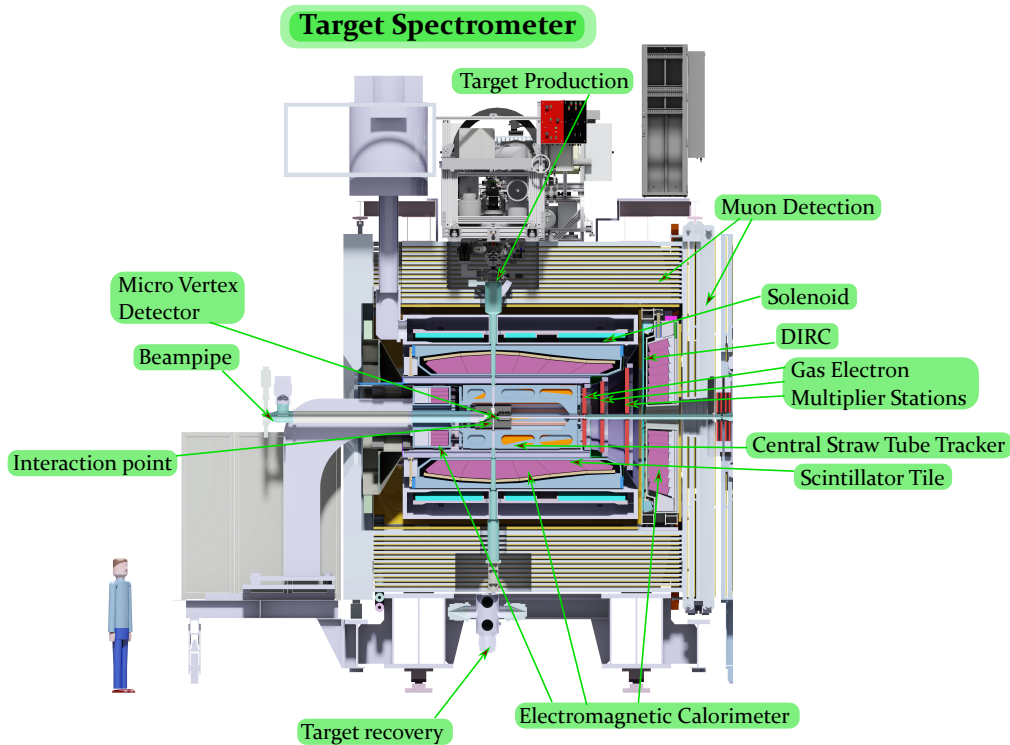


Figure 13: *Target Spectrometer* [65]. The Target Spectrometer is constructed according to the onion-shell principle.

Through injection pipes, the target material will cross the beam pipe. Radiant from the interaction point, the subdetectors are arranged from the inside to the outside as follows:

4.2.1 Target

The internal target concept of \bar{P} ANDA pursues two different drafts: **Frozen pellet targets** and **cluster-jet targets**. The requirements of the targets are on the one hand to provide a pure material with as few as possible admixtures and on the other hand to provide an areal target density below $\rho = 10^{16}$ nucleons/cm⁻² [34]. The first is able to reduce background signals, the latter is important to avoid multi-scattering and beam heating. Nonetheless, the target must be thick enough to provide the foreseen high luminosity of $L = 10^{32}$ cm⁻²s⁻¹. Therefore, a thickness of about $1 \cdot 10^{15}$ atoms/cm² is required for 10^{11} stored antiprotons in the HESR. The two major concepts are:

Cluster-jets: A gas is injected through a nozzle into vacuum and, while passing, the gas cools down to form a supersonic beam. At certain conditions, condensation can occur to convert the gas into nano-particles of which the cluster-jets are made up with up to 10^{15} atoms/cm². The advantages of a cluster beam are its homogeneous volume density together with a sharp boundary and a constant angular divergence. This results in a time-independent beam-target injection. Hence, the parameters like the cluster-jet thickness can be easily modified during operation. The substance will be mostly Hydrogen but it can be replaced by Deuterium, Nitrogen, Neon and other even heavier gases.

Pellet-targets are composed of frozen Hydrogen microspheres which pass the beam pipe as a stream of about 10,000 pellets/s at 70 m/s. Their size depends on the injection nozzle but is between 20 μ m and 40 μ m. The stream has a position uncertainty of ± 1 mm at a diameter of 3 mm, corresponding to 10^{15} atoms/cm².

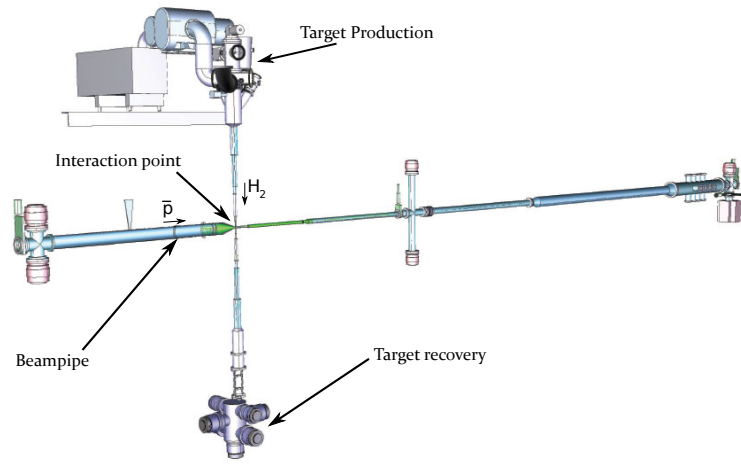


Figure 14: **Target system** [62]. Two different main systems will be used for distinct applications: The cluster-jet target and the pellet-beam target. Their applications depend on specific conditions. On the one hand the cluster target which is designed for a high precision, whereas, on the other hand, the pellet target will be used to provide a high luminosity. The targets will traverse the beam laterally through a pipe.

Due to a lack of momentum in beam direction, the targets can be regarded as fixed. Compared to each other, the pellet targets have a higher maximum density and a better point-like interaction zone. In contrast, the cluster target provides an adjustable and homogenous target density plus a better time structure. In the end, it depends on the specific experiment which target is more suitable. For a

- high luminosity up to $L = 10^{32} \frac{1}{\text{cm}^2\text{s}}$ and $\frac{\Delta p}{p} = 10^{-4}$ with $10^{11} \bar{p}$, it is the pellet target and for a
- high precision with $L = 10^{31} \frac{1}{\text{cm}^2\text{s}}$ and $\frac{\Delta p}{p} = 10^{-5}$ with $10^{10} \bar{p}$, it is the cluster target.

Both concepts share the same devices. Target material that did not interact with the beam will be recovered by the target beam dump.

4.2.2 Micro Vertex Detector

The MVD¹⁸ is designed to track charged particles and delivers **track** and **time information**. A minimum of at least four track points is necessary to reconstruct a particle's trajectory [142]. On this basis, it will strongly improve the transverse momentum resolution. Hence, to meet all the requirements of the according physics tasks, it will be capable of reconstructing displaced vertices. It is the very first detector around the interaction point due to its purpose to resolve primary interaction vertices on the one hand and secondary vertices of short-lived particles such as D-mesons and hyperons on the other hand, plus to provide a maximum acceptance close to the interaction point. The MVD has a length of 40 cm and a radius of 15 cm [33].

The vertex reconstruction will have a **spatial resolution of $< 100 \mu\text{m}$** and a **time resolution of $\leq 6.43 \text{ ns}$** . Mainly, the detector consists of two different parts: Four barrels of silicon detectors, of which two layers are radiation hard hybrid silicon pixel detectors and two layers are double-sided silicon strip sensors as well as six forward disks made of a mixture of the former ones. The spatial resolution is given by the pitch¹⁹, which is, e.g. $45 \mu\text{m}$ for the barrel layout and $70 \mu\text{m}$ for the disk layout. Ideally, the Micro Vertex Detector influences traversing particles as little as possible to leave the particles unaffected for the subsequent detectors. Right after the Micro Vertex Detector, further tracking information will be gathered by straw tubes or by the time projection chamber.

¹⁸Micro Vertex Detector

¹⁹Gap between strips

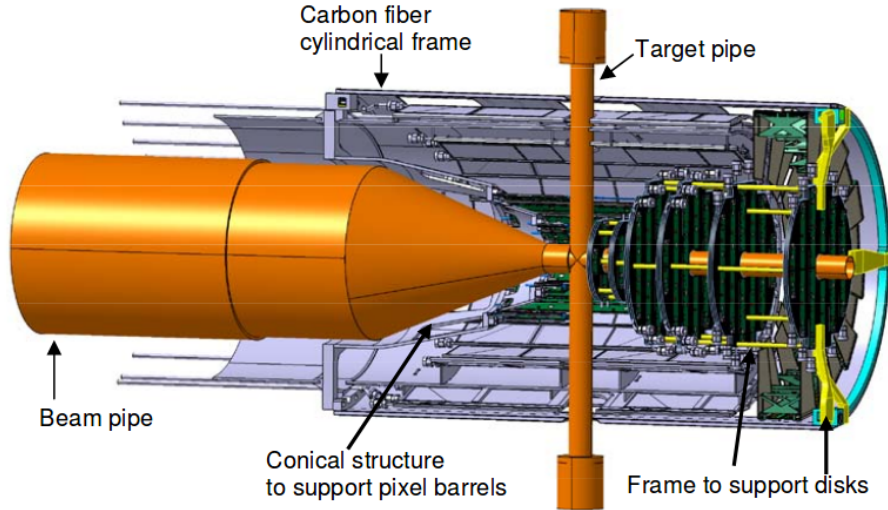


Figure 15: *Micro Vertex Detector* [22]. The Micro Vertex Detector is responsible to provide tracking and time information of charged particles. Furthermore, it has to detect primary and secondary vertices. Therefore, it comprises several layers of hybrid silicon pixel detectors and double-sided silicon strip detectors to cover a polar angle of 3° up to 150° . Additionally, six discs will be installed in the forward direction of which four are hybrid silicon pixel detectors and two are a mixture of a pixel and a double-sided strip detector.

4.2.3 Central Straw Tube Tracker

Besides the Micro Vertex Detector, the Central Straw Tube Tracker is another device to **track charged particles**. Hence, it will also measure particle energy losses with a resolution of $\sigma_E \leq 10\%$ for momenta up to $1 \text{ GeV}/c$ [66]. $\bar{\text{P}}\text{ANDA}$ provides two of such tube trackers. The one in the Target Spectrometer will be installed around the Micro Vertex Detector and will consist of 4636 self-supporting straw tube modules. These straw tubes are about 1 cm in diameter each and operated at over-pressure. Furthermore, the tubes will be glued together to form planar multi-layers. Then, these layers will form a hexagonal layout within the cylindrical volume. The tubes are skewed with respect to the beam axis enabling a position resolution of 2.9 mm in beam direction.

The cathode is made of an aluminized mylar film with a thickness of $27 \mu\text{m}$, whereas the anode is a gold-plated tungsten-rhenium wire of $20 \mu\text{m}$ diameter. Argon will be used together with 10 % CO_2 as quencher because of its good behaviour in high-rate hadronic environments since it does not react with the installed components. In consequence of the presence of the beam pipe, the detector is divided into two halves. Finally, the **transverse momentum resolution** will be about 1.2 % and a spatial resolution of $\leq 100 \mu\text{m}$ is expected [137].

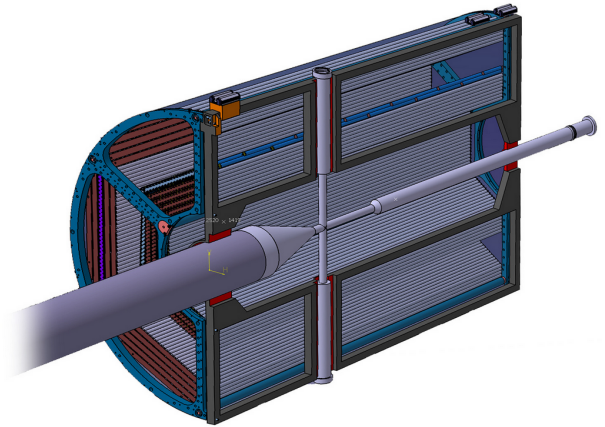


Figure 16: *Straw Tube Tracker* [63]. The Central Straw Tube Tracker detects charged particles outside the Micro Vertex Detector. It consists of 4636 straw tubes which act like a gaseous ionisation chamber. The tubes are arranged hexagonally around the Micro Vertex Detector.

4.2.4 Time-Of-Flight Detector

The main purpose of the TOF-detector is to measure the particles' velocity to discriminate different particles by their according **masses**. The detector itself will be a scintillating tile hodoscope containing 1920 small scin-

tillating tiles read out by 15360 Silicon Photomultipliers. The Barrel TOF will comprise 16 segments and, in turn, each segment will contain 120 scintillating tiles. A scintillator will be read out on two sides by four SiPMs connected in series [93]. The time is determined when particles propagate through a very fast organic scintillator. The time of flight, respectively the collision time t_0 , will be reconstructed by using track and velocity information of other subdetectors resulting in a resolution of about 55 ps, while t_0 will have a resolution of 2.3 ns. A time resolution of better than 100 ps is required together with an acceptance angle from 22° up to 140° .

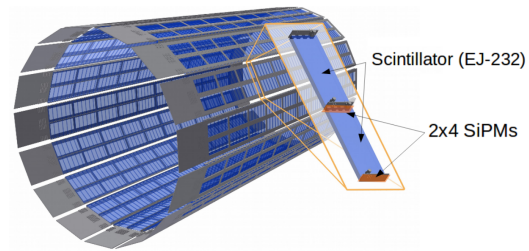


Figure 17: *Time-of-Flight detector* [94]. The collision time t_0 of the particle is recalculated via track and velocity information from other subdetectors. The time itself is measured when a particle traverses one of the 1920 scintillators which are read out by eight SiPMs each.

4.2.5 DIRC

The task of the DIRC²⁰-detector is to **identify** particles via Cherenkov radiation. Charged particles propagating through a medium with $\beta > 1/n$ will emit Cherenkov radiation at an angle of $\Theta_C = \arccos(1/\beta n)$. The detector comprises two parts, both housed within the Target Spectrometer: A barrel shaped detector to cover light at a polar angle between 22° and 140° and a planar end cap detector in forward direction for a polar angle down

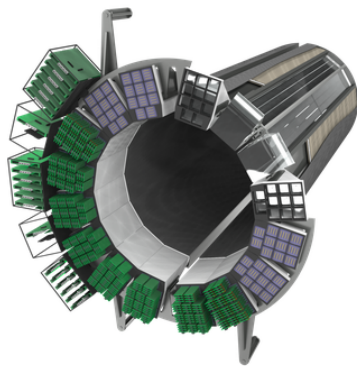


Figure 18: *DIRC Detector*. The DIRC detector uses time-of-propagation to extract the angular information of the Cherenkov photons traversing the radiator. It comprises 200 synthetic fused silica radiators with a thickness of 1.7 cm [64].

to 5° . It is necessary to design the DIRC-detector as thin as possible since it will be placed in front of the Electromagnetic Calorimeter. The barrel part contains 200 radiators with a thickness of 1.7 cm which are aligned in beam direction at a radius of 48 cm. These radiators are made of synthetic fused silica with a refraction index of $n = 1.47$ and guide the Cherenkov photons lengthways to a regular aerogel ring imaging cherenkov counter-system via internal total reflections. Particles at about $\beta \approx 1$ within such a radiator with $n = \sqrt{2}$ might always be reflected in total internally. Finally, the photons exit the radiator through focusing elements into an expansion volume which has a different refraction index. This causes a widening of the initial angle. There, the photons will be gathered by a photon detector array of micro-channel-photomultipliers which are usable within the magnetic field [137].

²⁰Detection of Internally Reflected Cherenkov Light

With the help of the hit position on the photon detectors, their initial direction can be calculated. The angle of the Cherenkov photons is determined via a comparison of the track of the detected photon and the direction of the particle's track from another detector. The larger the propagation time of the particles the larger the difference between photons generated by pions and kaons [108]. The concept design is close to the DIRC-detector of BaBar but provides some improvements like a more compact geometry, a focusing system and a fast photon timing. The DIRC will have a time resolution of about 100 ps [100].

4.2.6 Electromagnetic Calorimeter

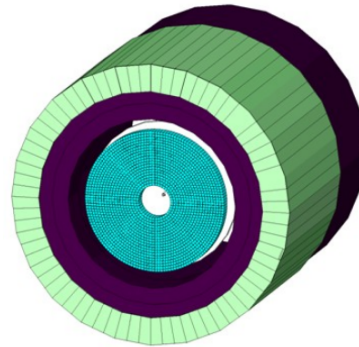
The Electromagnetic calorimeter is described in detail in section 5, Electromagnetic Calorimeter.

4.2.7 Muon Detection

The muon tracker will be the most outward detector and it will comprise an inner barrel with four planes and an outer barrel with six planes wrapped around the iron yoke. Each plane will consist of 3 cm thick layers of iron interleaved with MDTs²¹.

Therefore, the yoke of the Target Spectrometer is segmented in thirteen layers in total. All together, the muon system will be made up of 3751 MDTs [19]. A MDT is built up of eight anode wires while the cathode is made of an aluminum comb-like profile. The signals will be read out by external strip electrodes [82]. Absorbed muons are an important probe for e.g. J/ψ -decays and D-mesons. The muon system aims at identifying **primary muons** as well as those from the background. Therefore, the muon detection has to fulfill an important and complicated task. The spatial accuracy will be about 0.5 mm and a longitudinal accuracy of better than 200 μm .

Figure 19: *The Muon Tracker* [44]. The Muon detection is based on a segmentation of the iron yoke and contains thirteen layers interleaved with MDTs. Plastic scintillators behind the iron yoke will cover a polar angle in the lab system from 60° down to the dipole's opening angle. Muons at larger angles will be stopped by the iron yoke.



4.2.8 Tracking and Particle Identification

All information of the subdetectors have to be gathered to extract physics signatures for analysis purposes. This is not possible in a single process and, therefore, it is necessary to merge several signal inputs together to form a whole entity.

Thus, the previously described subdetectors can be grouped into four main categories:

- the Target system: Pellet beam target, cluster beam target or nuclear target
- the Tracking System: Micro Vertex Detector, Central Tracking Detector and Forward Mini Drift Chamber Stations
- the Electromagnetic Calorimeter and
- the Particle Identification: DIRC-detector, TOF-detector and the Muon Chamber

²¹Mini Drift Tubes

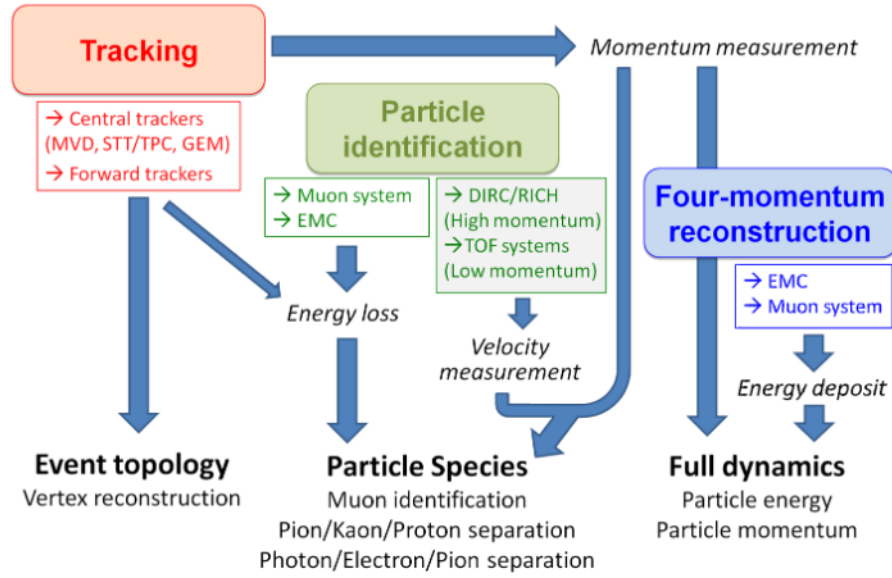
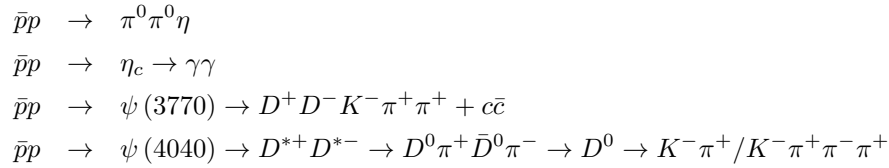


Figure 20: *Tracking & particle identification* [45]. The information of the particles can be addressed to various domains each of which is covered by a specific subdetector: Tracking aims at gathering the momentum and is done by the Micro Vertex Detector, Central Tracking Detector and Forward Mini Drift Chamber Stations. Particle identification is settled mainly by the DIRC detector, TOF detector and the Muon Chamber but also with small contributions from the Straw Tube Tracker. The Electromagnetic Calorimeter delivers crucial energy information.

Overall, the $\bar{\text{P}}\text{ANDA}$ -detector requires a high **momentum resolution** as well as a high **dynamic range** for γ -detection plus a very good **particle identification** from electrons over pions up to protons since pions are often more abundant than kaons. Some benchmark channels highlight the importance of a good π/K separation as well as the need for an excellent γ -detection since even a single γ can represent another reaction process [32], [100]:



$\bar{\text{P}}\text{ANDA}$ requires a separation of 3σ to separate π from K in the momentum range from $0.5\text{ GeV}/c$ up to $3.5\text{ GeV}/c$. Moreover, an identification of particles is generally needed for momenta up to $12\text{ GeV}/c$. The efficiency of the DIRC detector to separate pions from kaons is almost 100% [138].

Furthermore, pions will be the most dominant background channel and thus, a $e^{+/-}/\pi^{+/-}$ discrimination is crucial and, among others, done by the TOF-detector. The TOF can only measure relative times of flight between charged particles compared to each other since it consists of only a single depletion layer that is not located near the interaction point. There, the Micro Vertex Detector will play the role to determine vertices of very short-lived particles like D-mesons with a position resolution of less than $100\ \mu\text{m}$. In addition, the Straw Tube Tracker provides a position tracking resolution of less than $150\ \mu\text{m}$ and a momentum resolution of about 2%.

The DIRC-detector identifies particles with momenta $> 1\text{ GeV}/c$. Together with the velocity information derived from the Cherenkov angle Θ_c , the mass of detected slower particles can be determined. On the basis of this, likelihoods for e , μ , π , K and p are feasible.

The energy of the particles will be determined by the Electromagnetic Calorimeter with a resolution of about 2%. The mainly produced particles decay into $\gamma\gamma$, forcing the need of a detection of the γ 's as best as possible. The muon identification will be done primarily by the muon tracker but the Electromagnetic Calorimeter, the TOF-detector and the DIRC-detector can also improve the identification. Nevertheless, the muon system will enable information of the total path of the muons traversing the absorbers plus their according energy losses. Muons with energies below < 1 GeV will not reach the tracker and have to be covered by the DIRC and Electromagnetic Calorimeter.

5 Electromagnetic Calorimeter

Calorimetry is the detection of particles within a given material through total absorption. The benefit of such devices is to obtain **energy information**. A major aspect in designing detectors which contain a calorimeter is that, typically, these subdetectors absorb respectively dissipate all the particles to be measured - except of the muons. Since the particles will not be available anymore for further investigation done by other subdetectors, a calorimeter is usually placed at or close to the end of the subdetector chain (see Target Spectrometer on page 18).

The PANDA Electromagnetic Calorimeter, for example, is made out of (inorganic) **semiconductor crystals** which offer very good properties in gaining time and energy information. Their detection principle is based on electromagnetic showers (see Electromagnetic shower on page 30) which are generated when incident particles interact with the detector material.

The performance of an electromagnetic calorimeter is given through several aspects: The most important one is the so-called **calorimeter response** which describes “*the average calorimeter signal divided by the energy of the particle that caused it*” [131]. An electromagnetic calorimeter should have a constant response for a given particle energy and the global response should be a **linear** function of energy. An additional significant aspect is the energy resolution, quantifying the precision of measuring the deposited energy.

Though a linear response is an absolute necessity, the **energy resolution** is the most discussed facet. It is influenced by fluctuations of the energy deposition within the detector material and by the specific utilized read out devices. These factors can be expressed in a parameterized equation:

$$\frac{\sigma_E}{E} = \frac{a}{\sqrt{E}} \oplus \frac{b}{E} \oplus c \quad (1.3)$$

It includes several aspects which behave uncorrelated and thus, they affect the energy resolution $\frac{\sigma_E}{E}$. The coefficient a represents the fluctuations which are stochastic and almost unavoidable. Cardinally, fluctuations in signal productions caused by particles are assumed to follow a Poissonian behaviour. The coefficient b describes fluctuations, for example, generated by electronic noise and pile-up which are energy independent. c contains non-uniformities, for example, caused by the light propagation inside the crystal, imperfections due to the manufacturing processes, inter-calibration errors or shower leakages such as lateral and longitudinal energy losses. The latter coefficient c is the most dominant term. Overall, the formula describes the fact that the energy resolution improves with the energy due to a better statistic since more deposited energy generates more photoelectrons in the readout device. Further calorimeter aspects are the time and position resolution as well as the ability to discriminate particles from each other.

In homogenous calorimeters such as the PANDA Electromagnetic Calorimeter, the detector material is at the same time the **absorber** and **detector**. Various materials possess different dominant signal production mechanisms, for example, in case of BGO, BaF₂ and PbWO₄, the signal is produced mainly by scintillation while lead glass makes use of Cherenkov light and detectors operating with noble gases are based on ionization processes.

5.1 Interactions of radiation with matter

Particles can only be measured when they **interact** with the material of the detector. This requires a long enough lifetime but the majority of the particles of interest is short-lived. Hence, the ECAL will only be able to measure the final products and, with the help of the other subdetectors, the initial particles can be recon-

structured. In general, radiation interacts with matter in a wide scope and, in case of calorimeters, the information sought is their deposition of energy dE/dx . To determine a particle's energy, the kind of material (atomic number, thickness,..) the particle interacts with plays an important role. Hence, the possible processes can be separated into interactions of photons on the one hand and into interactions of charged particles on the other hand. One main difference is the absorption which results almost in a local drop in intensity in case of charged particles and in an exponential decrease in case of photons.

All these processes result in an energy loss along the particle's trajectory and are always connected to an **ionization** or **excitation** of the absorber material. The target particles can be almost considered at rest and the radiation processes as a two-body scattering. Then, the possible maximum energy transfer W will occur in head-on collisions and is found by $W_{\max} = (p^2 c^2) / (\frac{1}{2} m_e c^2 + \frac{1}{2} ((m/m_e) c^2 + \sqrt{p^2 c^2 + m^2 c^4}))$, under the assumption that the target particle is an electron. When the incident particles are massive like p , K , π and in a high relativistic region, the maximum energy transfer simplifies to $W_{\max} \approx pc \approx E_i$ [29].

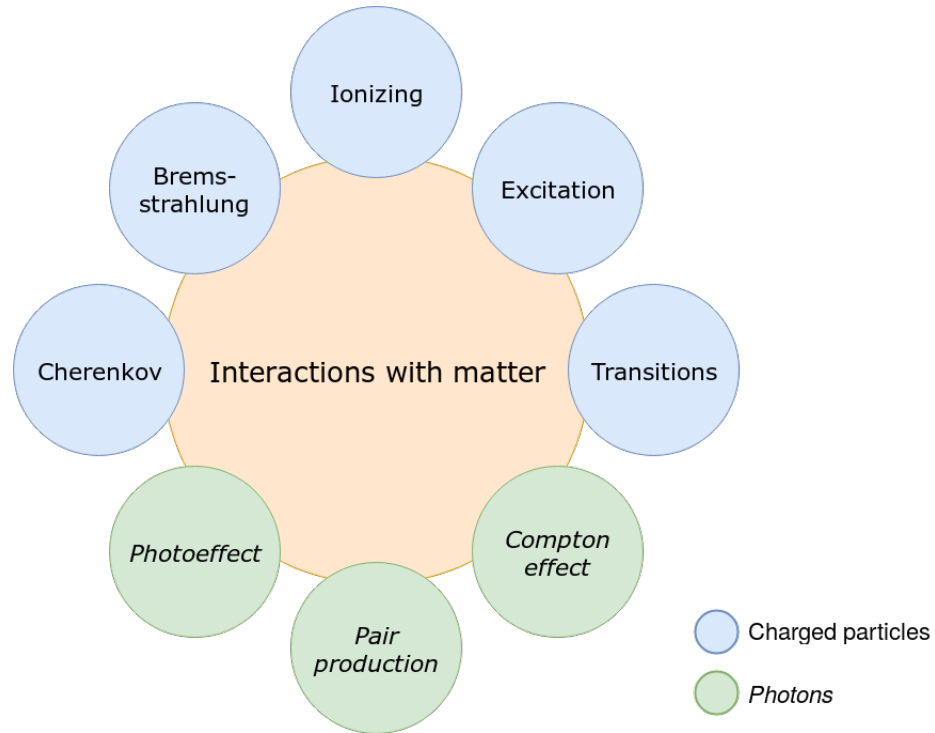


Figure 21: **Overview of interaction processes of particles with matter.** The possible interaction processes can be subdivided into those involving photons and into those involving charged particles. In case of photons, the energy is deposited completely in a single process except in case of the Compton effect. In contrast, the energy of charged particles decreases continuously along the trajectory. Charged particles interact mostly via ionization processes and, with respect to their mass, also via radiation emissions. As a thumb of rule, measuring charged particles is often less difficult than measuring photons.

An electromagnetic calorimeter can only detect particles which interact electromagnetically. Photon interactions can take place via the **Photoelectric Effect**, **Compton scattering** and **Pair Production** while charged particles interact mostly via ionization processes and radiation emissions. In the following, the interactions which are likely to occur within an electromagnetic calorimeter, will be described through some terms: The mass attenuation coefficient μ/ρ , the cross section σ and the ionization density dE/dx .

The attenuation of a photon beam behaves exponentially as $I(x) = I_0 \exp(-\mu x)$, where μ is the absorption coefficient, also called linear attenuation coefficient. It represents the fraction $\mu = N\sigma_{tot}$ of N absorbed photons per cm within the material.

The mass attenuation coefficient μ/ρ is a normalization of the linear attenuation coefficient μ per unit density ρ . It takes into account different magnitudes of absorption of different materials ρ . In return, the mass attenuation coefficient μ/ρ is similar to the cross section σ which uses the effective area per unit mass instead of particle numbers. The cross section is the probability of an interaction process: $dN/dx = -Nn\sigma$, where N is the number of particles, n the number of target scatterers and σ the **cross section**. It is connected with the scattering length $\lambda = 1/(n\sigma)$ for a certain cross section.

To consider all possible final states, the total cross section can be defined but, commonly, the differential cross section $d\sigma/d\Omega$ is used because it considers the dependency of the scattering angle θ with respect to the possibility to detect the particle within a given area.

5.1.1 Photon interactions

5.1.1.1 The photoelectric effect eliminates the incident particle and **transfers** all its energy E_γ to the atom, $E_T = E_\gamma$. The photon will wrest an (photo-)electron from an atom only if its energy exceeds the **binding energy** I of the electron $I \approx Z^2 \cdot 13.6 \text{ eV}$ (with Z as the atomic number). Secondary effects like characteristic X-rays and Auger electrons can happen. The cross section τ_K of the photoelectric effect can be described as

$$\tau_K = \frac{8}{3} \pi r_e^2 4\sqrt{2} \frac{Z^5}{137^4} \left(\frac{mc^2}{h\nu} \right)^{7/2} \quad (1.4)$$

with r_e representing the classical electron radius

by using the born approximation²² [29]. Through a more handy expression it can be simplified to $\tau = \frac{Z^n}{E_\gamma^m}$ with $n = 4$ and $m = 3$ for the K-shell and applied in an energy region of $E \approx 100 \text{ keV}$. K-shell electrons are the most tightly bound electrons, thus being the most important contribution to the cross section of the photoelectric effect since the K-edge absorption probability prevails other shells when the photon energy exceeds the K-electron's binding energy.

5.1.1.2 Compton effect describes the increase of the wavelength ($\lambda_0 \rightarrow \lambda$) of a photon due to **scattering** at an electron under the angle ϑ . Contrary to the photoelectric effect, the photon **is not absorbed** by the electron in this process. Instead, it is deflected because the Compton effect is not an elastic scattering but an elastic collision process. The energies of the scattered photon E_γ and of the electron E_e read

$$E_\gamma = \frac{h\nu_0}{1 + (h\nu_0/mc^2)(1 - \cos\theta)} \quad E_e = m_e c^2 \frac{2(h\nu_0)^2 \cos^2 \phi}{(h\nu_0 + m_e c^2)^2 - (h\nu_0)^2 \cos^2 \phi} \quad (1.5)$$

with $h\nu_0$ as the energy of the incident photon and $h\nu$ as energy of the scattered photon

At a collision angle of 180° , the Compton-edge, the energy transfer between photon and electron is maximum. There, the scattered photon remains with $E_\gamma = \frac{1}{2} m_e c^2$. The cross section σ of the Compton Effect is obtained by the Klein-Nishina formula which is based on Dirac's relativistic theory. The total cross section is given by

$$\sigma_C = \pi r_e^2 \frac{2 \ln(2(h\nu/m_e c^2) + 1)}{h\nu/m_e c^2} \quad (1.6)$$

in case of unpolarized radiation and when the reduced photon energy $h\nu/m_e c^2 \gg 1$ can be applied. This is a good approximation for photons with an energy of $E_\gamma > 1 \text{ MeV}$ and a material with a low Z . Equation eq. (1.6) already takes into account binding corrections but is not complete. An extensive description can be found in [79][29]. The **Klein-Nishina formula** shows a decreasing cross section when the photon energy increases.

²²The Born approximation is the first term in the Born expansion and takes into account only the incident particle's field, e.g. neglects induced emissions. This is a valid assumption when $\frac{2\pi Z e^2}{\hbar \zeta} \ll 1$, where $\zeta = \{v, v_0\}$ with v being the electron velocity after and v_0 before photon emission

The low-energy limit of Compton scattering is known as Thomson scattering and can be applied as long as the photon energy is much less than the electron energy: $h\nu \ll m_e c^2$. Its cross section is given by $\frac{d\sigma}{d\Omega} = r_e^2 (1 + \cos^2 \varphi) / 2$ [51] and together with the resonant and the Rayleigh-scattering it is one of the elastic scattering processes. These three processes occur when radiation perturbrates electrons at $\omega_0 = 2\pi\nu_0$ and differ in principle only in the compelled oscillator frequency: $\omega \gg \omega_0$: Thomson scattering, $\omega \simeq \omega_0$: resonant scattering, $\omega \ll \omega_0$: Rayleigh scattering.

5.1.1.3 Pair production is the most important interaction to an electromagnetic calorimeter due to its dominance at energies of $E_\gamma > 10$ MeV. Pair production **converts** a photon in the Coulomb field of a nucleus into an electron-positron pair above an energy threshold $E \geq 2m_e c^2 + 2\frac{m_e^2 c^2}{m_{nucleus}}$. The created particles will produce **Bremsstrahlung** as well as they will cause ionizations along their paths. In contrast to the electron, which is rather fast absorbed by an ion, the positron **annihilates** with an electron. Afterwards, two photons sharing twice the electron's rest mass will be produced. By taking into account screening effects [29], the cross section κ is

$$\kappa = \alpha Z^2 r_e^2 \left[\frac{28}{9} \ln \left(183 Z^{-1/3} \right) - \frac{2}{27} \right] \quad (1.7)$$

$$\text{with } \alpha = e^2 / (\hbar c)$$

For different energy regions the equation above can be split into simplified expressions as follows:

low photon energy	high photon energy
$\kappa \sim \ln(h\nu)$	$\kappa \sim \frac{7}{9} (A/X_0 N_A)$

In case of photons with an initial energy of $E_\gamma = 1$ GeV and Pb as target material, the difference between both approximations is about 7% [79][11]. The cross section increases with the particle's energy and is connected to the radiation length X_0 (see **Charged particle interactions** on the following page) [131]. The probability that a photon undergoes a conversion within one radiation length is given by $P \approx \sigma_{Pair} \left(\frac{\rho N_A}{A} \right) X_0 \approx 7/9$.

Each process has a separate contribution to the mass attenuation coefficient μ/ρ . Therefore, the **cross section** of attenuation of a photon beam can be written as

$$\sigma = \tau + \sigma_C + \kappa \quad (1.8)$$

photonuclear reactions like Rayleigh scattering are neglected due to the negligible energy transfer

Finally, it has to be noted that the cross sections of the interactions between photons and matter are much smaller than those of charged particles and matter. Therefore, for example, X-rays and γ -rays are more penetrating than charged particles. The separate cross sections are:

Process	Order	Incident photon energy
Photoelectric effect	$\tau \propto Z^4 / E^3$	≤ 1 MeV
Compton effect	$\sigma_C \propto Z / E$	$1 \text{ MeV} \leq E_\gamma \leq 10$ MeV
Pair production	$\kappa \propto Z^2 \ln(E)$	≥ 10 MeV

Table 2: **Comparison of interaction processes of light with matter** The dependency in E_γ and Z reveals the situation that it is, e.g., easier to cover against 10 – 20 MeV photons than against 3 MeV.

Even though the dependency of a cross section is always given in Z , the interactions also depend on the electron density ($\sim Z$) which is not strongly related to the atomic number Z of the medium since an increasing amount of electrons can cause a lower electron density due to Coulomb repulsion.

Furthermore, though the cross sections of the different mechanisms are energy dependent, they do not reveal how much energy will be transferred. While the Compton effect transfers only a fraction of the photon's energy according to $E_T = E_\gamma / (1 + (E/m_e c^2 (1 - \cos \theta)))$, the photopeak results in a complete transfer of the energy $E_T = E_\gamma$. In fig. 22 is the mass attenuation and the photon cross sections for the according interaction processes given:

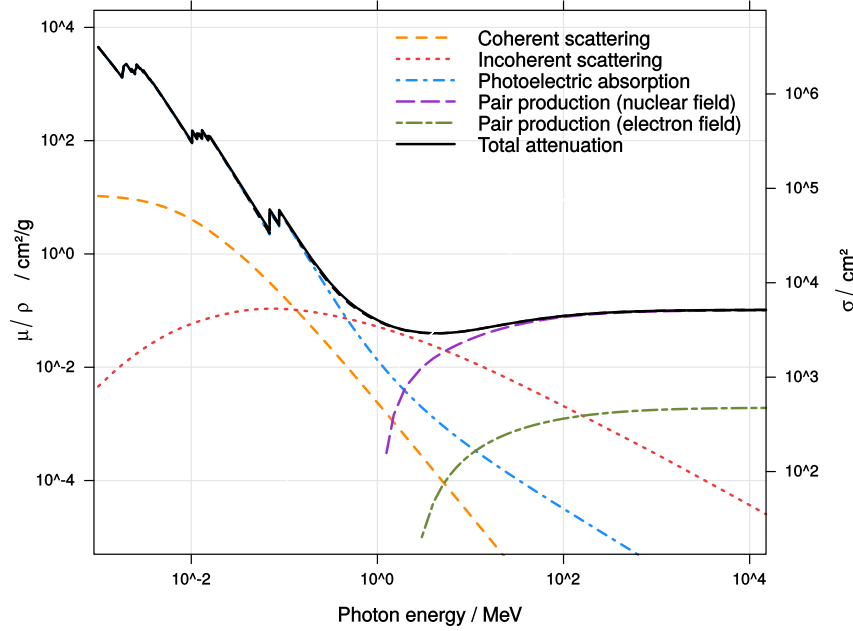


Figure 22: **Mass attenuation and photon cross section of $PbWO_4$.** The photon interactions at lead tungstate represent very well their general energy dependence: The photoelectric effect is dominant at energies up to about 0.5 MeV while scattering processes prevail within a rather small energy region from 0.5 – 6 MeV and from there on pair production is the most major interaction. The mass attenuation of $PbWO_4$ [111] is converted into the cross section via $\sigma = \frac{\mu}{\rho} \cdot \frac{m_A}{N_A}$ with $m_A = 455.0376 \frac{g}{mol}$ [35].

5.1.2 Charged particle interactions

Mainly, charged particles interact with matter electromagnetically whereas neutral particles require the detection of charged secondary particles. The interactions of charged particles can generally be subdivided into electrons/positrons on the one hand and heavy particles such as μ , π , K , p , d and α on the other hand. The latter are mostly based on **inelastic collisions** with shell electrons, causing an ionization or excitation of the atom. Starting with massive particles, Bohr was the first to describe the **energy loss of charged particles**. Bethe and Bloch extended this description quantum mechanically while Sternheimer added correction terms to consider effects of the shell electrons:

$$\frac{dE}{dx} = \frac{2\pi z^2 e^4}{m v_e^2} \rho N_A \frac{Z}{A} \left[\ln \left(\frac{2m v_e^2 W_{max}}{I^2 (1 - \beta^2)} \right) - 2\beta^2 - \delta - U \right] \quad (1.9)$$

ρ as the target density, Z representing the atomic number, I is the material dependent mean ionization potential, W_{max} the maximum of the transferable energy which is $W \approx 2m_e (c\beta\gamma)^2$,

ze indicates the incident charge, δ takes into account electric field corrections and U considers inner shell corrections

This expression is very accurate in an energy range of $0.1 < \beta\gamma < 100$ and the energy loss depends mainly on the velocity of incident particles, their charge and on the target material density. Above formula can be split up into three regions: A negative slope proportional to $(1/\beta)^2$ due to the fact that slow particles undergo more electric forces of atoms until they reach approximately $\beta\gamma \approx 3.5$ as well as a positive, logarithmic slope due to relativistic effects in which Lorentz transformations increase the transversal electric field according to $E \rightarrow \gamma E$

and a Fermi plateau at high energies as a result of polarization effects. Within a local minimum at $\beta\gamma \approx 3.5$, different particles suffer a very similar energy loss. There, the particles are called **MIPs**²³ and their energy loss is nearly independent of the material with approximately $2 \text{ MeV}/(\text{g}/\text{cm}^2)$. It is a meaningful property because particles with different mass but same momentum have different β and γ according to $p = \gamma mc$.

Typically, the energy loss is normalized to the **absorber density** ρ to $-\frac{1}{\rho} \frac{dE}{dx}$. The energy loss against the penetration depth is given by the so-called Bragg curve which indicates that the number of collisions increases with the remaining energy of a particle. Also, collisions with atomic electrons are much more likely than such with a nucleus. Thus, a low energy transfer is more likely than higher ones. Energy losses are a statistical process since the number of collisions N of a traversing particle varies with \sqrt{N} , according to a Poissonian distribution. Therefore, the energy loss varies typically with the thickness of the material: The energy loss in thin layers follows mainly a Poissonian behaviour while thick layers result rather in a Gaussian distribution. Especially in thin layers the calculated energy loss is less than assumed. This discrepancy becomes visible at higher energies above about $p = 100 \text{ MeV}/c$ but remains nearly the same from there on [103]. This is considered by the Landau distribution which represents almost a Gaussian behaviour but with an asymmetric tail at high energies. At very high energies, the energy loss is predominantly caused by **Bremsstrahlung** and less by ionization. However, electrons suffer energy losses foremost by the former process.

5.1.2.1 Bremsstrahlung is the emission of a photon when an electrically **charged particle** traverses matter. Such a particle will radiate in the vicinity of an electromagnetic field of a nucleus and atomic electrons due to deceleration. The emitted energy is converted into a photon and is proportional to the charged particle's energy loss. While radiation emission is almost negligible for heavy particles, it plays a significant role for **electrons** where this process is dominant at energies above $\geq 10 \text{ MeV}$. The point at which Bremsstrahlung prevails over ionization is called critical energy E_C which can be parameterized by $E_C = 610 \text{ MeV}/(Z + 1.24)$, applicable in case of solids and liquids. A comparison between electrons and muons indicates the fact that the energy loss of electrons is much higher according to $dE/dx \propto E/m^2$ [131]. The energy loss is as follows

$$-\left(\frac{dE}{dx}\right)^{rad} = n_A E_0 5.8^{-28} Z^2 \left[4 \ln \left(\frac{183}{Z^{1/3}} \right) + \frac{2}{9} - f(Z) \right] \quad (1.10)$$

$$\text{with } n_A = N\rho/A \text{ as the number of atoms per cm}^3 \text{ and } f(Z) = \begin{cases} 1.2021 (\alpha Z)^2 & \text{for low-Z} \\ 0.925 (\alpha Z)^2 & \text{for high-Z} \end{cases}$$

But an exact expression has to take into account screening effects[29]. The angle of emission Θ depends also on the particle's energy E_0 through $\Theta = mc^2/E_0$ and forms at high energies a bunched cone in forward direction. In contrast to ionization processes, where energy losses are almost continuous along the trajectory, energy reduced by Bremsstrahlung can be emitted already by one or two photons and results in large fluctuations. In this context, the **radiation length** X_0 characterizes the distance an electron lowers its energy by a factor of e and is:

$$X_0 = \frac{1}{\left[4n_A \Phi_c \ln \left(183/Z^{1/3} \right) \right]} \quad [\text{cm}] \quad (1.11)$$

$$\text{with } n_A = N\rho/A \text{ as the number of atoms per cm}^3 \text{ and} \\ \Phi_c = 5.8 \times 10^{-28} \alpha Z (Z + \iota) \text{ including } \iota \approx \ln \left(1440/Z^{2/3} \right) / \ln \left(183/Z^{1/3} \right)$$

but this is only valid when the born approximation can be employed. While X_0 is in terms of cm it is more useful to normalize it: $\rho X_0 \rightarrow X'_0$ [g/cm²]. The length of a detector device is often given in units of X_0 while the diameter is expressed in terms of the **Molière-radius** (see Electromagnetic shower on the next page):

$$R_M = \left(\sqrt{4\pi/\alpha} m_e c^2 X_0 \right) / E_C \quad (1.12)$$

²³Minimum ionizing particles

which is a material dependent value of the transverse dimension of an electromagnetic shower. It is defined such that 90 % of the energy is deposited within a cylinder at above radius, while two radii contain 95 % and three radii about 99 %.

5.1.2.2 Cherenkov radiation is another ionizing radiation emission and occurs when a charged particle moves faster through dielectric matter than light does, described by $v > c/n$ where n is the refractive index of the material. The cone of this emission is $\cos \theta_C = 1/(n(\nu)\beta)$ with ν as the photon's frequency. Every point in the particle's trajectory emits a spherical electromagnetic wave which all interfere constructively. The energy threshold to produce Cherenkov radiation is $E_{th} = mc^2/(\sqrt{1 - (1/n^2)})$. Thus, a proton in air emits Cherenkov radiation when an energy of 38.3 GeV is reached, whereas an electron will emit Cherenkov radiation at 20.8 MeV.

5.1.2.3 Transition radiation is the emission of radiation when a relativistic particle passes the boundary of two media with different refraction indices. The emitted energy is: $E_\gamma = \alpha z^2 \gamma \hbar \omega_p / 3$ with $\hbar \omega_p = \sqrt{4\pi N_e r_e^3 m_e c^2} / \alpha$ as a plasma frequency and N_e as the electron density [121].

Summarizing all processes, the energy of a charged particle changes along x as: $-(dE/dx)^{rad} = E_0/X_0 \Rightarrow E = E_0 e^{-x/X_0}$.

5.1.3 Electromagnetic shower

An electromagnetic shower is a **cascade** of photons, electrons and positrons. Incident **high energy particles** create an electromagnetic shower in consequence of a continuous emission of energy through Bremsstrahlung or via pair production. This means, a single initial particle marks a starting point from where a cascade of electrons, positrons and photons expands. An electromagnetic shower can be described with the Rossi-Heitler model and its assumptions are used and implied in the following. Each newly generated particle deposits energy and thus creates further particles, resulting in an avalanche of branched conversions.

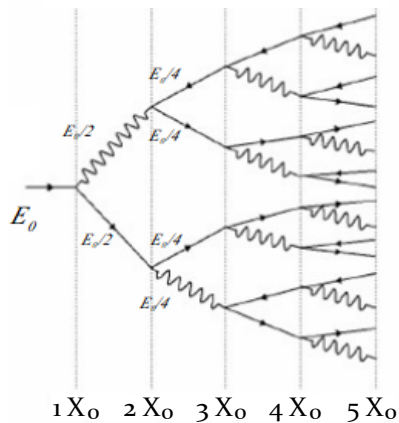


Figure 23: **Scheme of an electromagnetic shower**. After each radiation length the remaining energy is shared equally to new generated particles through Bremsstrahlung and pair production.

Such a shower propagates especially in longitudinal, but, less prominent, also in transversal direction. Appropriate terms to describe such a shower development is, in longitudinal direction, the radiation length X_0 and, in transversal expansion, the Molière-radius R_M . As a rule, an electromagnetic shower does not exceed a length of $22 X_0$ and a diameter of $3 R_M$, regardless of the material. In general, the exact dimensions of a shower depend on the initial particle respectively on its type and initial energy E_0 . At each branching of the shower, thus after each radiation length X_0 , the energy is **divided** in halves. The number of particles at the traversing depth $t = x/X_0$ follows exponentially with t through $N(t) = 2^t$ and is also linear to E_0 . The remaining energy after t is $E = E_0/N(t)$. This implies that t can be obtained via $t = \ln(E_0/E) / \ln(2)$ [164][107]. When $E = E_C$ is fulfilled, the shower has reached its maximum at approximately $7 X_0$. At this point, Bremsstrahlung and ionization rates are equal. The shower maximum increases logarithmically with the initial energy of the incident particle and, therefore, the required depth to contain the complete shower grows logarithmically, too. Afterwards, the number of particles decreases. The majority of the shower photons are within the Compton and photoelectric effect regime. Hence, about 60 % of the final shower particles have an energy below 4 MeV and roughly 40 % have an energy less than 1 MeV. Thus, only a very small fraction of particles deposits e.g. an energy more than 20 MeV. Nevertheless, the shower itself is mainly driven by Bremsstrahlung and pair production.

The deposited energy along the shower axis has a strong rise due to the growing number of secondary particles. The longitudinal shower profile is strongly dependent on the initial energy and can be parameterized, according to Longo, as $dE/dt = (E_0 \beta (\beta t)^{\alpha-1} e^{-\beta t}) / \Gamma(\alpha)$ where α, β are free parameters and Γ is the gamma function. This expression can be solved through $t = (\alpha - 1) / \beta = \ln(E_0 / E_C + C_{e\gamma})$. The coefficient $C_{e\gamma}$ enters as $C_{e\gamma} = -0.5$ in case of a shower induced by photons and for electrons as $C_{e\gamma} = -1.0$ [99][164].

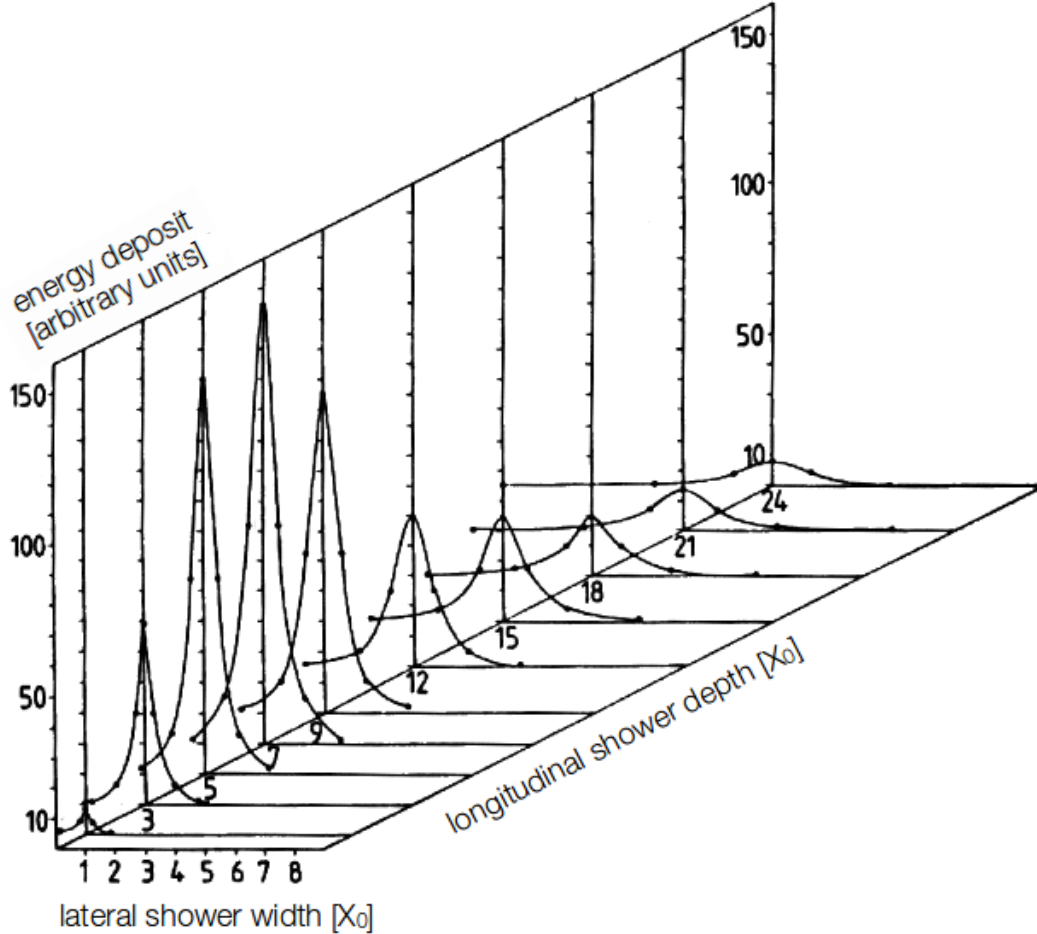


Figure 24: *Longitudinal and lateral development of an electromagnetic shower* [99]. The strong rise in longitudinal direction is caused by a rapid generation of secondary particles. In addition, the lateral size increases continuously with the shower depth. The shower production is mainly caused by Bremsstrahlung and pair production and stops expanding when the remaining energy E drops below the critical Energy E_γ . From there on, ionization processes are predominant and the photons will scatter a few more times via Compton till they are absorbed through the photoelectric effect.

The transverse shower profile depends mainly on the shower depth t and can be parameterized as $dE/dr = E_0 [\alpha \exp(-r/R_M) + \beta \exp(-r/\lambda_{\min})]$ where λ_{\min} is the range of low energy photons. The transverse shower consists of two main regions:

- The inner part consists of electrons and positrons which suffer multiple scatterings and diverge from the shower axis.
- The outer part contains mainly low energy photons and electrons which both move away from the shower axis, too. These particles are dominant beyond the shower's maximum.

In general, the lateral shower size increases longitudinally. The size profile is subject to the density of the material respectively if the material contains atoms with a high effective charge, then more nuclear charges influence the cascade due to greater accelerations caused by Coulomb repulsion. In fig. 25, examples of an electromagnetic shower for an incident electron at $E = 15$ GeV impinging different materials are shown:

Fe	[MeV]	[cm]	[g/cm ³]	Ne	[MeV]	[cm]	[g/cm ³]	PbWO ₄	[MeV]	[cm]	[g/cm ³]
Z	E_C	X_0	ρ	Z	E_C	X_0	ρ	Z_{eff}	E_C	X_0	ρ
26	21.68	1.76	7.87	10	67.02	24.03	0.9	73	9.64	0.89	8.28

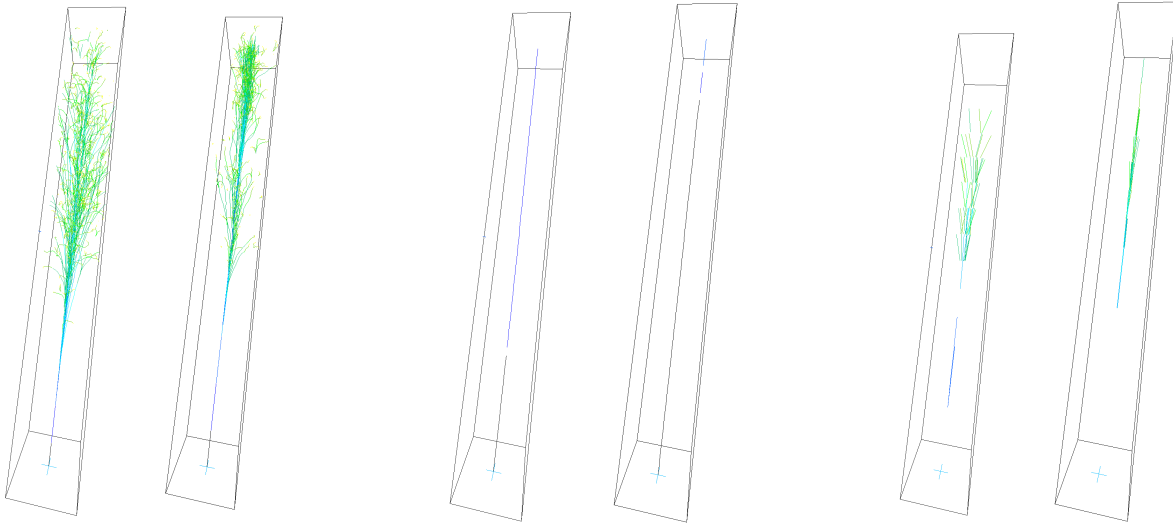


Figure 25: **Electromagnetic shower developments in iron, neon and lead tungstate.** Visualization of showers within different materials in case of an incident electron at $E = 15$ GeV impinging a volume with approximated PANDA-crystal geometries ($26 \times 26 \times 200$ mm³). Green corresponds to a low energy, blue to a mid energy and black to a high energy particle [151]. Each material is drawn without (*left*) and with a magnetic field of $B = 2$ T (*right*) perpendicular to the propagation direction. Material properties are taken from [122].

5.1.4 Scintillation

Scintillation happens when a high energy particle excites the material. Subsequently, the **de-excitation** will emit a time-displaced radiation according to: $h\nu + A \rightarrow A^+ + e^- \rightarrow A + h\nu$. There are some general categorizations to describe this de-excitation as follows:

- **Luminescence** describes the emission of photons after an absorption of energy in regard to the transfer process:
 - photoluminescence (Absorption of light),
 - chemiluminescence (Chemical reactions),
 - bioluminescence (Created by living organisms),
 - triboluminescence (Due to mechanical deformations),
 - sonoluminescence (Absorption of sound)
- **Fluorescence or scintillation** occurs after an excitation of atoms and molecules caused by ionizing radiation. The emission of light happens at a different wavelength than the impinging radiation has. It usually provides a fast decay time.
- **Phosphorescence** is the same as fluorescence but with a delayed re-emission

Scintillators are able to provide a **fast response time**. Some materials can be cheap which are, therefore, commonly used as material for electromagnetic calorimetry. However, some further aspects are also important:

A major criterion is a high quantum efficiency to convert as much of the energy as possible into emission light. Next, a transparency related to the own fluorescence light is mandatory to avoid catching instead of emitting it. Also very important is the decay time to cope with the high rates of an experiment. Some materials even provide a **fast** together with a **slow decay component**. Usually, it is pursued to suppress the latter to avoid an overlapping of the signals [148]. Due to quenching and the existence of several luminescence centers, e.g. materials like PbWO_4 , the de-excitation process is not an exponential behaviour but can be described by two, three or more exponential terms [97][53] or even hyperbolically [123]. However, many materials can be described by a simple exponential decay in the relaxation process as

$$N(t) = A \exp\left(\frac{-t}{\tau_f}\right) + B \exp\left(\frac{-t}{\tau_s}\right) \quad (1.13)$$

where $N(t)$ is the number of photons, A and B are proportional factors and τ_f, τ_s are fast and slow components

The scintillation mechanism depends on the material which can be divided into inorganic crystals, organic crystals and liquids, noble gases and plastic scintillators. In the following, inorganic crystals will be elaborated with respect to PbWO_4 : Inorganic scintillators are crystalline materials with periodically and highly ordered atoms which form an (in-)finite lattice. Each element of it has identic surroundings, called the basis. The neighbour lattice atoms are described in 3D-space by translation vectors \mathbf{a}, \mathbf{b} and \mathbf{c} . The general lattice vector is thereby $\mathbf{T} = n_1\mathbf{a} + n_2\mathbf{b} + n_3\mathbf{c}$ [152].

When radiation impinges on the crystal, **electron-hole-pairs** will be created. This means that the ionization will lift the electrons up from the Pb-O valence band into a band just below the W conduction band resulting in a loosely bound electron-hole-pair, also called exciton [123]. When the energy after the electronic excitation falls thermally below the ionization threshold, all excited electrons will be located at the bottom of the conduction band respectively within the exciton band and all holes at the top of the valence band (see fig. 27). This first stage is done within a picosecond.

The connection between a hole and the electron forms a so-called bound state, the exciton, which will propagate now along the crystal until it faces an electronic metastable level in the forbidden region which is created by a dopant. As a consequence, it will **recombine** with this attractive state which lacks an electron and transfers energy to it. This happens within about ps to μs .

The last step, the relaxation process, is the part of interest since it is the reason for the emission of light. The time from excitation until emission is usually in the magnitude of some ns and the energy of the emission can be related to the incoming radiation. Ionization via the photoelectric effect is more advantageous than by the Compton effect (see on page 27). For this reason, materials with a high atomic number are preferred.

Activator centers like Pb^{2+} increase the transition probability in such a way that they add discrete energy levels inside the band gap. The activator centers of PbWO_4 are a result of its stoichiometric excess of one of the constituents: The extra lead ions are the activator centers while the radiating centers are WO_4^{2-} . However, impurities within the lattice are not exclusively activator centers. They can also be traps preventing the charge carriers to contribute to the scintillation process. Hence, a transition can, moreover, occur radiationless, e.g., by producing secondary electrons such as Auger electrons. Traps, quenchings, phonons and scatterings of the charge carrier can influence the scintillation process massively [123]. Furthermore, also afterglowing is possible which is a relaxation process, too, but in the ms regime. In case of PbWO_4 , this results in $\sim 0.0005\%$ after 3 ms [102]. In general, the population of states N_0 emitting a photon ε_i depends on the absorbed energy via $N_0 = E_{\text{abs}}/\varepsilon_i$.

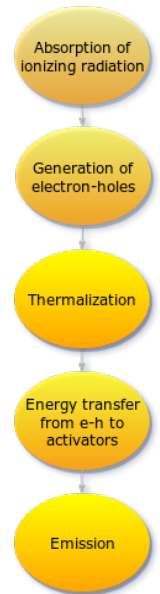


Figure 26: **Scintillation process**. The main sub processes are: Conversion, energy transfer and scintillation.

The decay time τ depends mostly on the lifetime of the activator's excited state. The time dependency of the rise is given through $I(t) \propto 1 - e^{-t/\tau_r}$ and of the fall by $I(t) \propto e^{-t/\tau_f}$. The pulse shape is the superposition of both edges. At room temperature, the decay time of PbWO_4 is $\tau_f = 5 - 15$ ns but the various parts of the emission spectrum provide different decay times [97][170]. One possible excitation of PbWO_4 is $\text{Pb}^{2+} + \text{WO}_4^{2-} \xrightarrow{h\nu=4.02 \text{ eV}} \text{Pb}^{2+} + (\text{WO}_4^{2-})^* \xrightarrow{h\nu_{em}} \text{Pb}^{2+} + \text{WO}_4^{2-}$. Therefore, excitation and emission are conducted by the tungstate anion [173]. Besides, emitted photons have a longer wavelength than the energy gap of the excitation represents. This is known as the so-called Stokes shift, enabling the detection of scintillation light which is then able to propagate through the crystal. PbWO_4 has a Stokes shift of 0.44 eV and four peaking emission bands at $\lambda_{em}=420$ nm, $\lambda_{em}=490$ nm, $\lambda_{em}=508$ nm and $\lambda_{em}=650$ nm. The excitation spectrum provides wavelengths at $\lambda_{em}=305$ nm, $\lambda_{em}=325$ nm, $\lambda_{em}=350$ nm and $\lambda_{em}=360$ nm [173], [3].

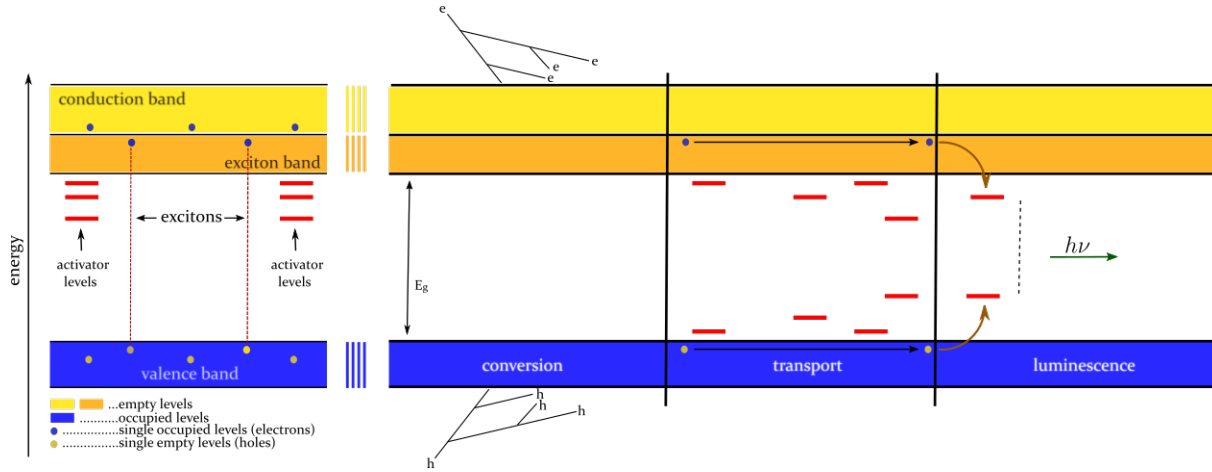


Figure 27: **Band structure of doped inorganic scintillators and stages of the scintillation mechanism.**

A scintillator is an extrinsic semiconductor in which impurities (traps and activators) add new energy levels. Ionizing radiation can lift electrons from the valence band up to the conduction band and create an exciton, an electron-hole pair. Then, thermalization causes electrons and holes to be energetically as close as possible to the band gap. The electron-hole pair will move along the crystal and when an activator is hit, a recombination process will result in the emission of scintillation light.

In general, the scintillation process can be described roughly by the efficiency $\eta = \beta S Q$ through three terms: β is the conversion efficiency and estimates the number of relaxed electron-holes per absorbed energy, S represents the energy transfer from those relaxed electron-hole pairs to the activator centers and Q is the luminescence yield.

5.2 $\bar{\text{P}}\text{ANDA}$ Electromagnetic Calorimeter

The EMC²⁴ of $\bar{\text{P}}\text{ANDA}$ has to meet some important requirements: As described before, a central requirement is an excellent **single-photon efficiency** over a wide dynamic range from a few MeV up to a few GeV. To ensure the targeted physics investigations, it is crucial to detect single photons since most of the observed reaction channels will have photons in their final states and already one might be able to represent a completely different reaction channel. π^0 and η will produce in the final state mostly photons, therefore some important benchmark channels are $\bar{p}p \rightarrow \eta_c \rightarrow \gamma\gamma$, $\bar{p}p \rightarrow \pi^0\pi^0\eta \rightarrow 6\gamma$ and $\chi_{c1} \rightarrow J/\Psi\gamma$. Thus, a detection of single photons is mandatory, for example, to be able to distinguish charmonium decays from the most abundant background particles like π^0 and η . This implies that the amount of undetected photons should be as small as possible by providing a large solid angle and a **low energy threshold**. As a consequence thereof another

²⁴Electromagnetic calorimeter

challenging aspect is the lack of a threshold for the DIRC-detector and results in the difficulty to separate pions from electrons and positrons in another way. The EMC tries to make up for this by providing lateral shower shape information [58]. These can be used together with the E/p -information to discriminate electrons and positrons from the background, thus, putting an energy resolution limit to about $\sigma_E/E \leq 1\%$ at high energies.

General properties	Required performance value
Energy resolution σ_E/E	$\leq 1\% \oplus \frac{<2\%}{\sqrt{E/\text{GeV}}}$
Energy threshold $E_{\text{thres, Cluster}}$	10 (20) MeV
Energy threshold $E_{\text{thres, single}}$	3 MeV
Noise (ENV) $\sigma_{E,\text{rms}}$	1 MeV

Table 3: **Requirements of the Electromagnetic Calorimeter of \bar{P} ANDA.** The EMC is designed to provide a high energy resolution of about 1% for the constant term and about less than 2% for the stochastic term. Hence, it is aimed to have a low energy threshold of 3 MeV/crystal to ensure the challenging physics program.

In addition, a proper mass determination affects the energy resolution and depends on the $1/\sqrt{E}$ term at low energies and on the constant term at high energies. This leads to the need of a constant term lower than 1% and of a stochastic term of lower than 2%. These conceptual design parameters result in specific requirements for the crystals in such a way that a single crystal must provide a threshold of $E_{\text{thr}} = 3\sigma_{\text{noise}} = 3\text{ MeV}$.

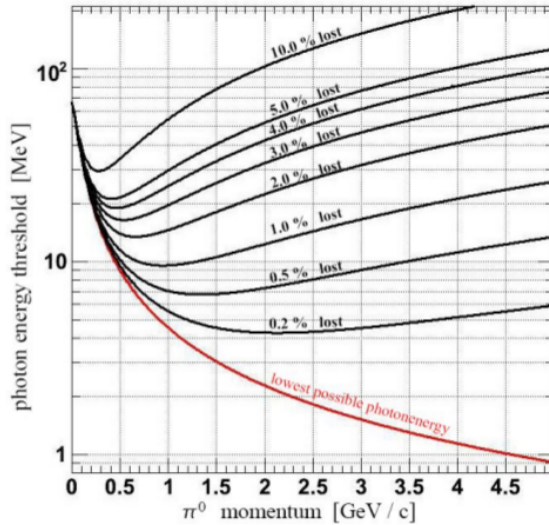


Figure 28: **Loss of π^0 against the energy threshold [154].** The amount of detected pions varies with the energy threshold which is related to the quantity of undetected photons. As long as the energy threshold is below about 50 MeV there is no significant loss to be expected.

When the electromagnetic shower extends over several crystals, a cluster energy threshold of 10 MeV is necessary. Furthermore, in case that more than one particle creates a shower, local energy maxima inside the shower cluster are tracked. If a cluster reaches a certain energy threshold of $0.5(N - 2.5) > E_{N,\text{max}}/E_{\text{local,max}}$, where $E_{N,\text{max}}$ is the highest crystal energy within this cluster and $E_{\text{local,max}}$ is a single crystal energy, its energy is then allocated to its local energy maxima via $E = \sum_i w_i E_i$.

The weight w_i of each crystal is calculated by $w_i = E_i \exp(-2.5r_i/r_m) / \sum_j E_j \exp(-2.5r_j/r_j)$. The distances $r_{i,j}$ are seen from the individual crystals to the local energy maxima. The spatial resolution is calculated through a center-of-gravity method with logarithmic weightings $W_i = \max(0, A(E_{\text{local}}) + \ln(E_i/E_{\text{local}}))$ because the energy decreases radial exponentially [154]. Based on the fact that, for example, π^0 and η leave no signal in the MVD due to the absence of electrical charge, their mass has to be determined by using the energy and opening angle θ via $s = 2\sqrt{E_1 E_2}(1 - \cos\theta)$. This task has to be

fulfilled by the EMC. The hits must not overlap and have to be at least two crystal widths apart from each other. A study about the position resolution revealed a spatial resolution of ≤ 1.1 mm [38]. Hence, a good time resolution of the signal of < 1 ns is also of high interest since it will serve as a time stamp for the EMC which will be operated triggerless. The time resolution depends mostly on the width of the signal noise σ_N , the signal slope dV/dt and the jitter σ . The most recent determination indicates a time resolution of about ~ 200 ps [156].

5.2.1 Design concept

The EMC is a **homogeneous** calorimeter and shaped like a **barrel**. Thus, it is divided into three appropriate subregions: The forward endcap, the barrel part and the backward endcap. The technical demands vary within the parts (see table 4 on on the next page). Due to the beam-target concept of \bar{P} ANDA, the three various sections of the EMC have to cover **different energy regions**: The deposited energy in the backward endcap goes up to about 0.7 GeV, in the barrel part up to 7.3 GeV and the forward part is confronted with almost the full energy of ≈ 15 GeV.

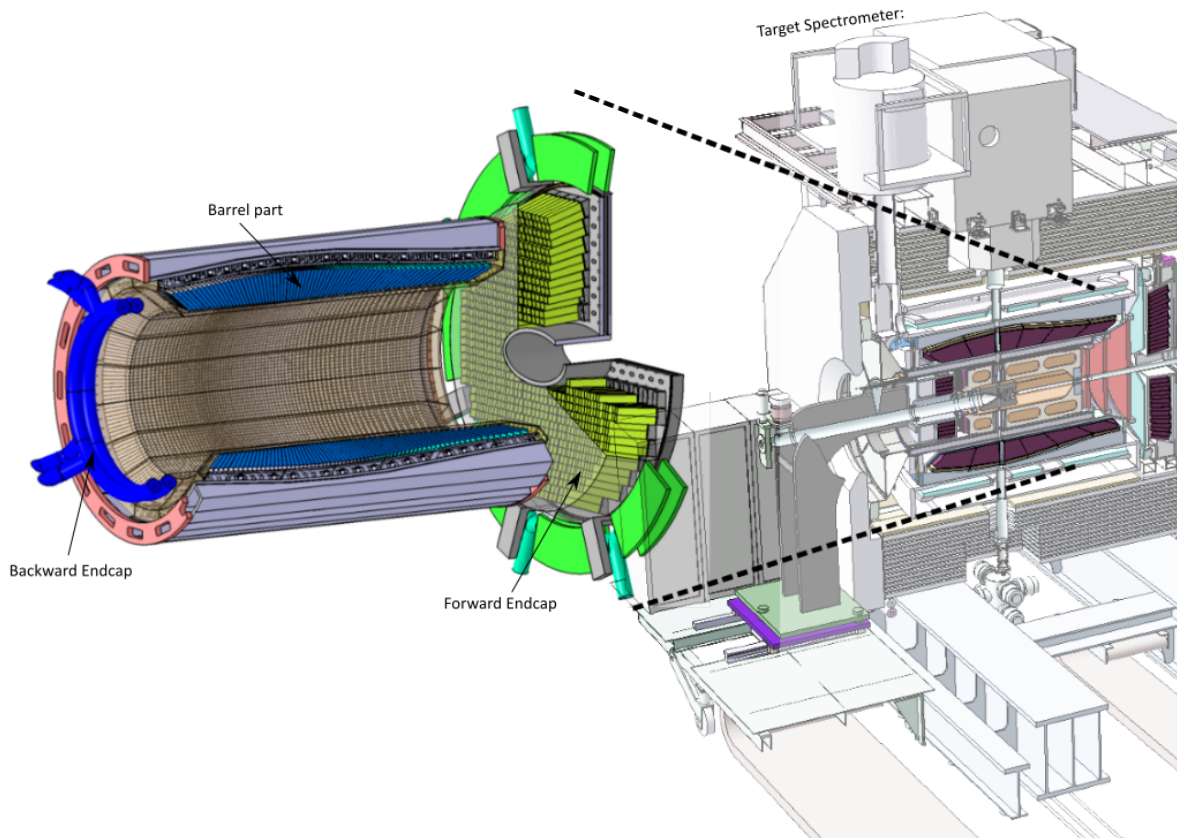


Figure 29: *Overview of the barrel part of the electromagnetic calorimeter* [154]. The EMC consists of 15552 crystals which have a tapered geometry and point towards the interaction point.

The EMC is located within the Target Spectrometer and complemented in the Forward Spectrometer with a shashlik sampling calorimeter. An important aspect is a solid angle coverage and is connected to the acceptance which is $\propto (\Omega/4\pi)^n$, where n is the number of electrons, positrons or photons in the final state. The goal is to cover about 99 % of 4π .

Subdetector properties	BEC ($\geq 140^\circ$)	Barrel ($\geq 22^\circ$)	FEC ($\leq 5^\circ$)
Energy range	0.7 GeV	7.3 GeV	14.6 GeV
Spatial resolution σ_θ	0.5°	0.3°	0.1°
Hit rate f_γ	100 kHz		500 kHz
Shaping time t_s	400 ns		100 ns
Radiation hardness	10 Gy		125 Gy

Table 4: *Requirements of the different parts of the Electromagnetic Calorimeter [154].* The forward region ($\leq 5^\circ$) has to manage most of the radiation exposure. Thus, important aspects are the high luminosity of the experiment, a fast response and radiation hardness provided by the components.

The EMC has a length of about 2.7 m and an inner radius of 54 cm and an outer one of 94 cm off to the beam line. The main part of the EMC are 15552 **scintillation crystals** which are housed in three different parts of the barrel: 11360 tapered crystals in the barrel part, 3600 slightly tapered crystals in the forward part and 592 straight crystals in the backward part. In the barrel, units of four crystals will be clustered to 40 crystals to form a module of 120 crystals in total and finally sum up to 710 crystals and constitute one of sixteen slices.

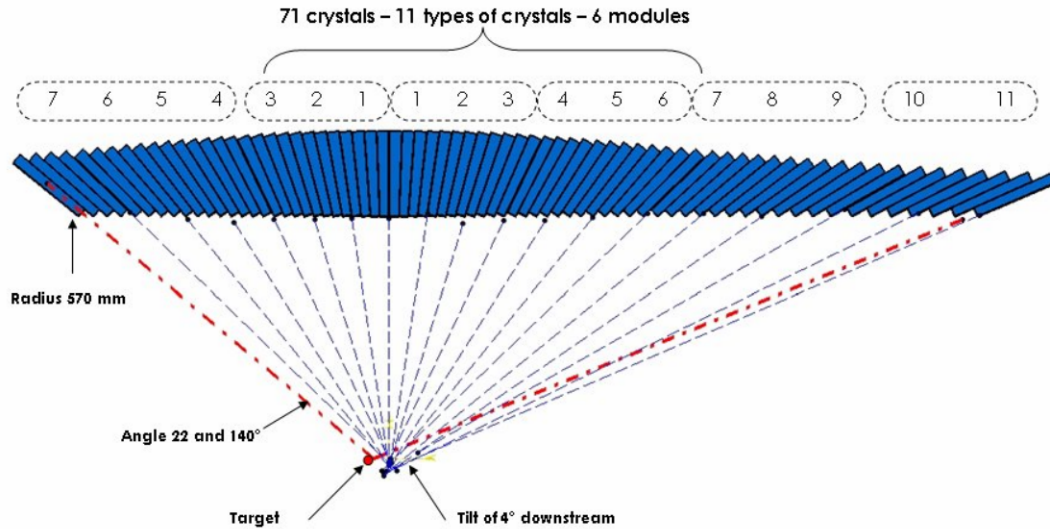


Figure 30: *Types of different crystal geometries in longitudinal direction of the EMC [154].* An angle of 4° on the focal axis ensures the crystals to point off-target, ensuring that particles will not pass along a dead zone in between the crystals. Thus, the crystals are designed in eleven different modules while each module contains 40 crystals. 18 modules along the beam direction build up the largest subdevice, a slice of 710 crystals. Then, 16 slices add up to the complete EMC.

In general, the crystals are formed as **right angle trapezoids** with an average mass of 0.98 kg. This geometry suffers less under a dead zone compared to straight crystals when arranged next to each other. According to the specific geometry of the EMC, the crystals are produced in consideration of several aspects: At first, the

crystals are subdivided into types from 1 to 11 while the types 1 to 7 appear twice. These crystals are designed **mirror-symmetrically**, seen from an imaginary plane through the interaction point and perpendicular to the beam direction. Type 1 is located closest to the interaction point, making it the least tapered type whereas type 11 is the most tapered one (see fig. 30).

Next, the crystals are subdivided into left and right (see fig. 31). A left crystal and a right crystal can be put together to form a flat surface. This allows an assembly of the crystals in such a way that the crystals altogether are almost arranged as a circular cross section (see fig. 32), when seen from the beam stream.

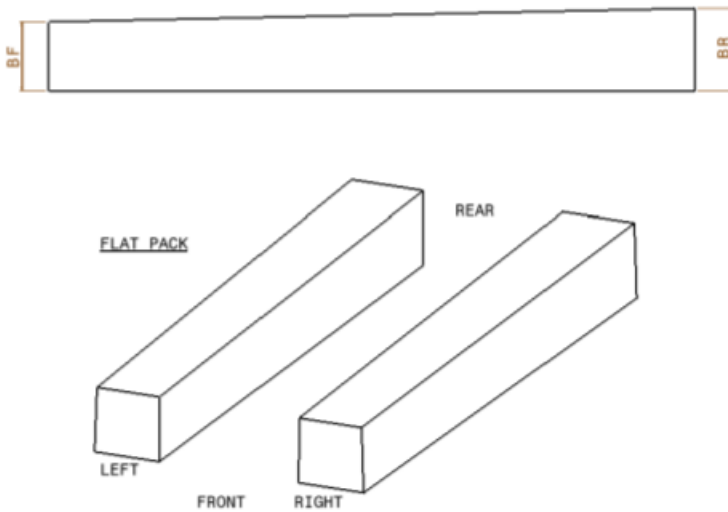


Figure 31: **Crystal geometry** [154]. All crystals have a smaller front face (*BF*) than backface (*BR*). The front height (*BF*) of 21.28 mm is the same for all types of crystals.

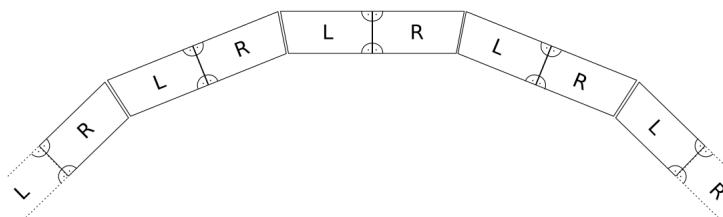


Figure 32: **Crystal geometry - left and right** [154]. In addition to the specific type geometry, the crystals are further subdivided into *left* and *right*. All crystals are designed as right trapezoids providing two right angles and a skewed side.

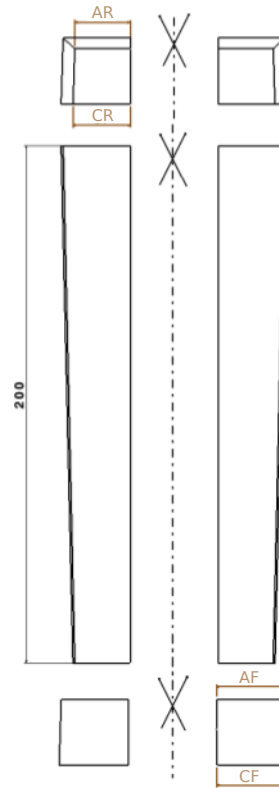


Figure 33: **Crystal geometry** [154]. Each crystal is 200 mm long but the front (*AF/CF*) and the rear faces (*AR/CR*) vary among the different types.

This specific geometry causes a varying light path inside the crystals and leads to a **non-uniformity** of the light yield. It has already been studied [148, 38] and depends mainly on the point of impact. Basically, the light yield comprises several quantities like the crystal quality, geometry, surface treatment and wrapping material [154]. The crystals are polished at $Ra < 0.02 \mu\text{m}$ and wrapped within a highly reflective foil.

5.2.2 PWO-II

All crystals of the EMC are made of **lead tungstate**, PbWO_4 respectively PWO-II, an improvement of the regular PWO material. Inherently, PbWO_4 is a member of the tungstate family and appears as one of three different polymorphs²⁵: stolzite, scheelite and raspite. The properties of the lattice are a space group with $14_1/a^26$ with the lattice parameters $a = b = 5.456$ and $c = 12.02$ [173]. At room temperature, it molds a scheelite-type tetragonal structure and provides a high density of 8.28 g/cm^3 [134]. The crystals produced for the PANDA-experiment are grown after the Czochralski method [156]. But this method makes it rather impossible not to retain molybdenum impurities which have a negative influence on the scintillation mechanism of PbWO_4 [20]. However, the concentration of it in PWO-II is below 1 ppm [154].

PbWO_4 is a transparent ternary transition metal oxide with the oxidation numbers +II and +VI. The energy of its band gap is about $E_g \approx 4.5 \text{ eV}$ [172] and the conduction band is less contributed by oxygen states compared with its valence band.

The low luminescence of PWO necessitated an **optimization** to enhance some of its initial properties like the light yield. A trivalent doping of Lanthanum and Yttrium, substituting lead, suppresses deeper trappings in the PbWO_4 structure which are connected to green and red emission spectra. At least the green spectrum seems to be the reason for some of the slow decay components [113].

Nevertheless, a reduction of the doping concentration of La^{3+} by a factor of two resulted in a better light yield by a factor of about 1.8, compared to the quality of the CMS crystals, where the material concept originates from. The concentration of La is then $< 50 \text{ ppm}$ [13] and now the improved material contains by a factor of two less Frenkel type defects [2]. The light yield enhancement can be summarized as an increase of the perfection of the crystal structure and as an activation with luminescent impurity centers [13].

PbWO_4 has a maximum emission at a wavelength of $\lambda = 420 \text{ nm}$ (FWHM=40 nm) and about 97 % of the scintillation light is emitted within **6.5 ns** and about 3 % within 30.4 ns [128]. Further wavelengths are $\lambda = 360 \text{ nm}$ and $\lambda = 620 \text{ nm}$. Hence, the optical transmission at each wavelength is well above the specification limit [117].

The radiation centers of PbWO_4 are transparent to the visible light spectrum and its luminescence region is far from the absorption edge [14]. Significant is that lead tungstate is a negative birefringent material with an ordinary refraction index of $n_o=2.24$ and an extraordinary refraction index of $n_e = 2.17$ [154]. Hence, PbWO_4 has a **light yield** which depends strongly on the **temperature** and its average gradient varies between 2 – 3 %/K [154]. At room temperature it is rather low, that is why the crystals will be operated at $-25 \text{ }^\circ\text{C}$ to provide an enhancement of the scintillation light by a factor of 4. The light yield amplification is achieved by reducing the thermal quenching²⁷ but the increase itself is assumed to be created by a lower concentration of traps. The decay time of $\sim 10 \text{ ns}$ changes only slightly [117]. The main properties of PWO-II in comparison to PWO are given in table 5:

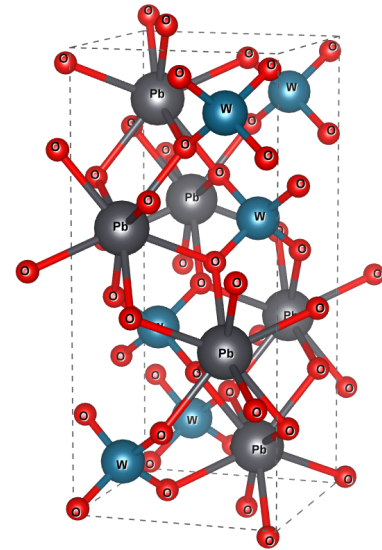


Figure 34: **Crystal structure of PbWO_4 .** W ions are surrounded by two types of oxygen tetrahedrons rotated to each other. The Pb ions are located within eight oxygen atoms shared with WO_4 tetrahedrons.

²⁵Different crystal structures at the same stoichiometry

²⁶The packing fraction a defines the number of atoms in a cell per volume

²⁷Quenching describes generally any de-excitation process without an emission

	La-/Y-conc.	Δk	LY	T
PWO	100	< 1.5	8 – 12	18
PWO-II	< 40	< 1	17 – 22	-25
	[ppm]	[m^{-1}]	[p.e/MeV]	[$^{\circ}C$]

Table 5: **Properties of $PbWO_4$.** PWO-II has a strong improvement of the light yield by reducing the concentration of Lanthanum and Yttrium [13][129].

Compared to other scintillation materials, $PbWO_4$ shows an ideal compromise between a short radiation length, decay time and material costs. Nevertheless, each of the materials has its advantages or disadvantages related to specific considerations. For example, CeF_3 and $PbWO_4$ are very radiation hard while BGO is weak against radiation. $PbWO_4$ has a relative low light yield, BaF_2 provides a very fast decay time and BGO, $PbWO_4$ and CeF_3 are not hygroscopic unlike NaI.

	ρ [g/cm ³]	λ_{em} [nm]	dLY/dT [%/ $^{\circ}C$]	LY	τ [μs]	R_M [cm]	X_0 [cm]
NaI:Tl	3.67	410	-0.2	100	0.245	4.13	2.6
CsI	4.51	310	-1.4	3.6	0.006	3.57	1.86
CeF_3	6.16	300/340	0.1	7.3	0.03	3.38	1.77
BaF_2	4.89	300/220	-1.9	4.1	0.001	3.1	2.02
BGO	7.13	480	-0.9	21	0.3	2.23	1.12
$PbWO_4$	8.3	440	-3.0	0.1	0.02	2	0.89
LYSO:Ce	7.4	402	-0.2	85	0.04	2.07	1.14

Table 6: **Comparison of inorganic scintillator materials** [132], [154]. $PbWO_4$ shows a short radiation length together with a fast decay time to fulfill the needs of PANDA but requires an operation at -25 $^{\circ}C$.

Another important aspect are the radiation damages to the crystals which will occur during operation. Similar damages are also caused, for example, by point structure defects of the host matrix meaning that already the growing processes have an impact on various material properties [2][153]. The growing procedure and irradiation has a great influence on the concentration of oxygen ions and can be changed by thermal treatment. The crystals recover already at room temperature and the necessary so-called annealing time depends on the injected radiation dose. In principle, after suffering a dose of 30 rad/h, the crystals need about 300 hours to achieve their initial weighted longitudinal transmission $EWLT = \int LT(\lambda) Em(\lambda) d\lambda / \int Em(\lambda) d\lambda$, which represents the light yield across the emission spectrum. The crystals will suffer an irradiation of about 1 – 2 rad/h during the experiment [139]. PWO-II is radiation tolerant up to about 7.2 rad/h [47] but cooling reduces the scintillation material's ability of self-annealing which might be connected with a change of tungsten oxides [18]. Radiation damages change the longitudinal absorption coefficient by $\Delta k = (\ln(T_b/T_a))/d$, where $T_{b,a}$ are the optical transmissions before and after irradiation. d corresponds to the thickness of the crystals which are irradiated with an integral dose of 30 Gy via γ -radiation before installed in the experiment. The change of the absorption coefficient $\Delta k_{420\text{ nm}}$ is specified to be lower than 1.1 m^{-1} which each crystal has to fulfill.

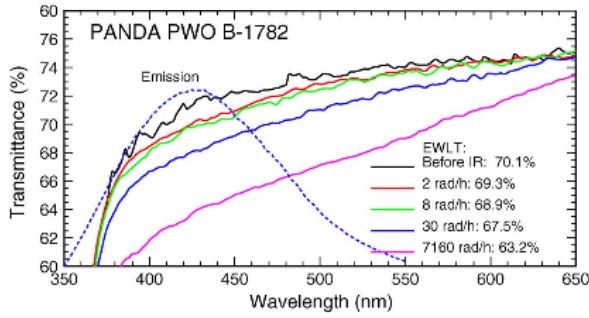


Figure 35: *Radiation damage* [47]. The damage increases with the radiation dose. In the forward part a high dose of 30 rad/h is expected. For such a dose, a recovery time of about 400 hours is needed to anneal the radiation damages at $T = -25^\circ \text{C}$.

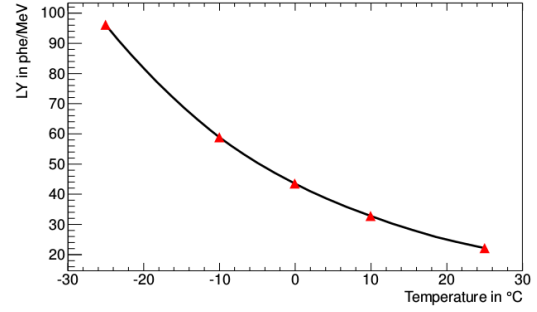


Figure 36: *Temperature dependency of the light yield of PbWO_4* [156]. The gradient of about 2 %/K has a slight linear tendency in the region of interest. The crystals will be operated at -25°C to gain a four times higher light yield compared to room temperature.

5.2.3 Avalanche Photodiode

The EMC will use APDs²⁸ as light detection devices because PMTs²⁹ are not suitable due to the applied strong magnetic field within the Target Spectrometer. Nevertheless, within the region of a small forward angle, VPTTs³⁰ come into play in the Forward Electromagnetic Calorimeter. VPTTs basically share the same principle as PMTs do with the slight difference that the dynodes are arranged in parallel to each other. This decreases the influence of a magnetic field significantly.

Generally, a **photo device** is sensitive to light of a certain frequency spectrum. Photo devices pick up the emitted light of the scintillator material and produce a correlated signal out of it. APDs³¹ put an extra **amplification** into this conversion by using a so-called **avalanche** process. To get started, the principles of semiconductors will be described in the following:

Electrons within a crystal are treated as nearly-free with a general probability density of $\rho = \Psi(\vec{r}) * \Psi(\vec{r})$. Atomic electrons have their own orbitals but the closer the atoms come to each other, the more their energy levels split and merge into new energy levels, thus, the more their wave functions overlap. And that is why they can be associated with the periodic bloch wave function $\Psi(\vec{r}) = e^{\pm i\vec{k}\vec{r}} u_k(\vec{r})$. However, when the energy levels overlap, they will generate continuous energy bands. There are two of these which are of high importance: The valence band and the conduction band. The former is energetically lower and provides at $T = 0 \text{ K}$ all the electrons with the highest energy, in contrast to the higher conduction band which usually lacks electrons but is finally responsible for the conductivity.

A special case emerges at the boundaries of the wave function, $x = \{0, na\}$ with a as the lattice period, where the band structure shows a discontinuity and forbidden energy states caused by bragg reflections. These regions can turn out to be a band gap which are in particular characteristic for insulators and semiconductors. In principle, no states are allowed there to be occupied and it represents the necessary energy $E_g = E_c - E_v$ to lift an electron up into the conduction band. The required energy to overcome is material and temperature dependent. Therefore, it follows phenomenologically $E_g = E_0 - \alpha T^2 / (T + \beta)$ with α and β as constants [162], but a more precise description can be found in [120]. It should be mentioned that, at room temperature (300 K), E_g of silicon is 1.12 eV [152].

Overall, the density of states $g(E)$ provides a view on the electron's probabilities to occupy energy states for

²⁸Avalanche Photodiodes

²⁹Photomultiplier

³⁰Vacuum photo triodes and tetodes

³¹Avalanche Photodiodes

which the Fermi-Dirac distribution yields the function:

$$f(E) = \frac{1}{1 + \exp((E - E_F)/k_B T)} \quad (1.14)$$

with E_F as the Fermi energy level³² [152]. In semiconductors, it lies within the band gap and is, moreover, in between the valence and conduction band. In case of holes, the density of states is $h(E) = 1 - f(E)$.

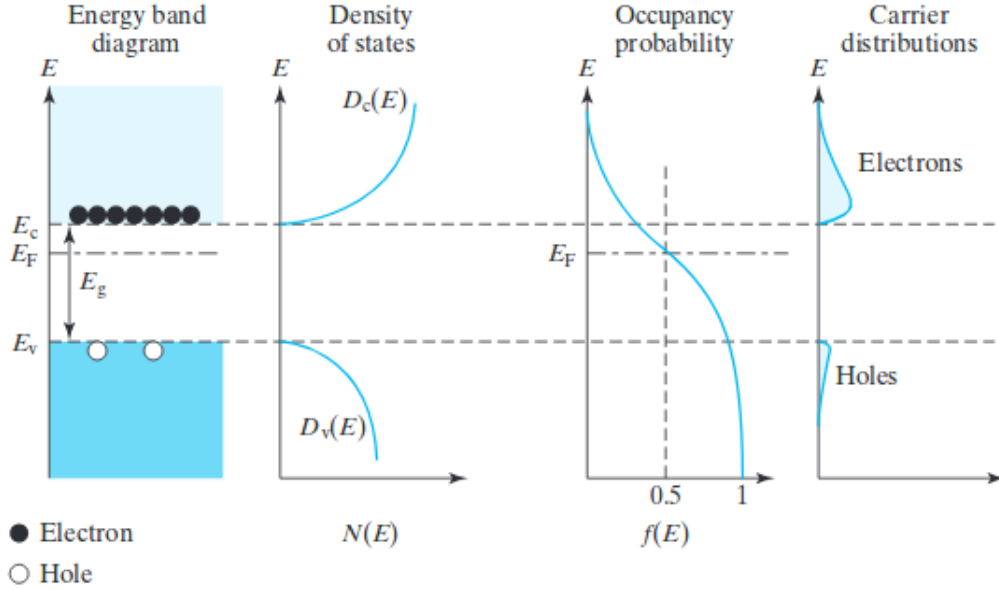


Figure 37: **Electronic band structure of intrinsic semiconductors** [24]. Due to thermal excitations, some electrons are at $E > E_F$ but the most are located below the conduction band. Overall, the density of states $g(E)$ is energy dependent, while the energy of electrons is measured upwards and the energy of holes is measured downwards. The Fermi-Dirac probability distribution $f(E)$ indicates that the probability of an electron to occupy a state is higher the lower the energy is and vice versa relative to holes. In doped semiconductors, $f(E)$ is shifted upwards (*n-type*) or downwards (*p-type*) and according carrier concentrations are bulked at the conduction band (*n-type*) or at the valence band (*p-type*) [152]. In general, $f(E)$ helps to describe the carrier concentrations: $\int n_E(E)dE$ yields the concentration of electrons n , respectively the concentration of holes p in case of $\int p_E(E)dE$.

The density of the states $g(E) = 0.5\pi^2 (2m^*/h^2)^{3/2} \sqrt{E}$, with m^* being the effective mass, is not temperature dependent and describes concisely states near the Fermi-level (a general expression can be found in [54]). In case of electrons, the square root expression of energy will be $\sqrt{E - E_C}$ and in case of holes it will be $\sqrt{E_V - E}$. Together with the Fermi probability distribution, the number of electrons within the conduction band can then be found via $n(E) = g_c(E)f(E)$. And since holes represent empty states in the valence band, their density is, in turn, $p(E) = g_v(E)[1 - f(E)]$. Overall, $g(E)$ is continuous in conducting materials as opposed to isolators. At room temperature, the effective density of states for silicon is $N_c = 2.86 \cdot 10^{19}$ and $N_v = 3.1 \cdot 10^{19}$ [105]. Finally, the concentration n_i can be obtained via $n_i^2 = N_C N_V \exp(-E_g/kT)$, whereas the electron and hole densities are the same in intrinsic semiconductors: $n = p$. Adding dopants with a surplus (*n-type*) or lack of electrons (*p-type*) in regard to a pure semiconductor crystal changes its properties due to the existence of new energy levels. Differences emerge in such a way that *n-type* impurities add energy levels slightly below the conduction band and *p-type* dopings add new ones slightly above the valence band. Depending on the doping

³²A particle's highest energy in the ground state

atoms (As, Ge, Mo,...), the additional donor levels are located 30–100 meV below the conduction band and acceptor levels 20–60 meV above the valence band [152]. Charge carriers there can easily participate in conduction respectively require little energy to move up from the valence band into the conduction band. Both doping levels vary from each other in the sense of their charge state: Donor levels are neutral when occupied and acceptor levels are neutral when unoccupied. If the donor level is empty it will be positively charged while the acceptor level will be negatively charged when occupied. Hence, doping will shift the fermi energy towards the conduction or valence band, depending on the type of doping.

Connecting differently doped materials will bend and connect the energy bands of the p-type and n-type layer. This results in a so-called pn junction and is the basis of each semiconductor. The dimension of the bending represents the differential voltage and is called the **built-in voltage** ϕ_{bi} . This potential is always present at the interface of doped materials.

Furthermore, at this region a thermally-driven diffusion of charge carriers will be created according to the corresponding concentrations of the materials: Surplus electrons of the n-type material will migrate into the p-type material and holes of the p-type will migrate to the n-type. In general, a diffusion current aims at compensating different concentrations and is proportional to the concentration gradient. This results in immovable ions N_a and N_d since the transfer of n-type electrons will cause positive donors on the n-side whereas missing holes create negative acceptors on the p-side. Consequence is the development of a depletion region with no mobile charge carriers: $n \approx 0 \approx p$. The n-layer and the p-layer are charge neutral which is required due to $n + N_a = p + N_d$. The depletion layer introduces a capacitance C_{dep} which follows a plate capacitor as $C_{dep} = A\epsilon_0 W_{dep}^{-1}$ with W_{dep} as the depletion layer width.

Both layers, in return, produce an electric field across the depletion region and result in a drift current. This current flows until an equilibrium is reached, where both currents, the diffusion and the drift current, will compensate each other.

Applying an **external voltage** influences a semiconductor in the manner of bending the energy bands, too. The slope of the energy bands represents the electric field [24]. According to the sign of the external voltage, the bending of the energy bands will be increased or decreased and results in a corresponding potential barrier. For example, a negative voltage at the p-side raises the required potential energy to overcome the space charge region.

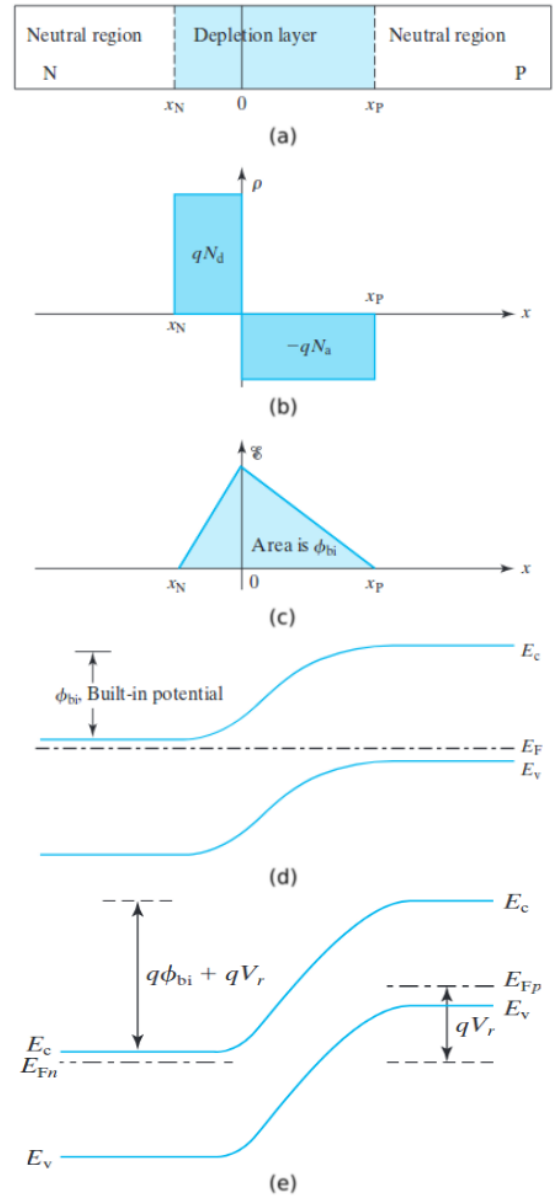


Figure 38: **pn junction** [24]. a) A semiconductor comprises the n-layer, the p-layer as well as the depletion region. All layers are charge neutral. b) The depletion region $W_{dep} = x_p - x_n$ can be obtained from the layer widths x_p and x_n [24]. c) The electric field along x results by incorporating the bias voltage ϕ_{bi} . d) The built-in potential is the differential voltage between the energy bands of the dissimilar dopings. Without any external voltage, the Fermi energy is constant across the whole semiconductor e) Applying a positive voltage V_R at the n-side changes the energy band diagram and increases the potential barrier by qV_R . Furthermore, the Fermi energy will be shifted.

Though a bending hardens the possibility of a charge carrier to participate in conducting, it enables a tunneling process as the bending of the energy bands causes the bands to be closer to each other as before [24]. When the bending becomes less, the potential barrier decreases and the current rises. Hence, the applied voltage plays a major role in developing the depletion region respectively the width of it: A positive voltage at the n-side will widen the depletion region.

Additional to an external voltage, light can also produce a current. When a photon impinges on a semiconductor, it can be absorbed when its energy E_γ is higher than the band gap energy E_g . If so, then two cases are possible: 1) The photon enters the semiconductor adjacent to the depletion region and lifts an electron up from the valence band into the conduction band. But due to a missing electric field, the generated electron-hole pair will not be separated and thus not produce an electric signal. 2) This is different when the photon hits the space charge region because of the electric field present there which splits the electron-hole pair. The electron moves to the n-side and the hole to the p-side.

The width of the depletion region can be modified by the applied voltage to increase the **conversion efficiency** and generates a higher photo current I_{ill} . In addition, to make a semiconductor more sensitive to impinging light, one possibility is to add an undoped layer in between. Such a device is called a pin-diode and can be used as basis for further devices like Zener or Avalanche Photodiodes. Zener diodes are heavily doped and provide a very thin depletion region in contrast to Avalanche Photodiodes.

Avalanche Photodiodes increase the sensitivity level through amplification by **impact ionization**. An APD covers a broad spectral response but has the disadvantage of a high noise in comparison with a pin diode as well as the need for a high voltage (typically between 100 – 200 V). The large amplification enables a measurement of even very low light levels at short times (\sim ns) but requires a precise control of the bias voltage to keep the gain stable which is, furthermore, also temperature dependent. This amplification is made possible by the special design of an Avalanche Photodiode. The mechanism of an APD is quite similar to that of a pin diode:

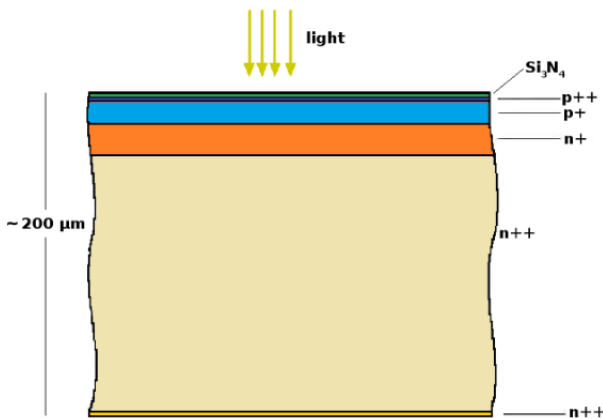


Figure 39: **Structure of an Avalanche Photodiode** [31].

An Avalanche Photodiode consists of a silicon-based semiconductor with a pn-junction. At first, photons enter the depletion layer p^- through the silicon dioxide layer. With the help of the special $p^{++}p^+n^+n^{++}n^{++}$ design, a very high multiplication avalanche is possible in the p^+n^+ -layer. The Si_3N_4 -coating reduces light reflection. The relative large n^{++} -layer reduces the nuclear counter effect because the amplification is initialized in the p^+n^+ -junction respectively charge carriers produced in the n^{++} -layer do rather participate in the multiplication process.

Incident light will pass the surface layer while the penetration depth depends on the wavelength. Afterwards, the photons will generate electron-hole pairs (in case of silicon, E_γ must be > 3.6 eV) in the depletion layer (p^+ -layer, also called π -layer) due to the inner photoelectric effect. Then, the individual charge carriers will be pulled apart by the external electric field. The electrons will drift towards the n^{++} -layer and the holes to the p^{++} -layer. Along their path, the charge carriers will likely collide with other ones and create additional electron-hole pairs. This will launch an avalanche process already within the n^+ -layer in which each of these charge carriers will cause additional ionizations. Special about these electrons is that, regardless of whether they collide with other electrons or not, they always have enough energy to excite further electrons and thus remain in the conduction band. The difference of generated electrons (α) and holes (β) is known as the **ionization rate** $k = \alpha/\beta$. The ionization rate of silicon includes much more electrons than holes and represents the fact that the exponential multiplication is mostly driven by electrons.

This large amplification M (see fig. 43) does not remain without negative consequences like the ENF³³ $F(M) = k \cdot M + (2 - 1/M) \cdot (1 - k)$. It describes the statistical nature of the avalanche gain and represents the statistical part of an APD's noise. The lower k and M the lower $F(M)$ will be and can be approximated through $F = 2 + kM$, in case of $k > 0.1$ and $M > 20$ [46]. Moreover, it is understood as the factor which compares the noise of an APD with a noiseless multiplier on the basis of Poissonian statistics which can be described by shot noise alone.

$F(M)$ influences the energy resolution by

$$\frac{\sigma_E}{E} = \frac{1}{\sqrt{E}} \sqrt{\frac{F}{N_{pe}}} \quad (1.15)$$

where $N_{pe} = N_\gamma QE$ takes into account a diode's asset to create primary charged carriers. It is one of the main factors influencing the possible energy resolution. In the following, the reverse bias region will be seen in a detailed view. An ideal diode shows two modes: If $V_D > 0$, it can be treated as a short-circuit and when $V_D < 0$, it can be seen as an open circuit. Thus, in reverse direction free charge carriers will become rare or even be totally absent so there are no charge carriers left to participate in conduction. Avalanche Photodiodes are specifically designed to operate in the reverse region ($V_D < 0$).

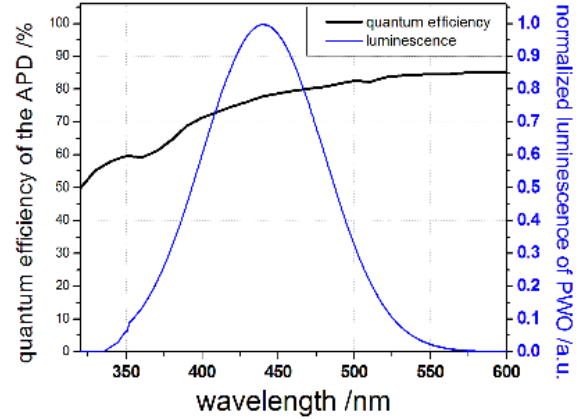


Figure 40: **APD quantum efficiency** [146]. The quantum efficiency of the APD begins at about $\lambda = 340$ nm and ends at about 800 nm. In between, the quantum efficiency rises for the most part. Within the luminescence spectrum of PbWO_4 , the QE is about 70 - 80 %.

Nevertheless, even before reaching the **breakdown voltage**, a small reverse bias leakage current I_R will flow because each increase in voltage will widen the depletion region adequately. Typically, this term, bias leakage current, is used in case of non-optical devices and in case of photodiodes it is called dark current I_D . There it is seen as the current the photodiode produces in the absence of any light:

$$I_D = I_S + M \cdot I_b \quad (1.16)$$

The dark current includes the bulk current I_b as well as the surface current I_S . The bulk current consists of thermally generated electrons and holes in the pn junction and the surface current is caused by surface defects. Therefore, an amplification process will increase the dark current too. In forward direction, the dark current becomes zero since the characteristic is reversed and the dark current becomes identical to the drift current. The total current can be expressed as

$$I^2 = 2e (I_{\text{ill}} (M = 1) + I_b) \Delta f M^2 F + 2e I_S \Delta f \quad (1.17)$$

with Δf as the bandwidth [75]. The slope of the reverse current is rather low but increases sharply when reaching $V > V_{Br}$. Then, the pn-junction can be destroyed but APDs are regularly produced such to operate safely there. The **multiplication gain** M of an Avalanche Photodiode can be calculated by [152]:

$$M = \left\{ 1 - \int_0^{w_D} \alpha \exp \left[- \int_x^{w_D} (\alpha - \beta) dx' \right] dx \right\}^{-1} \quad (1.18)$$

³³Excess noise factor

An **empirical expression** takes into account series resistances (especially the pn material itself and contact resistance) and is given by

$$M = \frac{1}{1 - \left((V_R - IR_s) \cdot V_{Br}^{-1} \right)^n} \quad (1.19)$$

with n as a constant that considers the material, doping profile and radiation wavelength. Finally, the multiplication gain M can **experimentally** be determined by

$$M = \frac{I_{ill}(V_R) - I_d(V_R)}{I_{ill}(M=1) - I_d(M=1)} \quad (1.20)$$

In the \bar{P} ANDA-EMC, the gain is yielded at a given temperature of -25°C and I_{ill} and I_d are observed with an illumination at $\lambda = 420\text{ nm}$ [154]. Thus, the gain is given by the ratio of $I_{il} - I_d$ at a certain reverse voltage and the voltage where no amplification occurs ($M = 1$).

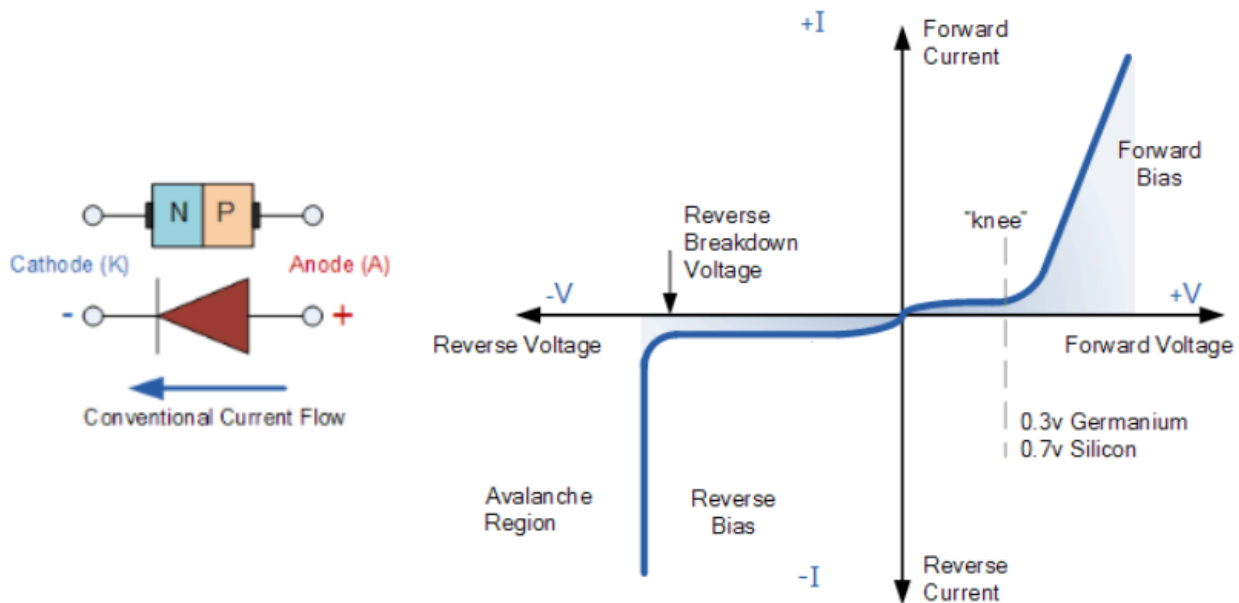


Figure 41: **Diode I-V curve** [5]. The I-V curve of an Avalanche Photodiode shows two distinctive regions: The *reverse bias* and the *forward bias*. Both can be further subdivided: The forward bias into the necessary voltage to prevail the space charge region and into the conduction driving voltage. The reverse bias provides a region with a moderate gain and applying a high voltage reaches the breakdown voltage where the amplification respectively the reverse current rises rapidly.

Applying a positive voltage at the p-side will reduce the depletion region and is known as forward-bias. Applying a negative voltage at the p-side will widen the depletion region and is called reverse-bias.

The Avalanche Photodiodes are manufactured by Hamamatsu and were used the first time in the CMS experiment. An advantage is the compact thickness which is only $200\ \mu\text{m}$ and the very thin conversion layer with only $10\ \mu\text{m}$ which reduces the NCE³⁴. The CMS version provides a rather small active area of $5 \cdot 5\ \text{mm}^2$.

³⁴Nuclear counter effect

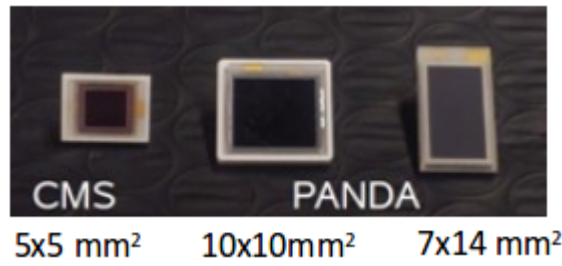


Figure 42: *APDs of CMS and PANDA in comparison* [89]. The APD used in PANDA originates from CMS. In order to achieve a better radiation hardness, the internal structure of the APD has been modified such that the conversion layer exists now of only 10 μm . Furthermore, to cover a larger rear area of the crystal, the geometry of the APD also has been changed allowing to place two APDs next to each other.

Therefore, Hamamatsu modified the geometric details and enlarged the active area to a final dimension of $14.5 \cdot 13.7 \text{ mm}^2$, now called **LAAPD**³⁵ (Hamamatsu S8664-1010, see):

$QE_{\lambda=420 \text{ nm}}$	M/T	ΔU_R	A	d	C	$ENF_{M=100}$	$\alpha (\lambda)$	d_{conv}	D
70-80	2.2	± 0.1	$14.5 \cdot 13.7$	200	270	2.33	$7.05 \cdot 10^3$	0.9	30
%	[%/°C]	[V]	[mm^2]	[μm]	[pF]		[1/cm]	[μm]	[Gy]

Table 7: *Parameters of the PANDA APD* [154]. Most critical operational parameters are the bias voltage and the temperature which must not differ by more than 0.1 V and 0.1 °C, respectively.

To increase the covered rear face of the scintillation crystals, two APDs will be mounted on each crystal which offers an improved S/N ratio of up to $\sqrt{2}$ together with a lower threshold level [154]. Furthermore, this enables the detection of fake events caused by neutrons by just comparing the measured signal of both APDs. Due to a possible suffering under irradiation, the photo devices have to be radiation tolerant.

Radiation damages can cause **surface** and **point defects**. Surface defects are common ionizations in which an electron-hole pair is created due to IEL³⁶. Especially in semiconductors, this is a reversible process but when located at surfaces, these defects can cause permanent damages and, in consequence, increase the surface current I_S . As a result, the quantum efficiency will decrease. Furthermore, there are bulk defects which will increase the dark current due to the knock out of atoms out of the lattice as a consequence of NIEL³⁷. While neutrons mainly cause point defects, protons are able to cause both. In solid-state devices, the most expected radiation damage will be point defects caused by neutrons. For example, in case of memory flashes, such transient effects can result in induced bit flips (e.g. 0 \rightarrow 1). Point defects are the consequence of vacancies or displacements of atoms within the crystal. This can change the doping profile of an APD and particularly the dark current suffers under radiation damages which then modifies the internal gain mechanism. Such defects appear proportionally to the neutron fluence Φ as the dark current rises in parallel: $\Delta I_d/V = \alpha \Phi$, with α as a material constant taking into account radiation damages. For CMS, α was observed as $\alpha = 14 \cdot 10^{-17} \text{ A/cm}$ [31]. The change of the dark current can be used to calculate the accumulated dose.

³⁵Large area Avalanche Photodiode

³⁶Ionizing Energy Loss

³⁷Non Ionizing Energy Loss

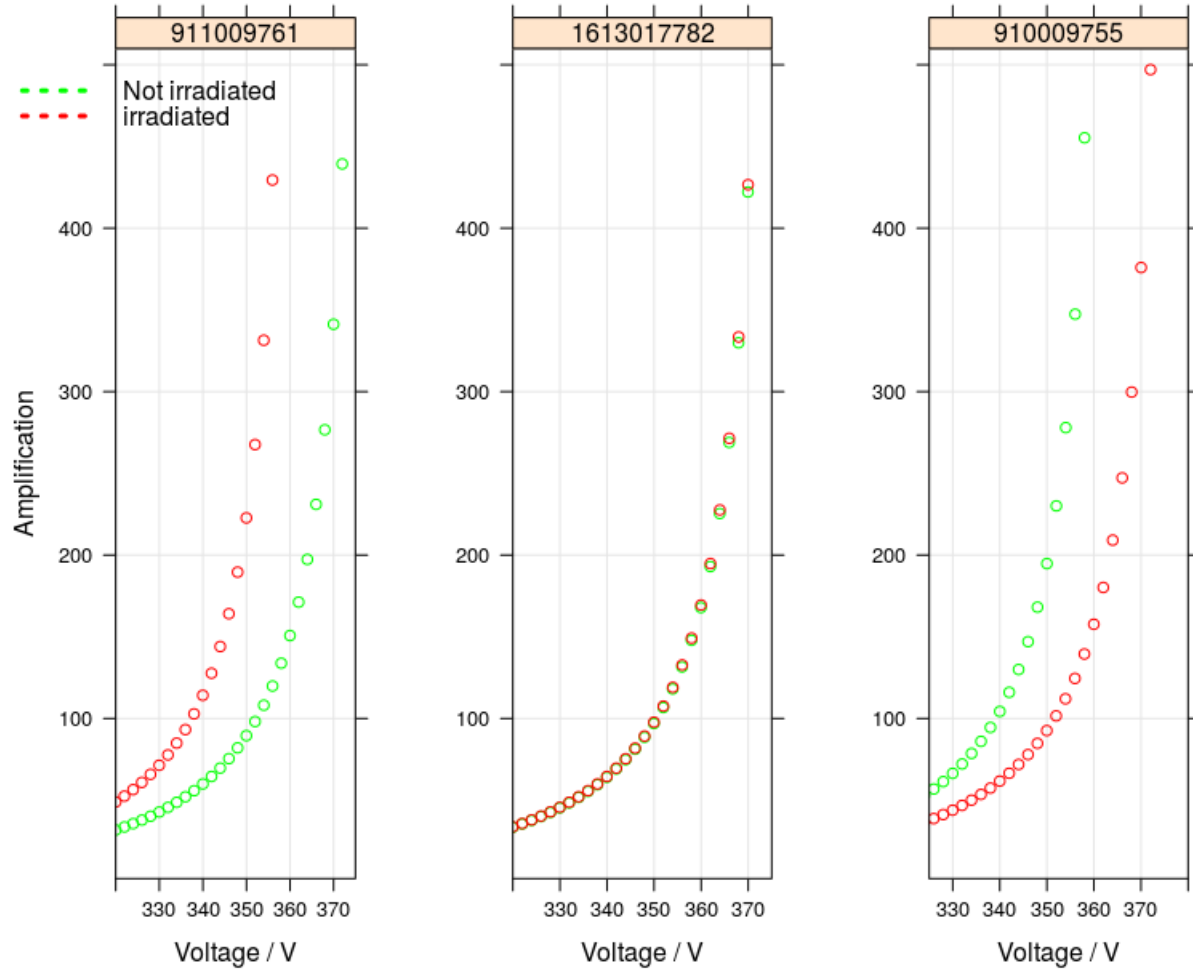


Figure 43: *Diode M-V curves of irradiated APDs.* APDs can show significant shifts due to the irradiation. Moreover, the behaviour is not necessarily systematic. The curve of APD 911009761 shifts towards lower voltages and the curve of APD 910009755 towards higher voltages. The APD 1613017782 shows almost no change.

Radiation damages, especially point defects, can vanish over time because they are not fixed within the lattice [15]. Thus, they are able to undergo a kind of **self-repair**, especially in a so-called annealing process in which devices are supplied with thermal energy. To make the APDs more radiation hard, so that possible damages occur less later in the experiment, they are irradiated with γ s ($\gamma_1 = 1.17 \text{ MeV}$, $\gamma_2 = 1.33 \text{ MeV}$ [28]) at the Strahlzentrum in Giessen by using ^{60}Co . The accumulated Dose is $D = 30 \text{ Gy}/90 \text{ min}$ at a stabilized room temperature of $T = 20 \text{ }^\circ\text{C}$. Such an irradiation can result in possible damages used before in the Experiment. This way it is possible to investigate irradiation influences and take them into account, for example for matching purposes (see Matching on page 53). Finally, irradiation can change the performance of an APD in general. The APDs which will be used in the EMC are radiation hard up to an integrated fluence of 10^{13} p/cm^2 [171]. Since the APDs will be attached directly to the crystals, they will also be operated at $-25 \text{ }^\circ\text{C}$. After producing an energy-correlated charge, the first device this charge is transferred to is usually a preamplifier.

5.2.4 Preamplifier

Preamplifiers convert the charge signal of the photosensor into a voltage signal. To achieve an optimal readout of the Avalanche Photodiodes, a LNA³⁸/LNP³⁹ is necessary. It lowers the influence of **noise** from subsequent electronic devices according to Friis. It is located close to the photo sensors and reduces signal losses in the feed line, for example, to avoid pick up and it is a key component in the readout circuit. The EMC will use the APFEL⁴⁰ which is based on a 350 nm CMOS technology. It is used in the barrel and backward endcap while the forward cap utilizes a preamplifier based on discrete components, the BASEL pre-amplifier, to cover the high rates of up to 500 kHz. The minimum energy deposit which should be covered is about 1 MeV and corresponds to an input charge of 2 fC while the input noise is equal to 0.67 fC [166].

The shaping time of the preamplifier should be longer than the scintillation decay time to ensure a collection of the entire signal.

The dark current I_d of the APD contributes to the parallel noise of the system APD-pre-amplifier. Especially in case of high shaping time periods, it will be the most dominant part of the noise [116]. The noise of an output signal which is based on an input signal can be evaluated by using the ENC⁴¹. It indicates the charge quantity at the input to generate a noise signal at the output. It comprises several factors such as the time gate, capacitance and amplification electronics [155]:

$$ENC^2 \sim 2e (I_S + I_B \cdot M^2 \cdot F) \cdot \tau + 4kT \left(R_S + \frac{0.7}{g_m} \right) \cdot C_{ges}^2 \cdot \frac{1}{\tau} + A \cdot C_{ges}^2 \quad (1.21)$$

and is about $\sim 4436 e^-$ for the APFEL [125]. Main aspects are the thermal noise current $i_{therm} = 4k_B T/R$ and the shot noise $i_{shot} = 2I_o e$ which both are frequency independent. At low energies, this noise term plays the major role with respect to the resolution [131]. The overall signal response has to be fast enough to allow a solid particle identification. On the other hand, to avoid signal losses, the shaping time of the preamplifier stage has to be longer than the decay time of the scintillator material. Hence, the shaping time must not exceed an upper limit to avoid pile-up signals.

C_f	P	f	δM	M	τ	ENC
8	50	350	0.64	10.000	250	$\sim 4436 e^-$
[pC]	[mW/ch]	[kHz]	[mV/fC]		[ns]	

Table 8: **Parameters of the APFEL** [125]. The APFEL has an ENC of about $4436 e^-$. Furthermore, it can be operated at 350 kHz and has a low power consumption of 50 mW/ch. The capacitance corresponds to 8 pC.

The APFEL has to provide a huge **dynamic range** from 1 MeV to 10 GeV and the amplification signal is quite proportional within this region. In addition to the amplification, the APFEL provides a third order shaper, consisting of integrators⁴², and finally a differential output.

The readout of the ASIC consists of an analog chain together with a digital part. The latter allows to set reference voltages which can be adjusted to suit the temperature. In the analog part, the first integrator, the APFEL splits each APD signal into two different channels, a low gain and a high gain. The high gain aims at an amplification of very low signals which have to be enhanced the most. The **high gain** can be set to an amplification factor of 16 or 32 relative to the **low gain**. Both of these subpaths are composed of two integrators of which the last delivers the differential output signal.

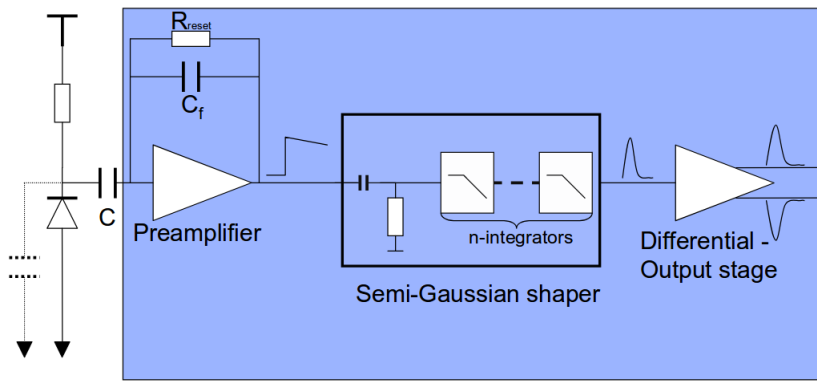
³⁸Low Noise Amplifier

³⁹Low noise and power

⁴⁰ASIC for Panda Front-end Electronics

⁴¹Equivalent noise charge

⁴²Inverted operational amplifier with a negative feedback



ASIC

Figure 44: *Preamplifier and shaper APFEL ASIC* [124]. The preamplifier stage is based on a folded cascode circuit and a source follower. The input transistor is the most dominant noise source. At first, the APD signal is amplified by the preamplifier. Next, a pulse shaper modifies the signal to a gaussian-like shape and sets a frequency window. The pulse shaper consists of an integrator of a third order, each with an integrated time of $\tau = 80$ ns. To measure the APD signal, a shunt resistor is used in an additional but not depicted circuit connected to the anode of the APD.

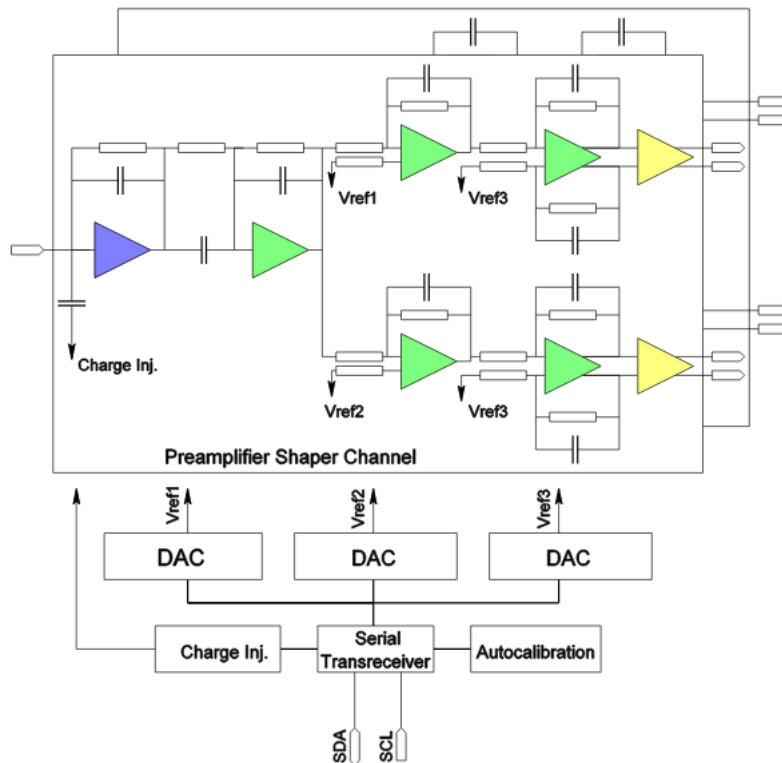


Figure 45: *Readout of the APFEL ASIC* [167]. Both readout paths include a charge sensitive preamplifier (blue), a third order shaper (green) and finally a differential output (yellow).

The digital part covers a serial interface for the autocalibration to adjust the DC voltages for a fixed temperature. Furthermore, a charge quantity can be injected to generate a testpulse for monitoring purposes. The 10 Bit DACs⁴³ provide voltage references to make differential voltage signals available [126]. Finally, the APFEL is used to drive the positive voltage signal via a $50\ \Omega$ line to the main readout device at a as high as possible S/N-ratio. Hence, it delivers the pulse height sampling for further processing.

5.2.5 Readout

The interaction rate of up to $2 \cdot 10^7\ s^{-1}$ results in an enormous data rate in the order of 200 GB/s. This makes a **trigger system** difficult and can't be realized in hardware. Thus, this data stream will already be filtered by a complete online event reconstruction. A reduction of the data volume is possible with the help of online information from the subdetectors by extracting physical signatures on the fly. On a first level based on FPGAs⁴⁴ and on a second level with the help of GPUs⁴⁵ or PCs. The circumstance that the subdetectors operate at different read out times results in an overlapping of the events. This will be solved by making use of SODANET⁴⁶ time stamps which were allocated to the respective subdetectors. The DAQ⁴⁷ system comprises an event building as well as a filtering [109].

Since several subdetectors contribute to the identification of a particle, the readout has to handle the input of various readout times. This makes a global trigger difficult or even impossible and, therefore, each subdetector will provide its own trigger. To do so, each subdetector is supplied with a pre-processing stage in which the hit information of this subdetector is already reduced to physical relevant information.

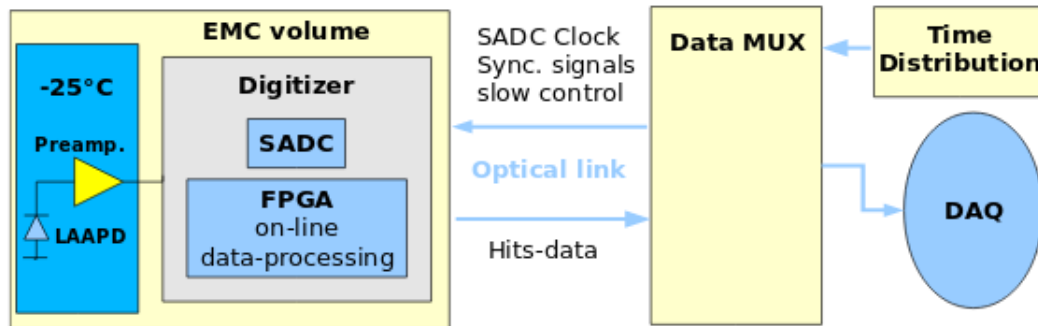


Figure 46: **Readout chain of the EMC** [92]. The clock signal is allocated to all SADC channels. In principle, the readout scheme consists of the hit detection and feature extraction (Front-end electronic), the data concentrator, the event selection and building and the compute node.

In case of the EMC, first of all, an APFEL is readout by a 14-bit SADCs⁴⁸ with 64 channels and 125 MSPS⁴⁹ which constantly digitizes the signal from the APFEL. Next, the data will undergo an online feature extraction⁵⁰ realized by FPGAs⁵¹ which can manage pile-up recovery. Each hit is assigned to a precise timestamp by a global clock at 1.25 GHz which initializes all SADC channels [92]. Afterwards, the hit information is extracted through a serial optical link connection cable into a DMUX⁵² module, outside the EMC. The DMUX is respon-

⁴³Digital to analog converter
⁴⁴Field-programmable gate array
⁴⁵Graphics processing unit
⁴⁶Synchronization of data acquisition
⁴⁷Data acquisition
⁴⁸Sampling analog-to-digital converter
⁴⁹Mega-samples per second
⁵⁰Signal height and event time
⁵¹field-programmable gate array
⁵²Data multiplexer

sible for pile-up recovery as well as for the time synchronization. In general, the readout consists of a digitizer, data concentrator as well as a DAQ⁵³. The DCON⁵⁴ then fulfills time ordering via leading edge, pile-up recovery as well as time synchronization. The final event selection which considers information of all subdetectors, is done by a compute node connected via a high bandwidth network which manages cluster finding and pattern recognition in a first stage. In a second stage event building is done by calculating physical parameters [127].

Finally, the complete process comprises particle detection over signal generation to event reconstruction as following:

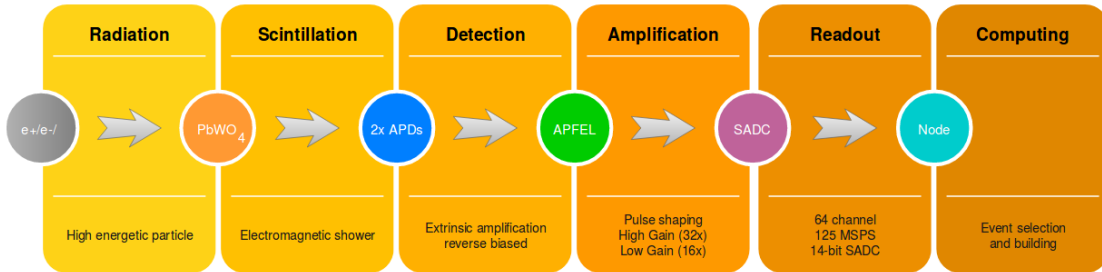


Figure 47: **Scheme of the complete process.** Radiation impinges on the scintillation crystal and causes an excitation by creating an electron-hole pair. De-excitation will result in the emission of characteristic light which enters the Avalanche photodiode. There, it will produce again an electron-hole pair and causes an avalanche multiplication where electrons lead to many ionizations. The APFEL preamplifier will pick this signal up, amplify and shape it. The signal will be forwarded to SADC where it will be digitized. Subsequently, the signals pass an online feature extraction. Finally, an event selection will be performed and build up the events.

⁵³Data acquisition

⁵⁴Data concentrator

Part 2

Matching

“A good decision is based on knowledge and not on numbers.”

Plato

The scintillation light of each crystal is converted into an energy-correlated charge quantity by two independent photodiodes. To achieve the highest possible benefit out of the APDs, it is important to assign them to each other in such a way that their **individual properties** are as **close to each other** as possible. Therefore, the operational parameters of each APD have to be determined very precisely. Furthermore, by taking into account these parameters before and after an irradiation process, the following approach attempts to ensure an identical behaviour of paired APDs not only when mounted but also throughout their experimental operation period. The APDs studied in the following are part of the first slice of the $\bar{\text{P}}\text{ANDA-EMC}$ which is being constructed as of this writing. These APDs were evaluated, matched and glued to crystals following an approach which showed potential for improvement. Thus, the approach presented here aims to improve the existing procedures and will highlight and clarify differences.

6 APD Parameters

The most fundamental parameter of an APD is its **bias voltage** since it determines an APD's internal multiplication factor or amplification gain M . Because the M - V curve of an APD is strongly nonlinear, the parameters change heavily with increasing voltage, especially when exceeding the reverse breakdown voltage. This makes it important to describe the **nonlinear** behaviour as precisely as possible. Another parameter of interest is the individual slope dM at the operation point of an APD which changes according to the applied bias voltage by:

$$\frac{1}{M} \frac{dM}{dV} = \epsilon \rightarrow dV \cdot \epsilon = dM/M \quad (2.1)$$

Considering the slope guarantees that assigned pairs of two APDs behave as similar as possible over time because irradiation influences are able to change the operational parameters (see [Radiation damages](#) on page 47). This means, when APD1 drifts in its parameters, for example, due to irradiation, APD2 should behave exactly the same - and in the same manner. The influence of fluctuations of the bias voltage of the APDs on the energy resolution has already been studied by [155].

The following ansatz is chosen to ensure that the readout signals of both APDs deliver the same output signal for an event. Overall, **four parameters** have to be determined:

$$U_{\text{bias}} \quad | \quad U_{\text{bias,irr}} \quad || \quad dM \quad | \quad dM_{\text{irr}}$$

Since these parameters were not measured directly, a regression modelling of the APD's M - V curve is necessary. This allows to determine the required individual bias voltage of each APD together with the corresponding slope. This certain voltage has to be obtained by an inverse regression because all the APDs provide the same multiplication gain of $M = 150$, in case of the barrel part of the EMC. The APDs of the backward endcap will operate at $M = 200$ and those of the forward endcap at $M = 100$. The CMS uses a gain of $M = 50$ which provides a compromise between noise and stability [46]. Further requirements are put on the APDs and their peripheral hardware like a temperature stability of $\Delta T = \pm 0.1$ °C at -25 °C and a voltage stability of $\Delta U_{\text{bias}} = \pm 0.1$ V [154].

6.1 APD screening

QA tests and measurements of the APDs are done by the PhotoSensitive Laboratory (PSL) at GSI. There, each APD is measured in regard to bias voltage, amplification and dark current. The devices are put in an opaque box and measured as long as a bias voltage of 500 V or a dark current of 100 μA is not reached. The incremental step size of the applied voltage is arbitrary (see 56). Hence, this procedure is performed at four temperatures.

Afterwards, the APDs will be **irradiated** with γ 's from a Cobalt source at the Strahlzentrum in Giessen. There, the APDs are staggered in receptacle boxes, each providing 20 APDs in a grid. The cobalt source is located at a certain height and the grids are placed in a fixed distance away from the cobalt sources. The conditions are an irradiation dosis of 30 Gy during a period of time of 90 minutes at $T = 20\text{ }^\circ\text{C}$. The APDs are operated with an applied bias voltage fulfilling a gain of $M = 100$.

In a next step, the APDs are annealed in an oven for 9 hours at a temperature of $80\text{ }^\circ\text{C}$ at a bias voltage of 300 V at the GSI. Then, the initial measurements are repeated. Finally, this procedure yields parameters of each APD before and after an irradiation.

Since major diode to diode variations occur in the gain-voltage curve, it is necessary to determine the quiescent point parameters for each APD **individually**.

6.1.1 Cluster analysis

To get started, the APDs have to be classified which is done by the manufacturer, **Hamamatsu**: The highest division is a lot which indicates that the production conditions for each APD in it are the same. Up to this writing, the latest produced lot is the one with the number 24 but some lot numbers in between are missing due to the manufacturer. The lots are subdivided into wafers while only a few lots comprise the maximum number 20 of wafers, again, due to the manufacturer. In contrast to the varying amount of wafers per lot, each wafer is cut into 20 APDs. Each single APD can be identified by its serial number which comprises the lot and the wafer number. This information, together with an additional number, the ID, forms the unambiguous serial number:

19	20	09913
Lot	Wafer	ID

The first two digits represent the lot in which the APD was produced in and the next two digits indicate the wafer from which the APD is diced. The general **hierarchy** is depicted in fig. 49:

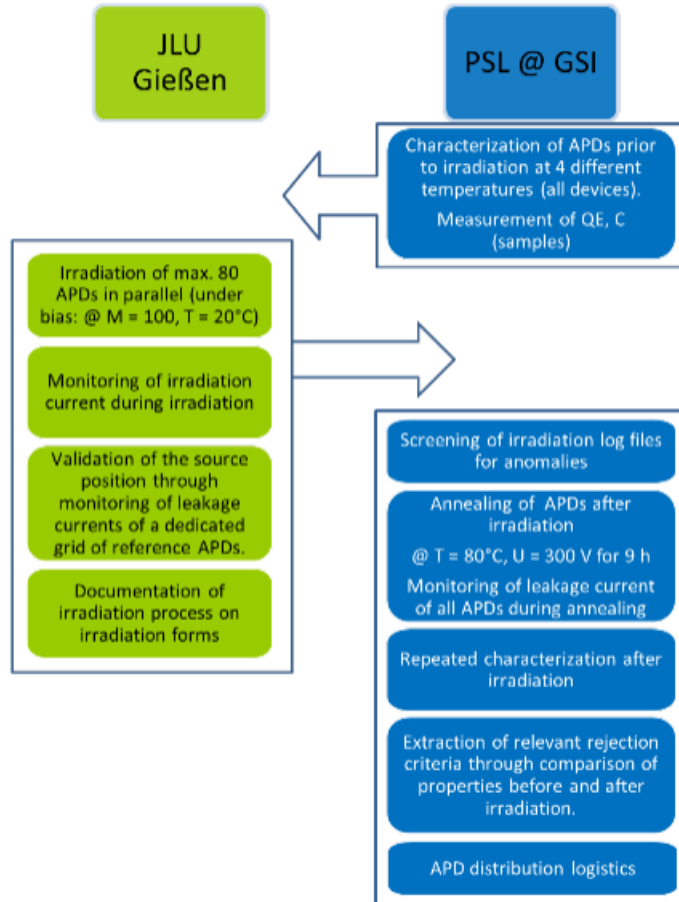


Figure 48: **Screening Flow Chart** [25]. The APDs are measured at the PSL, irradiated in Giessen and measured again at PSL.

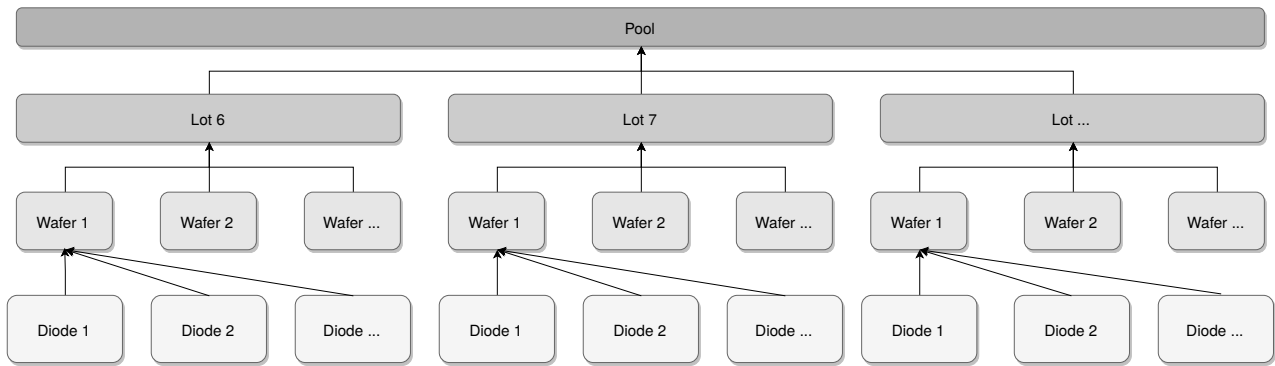


Figure 49: **Hierarchical structure of the Avalanche Photodiodes.** The pool comprises several lots which provide the same manufacturing conditions for all the APDs being part of the same lot. The lots are further subdivided into wafers of which each provides 20 APDs in total.

Within the following analysis, the wafers are labelled by adding the lot number to ensure an unambiguous assignment. For example, the „wafer 20” in „lot 19” is now tagged as „1920”. Since the APDs will be operated at $T = -25\text{ }^{\circ}\text{C}$, only measurements at this temperature will be considered from here on. From an analytical perspective it is useful to get an overview at first about the involved structures and clusters:

The structure of the APD pool can be clustered into 10 lots which split into 63 wafers. All these wafers together comprise 1,000 APDs. Only 1,000 APDs are considered here in this study though a slice contains 1,420 APDs. A list of these 1,000 APDs can be found on page 229.

Lots	Wafers	APDs
10	63	1000
Data points	Irradiated	not irradiated
147752	74064	73688

Furthermore, the data consists of 147752 data points which split up into 74064 data points after and 73688 data points before the irradiation. A data point refers to a single observation as a 2-tuple (V, M) of voltage V and amplification M . To the right in fig. 50, the share of lots is given relative to the pool of observations. There, some lots are much more present than others.

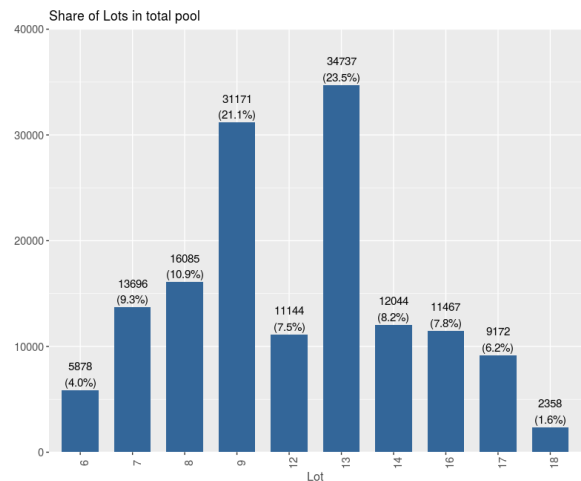


Figure 50: **Share of Lots relative to the pool of observations.** The Lots 9 and 13 are the most present while Lot 18 and 6 are hardly represented.

In addition to the share of lots (fig. 50), the share of wafers indicates that the number of wafers correlates to the number of lots (see 197). Since these classifications reflect manufacturing and/or measurement conditions, it is open whether deviations within the divisions will appear in the following. However, the data pool reveals some inconsistencies in these measurements (see fig. 51). Each APD comprises a certain amount of data points (V, M) and the start and end values of voltage and amplification differ in many cases. This points out the heterogeneity of the measurements and, especially in case of the upper amplification values, differences are obvious. A reason might be caused by the strong nonlinear behaviour of an APD because when the applied voltage exceeds the breakdown voltage, the amplification rises rapidly.

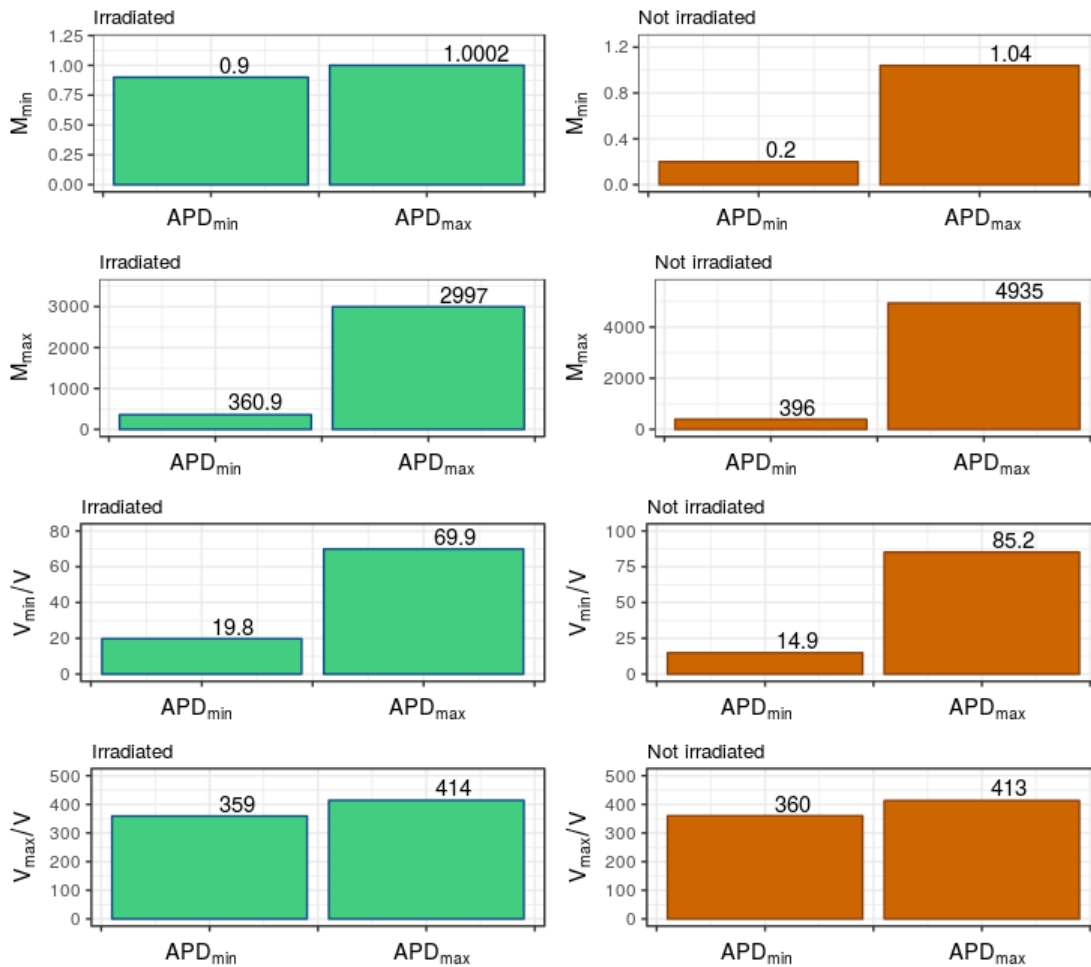


Figure 51: *Deviations in amplification and voltage measurement points.* Left - irradiated data. Right - not irradiated data. Each bar depicts a single APD with the lowest observed value (*min*) together with a single APD with the highest observed value (*max*), respectively.

The highest measured amplification gain of an irradiated APD is about 3,000 and the lowest value for the maximum amplification gain is about 360. In case of the APDs before the irradiation, the highest amplification gain is about 5,000 and the lowest maximum amplification gain is about 400. The corresponding applied bias voltages do not show such a discrepancy as the minimum and maximum voltages are quite similar before and after the irradiation. Despite from that, the measured minimum amplification gains are about 1 for the irradiated APDs but the data before the irradiation provides values even with 0.2. This reveals that the measurements were not taken systematically or something happened during the measurements. Especially when performing a regression analysis later, this circumstances have to be taken into account.

Since several parameters are of interest, it is worth to focus not only on univariate methods but also on multivariate ones. Thus, for example, a three-dimensional view of lot, voltage and amplification is potentially able to provide lot-to-lot differences (fig. 52):

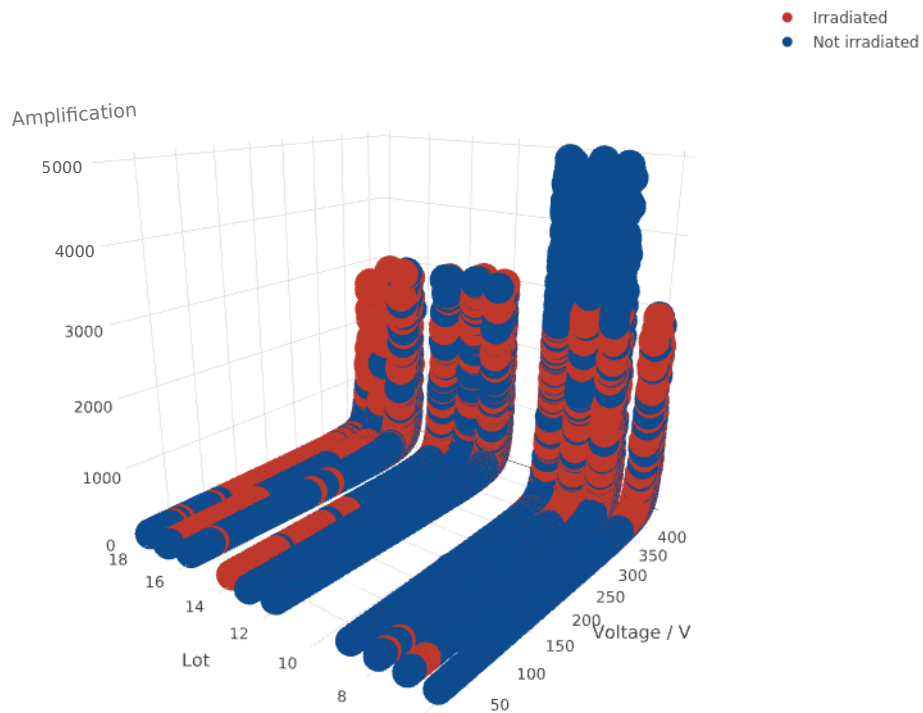


Figure 52: *Amplification as a function of voltage and lot.* The data pool shows that the APDs of the lots 7 to 10 reached a higher amplification than the other APDs did, but only in case of pre-irradiation data.

It turns out that the lots 7 – 9 provide much more data points before the irradiation respectively at least up to higher values. Despite that, the data pool looks similar across all lots. Nevertheless, due to the ratio of irradiated and not irradiated data points per lot it can be seen that the APDs were measured differently. In fig. 53 it is shown that the number of data points vary from APD to APD. Though, the greatest part provides the same amount of data points with a number of about 71 ± 5 . In general, a great part of the irradiated APDs provide about 2 data points more. As a consequence, for example, the settings of an interpolation model might have to be adjusted differently for some APDs.

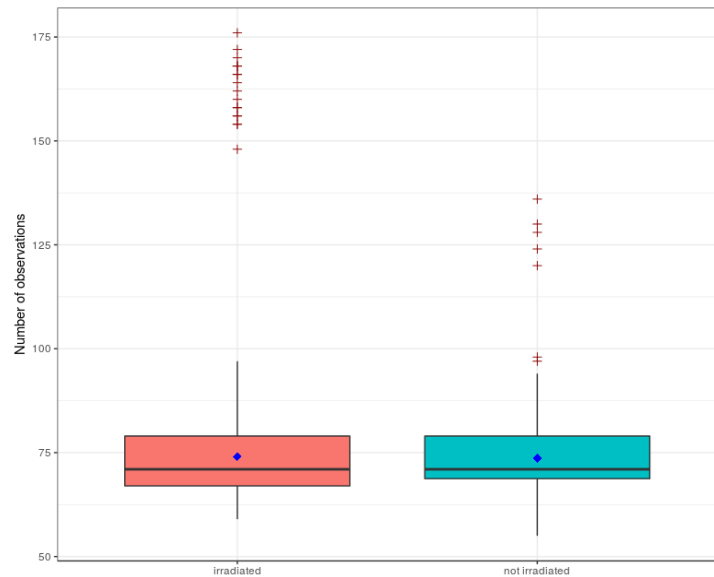


Figure 53: *Number of data points per APD.* The number of data points as a box plot with a mean of about 73 and a median of about 70.

6.2 Parameter extraction

“All Models are wrong, but some are useful.”

Thomas Bayes

Diodes can be described in very different ways and each method provides different requirements and advantages. Though ASA⁵⁵ is a quite common method to describe electronic components and to discover defects, it is not applicable to determine the operational parameters, as a comparison between the measured characteristic curve and a reference curve will not yield any properties for application purposes. Accordingly, it is commonly applied in earlier stages, for example by the manufacturer or in the QA stage of the client. Nevertheless, even then variations among the devices can hardly be avoided and tolerance limits will dictate their further usage. Generally, as already described in Avalanche Photodiode on page 41, diodes provide a **strong relationship** between voltage and current. The way how a diode follows this connection represents commonly its type. For this reason, several models exist to describe the variety of diodes specifically and it has to be decided whether these models are sufficient respectively applicable.

This topic is under the general situation that the present APDs do not provide data points at the specific gain of $M = 150$. Hence, the goal to determine the corresponding bias voltage results in an **interpolation** task. In the following, on the basis of a simplification, the axis on the plots will often be depicted without units. In such cases, the unit of the independent axis is given in Voltage [V] and the dependent axis is unitless and represents the amplification M . Furthermore, irradiated data will be colored in **green** and not irradiated data in **orange**.

6.2.1 Diode regression modelling

Generally, a method is required to study the relationship between a response variable y and its explanatory variable x . Diodes, especially APDs, possess a strong **nonlinear** characteristic according to $c \cdot M(V) \neq M(c \cdot V)$. Thus, such a device does not provide a simple characteristic curve which can easily be solved mathematically. Furthermore, since the goal is to determine the corresponding bias voltage at which the diode provides a gain of $M = 150$, the need for an inverse regression arises. Given that, not $E[M|V=v]$ is required but $E[V|M=v]$. The aimed point on the curve providing a specific bias current and voltage is called the **q-point**⁵⁶.

In electronics, a common way to describe the non-linear behavior of diodes is to use signal modelling. The signal model of a diode is given by $I_D = I_S (e^{U_F/nU_T} - 1)$, with U_F as the forward voltage, I_S as the reverse current and $U_T = k_B \cdot T/q$ as the temperature voltage. Since this expression is used for a large signal behaviour and rather used for the forward region, it is not assumed to be applicable to the reverse region. Additionally, the needed input parameters are not available anyway.

Another approach is to calculate the q-point by using the specific knowledge of the electronic circuit. This is not applicable too, as all devices provide certain parameter tolerances and specific property deviations.

A quite simple and fast method is the piecewise linear model in which the characteristic curve is broken down into several linear segments (see fig. 54). Considering only two segments, the curve, until the breakdown voltage is reached, could be described by a line segment with almost no slope and a line segment describing the rise of the curve, embodying the breakdown voltage as a tangent. Despite many uncertainties among the present APDs like varying slopes, unequal numbers of data points, different incremental steps and so on, this is a quite satisfactory solution to roughly determine at least the breakdown voltage, as it behaves approximatively as a tangent of the characteristic curve. However, this approach is in general not as precise as necessary and the bias voltage cannot be obtained this way anyhow. Therefore, it has to be determined through a regression analysis.

Regression analysis is the determination of an analytic expression to describe the relationship between two (or more) variables. One is the so-called **predictor** variable or independent variable, and the other is the **response** variable or dependent variable.

Standard regression models do not account for measurement errors in the predictor variables and assume that

⁵⁵Analog signature analysis

⁵⁶Quiescent point

the measurements were observed without errors. Since available voltage meters and especially ammeters are quite precise, measurement errors are omitted in this analysis. Hence, EoV⁵⁷-models are not considered here. Furthermore, as an **inverse regression** is targeted, it has to be kept in mind that regression is not symmetric to the variables since predicting the dependent variable by the independent one is different from predicting the independent variable by the dependent variable. In principle, an expression is sought which can be shortly described as $Y(x) = f(x) + e$, where $Y(x)$ is the targeted response variable, $f(x)$ is the analytic function to describe the relationship between x and $Y(x)$, and e is a stochastic error term.

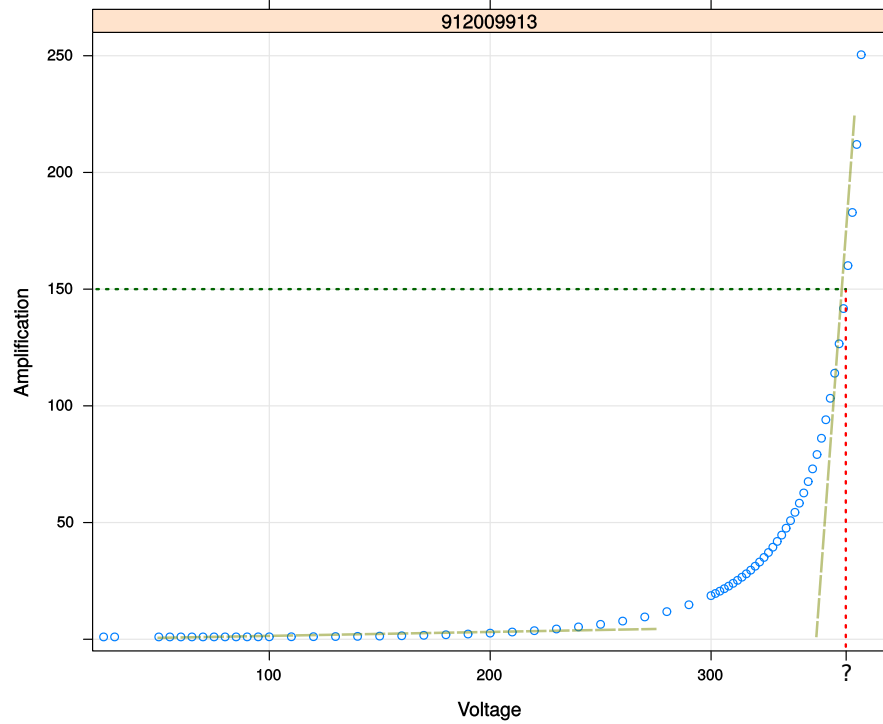


Figure 54: **Determining the bias voltage.** To calculate the individual bias voltage, an inverse regression is necessary because the amplification is preset. Depicted data is taken from the irradiated APD 912009913.

6.2.1.1 Estimation methods and coefficients of determination To perform a regression model, several methods are available and some are very similar to each other and may differ very specifically in minor aspects. The most important term is the **residual** $\hat{\epsilon}_i$ which represents the vertical distance between a measured point (x_i, y_i) and the estimated point \hat{y}_i . In case of a simple linear regression it is given by $\hat{\epsilon}_i = y_i - \hat{y}_i = y_i - \hat{\beta}_0 - \hat{\beta}_1 x_i$ which represents a linear model. There, y_i is the response vector, β_i are unknown parameters which have to be estimated and x_i is a vector of observations which represents the predictor variable. The relationship between the dependent and the independent variable is explained by the **linear parameters** β_i .

A linear model is often expressed with the help of a design matrix X which contains the explanatory variables x_i while the parameters β_i are collected in a parameter vector β [160]:

$$Y = X\beta + \epsilon \quad \epsilon \sim \mathcal{N}(0, \sigma^2) \quad (2.2)$$

The error term ϵ collects all factors that influence the response variable differently than the predictor would do exclusively, also known as noise or disturbance. In linear models these errors are assumed to be distributed normally around an expectation value $E(Y)$ with variance σ^2 . A useful tool to describe how well a function

⁵⁷Errors-in-variables

describes the relationship between y_i and x_i , is the $RSS^{58} = \sum_{i=1}^n (y_i - f(x_i))^2 = \sum_{i=1}^n (\hat{\epsilon}_i)^2$. Actually, RSS is the sum of squares of the residuals and $f(x_i)$ is the predicted value of y_i and in other terms: $RSS = \hat{\epsilon}^T \hat{\epsilon} = \|\hat{\epsilon}\|^2$. A small RSS presents a close approximation of the model to the data. A model is considered as the best candidate when it provides the best value of an objective function. For nonlinear models, R^2 is not available as it is based on linear models due to the sum of the errors [55], therefore $\chi^2 = \sum_{i=1}^k (O_i - E_i)^2 / E_i$, with o as an observed value and e as an expected value, is a better choice. The selection of a model can be performed by utilizing additional tools:

Least squares In the actual context, the least squares method aims at minimizing the value of $RSS = S \Rightarrow \min S$. It can be found by setting the gradient to zero: $\partial S / \partial \beta_j = 2 \sum (y_i - f(x_i)) \partial (y_i - f(x_i)) / \partial \beta_j$, with $j \in [0, m]$ as the numbers of parameters m . To perform the least squares technique, a few prerequisites must be fulfilled, e.g., the residuals must be distributed normally. To solve nonlinear relationships, a ML⁵⁹-method is often preferred over least squares. The same applies if the sample is rather small because least squares is very prone against outliers.

Maximum Likelihood The ML⁶⁰ estimation takes the observations and chooses parameters which make them most likely. This method is based on the assumption that each part of a set is member of the same distribution. The total likelihood L of a set of independent observations x_i with the parameters θ_i is the product of the likelihood of each:

$$\begin{aligned} L(x_i|\theta) &= p(f(x_1|\theta)) \cdot p(f(x_2|\theta)) \cdot p(f(x_3|\theta)) \cdot \dots \cdot p(f(x_N|\theta)) \\ &= \prod_{i=1}^n p(f(x_i|\theta)) \end{aligned}$$

and is normalized to 1 according to a probability density function: $\int L(x_i|\theta) dx_i = 1$. To achieve a better calculation, the logarithm can be utilized which allows using sums instead of a product [160]:

$$\begin{aligned} \ln(L(x_i|\theta_i)) &= \ln(p(f(x_1|\theta)) \cdot p(f(x_2|\theta)) \cdot p(f(x_3|\theta)) \cdot \dots \cdot p(f(x_n|\theta))) \\ \mathcal{L}(x_i|\theta_i) &= \ln(p(f(x_1|\theta))) + \ln(p(f(x_2|\theta))) + \ln(p(f(x_3|\theta))) + \dots + \ln(p(f(x_N|\theta))) \\ &= \sum \ln(p(f(x_i|\theta))) \end{aligned}$$

Maximizing $\mathcal{L}(x_i|\theta_i)$ means to find $\hat{\theta}^{ML} = \arg \max [\mathcal{L}(x_i|\theta_i)]$ which requires to solve $\partial \mathcal{L}(x_i|\theta_i) / \partial \theta_i = 0$ and $\partial^2 \mathcal{L}(x_i|\theta_i) / \partial^2 \theta_i < 0$. This leads to a drawback of the likelihood method as it often makes numerical approaches necessary which can result in difficult optimization problems and faulty interpretations. The variance of the ML estimator $\hat{\theta}^{ML}$ can be extracted from the inverse of the information matrix $\text{Var}(\theta) = [I(\theta)]^{-1}$ and can be found by using the negative of the expected value of the Hessian matrix: $i(\theta) = -E[H(\theta)]$ with $H(\theta) = \partial^2 \ln \mathcal{L}(\theta) / \partial \theta \partial \theta'$. Consequently, the standard errors of $\hat{\theta}$ are the square roots of the diagonals of the variance-covariance matrix: $\text{sqrt}(i(\hat{\theta})_{jj}^{-1})$ [160].

Another tool is the **anova**⁶¹-test which is helpful to make a decision between a set of models. It analyzes the influence of factors to the dependent variable. A variance analysis is performed such that, for example, the hypothesis H_0 is checked that the mean values, μ_i, μ_j with $i \neq j$, of two (equivalent to a t-test) or more (anova) sets are different:

$$\begin{aligned} H_0 : \mu_i &= \mu_j && \text{Null hypothesis} \\ H_1 : \mu_l &\neq \mu_m && \text{Alternative hypothesis} \end{aligned}$$

⁵⁸Residual sums of squares

⁵⁹Maximum Likelihood

⁶⁰Maximum likelihood

⁶¹Analysis of variance

where μ_l and μ_m are the mean values of samples being not part of the test. The null hypothesis is valid when there is no significant difference between the sample means. This leads to the assumption that they are part of a larger set of the same sample. Finally, anova looks at variations in the data and compares the amount of deviations *within* groups with the amount of deviations *between* groups, according to $x_{ij} = \mu_i + \epsilon_{ij}$. There, x_{ij} represents the individual data points and ϵ_{ij} is the unexplained variation. This means, the null hypothesis aims at the assumption that it is valid for the sample and differences among different sets are consequence of random chances. To evaluate if differences are significant or not, the p-value will be used which can e.g. be obtained by using the chi-squared test $\chi^2 = \sum (o - e)^2 / e$, where o is the observed value and e is the expected value. With the help of look-up tables, the p-value can be achieved. A large **p-value** > 0.05 represents a weak evidence against the null hypothesis. It should not be confounded with an estimate of an error since a p-value indicates only the probability that the null hypothesis can statistically be regarded as true, without knowing if it is really true.

Pearson correlation To measure the linear correlation between two variables, the Pearson correlation coefficient r can be used:

$$r = \frac{\sum_{i=1}^n (x_i - \bar{x})(y_i - \bar{y})}{\sqrt{\sum_{i=1}^n (x_i - \bar{x})^2} \sqrt{\sum_{i=1}^n (y_i - \bar{y})^2}} \quad (2.3)$$

Varying between -1 and $+1$, it indicates if a variable is correlated positively or negatively with another variable. A value of 0 indicates no linear relationship, however nonlinear relationships are possible. Even if we can measure the correlation, we still need to determine how good any value of r is. r^2 (nonlinear) or R^2 (linear) represents the coefficient of determination. This is possible by having a look at its significance which represents the probability of the targeted variable to be true. Hence, R^2 represents the ratio between the explained variance and the total variance of the explanatory variable. In addition, there is the so-called adjusted R^2 which was introduced to solve a problem which arises by using R^2 : The more explanatory variables are used the higher the value of R^2 will be, leading to a so-called “overfitting” and favouring the largest model. Such a model will provide bad prediction performances. Therefore, the adjusted R^2 considers the number k of independent variables and penalizes the outcome accordingly. Furthermore, it takes into account the sample size n [88]:

$$R_{adj}^2 = 1 - \frac{RSS / (n - k)}{TSS / (n - 1)} \quad (2.4)$$

with TSS as the total sums of squares, given by $TSS = \sum_{i=1}^n (y_i - \bar{y})^2$. The higher this value, the more precise is the candidate model. A possibility to compare different models are AIC ⁶² and BIC ⁶³ [87]:

$$AIC = 2k - 2 \log(L) \quad (2.5)$$

$$BIC = \log(n)k - 2 \log(L) \quad (2.6)$$

Both criteria use the log-Likelihood method which makes use of the maximum value \hat{L} of the likelihood function. The better a model can explain the underlying data, the lower both values will be. To avoid preferring models which are complex, a penalty is taken into account again which, in turn, increases both values when parameters are added. The AIC and BIC differ from each other such that they penalize in another way as it is $2k$ in case of AIC and $\log(n)k$ in case of BIC . Nevertheless, both criteria should be applied for distinct purposes: AIC is a better choice to select the model which has to describe unknown data with many dimensions. While AIC is assumed to fit complex data better, it actually does not consider if the candidate models are true. BIC is more suitable to find the true model of the former candidates.

⁶²Akaike-Information-Criterion

⁶³Bayesian-Information-Criterion

6.2.1.2 Empirical relationship In the following, the response variable Y and the amplification gain M will be used simultaneously and the same is valid for the explanatory variable X and the voltage V . An empirical relationship to describe the functional behaviour of an APD is given by

$$M = \frac{I - I_{MD}}{I_p - I_D} = \left[1 - \left(\frac{V_R - IR_S}{V_B} \right)^n \right]^{-1} \quad (2.7)$$

which makes use of the circuit components or rather of the applied and measured values. I_{MD} is the multiplied dark current, I_p is the primary photocurrent and I_D is the primary dark current. Instead of the currents, the voltages can be used as well: V_R is the reverse bias-voltage, V_B is the breakdown voltage and n is a constant that depends on the semiconductor properties, especially on the doping profile [152]. A deduced, common and more handy expression is the so-called “Miller-fit”, [104], [143]:

$$M(V) = \frac{1}{1 - \left(\frac{V}{p_0} \right)^{p_1}} + p_2 \quad (2.8)$$

The parameters are given as following: V is the applied voltage, p_0 represents the breakdown voltage and p_1 , p_2 are fit parameters. The PSL database provides two series of measurement data: Raw data measurement points and fitted values obtained by performing the Miller fit. Both do not provide the needed bias voltage at $M = 150$. Thus, a Miller fit is performed via the CERN ROOT framework. The following plot shows the Miller fit for the diode 711006317:

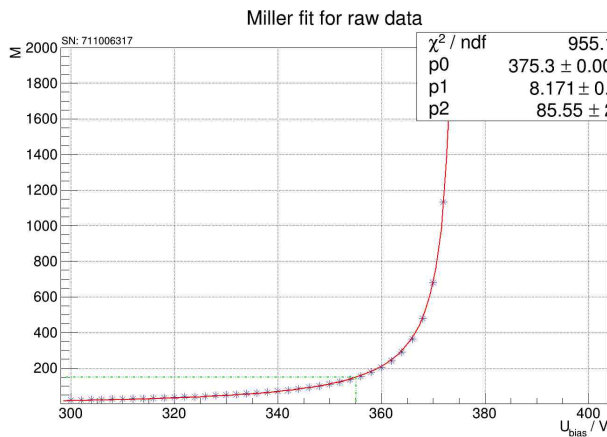


Figure 55: *Miller Fit for irradiated APD 711006317.*

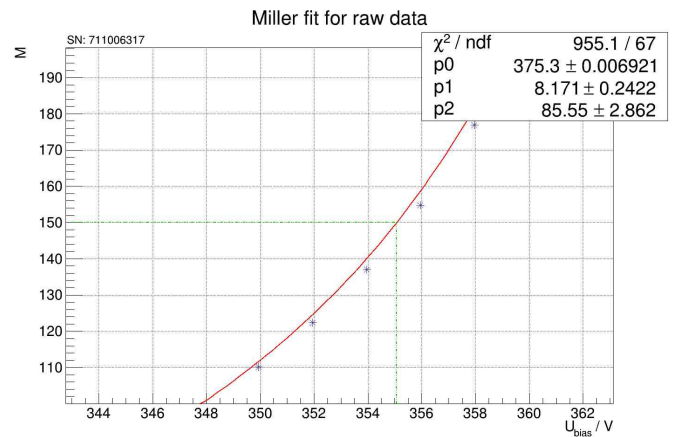


Figure 56: *Miller Fit zoomed.*

Table 9: *Parameter influence on the fit in ROOT.* The initial parameters are $p_0 = 375$, $p_1 = 1.2$ and $p_2 = 1.0$. Two parameters are fixed to these values when changing the third. To the right, the exemplary influence of these parameters is studied for the APD 711006317:

p_0	U_{bias}	p_1	U_{bias}	p_2	U_{bias}
340	355.054	0.9	355.45	0.7	355.45
350	354.084	1.0	355.45	0.8	355.45
360	355.45	1.1	355.45	0.9	355.45
370	355.45	1.2	355.45	1.0	355.45
380	355.45	1.3	355.45	1.1	355.45
390	355.45	1.4	355.45	1.2	355.45

The estimated bias voltage is quite independent from the choice of parameters, only the breakdown voltage affects the estimation. When p_0 is not adjusted individually for each APD, it will result in a bad fit. Overall, it is quite time-consuming to check the parameters for each APD manually. The Miller fit works well at high gains but the estimated values are often rather poor in moderate gains up to 200. Nevertheless, it is a solid expression and fast to implement but the fit results are not satisfying enough. It remains open how to apply the Miller fit. How well the fit can describe the data depends strongly on the diodes. In the majority, it is sufficient to check the APDs by eye. In the following an overview of 14,000 not irradiated APDs:

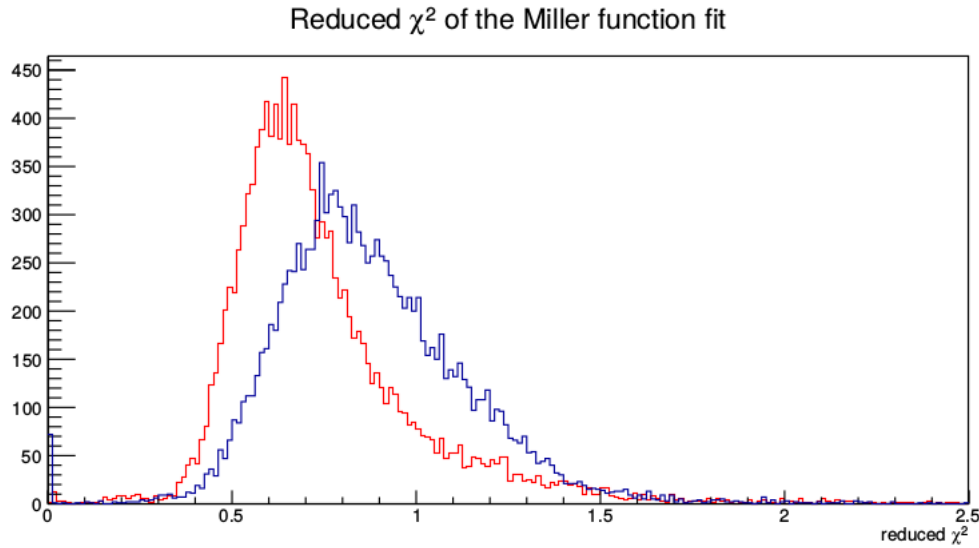


Figure 57: χ_{red}^2 of the Miller fit [157]. The blue lines represents data at $-25\text{ }^\circ\text{C}$ and the red line at $20\text{ }^\circ\text{C}$. Here, a slightly modified Miller formula is used: $M(V) = p_2 / (1 - (V/p_0)^{p_1}) + 1 - p_2$.

The expectation value of χ^2 is 1. Goodness of fit is $\tilde{\chi}_{red}^2 = \chi^2 / ndf$ with ndf as the number of parameters and when $\tilde{\chi}_{red}^2$ differs significantly from 1, it indicates that the regression formula is not describing the relationship very well. A very low χ_{red}^2 occurs, e.g., when using too few data points and indicates that it is at least misleading to measure the goodness of the fit.

Nonlinear least squares The Miller-Fit is checked with another approach to ensure that the unclear results are not based on ROOT and that the outcome is not too dependent on the choice of parameters. Hence, the bias voltage is estimated with a self-starting nls-model⁶⁴. A **nonlinear** model is given by:

$$Y = f(X, \beta) + \varepsilon \quad (2.9)$$

where the unknown parameters β_i are not linear anymore. The method of least squares remains to estimate their values. Thus, the task is to find a minimizer β^* of f , therefore: $\min_x f(\beta) = (1/2) \sum_{i=1} r_i^2(\beta)^2$. This must not be confounded with the situation when also linear parameters show nonlinear effects. Nonlinear models are advised to be applied when the underlying relationship satisfies a nonlinear assumption, like growth models do. Nonlinear least squares extend the linear regression with a larger set of functions which is the most important advantage over other techniques. The **parameters** of the Miller formula are nonlinear, thus, it is assumed that a nonlinear approach is more succesful. Hence, this method could describe an asymptotic process quite well which is the case when an APD reaches the breakdown voltage. The nonlinear approach is conducted by using

⁶⁴Nonlinear least squares

the *nls* model of the *nlme*⁶⁵ package, available for R⁶⁶ [86]. Since *nls* is a self starting model, the self starting values have to be estimated in advance:

$$\frac{p_0}{\max(V) \cdot 1.01} \quad \left| \quad \frac{p_1}{0.1} \quad \left| \quad \frac{p_2}{-10} \right. \right.$$

The parameter p_0 is estimated such that the maximum available voltage value is extracted and multiplied by 1.01. This calculation estimates the breakdown voltage. The parameters p_1 and p_2 are obtained empirically. When the parameters are not estimated in advance, they will be guessed rather poorly.

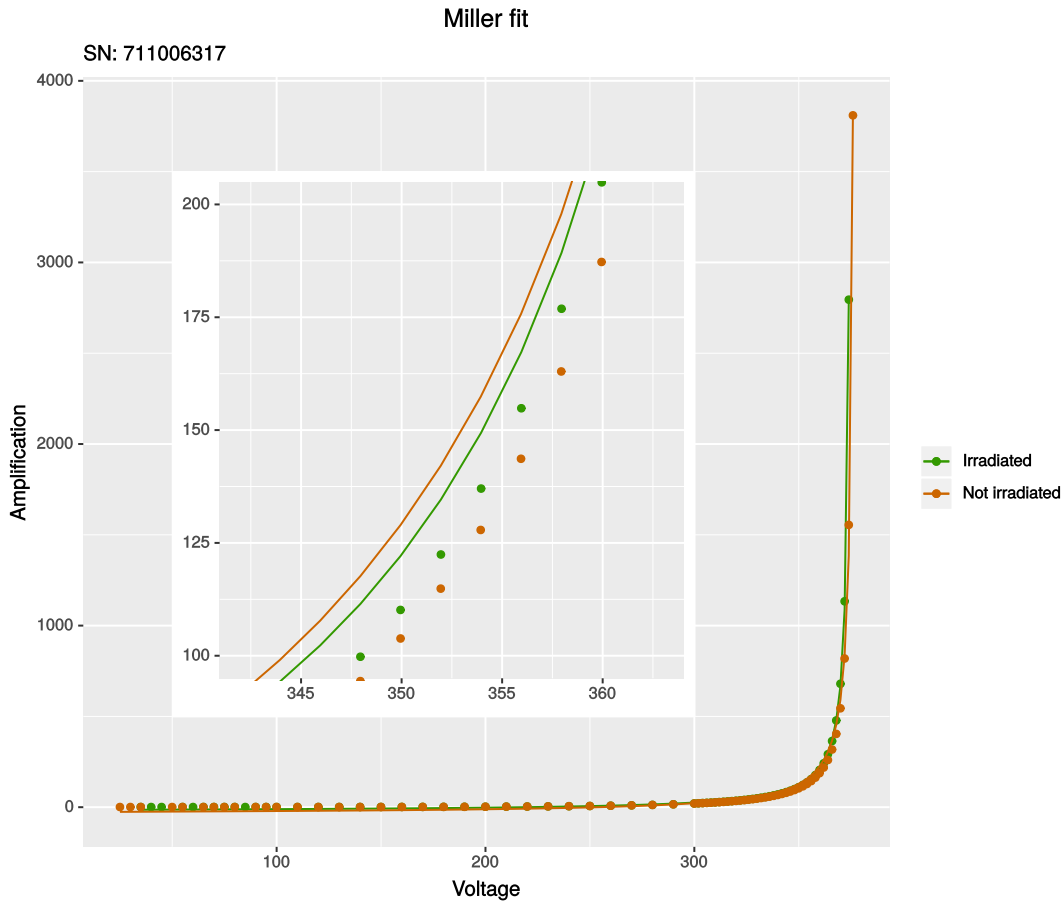


Figure 58: **Nonlinear least square fit.** The *nls* model is performed within the *nls* framework of R. The fit does not match the data precisely, especially in case of the pre-irradiation data.

The value of p_2 is already indicating that this fit is not matching the data perfectly. The *nls* models performs quite well but it does not converge in many cases for the not irradiated data. For example, for the irradiated APD 6080004649 no self-starting values can be found whereas for the APD 711006317 self-starting values are very easy to estimate. Limiting the range of the independent variable does not help to solve this problem. It seems that the nonlinear model is ill-posed as the data indicates asymptotes at $M = 1$ and $V = 370 - 400$ which fix p_0 and p_2 , leaving only p_1 to match the rest of the data (see table 10). Hence, the model cannot converge. Adding further parameters to the function does not help either. In the following, the investigated parameters for the *nls* Miller-Fit are:

⁶⁵Linear and Nonlinear Mixed Effects Models

⁶⁶Programming language for statistical computing

p_0	U_{bias}	p_1	U_{bias}	p_2	U_{bias}
340		0.9	354.0337	0.7	354.0337
350		1.0	354.0337	0.8	354.0337
360		1.1	354.0337	0.9	354.0337
370		1.2	354.0337	1.0	354.0337
380	355.45	1.3	354.0337	1	354.0337
390		1.4	354.0337	1.2	354.0337

Table 10: **Parameter influence on the fit in R.** Only the selection of parameter p_0 lead to a converging result for the APD 711006317. Then, the bias voltage is the same like it is in the ROOT framework. However, this does not work for many other APDs. The standard parameters are chosen as $p_0 = 380$, $p_1 = 1.2$ and $p_2 = 1.0$. Fixing the parameter p_0 and a change of the other parameters does not result in any changes of the bias voltage.

A general drawback of nls is the necessary effort to conduct iterative optimization procedures. In comparison to linear regression models, the parameters can hardly be calculated analytically. This makes the use of start values mandatory which have to be estimated already close to the optimum values. Otherwise, the model will not converge. Even if it does, there is a significant probability that local minima are found instead of the global minimum. Furthermore, nonlinear regression models are sensitive to outliers. The nls package works in optimizing a fit through χ^2 . Since the goodness of a fit is more a subproblem in the larger task of determining a proper model, it is not investigated here as the model is not matching the data sufficiently. Other approaches are briefly explained in the following:

Linear transformation Another approach is to transform the data to remove the nonlinearity behaviour as good as possible. This can be done via defining the amplification value $M = 150$ as a reference to which the other data points (M_i, V_i) relate to by the mean of a difference. This means, that all data points below this value will lie in a negative range and the values above in a positive one. The zero of a curve crossing the line indicates the demanded amplification and the bias voltage. But due to the nonlinear behaviour even in the local environment of $M=150$ it is not assumed to embody the best choice.

Kernel smoother This local regression provides a rectangular window and considers only the data in there. Then, some properties can be applied like how smooth the fit shall be but it is complicated to perform as its necessary boundary conditions, like the bandwidth or distance size, are hard to determine reasonably. A special case of a Kernel smoother is the so-called moving average and is achieved by using a zero degree polynomial.

Differential fit Another model to use is a differential fit: $\partial Y \left(a(Y - 1)^b + c(A - 1)^d \right) = \partial X$. This fit is quite precise but since it is a differential fit it is susceptible to data fluctuations. Due to some inconsistent data structures, this fit is supposed to be applied only when the diodes are measured without any uncertainties like (local) measurement device failures or an noberved change of environment settings, for example, temperature or humidity. These are problems in general but a differential fit is prone to any single data point. In principle, this is a very precise fit and in the long run, it might be best choice but it requires quite a lot of calculation time of about 20 – 40 minutes per APD and each fit should be verified manually.

6.2.1.3 Polynomial A polynomial is mostly only an approximation of the true relationship but it can be assumed that it describes the relationship quite well in certain ranges. An important assumption of a polynomial is that the underlying relationship can be described by a smooth function. $n + 1$ datapoints can be described by a polynomial of n -th degree:

$$p(x) = \beta_0 + \beta_1x + \beta_2x^2 + \dots + \beta_nx^n \quad (2.10)$$

Generally, a polynomial of an order > 4 is dangerous as it may lead to over-fitting because an increasing degree results in a stronger oscillation between the supporting points (known as Runge phenomena). A high order polynomial will always fit the data better but it will result in poor prediction results.

Spline fits are single polynomials. A piecewise polynomial $f(x)$ is constructed by dividing X into contiguous intervals which are then represented by a separate polynomial in each interval: $p(x) = \beta_0 + \beta_1x + \beta_2x^2 + \dots + \beta_nx^n + \sum \beta_{n+k}(x - \kappa)^n$. Each of these polynomials is able to be of a different degree and describes only a certain range of data but being joined together at the knots⁶⁷ to reduce oscillation between the data points. The level of smoothness depends on the selected number of knots n . Finally, splines are piecewise polynomials embodying polynomial interpolations by losing the original relationship.

Whether a polynomial is able to describe the data can be simply checked by transforming the data: Since the diode behaviour is strongly nonlinear and the diode formulas for the forward region are containing an exponential function, it is assumed that a logarithmic transformation will make the relationship linear.

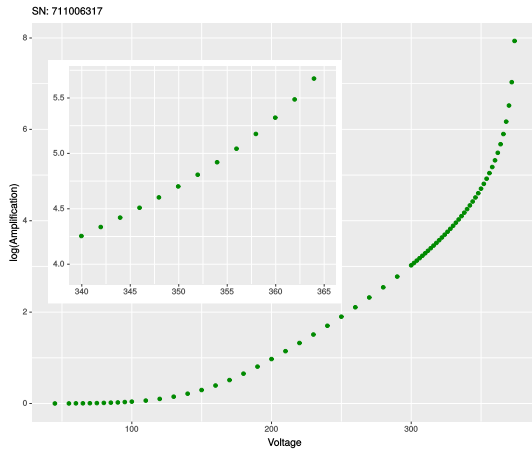


Figure 59: **Logarithmic transformation of APD 711006317.** The range of the zoomed region spans from $\ln(50) = 3.912$ to $\ln(300) = 5.7038$.

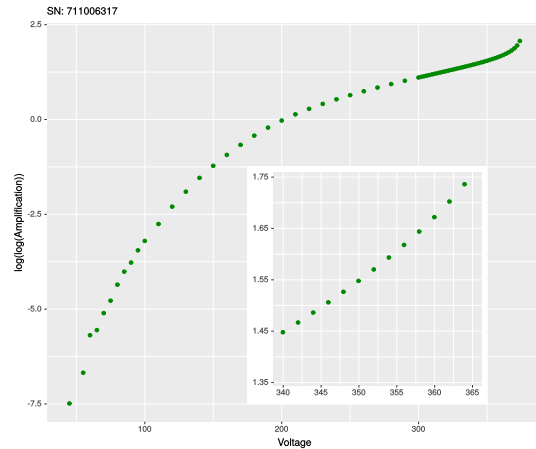


Figure 60: **Double logarithmic transformation of APD 711006317.** The range of the zoomed region spans from $\ln(\ln(50)) = 1.364$ to $\ln(\ln(300)) = 1.7411$.

Data points with an amplification < 1 are neglected in fig. 59 and in fig. 60. Furthermore, in R, “log” represents the natural logarithm “ln”. A general advantage of logarithms is that they are fairly stable against noise. Nonlinear shapes are still present, thus, a second logarithm transformation is performed (see fig. 60). Now, the data almost seems to satisfy a linear behaviour in the targeted region of $M = 100 - 200$.

To proceed, the data is fitted with raw polynomials of a 2nd and 3rd order for the logarithmical data as well as for the double logarithmic data. In addition, the R^2 -values and p -values of the corresponding models will be checked with anova for the APD 711006317:

⁶⁷interval endpoints

Logarithmic, polynomial 1st order

	p-value
Intercept	-2.0397745
1st order term	0.0188504
ndf	66
Multiple R^2	0.8771
R^2_{adj}	0.8752
F-statistic	471
p-value	2.2^{-16}

Table 11: *Goodness of fit: log-pol(1).*

Double logarithmic, polynomial 1st order

	p-value
Intercept	-5.6213131
1st order term	0.0216411
ndf	66
Multiple R^2	0.8938
R^2_{adj}	0.8922
F-statistic	555.4
p-value	2.2^{-16}

Table 12: *Goodness of fit: loglog-pol(1).*

Logarithmic, polynomial 2nd order

	p-value
Intercept	0.000101
1st order term	6.24^{-10}
2nd order term	2^{-16}
ndf	65
Multiple R^2	0.9724
R^2_{adj}	0.9716
F-statistic	1146
p-value	2.2^{-16}

Table 13: *Goodness of fit: log-pol(2).*

Double logarithmic, polynomial 2nd order

	p-value
Intercept	2^{-16}
1st order term	2^{-16}
2nd order term	2^{-16}
ndf	65
Multiple R^2	0.9812
R^2_{adj}	0.9807
F-statistic	1700
p-value	2.2^{-16}

Table 14: *Goodness of fit: loglog-pol(2).*

Logarithmic, polynomial 3rd order	
	p-value
Intercept	0.0.01392
1st order term	0.00498
2nd order term	0.00142
3rd order term	1.92^{-7}
ndf	64
Multiple R^2	0.982
R^2_{adj}	0.9812
F-statistic	1164
p-value	2.2^{-16}

Table 15: *Goodness of fit: log-pol(3).*

Double logarithmic, polynomial 3rd order	
	p-value
Intercept	2^{-16}
1st order term	2^{-16}
2nd order term	2^{-16}
3rd order term	2^{-16}
ndf	64
Multiple R^2	0.9987
R^2_{adj}	0.9987
F-statistic	16860
p-value	2.2^{-16}

Table 16: *Goodness of fit: loglog-pol(3).*

The p -value is determined by checking the null hypothesis that a polynomial coefficient is zero and the listed p -values in the bottom row consider the necessity of all implemented coefficient terms. A double logarithmic transformation promises the highest R^2 -value and the anova tests reveal that a polynomial of a third degree is the best model.

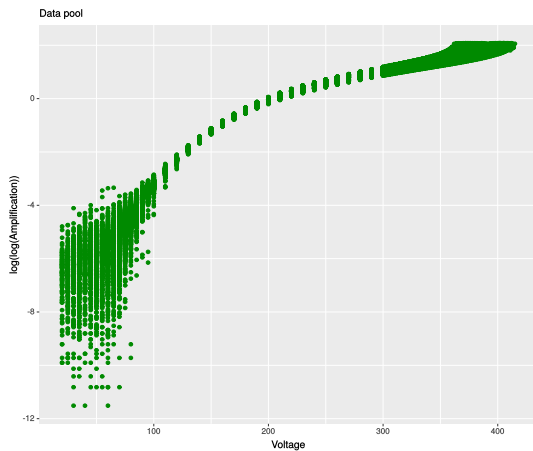


Figure 61: *Double logarithmic transformation of the irradiated APD pool.*

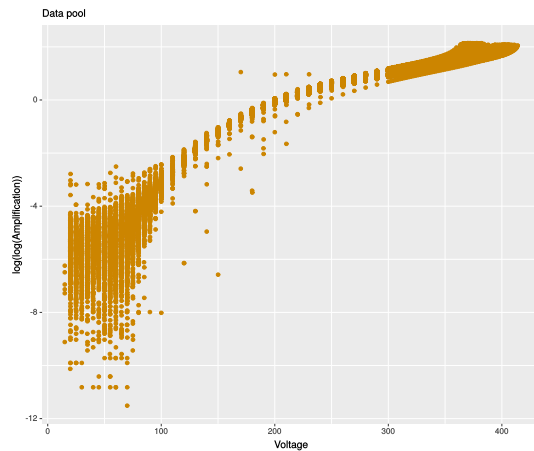


Figure 62: *Double logarithmic transformation of the not irradiated APD pool.*

The double-logarithmic data of the complete APD pool after and before the irradiation shows a quite identical shape though the non-irradiated data provides more outlying data points. Both courses show a behaviour that corresponds to that of a third polynomial. Next, the linear approach is used as a basis and extended to a **mixed model**. Mixed models take into account the variation between groups and are often applied when objects or subjects are measured multiple times or when observations are taken on the same unit over time.

Hence, they are often used in clinical trials where one group receives a drug and another not. Mixed models are also used to analyze semiconductor manufacturings [112]. Using a double logarithmic transformation of the data and applying a mixed model (see a deeper description of **Linear mixed model** on page 199), it is now:

$$\ln \left(\ln \left(\hat{Y}_{ij} \right) \right) = \sum_{k=0}^3 \left(\hat{\beta}_k + \hat{\gamma}_{ik} \right) X_{ij}^k + \varepsilon_{ij} \quad (2.11)$$

with i denoting the individual APD and j corresponding measurement observations

Y represents the amplification as the response variable, X is the predictor variable and i is the number of observations per APD j . With a suitable model on hand, the bias voltage can now be determined:

Inverse regression `lme4` does not provide inverse prediction for mixed models at the moment but it is currently under development. Hence, the sought bias voltage has to be calculated with the help of the coefficients provided by the mixed model. Since $X[Y = 150]$ is sought and a polynomial of a third degree is involved, a cubic equation has to be solved. The solution for it is Cardano's method which is rather circumstantial due to the necessary case distinction of real and imaginary solutions. To circumvent this situation, the zero of the inverse ($f(x) - 150$) is calculated via `uniroot()`. This function yields the zero of a continuous univariate function within a specified interval. Hence, the function must provide opposite signs at the initial endpoints to be able to perform a calculation. The corresponding interval is sometimes not easy to determine, especially when raw polynomials are used. For the mixed model it could be successfully defined as $\{350, 450\}$ which corresponds mainly to the region where the APDs provide their strongest amplifications. By extracting the estimated coefficients of the mixed model [59], the bias voltage can be calculated.

6.3 Results

6.3.1 Polynomial degree

At first, to study the degree of the polynomials for the fixed and random effects, the data is shrunk such that all amplification values $M < 2$ are removed. This allows a better convergence of the model (see **Numerical convergence** on page 75) by reducing the number of data points from 74064 down to 55064 in case of the irradiation data. The anova takes into account that the models have to be fitted per ML instead of REML [8] and the following models are tested:

Ref	Degree of fixeff	Degree of ranef	Degree of freedom	AIC	BIC	logLik	p-value
#	1	1	6	-154370	-154317	77191	
	1	2	9	-154747	-154667	77383	2.2^{-16}
#	1	2	9	-154747	-154667	77383	
	2	2	10	-156039	-155950	78030	2.2^{-16}
#	2	2	10	-156039	-155950	78030	
	2	3	14	-228589	-228465	114309	2.2^{-16}
#	2	3	14	-228589	-228465	114309	
	3	3	15	-235660	-235526	117845	2.2^{-16}

Table 17: **Anova test for model selection.** The APDs are treated as random effects. The hashtag in "Ref" indicates the model against which is tested, means, the lower one (without #) is tested against the upper one (with #). *fixeff* represents the degree of the polynomial for the fixed effects and *ranef* analogously in case for the random effects.

A model is considered as being superior when the AIC or BIC values are low while the logLik-value is high. Also important is the p-value when comparing a higher model with a lower one, for example, due to additional degrees of the polynomial. A low p-value indicates that the higher model provides a significant improvement. Due to previously described consequences which arise when using degrees greater than three, higher polynomials are not considered.

In the following, the mixed model regressing the APD pool is shown:

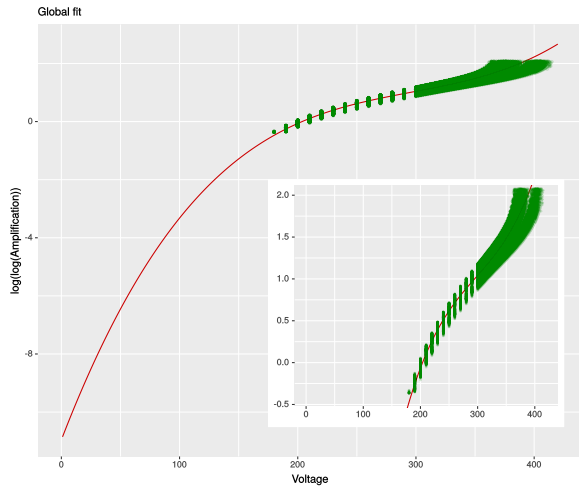


Figure 63: *Global fit for the transformed irradiated APD pool.*

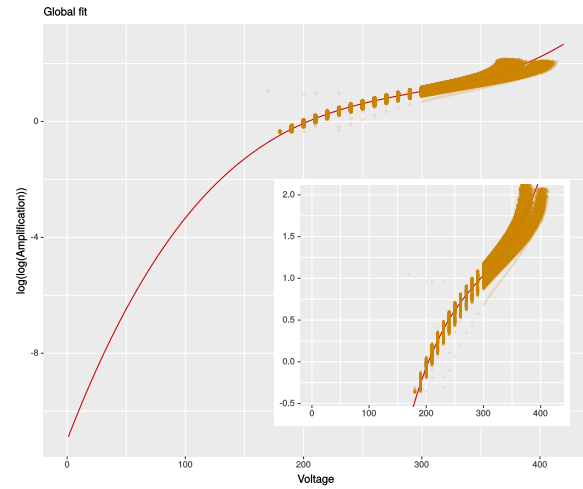


Figure 64: *Global global fit for the transformed not irradiated APD pool.*

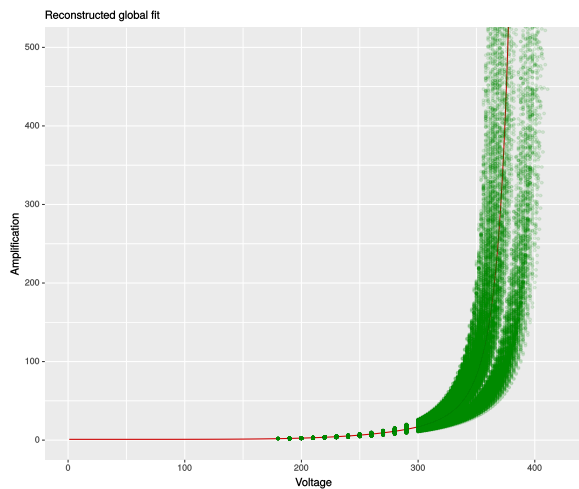


Figure 65: *Reconstructed global fit for the irradiated APD pool.*

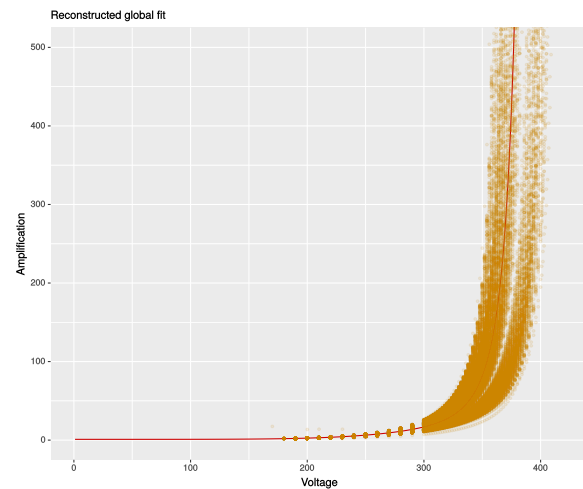


Figure 66: *Reconstructed global global fit for the not irradiated APD pool.*

All data points with $M < 2$ are neglected here. The global fit represents the functionality of the whole APD pool by using only the fixed effects. Next, an individual fit for three single APDs:

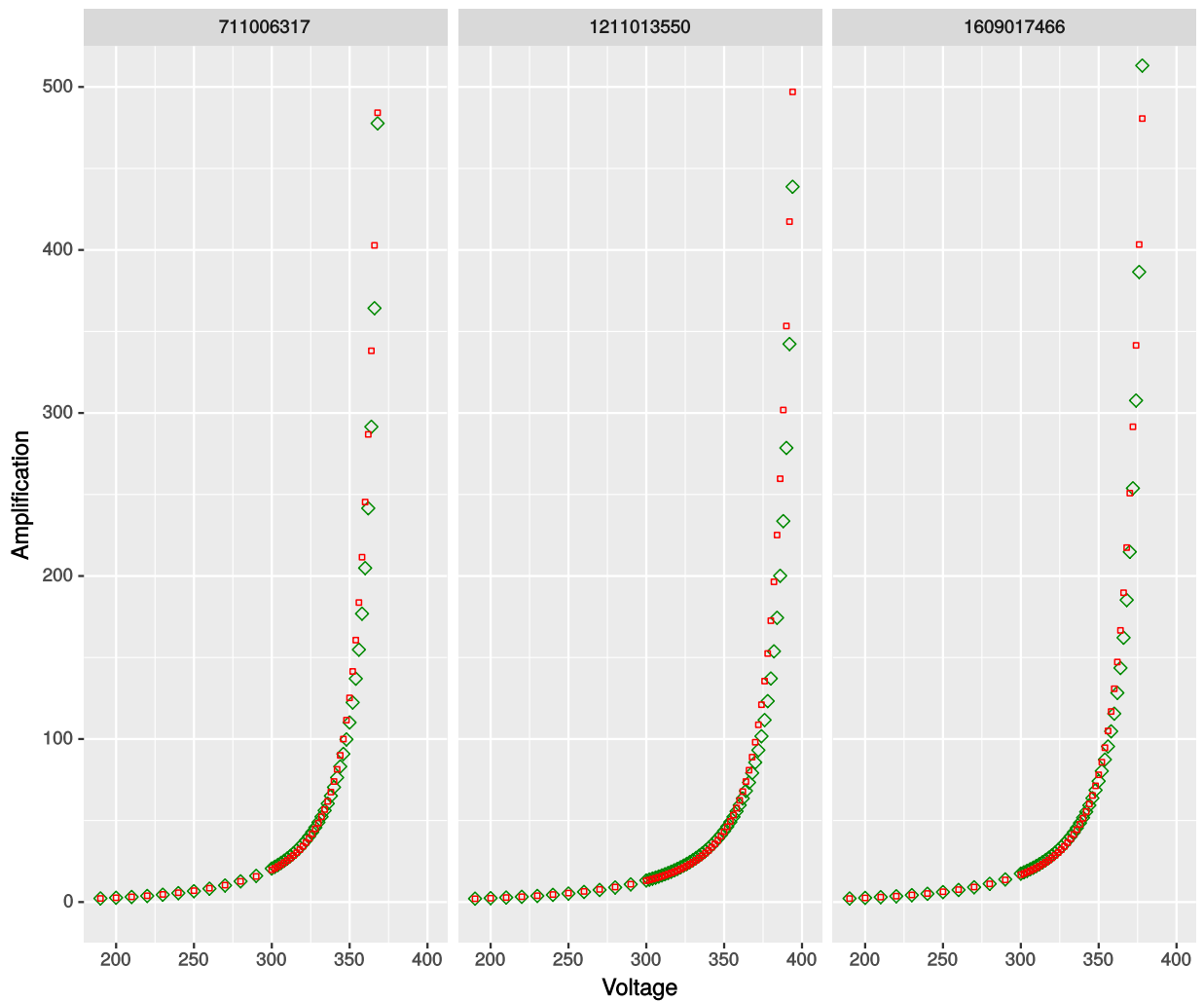


Figure 67: **Individual linear mixed model fits.** The green data represents measured data and the red data represents the individual fit which does not match the data as demanded.

The model seems to describe the APDs quite well, especially in the moderate gain region up to an amplification of about $M = 100$. From there on, slight deviations are visible. However, the prediction results match the data over the entire range.

Since the task is less to find a fit describing the total data region (see fig. 67) but to find a fit which yields the q-point very precisely, a closer look is necessary (see fig. 68). It turns out that the model cannot satisfy the needs:

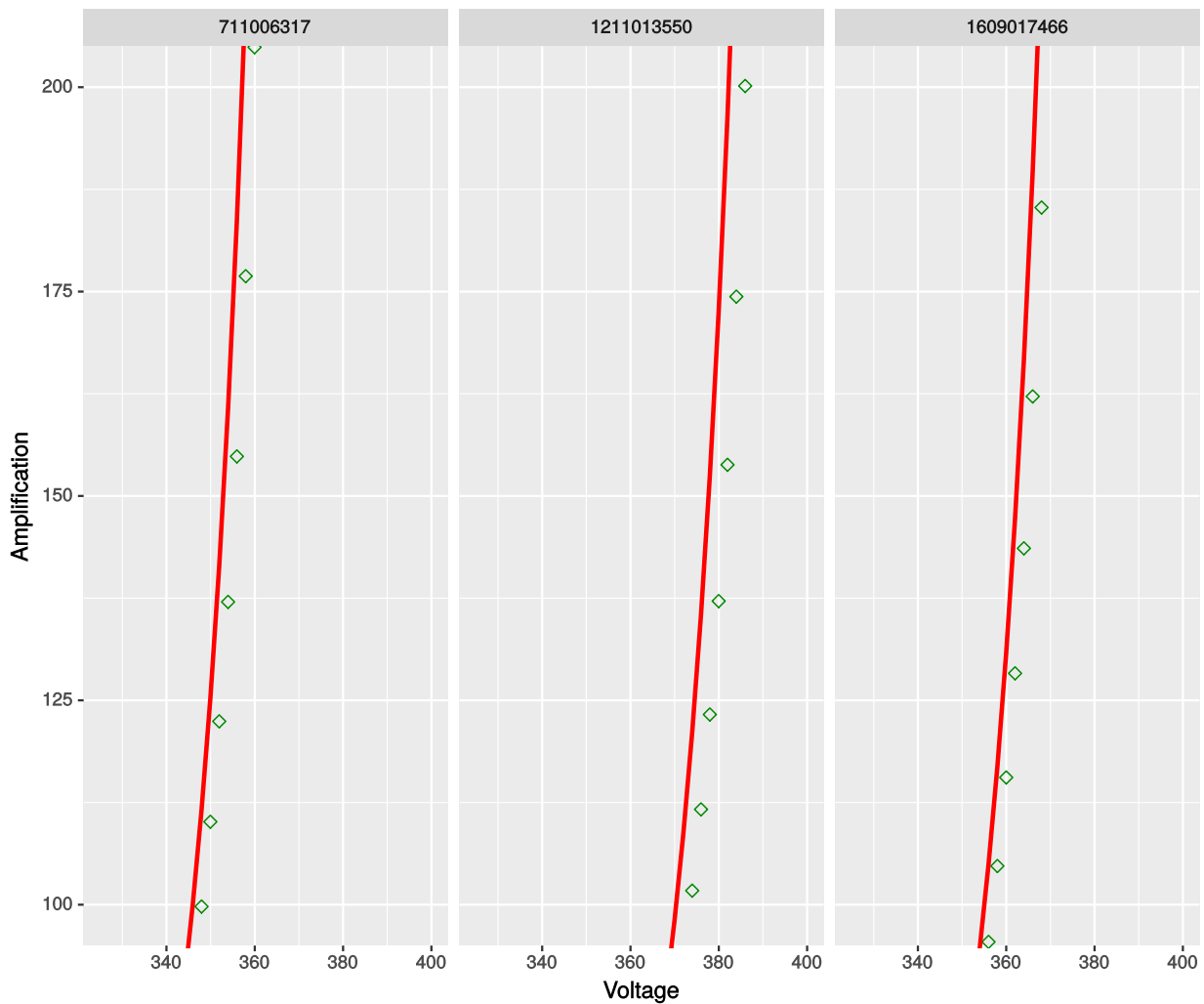


Figure 68: **Individual linear mixed model fits.** The green data represents measured data and the red data represents the individual fit which does not match the data as demanded.

The individual fits are able to emulate the data but not as precise as demanded. Above all the APD 1211013550 shows evident deviations. To improve the model, some modifications are necessary, foremost the reduction of the underlying data range:

In the following, the influence of data points is studied by tracing the pearson **residuals** according to the considered number of data points. Number of data points n is the amount of considered data points each below and above a threshold of $Y = 150$. Hence, the specification of a number of three data points describes six data points in total.

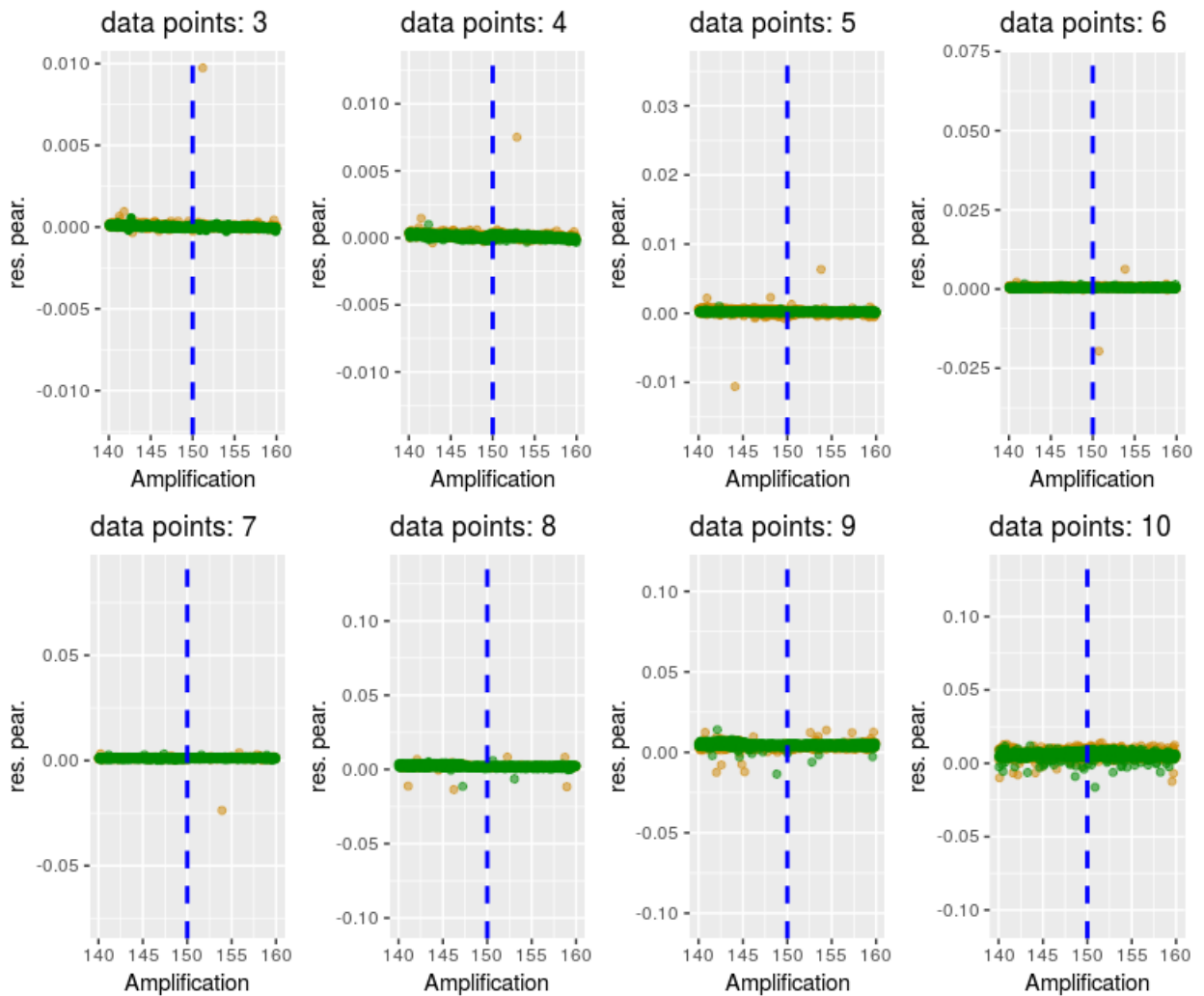


Figure 69: *Residual plot - zoomed*. On the y-axis are the pearson residuals and the x-axis represents the amplification No structures can be seen. The magnitude of residuals is quite independent from the number of data points. The raw residuals are divided by $\sqrt{V(\mu)}$

Residuals of less than six data points are not investigated because a polynomial of a third degree cannot be applied. In order to know whether a fit describes the data well, the residuals must not show any structures. The magnitude of the residuals does not play the major role as long as the residuals are normally distributed. Otherwise, this would indicate that the model provides a systematic structure due to its deficiency. The model describes the irradiated data well within the local amplification region at $Y = 150 \pm 10$ as no structures or patterns are visible. This changes when the data range is not limited:

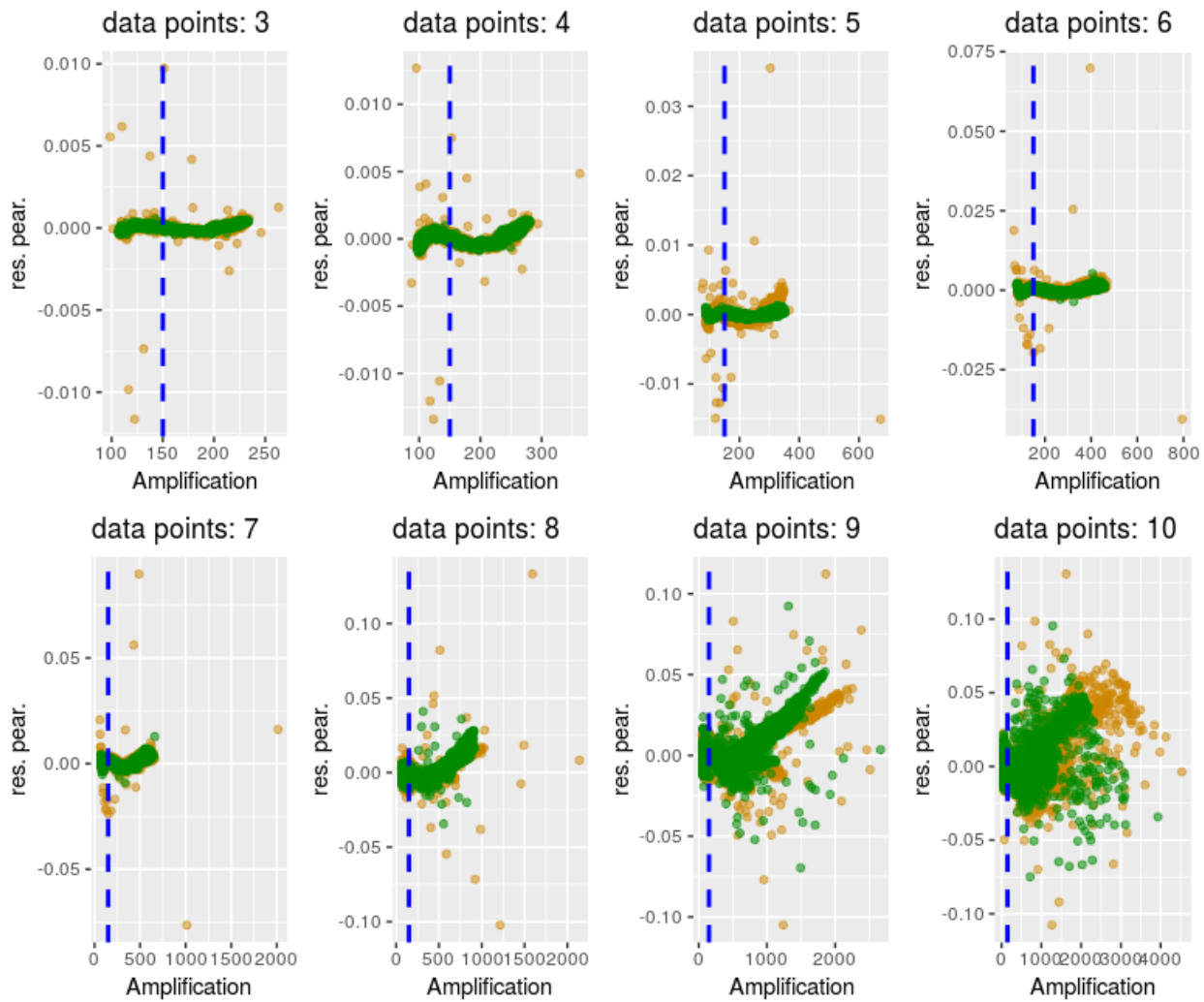


Figure 70: **Residual plot.** The $M=150$ line is moving further to the left the more data points are included due to the strong amplification rise when increasing the voltage. Additionally, particularly in this region the residuals spread as the model becomes poorer the more data points are involved.

In contrast to the local window at $M = 150$ (see fig. 69), structures are now emerging. The residuals are spreading more the more data points are available, especially in case of the not irradiated data. In addition, the residuals seem tendentially to be located in the positive range. Furthermore, the residuals vary also characteristically among the lots (see Residual plot of the lots on page 201).

Finally, it turns out that local constraints in the form of a limited number of data points are meaningful to be applied. Thus, only the **six local support values** surrounding the value $M = 150$ will be used from now on. Therefore, the polynomial degree is studied against to ensure that the utilized model is reasonable (table 18):

Ref	Degree of fixe	Degree of ran	Degree of freedom	AIC	BIC	logLik	p-value
#	1	1	6	-45645	-45605	22829	
	2	2	10	-60743	-60676	30382	2.2^{-16}
#	2	2	10	-60743	-60676	30382	
	3	2	11	-66462	-66388	33242	2.2^{-16}
#	3	2	11	-66462	-66388	33242	
	3	3	15	-68408	-68303	34219	2.2^{-16}

Table 18: *Anova test for reduced data range and model selection.*

Hence, a polynomial of a third order in the fixed and random effects will be used for the reduced data range, too. Since the hierarchy of the data pool represents a clustered data (Lots → Wafers → APDs), the two-level hierarchical influences are also tested by considering the wafers as a nested factor within the model:

Ref	Level	DoF	AIC	BIC	logLik	p-value
#	APD	15	-235660	-235526	117845	
	APD + Wafer	25	-235238	-235015	117644	1

Table 19: *Anova test for the levels.* The APDs are treated as random effects nested within the wafers.

Contrary to the expectations, the additional degree of freedom does not improve the model. This means, that it is sufficient to treat the APDs as individuals within the APD pool and without considering them being part of a group of wafers.

6.3.2 Numerical convergence

lme4 uses general-purpose nonlinear optimizers to estimate the variance-covariance matrices of the random effects and up to this writing the convergence topic of lme4 is subject to be improved. Optimizers stop searching when the loss function cannot be improved further. Difficulties can occur, for example, when a random effect is not necessary so the variance of it is zero. This might be something like a trap for the optimizer and it is hard for it to proceed or rather to converge. When calculating the models, several convergence warnings emerge: The scaled gradient cannot be evaluated and the model fails to converge due to negative eigenvalues in the Hessian. The negative Hessian eigenvalues vanishes when the data is cleared as following: Duplicates of the APDs are removed, each APD provides an irradiated and not irradiated data set and APD data points do not occur more than once. These issues are present due to a faulty database and have to be cleared manually. Generally, they did not occur before studying the numerical difficulties though verification tools are used and performed in advance but it is hard to predict each possible issue.

The remaining issues are picked up and investigated according to [135], [9]. The package influence.ME [130] provides a Cook's distance to calculate the impact of single APDs to the model (see Influence of single APDs on page 200) but removing outlying APDs does not improve the convergence respectively will not eliminate its warnings. Computing the gradient with Richardson extrapolation yields the same results. Hence, switching to different optimizers by using the optimx-package [85] yields the same results with regard to the estimated bias voltage but throws warnings, too. Using the nonlinear optimizer BOBYQA finally shows no warning but the estimated bias voltages do not change anyhow.

6.3.3 Diagnostics

In the following, the assumptions of the mixed model are checked. The first aspect to study is the standard distribution of the residuals. If this is valid, then the residuals have to follow a straight line:

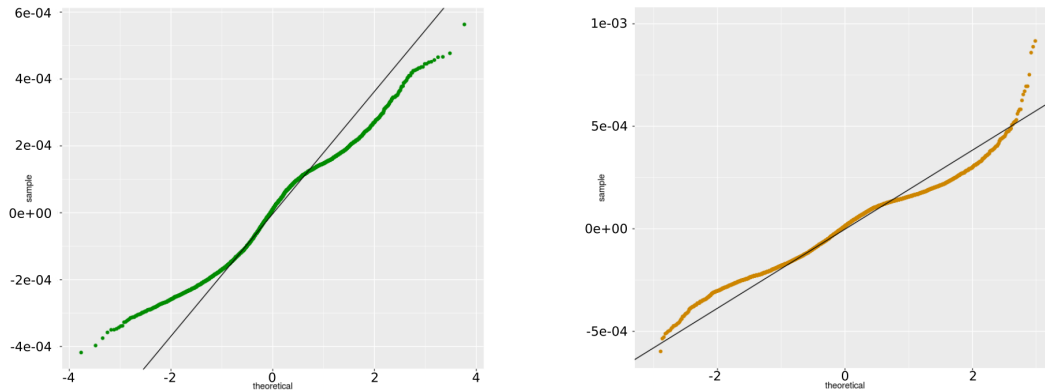


Figure 71: **qq-plot**. Empirical quantiles are plotted against theoretical quantiles of a standard normal ($\mu \approx 0$, $\sigma \approx 1$). Light tails are present but the tails for the non-irradiated data are more characteristic.

Though the residuals provide deviating tails, this assumption can be verified in principle. Nevertheless, though it is a quite common standard, [57] do not even recommend diagnostics of the normality assumption but it is quite common though. Again the homogeneity of variance (fig. 69) but next with a zoomed y-axis:

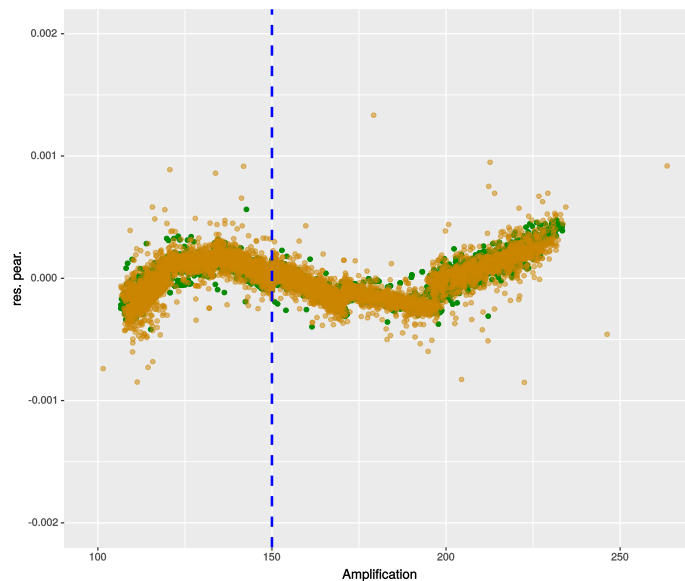


Figure 72: **Residual plot - zoomed**. The residuals are mainly within ± 0.001 .

The irradiated and the non-irradiated data are quite similar. Nevertheless, the latter spreads more but both are of the same magnitude. The residuals spread almost equally within the complete region, hence, the variance is homogeneous. Next, the residuals within the lots are studied:

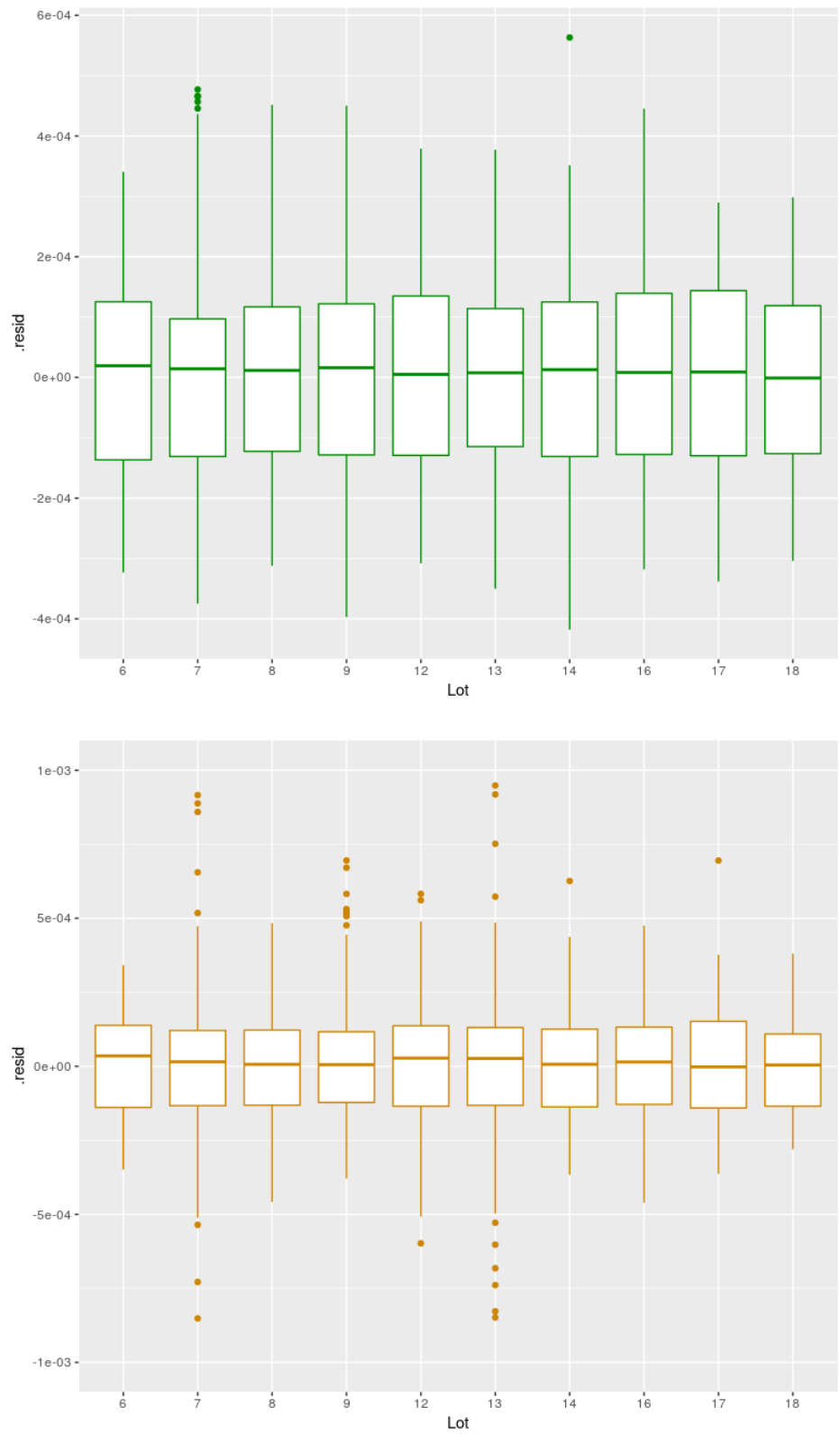
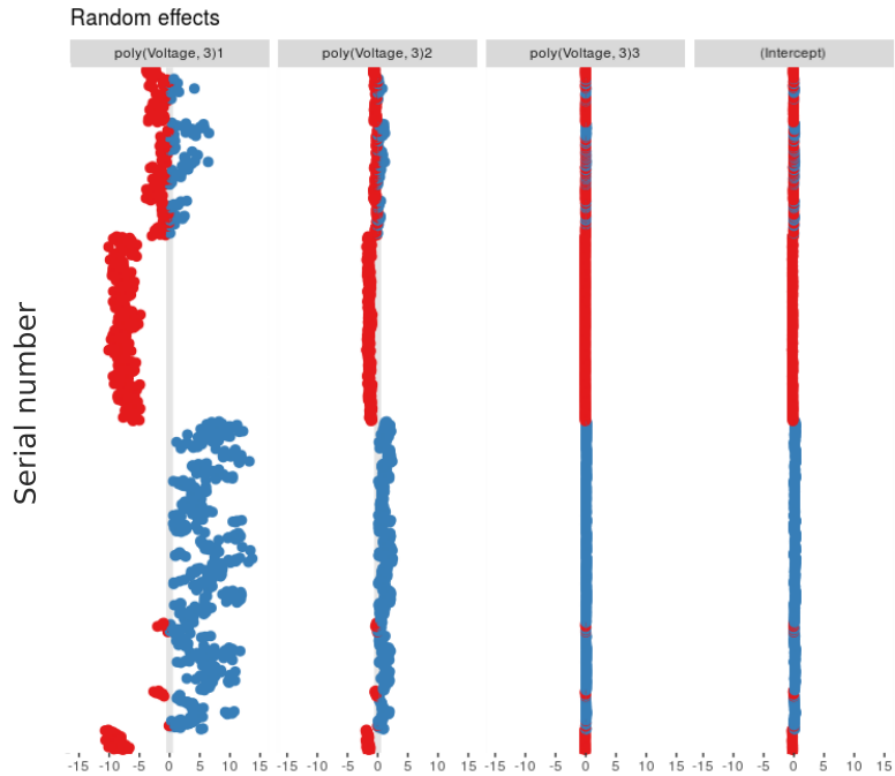


Figure 73: **Residuals of the lots.** The residuals are depicted as a boxplot. There, the straight line indicates the median and the box represents 50 % of the data while the whiskers represent 99 %. Nine residuals of the non-irradiated data (*orange*) are neglected here due to their relative large value.

The residuals of the irradiated APDs are about a magnitude lower than those of the non-irradiated APDs. Differences between the single APDs become clear when having a look at the coefficients of the corresponding polynomials across the whole pool:

Figure 74: *Random coefficients of the mixed model.* The values of the single coefficients of the random terms γ are given in blue or red, according to their sign. The term $poly(Voltage, 3)1$ refers to the linear term, $poly(Voltage, 3)2$ to the quadratic term and $poly(Voltage, 3)3$ to the cubic term. Due to the large amount of serial numbers, the y-axis is hidden here which provides increasing values of the serial numbers upwards. Thus, APDs of the lot 6 are at the bottom and APDs of the lot 18 are at the top.



The APDs share almost the same intercept and coefficients of the third degree of a polynomial but differ in case of the coefficients of the second order and especially of the first order. It also turns out that about three fourths of related APDs can be divided into two sets which provide the same signs of their coefficients of the first and second polynomial terms. As the anovas showed in table 18, the third degree of the polynomial improved the model only a bit, so the APDs share almost the same coefficients there. In Residual plot of the lots on page 201, further residual plots are provided. The fixed effect parameters of the mixed model are given below:

Irradiated			
β_0	β_1	β_2	β_3
-7.408418	6.703024^{-1}	-2.004057^{-3}	2.016638^{-6}
Not irradiated			
β_0	β_1	β_2	β_3
-7.325646	6.631535^{-1}	-1.983152^{-3}	1.995987^{-6}

Table 20: *Fixed effects parameters.* The intercepts differ the most.

6.3.4 Q-point

The reconstructed q-point is studied in dependency on the number of data points and the mixed model is compared to polynomials in addition. This is done to check whether the rather effortful programming framework behind the described mixed model is necessary. The task is how to determine the real q-point as it depends on the amount of data points and the degree of the polynomial. The q-points for various amounts of data points:

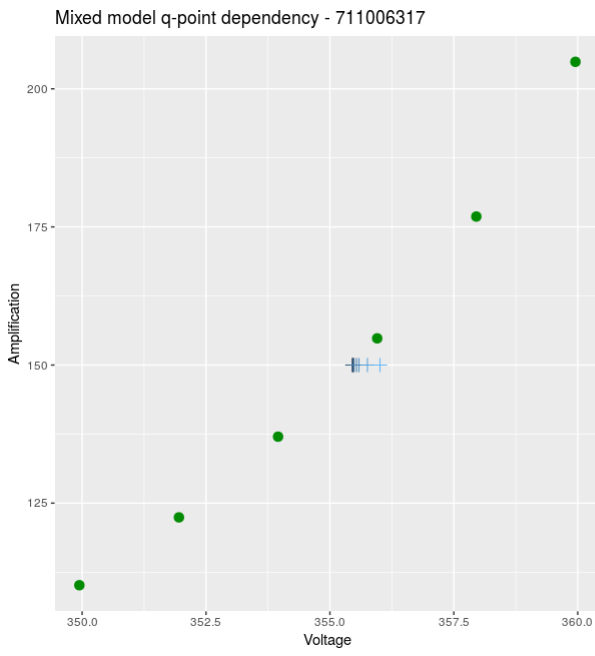


Figure 75: *Q-point against amount of data points for mixed model.*

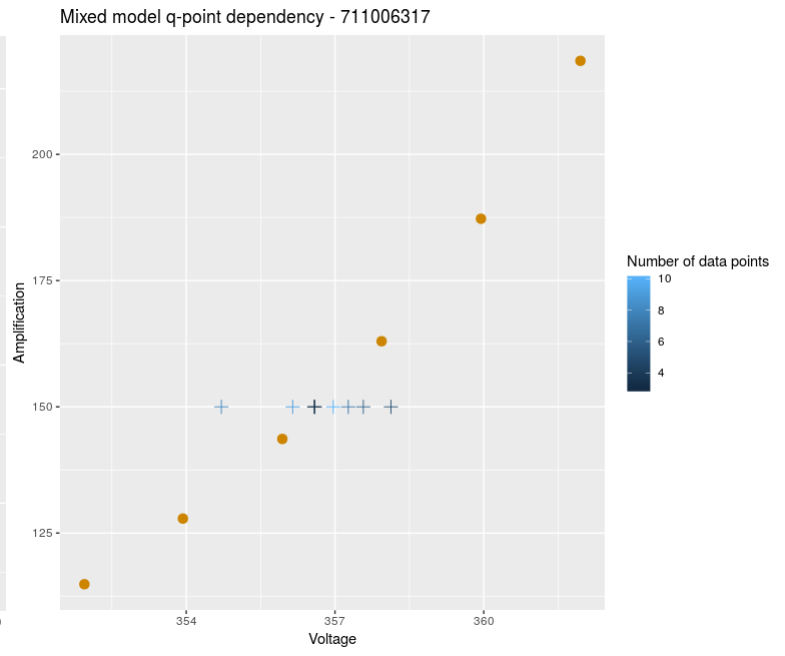


Figure 76: *Q-point against amount of non-irradiated data points for mixed model.*

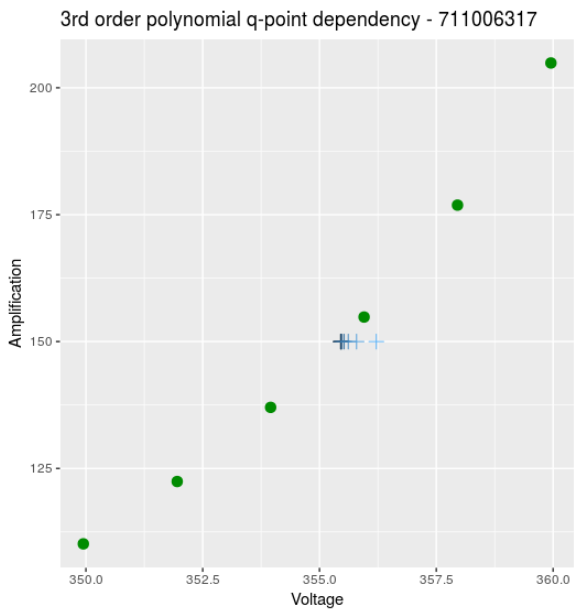


Figure 77: *Q-point against amount of data points for polynomial.*

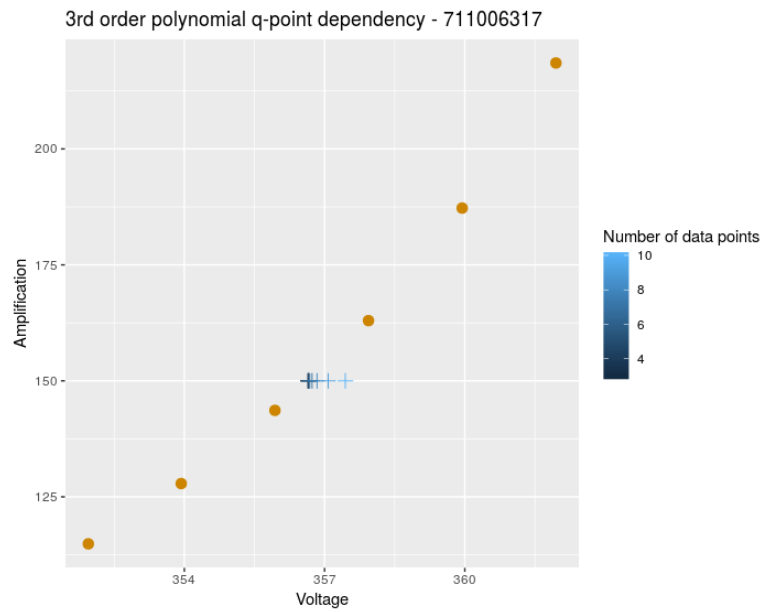


Figure 78: *Q-point against amount of non-irradiated data points for polynomial.*

The other APDs (1211013550 and 1609017466) can be seen in Q-point on page 203. The leverage of data points is more present the more data points with a high amplification are involved, thus, shifting the q-point (see fig. 76). Nevertheless, the other two APDs do not show this behaviour. This might be connected to the circumstance that these single APD measurements do not provide visible abnormalities (see e.g. *APD 711006317 curve* on page 198) but, yet, the pool of the non-irradiated data shows some (see fig. 62) and because the mixed model takes into account the complete pool and not only single APDs, it seems that the correlations within the pool cause these strong deviating q-points. This is in contrast to the polynomial model which treats an APD as an isolated object. Nevertheless, it remains open why this occurs only for the APD 711006317. To circumvent such issues in the future, for example, only defined monotonously rising amplification values could be considered. The decision to make is which result describes the q-point as best as possible: This is without an uncertainty not possible but it is assumed that, according to the corresponding residuals, the mixed model with six data points together with polynomials of a third degree in the fixed and random effects is representing the q-point as precise as possible. In the following, the bias voltage of all APD through a mixed model, a raw polynomial model and an orthogonal model:

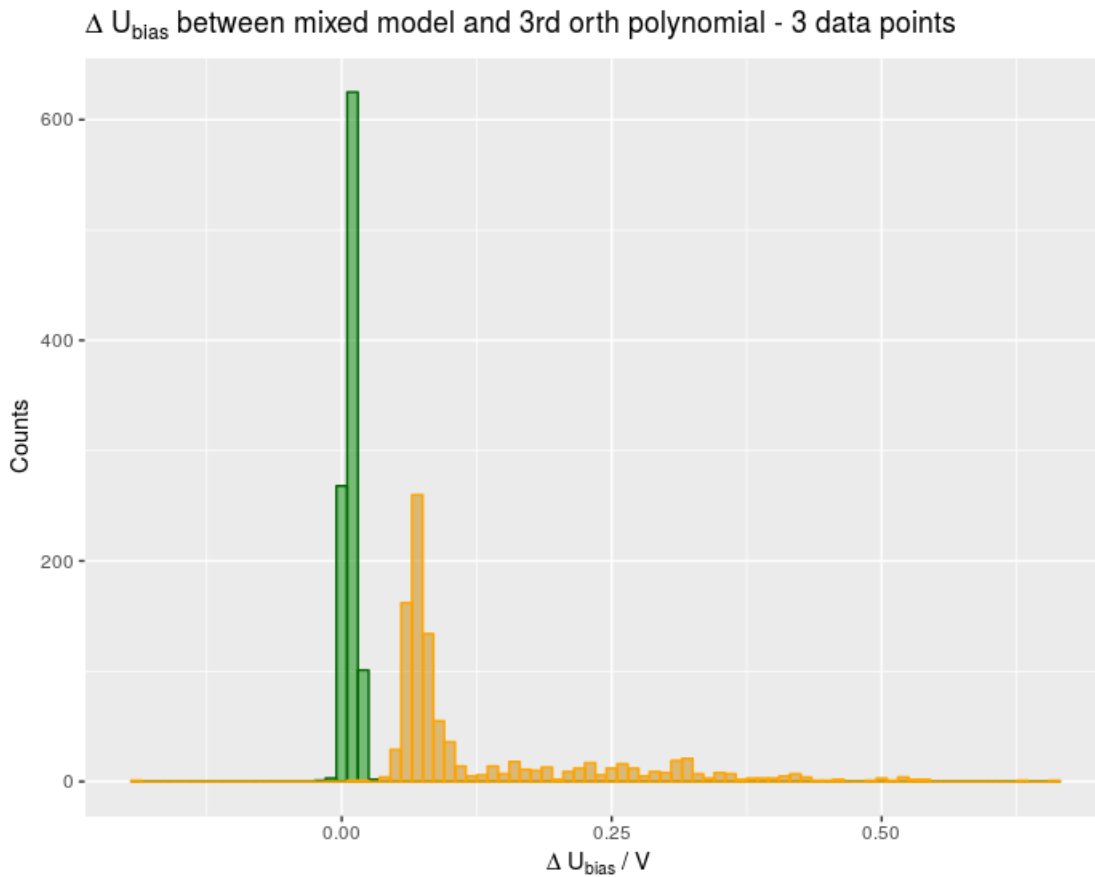


Figure 79: *Change of bias voltage between mixed model and 3rd order orthogonal polynomial.*

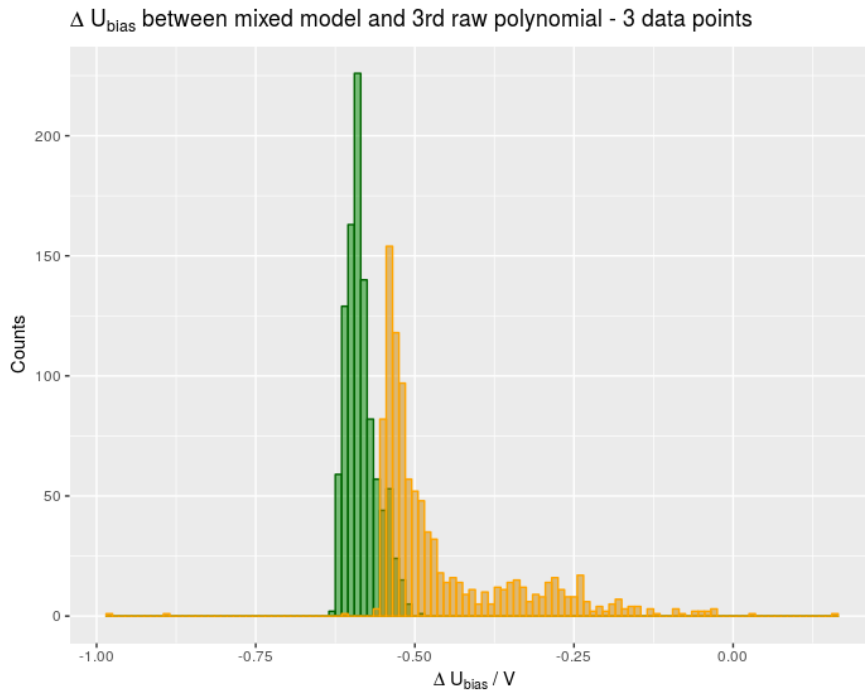


Figure 80: *Change of bias voltage between mixed model and 3rd order raw polynomial.*

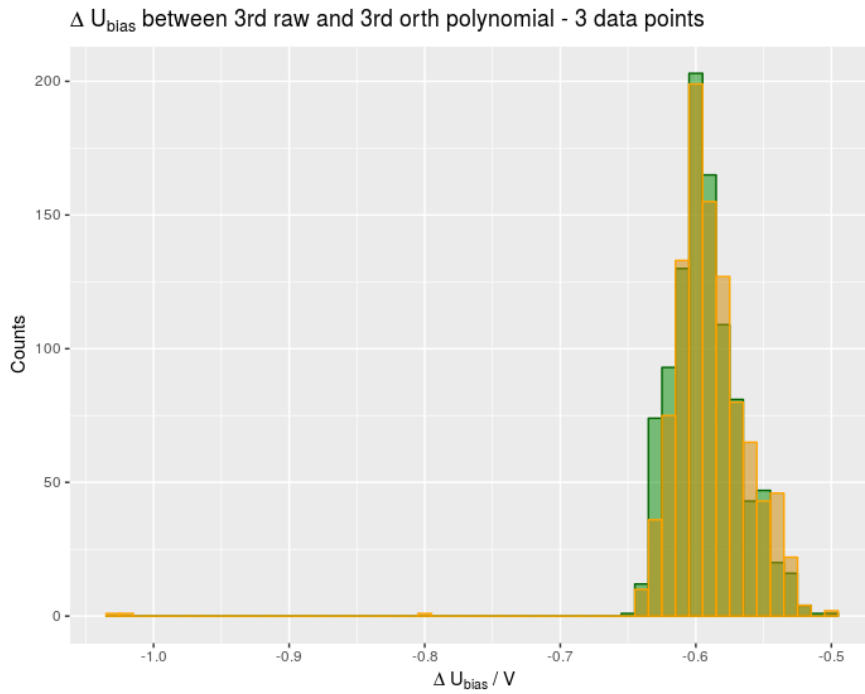


Figure 81: *Change of bias voltage between 3rd order raw and orthogonal polynomial.*

The inverse regression for the polynomial model is performed with the *invest()* function of the *investr*[16] package. The change of the bias voltage between the mixed model and the 3rd order orthogonal polynomial is quite small or even not really present, at least in the case of the irradiated data. For the data before the irradiation, most of the devices do not change more than about 50 mV. Differences become clearer when the mixed model is compared to raw polynomials. There, the average change is at about 450 mV for the non-irradiated data and at about 600 mV for the irradiated data. Lastly, the raw and orthogonal polynomials are compared to other and their difference is quite clearly 600 mV for both measurement series.

Next, the mixed model and the polynomial model are compared with each other when the two inner data points around $M = 150$ are removed. This means that, in return, two outermost other data points are considered instead, so this will give a rough impression about the stability of the model:

APD	Mixed model	Mixed model*	ΔU	Poly*	ΔU	Irradiated
711006317	356.58 V	356.6 V	0.04 V	356.65 V	0.07 V	no
711006317	355.45 V	355.45 V	0 V	355.46 V	0.01 V	yes
1211013550	380.54 V	380.51 V	-0.03 V	380.76 V	0.22 V	no
1211013550	381.55 V	381.55 V	0 V	381.55 V	0 V	yes
1609017466	364.81 V	364.82 V	0.01 V	364.9 V	0.08 V	no
1609017466	364.74 V	364.73 V	-0.01 V	364.75 V	0.01 V	yes

Table 21: **Change of bias voltage due to removal of data points.** The data of these single APDs is modified by removing the two inner data points (indicated by *) and replacing them with the next two data points further out to study changes of the bias voltage against measurement variations.

For these three APDs, the mixed model is more stable against data perturbations, yet, the changes are quite small again.

Besides the bias voltage, the slope and the breakdown voltage play a role, too, for the technical operation later on. The bias voltage will be regulated technically and thus, the slope implicitly, too, since it is linked to the bias voltage. Nevertheless, the slope has to be determined as well:

6.3.5 Slope

The slope can be calculated by using the derivative $d(\ln(\hat{Y}_{ij}))/dX = \sum_{k=0}^2 (\hat{\beta}_k + \hat{\gamma}_{ik}) X_{ij}^k + \varepsilon_{ij}$, together with the gained bias voltage X_{ij}^k and the coefficients of the used model. In case of the polynomial model, the slope can be obtained through the *derivative()* function inside R.

For the Miller fit, a typical expression for the slope is to normalize it with respect to the set amplification gain Y by $(1/Y) \cdot dY/dX$. Since a derivative is sensitive to nonlinear transformations (because the log function is not linear), the calculated slopes will not be re-transformed.

6.3.6 Breakdown voltage

Hamamatsu defines the breakdown voltage through the dark current, when reaching a value of 100 μA . In contrast, the CMS experiment defined that an APD reaches the breakdown voltage when it exceeds an amplification of $M = 500$. According to regular electrical engineering literature, the breakdown point is subject to the dark current and is reached when $I_D \rightarrow \infty$. The dark current of the APD data pool cannot be used due to major troubles like missing values, falsely calibrated measurement devices and too strong deviations within the measurements. Therefore, the breakdown voltage has to be estimated, too. It can be calculated with a nonlinear least squares approach [163], [60]:

$$\log(V_i) = \alpha + \beta \rho^{A_i} + \varepsilon_i \quad (2.12)$$

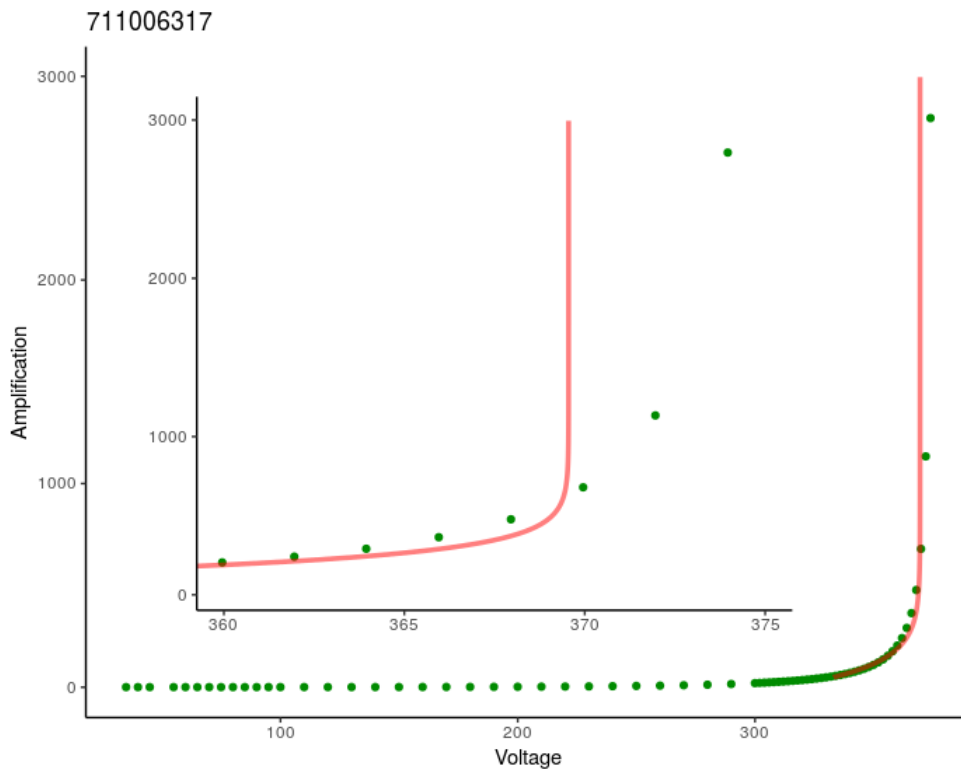
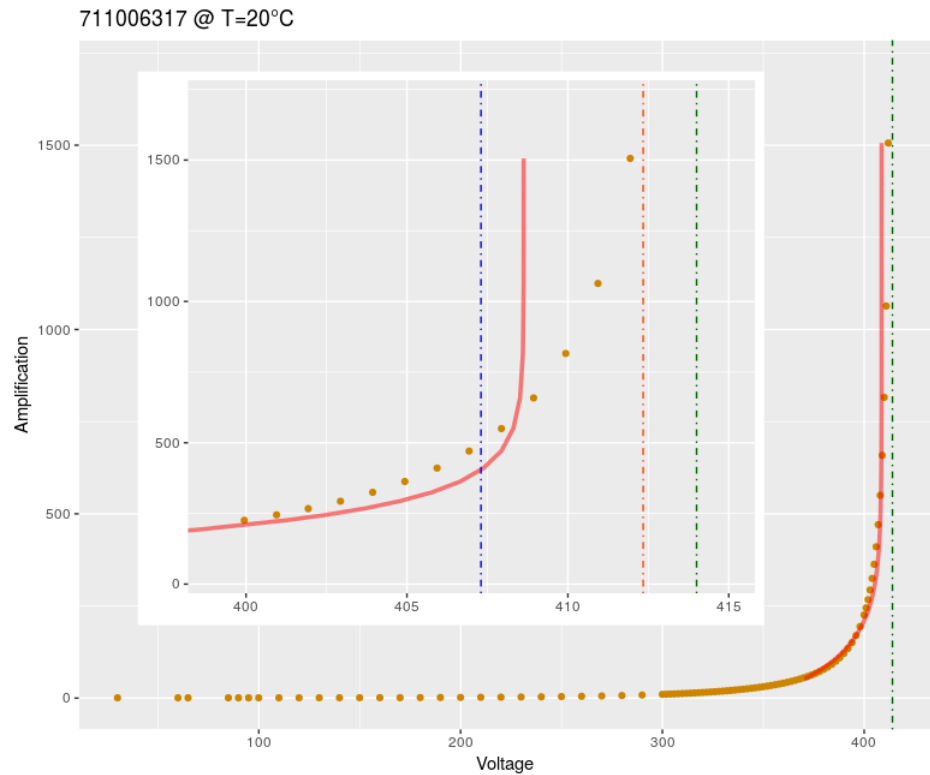


Figure 82: *break-down voltage fit of APD 711006317 at $T=-25^{\circ}\text{C}$* . The breakdown voltage is determined at 369.552 V.

The fit catches the strong amplification quite well without taking into account the large amplification values where the breakdown voltage has already been exceeded. The parameters will be guessed by the model itself and adjusted throughout the optimization. In Breakdown voltage on page 205, further APDs are depicted together with their fitted breakdown voltage.

Figure 83: *break-down voltage fit of APD 711006317 at $T=20^{\circ}\text{C}$* . The breakdown voltage given from Hamamatsu is 414 V and determined at 408.62 V by the fit. The voltage at $M = 500$ is ~ 407.3 V and the voltage through eq. (2.13) is 412.34 V. Major differences occur between the approaches.



Another method and the most easy way to determine the breakdown voltage is to use the data itself through

$$V_{br} = 1.001 \cdot \max(V_i) \quad (2.13)$$

This might be good enough since the $M - V$ curve behaves as an asymptote to the breakdown voltage. But this approach is sensitive to the data itself as it is subject to the number of data points respectively it depends on the measured maximum voltages. Finally, it is in principle the same concept the CMS uses as they take the voltage at $M = 500$. Besides, Hamamatsu provides the breakdown voltages for all APDs at $T = 20^\circ\text{C}$. Hence, the data there can be used to compare the different approaches (see fig. 83). The voltage from the fit and the CMS-approach are only 1.3 V distant from each other and located in a reasonable region. In contrast to the the Haamatsu value and eq. (2.13) which both provide values where the breakdown already happened.

6.3.7 Data pool

Now, the obtained parameters of all APDs will be depicted in regard to the way how they are generated. Firstly, the **bias voltages** by using the orthogonal polynomials of a third degree:

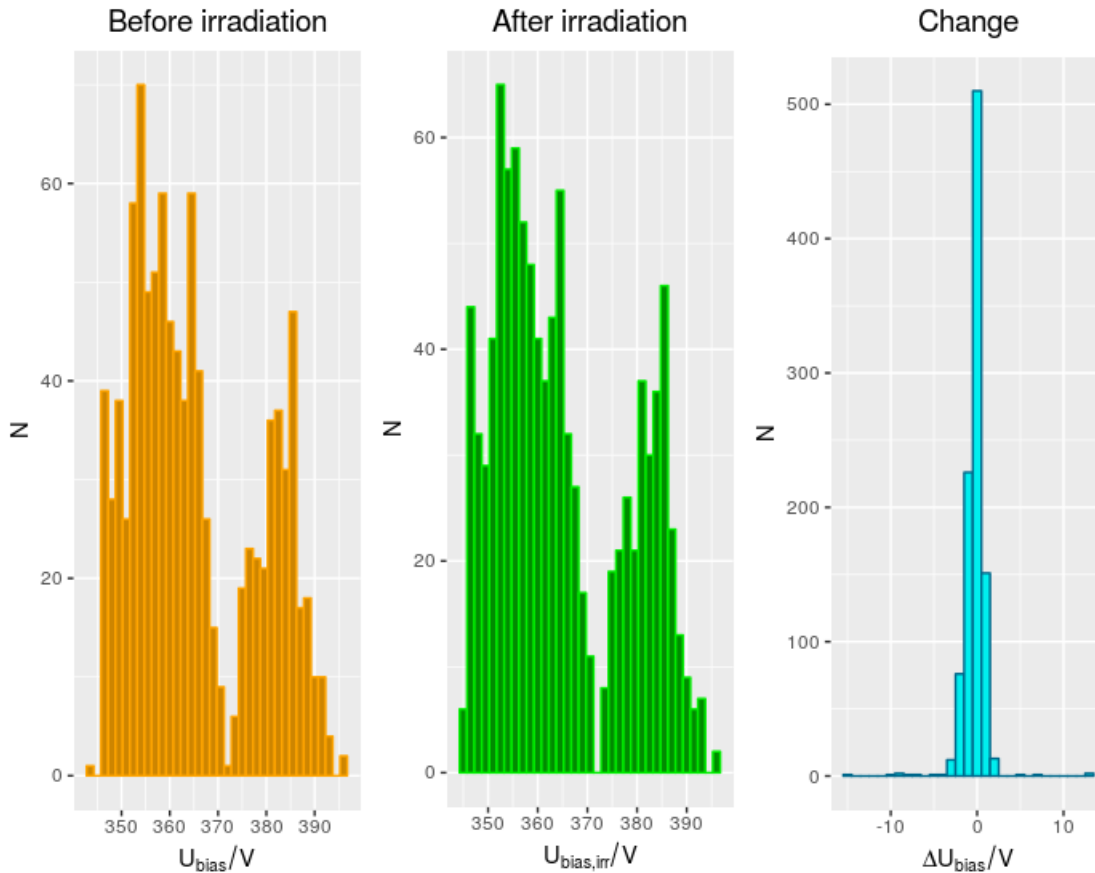


Figure 84: **Distributions of the bias voltages of the pool.** The bias voltages of the APDs spread over a range of about 50 V. Most of the APDs did not change their voltages significantly but some APDs did within ± 2 V.

Both voltage distribution are shaped like a bimodal distribution. The characteristic shape of the distributions might be caused due to manufacturing processes (see fig. 94). On the contrary, the distribution of the voltage changes embody a Gaussian behaviour and most of the APDs change within 0 ± 2 V.

Subsequently, the distributions of the **slopes** which are gained by calculating the derivative of the orthogonal polynomial model:

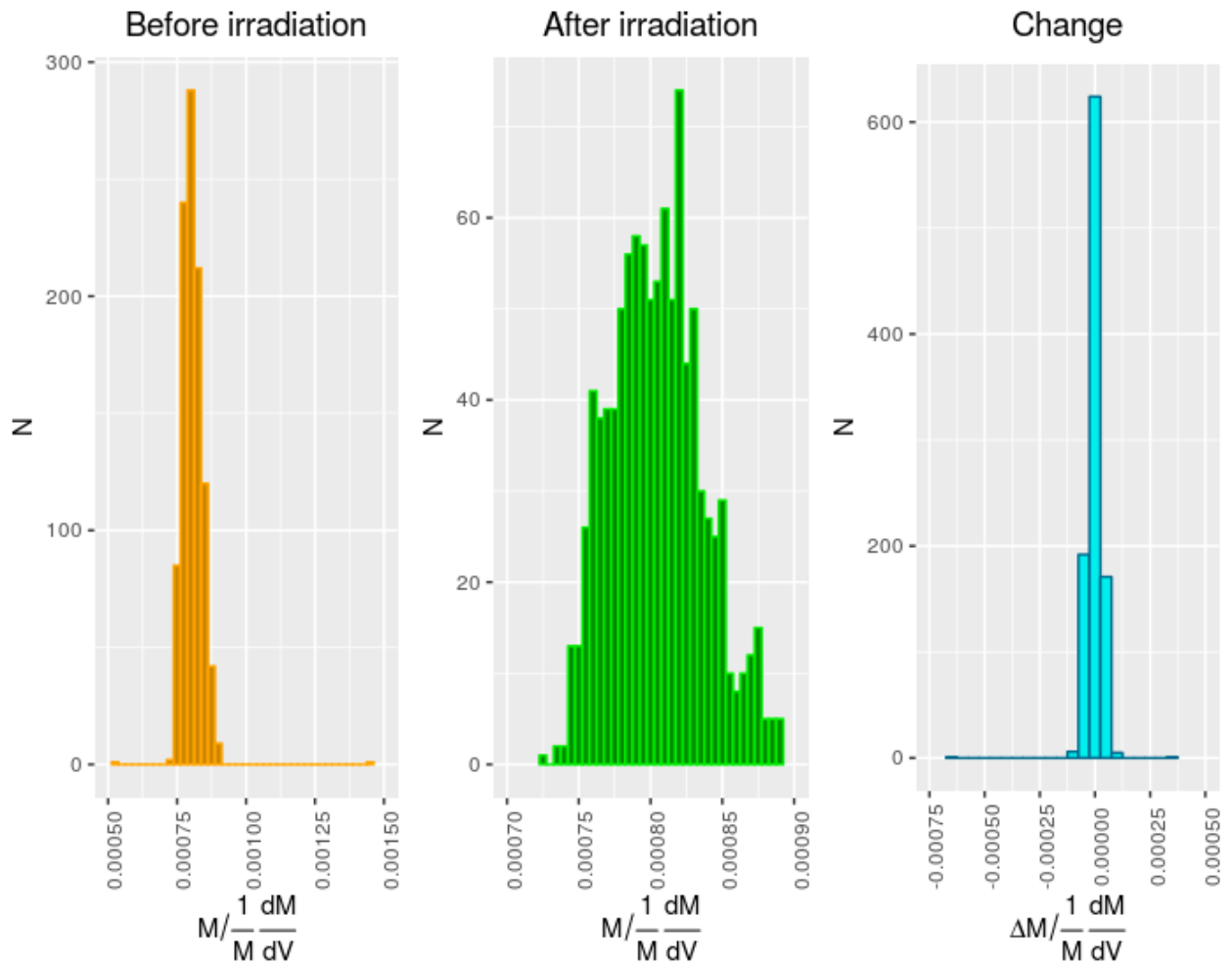


Figure 85: *Distributions of the slope of the pool.* Most of the slopes do change even less due to the irradiation process.

All three distributions behave quite well like a Gaussian and the change due to irradiation has a width of about $2 \cdot 10^{-4}$. Like the voltage changes due to irradiation, the changes of the slopes are centered at 0, too. However, the width of the slope distribution of the non-irradiated APDs is broader but reduced by the irradiation (see fig. 85).

The **breakdown voltage** distribution obtained by using the nls model, see eq. (2.12), is:

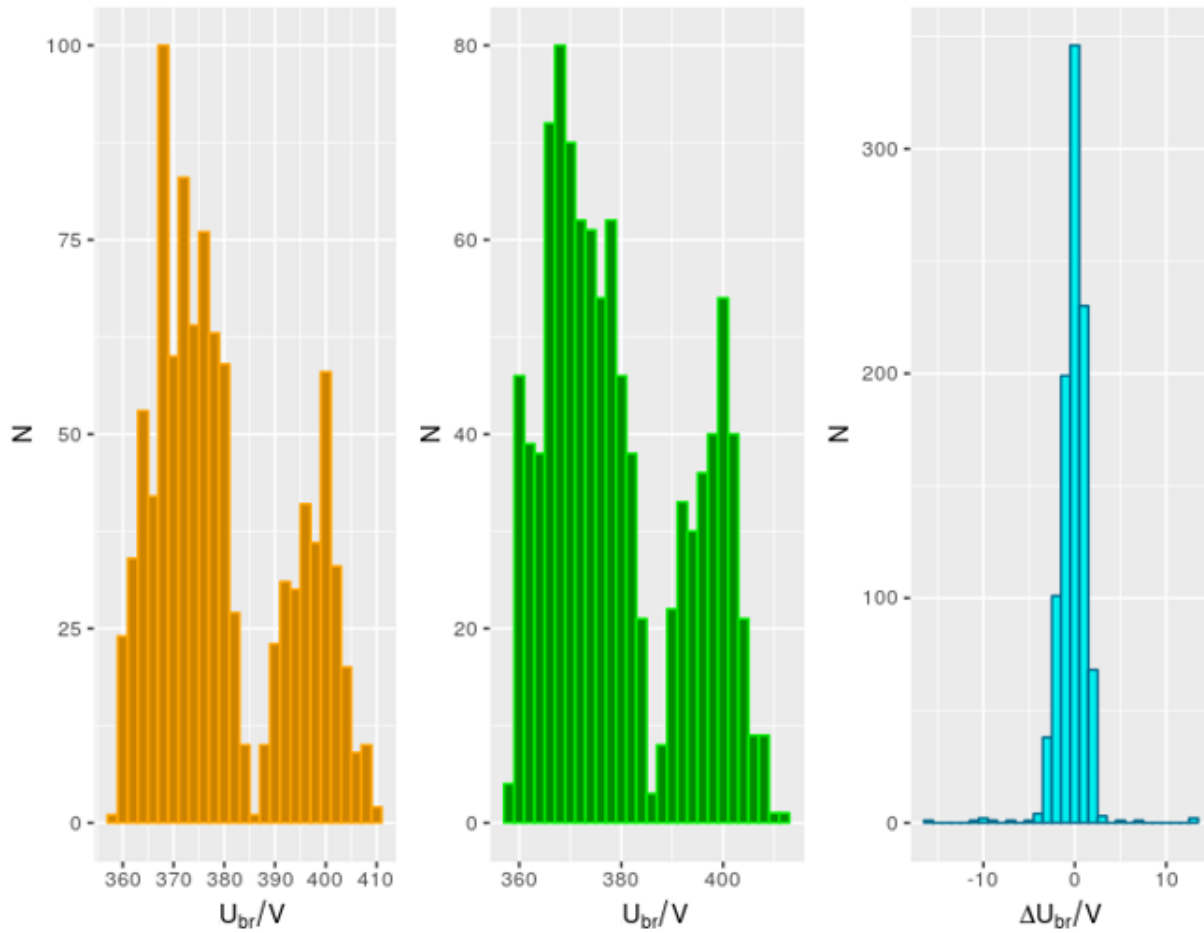


Figure 86: *Distributions of the breakdown voltages of the pool.* Like the change of the bias voltage, the breakdown voltage changes are also within about 0 ± 2 V.

Basically, it is the same distribution as in fig. 84 but shifted by about 20 V. The changes due to irradiation are of the same magnitude, too, thus, it seems that the irradiation puts a constant shift onto the voltage curve of the APDs.

And the breakdown voltages obtained by using eq. (2.13):

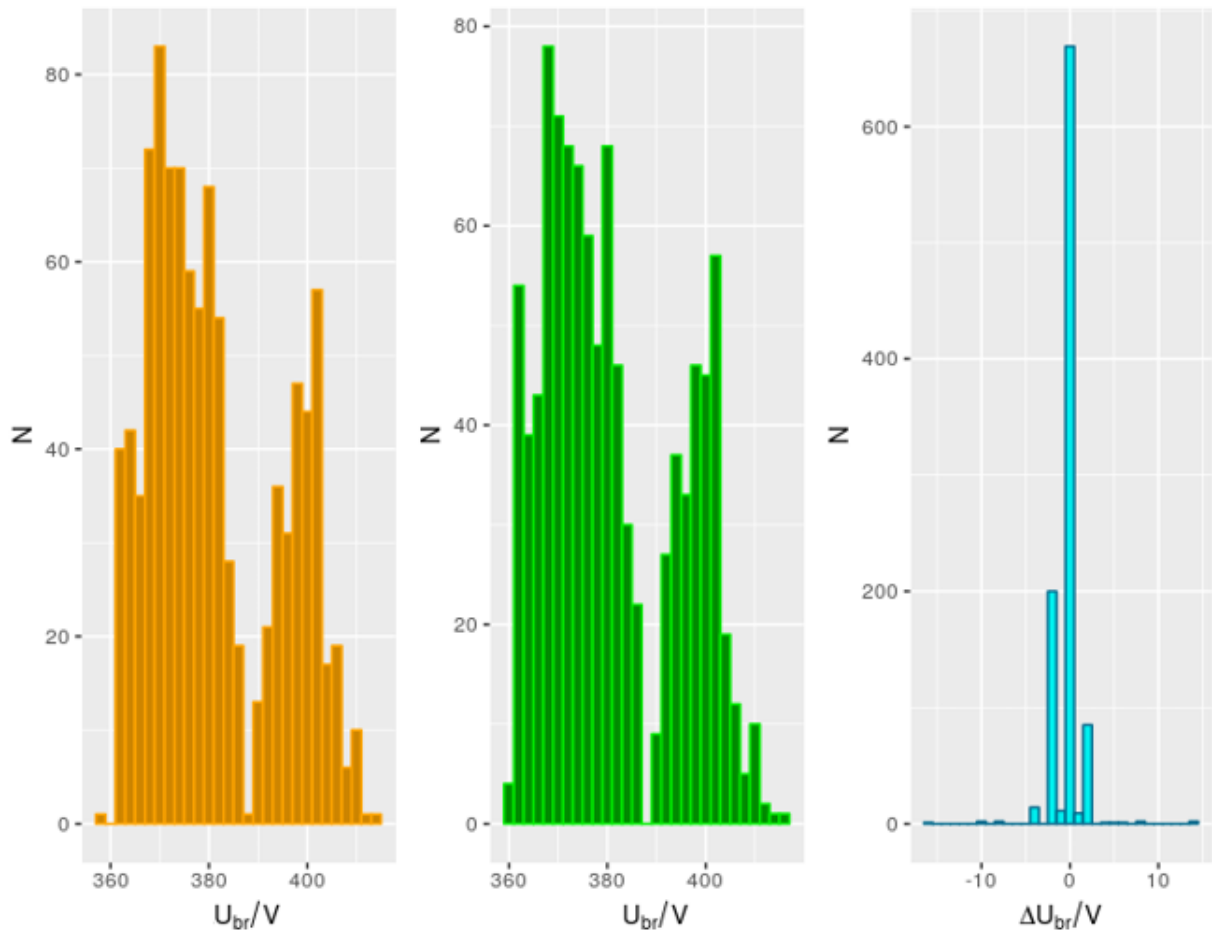


Figure 87: *Distributions of the breakdown voltage of the pool through the max values.* The breakdown voltage changes are not as Gaussian as the fitted voltages in fig. 86.

The breakdown voltages are difficult to separate from fig. 86 but the change is clearly different, yet, of the same magnitude. However, the not quite continuous voltage distribution can probably be explained by the fact that the voltages were determined on the basis of their maximum values. And these vary, especially within the lots (see fig. 52). Hence, the breakdown voltage determination through the fit seems to be more reasonable as it does depend less on the data and the distribution of the voltage change fulfill a Gaussian behaviour quite good.

To achieve a better comparison, the fitted breakdown voltages are sketched against measured values from Hamamatsu. The company provides only data for non-irradiated APDs at $T = 20^{\circ}C$:

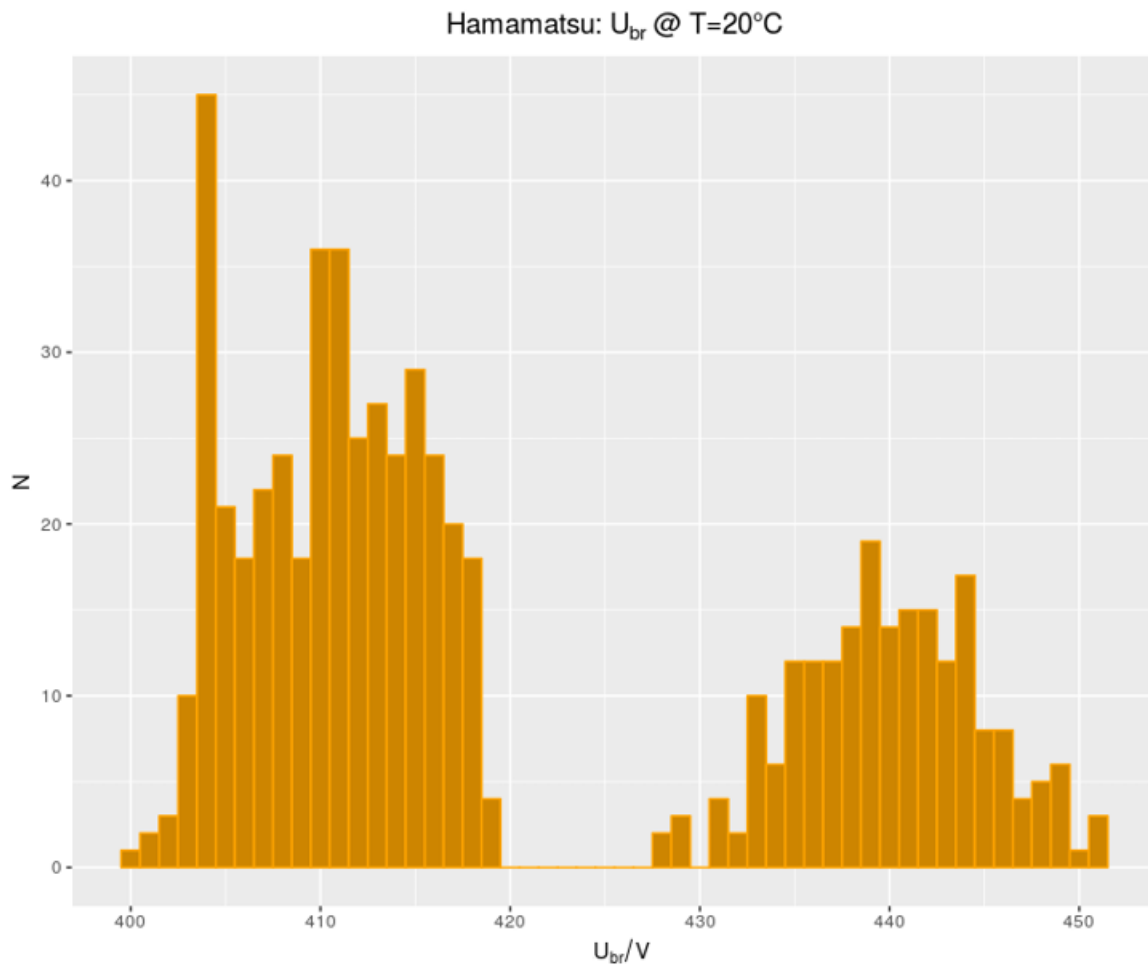


Figure 88: *Distribution of the breakdown voltage of the pool given by Hamamatsu.* These voltages are from Hamamatsu at $T = 20^{\circ}\text{C}$.

The Hamamatsu data provides a clear gap between 420 V and 430 V which is also present in the distributions but much less distinctive. Furthermore, the voltages are shifted by about 30 – 40 V compared to fig. 87 and fig. 86. However, those values are gathered from measured APDs at $T = -25^{\circ}\text{C}$ while the ones in fig. 88 are taken at $T = 20^{\circ}\text{C}$. Therefore, the APD measurements at $T = 20^{\circ}\text{C}$ are studied as well to enable a direct comparison (see fig. 89).

In the following, the same APDs with fitted breakdown voltages:

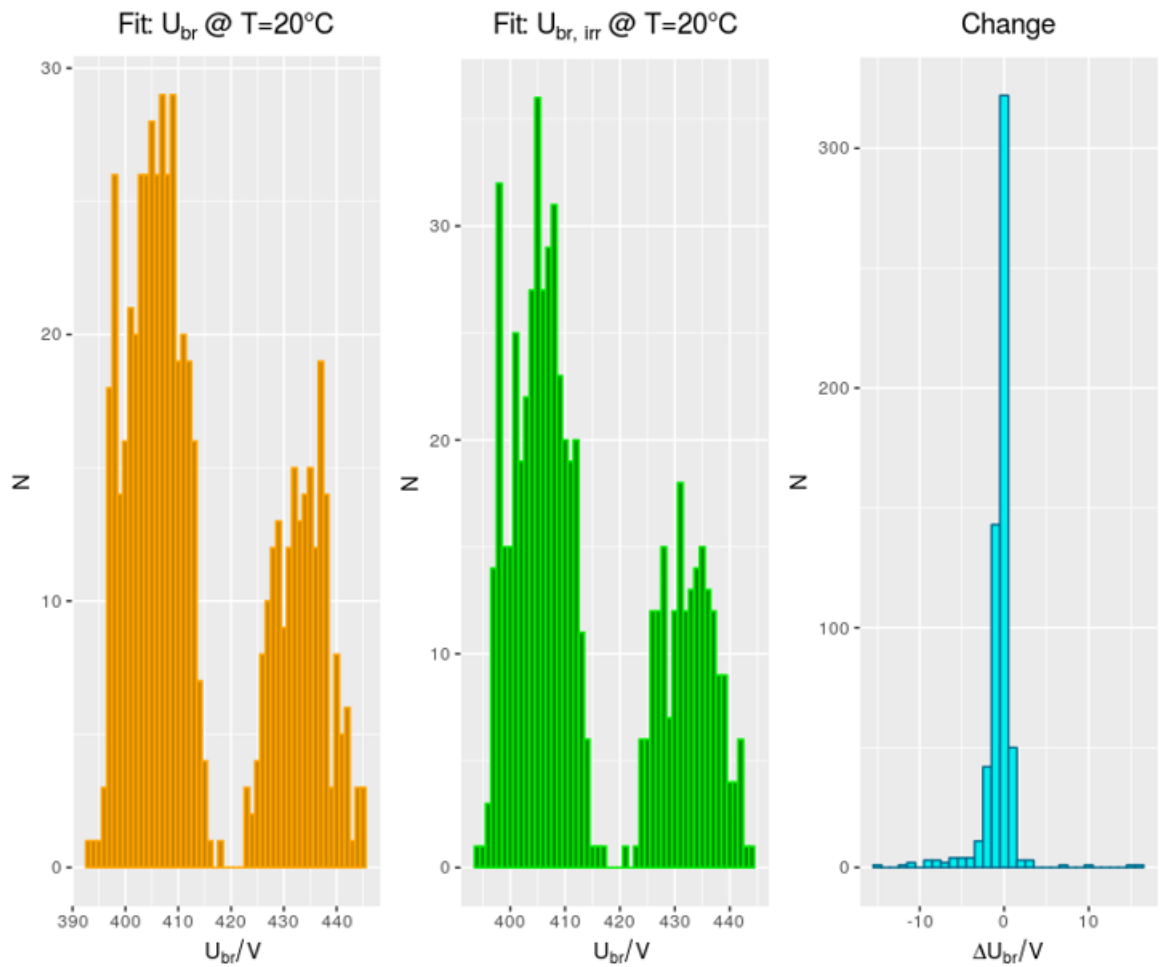


Figure 89: **Distribution of the fitted breakdown voltages of the pool.** The breakdown voltages are obtained on a basis of measurement data for APDs at $T = 20^\circ\text{C}$ provided by PSL.

The gap between 420 V and 430 V is present again but less marked compared to the Hamamatsu data (see fig. 88). Nevertheless, the values of the non-irradiated APDs should be comparable. The corresponding widths of the distributions are relative similar with an upper limit of 450 V and a lower limit of about 390 – 400 V which differs slightly between Hamamatsu and the fit. The irradiation causes a change of the voltage values of about $\sim 0 \pm 2$ V and represents a Gaussian behaviour again (as in fig. 86).

To reveal any differences between the Hamamatsu and the fit values, they are put in a direct comparison (see fig. 90):

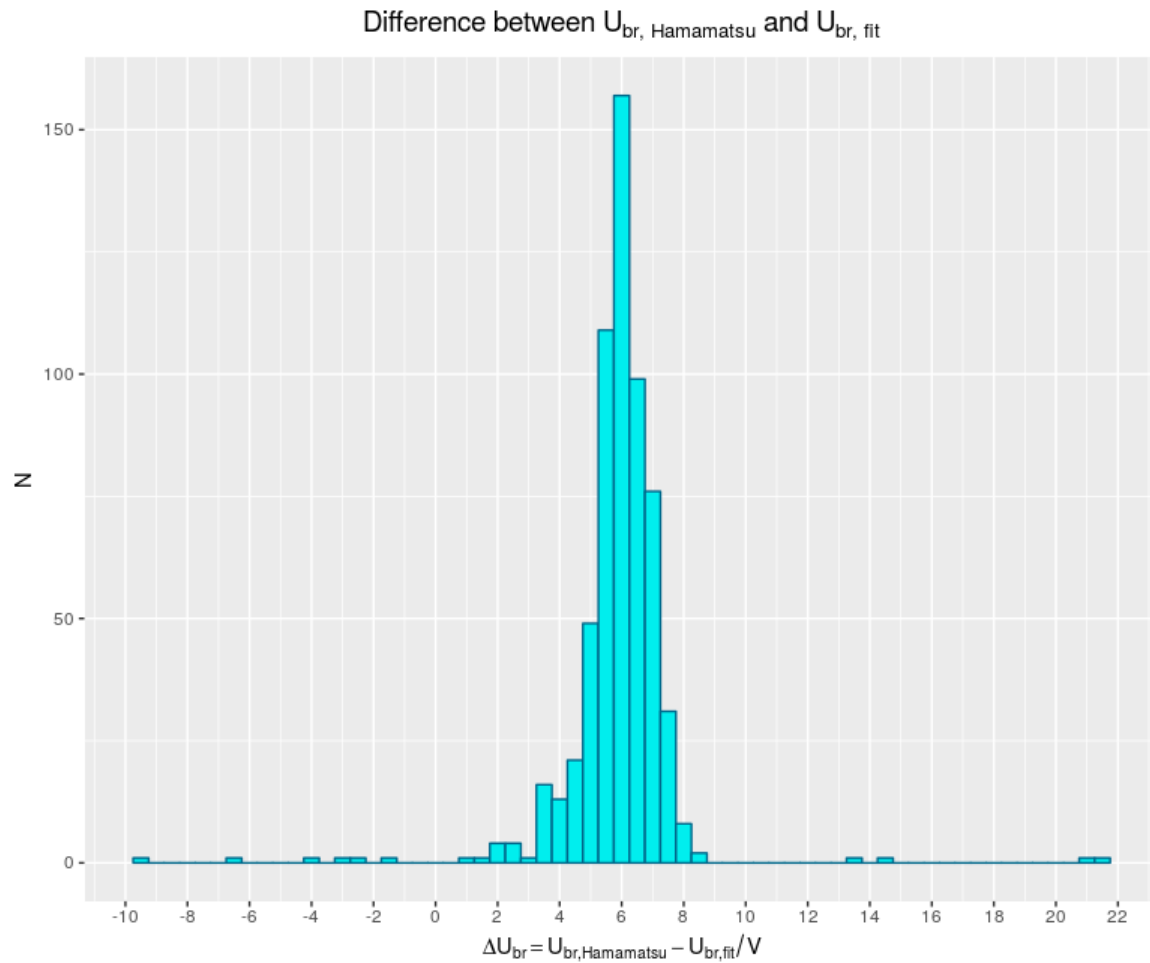


Figure 90: **Differences between Hamamatsu data and the fit.** Data at $T=20^{\circ}\text{C}$ is used as Hamamatsu provides only values at this temperature. The differences between Hamamatsu and the fit are mainly about 6 V.

The calculated differences are quite constant with about 6 V in average and almost each voltage distance is positive when using the Hamamatsu values as the higher ones. For example, in fig. 83, it can be seen that the Hamamatsu value is significant higher. It is assumed that it is safer to operate the APDs at the lower voltage than at the higher voltage. Therefore, the voltages determined by the fit should be preferred over the Hamamatsu values. On the other side, Hamamatsu does not provide breakdown voltages at $T = -25^{\circ}\text{C}$ anyhow. The correlation between the fitted breakdown voltages and the Hamamatsu values is 0.96. For this reason, the fit provides a reasonable approach to obtain the required breakdown voltages.

For the operation in the experiment later, the voltage distance between the breakdown voltage and the bias voltage is also of interest. At first, utilizing the breakdown voltages via eq. (2.13):

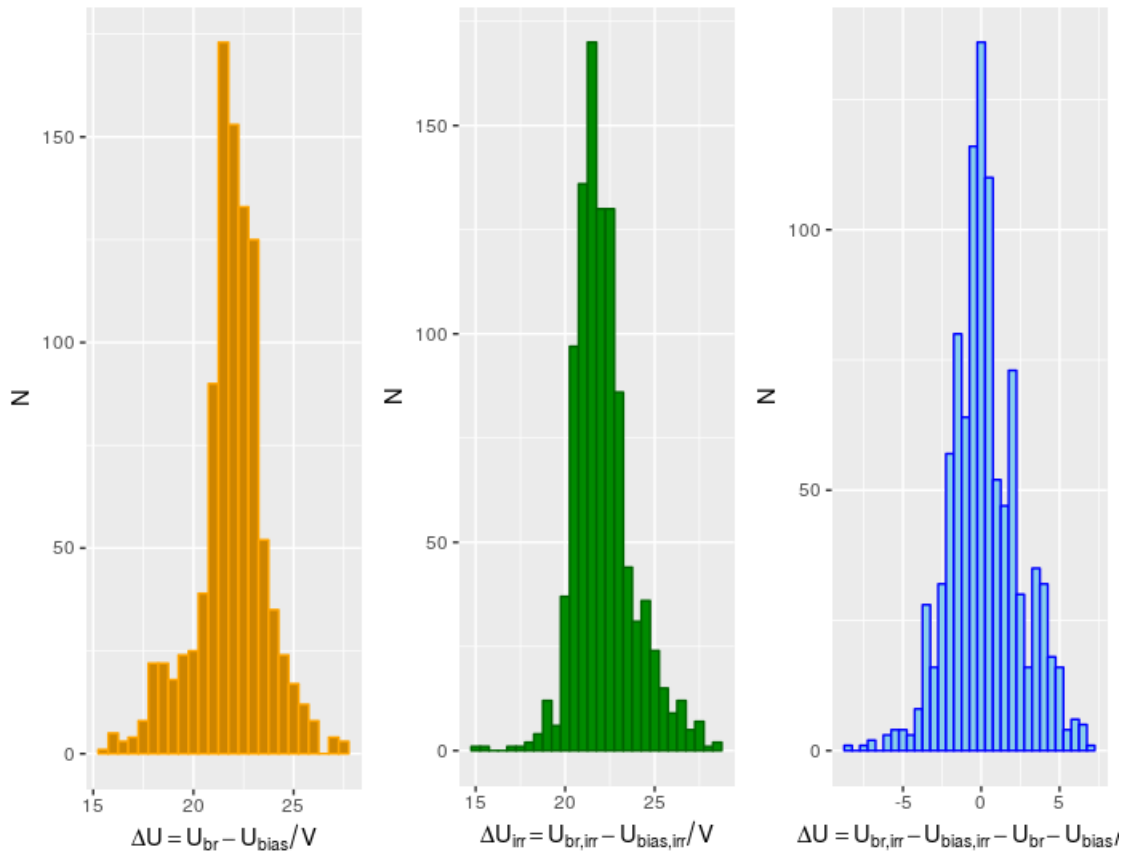


Figure 91: **Distances between bias voltage and breakdown voltage via max voltage values.** The breakdown voltages are obtained by calculating $U_{br} = \max(V_i) \cdot 1.001$.

The distances ΔU are about the same in case of the non-irradiated and irradiated APDs. Hence, the distance changes are distributed around 0. Nevertheless, many changed within ± 5 V. In general, the voltage distance between the bias voltage and the breakdown is about 20 – 25 V.

The distances when using the maximal amplification values below $M = 500$ as breakdown voltages:

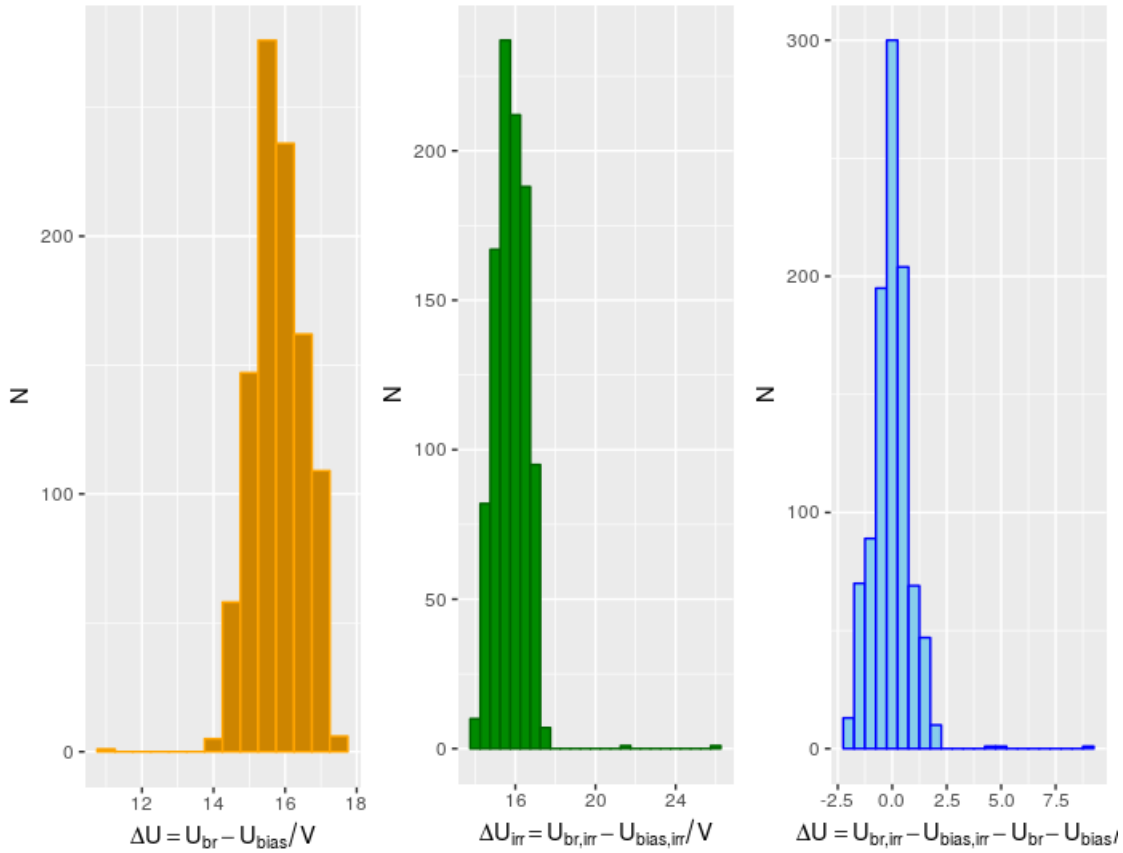


Figure 92: **Distances between bias voltage and breakdown voltage at $M=500$.** The breakdown voltage is obtained by calculating $U_{br} = \max(V_i | < M = 500) \cdot 1.001$.

The voltage distances are now notable smaller with about 16 V in average. The distance changes due to irradiation are also smaller with 0 ± 2.5 V. This is the approach the CMS uses to determine the breakdown voltages. Compared to fig. 91 and though the amplification is very steep, the diode curves still increase by about 10 V until they reach their maximal measured voltage values. Therefore, the highest available voltage values should not be used to determine the breakdown voltage since these values vary anyway heavily from APD to APD. In addition, the breakdown voltage is not just an asymptote to the diode curve as the APDs reach and pass this voltage somewhere. Determining the breakdown voltages by using the maximal values below $M = 500$ seems to be reasonable and is a fast and efficient method.

And the voltage distances when using the fit based on eq. (2.12):

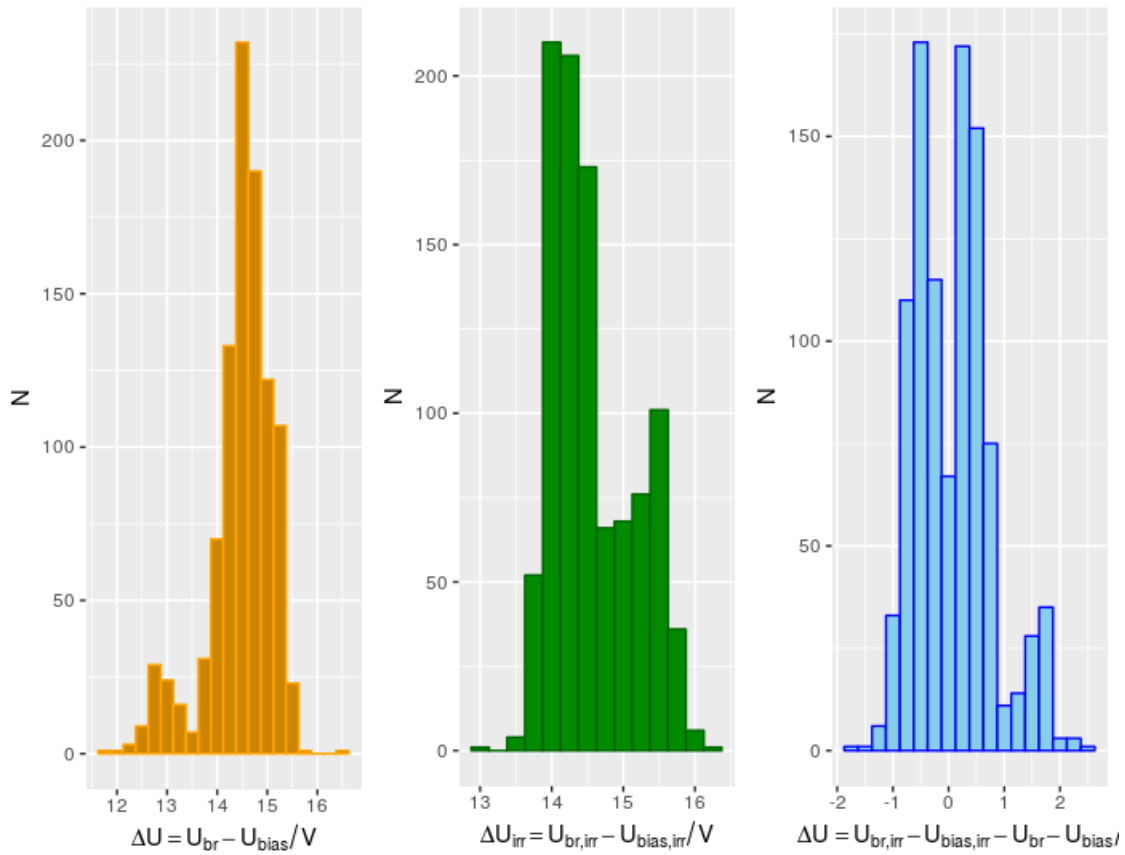


Figure 93: *Distances between the fitted bias and breakdown voltages.* The fit is performed via the nls model eq. (2.12).

The distribution in fig. 93 is quite similar to the voltages gathered by using the maximal values below $M = 500$ (see fig. 92). Generally, they differ only of about 1 V in average and the changes caused by irradiation are similar too with 0 ± 2 V. The fitted voltages are not as Gaussian as in fig. 92 but the fit depends less on the data points itself, like the incremental steps. In addition, the maximal values can vary by many voltages as the highest available data point below $M = 500$ is taken. For this reason, the fit is more trustworthy as it does not weight the high amplification values so much.

Another aspect is the irradiation influence: In general, irradiation can affect semiconductors in various ways (see on page 39). Therefore, the change of the operating parameters is used as a basis to describe how radiation-hard a device is. These changes were already depicted previously but in the following, the changes due to **irradiation** will be studied in regard to their lots:

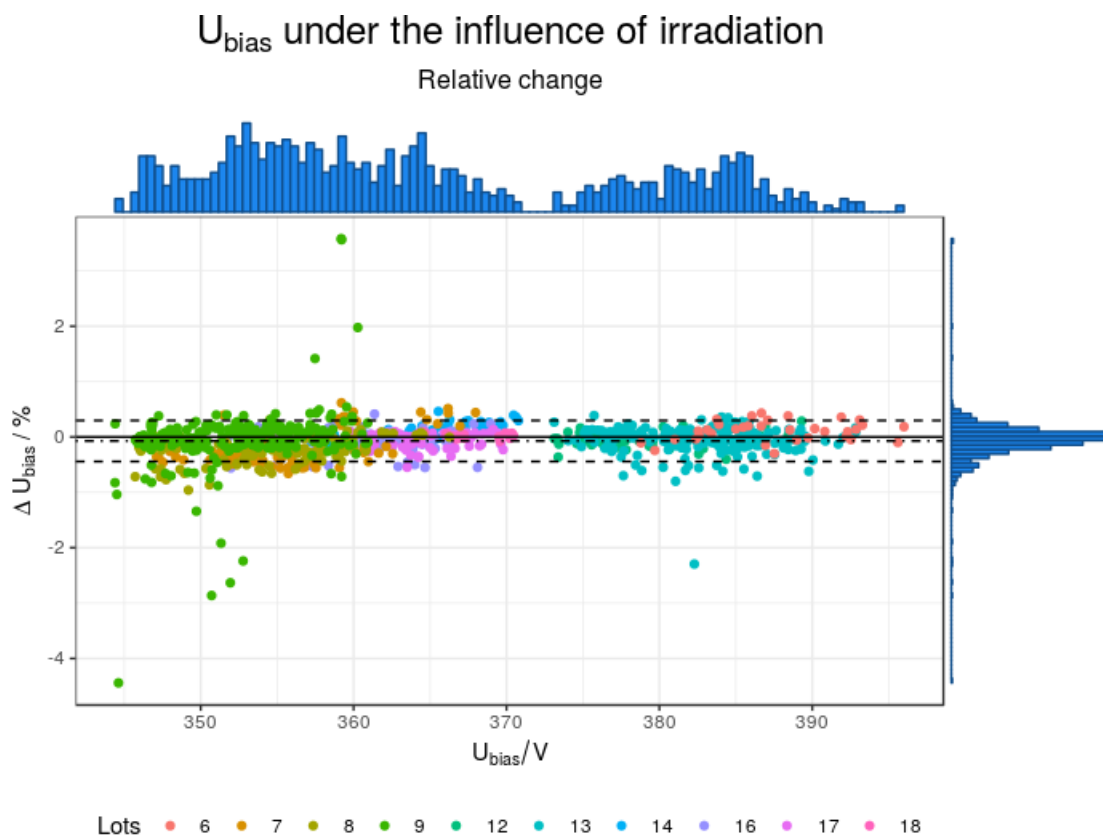


Figure 94: **The change of the bias voltage due to irradiation.** The dashed line represents one standard deviation and the dot-dashed line is the mean value. Taking a bias voltage of 375 V, a change of 1 % equals to 3.75 V.

Irradiation changes U_{bias} almost in the same manner across all lots. Hence, the greatest part of APDs does not provide a deviant behaviour from the pool. Only lot 7 and 9 show several outliers, both contain also most of the APDs.

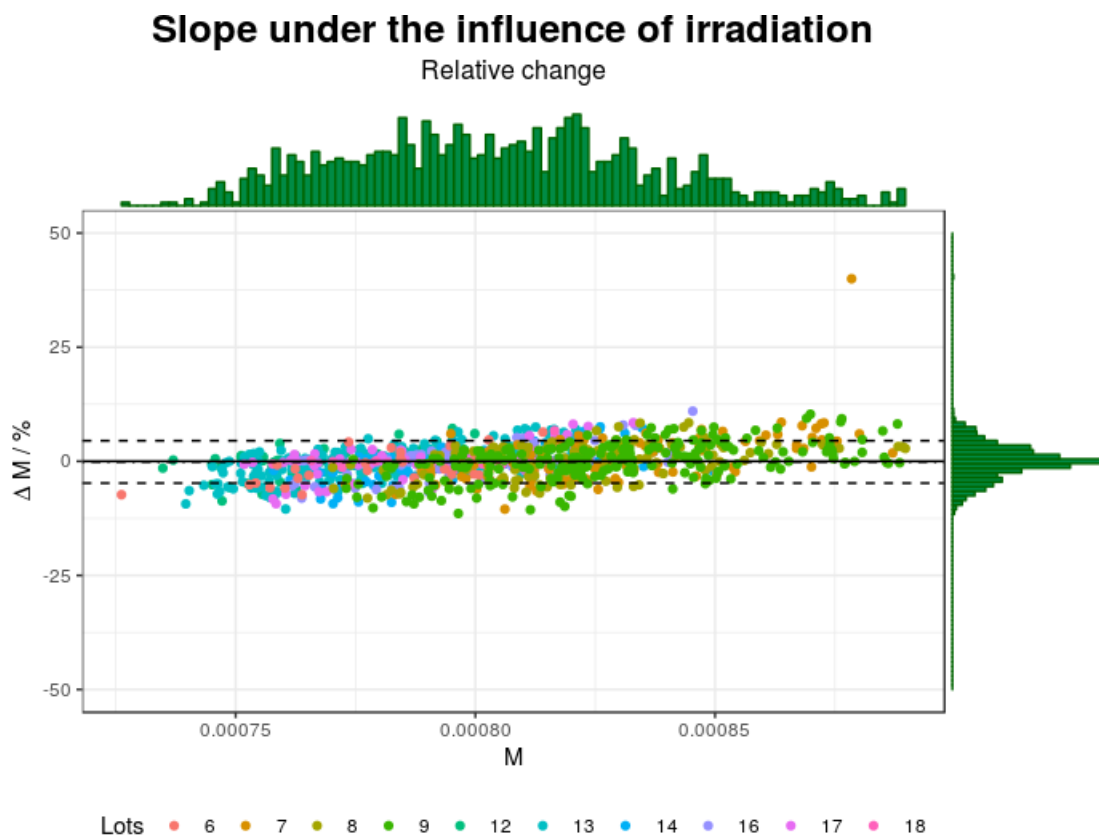


Figure 95: *The change of the slopes due to irradiation.*

The slope of the APDs are distributed homogenous across the lots but the pool as a whole shows slight deviations at lower slopes tend towards negative deviations and higher slopes towards positive deviations. Nevertheless, the changes in general are very Gaussian but also higher (up to 10 %) than the voltage changes which differ less than 2 % due to irradiation.

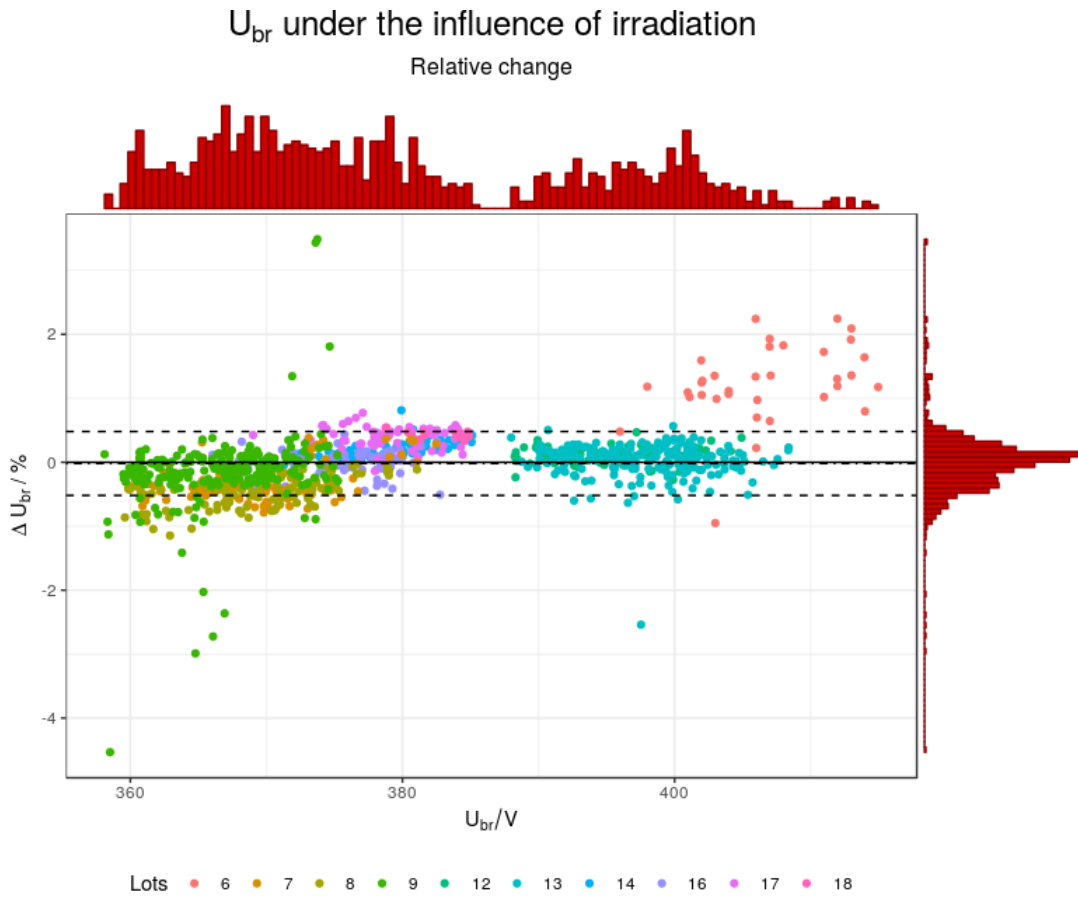


Figure 96: *The change of the breakdown voltages due to irradiation.*

Compared to the bias voltages in fig. 94, the breakdown voltages are spread almost the same, except of several outliers of the lot 6 and 9. The voltages change mainly less than 1 %. Furthermore, the APDs of a lot are very clustered and can easily be separated from APDs of another lot.

The parameter changes caused by the irradiation are also given in absolute values in Influence of irradiation on on page 215.

6.4 Conclusions

Ionizing particles traversing a scintillation crystal will put it in an excited state. After a certain time it will return to the ground state and emit characteristic light. Then, photodetectors convert this light into energy-correlated electrical signals. Since APDs are used here, even very small amounts of light are sufficient to construct a signal, since the amount of electrical charge is amplified many times by internal mechanisms in the APD (see [Avalanche Photodiode](#) on page 41).

The specific operating point determines the height of the gain and it indicates also what the noise ratio of this signal looks like, for example. The operating point is set to $M = 150$ and in [Parameter extraction](#) on page 58 it is examined how the associated bias voltage can be determined as precisely as possible. This voltage determines the multiplication factor, since the applied bias voltage is strictly related to the gain of the APD.

The measurement data are gathered by the PSL in Darmstadt and the APDs are measured at $T = -25\text{ }^{\circ}\text{C}$ and $T = -20\text{ }^{\circ}\text{C}$. Each APD provides a series of data points with amplification versus voltage values. In addition, the data set of each APD contains such a measurement series before and after an irradiation with γ 's of 30 Gy. In the barrel part of the EMC, the amplification gain of the APDs is set to 150 and is connected to an individual q-point. The corresponding bias voltage and slope for each APD has to be determined since the available measurement series do not provide data points at this specific amplification gain.

To determine the individual q-point of each APD as precise as possible, several regression models were studied in this work because the common model, the so-called Miller-fit, is not precise enough. Studying its coefficients in a wide range of values is not a solution nor adding additional terms to the Miller-Fit. To ensure that any inaccuracies are not caused by the commonly used framework ROOT, the Miller-Fit is also performed in R, with a non-linear least squares model and with a non-linear mixed model. The latter could not be conducted at all and the former provides not usable results as it can be applied to fit the irradiated data but not to fit all non-irradiated data.

Therefore, especially a linear mixed model and a polynomial model are analyzed more deeply without utilizing the Miller-formula. In addition, a differential fit is promising, too, but due to the strong dependency on the data points it is not investigated further since the measurements show a quite heterogeneous structure and a differential fit is very sensitive to the single data points. Therefore, each fit would have to be checked manually to prevent false results. Moreover, the calculation time required for each APD is considerable. For this reason, the mixed model is examined more closely. A mixed model takes into account pool information and is a common method, for example, to study drugs by testing a group against another. In physics and engineering, it is used when units are measured over time or when measurements are taken by the same device. Related models are used to analyze and to evaluate semiconductor manufacturers where processes are interrelated. However, each mixed model contains fixed effects and random effects. Fixed effects are those which provide information valid for all parts of the pool whereas the random effects utilize or represent individual information (see [Linear mixed model](#) on page 199 for further explanations).

Here, the underlying function of the mixed model is a polynomial function and it has been investigated which order provides the best results. In addition, the use of R^2 -values reveals how well a function describes the data and leads to the fact that the transformation of the data into a double logarithmical scale provides the best benefit as the amplification-voltage relationship approaches quite closely a behaviour of a polynomial of a third degree (see [fig. 60](#) and [table 16](#)). Furthermore, anova tests were performed to compare models with a different order of degree and ultimately to find the most precise relationship between amplification and voltage (see [table 18](#)).

Mainly, all investigations were performed with the help of three different APDs and it turned out the model is also not as precise as necessary in the envisaged region of $M = 100 - 200$. Therefore, it has been investigated how much the q-point depends on the involved number of data points. To do so, a set of data points with in total 6 to 20 is studied and compared with the location of the q-point (see [fig. 75](#)). The q-point shifts with the number of data points and in case of one of the three studied APDs, the q-point jitters even a lot (see [fig. 76](#)). Therefore, the mixed model is compared to a regular model with orthogonal polynomials which does not consider any pool information. If this model is used, the q-point does not change so much with any APD. Using only six local data points in total, three each above and below $M = 150$, delivers the best respectively the most stable results. The CMS uses a set of close points at the aimed gain as well [[133](#)] and this study here

proves that this is suitable. The bias voltages obtained by the mixed model serve as a reference to be compared to bias voltages of less advanced models like regular polynomials. Therefore, when comparing the q-point of each individual APD with both models, it turns out that the differences are rather small, in most cases below 100 mV (see fig. 79). For this reason, it is stated that the mixed model does not justify the programming and performing effort for future researches like in *Assignment & Matching*.

There, the slopes at the characteristic q-points will be used as well as they indicate how much an APD will drift in its amplification in case of a non-automatic regulation. In that sense, the parameter values before and after the irradiation represent how much they change over time in general due to external influences like being hit by particles later in the experiment, for example. The slopes are gained by using the derivative of the polynomial model and in addition, they are normalized to the amplification value of $M = 150$.

Though it is not used for the assignment task in *Assignment & Matching*, the breakdown voltage of an APD features an important parameter, too. The breakdown voltage of an APD indicates when an APD gets very sensitive due to a high applied voltage. There, a single photon will result in an enormous multiplication. In the Miller formula, the breakdown voltage is an open parameter and has to be estimated. Since the Miller-fit is not applied here, another method is necessary to determine this voltage. The diode curve acts like a tangent to the breakdown voltage and to estimate it, the highest available amplification value A_i is used via $U_{br} = \max(A_i) \cdot 1.001$. Another approach is to use the corresponding voltage where an amplification value of $M = 500$ is reached. This is the way the CMS determines this voltage. An additional method is to perform a regression with a nonlinear least squares models and with the underlying function $\log(V_i) = \alpha + \beta \rho^{A_i} + \varepsilon_i$. The CMS approach and the nls model provide very similar results with a difference of about 1 V in respect to the pool distribution (see fig. 83, fig. 92 and fig. 93). Therefore, both approaches deliver reasonable outcomes. The regression model depends less on the measurement data which varies in terms of available number of data points and the incremental sizes in between (see fig. 51 and fig. 53). Hence, the nls model is the better choice if in doubt. Hamamatsu provides breakdown voltages of the APDs at a temperature of $T = 20$ °C but not at $T = -25$ °C. To see, how the regression model performs in comparison with the official values, the APDs are also regressed at $T = 20$ °C (see fig. 90). This reveals that there is a very constant difference between the Hamamatsu values and the values provided by the nls model of about 6 V in case of almost each APD. Since the difference is positive and calculated by using $U_{br,Hamamatsu} - U_{br,nls}$, it is the fact that the Hamamatsu values are almost located at very large amplification values of $M > 1500$ where the breakdown likely already happened.

Finally, the changes of the parameters due to the irradiation are investigated in case of the entire pool (for example, see fig. 84). The bias voltages change in average by about 0 ± 2 V, respectively by less than 2 % (see fig. 94) whereas the relative changes of the slopes are greater with an upper limit of about 10 % (see fig. 95). The breakdown voltages change the least with less than 1 % in average (see fig. 96).

7 Assignment & Matching

*“Begin at the beginning,” the King said, very gravely,
“and go on till you come to the end; then stop.”*
Lewis Carroll

Assignment

Assigning subjects or objects to each other in a specific manner is a very common task. An assignment task is basically an optimization problem which usually requires complex patterns to solve. This is because many possible combinations have to be taken into account regularly. Imagine the observable matter content of the universe which is about $1 \cdot 10^{80}$ nuclei, a number which is already reached by the combination possibilities of only $60!$ objects [67]. Optimization problems have a very extensive application range: From logistic loadings through radiotherapy to data analysis to the diet problem [150], which was actually one of the first optimization tasks, while the most popular one is the so-called marriage problem. Everyday problems are, for example, the proper assignment of wlan devices to a router within a mesh or clients to servers in general and also the routing of self-driving cars. Furthermore, it has often to be decided whether an approximative solution, like a genetic algorithm, is sufficient or not.

Problems can be static or dynamic and underlying systems can be deterministic or stochastic. Furthermore, optimization problems can be divided into decision tasks, optimization tasks and search tasks. The **assignment problem** is a special case of the transportation problem, which is, in return, a special case of the minimum cost flow problem. This, again in return, is a special case of linear programming. Assignments are usually subject to constraints. The basics are linear functions which are optimized over a set of solutions and can be shortly expressed as [56]:

$\max (c^T x)$	linear target function
$Ax \leq b$	constraint
$x \geq 0$	constraint

where x is a vector of variables. This is called a primal program. The use of slack variables $z \geq 0$ can transform an inequation, $Ax \leq b$, into an equation: $Ax + z = b$. This reduces the complexity of a problem which can be given generally in terms of DTIME. The expressions

$\min (b^T y)$	linear target function
$A^T y \geq c$	constraint
$y \geq 0$	constraint

represent the dual program of the primal program above and provide a variable for each constraint of the primal. This allows to solve the primal problem faster since the optimum of the primal is now limited by an upper bound which is the optimum of the dual: The constraint of the primal problem is now the target function in the dual problem and vice versa. This leads to the situation that the maximization of the primal problem seques into a minimization of the dual problem.

Furthermore, the required run time depends also strongly on the number of the objects and connections in between but is also subject to the searching algorithm used like BFS⁶⁸, DFS⁶⁹ and Distrijka. Finally, it is about to determine the extrema of a function, either it is a maximization or a minimization problem. This corresponds to a matching in a weighed **graph** which will be the basis of this topic and discussed in the following.

⁶⁸Breadth-first search

⁶⁹Deep-first-search

7.1 Similarity measure

Each single APD is represented by its individual parameters. Here, two parameters are of major interest, the bias voltage and the slope as well as their changes due to irradiation. Since a lot of APDs are involved, specific characteristics or rather peculiarities of the operational parameters might appear across the APD pool. Therefore, the APD pool is studied as a whole to get a deeper understanding of the underlying structures in general and in specific due to the irradiation. At first, all **correlations** between the parameters are calculated (fig. 97):

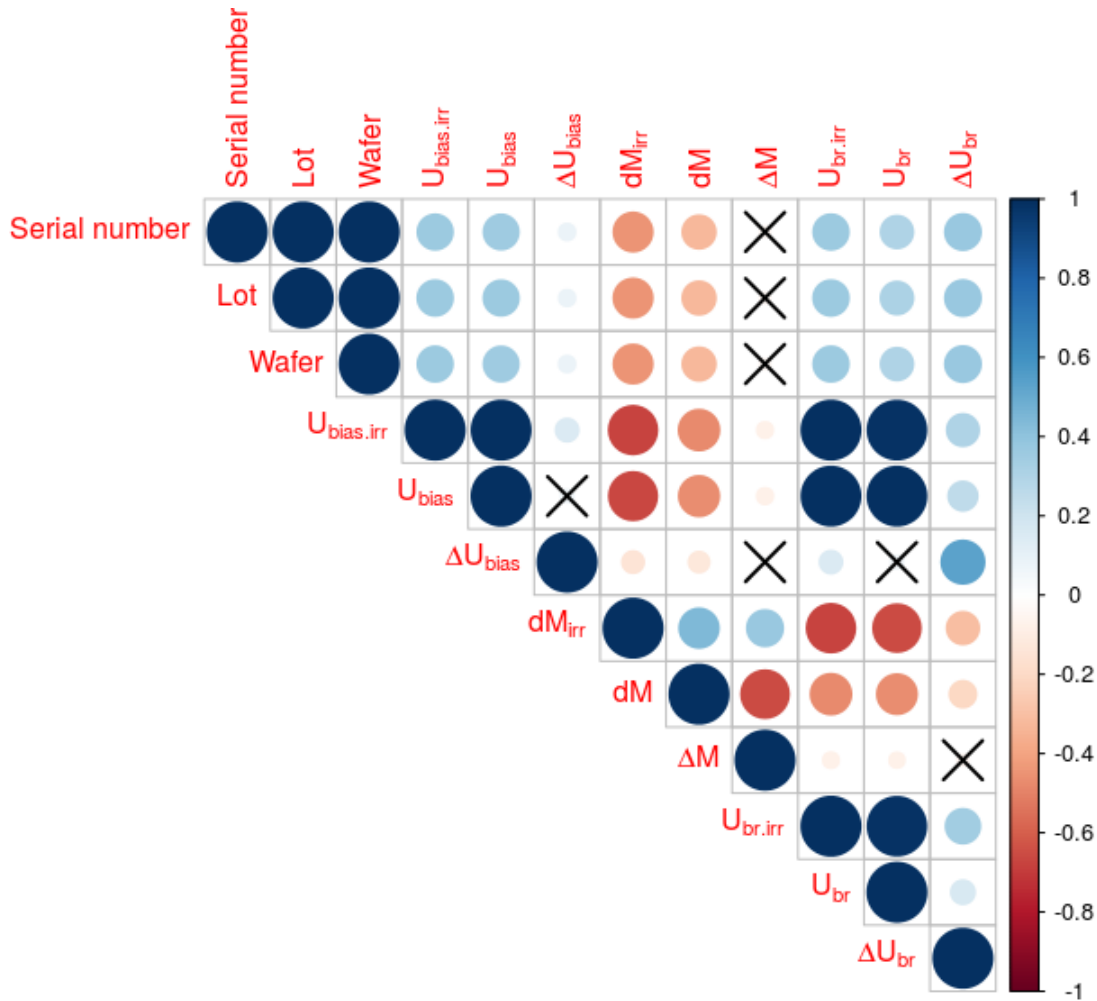


Figure 97: **Correlations among all parameters.** The changes ΔU_{bias} , ΔM and ΔU_{br} are calculated by using the values before and after the irradiation process, the latter indicated by an index *irr*. A significance test with a p-value of 0.05 is applied.

Most relationships provide a correlation, only except of those where the slopes of the diodes are involved. It is worth noting that the bias voltage is clearly negatively correlated with the slope. In general, the APDs tend to provide higher voltages when seen on a time scale, represented by their serial numbers (see fig. 97 and fig. 238). Since the APDs have to be assigned to each other in a specific way, it is necessary to determine under which rule this has to be performed. To get a better impression of the distributions of all bias voltages and slopes, the APD pool is visualized as the corresponding parameter space (see fig. 98):

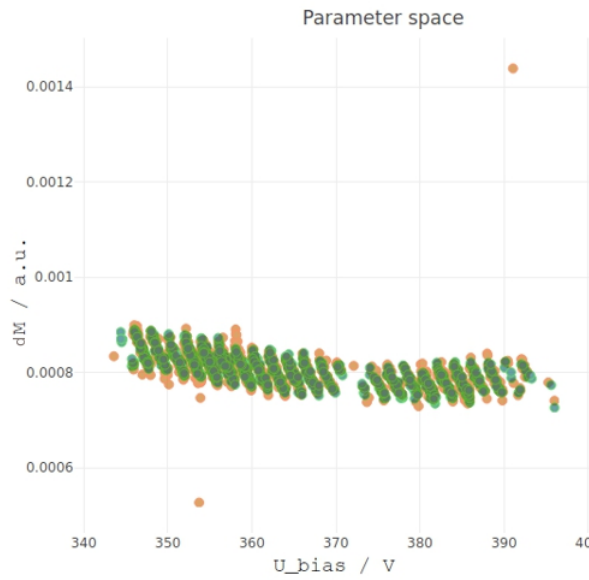


Figure 98: *Parameter space*. Two prominent outliers are present.

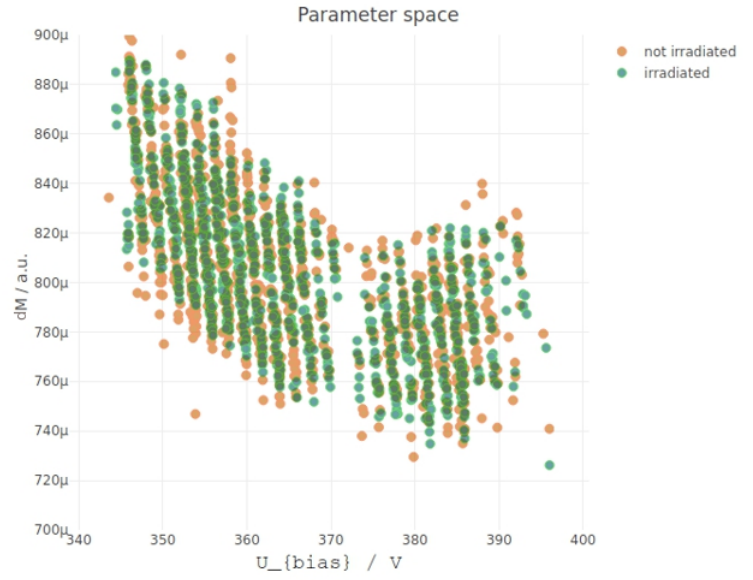


Figure 99: *Parameter space - zoomed*. Without the outliers, the shape is now a bit more characteristic as the pool provides a decreasing course.

The parameters are distributed very differently in fig. 98. The bias voltage provides a much more stretched shape than the slope does, both for the irradiated and for the non-irradiated data as well. To measure a similarity, this peculiarity must be taken into account because they have to be weighted accordingly in order to avoid a preference of a parameter over the other. The outliers in fig. 98 are neglected in fig. 100.

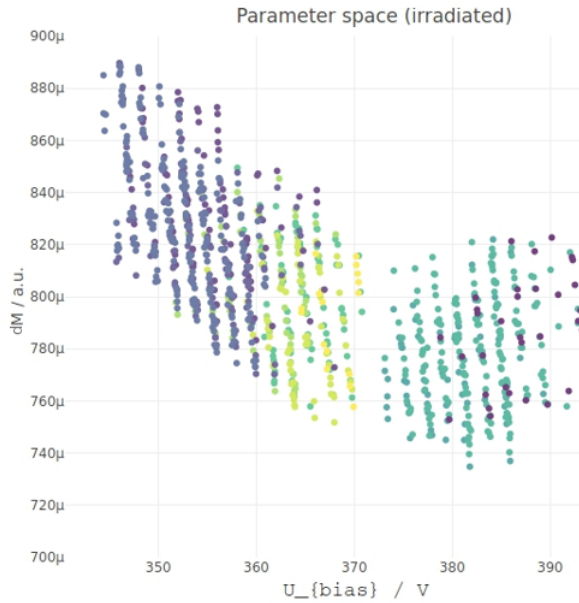


Figure 100: *Parameter space - irradiated*.

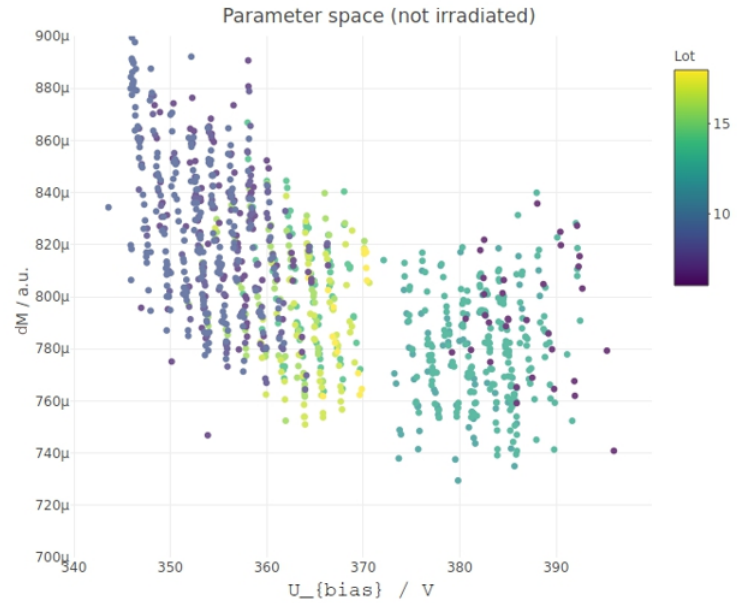


Figure 101: *Parameter space - not irradiated*.

The parameter space in fig. 98 can be divided into a set before and into a set after the irradiation and, in addition, with respect to the lots of the APDs (see fig. 100 and fig. 101). The data points of the same lots tend to cluster like they do when having a look at their single parameters only (see fig. 94 and fig. 95). The first lots, especially lot 6, spread across the parameter space. The changes of these parameters because of the irradiation can also be visualized in a two dimensional space:

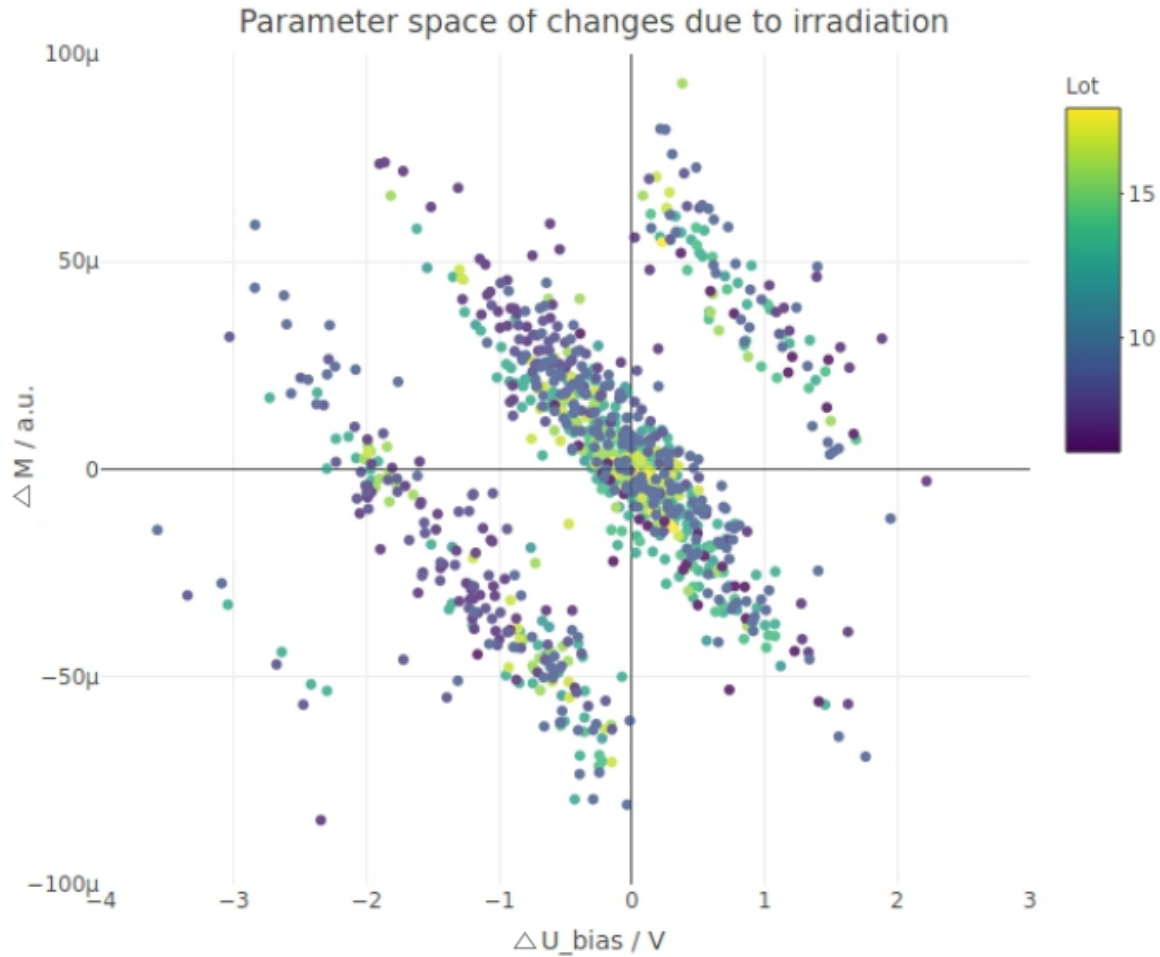


Figure 102: **Change of the parameter space.** The non-irradiated values are subtracted from the irradiated values. Clear structures are present but independent from the lots.

The parameter space of the changes reveals a clear structure: The entire pool is divided into three or four separate clusters. Since the APDs of the lots are rather grouped across the entire pattern (see fig. 100), this characteristic structure cannot be explained through different manufacturing properties. The fact that most changes are centered at the origin is an indicator for a Gaussian behaviour. Furthermore, the inclination seems to represent a systematic reason caused by the irradiation. The next task is to find a proper method how to assign the APDs to each other.

7.1.1 Metric

In order to find out which devices are similar to each other, a suitable measuring instrument is needed first. A feasible method is the usage of a distance measurement: Imagine the devices are space points in a four-

dimensional space $\vec{x} = (dM, dM_{\text{irr}}, U_{\text{bias}}, U_{\text{bias,irr}})$ and the distances between the APDs represent their similarities:

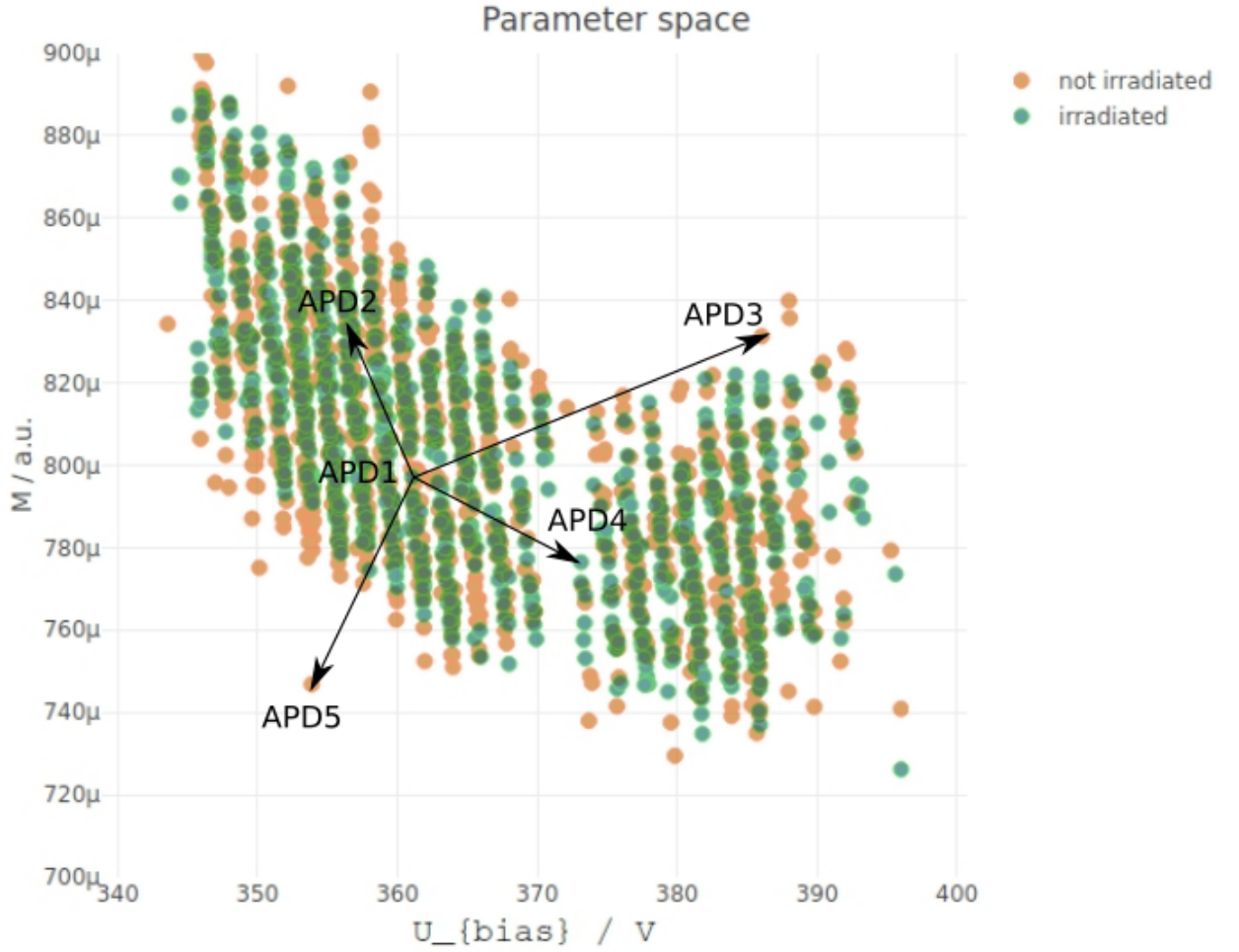


Figure 103: *Parameter space - similarity measurement.* The similarities are represented by the distances between the APDs.

The task is to measure a meaningful distance by making use of a real-valued function. The Euclidean distance is the most common distance and applicable plus sufficient in many situations:

$$d_{\text{eucl}}(\vec{x}, \vec{y}) = \|\vec{x} - \vec{y}\| = \sqrt{(\vec{x} - \vec{y})^2} = \sqrt{(x_1 - y_1)^2 + \dots + (x_4 - y_4)^2} \quad (2.14)$$

where $i = 1, \dots, 4$ represent the parameters of an APD. When calculating distances in a multivariate space, this distance has the disadvantage that the units of the different variables will provide varying magnitudes in their dimensions. The **Mahanobolis** distance takes up on this by measuring the distance from an observation \vec{x} to the mean $\vec{\mu}$ of a set:

$$d_{\text{mahal}}(\vec{x}) = \sqrt{(\vec{x} - \vec{\mu})^T S^{-1} (\vec{x} - \vec{\mu})} \quad (2.15)$$

in terms of the standard deviation. S is the covariance matrix:

$$\begin{aligned}
S &= Cov(X) = E\left((X_i - \mu_i)(X_j - \mu_j)^T\right) \\
&= E\left(\begin{array}{cccc}
(X_1 - \mu_1)^2 & (X_1 - \mu_1)(X_2 - \mu_2) & \dots & (X_1 - \mu_1)(X_n - \mu_n) \\
(X_2 - \mu_2)(X_1 - \mu_1) & (X_2 - \mu_2)^2 & & \\
\vdots & & \ddots & \vdots \\
(X_n - \mu_n)(X_1 - \mu_1) & & & (X_n - \mu_n)^2
\end{array}\right) \\
&= \begin{pmatrix}
Var(X_1) & Cov(X_1, X_2) & \dots & Cov(X_1, X_n) \\
Cov(X_2, X_1) & Var(X_2) & & \\
\vdots & & \ddots & \vdots \\
Cov(X_n, X_1) & & & Var(X_n)
\end{pmatrix} \\
&= \begin{pmatrix}
\sigma_1^2 & \sigma_{1,2} & \dots & \sigma_{1,n} \\
\sigma_{2,1} & \sigma_2^2 & & \\
\vdots & & \ddots & \vdots \\
\sigma_{n,1} & & & \sigma_n^2
\end{pmatrix}
\end{aligned}$$

Covariances are able to take into account irregular shapes in a multivariate space (see fig. 99), like elliptic shapes which are often a result of the multivariate units. In contrast, the Euclidean radius can be applied only when the parameter space can be described by a circle. If S is the identity matrix, which is given when the variates are uncorrelated, then the Mahalanobis distance falls back to the Euclidean distance.

The expectation values $E[\mu_i]$ and $E[X_i]$ are part of the covariance matrix but due to $E[X_i] = \sum_{i=1}^n x_i p_i$, the variable x_i is assigned with an individual probability p_i and can hardly be calculated. Therefore, the estimated mean $\hat{\mu}_1 = \frac{1}{n} \sum_{i=1}^n x_{1,i}$ is suitable because x_i follows the true underlying distribution. This is valid through the law of large numbers by making use of the linearity of the expectation value: $E[\hat{\mu}_1] = E[\frac{1}{n} \sum_{i=1}^n x_i] = \frac{1}{n} \sum_{i=1}^n E[x_i] = \frac{1}{n} n E[x_i] = E[x_i]$. With enough samples n , e.g. $n \rightarrow \infty$, the mean can be estimated precisely $\hat{\mu}_1 \rightarrow \mu_1$ and thus, $\frac{1}{n} \sum_{i=1}^n x_{1,i}$ can be used to approximate $E[\mu_1]$. The Mahalanobis distance can also be used to calculate the distance between two random vectors \vec{x} and \vec{y} of the same sample set:

$$d_{mahal}(\vec{x}, \vec{y}) = \sqrt{(\vec{x} - \vec{y})^T S^{-1} (\vec{x} - \vec{y})} \quad (2.16)$$

An advantage of the Mahalanobis distance is its invariance against **scaling** and **correlations**, in contrast to the Euclidean distance. Thus, it can be applied for spaces spanned by variables with different units.

Beside the Euclidean and the Mahalanobis distance, there are other metrics as well. Transforming the parameters into defined ranks is another method but some ranks next to each other might have low similarities. Two others are worthy to note which is the Manhattan distance on the one hand and the cosine similarity on the other hand. The Manhattan distance $d(x, y) = \sum_i |x_i - y_i|$ is used when, e.g., a movement through a city is only allowed horizontally or vertically. As the parameter space of the APDs is quite continuous, this metric is assumed to be not meeting the requirements. The cosine similarity has an advantage in measuring the cosine angle $\cos(\theta)$ between vector \vec{x} and \vec{y} : $\cos(\theta) = x \cdot y / (||x|| \cdot ||y||)$. It does not consider the distance between x and y themselves but indeed how similar the vectors are. In case of APDs, it is important that not only the angle is considered but also the vector length $||APD||$ of an APD as it represents how strong its properties are. A cosine similarity would neglect this. On the other hand, for example, considering the distance only could lead to situations where APDs are located very close to each other at the origin but provide opposite properties. Thus, they will be treated as similar due to their short distance.

With the Mahalanobis distance d_{mahal} in the inventory, the similarities of the APDs can now be determined. In the first instance, the Mahalanobis distance is used to identify **outliers**. In the following, the APD pool is sketched in terms of the Mahalanobis distance against the number of standard deviations. Though only two parameters are used to visualize the pool, the APDs are represented by four parameters in both images.

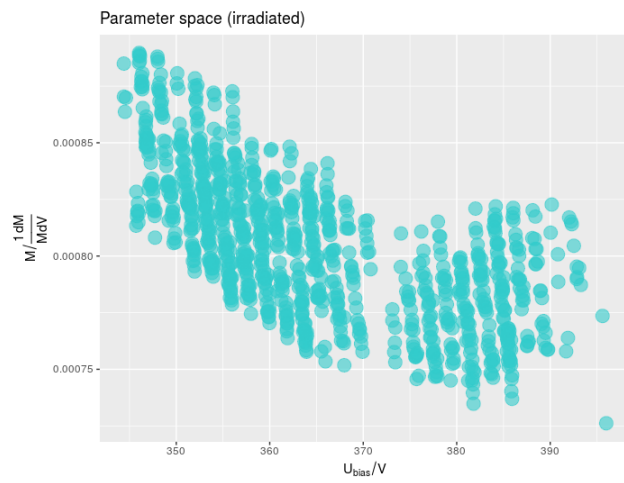


Figure 104: *Outlier identification for irradiated data with a threshold of 0 std.*

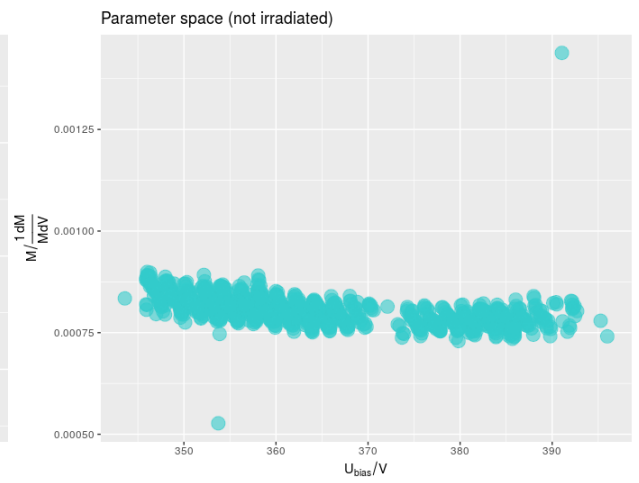


Figure 105: *Outlier identification for not irradiated data with a threshold of 0 std.*

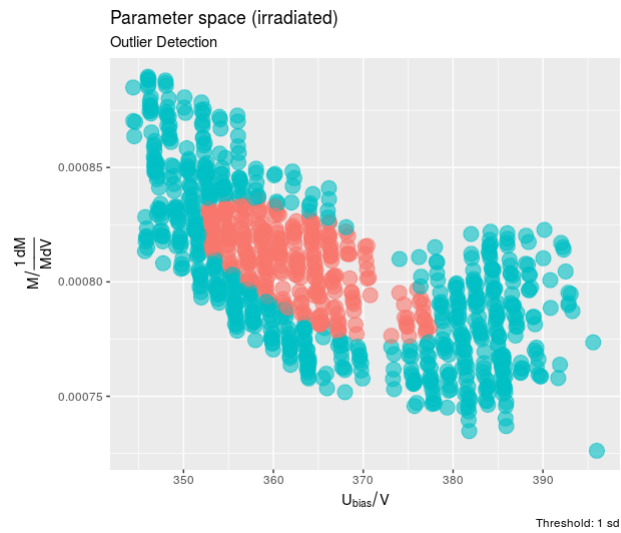


Figure 106: *Outlier identification for irradiated data with a threshold of 1 std.*

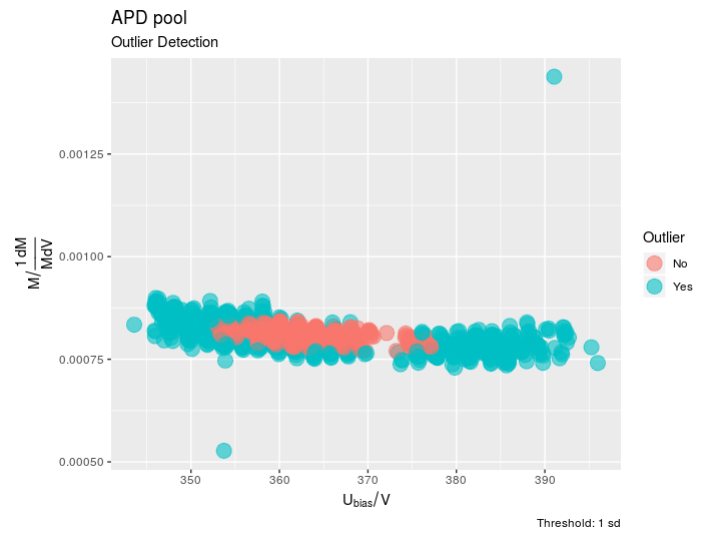


Figure 107: *Outlier identification for not irradiated data with a threshold of 1 std.*

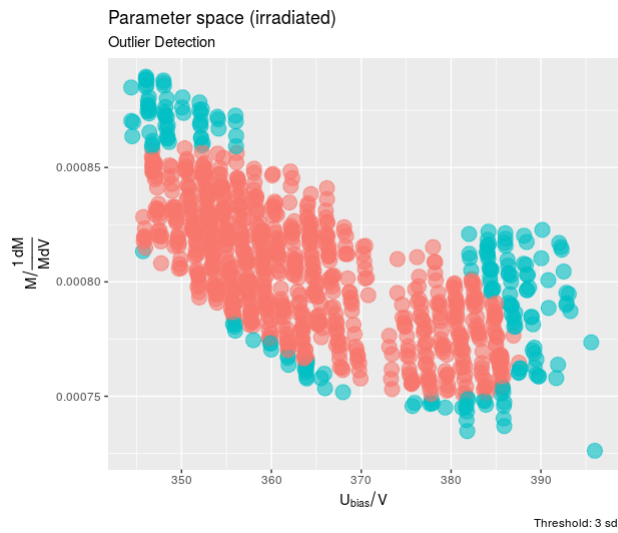


Figure 108: *Outlier identification for irradiated data with a threshold of 3 std.*

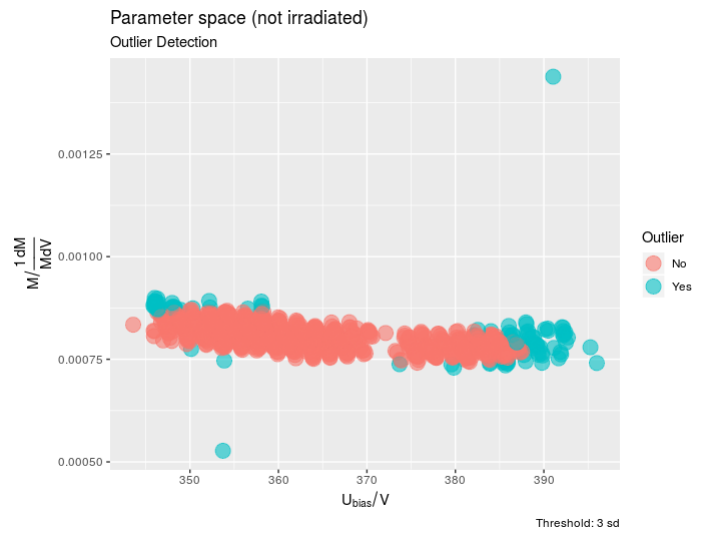


Figure 109: *Outlier identification for not irradiated data with a threshold of 3 std.*

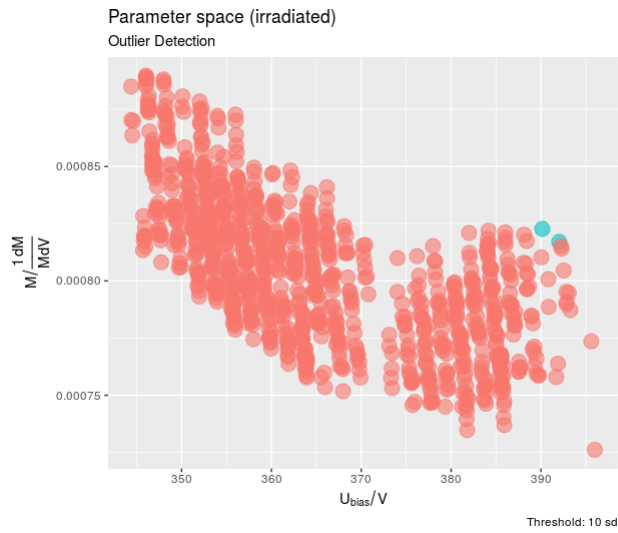


Figure 110: *Outlier identification for irradiated data with a threshold of 10 std.*

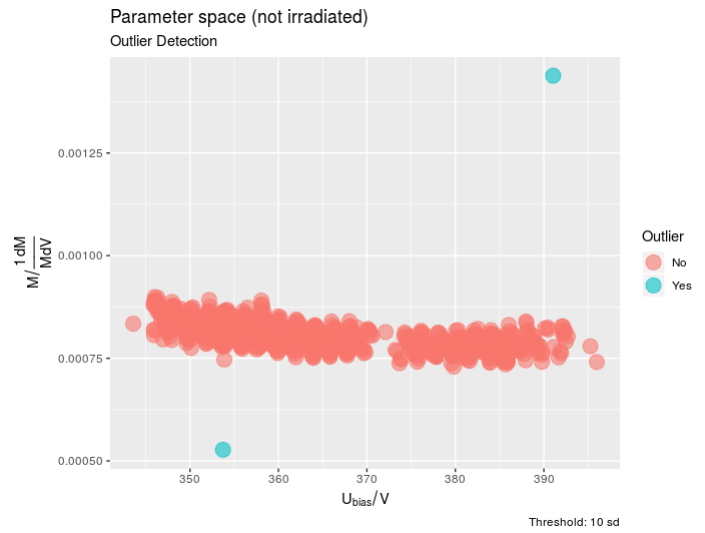


Figure 111: *Outlier identification for not irradiated data with a threshold of 10 std.*

The outlier analysis shows that the majority of the APDs differs in their properties but, yet, most are within 3 standard deviations. In **Similarity measure** on page 214, the similarities are also measured as a function of the lots. An outlier detection can be used to identify suspicious APDs before they enter the matching processes - without using predefined tolerance limits. On the other hand, two outlying APDs could be that similar that they form a valid pair. However, the possibility remains that both APDs are just bad APDs. Regarding the outliers in fig. 111, it turns out that only their slope is strange and the strong characteristic vanishes due to the irradiation (see fig. 110).

To now assign APDs to each other with respect to their distance, a suitable method has to be found. In the following, some approaches will be presented. The algorithm ultimately used is Edmond's algorithm described on page 109. In the following, some concepts and the starting point will be discussed. However, the simplest method to use is a greedy algorithm:

7.2 Greedy algorithm

Greedy algorithms always make choices which seem to be the best at the current state and disregard future or past steps. Thus, they can hardly determine a global optimum as they will likely step into a **local optima**. Such an approach is also widely known as heuristic technique. In some cases greedy algorithms are able to prevail in comparison with more advanced algorithms due to their fast and simple approach. Hence, they are preferred when an approximative solution is sufficient, even when it is only half as good.

This method marks the starting point and has already been used for Proto120 [147]. For it, the procedure was as following: Match the initial APD with the next APD of a table which is within a certain Euclidean distance. Afterwards, remove this pairing from the table and move on to the next APD (fig. 112):

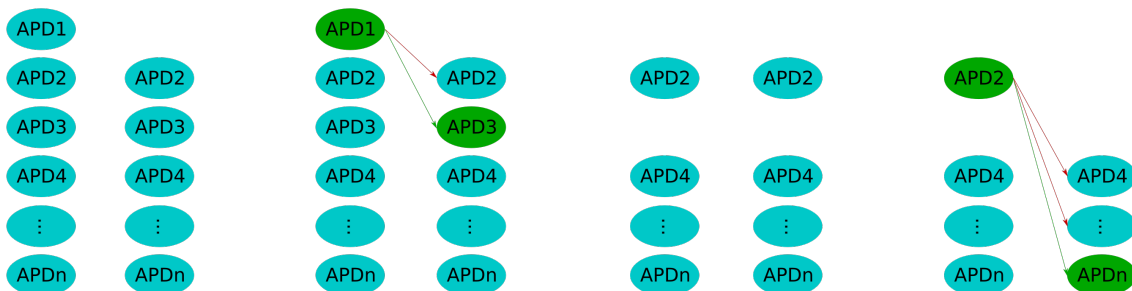


Figure 112: **Greedy algorithm.** Each APD will be matched with an APD which is next inside a defined radius.

This technique considers only one single matching and is very greedy as only a single path through the tree is taken into account (see **Graph theory** on page 216). When utilizing such an algorithm, the situation occurs that, for example, the output of the algorithm will be only a subset of the available APDs. Hence, not all available APDs will be matched as a result of searching for local optima only. For this reason, in this approach the quality of the matching is measured by the achieved amount of assigned APDs.

The first step to improve the matching is to increase the amount of possibilities by looping over the whole pool to find out which APD is the best to start with. The sum of weights of each iteration is stored and finally compared among the iterations. On this basis, the iteration with the highest amount of APDs is selected and performed again.

The distances between the APDs are calculated via

$$d_{\text{eucl}} = \sqrt{\left(\frac{|dM_{APD1} - dM_{APD2}|}{\Delta dM}\right)^2 + \dots + \left(\frac{|dU_{bias,APD1} - dU_{bias,APD2}|}{\Delta dU_{bias}}\right)^2}$$

and normalized due to the mixed attributes involved here. This will prevent the covariate with the highest variance from driving the pairing. The matching limits were set to $\Delta dM = 0.1 = \Delta U_{bias}$ together with a combined limit taking into account both: $\Delta R = \sqrt{(\Delta dM)^2 + (\Delta U_{bias})^2} = 0.14$. Hence, the APDs of a pairing were not allowed to extend the limits of ΔdM , ΔU_{bias} and ΔR . In daily operations, this approach results in the circumstance that a varying number of APDs will not be used though maybe needed. In such a case, the matching limits were enlarged in the past and disregarded APDs were put into the pool again for the

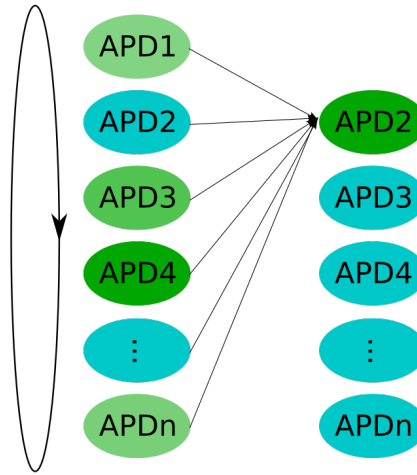


Figure 113: *Greedy algorithm - enhancement.*

next routine. Tasks like the assignment problem (and for example other ones like the Travelling salesman problem or the Knapsack problem) require a more elaborate method because these problems are NP-hard⁷⁰. Therefore, the need for something more advanced like the hungarian algorithm arises. The most efficient methods use **graph theory** as a basis (see **Graph theory** on page 216).

7.3 Hungarian algorithm

Kuhn was in 1955 the first to solve the maximum-weight problem on a **bipartite graph** [78]. Because the approach is based on the work of two hungarian mathematicians, Dénes König and Jenő Egerváry, he called the algorithm the Hungarian method. The following theorems play an important role:

Berge's lemma: A matching is maximum when there is no alternating path

Theorem from König and Egerváry: The number of edges in a maximum matching is equal to the number of vertices in a minimum vertex cover

Marriage theorem from Philip Hall: A graph $G = (V, E)$ with $V = A \cup B$ provides a matching that covers A if and only if for all vertices of $S \subseteq A$ is: $|S| \leq N(S)$, where $N(S)$ are all the neighbors.

Two years later Munkres improved the algorithm which is known as the Kuhn-Munkres algorithm from then on. The approach is based on the primal-dual method which corresponds to the finding of a maximum matching and a minimum vertex cover on a bipartite graph. The Kuhn-Munkres theorem is:

Be G_l a spanning subgraph of G . If G_l contains only those vertices (x, y) which satisfy the condition $(x, y) \in E_l \Leftrightarrow E \wedge I(x) + I(y) = w(x, y)$, then it is an equality (partial) graph. The relationship between maximum-weighted matching and a perfect matching in the equality graph is: If M^ is a perfect matching in G_l , then M^* is a maximum-weighted matching in G .*

Basically, the theorem transforms the problem from finding a maximum weighted matching into the problem of finding a perfect matching. The scheme of the Kuhn-Munkres algorithm is basically as follows [136]:

⁷⁰non-deterministic polynomial-time

1. Find maximal matching in E_l
2. Check for a perfect matching, otherwise construct root tree
3. Find an augmented path in the root tree
4. Enlarge matching through exchanging the edges

The Hungarian algorithm is only applicable to bipartite sets but it is assumed to be feasible nevertheless according to the following idea: In each iteration the algorithm fixes a specific APD, e.g. APD 1. Then, the APD 1 represents a set containing only this single element and all the remaining APDs embody the other set to fulfil the bipartite requirement. In the next iteration, the sets will change such that the former single APD 1 is now part of the set containing all APDs except of a another APD, e.g. APD 2.

The results show that this idea cannot work because the according tree growing on the graph does not know about the separation of the APDs into sets with only one single APD and all other APDs in the other set. Hence, the algorithm can never deliver satisfying results because many APDs will be matched twice.

7.3.1 Adjustment to a single set

Due to the restrictions of the Hungarian method, the approach “*The Hungarian Algorithm with a Single Input Set*” [48] is realized which is built on the Hungarian algorithm but extends it such that an unipartite set can be used (see *Adjustment to a single set* on page 218). Due to conceptual flaws this method cannot be applied to unipartite sets. An algorithm that is able to solve the assignment problem on a single set is Edmond’s algorithm.

7.4 Edmond’s algorithm

The Edmond’s algorithm [81], also called blossom algorithm and developed in 1965, takes up on the Hungarian method by considering also non-bipartite graphs. In the last decades several improvements were achieved e.g. by Lawler [96], Gabow and Tarjan [77] and finally by Kalmogorov [165] by combining the idea of updating dual variables and making use of priority queues. As the first computer implementation is labelled Blossom-I, the according algorithm by Kolmogorov is now called the Blossom-V algorithm.

Non-bipartite graphs can be handled because Edmond introduced the ability to take into account odd-length cycles. When the algorithm enters such a cycle, it will be treated as a single vertex through edge contraction, representing the **blossom**. Then, the algorithm will continue along the origin path [145]. A blossom B is a cycle with $2k + 1$ edges of which k edges are in M . Hence, a vertex v of such a cycle must provide an alternating path to an exposed vertex y , making v a root.

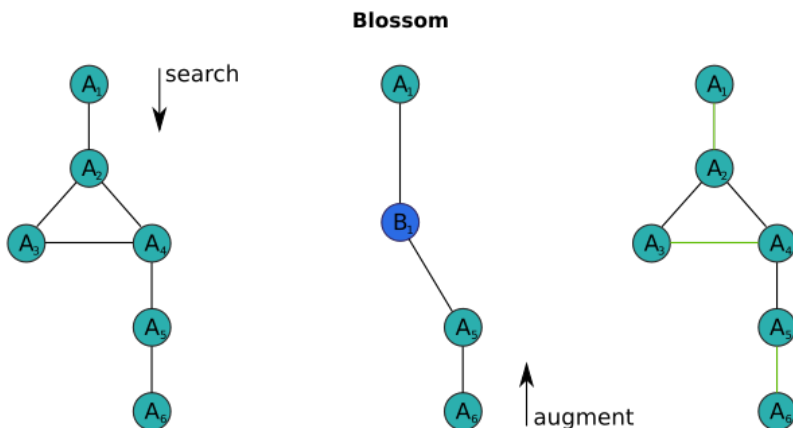


Figure 114: **Blossom shrinkage and expansion.** A blossom is an odd-length cycle with $2k+1$ edges. Edmond’s algorithm shrinks such a blossom to a single vertex and continues its search along the alternating path. After reaching the end, the algorithm returns and augments this path. When the blossom B is met, it will be expanded. Shrinking to a single vertex enables the toggling of the edge, e.g. (a_1, a_2) to (a_1, a_3) , which connects the blossom with the alternating path.

The steps of the algorithm:

1. Initialize with a greedy matching
2. Construct root tree, shrink any blossoms
3. Check root tree for augmented path
4. Expand blossoms
5. Enlarge matching through swapping the edges

7.4.1 Implementation

To get started, the distance of each single APD i has to be calculated in regard to each other APD j . The most common way to do so is to represent the APD pool as an **adjacency matrix**. Then, the distances $d(i, j)$ among the N APDs are represented as elements of a $N \times N$ matrix, the distance matrix (see table 22). There, each cell represents the distance between the corresponding APD i and APD j . This arrangement makes it easy to equip bad pairings with an infinite distance. Given four APDs, it looks as following:

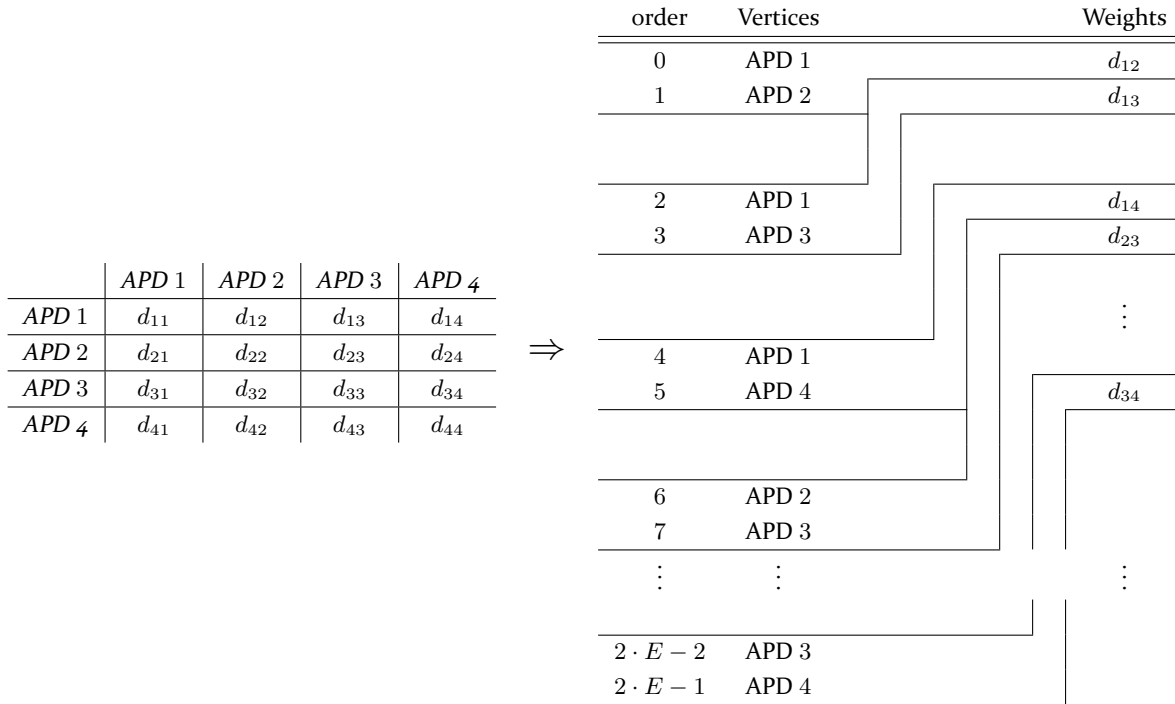


Table 22: **Adjacency matrix.** The adjacency matrix contains all distances between the APDs.

Table 23: **Data structure of the blossom algorithm.** The adjacency matrix is converted into a vertex and an edge table. The handshaking of the APDs is already taken into account. E is the total number of edges.

Instead of a matrix, the algorithm expects a specific input arrangement, a list with two different **tables**: The one holds the vertices and the other the corresponding weights of the edges connecting them. Two subsequent entries, $2 \cdot i$ and $2 \cdot i + 1$, of the vertex table are always incident to the edge i . The data set is extracted from the symmetric adjacency matrix by using only a **“triangular matrix”** without the diagonals. This is because the APD pool is a unipartite set and therefore one has to take into account self-loops. This ensure that each assignment is considered only once and self-loops will be neglected. Furthermore, the algorithm requires the

total number of assignments E in advance. In general, to calculate the number of possibilities to take a subset of k objects out of a set of N objects, the binomial coefficient can be applied:

$$\binom{N}{k} = \frac{N!}{k!(N-k)!} \quad (2.17)$$

1,000 APDs provide $E = 1000!/(2! \cdot (1000 - 2)!) = 499500$ edges. Basically, the number of edges of the APD pool can be transferred to the **handshake** problem: How often will hands be shaken when every guest shakes hands with every other guest? Thus, the possibilities can finally be calculated by $E = (N \cdot (N - 1)) / 2$. On a bipartite graph it just would be N^2 . In the case that all these edges are available, then the underlying graph is considered as a complete graph. Since these edges provide weights, it is an edge-weighted graph.

The Mahalanobis distance is calculated with the help of the **Eigen** library which is a template library for C++ for linear algebra. There, the parameters of the APDs are given as a population matrix (P_{ij}), where each row i represents the parameters j of a single APD:

$$P_{ij} = \begin{pmatrix} dM_1 & U_{bias,1} & dM_{irr,1} & U_{bias,irr,1} \\ dM_2 & U_{bias,2} & dM_{irr,2} & U_{bias,irr,2} \\ \vdots & \vdots & \vdots & \vdots \end{pmatrix} \quad (2.18)$$

Next, a centered mean matrix $C = (P_{ij} - \bar{P}_j)$ is calculated with the help of partial reduction templates within Eigen:

$$C = \begin{pmatrix} dM_1 - \overline{dM} & U_{bias,1} - \overline{U_{bias}} & dM_{irr,1} - \overline{dM_{irr}} & U_{bias,irr,1} - \overline{U_{bias,irr}} \\ dM_2 - \overline{dM} & U_{bias,2} - \overline{U_{bias}} & dM_{irr,2} - \overline{dM_{irr}} & U_{bias,irr,2} - \overline{U_{bias,irr}} \\ \vdots & \vdots & \vdots & \vdots \end{pmatrix} \quad (2.19)$$

Now, the covariance matrix S can be obtained by using the adjoint of C :

$$S = \frac{1}{N-1} \cdot C^T \cdot C \quad (2.20)$$

Next, the difference between the APDs i, j , with $i \neq j$, is given by

$$d = APD_i - APD_j \quad (2.21)$$

The implementation of the Mahalanobis distance is now complete to calculate the edges between all APDs via: $d_{Mahal} = \sqrt{d^T \cdot S^{-1} \cdot d}$ (see eq. (2.15)). It is important to consider that the APDs are samples and, thus, the specific distances are subject to the pool they are selected from respectively to the covariance matrix S . When the pool is small, for example, containing only 10 - 20 APDs, then the distances change significantly (see fig. 119). In case of even less APDs, some eigenvalues of the covariance matrix might provide very small numbers, e.g. $\sim 1 \cdot 10^{-14}$, which can cause to be seen as negative due to rounding issues. Then, the covariance matrix is **singular** because the parameters of such few APDs will only exist in a linear subspace. Since only matrices which are positive semidefinite respectively which are not singular can be inverted, these eigenvalues might lead to wrong distances. A common method for such a situation is to perform a PCA⁷¹ but information might be lost afterwards. In [101] it is advised to correct or even to truncate the distance then. Another solution is to use the Moore-Penrose inverse but the implementation is not considered here as it is assumed that APDs will not be matched unless a proper number is available. Therefore, the calculation of the distances will be tracked and an error will be thrown when the covariance cannot be inverted or when a distance is negative. In case of the APD pool used in this work, the calculation succeeds when the number of APDs is higher than 7.

⁷¹Principle component analysis

Another problem arises when the ROOT library is linked because some memory-errors might appear. The reason could be identified via Valgrind⁷² which narrowed down the possibilities. Blossom and ROOT seem to use some same memory addresses which cause the problems and declaring all arrays used to transform the tables of the vertices and edges into the input list, with the help of the *new*-operator in C++, turned out to be the solution.

7.5 Sequence

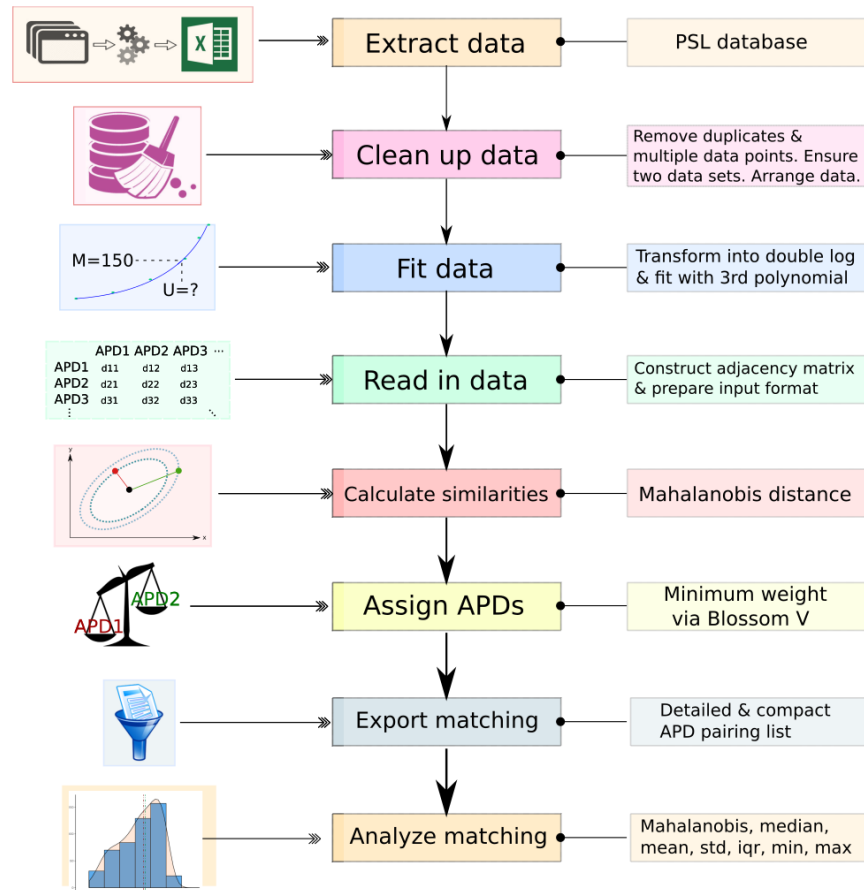


Figure 115: *Sequence*. The APD measurement data points are extracted from the PSL database. The data has to be cleaned and prepared for further steps. At first, the individual q-point of the APDs have to be determined. Afterwards, the APD parameters are imported into the matching routine where their similarities are calculated. On this basis, the APDs will be grouped into pairs of two via a minimum weight. Next, the matching is exported and can be analyzed in terms of global weight and statistical parameters like median and mean.

Initially, the APD data is extracted from the PSL database. An APD set contains the measurement series of an APD at a certain temperature and, thus, especially the amplification against voltage values. In the next step, the data is cleaned and verified by some routines which identify APD duplicates, multiple data points and sets. It is also ensured that an APD provides two data sets (non-irradiated & irradiated data). In addition, there are features to filter the APDs by grid numbers and other options like neglect matched or mounted APDs. Furthermore, it is verified that the serial numbers are correct and present in the database. Such **verification tools** are also available for the crystal database in regard to the APDs which are glued to specific crystals. However, in both cases mistakes have to be checked and corrected manually. Up to now, several routines and classes in C++ are used for that. As at the last step, the data format is modified to be imported in R.

In the next stage, the data of all APDs is **transformed** into a double logarithmical scale and each APD is **fitted** separately by a polynomial of a 3rd degree. For each APD data set only six data points are taken into account in total, three below $M = 150$ and three above. Each APD is fitted **twice**, once for the non-irradiated data set as well as for the irradiated data set.

Afterwards, all APD data sets are exported and read in by the matching program. There, some choices can be made like defining parameter limits. Next, the Mahalanobis distances between all APDs are calculated and stored in an **adjacency matrix**. Then, only a triangular matrix without the diagonal elements is converted

⁷²Debugging and profiling tool for memory-related errors

into a vertex and an edge table and passed to the Blossom V algorithm where a minimum weighted matching is calculated. The efficiency of the algorithm yields a **matching** result in less than a second. Performance studies on the algorithm have already been conducted [23]. The matching is exported in two **output** formats: One that contains detailed information about the pairings like the properties of the APDs and their similarity and another one that provides only the serial numbers of the matched APDs.

Then, the matching results can be analyzed in R where the **weight** of the matching is calculated by an independent Mahalanobis distance calculation. In addition, the matching quality can be visualized by putting the weights of the pairings into a histogram. Statistic tools like median, mean, iqr and so on deliver quantitative values about the matching.

7.6 Results

The result and purpose of an assignment algorithm is the matching which provides the information about which objects are ultimately paired. To analyze the quality of a matching, the sum of the pairings' weights is the most important aspect. To study how the matching can be influenced to meet some technical requirements like maximum tolerance limits, several statistical calipers are also useful. However, the basic input is the one that provides no limits or restrictions in its assignments. Only self-loops are forbidden. Hence, all other edges will be taken into account, making it a dense graph which is called the **basic graph** or **basic network** from now on. With the help of Gephi [7], a network can be visualized and studied in detail.

7.6.1 Basic network

7.6.1.1 Blossom algorithm

Vertices	1,000
Edges	499500
Average degree	999
Average weighted degree	2420.574
Network diameter	1
Graph density	1
Average cluster coefficient	1
Modularity	-0.001
Communities	461

Table 24: *Properties of the basic graph.* The basic graph uses no distance limits or other constraints to determine the perfect matching.

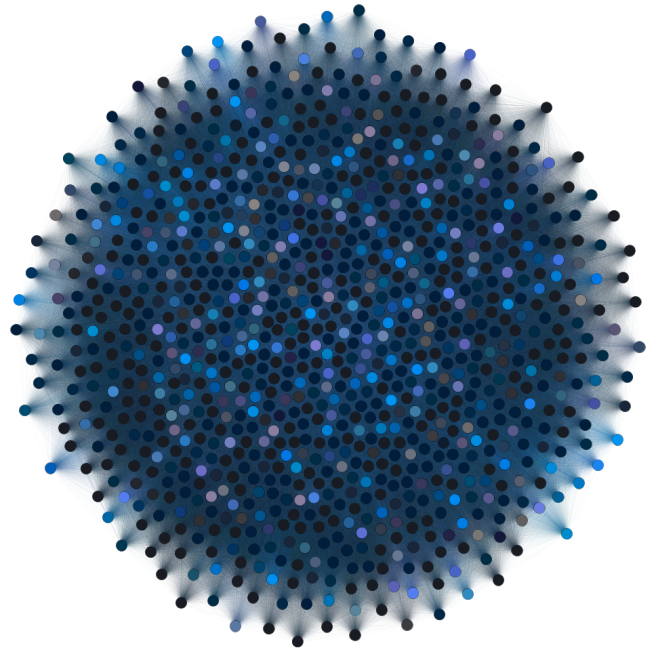


Figure 116: *Edges of the basic graph.* All 499500 edges are drawn. The Force Atlas2 algorithm is used to visualize all connections by using repulsion and gravity to place the vertices. Furthermore, each of the 461 communities is colored.

In the basic graph, the average degree of each vertex is 999 and the average weighted degree is 2420.574. Since all edges between all available APDs are present, the average degree represents minimum and maximum at the same time. A weighted degree sums up the weights of all edges which are incident to the specific vertex. The network diameter, the graph density and the average cluster coefficient are all equal to 1. The latter indicates how complete the neighborhood of a vertex is. In addition, the modularity is -0.001 with a number of communities of 461. A modularity number of 1 indicates a very strong community structure, it can be within $\{-1, 1\}$ and measures how much a network can be subdivided into communities or groups. The connections within such clusters are much more dense than the inter-connections between the clusters. Thus, 461 communities reveal that only very few APDs, almost only two each, are similar to each other. In **Reduced graph** on page 227 information are available about the sparse graph considering only edges with distances below 1. Next, the matching itself is studied by analyzing in R. The similarity (or weight or distance) of each of the 500 pairings is calculated again and independent from the Mahalanobis implementation inside the matching sequences. There, the sum of the weights is 370.653 and in R it is 370.6534. This proves that the calculation of the Mahalanobis distance is implemented correctly. All the single distances will form a specific distribution which is not forced to follow a normal distribution, hence, the median and the interquartile distance will be used as **statistical calipers**. Nevertheless, the mean and the variance will be recorded, too. The advantage of the median over the mean is that it is not sensitive to outliers. With the help of these values, several modifications of the assignment rules will be studied (see **Modified network** on page 123). In fig. 117, the distribution of the “basic” matching is depicted:

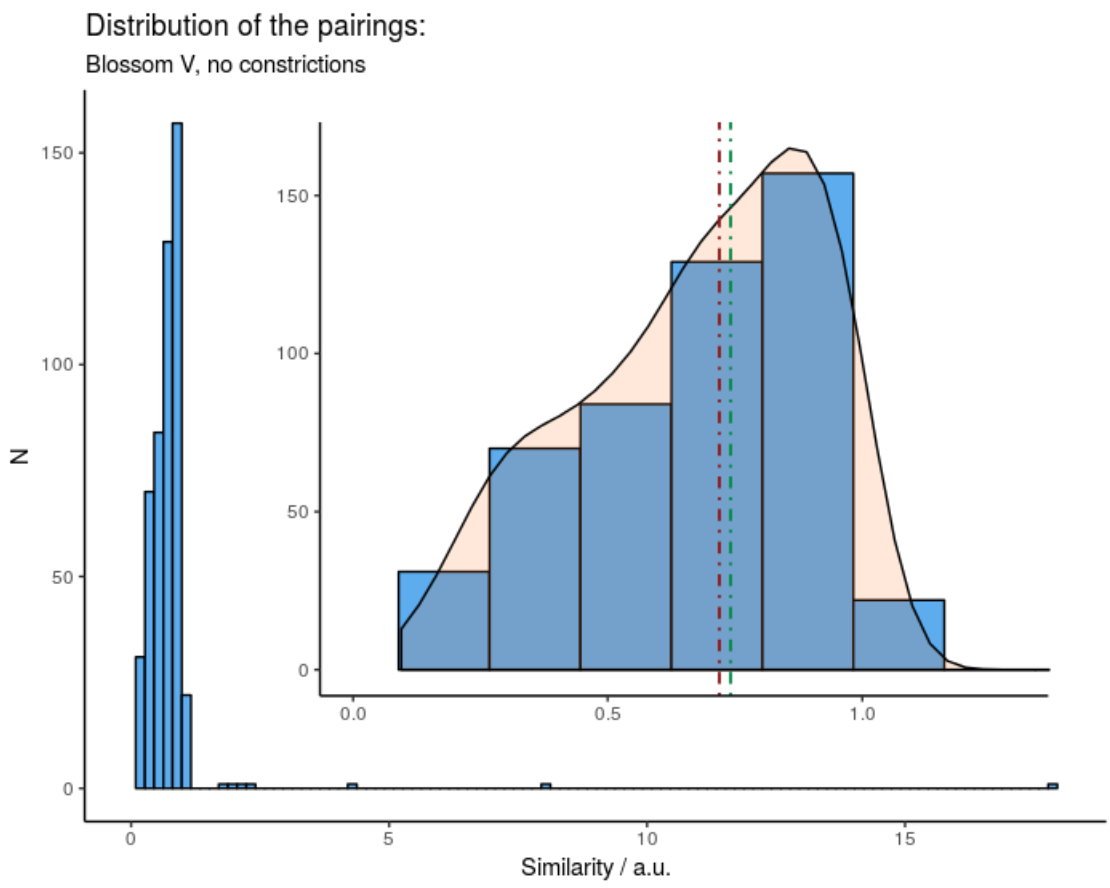


Figure 117: **Distribution of the pairings.** The median is given in red and the mean in green. In addition, a density curve is drawn over the histogram.

In this matching, none of the four parameters is preferred over to the others. The matching provides almost only pairings with a distance below 1 where a quite sharp edge is located. Only a few pairings exceed this distance value. Hence, the median is located at 0.719 ± 0.38 and the mean at 0.7413 ± 0.8864 .

7.6.1.2 Greedy algorithm Though the blossom algorithm is the main subject of investigation it will be briefly compared to the greedy algorithm in the following. To enable a comparison, the greedy algorithm is equipped with the Mahalanobis distance, too. The greedy algorithm provides a different pairing distribution:

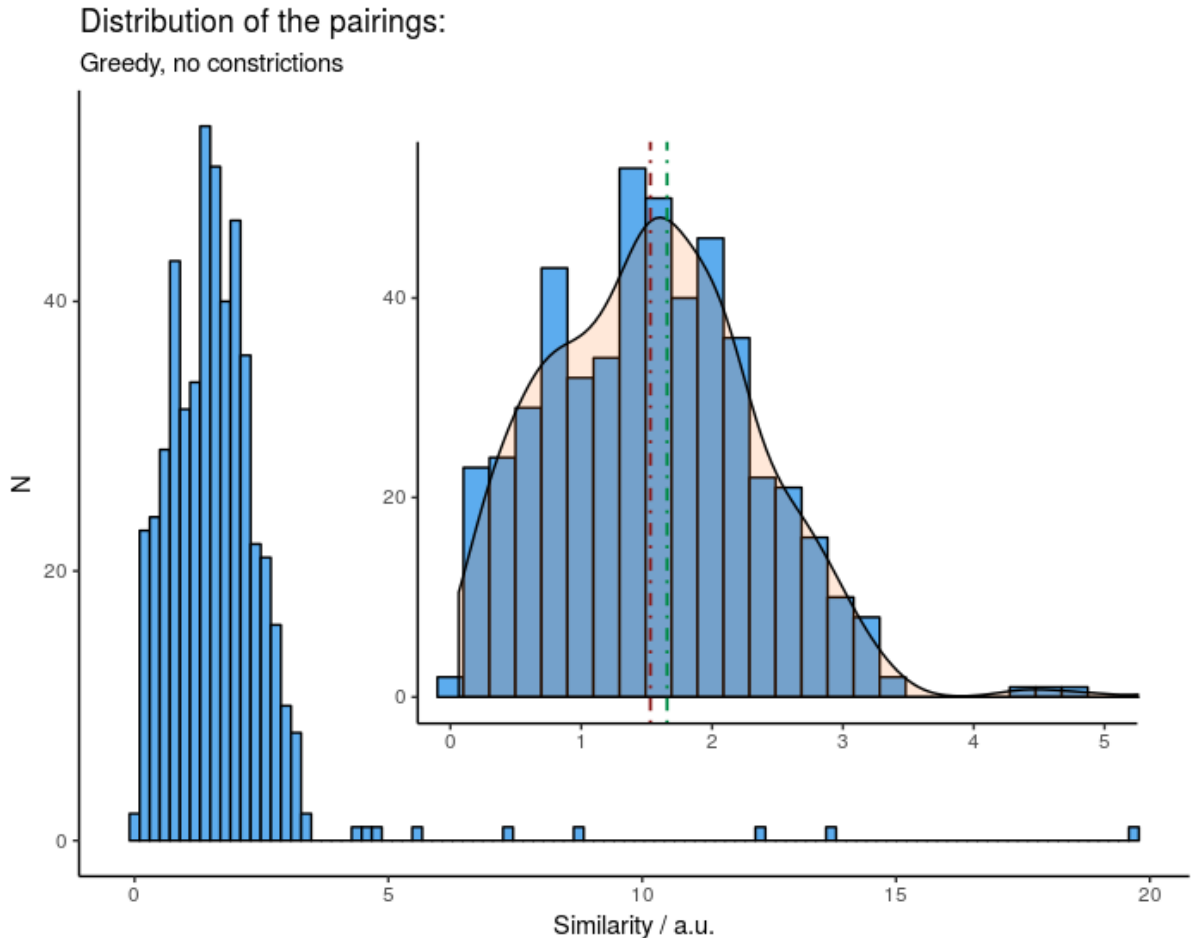


Figure 118: *Distribution of the pairings for the greedy algorithm.* The median is given in red and the mean in green. Compared to fig. 117 the distribution is much broader.

The matching of the greedy algorithm without any constraints provides a sum of weights of 828.1. Thus, the sum is about three times as much as the Blossom-V algorithm yields. The median is 1.528 ± 1.13 and the mean is 1.656 ± 1.41 , thereby, it is about as twice as much compared to the Blossom-V result. In both algorithms, the mean and the median are not far from each other. Because the greedy algorithm is not operating on a graph, the underlying network can neither be visualized nor analyzed.

7.6.1.3 Pool influence on the similarity measurement The Mahalanobis distance takes into account the means of the parameters of the APD pool. These means are subject to change according to the currently involved APDs. This dynamic adjustment can be seen as an advantage or as a disadvantage. In the situation that all APDs shall be assigned by disregarding any deviation limits, the changing pool means will not affect anything. When APD pairings exceed a certain parameter difference, further deliberations on the consequences have to be performed (see *Modified network* on page 123). In any case, it does only matter when distance limits are applied to the adjacency matrix. In fig. 119 the similarities between three constant APD pairs are measured during enlarging the available APD pool:

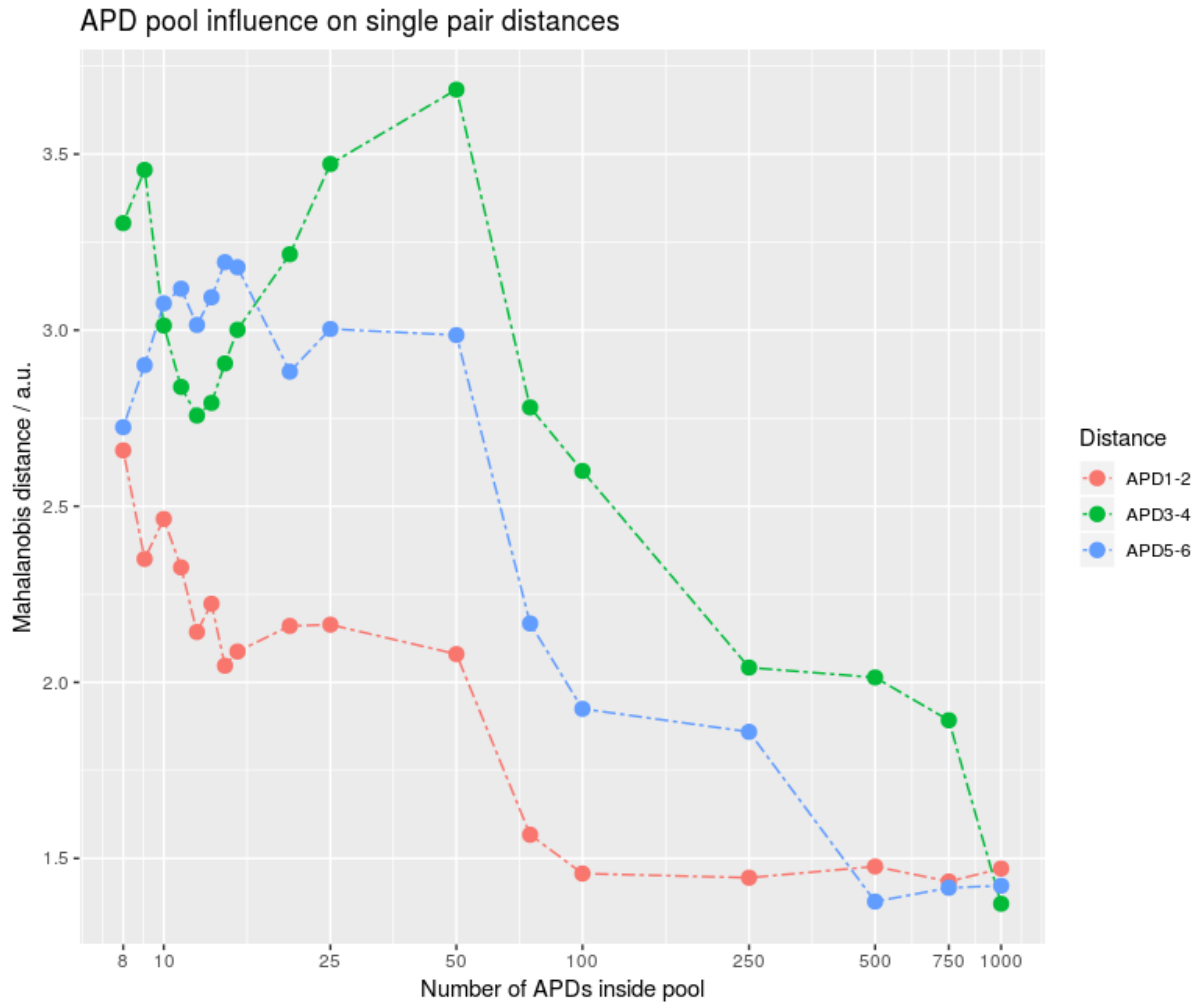


Figure 119: *Influence of the APD pool on the single distances.* The distances between fixed APDs vary with the pool they are part of. Because the covariance matrix uses the mean of each parameter, the distances change according to the pool. Above distances are calculated between following pairs:

APD₁₋₂: 1205013067 and 1205013069 | APD₃₋₄: 1205013070 and 1205013071 | APD₅₋₆: 1205013072 and 1205013073

The similarities between the APDs change with the number of participating APDs. The pairings tracked in fig. 119 consist of APDs which should be very similar to each other with regard to their manufacture as they originate from the same wafers. This is not noticeable in the first place when only a few APDs participate but with more APDs being in the pool, the more these APDs become similar to each other.

7.6.1.4 Metric The APDs of the first slice were assigned by using a greedy algorithm together with an Euclidean distance. Furthermore, these 1,000 APDs subdivide into 500 pairings and the difference in choice between Euclidean and Mahalanobis is studied in fig. 120:

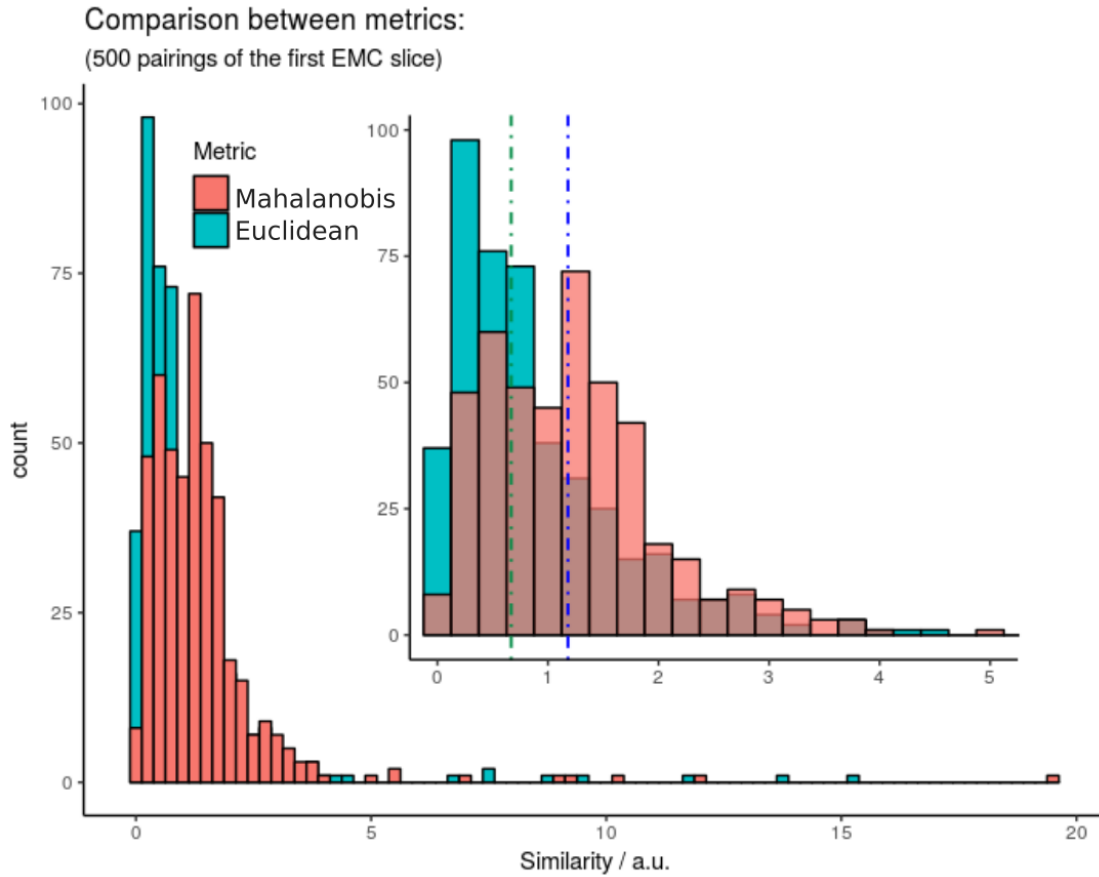


Figure 120: *Comparison between the metrics for the pairings of the 1st slice.* The pairing similarities calculated with the Mahalanobis distance result in a distribution broader than when using the Euclidean distance. The median of the Euclidean distance is colored in green and the median of the Mahalanobis distance is given in blue. The metrics and the resulting distributions are not comparable.

The shape of the distribution is used to compare the Mahalanobis distance with the Euclidean distance though the latter is not a proper tool to measure distances between multivariate variables. Therefore, it has to be kept in mind that fig. 120 is only for visualization purposes. To enable a direct “comparison”, only the irradiated parameters were used here. The Mahalanobis distance provides the valid similarities of the matching of the first slice. The table on the right holds the statistical values for both metrics.

	Mahalanobis		Euclidean
Median	1.81	Median	0.667
IQR	1.07	IQR	0.9
Mean	1.37	Mean	1.04
Std.	1.486	Std.	1.5

Table 25: *Properties of the slice.*

7.6.1.5 Parameter deviations The differences between the same parameters of a pairing play an important role in addition to their similarities in general. To get a better comparison between the blossom algorithm, the greedy algorithm and the first slice, the corresponding matchings are investigated with respect to their parameter differences. In fig. 121, the distributions of the voltage differences between the matched APDs of the first slice are depicted. The pairings of the 1st slice were generated by using distance limits (see Greedy algorithm on page 107).

7.6.1.5.1 Voltages

1st slice

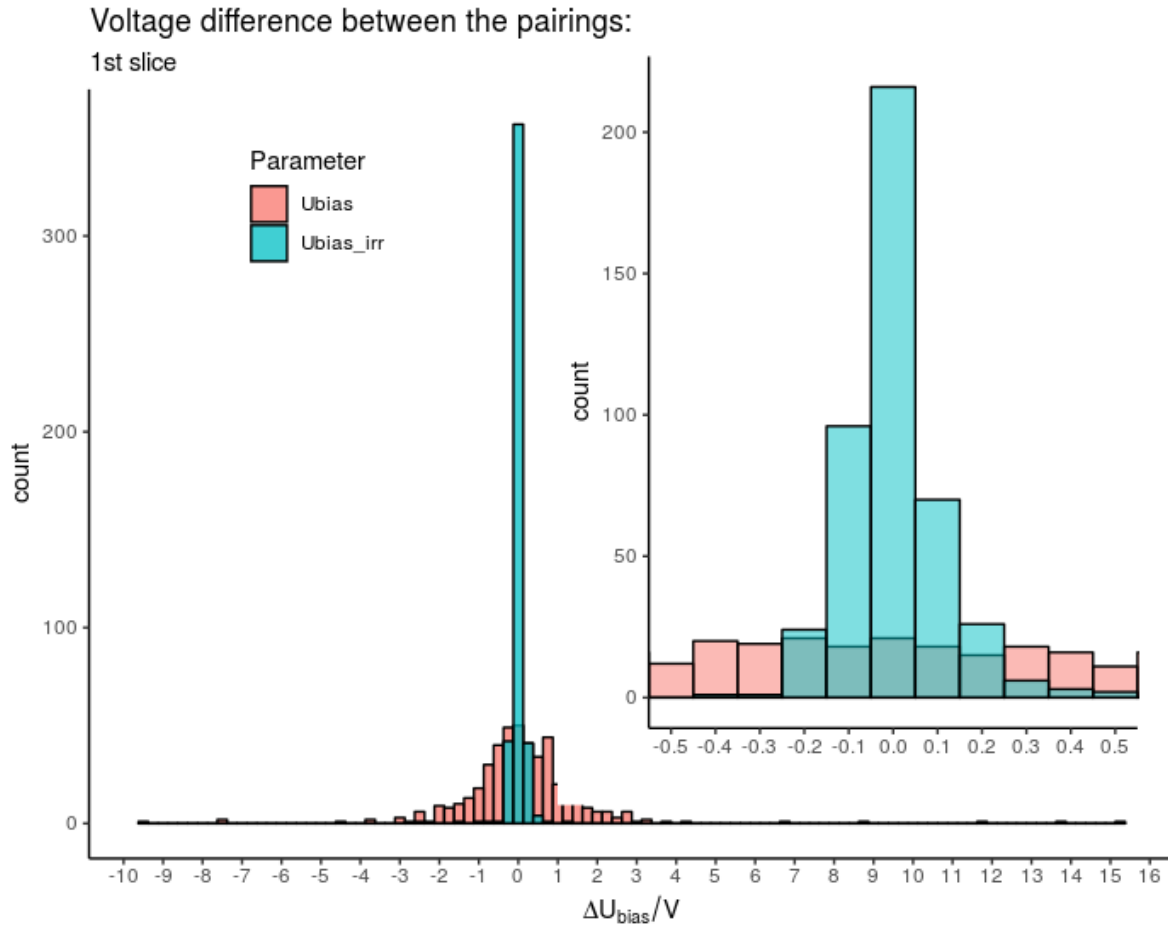


Figure 121: **Voltage differences among the pairings of the 1st slice.** The irradiated voltage differences are closely within about ± 0.2 V. Because only parameters after the irradiation were taken into account, the differences between the voltages before the irradiation are quite widely distributed.

Considering only the irradiated voltage differences, the voltage differences between the matched APDs are quite small as according voltage limits were applied. Since only the irradiated values were taken into account to construct the matching, the differences between the non-irradiated values are much bigger. In contrast to the first slice, the algorithms in fig. 122 and in fig. 123 do not limit their assignments. This means, that all parameters are treated equivalently and neglect any technical restrictions. In the following, a distribution is given how the greedy algorithm assigns APDs without any limits in opposition to fig. 121.

Greedy

Voltage difference between the pairings:

Greedy algorithm: no constrictions

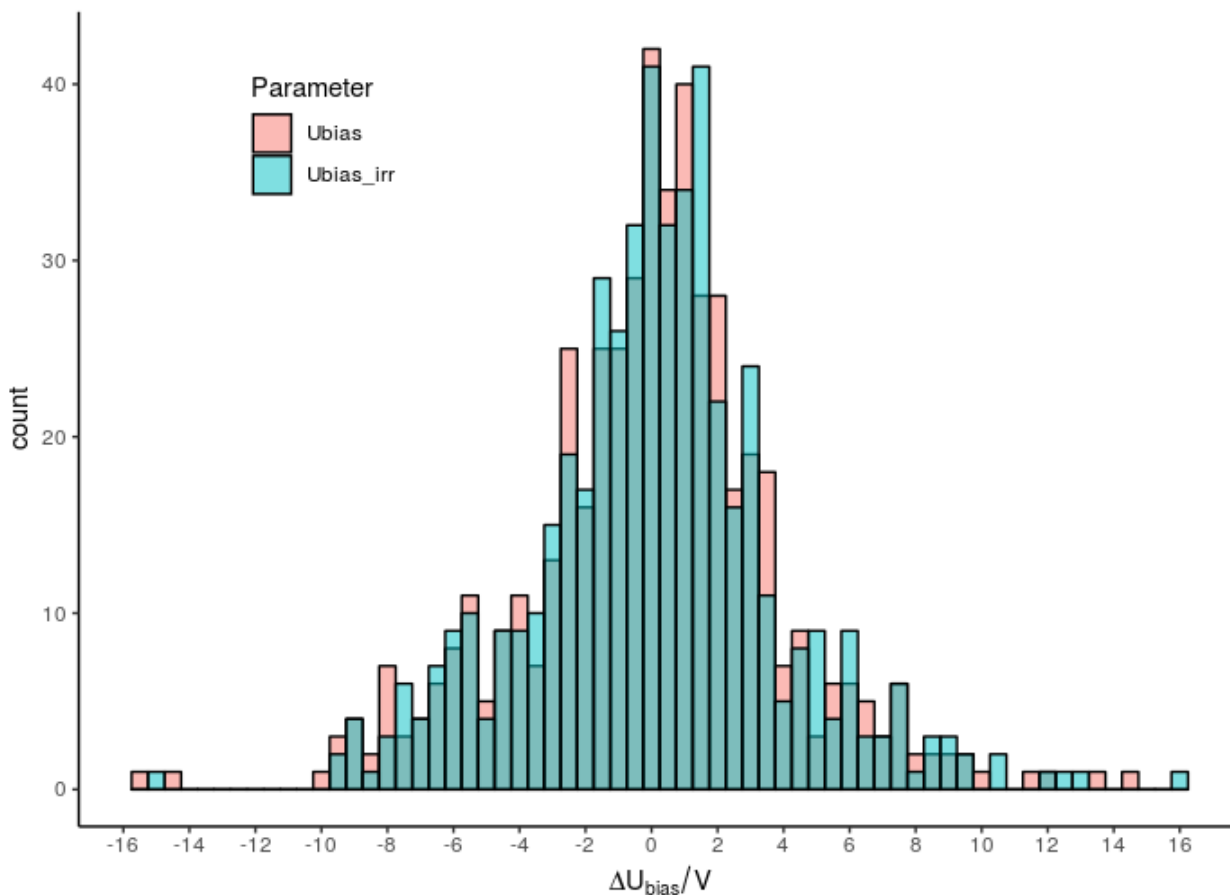


Figure 122: **Voltage differences among the pairings from greedy algorithm.** The voltage differences are quite normally distributed within almost only $\{-10, 10\}$ V.

No metric respectively no distance function is applied here to study the results of the algorithm only. The distribution is not as narrow like in fig. 121 and the irradiated and the non-irradiated distributions are quite identical. Both start at about -10 V and end at about $+10$ V while they are centered at around 0 V.

Blossom

Voltage difference between the pairings:

Blossom algorithm: no constrictions

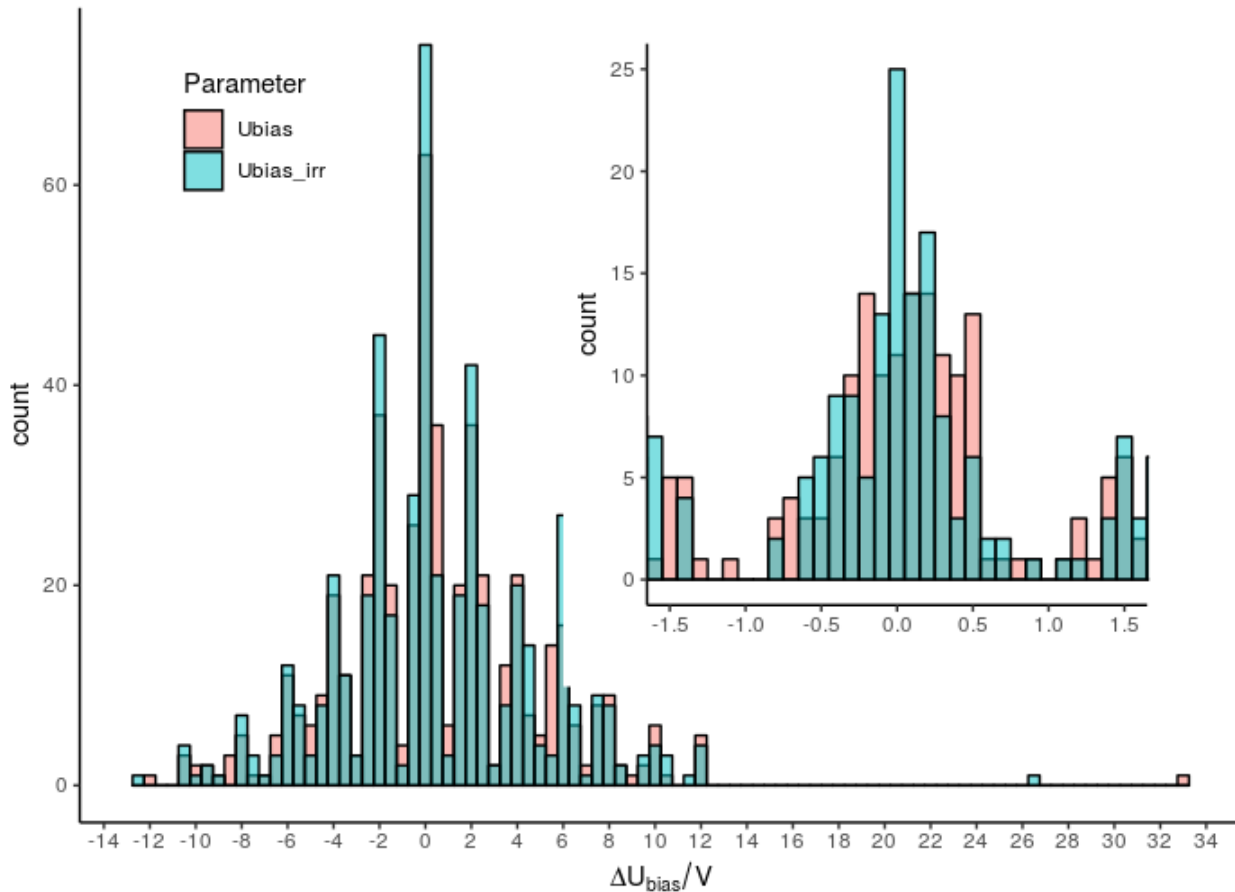


Figure 123: *Voltage differences among the pairings from blossom algorithm.* The blossom algorithm provides a characteristic distribution of the voltage differences between the pairings.

The voltage differences between the pairings are distributed almost over the same region like the ones from the Greedy algorithm in fig. 122. There, the distributions are rather continuous whereas periodic spikes are present in case of the Blossom algorithm. This might be either a result of the Dijkstra searching algorithm used in the Blossom algorithm or maybe due to the structure of the APD pool within the four dimensional parameter space (see fig. 102 on on page 102).

Beside the voltage, the slope is of interest as well. Therefore, the slope distributions of the previous matchings are depicted subsequently:

7.6.1.5.2 Slopes

1st slice

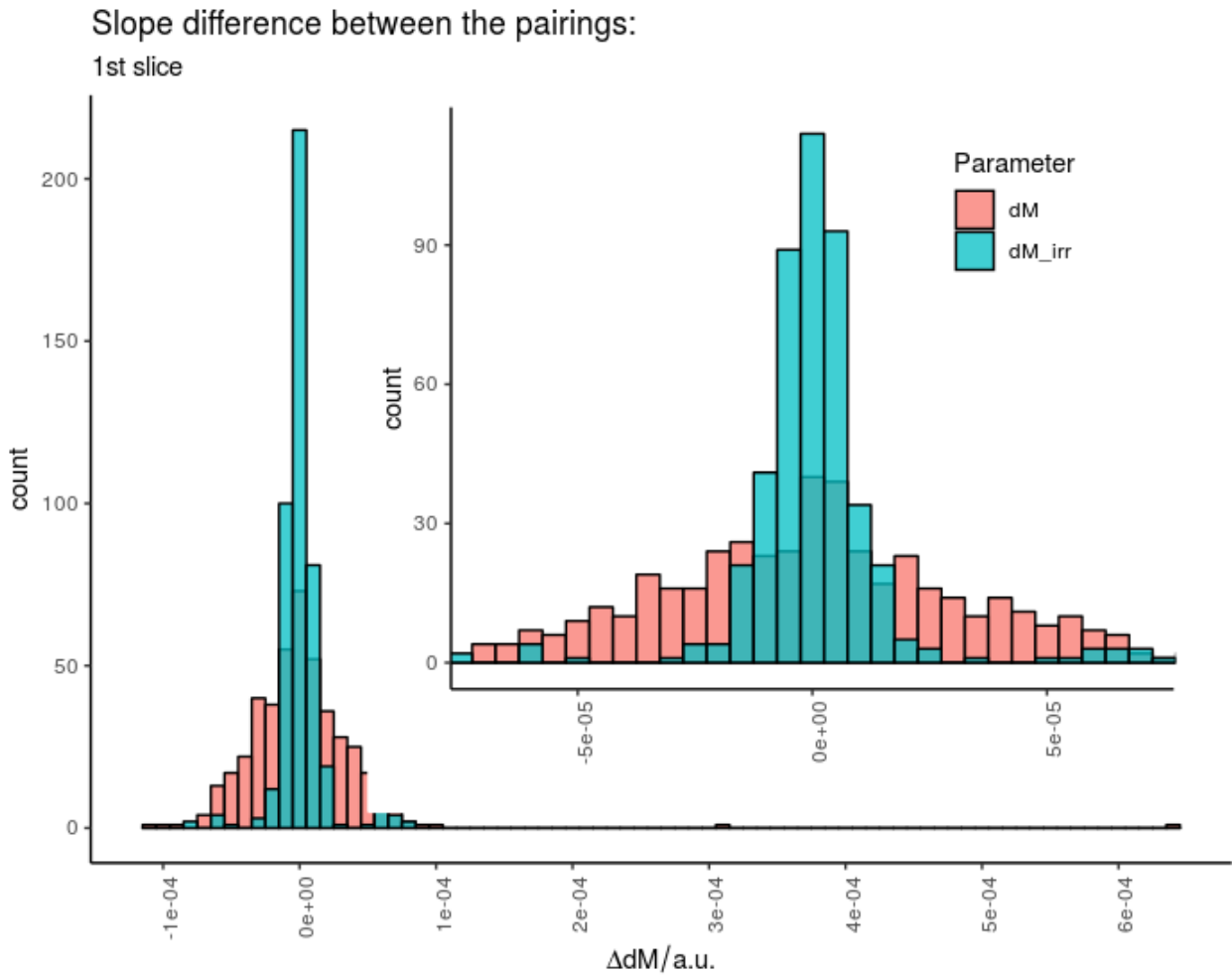


Figure 124: *Slope differences among the pairings of the 1st slice.* Only the irradiated values are located within a small region around zero.

Similar to fig. 121, only the irradiated values provide a narrow distribution. The width of the irradiated data is $\approx 5 \cdot 10^{-5}$ a.u., but some outliers are present. The non-irradiated data is much broader with a width of about $15 \cdot 10^{-5}$ a.u..

Greedy

Slope difference between the pairings:

Greedy algorithm: no constrictions

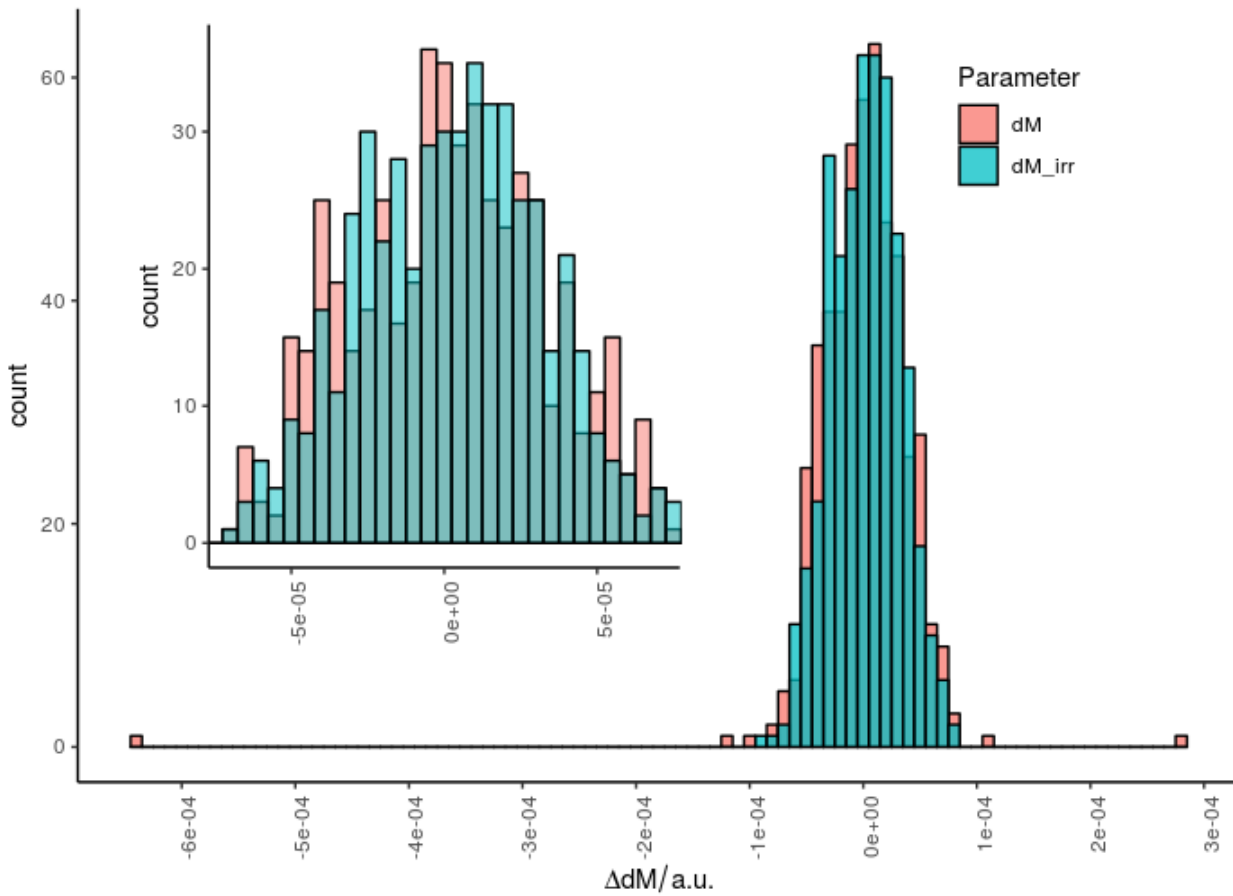


Figure 125: *Slope differences among the pairings of the greedy algorithm.* The slope differences are with $2 \cdot 10^{-4}$ a.u. much broader than in the matching of the first slice.

The greedy algorithm provides a rather broad distribution of the slope differences with a width of $2 \cdot 10^{-4}$ a.u.. Compared to the matching of the first slice, it is about 4 times as broad.

Blossom

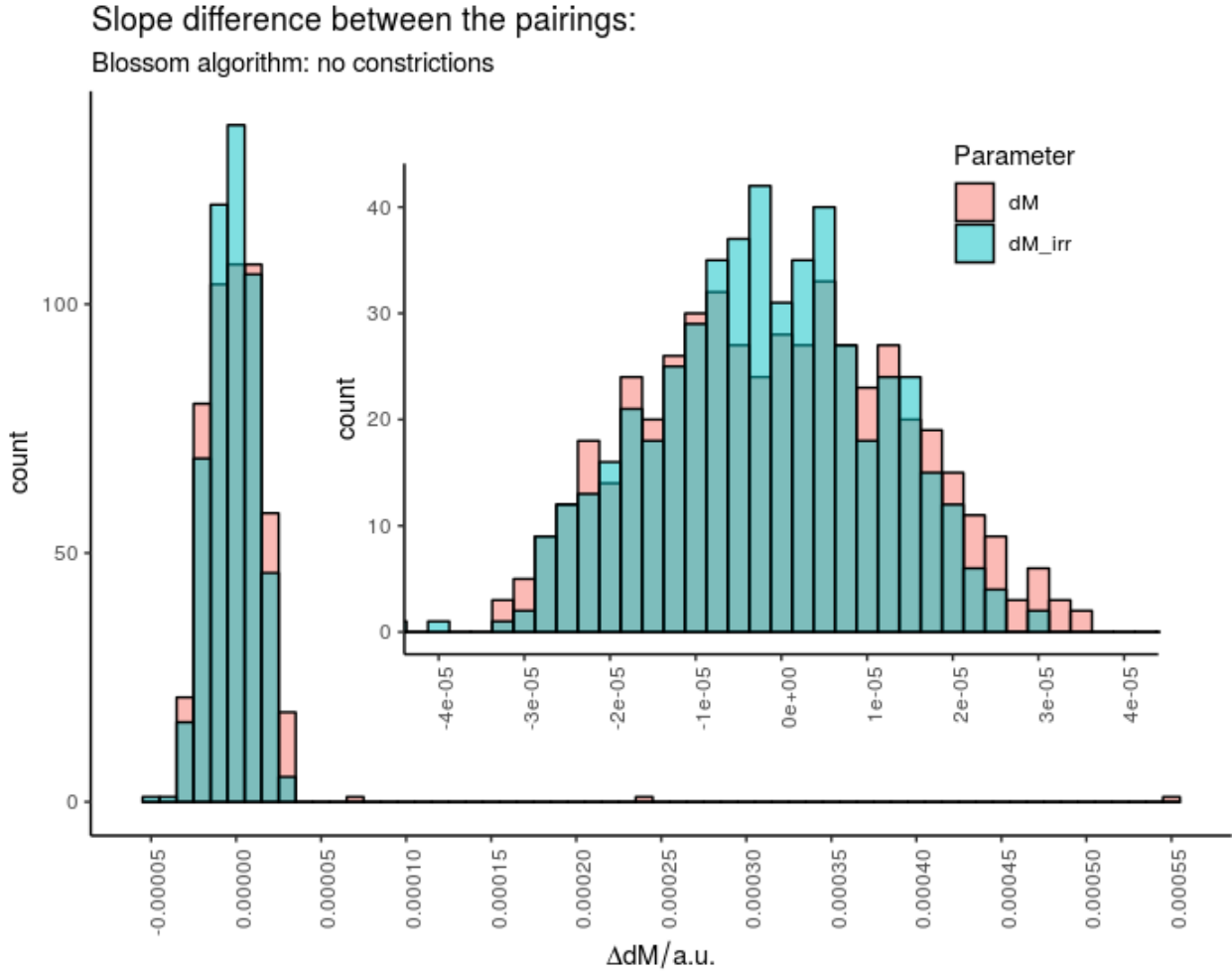


Figure 126: *Slope differences among the pairings of the Blossom algorithm.* The slope differences are very normally distributed with a width of $6 \cdot 10^{-5}$ a.u.

The slope distribution of the matching provided by the Blossom algorithm is with a width of only $6 \cdot 10^{-5}$ a.u. as narrow as the one from the first slice in fig. 124.

7.6.2 Modified network

To achieve a global optimum, some considerations should be kept in mind. In the first place, the most handy method to assign objects is to use the metric of choice and apply it on top of an assignment algorithm. This will result in the global optimum but by using boundary conditions it is possible to influence the similarities between the APDs. By using a binary decision when the distances exceed a certain limit, these constraints are able to have a huge impact on the matching. When the parameter deviations between the APDs are too strong, the corresponding assignments will receive an infinite weight. Hence, when reducing or increasing the distance limit, the amount of matched APDs might change accordingly. When applying no limits, all APDs will be treated as a possible partner for each other APD. Though such a matching will represent the global optimum, it might turn out that some of these assignments are not suitable due to technical requirements to build up a pair. This is because the voltage range of the HV-backplane provides a chosen **limit** of 50 V. Due

to the voltage resolution provided by a 10-bit DAC, which regulates the applied voltages, the APDs shall not extend a bias voltage deviation of more than $50 V / 2^{10} \approx 0.05 V$. In the following, the separately investigated voltage limit is 0.1 V which marks the starting point.

In this context, the question arises whether an assignment with technical limits will yield a better matching than one without any. Accordingly, the term “**best matching**” has to be defined first to be able to make any evaluations on it. In general, the purpose of a matching is to provide suitable and as many as possible assignments among all pairs with respect to their similarities. Furthermore, it shall provide the best matching represented by a **minimum weight** which is assumed to result in the most narrow parameter distribution of all matchings.

As previously mentioned, restrictions towards the distances will flag pairings binarily as “assignable” or as “not assignable”. This is implemented such that not assignable pairings receive an infinite distance to represent a very high weight. Hence, the algorithm will treat it as a very bad choice but nevertheless such an assignment is still be possible to enter the matching finally. Each APD represents a position in the four dimensional parameter space and, therefore, to determine a potential matching partner, a **sphere** around the initial APD can be constructed:

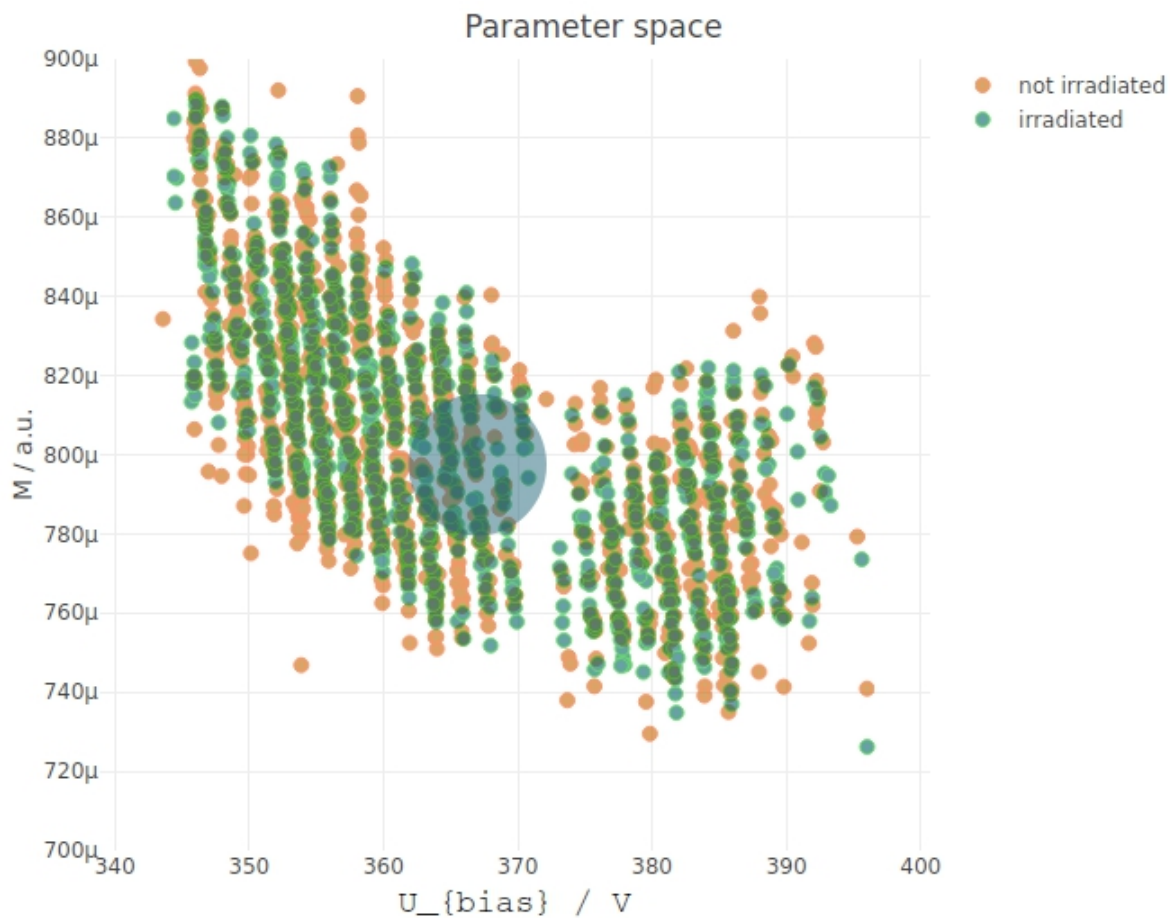


Figure 127: *Parameter space - sphere*. When limits are applied to the utilized metric, a circle around the targeted APD will represent all APDs in question. The weights are given by the calculated similarity through the Mahalanobis distance. All APDs outside this circle will receive an infinite weight.

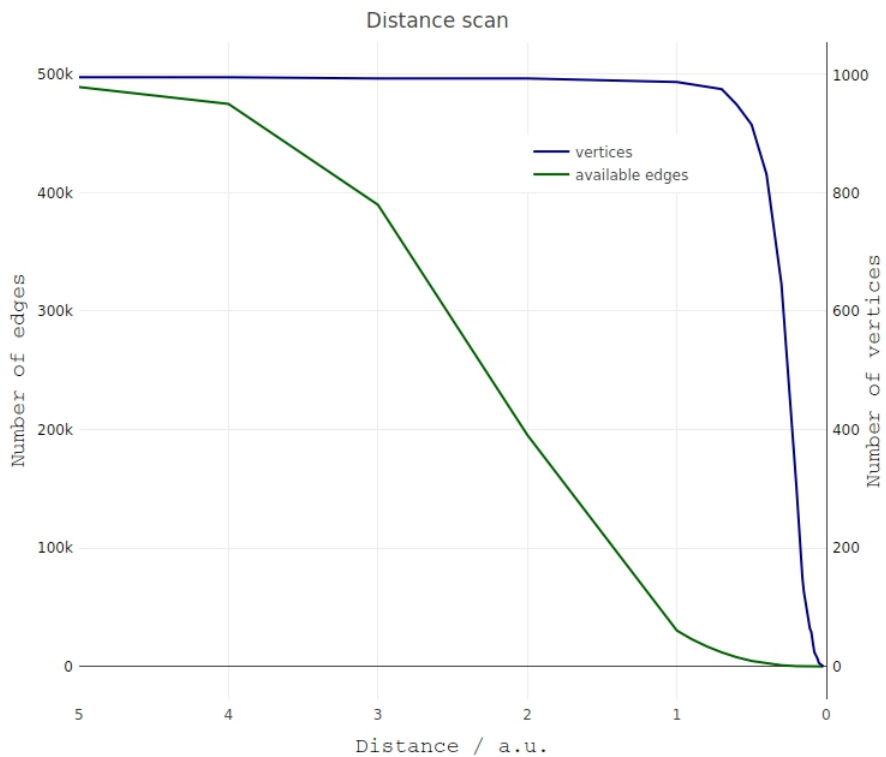
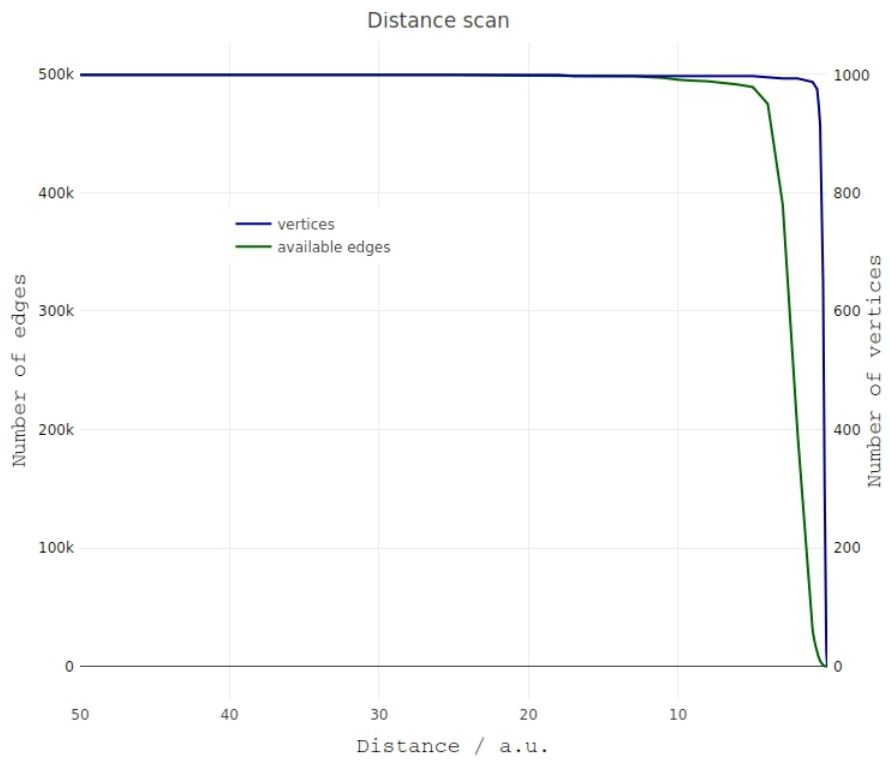


Figure 128: **The number of vertices in dependency on the number of edges.** The number of edges decrease already before the number of vertices decrease. In contrast to the number of edges, the number of the vertices drops rapidly from a distance limit of about 0.8 on. However, the edges and the vertices are not affected until a distance limit of about 5 is reached.

The number of edges which meet the limit vary according to the applied threshold. In fig. 128 it is quite constant over a long distance region and decreases continuously after reaching a distance limit of about 5. Up to a distance threshold of roughly 1, the amount of vertices is not affected by the number of available edges but from $d \approx 0.8$ on, it decreases sharply. The number of the vertices remains quite constantly until when only few edges are left. This can be explained by the fact that the Blossom algorithm builds up the matching on only few edges since it seeks the optimized network. A matching of 1,000 APDs means basically, that only 500 edges are required.

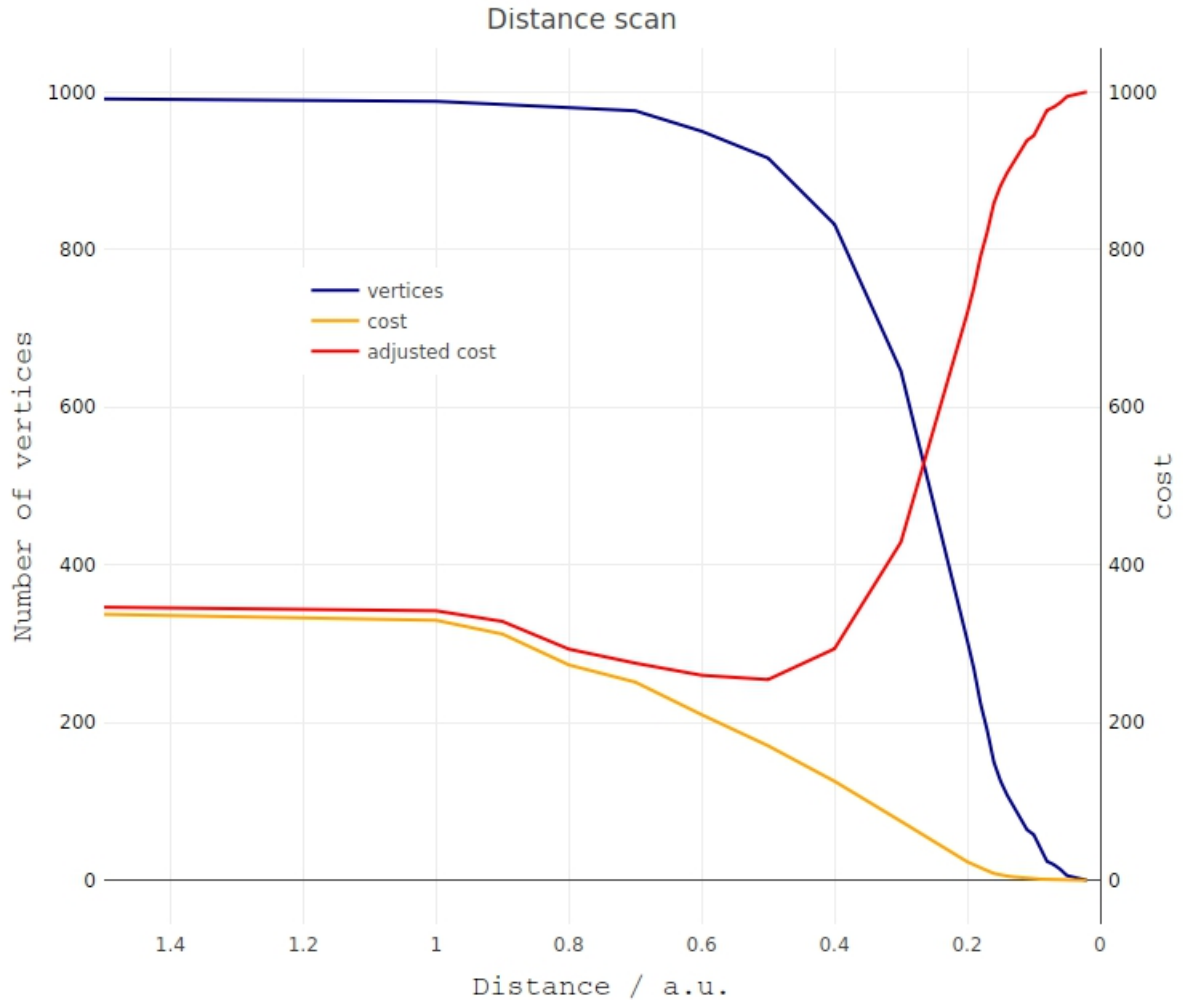


Figure 129: *The costs in dependency on the number of vertices.* The number of vertices decreases with both costs while the adjusted cost increases after a minimum at $d = 0.5$. There, the scan reveals a best adjusted cost of 254.99. Afterwards, the adjusted cost increases continuously.

While the number of APDs decreases continuously from a distance of 1, the costs decrease even faster up to the optimum of $d = 0.5$. Then the situation turns around. The costs are strongly related to the number of detectors, which in turn do not decrease until a little later. Hence, the algorithm will use more and more less efficient edges in total though the edges represent more and more a higher similarity with an increasing distance limit. This is because in some cases the global optimum prefers in some instances worse edges to achieve a better matching.

Next, the cost and the adjusted cost are analyzed with respect to the amount of available edges:

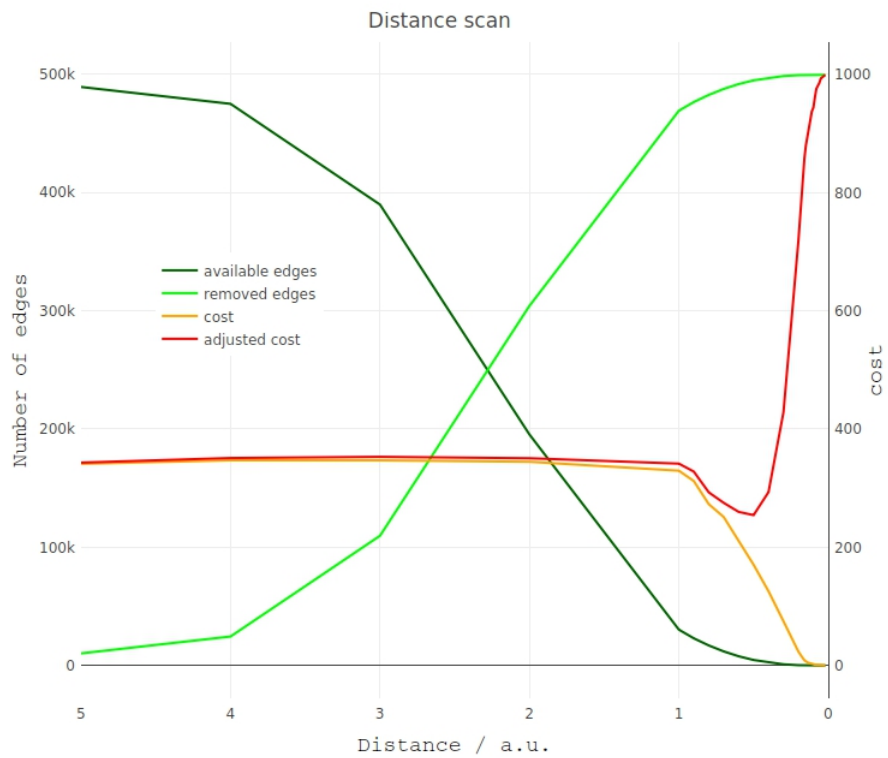
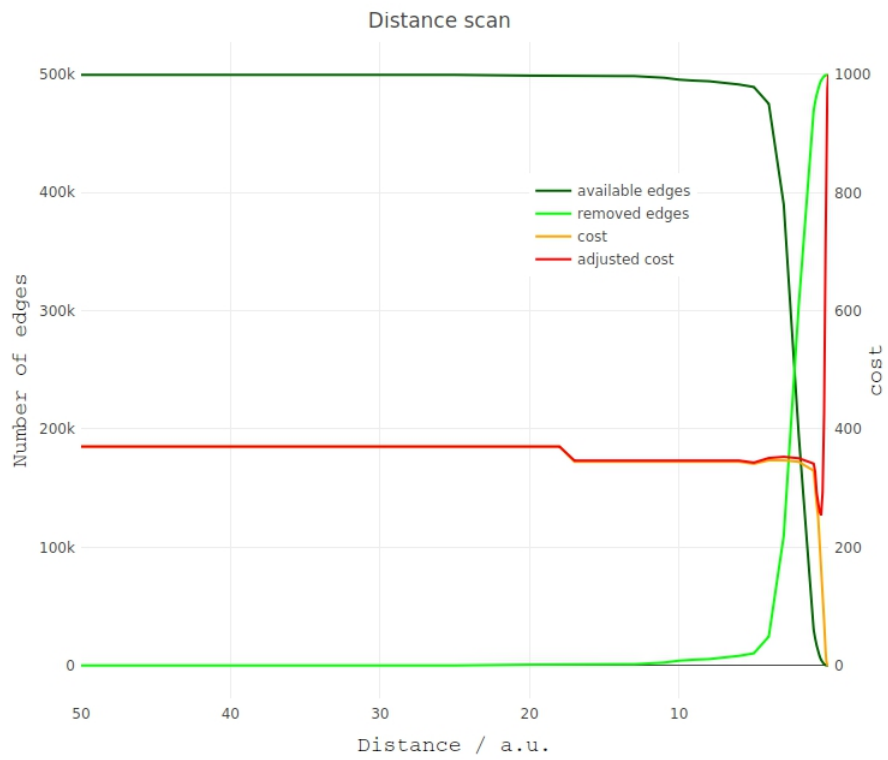


Figure 130: *The costs in dependency on the number of edges.* The number of available edges does hardly vary before a distance threshold of about 5 is reached. An adjusted cost of 1000 represents zero assigned APDs. The number of edges is halved at about a distance limit of ~ 2.5 .

Both cost types behave very similar in regard to the number of edges and remain almost unchanged over a wide range. The number of edges does not change until a distance limit of about 13 is reached. In opposite to the edges, both costs drop slightly at a distance of 17. There, a single pairing is removed from the matching, changing the cost from 370.553 to 344.976 and the adjusted cost from $\text{cost} = 344.976 + 2$ to 346.976. Applying stronger distance limits affects the matching more and more (see fig. 130). While the number of edges decreases already from a distance threshold of about 5, the costs remain rather constant up to a distance value of 1 but from there on, the number of edges and the costs change a lot (see fig. 131).

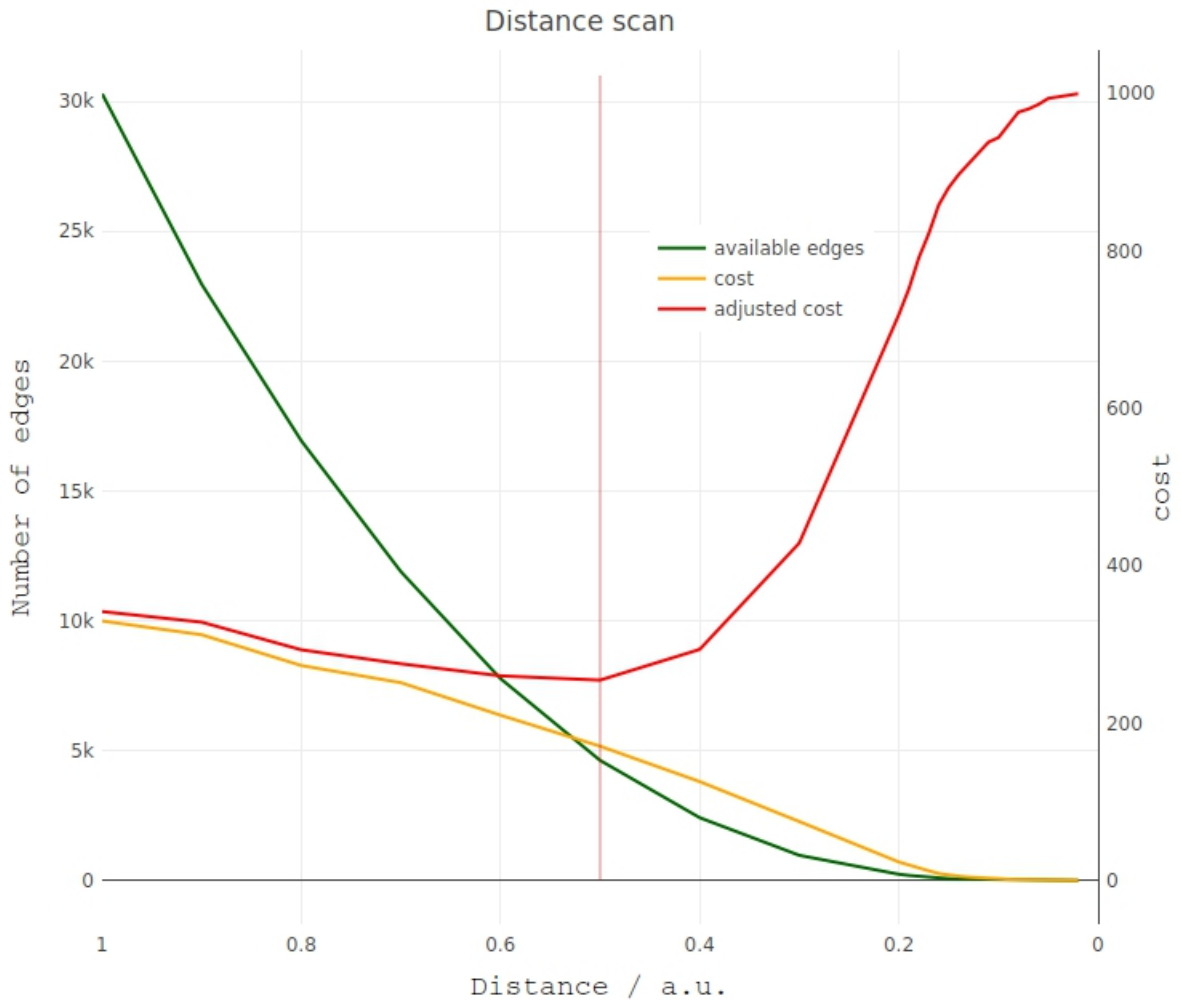


Figure 131: *The costs in dependency on the number of edges - range from 1 to 0.* While the cost is zero with none available APDs, the adjusted cost represents a solid compromise between the number of APDs and the cost of the matching. Hence, it is assumed that the matching is best at the adjusted cost's minimum which is located at a distance limit of 0.5.

While the cost decreases with the number of APDs, the adjusted cost takes into account this situation and considers the number of APDs in the corresponding matching. Thus, the matching provides a good compromise between the amount of successfully assigned APDs and their matching quality at a distance limit of 0.5 where it provides an adjusted cost of 254.599 and a cost of 170.599. There, the number of edges has dropped to about 5,000 with 458 pairings. Finally, the matching will be studied with the help of the five numbers median, +iqr, -iqr, min and max:

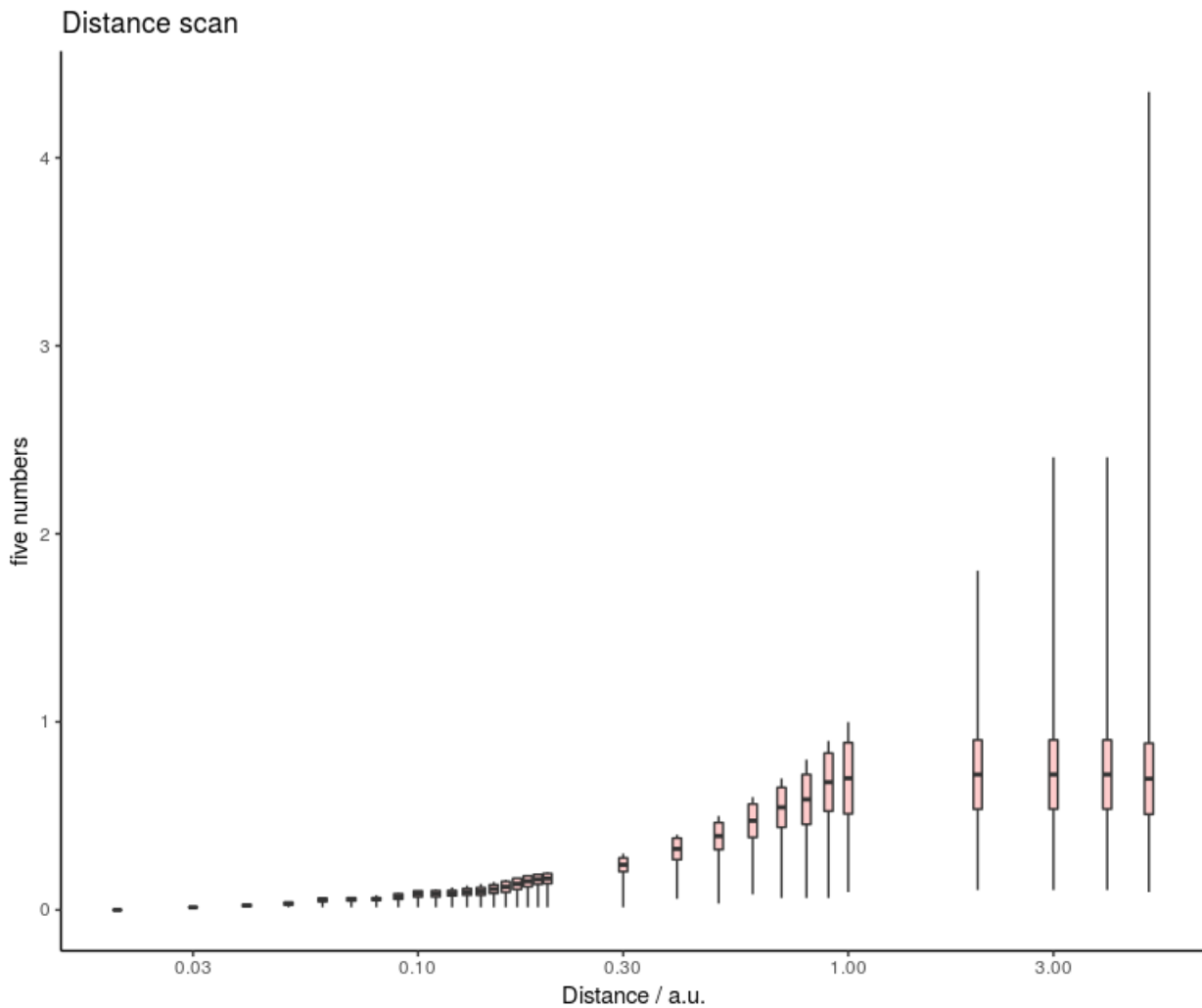


Figure 132: *Five numbers in the range of {0,5} of the distance scan.* The boxes contain \pm iqr while the line crosswise in the box represents the median. The top and bottom values of the lines represent the maximum respectively the minimum. The y-axis provides the numbers in terms of the weights of the matching respectively the similarities of the APDs. The dependent axis represents the Mahalanobis distance between the APD pairings.

In fig. 132 it can be seen that increasing the distance limit does hardly change the median up to a limit of about 1. Instead, almost only the maximum values decrease respectively the most inefficient edges are removed. At a distance limit of 1 and below, the maximum value is quite close to the box which is now more distant to the minimum value.

At a distance limit of 0.5, the matching provides the highest quality. Thus, the corresponding network with an applied distance limit of 0.5 will be studied in detail in the following. At first, the generated matching is depicted in regard to the distribution of the similarities (see fig. 133):

7.6.2.1.1 Optimal distance threshold

The distribution of the similarities of the matched APDs delivers a deeper insight into the matching's quality. The median and the mean represent its average value and thus embody the most important parameter beside the applied distance limit.

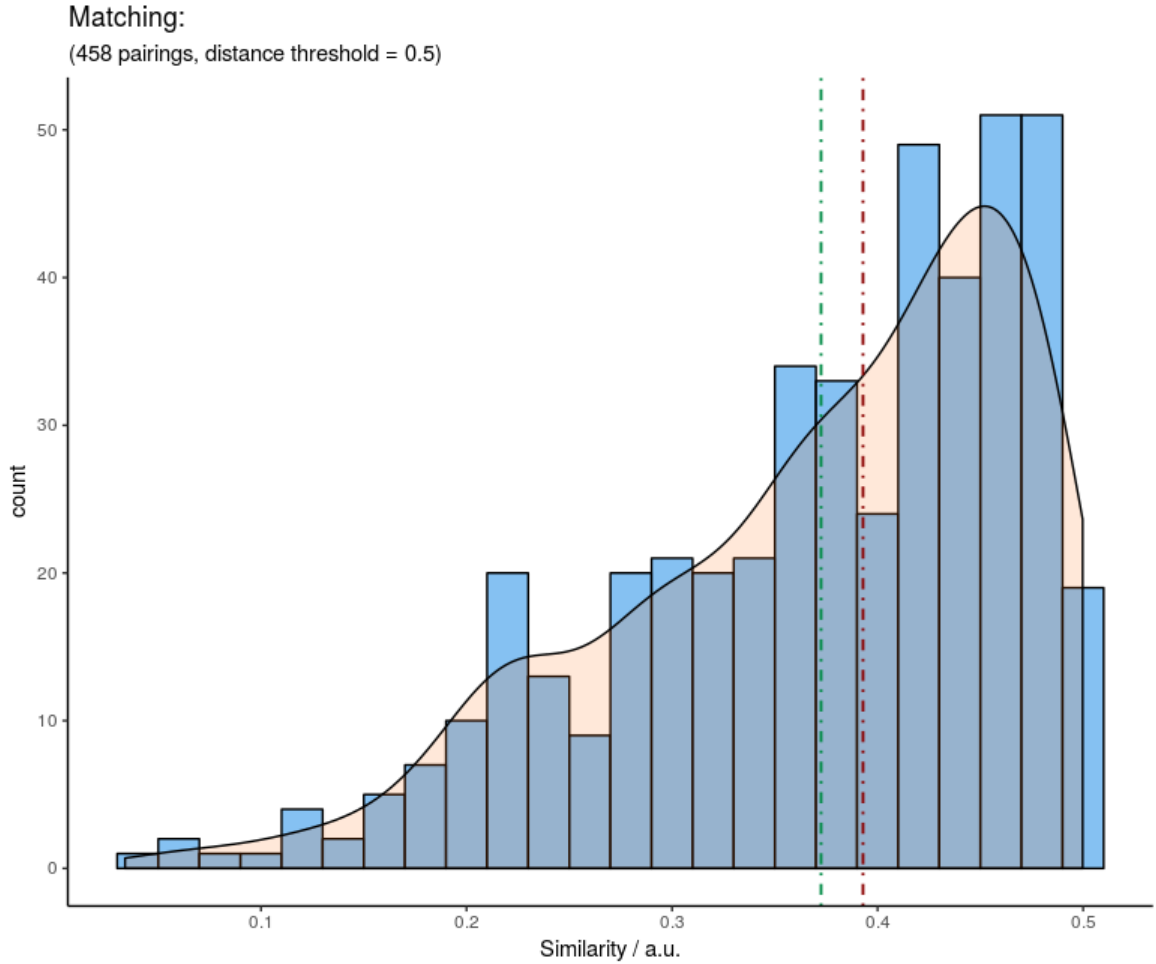


Figure 133: **Matching at a distance limit of 0.5.** The median is given in red and located at 0.393 ± 0.144 and the mean is given in green at 0.373 ± 0.098 .

Most of the pairings are located near the distance threshold. Hence, the median is located at 0.393 ± 0.144 and the mean at 0.373 ± 0.098 .

Since the matching is measured with the help of the Mahalanobis distance which does not prefer any of the parameters, it is important to check how the APDs are assigned with respect to their technical parameter differences. At first, in fig. 134, the voltage differences between the pairings are shown.

Voltage difference between the pairings:

Constrictions: $d < 0.5$

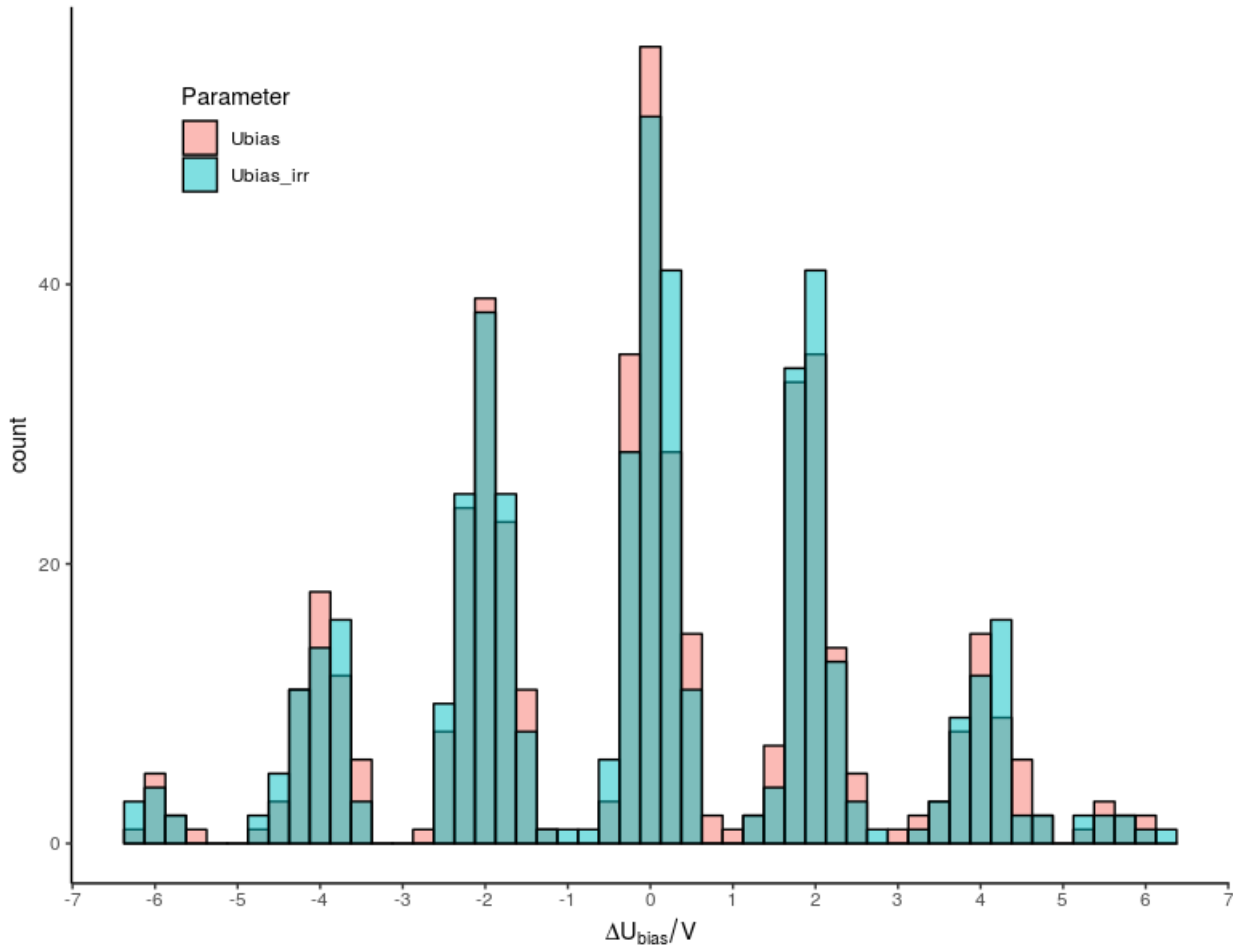


Figure 134: **Voltage and slope differences at a distance limit of 0.5.** The maximum voltage differences are about ± 6 V.

Both data sets, the irradiated and the non-irradiated sets, are very similar to each other. In addition, both data sets provide the same periodic “distributions” or “peaks” within the distribution itself. In other words, distinct gaps are periodically present though the distribution follows basically a Gaussian. Each such a peak has a width of approximately 1.5 V. These show the same structure like in fig. 123, where none distance limit are applied. Compared to that, the range of the voltage deviations is now reduced from ± 14 V to ± 6 V.

Next, the slope differences are depicted (see fig. 135):

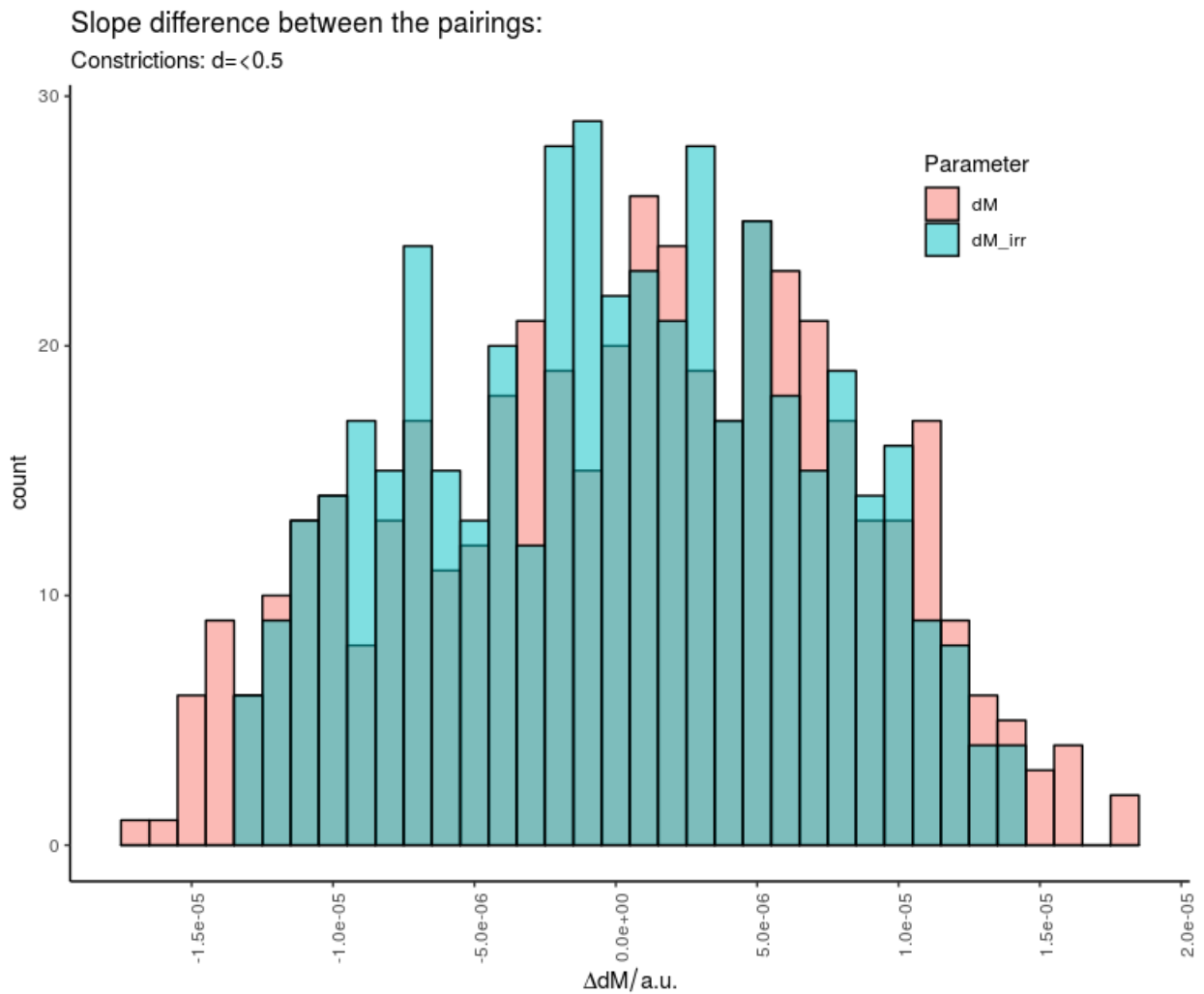


Figure 135: *Slope differences at a distance limit of 0.5*. The slope differences are very normally distributed with a width of about $2 \cdot 10^{-5}$.

The slope differences between the APD pairings are very normally distributed within a range of $\pm 1 \cdot 10^{-5}$. Both data sets follow almost the same distribution. Next, the network itself is investigated:

The network of the graph with edges only below 0.5 (see fig. 136) is much less dense than the basic graph (see fig. 116). Due to the limited connections within the graph, the formation of the communities is quite distinctive since they divide into 43 communities. Nevertheless, most of the APDs can be assigned to each other while some provide only few possible partners. However, only about 5,000 edges (1 %) are necessary to enable a matching of about ≈ 900 APDs (90 %).

Vertices	916
Edges	4622
Average degree	9.972
Average weighted degree	3.753
Network diameter	19
Graph density	0.011
Average cluster coefficient	0.571
Modularity	0.807
Communities	43



Table 26: *Properties of the graph with a distance limit of 0.5.*

Figure 136: *Visualized network with a distance limit of 0.5.*

With an average weighted degree of 3.753, the APDs of this subnetwork provide very few edges in general. Taking the maximum weight 0.5 of an edge, the APDs provide at least more than 7 edges in general. And indeed, the average degree is 9.972.

Comparison with the greedy algorithm:

At a distance limit of 0.5, the Blossom algorithm provides 458 pairings and the greedy algorithms provides 422 pairings again. Below in table 27, both matchings are compared to each other.

Blossom		$d = 0.5$	Greedy	
Cost	170.6		Cost	152.07
Cost _{adj}	212.6		Cost _{adj}	230.07
APDs	458		APDs	422
Median	0.393		Median	0.3792
IQR	0.14		IQR	0.152
Mean	0.37		Mean	0.36
Std	0.097		Std	0.102

Table 27: *Comparison of the matching with a distance limit of 0.5 between Blossom and Greedy.* The median and the mean are related to the Mahalanobis distance.

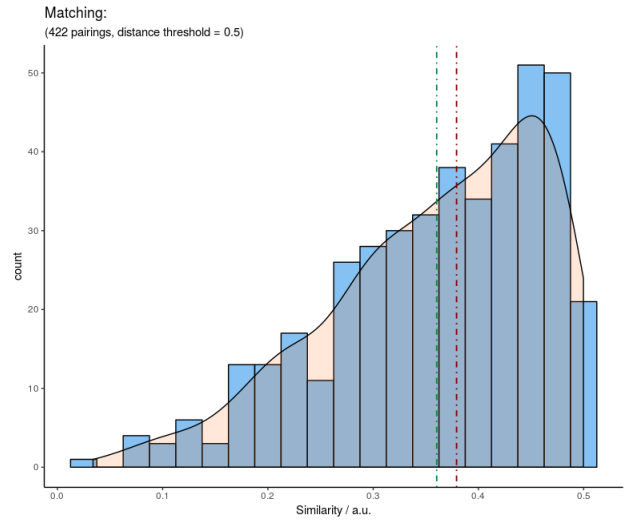
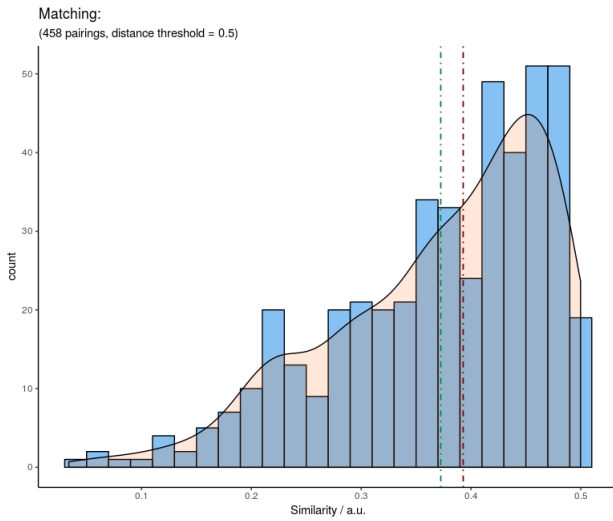


Figure 137: **Comparison of the matching with a distance limit of 1 between Blossom and Greedy.** The shape of both matchings shows a comparable distribution. Some specific peaks (e.g. at ~ 0.5 a.u.) can be identified in both matchings. Additionally, the matching of the Greedy algorithm is more right-skewed.

The distribution patterns of both matchings look very similar to each other. Most of the assignments in both matchings provide a similarity close to the distance threshold. Furthermore, even a gap at about 0.25 a.u. emerges in both distributions. Nevertheless, the distribution of the Greedy matching is more continuous. Subsequently, the parameter deviations are shown with the voltage differences at first (see fig. 138):

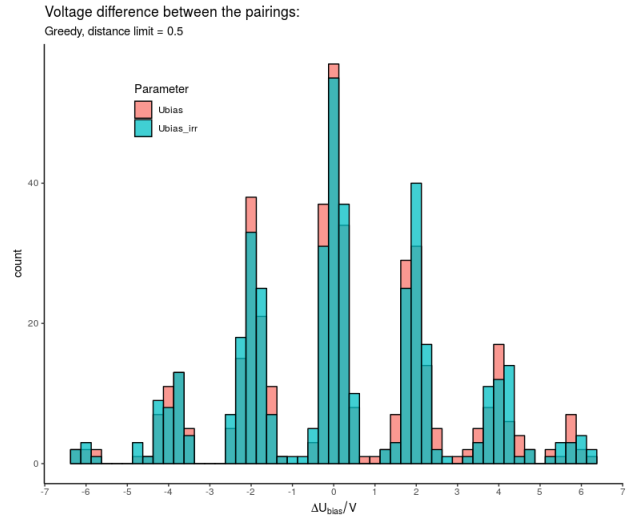
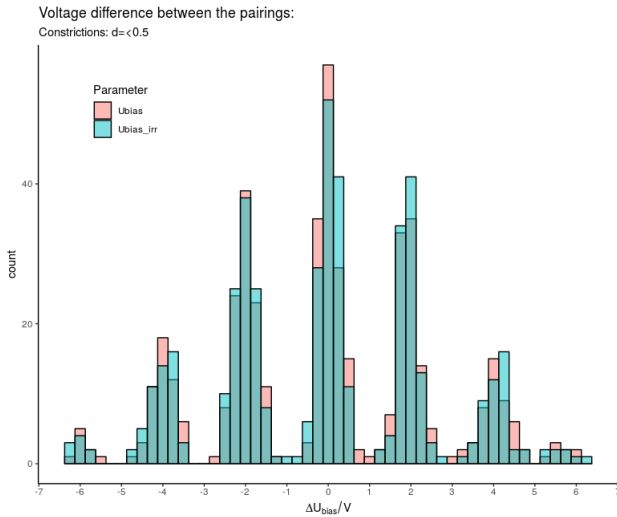


Figure 138: **Comparison of the voltage difference between Blossom and Greedy at a distance limit of 0.5.** Blossom: median = -0.018 ± 3.8 & mean = -0.1 ± 2.5 . Greedy: median = 0.047 ± 3.7 & mean = 0.15 ± 2.5 .

The voltage difference distribution of the Greedy algorithm resembles the one from the Blossom algorithm and unlike to fig. 122, the Greedy algorithm provides also a characteristic distribution when limits are applied. Next, the slope differences distributions are depicted as well:

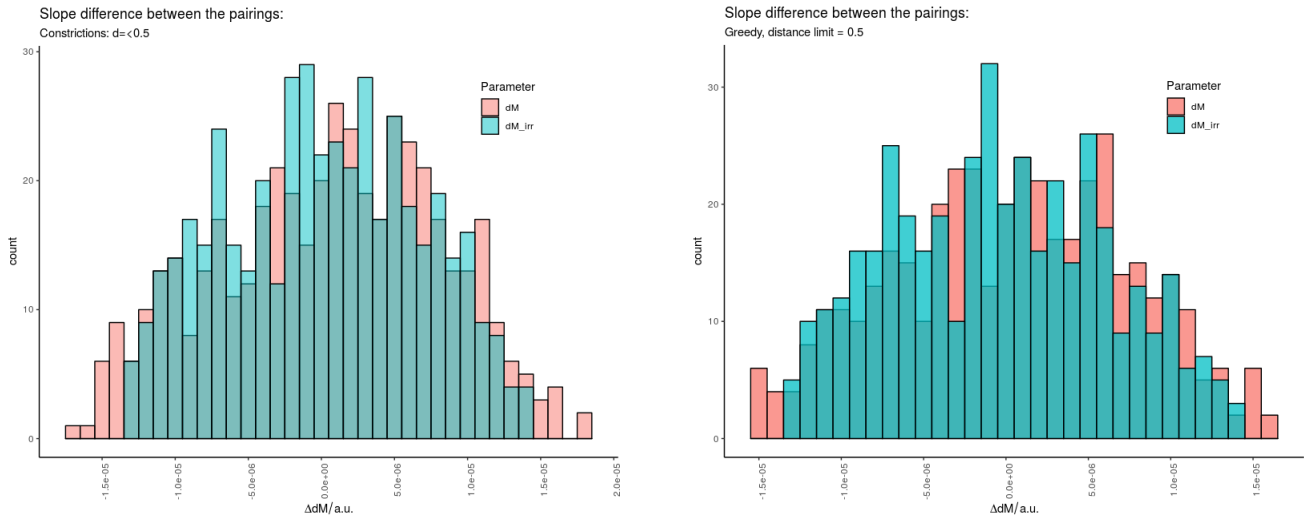


Figure 139: *Comparison of the slope difference between Blossom and Greedy at a distance limit of 0.5.* Both distributions are within a range of $\pm 1 \cdot 10^{-5}$ a.u., thus both are centered around 0.

Like the voltage differences in fig. 138, the distributions of the slope differences are also very similar to each other. It seems that the utilized metric, the Mahalanobis distance, plays a higher role than the assignment algorithm. This applies at least to a distance limit of 0.5. To see how the limit affects the matching quality, the same study is repeated with a distance limit of 1 in the following:

With a distance threshold of 1, the Blossom algorithm provides a matching where 494 APDs get successfully assigned. The Greedy algorithm is slightly worse with 483/500 pairings or 487/500 when picking the most efficient iteration.

Blossom		$d = 1.0$	Greedy	
Cost	329.7865		Cost	336.835
$Cost_{adj}$	341.7865		$Cost_{adj}$	362.835
APDs	988		APDs	974
Median	0.70		Median	0.74
IQR	0.38		IQR	0.38
Mean	0.67		Mean	0.69
Std	0.23		Std	0.23

Table 28: *Comparison of the matching values with a distance limit of 1 between Blossom and Greedy.* The Blossom algorithm provides a better matching in terms of statistical values and a higher number of assigned APDs.

In **Reduced graph** on page 227, the corresponding network is analyzed. Next in fig. 140, the quality of both matchings is shown:

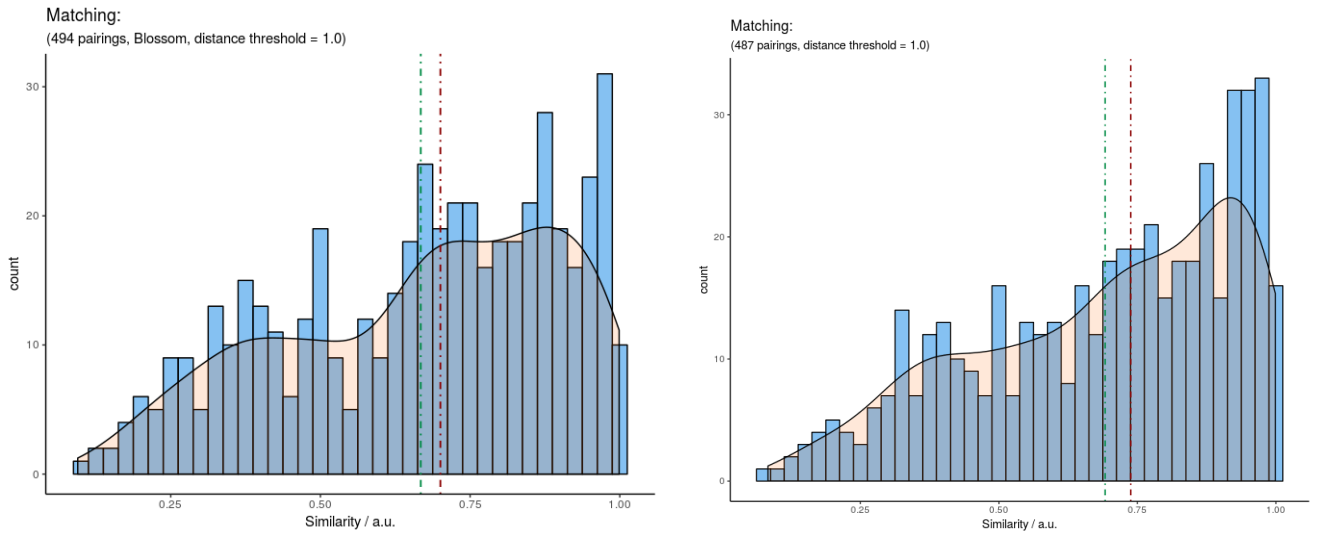


Figure 140: **Comparison of the matching with a distance limit of 1 between Blossom and Greedy.** The shape of the matching distribution shows a similar course. Some specific peaks (e.g. at ~ 0.5 a.u.) can be identified in both matchings

The similarities of the pairings tend towards the distance threshold again. Especially the matching of the Greedy algorithm is more right-skewed. Noticeable is that in both matchings a characteristic peak emerges at the previously discovered optimal distance threshold of 0.5 a.u. Anyhow, the height of it differs as it represents more than 30 pairings in case of the Blossom algorithm but only about 17 in case of the Greedy algorithm. Therefore, it might be only a coincidence whereas the shape of both distributions is comparable in general. In the following, the corresponding parameter differences with the voltage values at first (see fig. 141):

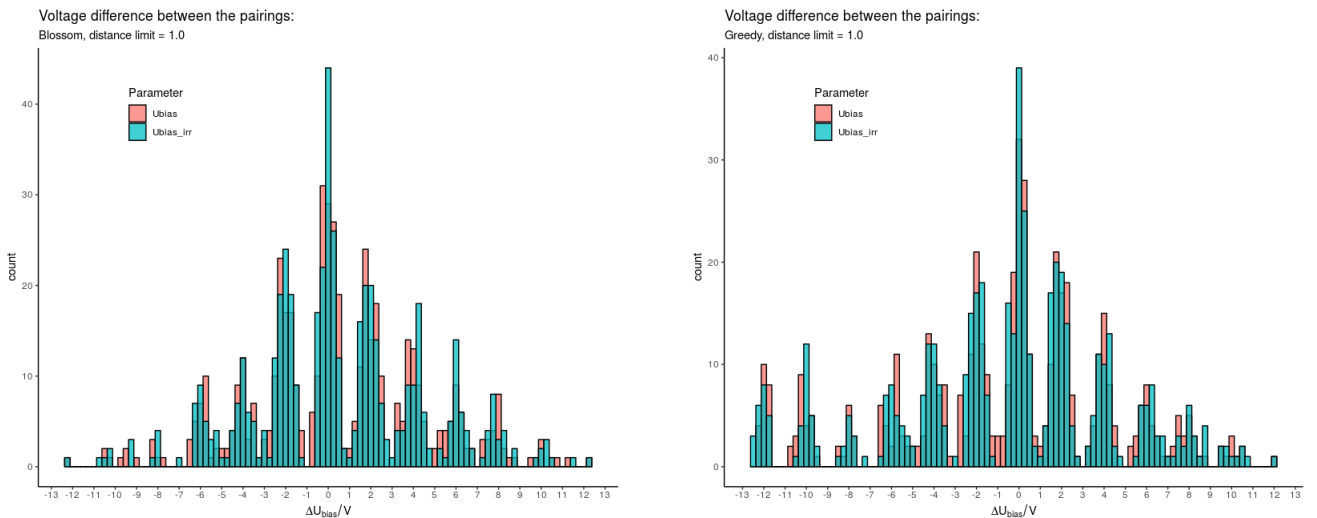


Figure 141: **Comparison of the voltage difference between Blossom and Greedy at a distance limit of 1.** Blossom: median= 0.122 ± 4.5 & mean= 0.43 ± 3.9 Greedy: median= -0.017 ± 5.9 & mean= -0.67 ± 5 .

Both distributions are very similar again with the same range of ± 12 V and the characteristic peaks and gaps at the same positions. Next, the slope differences (see fig. 142):

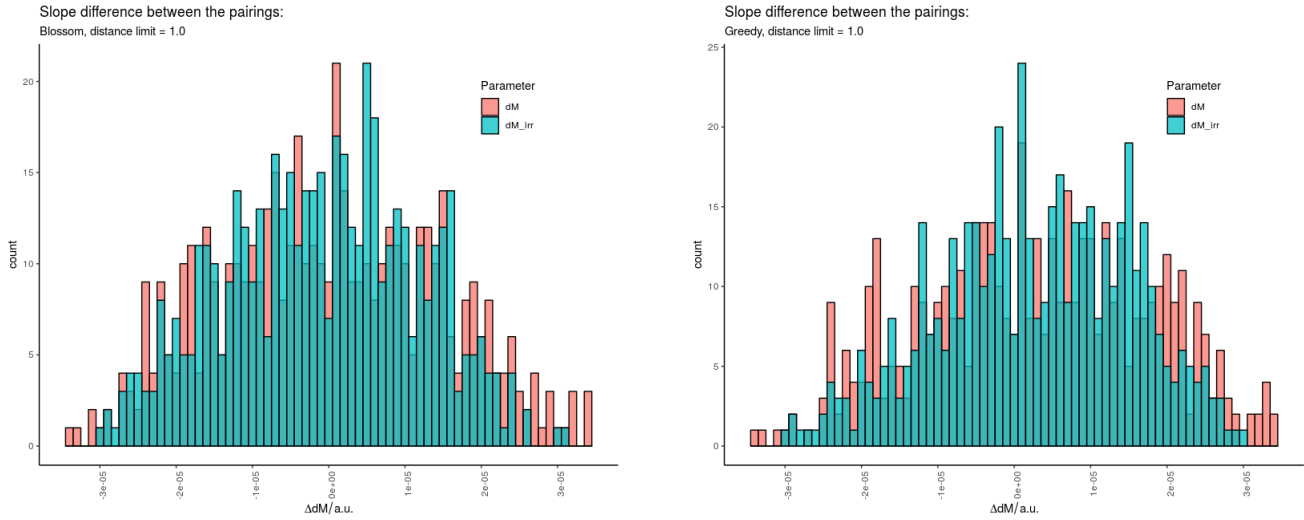


Figure 142: **Comparison of the slope difference between Blossom and Greedy at a distance limit of 1.** Blossom: median $\approx 0 \pm 2^{-5}$ & mean $\approx 0 \pm 1.4^{-5}$. Greedy: median $= 2.82^{-6} \pm 2^{-5}$ & mean $= 2.6^{-6} \pm 1.37^{-5}$.

The slope difference distributions are very similar, too, at least the shape and the range of $\pm 3 \cdot 10^{-5}$ a.u. while the peak heights differ slightly.

To fulfill technical considerations such that an APD pairing should share almost the same voltage, studies on the limitations related to specific parameters only are performed in the following. In other words, the matching is analyzed, for example, with respect to limiting the voltage distances only. The optimum of the distance limit offers the best matching but a voltage limit might provide the most meaningful matching in terms to a technical realization. At first, the limiting of the slope is investigated:

7.6.2.2 Slope limit To study the effect of slope limits, only the slope will be constrained. Furthermore, because the APDs are irradiated, only the irradiated slope values will be limited. In the following, the number of vertices against the number of edges (see fig. 143):

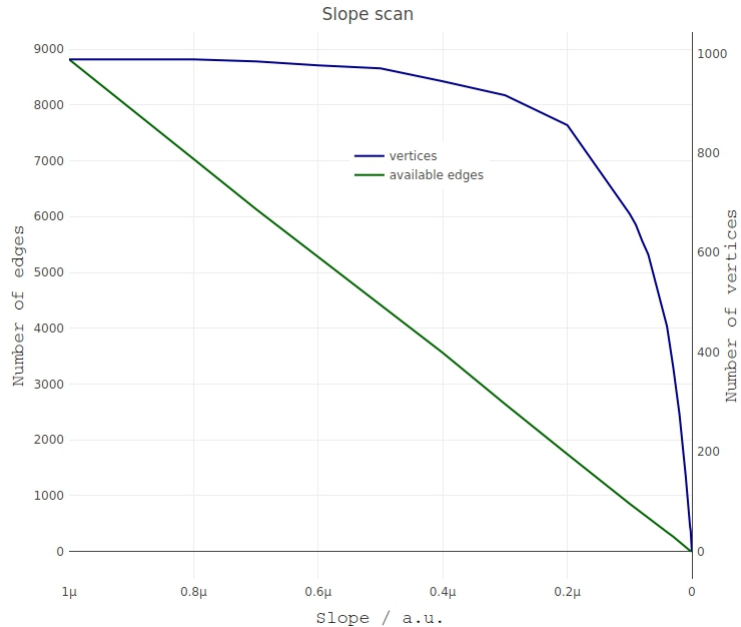


Figure 143: **Vertices and edges slope.** The number of assigned APDs changes hardly before a threshold of about $0.8 \cdot 10^{-6}$ is reached.

The number of the available edges decreases very linearly whereas the vertices rather drop rapidly with the strength of the slope distance. However, when the slope limit rises, the number of successfully assigned APDs will also decrease though only few edges of about 9,000 are necessary to maintain an almost complete assignment of the APD pool. Subsequently, the costs and vertices are shown in dependency of the slope limit (see fig. 144):

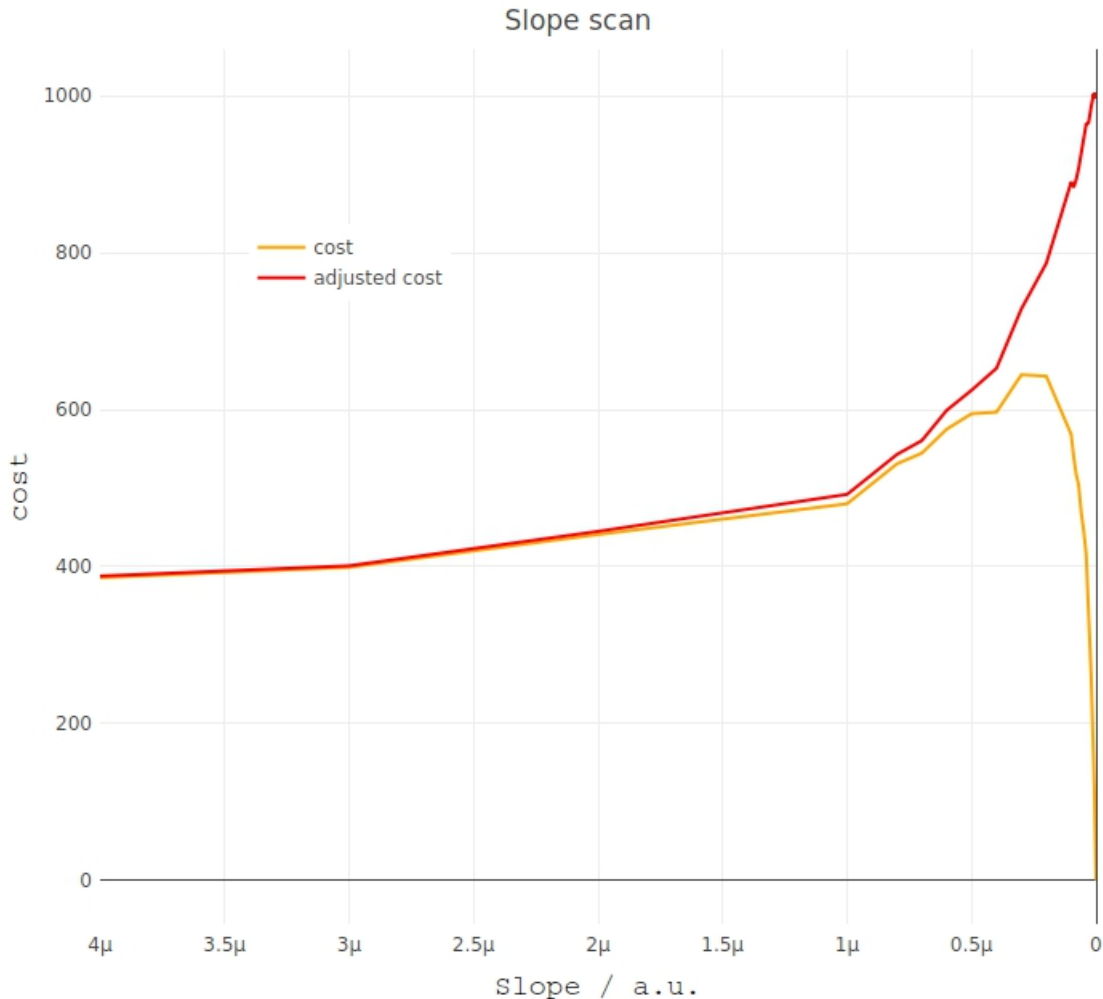


Figure 144: **Slope limits against cost and adjusted cost.** Limiting the slope has almost no effect over the large slope range and will result only in a higher cost.

Both costs and the number of available vertices is nearly independent from any slope limit over a large range until a slope limit of about $4 \cdot 10^{-6}$ a.u. is reached. From there on, both rise and the cost decreases fastly at a threshold of $0.2 \cdot 10^{-6}$ a.u. Hence, the matching is getting worse in terms of the cost which does not consider the number of assigned APDs. At this certain treshold, 856 APDs can be successfully paired.

The adjusted cost provides a slight minimum at $9 \cdot 10^{-5}$ a.u. which is shown in fig. 145. There the cost is 360.461 and none APD is removed at this threshold. Therefore, the matching could be improved by leaving the data pool unchanged. The only reason for that is the specific procedure of the Dijkstra search which operates now differently according to the modified underlying edges. Below in fig. 145, the number of edges is depicted against the costs:

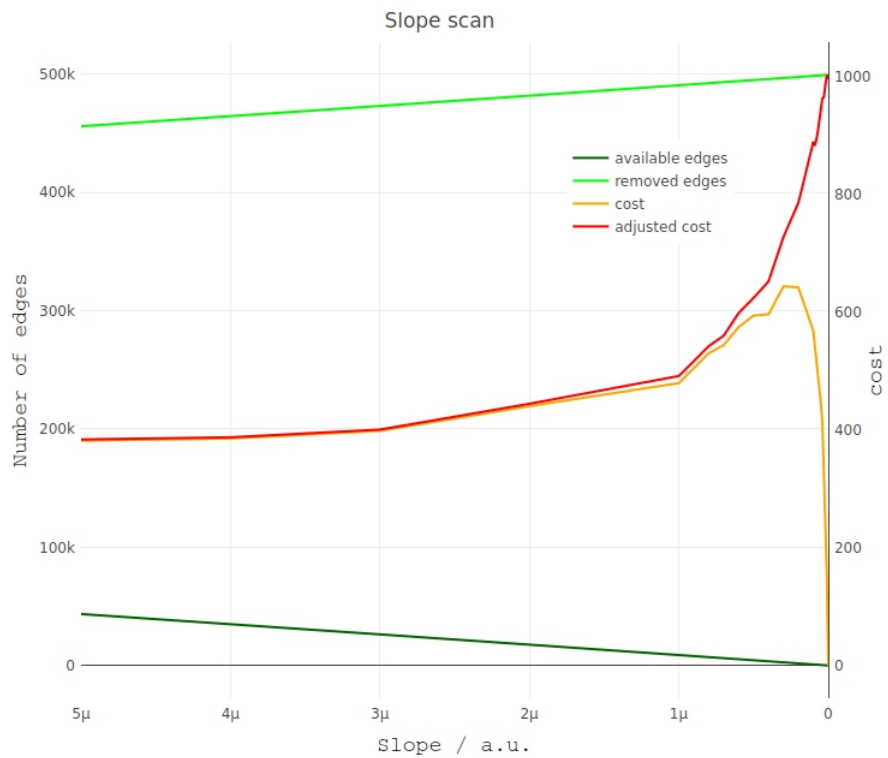
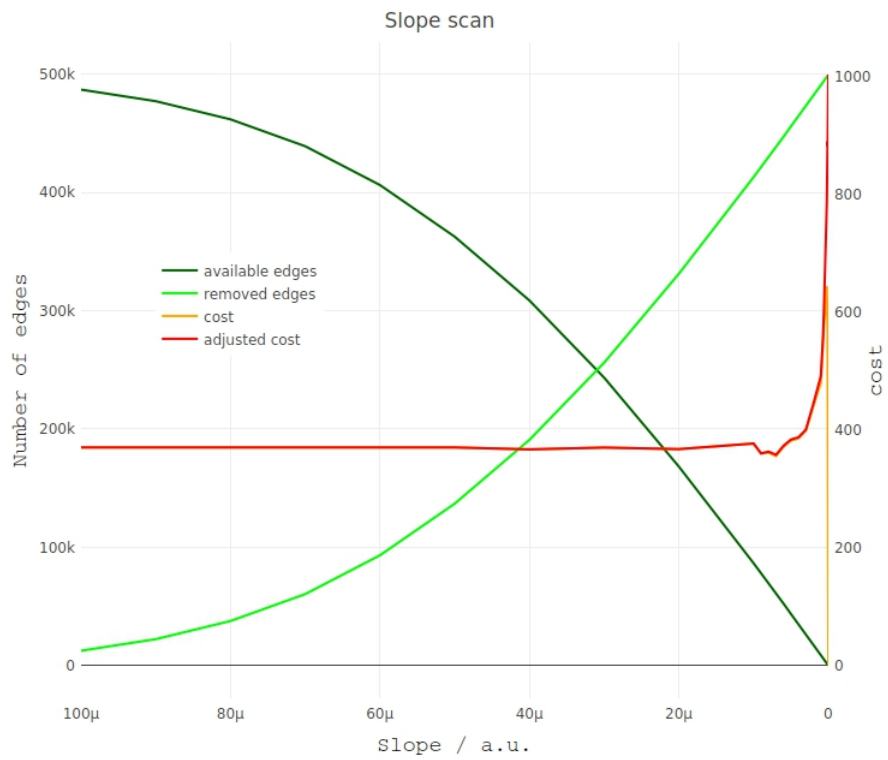


Figure 145: **Costs against slope limit.** The number of edges is halved at about a slope limit of $\sim 30 \cdot 10^{-6}$ a.u. and the adjusted cost provides a slight minimum at a slope limit of 0.000007 (top). Stronger limits will make the matching only worse (bottom)

The number of edges decrease continuously with the applied slope limit though the amount of available edges is quite constant over a long range until reaching a slope limit of $1 \cdot 10^{-4}$ a.u. Then, the quality of the matching is almost only getting worse when increasing the slope limit. Hence, the adjusted cost does not provide an optimum. At the slope limit of $7 \cdot 10^{-6}$ a.u., the adjusted cost provides a minimum of 358.088 and a cost of 356.088. When the minimum is reached, the median of the pairings changed from 0.7 ± 0.37 to 0.62 ± 0.45 , the minimum slope from 0.094 to 0.064 and the maximum slope from 17.77 to 20.33. The mean changed from 0.741 ± 0.886 to 0.72 ± 1.16 .

Finally, the matching can be traced with the help of the five numbers median, +iqr, -iqr, min and max (see fig. 146):

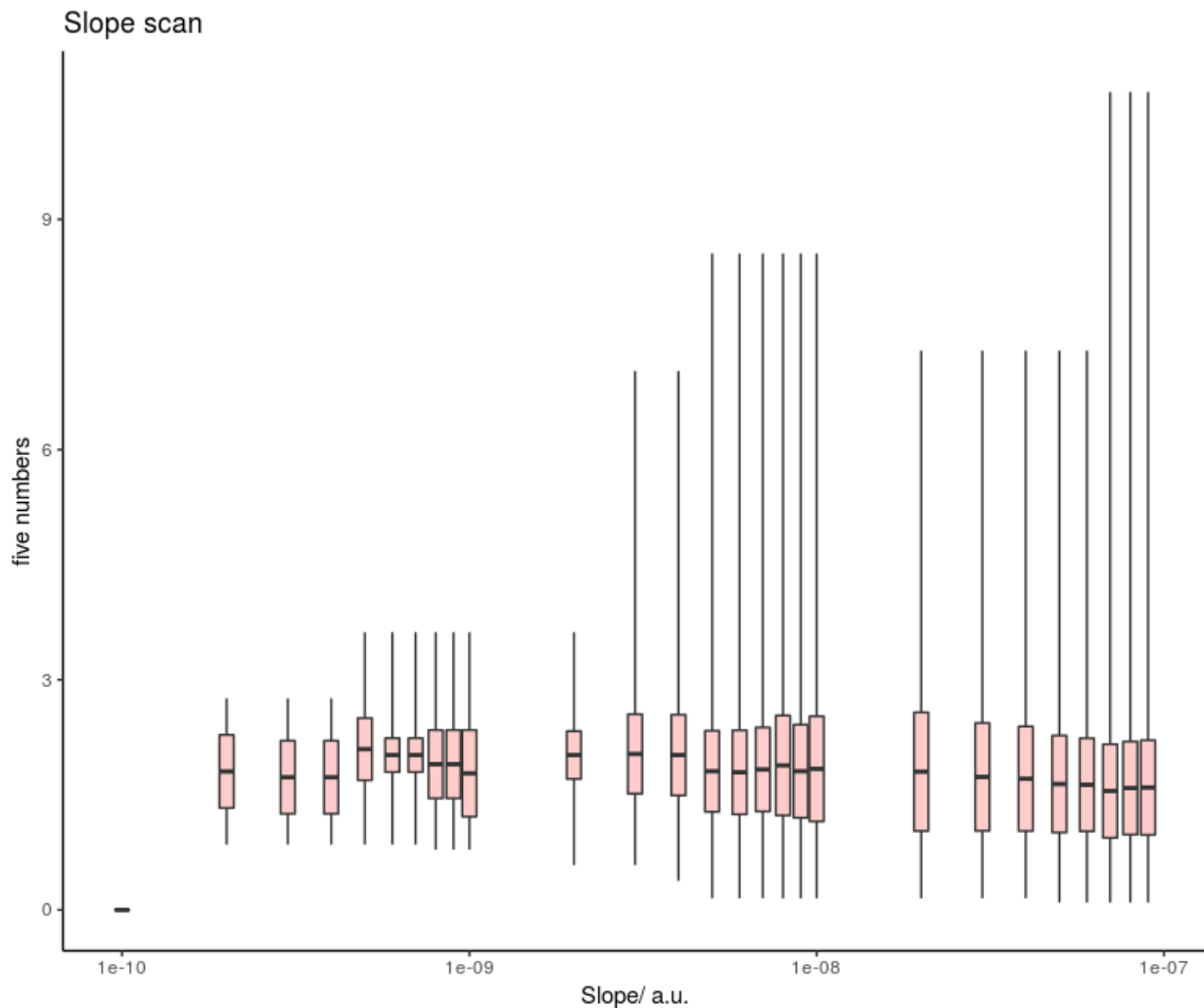


Figure 146: *Five numbers of the slope scan in the range of $\{1 \cdot 10^{-10}, 1 \cdot 10^{-7}\}$.* The median jitters slightly along the slope limits. The dependent axis represents the Mahalanobis distance between the APD pairings.

The median oscillates slightly with the applied slope limit. When increasing the limit, the maximum and minimum values change accordingly though only the maximum values are removed continuously. Nevertheless, it seems that a better global minimum matching can be obtained when selecting not only edges with the lowest value. In the following, the matching at the optimum of the slope limit $7 \cdot 10^{-6}$ a.u. will be investigated in detail:

7.6.2.2.1 Optimal slope threshold

In contrast to the matching distribution of the optimal distance limit (see fig. 133) which assignments tended to the limit, the distribution of the optimum slope limit follows a Gaussian behaviour (see fig. 147):

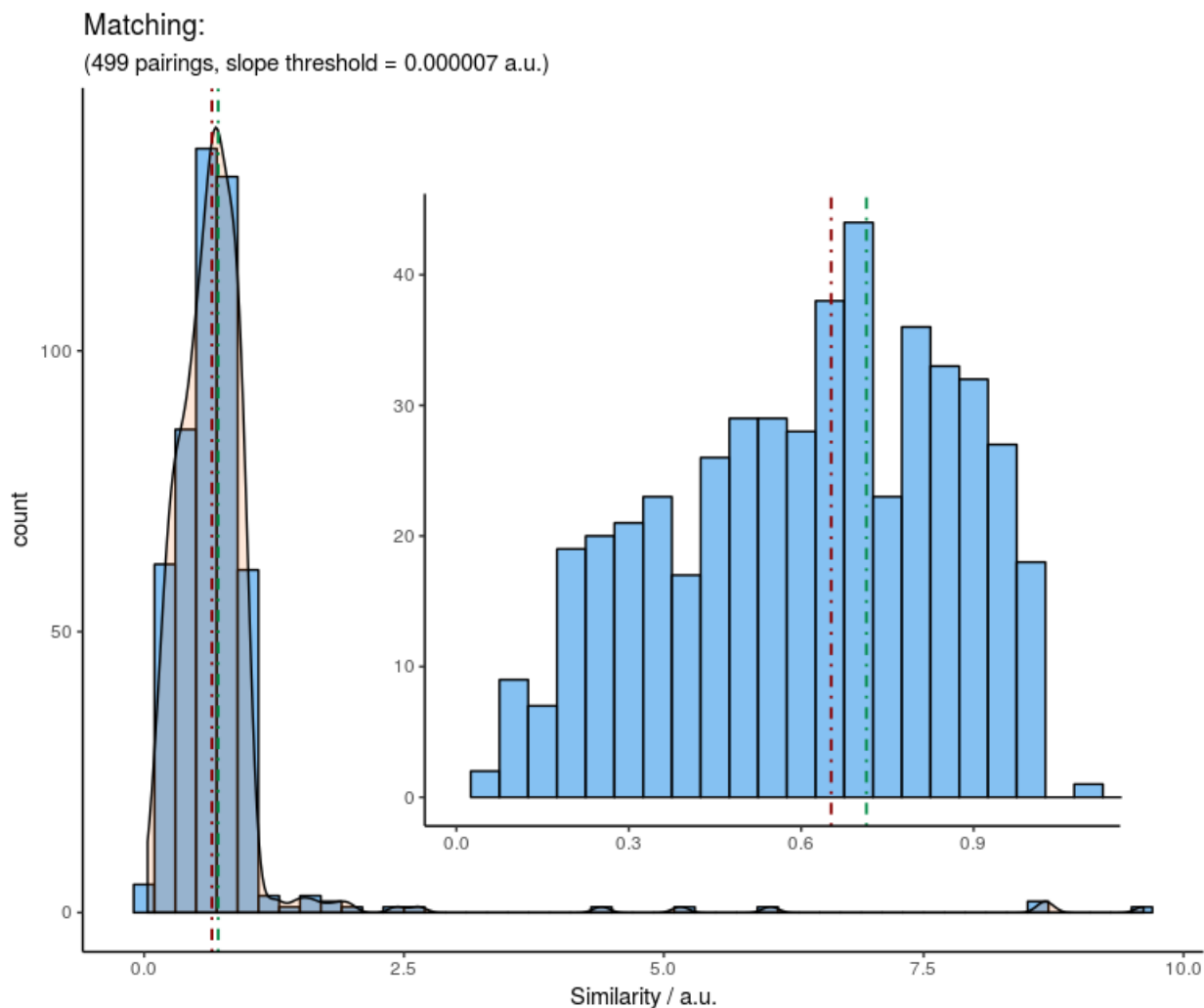


Figure 147: *Matching of the optimal slope limit.* The median is at 0.652 ± 0.393 and the mean at 0.7136 ± 0.795 .

Most of the pairings provide a similarity below 1 a.u. while the one half is located below ~ 0.7 a.u., both given in terms of the absolute Mahalanobis distance. Nevertheless, some outliers are present. The distribution of the slope differences is depicted in the following in fig. 148:

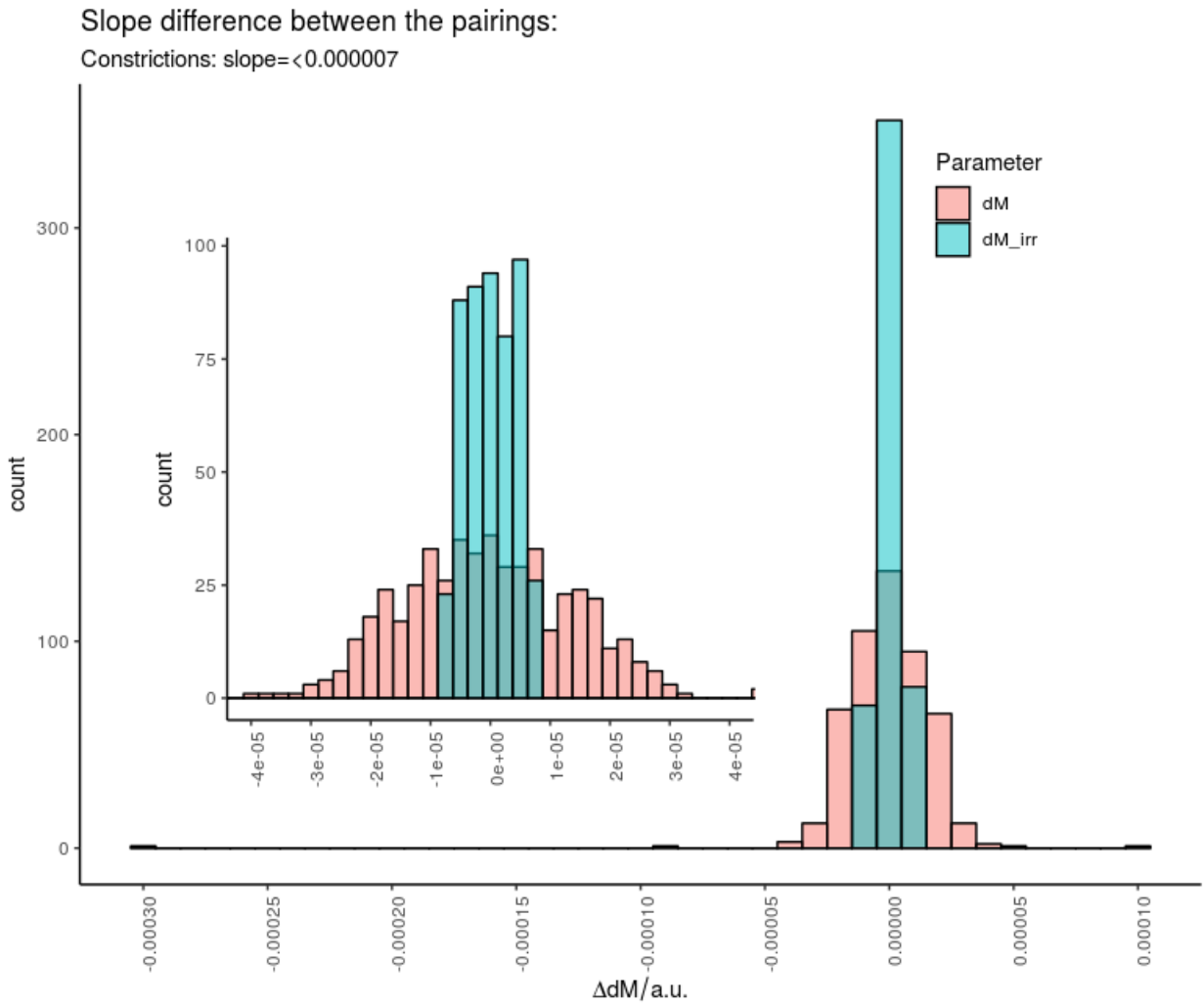


Figure 148: **Slope differences at the slope optimum.** The irradiated slope values are located within the given threshold of $7 \cdot 10^{-6}$ a.u. and the non-irradiated values provide a broader distribution within about $3 \cdot 10^{-5}$ a.u.

The non-irradiated slopes provide a Gaussian-like distribution whereas the irradiated slopes are located within a narrow distribution due to the applied limit. The technically more significant part is represented by the voltage differences between the APDs of each pairing (see fig. 149):

Voltage difference between the pairings:

Constrictions: slope=<0.000007

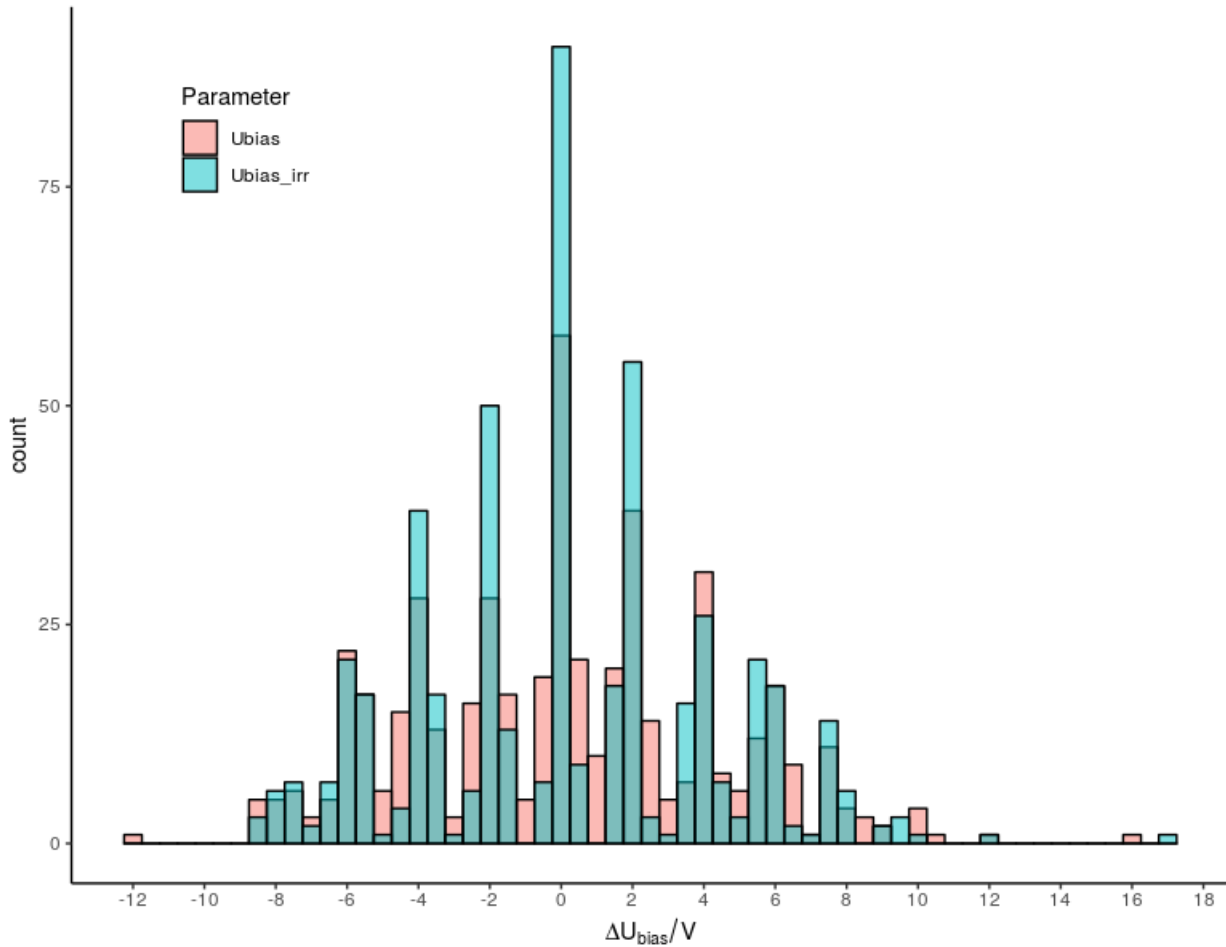


Figure 149: ***Voltage differences at the slope optimum.*** The pairings provide voltage differences with a wide distribution within about ± 10 V though it is centered at 0 V.

Similar to the distributions of the voltage differences of the optimal distance limit (see fig. 134) and the basic graph (see fig. 123), the optimal slope limit provides a similar characteristic distribution of the voltage differences (see fig. 149). Many pairings provide a voltage difference of ± 0 V and most of the pairings are within a lower voltage limit of $\Delta U = -8$ V and an upper one of $\Delta U = 10$ V.

Since the voltage is the only real parameter that is technically regulated in the experiment, the limitation of it is also examined in more detail in the following.

7.6.2.3 Voltage limit

Applying a voltage limit is more meaningful than a limitation of the slope because the APD's bias voltages will be set electronically and the corresponding slopes are connected to the regulated bias voltages anyway. The scan will begin with an applied voltage limit of 100 V and end with a limit of 100 μV . A limit of 0.1 V marks a special value as it was used for the first slice. To get started, in fig. 150 the number of vertices is shown against the applied voltage threshold:

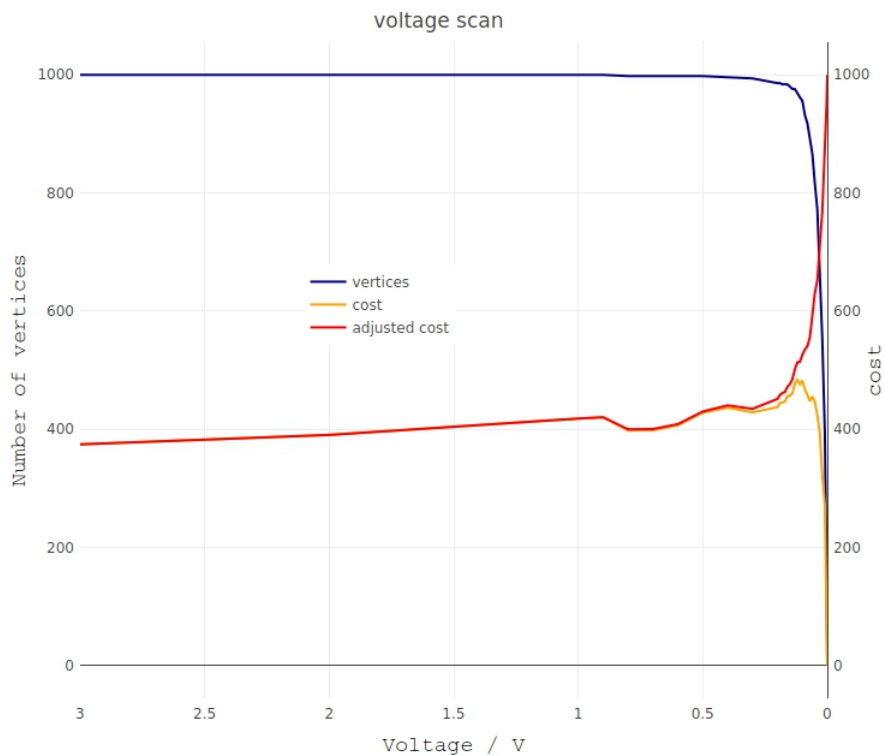
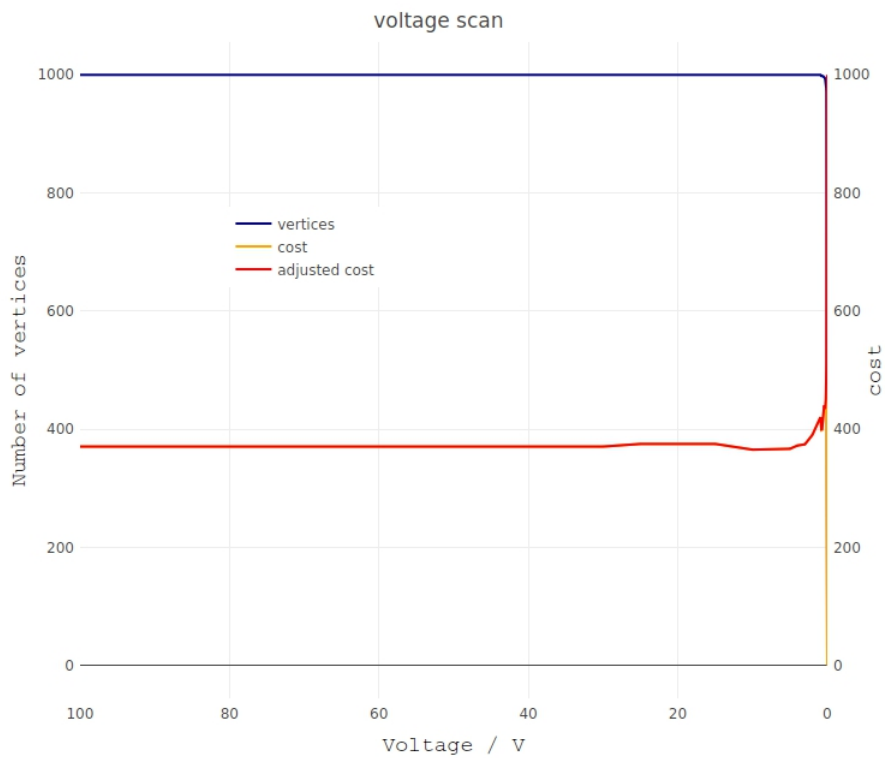


Figure 150: ***Number of vertices and costs against voltage limit.*** The number of vertices and the costs are constant almost over the entire voltage range until a voltage limit of 1 V is achieved. Then, two APDs are removed from the matching. By reaching a voltage threshold of 4 V, the adjusted cost increases slowly up to a voltage threshold of 900 mV and decreases then slowly until about 700 mV, then it rises again. Both costs do not provide a characteristic minimum below 500 mV.

The number of vertices and both cost types do not change until a relative high voltage limit < 1 V is reached. A minimum is located at a voltage limit of 10 V where the cost is 365.41 with 1,000 assigned APDs (see fig. 150). Accordingly, the adjusted cost is 367.41. At 800 mV, the cost encounters a local minimum with a cost of 397.903 respectively with an adjusted cost of 399.903 and 998 APDs. Though this threshold represents the optimum, it is too broad and motivates further investigations. Hence, in the following (see fig. 151), the voltage differences are scanned below a voltage value of 300 mV.

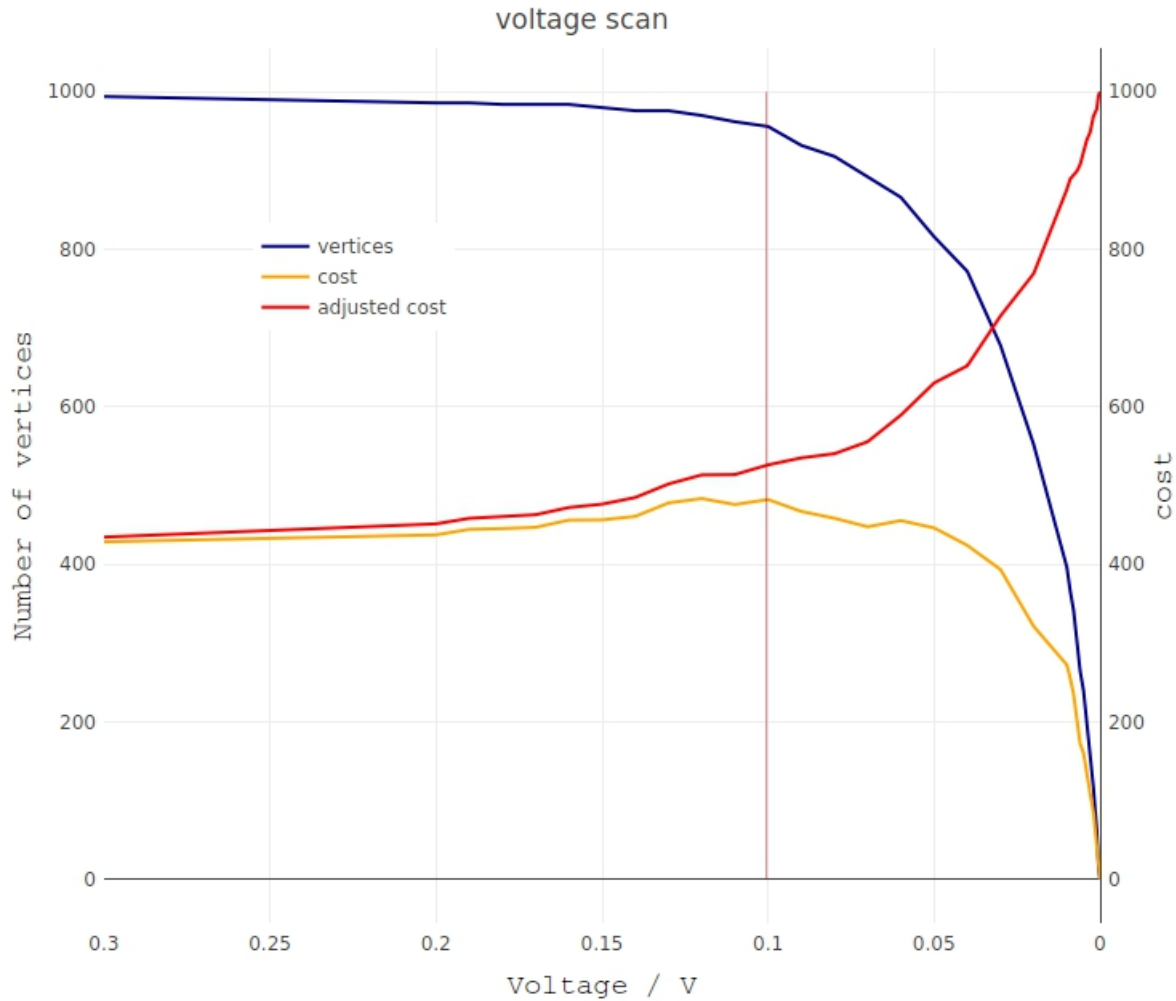


Figure 151: **Voltage limits against cost and adjusted cost.** From 200 mV on, the number of APDs decreases continuously together with the cost. The adjusted costs are only increasing.

The cost is rising until a voltage limit of 120 mV is reached with 970 APDs. The cost will decrease with a stronger threshold while the adjusted cost continues to rise. The cost decreases quite steeply together with the number of APDs when a voltage limit of about 50 mV has been exceeded (see fig. 151). Next, the number of edges against the voltage limit (see fig. 152):

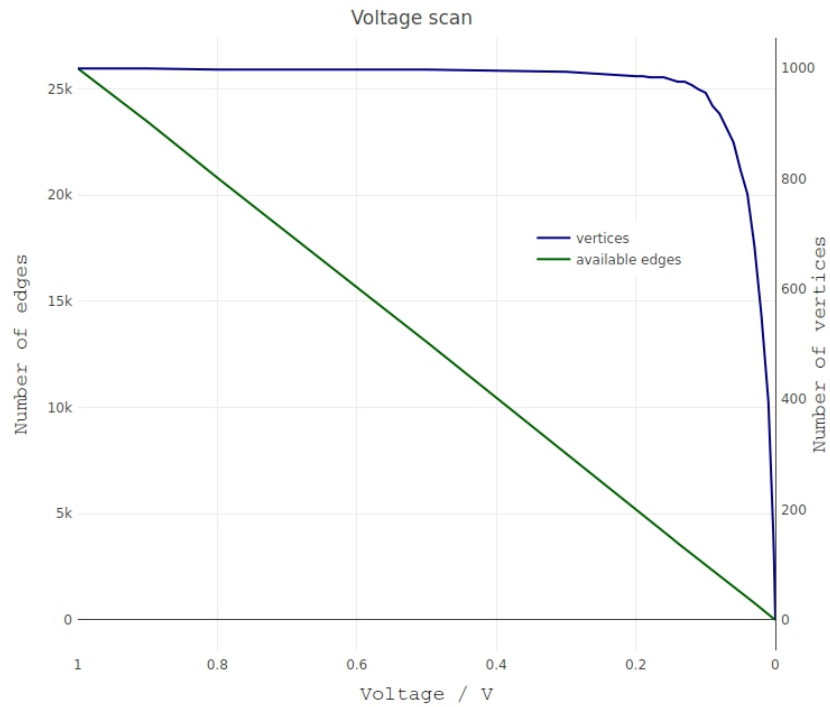
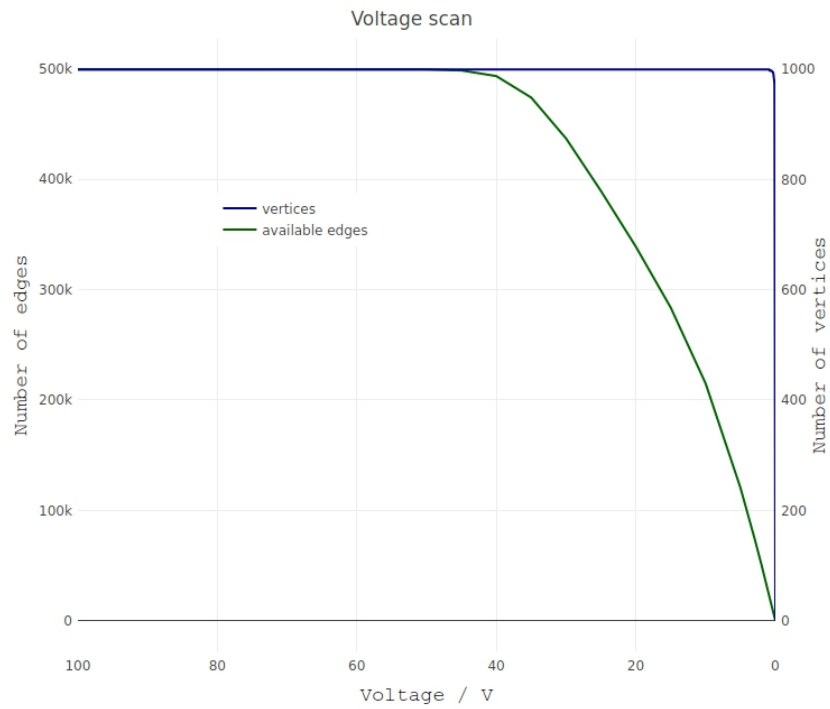


Figure 152: *The number of vertices against the number of edges in dependency on the voltage limit.* The amount of edges does not change until a voltage limit of about 40 V is reached and the vertices do not decrease up to a threshold of about 200 mV.

The number of APDs does not decrease until only about 5,000 edges are left. Afterwards, the number of APDs is dropping quite fast. In the following (see fig. 153), the costs are compared to the number of edges and APDs:

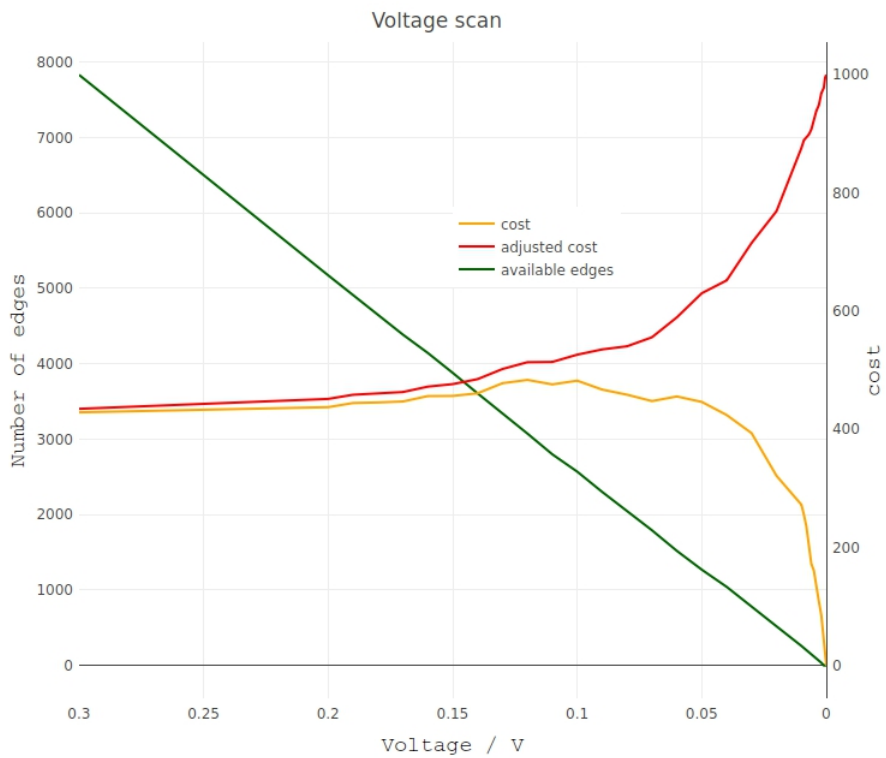
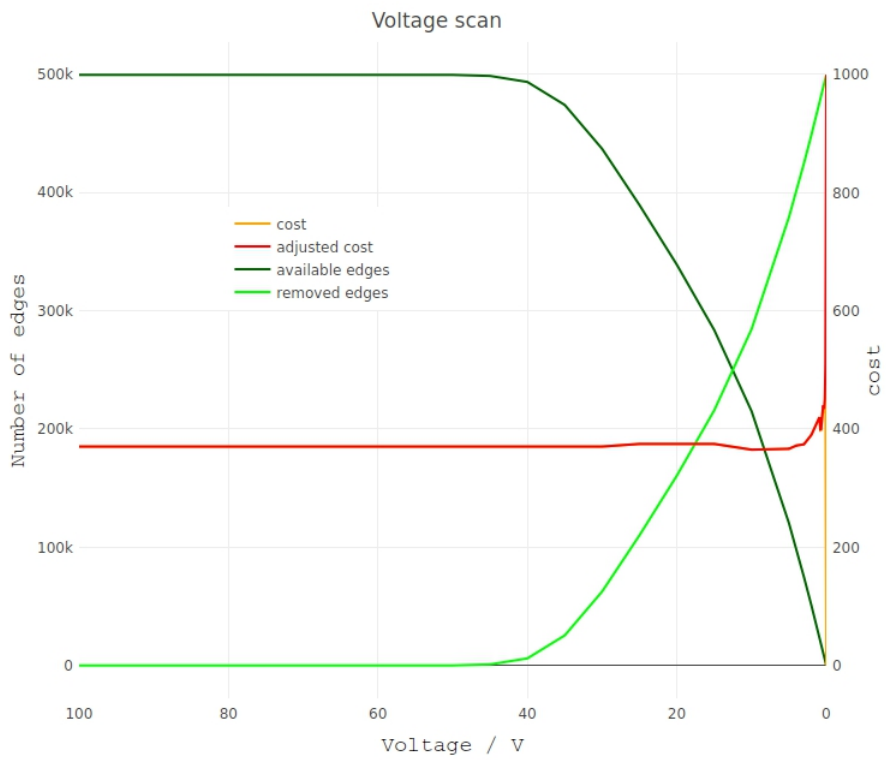


Figure 153: **Cost and edges against voltage limit.** The number of edges is halved at a voltage limit of about 12 V. In addition, the matching cannot be improved when selecting higher voltage thresholds. On the contrary, it only gets worse.

The edge number is already decreasing from a threshold of about 40 V on though it does hardly affect the matching. Finally, both costs provide only one optimum at a voltage limit of 800 mV (see fig. 150). In fig. 154, the voltage scan shows how the five numbers change with the applied voltage threshold:

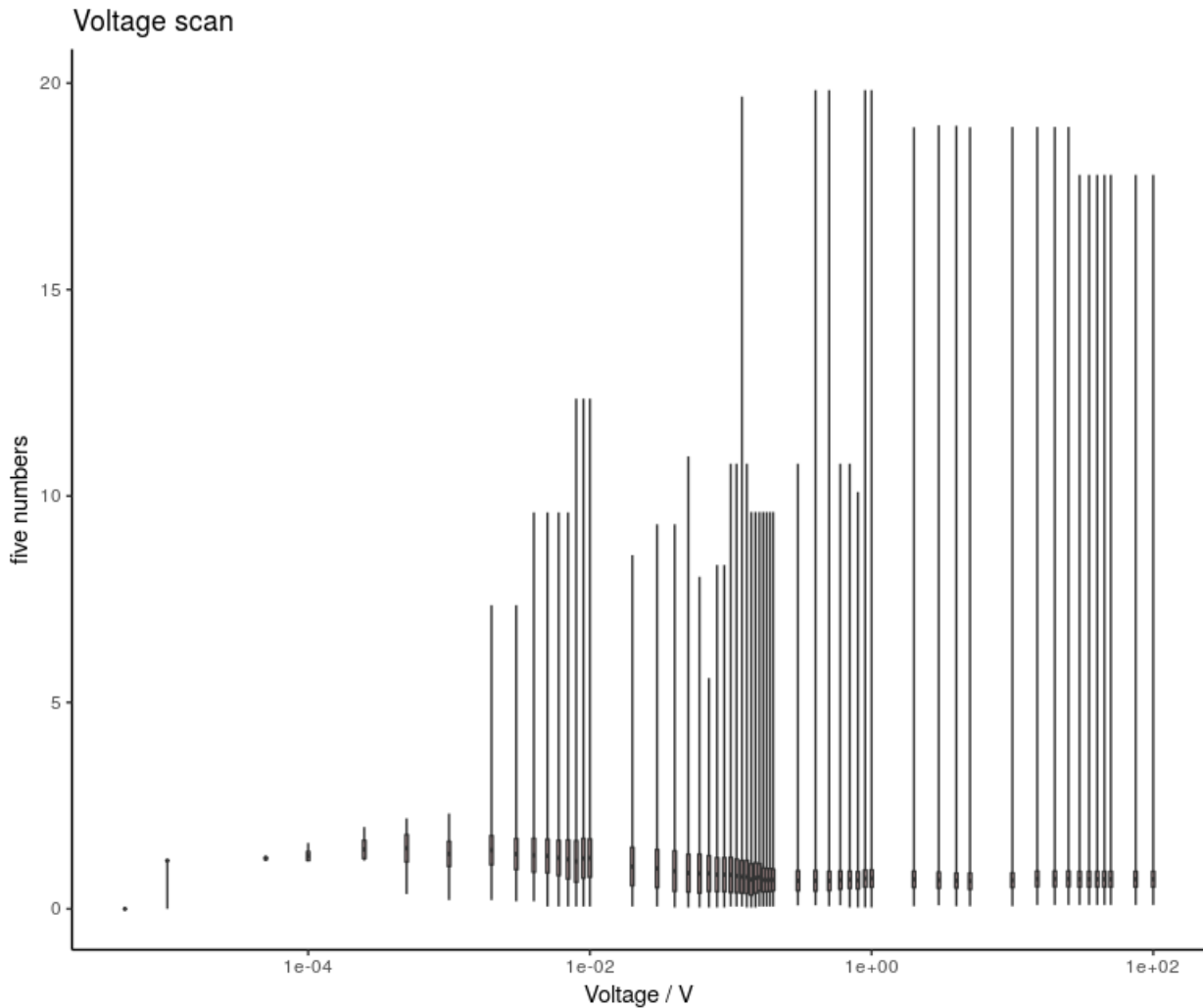


Figure 154: *Five numbers in the voltage limit range of 0 – 100 V.* The median changes with the applied voltage threshold. The dependent axis represents the Mahalanobis distance between the APD pairings.

The median increases with a stronger voltage threshold. The minimum weight increases, too, while the maximum weight decreases. It has to be kept in mind that these numbers represent the edges of the matching and not the original network itself from which the matching is formed. At a voltage limit of 800 mV, the median is 0.693 ± 0.412 with a minimum edge of 0.033 and a maximum edge of 10.1. The mean is 0.797 ± 0.779 . It is worth mentioning that sometimes the matching includes higher weighted edges at a higher threshold than at lower ones, e.g. when going from $\Delta V_{\max} = 600$ mV to $\Delta V_{\max} = 500$ mV.

7.6.2.3.1 Optimal voltage threshold:

Since the optimum of 800 mV is greater than the aimed threshold of 100 mV, only the matching of 100 mV will be studied in the following. Furthermore, this voltage limit will be treated as the voltage optimum from now on though the costs do not represent it as such. Its usage is justified on the part of the technical background. First, the corresponding matching in fig. 155:

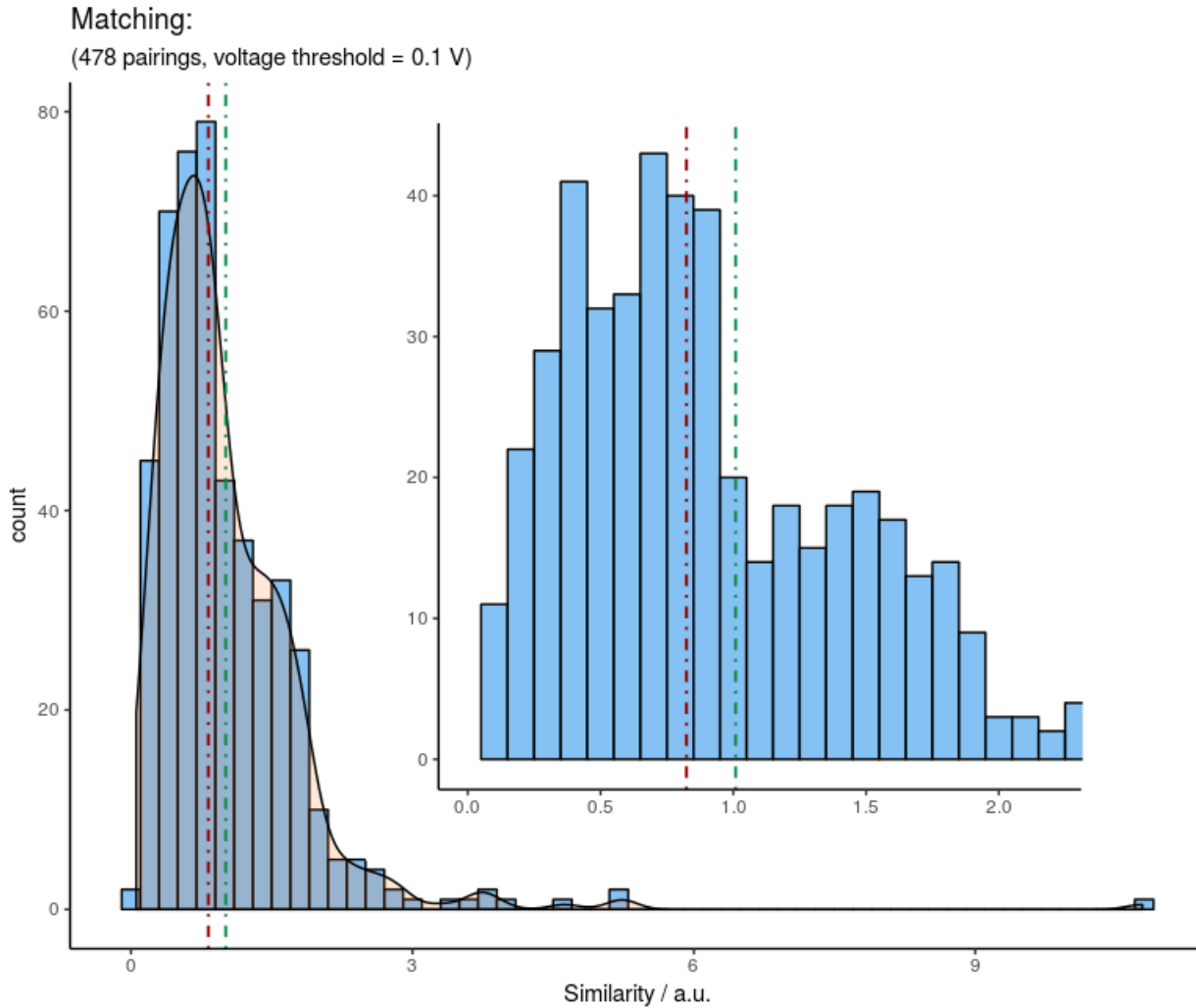


Figure 155: **Matching at a voltage limit of 100 mV.** The median is 0.824 ± 0.85 and given in red and the mean is 1.08 ± 0.84 and given in green.

The matching at the voltage limit of 100 mV provides 478/500 pairings. The corresponding distribution is slightly left-skewed which is desirable since lower values on the independent axis represent a higher similarity between the APDs. One half of the APD pairings provides a similarity of less than 0.823 and almost the entire other half is below a value of 3, each in terms of the Mahalanobis distance. Some outliers are present. Overall, the median of all pairings is at 0.824 ± 0.85 and the mean at 1.08 ± 0.84 . In fig. 156, the voltage differences of the matching are shown:

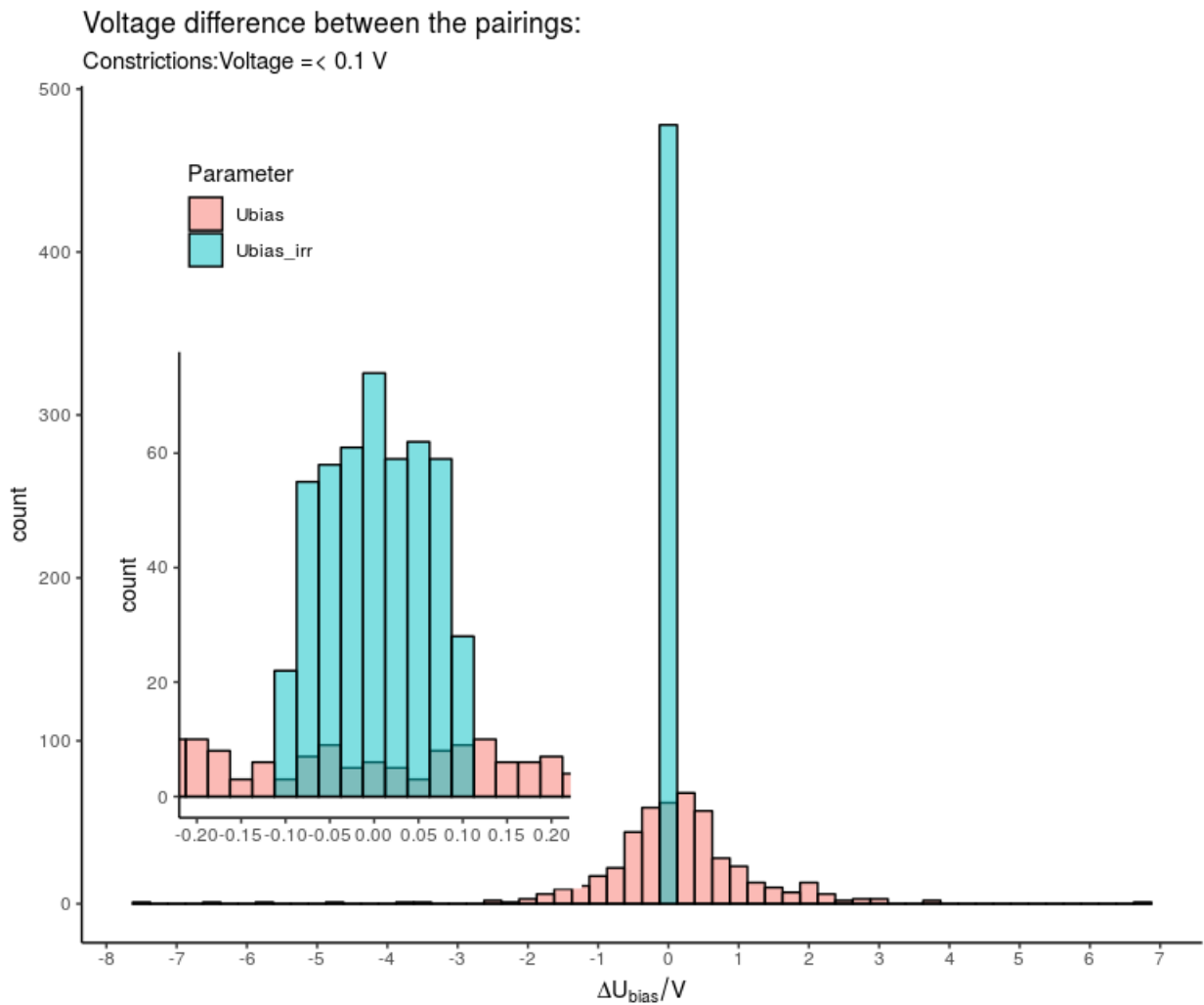


Figure 156: **Voltage differences at a voltage limit of 100 mV.** The irradiated values are located within the applied voltage threshold of 0.1 V.

All the voltage difference values are located in a very narrow window accordingly to the threshold. The non-irradiated data, on the other hand, are spread outwards over a large area of about ± 2.5 V. Though only the irradiated values are constrained, the similarities are calculated by using all four parameters. In other words, the irradiated values not exceeding the threshold are equipped with a very high weight, forcing the algorithm to avoid creating pairings out of them. Hence, the other parameters respectively the weights of the other edges are not modified. This explains why the non-irradiated values distribution is so broad compared to the distribution of the irradiated values. In [Voltage scan](#) on page 224, the network with applied thresholds on the irradiated values together with the non-irradiated values is analyzed, too. Next, the slope differences are depicted in fig. 157.

The distribution of the irradiated slope values is smaller than the one of the non-irradiated values and form both a Gaussian distribution. The distribution of the irradiated values has a width of $\pm 2 \cdot 10^{-5}$ a.u. and the distribution of the non-irradiated values has twice the width with approximately $\pm 4 \cdot 10^5$ a.u.

Slope difference between the pairings:

Constrictions: Voltage = < 0.1 V

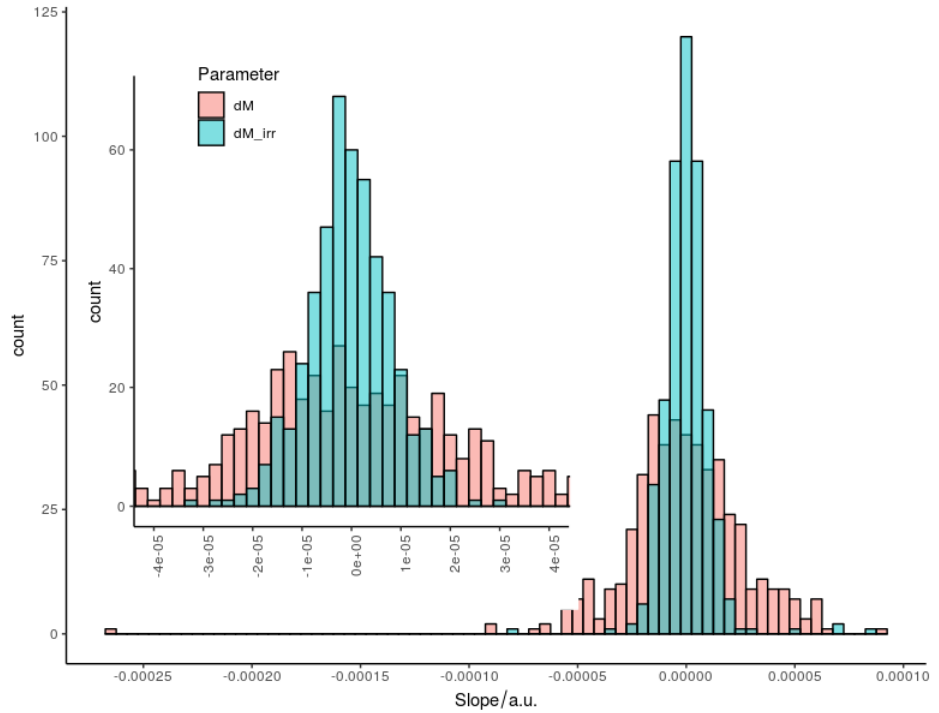


Figure 157: *Slope differences at a voltage limit of 100 mV.* Both data sets form a Gaussian distribution.

In the following, deeper insights into the network of the matching at a voltage limit of 100 mV are provided:

Vertices	956
Edges	2600
Average degree	2.661
Average weighted degree	3.882
Network diameter	8
Graph density	0.005
Average cluster coefficient	0.571
Modularity	0.962
Communities	98



Table 29: *Properties of the graph with a voltage limit of 100 mV.*

Figure 158: *Visualized network with a voltage limit of 100 mV.*

The corresponding network of the voltage limit of 100 mV provides a low density of only 0.005 and a community number of 98 with only few connections among themselves. Several communities are isolated, thus, many APDs do only have a small numbers of possible assignments. This is also indicated by a low average degree of 2.661. Finally, all optima are summarized in table 30.

7.6.2.4 Comparison between all optima

In the previous studies, thresholds were applied for the respective parameters and their change and effect on the matchings were observed. In order to assess this according to quality of the matching, the so-called adjusted cost function was set up and, where this has a minimum, the matching is assumed to provide optimum properties in regard to the similarities between all the APD pairings. These are compared below in table 30.

Minima of applied limits			
	Distance	Slope	Voltage
	0.5 a.u.	$7 \cdot 10^{-6}$ a.u.	100 mV
APDs	916	998	956
cost	170.599	356.088	482.247
cost _{adj}	254.599	358.088	526.247
$ \max(\Delta V) / V $	6	10	0.1
median	0.393	0.652	0.824
iqr	0.144	0.393	0.85
mean	0.373	0.7136	1.08
std	0.098	0.795	0.84

Table 30: *Comparison between the limits.* The median and mean are related to the Mahalanobis distance. Therefore, the optimum of the distance limit offers the best matching while the voltage limit provides the most meaningful matching in terms to a technical realization. The optimal slope limit offers the best matching with respect to the number of assigned APDs.

If all parameters were equivalent, then limiting only the distance d would provide the best matching in terms of the Mahalanobis distance. Since the irradiated parameters are more important in general, the distance d offers too great parameter differences, especially in regard to the voltage values as the previous analysis showed. Hence, it should not be simply used as an indicator for the goodness of the matching of the APDs. Therefore, due to the parameter difference each threshold is connected with, a limitation of the irradiated voltage values remains as the most reasonable way to pair the APDs. While a distance limit of 0.5 a.u. offers the best numbers with respect to a statistical measure of the matching, a limit in the irradiated voltage of 100 mV prevails in a technical context and, thus, in fact namely with regard to the voltage differences between the APDs.

The APDs will not only be assigned as pairs of two but in total also in groups of eight since one backplane will supply eight APDs with high voltage. The corresponding clustering, described next, will be studied by using 100 mV as a voltage threshold for each APD pairing.

7.6.2.5 Group APD pairings to a cluster of four pairings

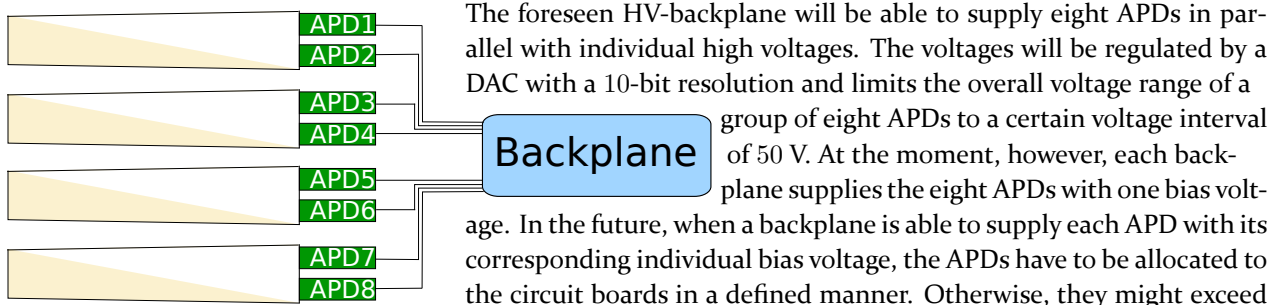


Figure 159: **High voltage supply to operate eight APDs.**

The foreseen HV-backplane will be able to supply eight APDs in parallel with individual high voltages. The voltages will be regulated by a DAC with a 10-bit resolution and limits the overall voltage range of a group of eight APDs to a certain voltage interval of 50 V. At the moment, however, each backplane supplies the eight APDs with one bias voltage. In the future, when a backplane is able to supply each APD with its corresponding individual bias voltage, the APDs have to be allocated to the circuit boards in a defined manner. Otherwise, they might exceed the voltage range of the backplane or decrease the possible voltage resolution. To do so, in the first instance the APDs have to be grouped into pairs of two and will be glued at the back of a crystal. Next, four crystals respectively eight APDs now have to be assigned together. This means, that a multi-matching of three partitions is necessary. Up to now, there is no such approach available, thus, a remedy is requisite. The idea is

to assign the APDs multiple times (see fig. 160): In the first layer, the APDs will be paired into groups of two. Now, such a pair will be seen as a virtual APD (APD12). In the next layer, two such pairs (APD12 and APD34) will represent another virtual APD (APD1234). Thus, two APD pairs will be assigned to a quartet. In the third layer, this procedure will be repeated and two virtual APDs, each comprising four APDs (APD1234 and APD5678), will finally be clustered into a group of eight APDs (APD12345678). A virtual APD is created by using the mean values of the parameters of both APDs of the former pair.

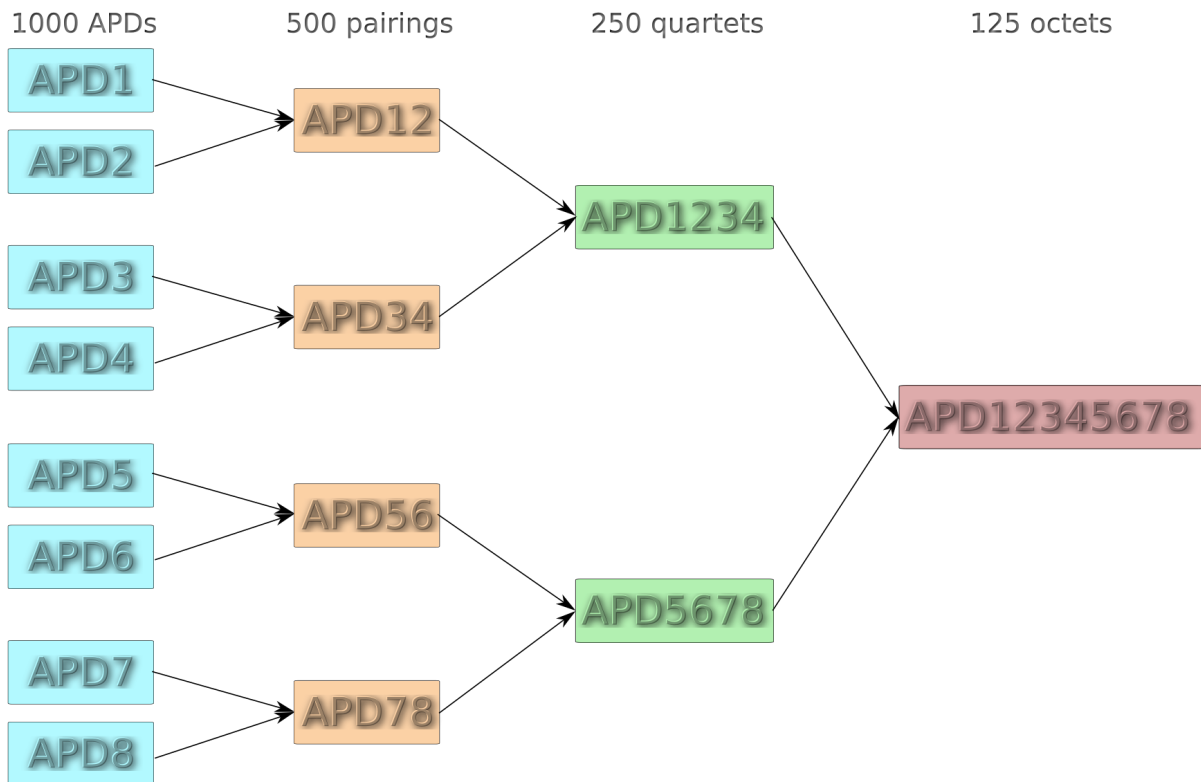


Figure 160: **Multi matching.** Four pairings, each containing two APDs, will finally be grouped into a cluster of eight APDs by using virtual APDs for the multiple layer assignment.

7.6.2.5.1 Assigning the APD groupings via Mahalanobis

As previously described, the APDs will be supplied by the HV backplanes in groups of eight. To cluster them, the assignment process is performed three times in total. The initial pairing of the APD is of the highest importance and performed by using the Mahalanobis distance to measure the similarity. In the subsequent assignment stages (for example, when clustering pairings into quartets), specific rules can be applied again like in Distance limit on page 125. Since the goal is to cluster eight APDs such that all bias voltages match the voltage range of the HV backplane, this topic is investigated only in regard to the irradiated voltage values. To get started, no constraints are applied in each assignment stage. In fig. 161, a distribution of the maximum differences between the bias voltages of each APD grouping is shown: $\Delta U_{\text{bias}} = \max U_{\text{bias,irr}} - \min U_{\text{bias,irr}}$.

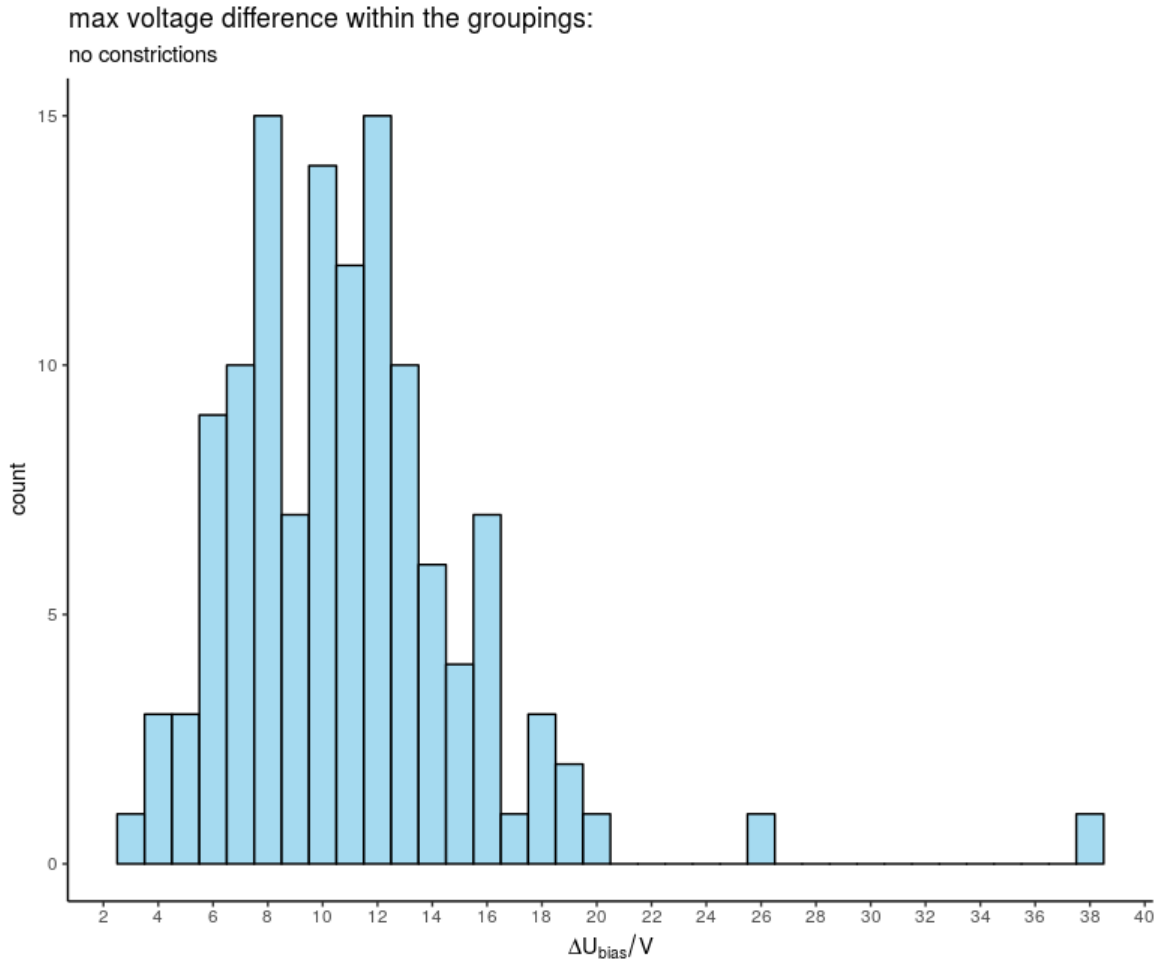


Figure 161: **Maximum voltage difference of the 8-APD cluster via Mahalanobis distance.** No limits are applied and all clusters provide a maximum voltages range below 40 V.

When no limits are applied, most of the backplanes have to cover a voltage range of about 20 V. Two backplanes need to provide a voltage range of 26 V or 38 V, respectively. Some backplanes can even operate with a voltage range of less than 5 V. However, though the technical requirement of a voltage range < 50 V is fulfilled, the initial APD pairings are not optimized with respect to their similarities in their voltages. Next, the layers will be modified via constraints.

7.6.2.5.2 Assigning the APD pairings via voltage limits

Before in fig. 161, all layers were grouped by using the Mahalanobis distance. Now, the pairings of the first layer will be assigned by considering only the irradiated bias voltages and the quartets and octets by using the Mahalanobis distance (see fig. 162).

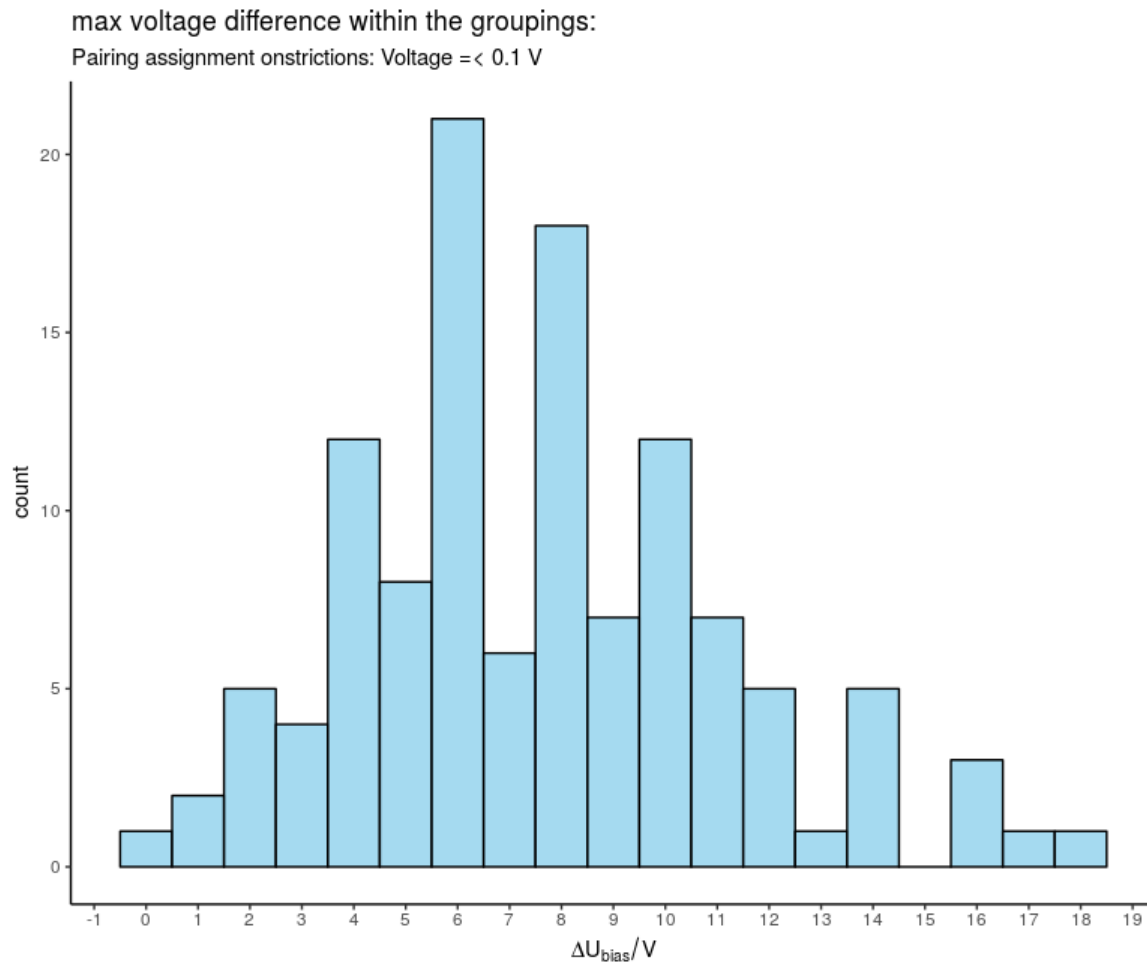


Figure 162: **Maximum voltage difference of the 8-APD cluster by assigning the quartets via irradiated bias voltages.** The APDs are paired with a voltage limit of 100 mV. The quartets and octets are assigned by using the Mahalanobis distance. Hence, voltage constraints are applied on one of the three layers.

The maximum voltage difference changed from 38 V to 20 V when the pairings are created with a voltage limit of 100 mV and the octets and quartets by using the Mahalanobis distance. Hence, the results are again within the required voltage range of 50 V. It remains to be seen, how the distribution will be when all layers are assigned by using voltage values only (see fig. 163).

max voltage difference within the groupings:

Pairing assignment onstrictions: Voltage = < 0.1 V
quartet and octet assignments via irradiated bias voltage value only

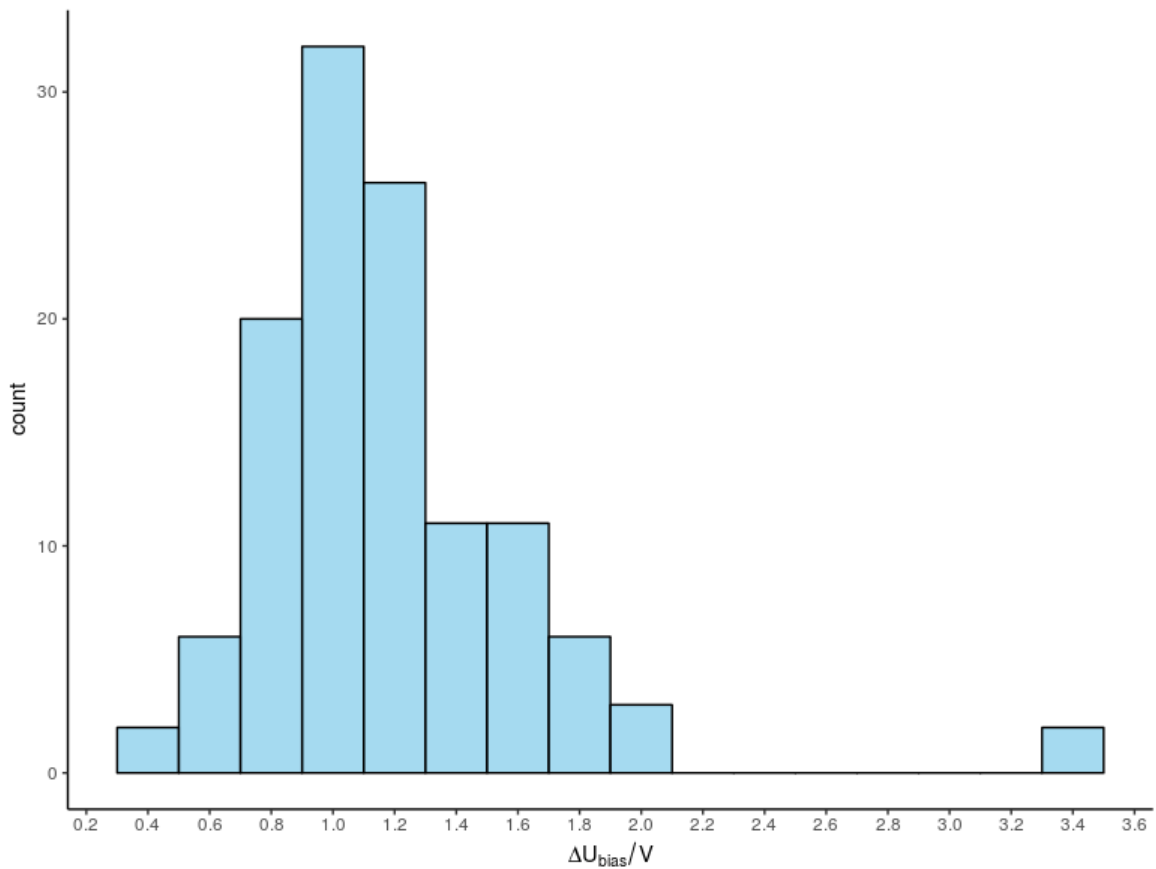


Figure 163: **Maximum voltage difference within the APD clusters via voltage assignment only.** The similarity between the APDs is calculated with the help of the Mahalanobis distance but combined with a voltage limit of 100 mV in the irradiated bias voltages. The octets and quartets are assigned by using only the bias voltage values.

At first, the APDs are paired via their Mahalanobis distances constrained but by using a voltage limit of 100 mV in the irradiated bias voltages and the quartets and octets are both assigned via their voltages only. Now, all HV backplanes need to provide only a voltage range of 5 V. This low voltage range would allow the DAC to regulate the voltages at a very high voltage resolution.

Note: The APDs of the first assignments, the pairings, can be glued at single crystals without taking into account information of the crystal geometries. This changes when the assignments are repeated for the second and third layer. In other words, when the pairings are partitioned into quarts and octets. Then, a special attention has to be paid to the crystal geometries because the HV backplanes supply the APDs in a local environment, thus, putting restrictions onto the crystals geometries in their vicinity.

7.6.3 Conclusion and outlook

Since two APDs will always be attached to a scintillation crystal, mainly in order to still be able to make measurements in the event of a failure, but also to reduce the NCE (see [Avalanche Photodiodes](#) on page 44), it is important to define this pair of 2 APDs in such a way that the APDs are as similar as possible. In order to determine how similar two APDs are, it must first be determined what similarity means in the sense of electronic components. It is specified that the operating parameters are located in a four-dimensional space, namely: Bias voltage and slope, both before and after irradiation of Co-60 with a dose of 30 Gy. These four parameters span a multivariate space in which the APDs are each represented by a specific position (see [fig. 103](#)). The spatial distance between the APDs embodies their similarity to each other. In order to be able to represent this quantitatively, special metrics or distance functions are normally used. For the first slice the similarities were calculated with an Euclidean distance. However, this distance is not suitable for multivariate spaces. In this context, the Mahalanobis distance is chosen as it can be used in multivariate spaces and it is independent of transformations (see [Metric](#) on page 102). It considers possible correlations between the parameters by using a covariance matrix. This metric can be used to identify outliers where the reference can be, for example, either the entire pool or the lots and it turned out that most of the APDs are not similar to each other (see [fig. 108](#)). When the reference is not the pool anymore but instead the lots, then the number of similar APDs even decreases from initially 600 being within 3 standard deviations to then only 471 being within 3 standard deviations.

The Mahalanobis distance can also be used to calculate the similarity between single APDs which is used and implemented for the assignment process. Though the distances do not refer to the pool mean, the parameter means are still utilized in the calculations. Hence, the distance between two APDs is subject to the currently observed population respectively sample size (see [Pool influence on the similarity measurement](#) on page 116). It is assumed that ever all currently available APDs are part of the pool which has to be partitioned into pairings and, therefore, this sample dependency matches the situation properly. Nevertheless, it would be preferable when all 22720 APDs of the EMC barrel could be grouped all at once but this is not possible due to manufacturing processes. For this reason, the APDs must be assigned in the way that is at a moment the most favorable. All calculated similarities will be stored in an adjacency matrix where the distances are now seen as edges with weights. In order to assign the APDs to each other, a proper method is necessary, which takes into account that the individual APD pairs are as identical as possible on the one hand, but on the other hand also takes into account that a maximum number of APDs are generally grouped together. This embodies a combinatorial optimization problem. For the assignment of the first slice a greedy algorithm was used which operates basically on a table where each entry, respectively an APD, will be assigned with the next entry that lies within the applied distance (see [Greedy algorithm](#) on page 107). A Greedy algorithm, as such, can only find local optima and, thus, it will produce in some situations a worse result or none at all. To overcome this, the Blossom V algorithm (see [Edmond's algorithm](#) on page 109) is implemented (see [Implementation](#) on page 110) which provides a perfect weighted minimum matching (see [Graph theory](#) on page 216). This means that all APDs are assigned to each other in such a way that each pairing is as similar as possible together with the surplus that all available APDs will be assigned. Hence, it will yield the global optimum of all matchings. But still, beyond that it is possible to modify the matching according to various restrictions. For example, the basic network (see [fig. 116](#)) represents a complete graph (see [fig. 257](#)) which provides all possible edges. By applying limits to the edges, it is possible to restrict the assignments and is done by equipping edges that exceed a certain threshold with an infinite weight. This changes the network and forces the Dijkstra algorithm, the search algorithm the Blossom V algorithm utilizes, to operate differently and to select the vertices and edges differently in its priority list. Applying thresholds will remove pairings which do not meet these constraints. Thus, it is possible to demand that the bias voltage difference within a pairing must not exceed 100 mV. How this, in return, affects the matching was analyzed in detail in regard to the irradiated bias voltages and slopes. Limiting the total distance was studied as well. The evaluation of a good matching is connected with its cost which is the sum of all weights between both APDs of all pairings. Since the cost decreases typically with the number of assigned APDs, another term is introduced to consider this: The adjusted cost of a matching $cost_{adj} = cost + k$, where k represents a penalty term for each APD that is removed from the matching due to the applied matching limits (see [Modified network](#) on page 123). Furthermore, the quality of the matching can also be measured due to its distribution.

To do so, the median is mainly used to deliver a value of the goodness of the matching together with the interquartile range.

Scanning several thresholds, it turns out that there is a distinct optimum for constraining the Mahalanobis distance at $d = 0.5$ (see fig. 129). At this limit, 42 pairings are removed from the matching which results in a better quality as consequence. The adjusted cost is 254.599 and the cost is 170.599. The matching is further evaluated by analyzing all its pairs. The median of all assignments of this matching is 0.393 ± 0.144 a.u. and the mean is 0.373 ± 0.098 in terms of an unitless similarity (see fig. 133). The drawback is the maximum voltage difference of a pairing of $\Delta 6$ V which does not meet the technical requirements of a maximum voltage difference of about 100 mV. The maximum difference of the irradiated slope values is $2 \cdot 10^{-5} (1/M) \cdot (dM/dV)$. When using only a single parameter to constrain the matching, like the irradiated bias voltage values, the similarities of the APDs will still be calculated by using the the Mahalanobis distance but only those within the specified limit will be assigned.

Limiting the irradiated slope provides only a weak optimum which is located at $7 \cdot 10^{-6} (1/M) \cdot (dM/dV)$. But there, nearly all APDs (499 pairings) get assigned. The adjusted cost is 358.088 and the cost 356.088. The maximum voltage difference of a pairing is $\Delta 10$ V which is also not usable for the EMC. The median of the matching is 0.652 ± 0.393 a.u. and the mean is 0.7136 ± 0.795 a.u. (see fig. 147).

The matching with constraints in the bias voltage provides an optimum at 800 mV which exceeds the requirement of $\max(\Delta V) = 0.1$ V, too. For this reason, this optimum is not further investigated. Since other optima are not available (see fig. 150), the aimed voltage threshold of 100 mV is investigated in detail. Restricting the voltage differences to 100 mV leads to a matching of 956 APDs with a median of 0.824 ± 0.85 a.u. and a mean of 1.08 ± 0.84 a.u (see fig. 155). The adjusted cost is 526.247 and the cost is 482.247. Though the irradiated bias voltage values are restricted by a threshold, the non-irradiated voltage values are not. For this reason, the width of the corresponding distribution is not 200 mV but 2.5 V. The matching obtained by the voltage limit of 100 mV uses only about 2600/495000 edges and its corresponding network is very sparse (see fig. 158).

The Greedy algorithm is briefly compared with the Blossom V algorithm via using the total distance as similarity measure (see Optimal distance threshold on page 134): The Greedy algorithm provides 422 APD pairings and the Blossom V algorithm provides 458 APD pairings. The adjusted costs are in case of the first 212.6 and in case of the latter 230.07.

Finally, the best matching is provided by putting a threshold of $d = 0.5$ on the absolute distance but since it does not meet the technical requirements of $\max V = 0.1$ V it cannot be used as a basis for the matching process. Though the corresponding matching is only one third as good as the optimal matching provided by the absolute Mahalanobis distance, it is necessary to simply constrict the assignments by demanding that the maximum voltage difference has to be lower than 100 mV.

After pairing the APDs, they will be glued at the rear of a crystal. The next step is to assign eight APDs such that their bias voltages match the voltage range of the backplane which is set to 50 V. This requires a multi-matching algorithm which has not yet been discovered up to this writing, therefore, a remedy is necessary. The idea is to perform a multi-layer assignment process (see fig. 160) by making use of the Blossom V algorithm again. The first layer will be the regular assignment described previously but in the second layer, a group of two APDs will be treated as one virtual APD by using the mean values of their respective operational parameters. Now, two such virtual APDs can be assigned to result in a grouping of four APDs. Repeating this step in the third layer will finally provide a cluster of eight assigned APDs. This assignment process can also be studied with respect to specified restrictions. Since it is now only a question of the voltage values of the APDs, so that they all fit to the circuit board, only this parameter is examined accordingly. Nevertheless: If the Mahalanobis distance is used as similarity measure in all layers, the largest voltage difference between two APDs of a group of 8 is 40 V (see fig. 161). Hence, this corresponds to the requirement of 50 V as voltage range but violates the condition of 100 mV as maximum deviation within a pair of 2 APDs. If the voltage deviation of the irradiated values is limited to 100 mV in the first layer and the Mahalanobis distance is still used in the other layers, this results in a maximum voltage difference of about 20 V within a group of eight (see fig. 162). This already fulfills all requirements, but the effect is also investigated, if also the second and third layer is limited solely according to irradiated voltage values. The maximum voltage difference within an 8-cluster is then only 5 V (see fig. 163).

When partitioning the APD pairs into clusters of 4 pairings to get connected to the same backplane, it has to

be kept in mind that the type of the crystals, where the APDs are glued at, determine the position inside the EMC and, therefore, also if these 4 pairings can be grouped together.

Up to now, most steps of the sequence (see 112) are divided in separated framework stages. For a better convenience in the future, the regression of the APDs, which is actually done in *R*, could be implemented in *C++* through an according API. The q-point of the APDs can also be determined directly via ROOT when the APD data is read in. This is already included but it should be verified that the regression in ROOT is adequate to *R*. Furthermore, the construction of a GUI might help on a daily basis due to the regular usage of the matching procedure.

Part 3

Light coupling for the monitoring system of the Electromagnetic calorimeter

„And these Pictures propagated by Motion along the fibers of the Optick Nerves into the Brain, are the cause of Vision.“

Sir Isaac Newton

Fiber coupling

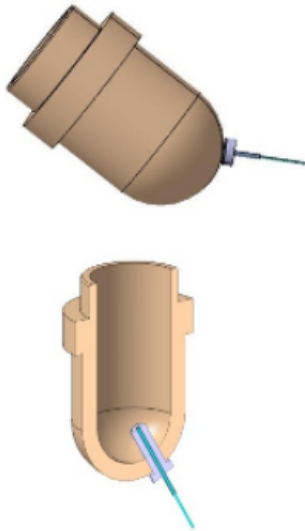


Figure 164: **Basic fiber coupling device.** A cap will be used to attach fibers to it to couple light into the crystal.

It was known that a **fiber coupling device** is needed to guide light from the light pulser into the scintillation crystals. The last beam time (see *Beam time with Proto120 in Main* on page 232) made this need obvious to investigate how best to couple light into a crystal. This study is guided by the fact that a fiber coupling is constrained by the limited bending radius of the fibers and the available space in general. This leads to a basic draft which is discussed in the following.

For the **measurements**, two light sources have been used: A light pulser constructed in Novosibirsk as well as a light pulser made in Bochum. The latter will be used in the experiment. The studied main parameters are the coupling angle and the coupling depth of the fiber. Reference value is the obtained amount of light reaching the photodetector.

In addition to experimental studies, the cap, the crystal and further components are simulated in *SLitrani* to gather results of methods how to optimize the coupling efficiency. Among several aspects, the light yield depends also on the geometry of the crystal as the tapered geometries of the $\bar{\text{P}}\text{ANDA}$ -crystals provide a non-uniform behaviour which has already been studied in case of γ 's [38, 148]. The following **simulation** extends present simulations by using light of a wavelength which will not generate electromagnetic showers in lead tungstate which is correctly treated as negative birefringent. For this reason, more popular frameworks like *Geant4* are not used because they are not able to treat such a material correctly.

The basic cap is made of PA⁷³-12 and is produced by Hasenauer & Hesser following a design made by IHEP⁷⁴ Protvino. It has a length of 22 mm and an inner radius of 5 mm (see). This enables a seamless transition (see fig. 165) at the crystal front. For this purpose, the front-inserts provide a hole with the same dimensions. Furthermore, the cap has a wider edging so it can be plugged in reproducibly and prevents the crystal from mechanical impacts when plugging and unplugging.

⁷³Polyamid

⁷⁴Institute for High Energy Physics



Figure 165: *Wrapped crystal without cap.*



Figure 166: *Wrapped crystal with cap.*

The fibers are inserted only from one direction (see fig. 167 and fig. 168) since the light pulser is located at the upstream side because on the downstream side no space is available. Not all crystals need to be provided with a cap as those in forward direction can be equipped directly with fibers (see fig. 168):

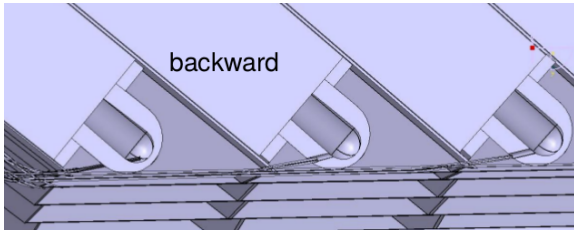


Figure 167: *Crystal types 7 to 1 in beam direction.* The first 7 submodules contain the types 7 to 1 which are orientated backwards with respect to the beam direction. These crystals require a cap to be equipped with fibers.

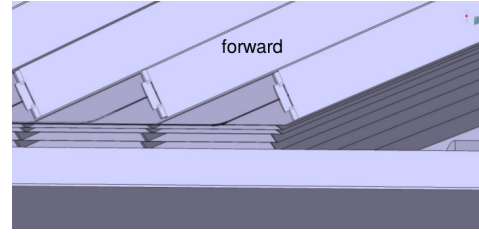


Figure 168: *Crystal types 1 to 11 in beam direction.* The submodules which contain crystals orientated along beam direction are aligned such that fibers can be attached to the crystals directly. Hence, these crystals do not require a cap.

Light propagation

Light can be described as solutions of the wave equations and as part of an electric field $\vec{E} = \text{Re}[\vec{E}_0 \exp(i(\omega t - \vec{k} \cdot \vec{x}))]$ and a magnetic field $\vec{B} = \text{Re}[\vec{B}_0 \exp(i(\omega t - \vec{k} \cdot \vec{x}))]$ [110]. In general, all optical properties are given by electromagnetic wave properties. Furthermore, light is polarized at any time but the corresponding condition changes in such short periods of time that it is rather impossible to predict a condition.

The speed of light in vacuum is given as $c = \varepsilon_0 \mu_0^{-1/2}$ with the electric field constant ε_0 and the magnetic field constant μ_0 . In a medium, the electric permittivity ε_r and the magnetic permeability μ_r will come into play too and result in $c_m = c/\varepsilon_r \mu_r^{-1/2}$. The ratio of both velocities represents the refractive index $n = c/c_m$ and can further be used to describe the absorption of a medium. For this purpose, the refraction index can be expressed as a complex number:

$$\vec{n} = n(1 - i\kappa) \quad (3.1)$$

The real part n represents the refraction whereas the imaginary part $i\kappa$ describes the absorption. Both together form the reflectivity:

$$R = \frac{(n-1)^2 + (n\kappa)^2}{(n+1)^2 + (n\kappa)^2} \quad (3.2)$$

This expression is known as the Beer formula [10]. In case of two media, where n_2 is absorbent, the reflectivity is:

$$R = \frac{(n_2 - n_1)^2 + (n_2\kappa)^2}{(n_2 + n_1)^2 + (n_2\kappa)^2} \quad (3.3)$$

Light with an initial intensity I_0 propagating through media can be expressed as the sum of all participating processes: $I_0 = I_R + I_A + I_S + I_T$. These parts are I_R for the reflective part $R = I_R/I_0$, I_A for the absorptive part $A = I_A/I_0$, I_S as the scattering part $S = I_S/I_0$ and I_T as the transmission part $T = I_T/I_0$. Neglecting absorption, it is then: $R + T = 1$. In general, when a photon reaches a boundary, it faces two different aspects: Reflection or transmission. Overall, the intensity of a light beam is given by the Poynting vector $S(x, y, z, t) = \text{Re}(E(x, y, z, t) \times \text{Re}(H(x, y, z, t)))$ with the magnetic field strength $\vec{H} = \vec{B}/\mu$. The intensity of light through a medium along x is determined by the Lambertian law $I = I_0 \exp(-\alpha x)$ with the absorption coefficient $\alpha = 4\pi\kappa/\lambda$. Together with the refraction index, these values are mainly given by the optical properties of a medium.

8 Experimental setup

The goal is to determine under which parameters most of the light can be coupled into the crystal. Main parameters are the **position** of the fiber end inside the cap and the **angle** under which the fiber is led in. To determine and to compare the measurements, the light yield is used which represents the amount of generated electric charge per detected light:

$$LY = \frac{P_C - P_{Ped}}{P_{SEP} - P_{Ped}} \cdot \frac{1}{E_\gamma} \left[\frac{phe^-}{MeV} \right] \quad (3.4)$$

The single photon peak P_{SEP} is determined at 83.6 ch, the pedestal peak value P_{Ped} at 57.2 ch and $E_{\gamma, Cs137}$ corresponds to 0.622 keV. P_C is the measured signal. The according gate length of the readout is 100 μ s respectively 140 μ s with a 40 μ s electronical delay. The signal threshold is set to 49 mV, the temperature to +18 $^\circ$ C and the crystals provide the classification 6R-3 and 6L-1 to represent an average geometry among all crystal types. Each measurement is preceded by 30 minutes for temperature stabilization by a climate chamber while the time of a single measurement is 5 min. In fig. 169. The readout setup concept and its components are shown in fig. 169:

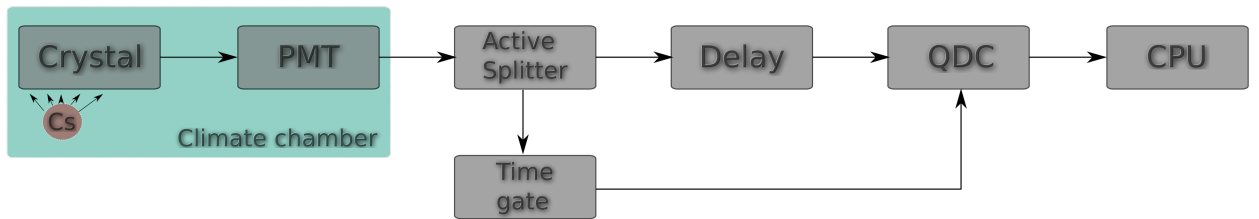


Figure 169: **Readout chain of the light yield setup.** The crystal and the photomultiplier are housed by a climate chamber to ensure a temperature of 18 $^\circ$ C.

The utilized main components are:

Component	Function	Description	Standard
CAEN 7805	CPU	Read out controller	VME
CAEN V775N	QDC	Charge-to-Digital converter	VME
Hamamatsu R2059	PMT	Photodetector	
PWO 6R-3	Crystal	Scintillation crystal	

Table 31: *Readout components of the light yield setup.*

8.1 Stability test

In the following, a radioactive source is used and placed on top of the crystal which is not equipped with a cap. Of first interest is to measure how long the setup needs to settle to achieve a thermal stabilization:

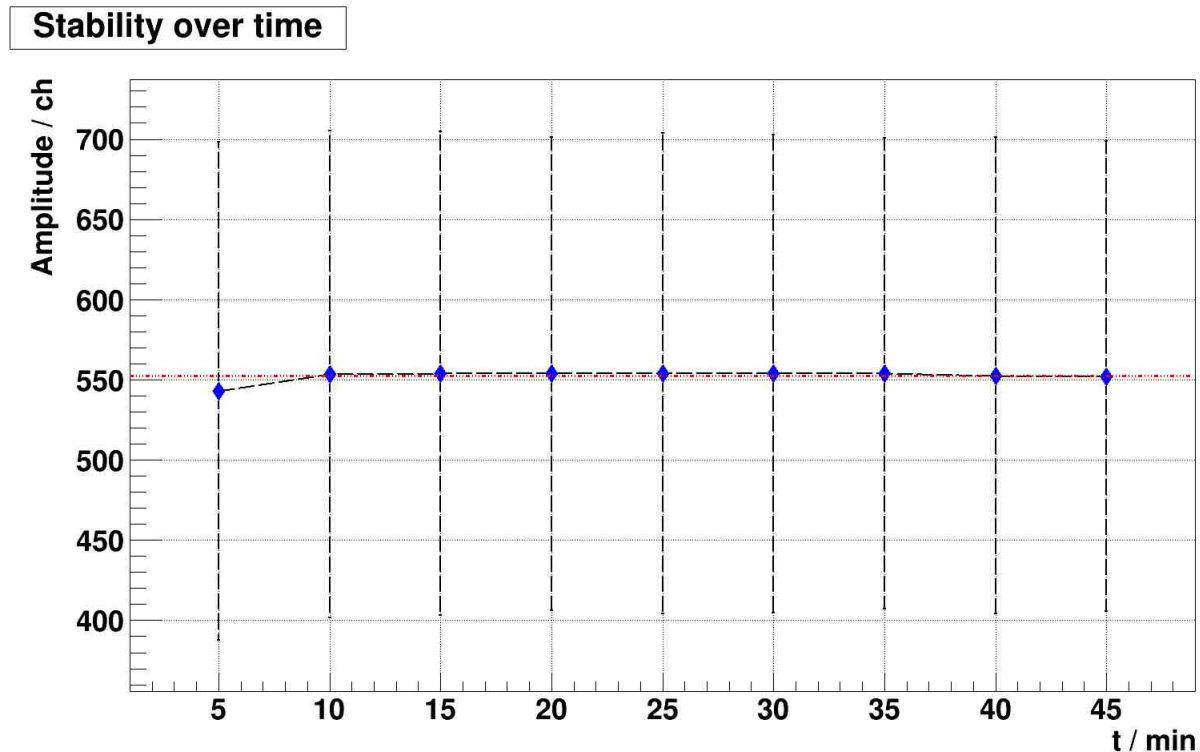


Figure 170: *Stability study over cooling time.* After ten minutes, the environment reached a thermal stabilization. The error bars represent the standard deviation from the corresponding signal. The mean is 552.3256 ch with a standard deviation of 3.509662 ch.

This measurement is done for 45 minutes and reveals that a cooling time of ten minutes is sufficient. Nevertheless, for safety reasons, a cooling time of 30 minutes is chosen for all subsequent measurements. Another aspect is to ensure the repeatability of the measurements in regard to assembling and disassembling: Each measurement is done by reattaching and sticking the crystal to the PMT afterwards:

Repeat study

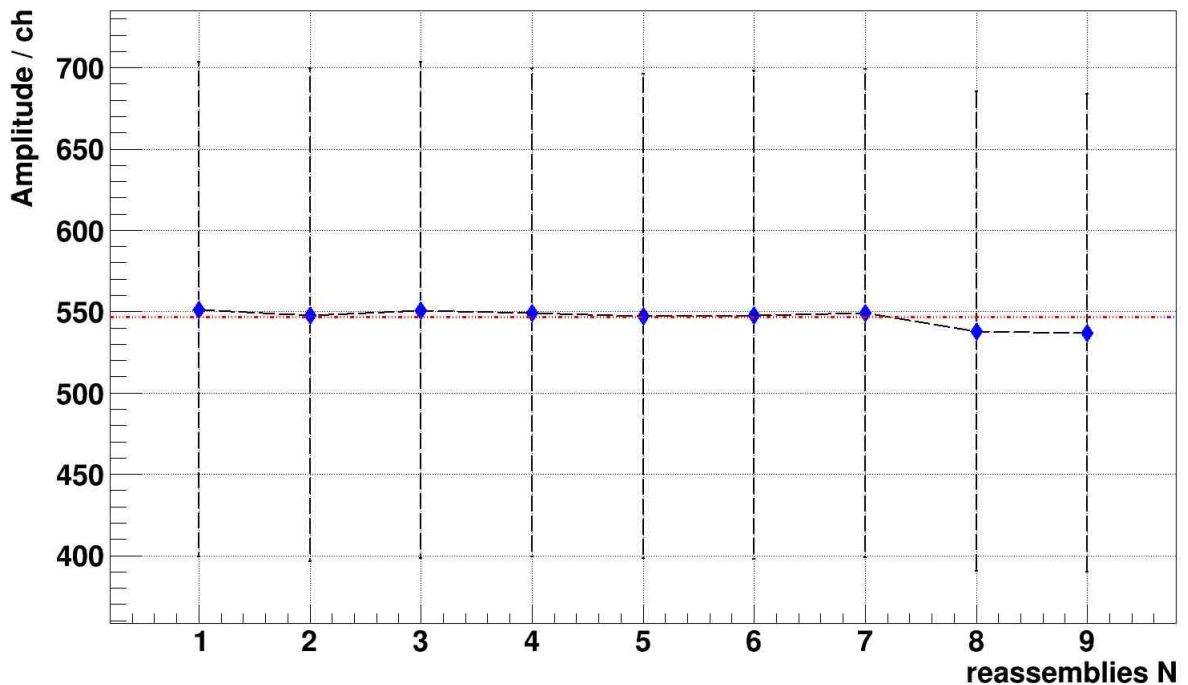


Figure 171: *Repeatability study*. The components are completely assembled and dismantled several times. The variations in each setup routine are quite small. The mean is at 546.45 ch with a standard deviation of 5.373986 ch.

When building up the experiment at the eighth time, something changes but the measured amplitude differs only with about ~ 10 channels which is twice the standard deviation of the average signal while the standard deviation of the measured signal itself corresponds to about 150 channels. Hence, the measurements are assumed to be stable against repetitions.

8.2 Material analysis for coating

Since the cap is solely made of PA-12, coatings will be considered to increase its reflectivity. The targeted coating material is **barium sulfate** because it serves as a quasi-standard with respect to reflectivity materials. However, the reflectivities of some other materials are studied as well. To obtain a reference, the light yield without a cap but with reflector foil inside the opening of the front insert is measured, too. Next, a basic cap is used without any coating or painting, respectively. Since barium sulfate is assumed to be the material with the highest diffused reflectivity and set as a reference for such purposes [72], the way of application is also examined. Barium sulfate is an emulsion paint, hence, it can be mixed with paint to increase its durability but this would result in a lower reflectivity. Finally, it is sprayed, brushed and plunged but it can be easily rubbed off by accident. Thus, to exclude human errors, both barium sulfate and aluminum are applied to the cap by an external company. For each method, a separate cap is used and all studies are performed with two crystals: 6R-3 and 6L-1 (see fig. 172). These are chosen to represent the geometric average of all crystal types. Each measurement is done twice: Once with the source taped at the top of the crystal and once with the source taped at the bottom. Each time the source is fixed such that the edge of the source matches with the upper or lower edge of the crystal. The measurement period is 300 s and the temperature is set to 18 °C.

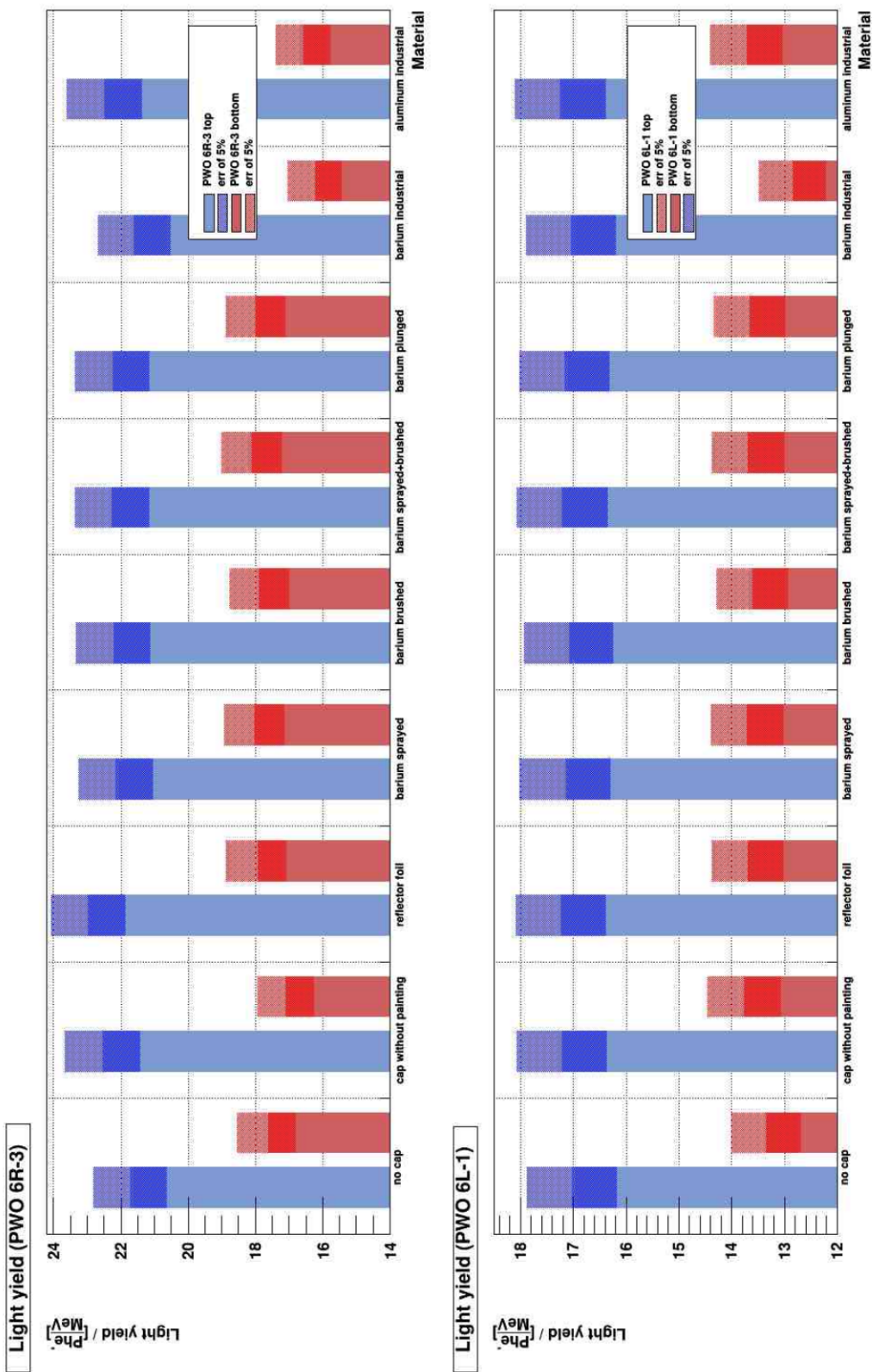


Figure 172: *Comparison of overall light yield for various materials and coatings.* Light source is a radioactive source, Cs-137, attached to the crystal. Each time at the top and again at the bottom. The reflector foil serves as a reference and, in general, a measurement uncertainty of 5 % is assumed and validated (see fig. 170).

The measurements show that there is not a strong difference by changing the coating nor by the way to apply it. This might be connected to the circumstance that a high amount of the generated light is not leaving the crystal at the top side. To ensure that the barium sulfate does not change under the influence of irradiation, two caps are irradiated with 30 Gy of a Co-source at the Strahlenzentrum Giessen (see fig. 173). The irradiation changes the LY of the caps which are sprayed with barium sulfate, or sprayed and brushed to enhance the covering quality (see fig. 173). However, all changes are small and within an uncertainty of 5 %.

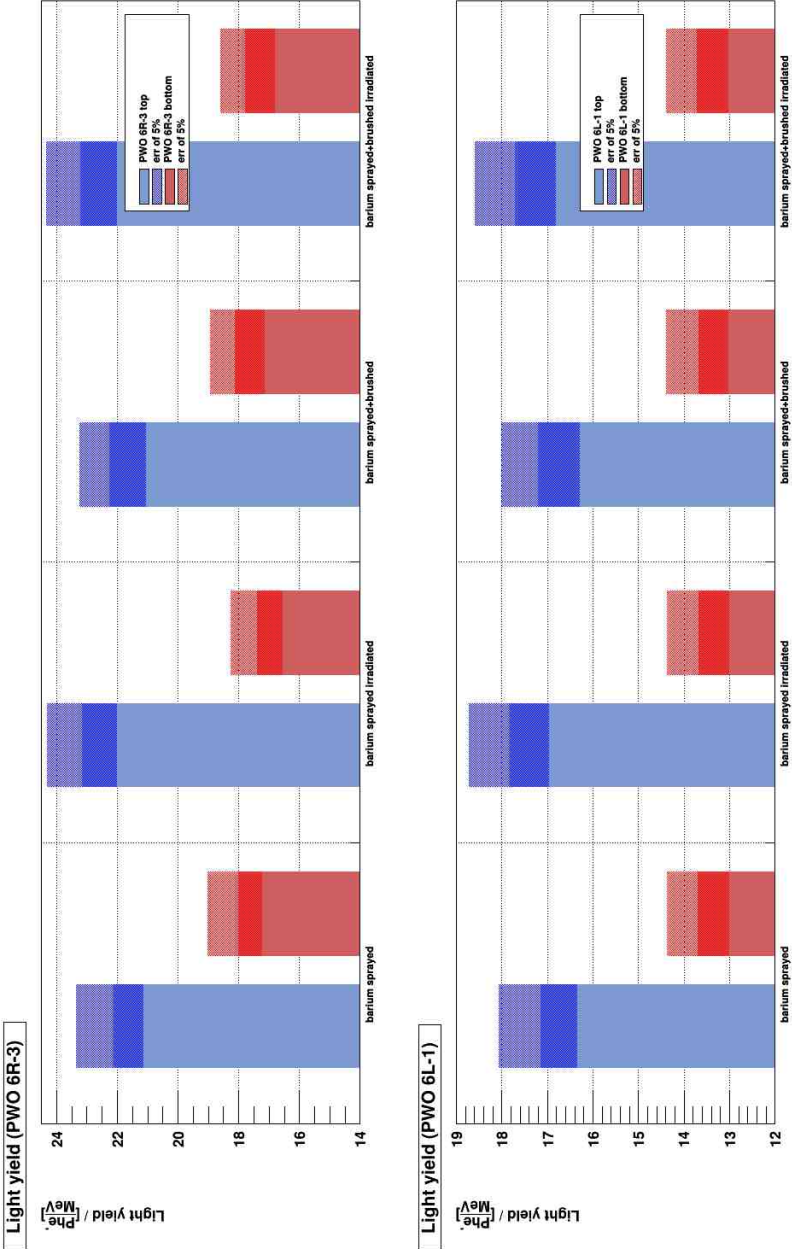


Figure 173: **Influence of irradiation on light yield for several application methods.** The caps were irradiated with 30 Gy and measured before and afterwards. The way how to apply it was studied, too.

Up to here, only the LY is measured and in the following the amount of transmitted light will be studied. Therefore, the setup changes slightly as the radioactive source is exchanged with a light pulser.

8.3 Position study

The analysis of the positioning of the **fiber** is done with the Novosibirsk light pulser system (see fig. 174) and a fiber, CeramOptec UV 200/220, guiding the light from the light pulser into the crystal. The length of the fiber is exactly 2 m. The technical properties remain unchanged with a cooling time of 30 minutes and a measurement time of 5 minutes.

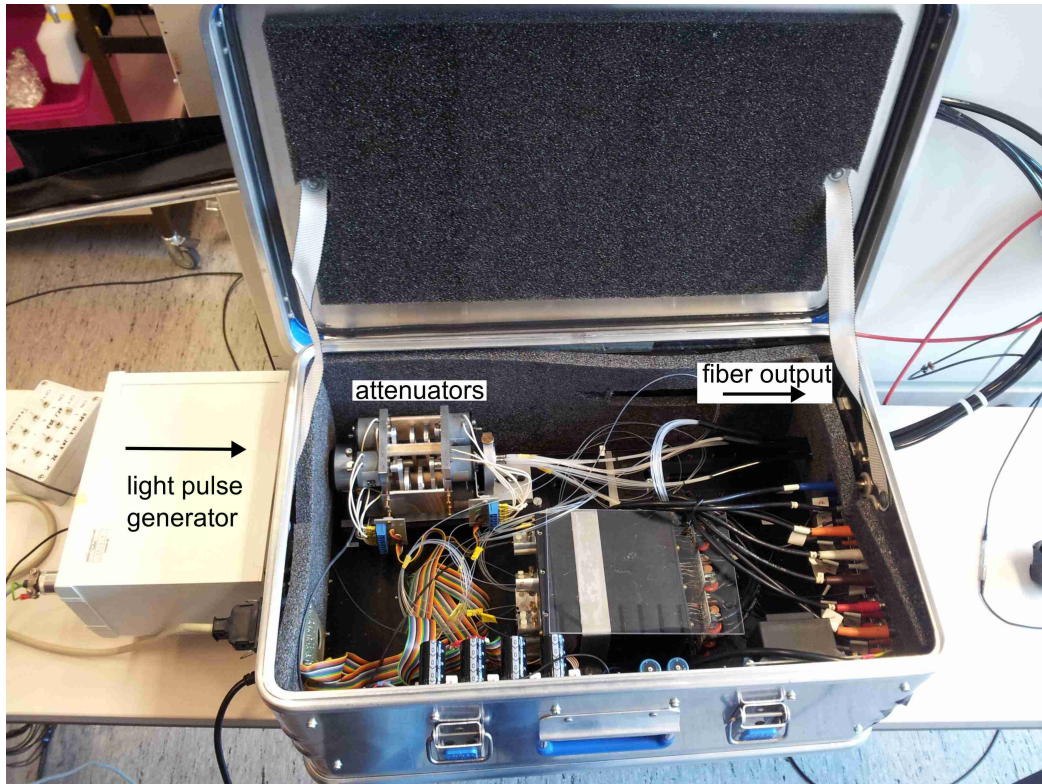


Figure 174: *Novosibirsk light pulser system [104]*. The attenuation filters can be swapped in and out mechanically by demand.

It is difficult to determine a proper coupling depth because the corresponding readout signal is either in the saturation region of the PMT or below its minimum amplification factor due to the limited dynamic range of the readout system and the large variation of the coupling efficiency. Therefore, calibrated in-built light attenuators are necessary for the efficiency evaluation of all coupling scenarios. Each of these attenuators can be put in and out of the light beam to allow combinations of the filters. The filter system contains 8 filters in total, each with a different attenuation (see fig. 175). For each measurement, the filters are chosen such that the light pulser signal can be measured in the dynamic range of the readout system. This means, a full Gaussian peak can always be recorded. The threshold of the readout system is set to 52 mV. All filters are measured with a coupling depth of the fiber of 5 mm which is attached to the cap at the top. The high voltage of the PMT is set to 1.822 kV and the current to 1.502 mA and each measurement is done for 10 min. Since the filters provide different attenuations, it is not possible to determine all filters using the same device parameters. Thus, for the filters 2 and 3 it is necessary to change the high voltage: In case of filter 3 it is 2.173 kV at 1.796 mA which makes it possible to receive a signal of the filter 4 and filter 3 under the same conditions. Finally, filter 4 can be used as a reference for filter 3. Same applies to filter 2 and 3, both at a high voltage of 2.395 kV and 1.996 mA.

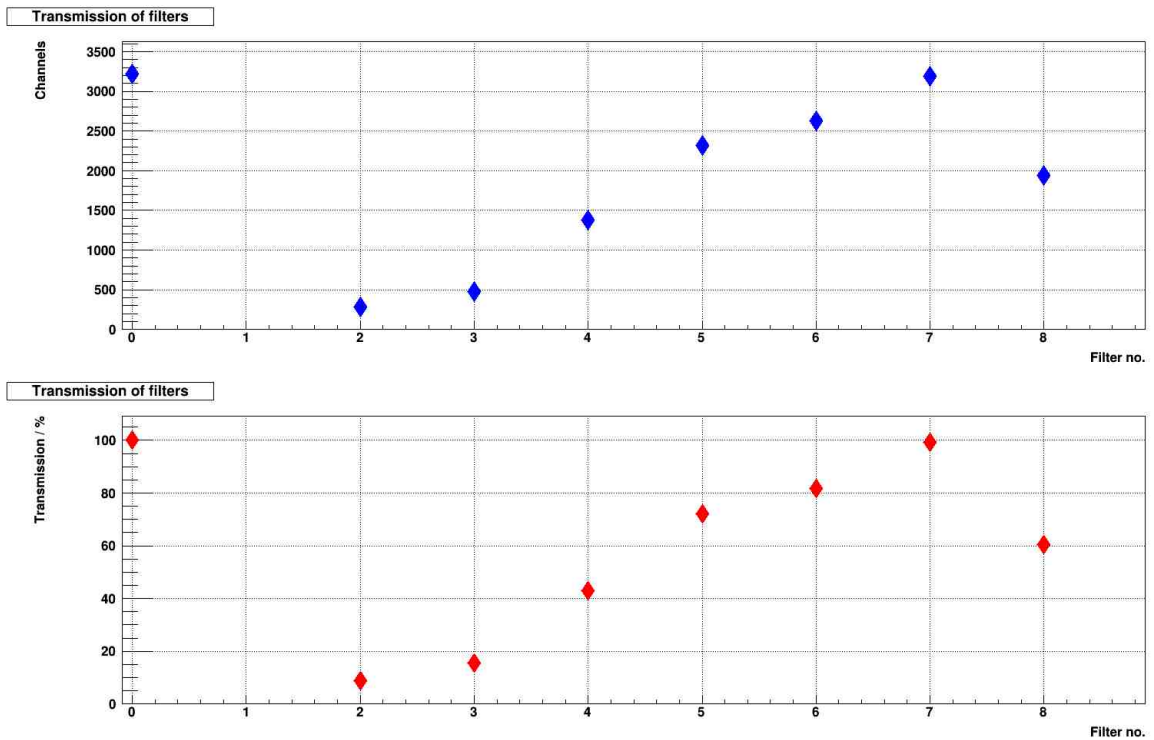


Figure 175: *Transmission of the filters of the Novosibirsk light pulser system.* Filter 1 does not yield any measurable transmission.

8.4 Energy injection at various positions

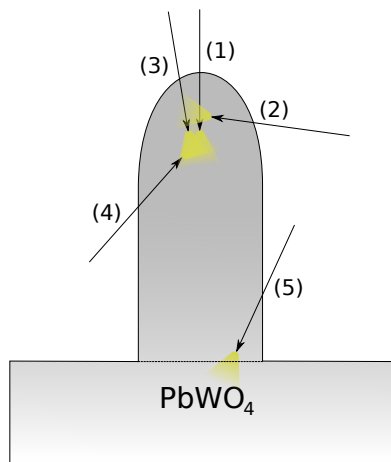


Figure 176: *Cap-fiber coupling.* Five positions/angles were chosen to be studied in detail: 1) 2° 2) 80° 3) 15° 4) 112° 5) 40°, relative to the perpendicular.

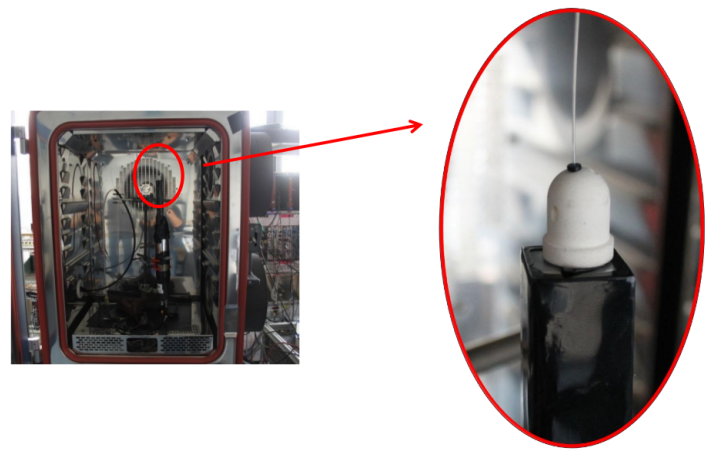


Figure 177: *Lab setup [104].* The cap is attached on top of the crystal. Fibers are fixed to the cap with the help of adhesive tapes at specific positions to ensure a fixed coupling depth.

To study the cap, several drillings are made into the cap to provide several coupling possibilities with different angles to emulate some “best” and “worst” angles of the fiber (see fig. 176) inside the slice later (see fig. 30). The cap is attached to the front side of the crystal with a fiber guided through one of the drillings and fixed at certain coupling depths (see fig. 177). Drilling position (1) is used as a reference since it points straight towards the crystal. Position (3) is a variation of that, (2) and (4) are considered as one of the least efficient angles and (5) is assumed to be the most efficient one.

The fiber is attached to the cap such that it reaches 8 mm or 12 mm into the cap. The length is given from the tip (see the black insert in fig. 178) to the end point of the fiber. The tip has a length of 5 mm so the fiber reaches finally 3 and 7 mm outside of the tip into the cap. In the following, the coupling depth is always given without considering the tip length, thus, only providing the absolute depth inside the cap. The results show that differences in the obtained light yield are present as expected. A strong angle and distance dependency is clearly visible and leads to differences in light injection up to a factor two in comparison:

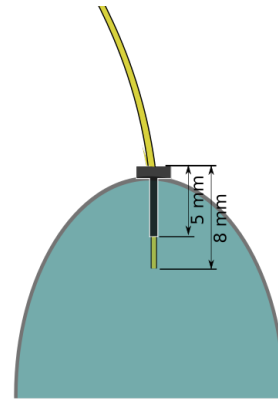


Figure 178: *Tip insertion.* The fiber is inserted into the cap with a tip which fixes the fiber. To enhance this, a glueing stripe is attached to the fiber at a specific point.

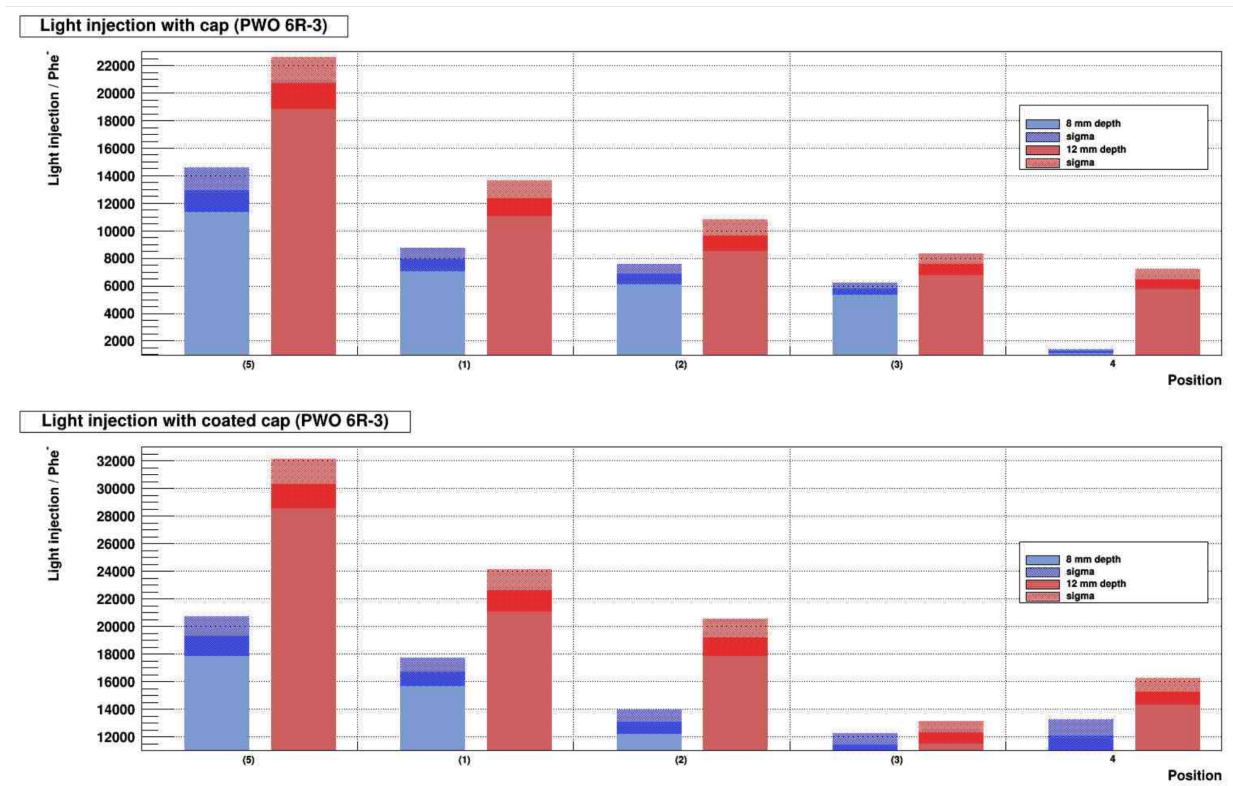


Figure 179: *Light injection dependency on position and angle of the fiber entry.* The intensity of detected light depends strongly on the coupling angle.

At first, the coating influence is studied and the light injections show significant differences: Due to the various coupling depths, the variations between the regular cap and a coated cap are about $10,000 \text{ phe}^-$ in case of the positions (5), (1), (2) and (4) and about $6,000 \text{ phe}^-$ in case of (3). Therefore, appropriate filters are required to use (see **Experimental settings** on page 248). A fiber directly attached to the crystal results in a light yield of 229823.15 phe^- . There, three filters (2 + 3 + 4) are necessary to obtain a measurable signal. Hence, using a fiber at a total distance of about 15 mm away from the crystal decreases the light intensity of a factor of about 10. Finally, the maximum observed signal by using the cap is about 10.5 % at the positions and distances given in fig. 179.

8.5 Absolute light yield

Since the previously utilized Novosibirsk light pulser system will not be used in the experiment later on, a reference study is done at position (1) with the **Bochum light pulser**. It is a system of a module which consists of a LED driver together with four LEDs, a LCD attenuator and its driver together plus a microcontroller board which houses all the electronic components [26]. In addition, a light mixer is also included. The LED has a power of 425 mW and the DAC for the LCD transmission is set to 0 V.

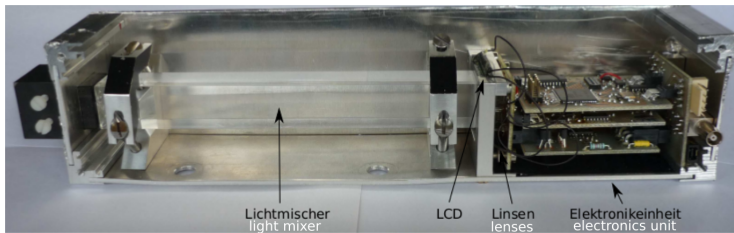


Figure 180: **Bochum light pulser**. The light pulser consists of the LEDs, LCD attenuator, the drivers, lenses and a light mixer [26].

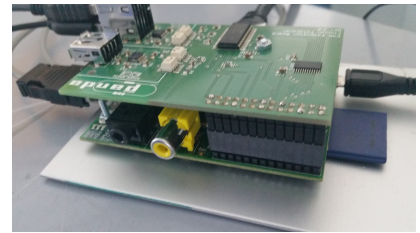


Figure 181: **Driver**. The control unit of the light pulser.

The system is designed such that the emission signal is similar to PbWO_4 . The decay time of the light pulser signal is 15 ns [26]:

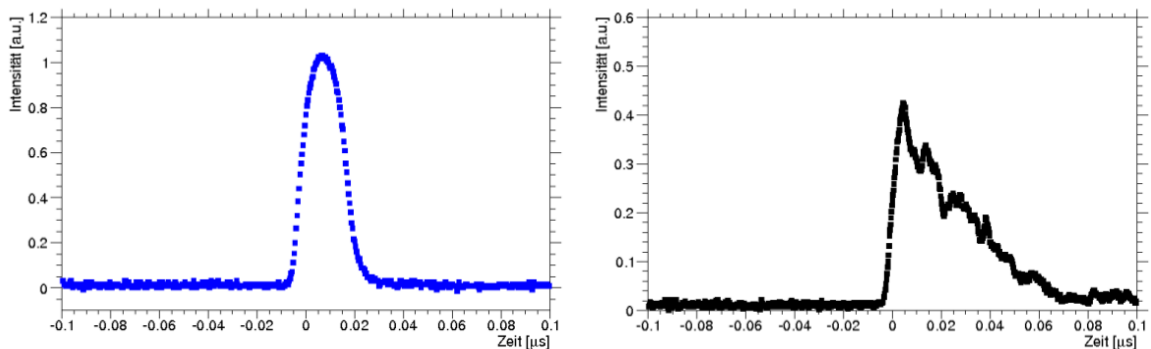


Figure 182: **Shape of the light pulse of the Bochum light pulser** [26]. Light pulse of the blue LED (left) and light pulse of PbWO_4 at $-25 \text{ }^\circ\text{C}$ (right).

The voltage of the light pulser is set to 675 V because below 650 V no pulse will be generated and the upper limit of 700 V is given by the voltage-proofness of the used transistors of the LED driver. The chosen operational parameters are:

Voltage:	0.675 kV
Current:	0.224 mA
Frequency:	15 Hz
Measure time:	5 min
Additional filters:	0.12 % + 0.03 %

Table 32: **Light pulser specifications.** A specific and stable high voltage is the most important parameter together with appropriate filters.

Two filters with a transmission of 12 % and 3 % are used to enable a measurement of the signal with the utilized readout. Subsequently, a calibration is performed by utilizing several radioactive sources.

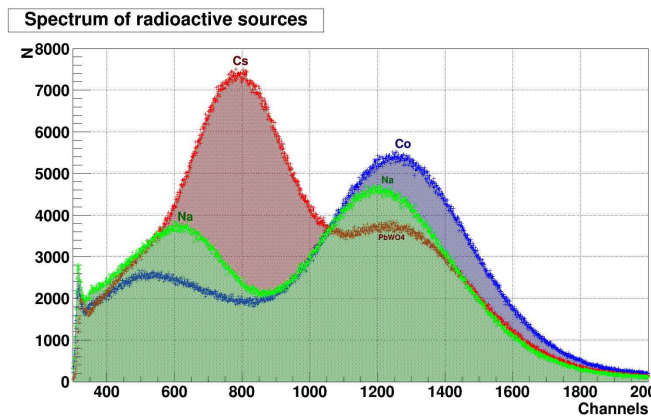


Figure 183: **Spectrum of radioactive sources.** The second peak of Caesium is attributed to an intrinsic emission of lead tungstate. All signals are measured at 18° C.

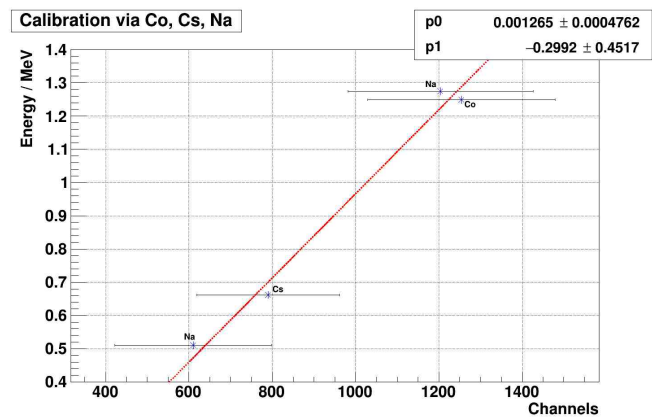


Figure 184: **Calibration with known γ -emissions of radioactive sources.** The calibration slope is 0.001255 MeV/ch.

The next task is to obtain comparative values of the absolute injected energy. According measurements are taken by shifting the fiber along the height perpendicularly in mm steps above the crystal (see fig. 185). The injected energy changes quite linearly with the height of the fiber. At the most distant position it provides a minimum of about 650 MeV and reaches a maximum of about 1050 MeV close to the crystal.

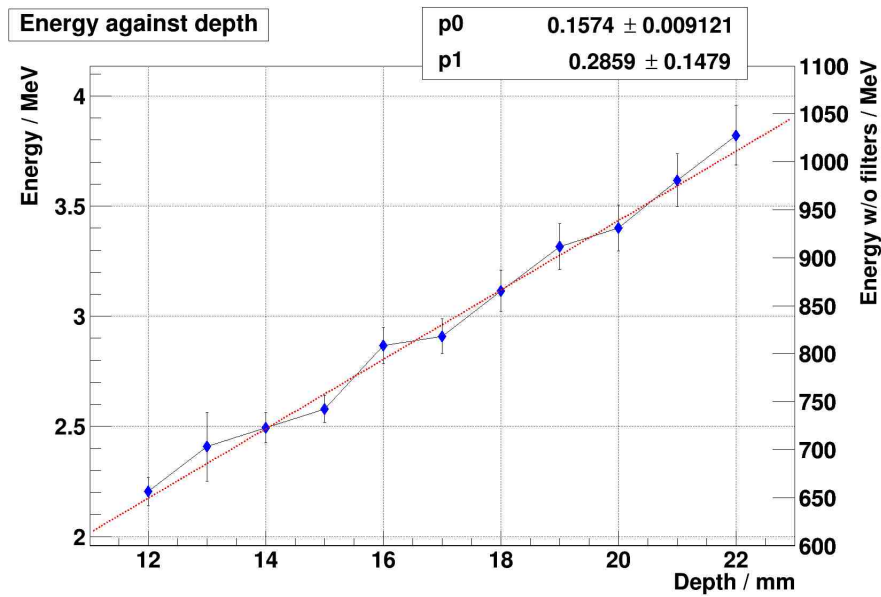


Figure 185: *Energy injection dependency of the coupling depth.* The injected energy changes with the coupling depth along the height of the fiber placed above the crystal. The detected energy varies in the magnitude of about 650 MeV without using the transmission filters.

8.6 Polishing dependency

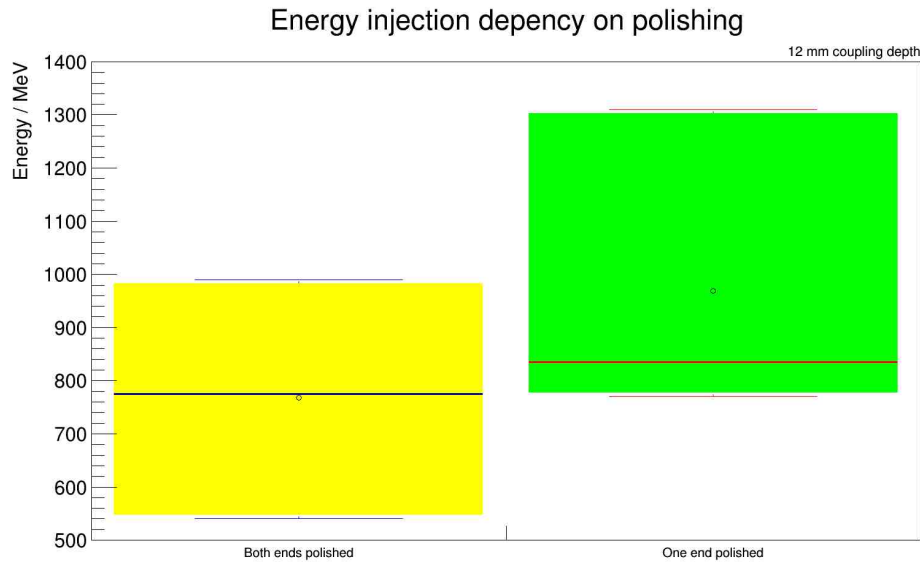


Figure 186: *Influence of polishing the fiber end.* Boxplots of the dependency of polishing with regard to the light injection. The colored lines represent the median and the dots represent the mean value. The fibers with only one side polished are arranged in such a way that the polished side corresponds to the collecting fiber end at the light pulser.

Besides the coupling depth and the angle, the amount of injected light has also to be related to the polishing of the fiber end. To study this, in total six fibers were prepared while three were only polished at one end and the other three at both ends. Polishing is done with a MD Fuga Remarks 800 polishing disc at a polishing machine for about 5 min each time for each fiber. All fibers have a length of 2 m and are severed with a cutter. The fibers are placed exactly with a depth of 12 mm above the crystal and point straight towards the crystal's front face. The results show that polishing affects the amount of injected amount of light (see fig. 186). While polishing both ends reduces the absolute injected energy, it seems to decrease its standard deviation in parallel. However, a sample size of six fibers is probably too small to be able to make a binding statement about the quantitative influence of polishing. Finally, one out of six fibers provides a greater light emission in comparison to the other five fibers.

9 Simulation & Implementation

9.1 SLitrani

SLitrani is a **light simulation software** written in C++ by François-Xavier Gentit and is based on CERN ROOT. The development of it has stopped, but the CCC⁷⁵ is hosting its source code [36]. SLitrani⁷⁶ is a further development of Litrani⁷⁷ and makes use of the *TGeo* class of ROOT which was developed within the CERN ALICE experiment. This means volumes are created by ROOT and linked with optical properties by SLitrani. SLitrani provides a built-in library of optical properties for several materials. Nevertheless, an important aspect of using SLitrani is to use the exact optical properties of each used material and also to set up the surfaces, boundaries and transitions properly within SLitrani. This software has been chosen because it is able to manage anisotropic and birefringent materials like PbWO₄.

SLitrani uses the Monte Carlo method to estimate the propagation of light. Thus, it is not based on deterministic calculations but on probability distributions like Gaussian and log normal. Hence, it delivers approximative solutions. Each Monte Carlo simulation is calculated by using a different, randomly generated set of initial parameters which follows specific probability distributions. Such a set is called a sample from here on.

SLitrani requires the input of parameters like the geometry dimensions, cross sections of processes, light yield, emission spectra and decay time of scintillators as well as further optical properties like roughness and diffusion lengths. Another important parameter is the quantum efficiency of the implemented detector. Then, the simulation can yield quantities like the energy deposit, the number of successfully generated photons, their propagation as well as their detection.

9.2 Birefringence

PbWO₄ is correctly treated in SLitrani as **negative birefringent**. The physics of SLitrani are based on the Feynman lectures Vol. II. To transition these fundamentals into SLitrani to consider lead tungstate correctly, the dielectric constant ε is treated as a symmetric tensor while the magnetic permeability μ is not [52]. A birefringent crystal differs from regular crystals in such a way that it separates impinging light into two partial rays. A description of the dielectric constant in anisotropic media requires the use of a tensor. The spatial components of such a tensor can be connected to the according wave velocities by $c/\sqrt{\varepsilon_i} = v_i$ and represent the main light speed inside the crystal [4]. If two of these components are equal to each other, then such a crystal is called uniaxial. The axis, for which these two speeds coincide, is called the optical axis.

Light whose polarization is perpendicular to the optical axis is called the ordinary beam o . Light with a polarization in direction of the optical axis is called the extraordinary beam e (see fig. 187). Both are linearly polarized and the ordinary beam follows Snellius' Law but the extraordinary beam does not. Additionally, as opposed to isotropic media, the angle of reflection is not the same as the incident angle. Two different refractive indices, n_o in case of the ordinary beam and n_e in case of the extraordinary beam, are responsible for that, a special feature of anisotropic media. The difference $\Delta n = n_e - n_o$ is a measure of the birefringence.

⁷⁵Crystal Clear Collaboration

⁷⁶Super Light TRansmission in ANIsotropic media

⁷⁷Light TRansmission in ANIsotropic media

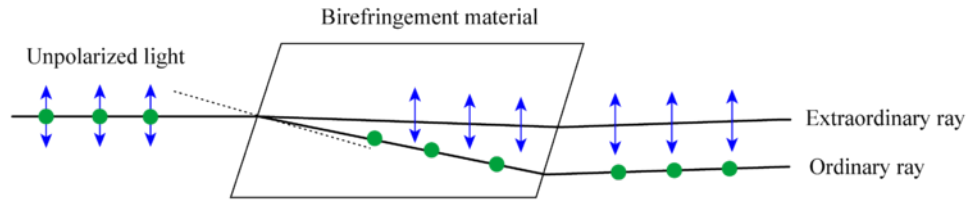


Figure 187: **Birefringence** [169]. Birefringent material will produce two different rays out of one impinging ray: An extraordinary e and an ordinary ray o .

The sign of this difference makes an anisotropic media positive or negative birefringent. A negative sign indicates that e moves away from the optical axis and vice versa [144]. The refractive indices of PbWO_4 can be found in [6].

9.3 Geometrical and optical parameters of the components

Some components of the simulation provide specific optical properties. In principle, SLitrani has these already implemented but the interactions among each other have to be specified clearly. SLitrani distinguishes two material definitions: An optical medium or a wrapping. A medium is treated as a volume which can be passed by photons. A wrapping or revetment is characterized by its reflection properties. Both media can be assigned to a TLitMedium constructor but when connecting both, SLitrani creates a thin slice automatically in between. These aspects are very important to obtain reasonable physical properties and processes.

In general, **fibers** are resonators with open end faces. This allows stationary waves as well as continuous waves. Since the benefit of fibers is to transmit waves along the core, these have to be reflected at the cladding via total reflection. Core and cladding require a different refractive index such that $n_{cladding} < n_{core}$ is fulfilled together with an angle of refraction larger than 90° . Hence, the law of Snellius $\sin \phi_1 n_{core} = \sin \phi_2 n_{cladding}$ changes to $\phi_c = \arcsin(n_2/n_1)$ and contains the critical angle ϕ_c which represents the minimum angle under which total reflection is possible.

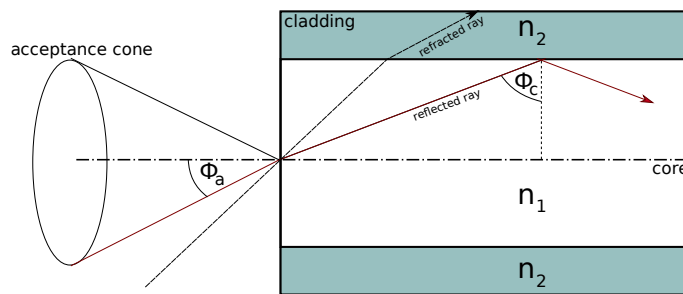


Figure 188: **Scheme of ray propagation inside a fiber**. The acceptance angle is connected to the numerical aperture of a fiber. Once entered, the light inside the fibre will follow a zigzag path.

In contrast, the maximum light entrance angle is called the acceptance angle ϕ_a . Utilizing Snellius' law again yields $n_0 \sin \phi_a = \sqrt{n_1^2 - n_2^2}$. The square root term represents the numerical aperture NA . Assuming air to be the surrounding medium, NA equals to $\sin \phi_a$. Rays entering the fiber within the acceptance cone will be guided without losses only if the reflected waves overlap constructively. Such a beam is called a mode.

In the simulation, the fiber is set as a source of photons with the help of the *SetEmission* constructor. The emission type is given as *sinuscosinus* which represents a non-isotropic distribution following $\sin \theta \cdot \cos \theta \cdot \delta \vartheta \cdot \delta \Phi$. The angle θ limits the upper angle by using the parameter t_{\max} while the emission has a slight favouring along forward direction. t_{\max} can be achieved by using the numerical aperture NA because it corresponds to the half of the opening angle $\sin(\alpha)$. For this reason, it is:

$$\alpha = \arcsin(NA/n) = \arcsin(0.28) = 16.2^\circ \quad (3.5)$$

with $n = 1.0003$ as the refractive index of the surrounding air. This results in $t_{\max} = 2 \cdot \alpha = 32.4 \approx 35^\circ$. The source of photons itself is generated somewhere inside the fiber with its edges as constraints. Hence, the photons are not emitted directly at the face of the fiber and because of that, there is a probability that photons do not leave the fiber. The beam of photons itself is located with the *TLitSpontan* constructor.

The **cap** is made of polyamide and coated with barium sulfate. Since SLitrani does not provide the possibility to set a coating, the cap is implemented as made solely out of barium sulfate. Therefore, the coating is treated as a revetment because photons must not be able to travel in it but to be reflected or absorbed. The diffusion angle is set to 90° . SLitrani simulates diffusion by absorbing the photon and re-emitting it with identical properties but at a different k-vector.

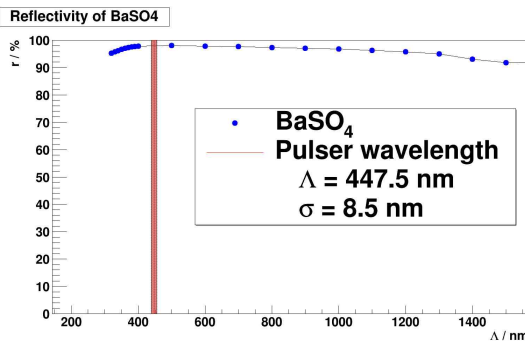


Figure 189: **Reflectivity of barium sulfate** [119]. Barium sulfate is highly reflective, especially in the wavelength range from 400 nm to 800 nm.

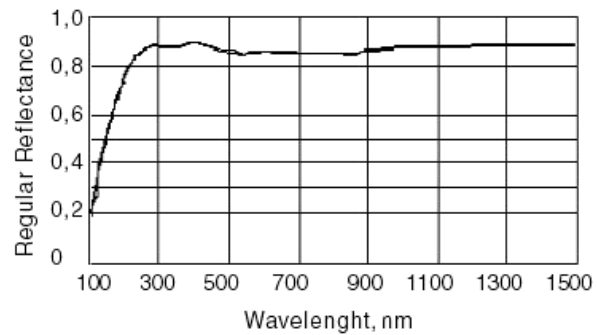


Figure 190: **Reflectivity of aluminum** [37]. Aluminum is highly reflective, too, and provides a similar reflectivity property as barium sulfate.

The necessary optical properties of barium sulfate, like the real and complex refractive indices, are partly unknown, thus, those of aluminum are chosen because it provides a similar reflection behaviour as barium sulfate and it is already implemented properly in SLitrani.

The **wrapping** of the crystal is made of DF2000MA, also known as VM2000. Like the cap, it is also set as a wrapping by the call *SetAsWrapping* and is supported naturally by SLitrani. In addition, it is set as isotropic by the call *IsIsotropic*. Between the wrapping and the crystal, there is a very thin layer of air. It is the *world medium* and allows total reflections.

The **crystal** is designed as a type 6 crystal in left orientation. The mounting of the crystals inside the slice is foreseen such that the long side of the APDs is orientated in beam direction. Hence, the running parameters of the simulation are only considered in a two dimensional space as the fiber will only move or rotate with respect to the beam direction. Furthermore, since the light pulser's wavelength of 447 nm and the excitation wavelength of $PbWO_4$ of 350 nm do not match, the possibility to create electromagnetic showers is neglected by not making use of the *TLitCascade* class. $PbWO_4$ is strongly anisotropic and induces a negative birefringence and is implemented with the call *IsUniAxialNegBirefr*.

The **APDs** are always located at the same place of the backside by arranging them with respect to the right angles of the crystals (see). They are treated as APDs by using the *TLit_Detector* constructor. In general, the components are positioned in xyz by the translation constructor *TGeoTranslation* and rotated by the Euler

angles ϕ , θ , Ψ through the rotation constructor *TGeoRotation*. The angle ϕ is the rotation around the z-axis and applied first. Next, the angle θ is the rotation about around new y-axis. Afterwards, the angle Ψ is applied with respect to the new axis z. The APDs have a thin slice which represents an entrance window. Between an APD and the crystal there is another slice which consists of the glue Dow Corning 3145. The gain profile of the APD is taken from the CMS APD as it is the same architecture. The running parameters, mainly the rotation angle of the fiber, are obtained by calling *MoveCradle*. It is the last stage in the simulation routine behind the geometry setup. In fig. 191 - fig. 194, some raytracing images are representing various beam paths:

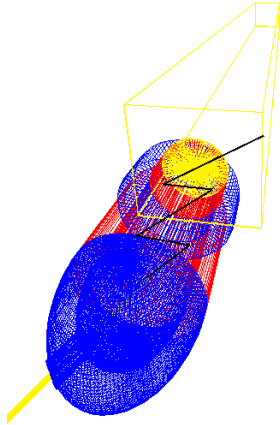


Figure 191: **Reflections within the cap.** The ray is entering the crystal and absorbed by the wrapping.

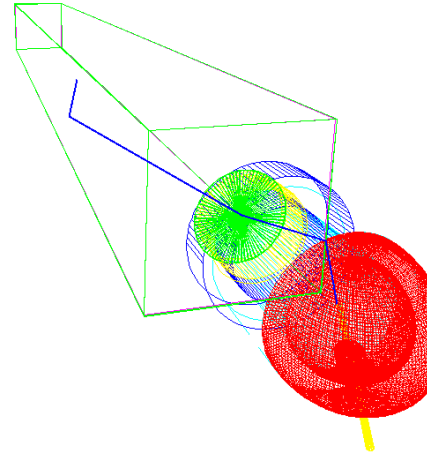


Figure 192: **Absorbed beam.** The ray is entering the crystal almost directly but absorbed already after the first reflection of the wrapping.

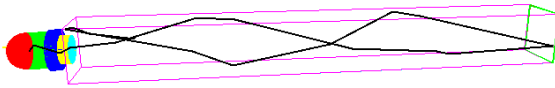


Figure 193: **Backscattering of the beam.** The beam did not hit one of the APDs and thus is scattered backwards and absorbed at the front face of the crystal.

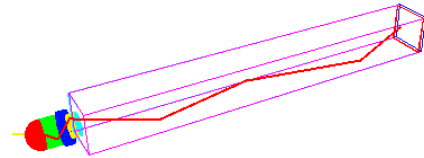


Figure 194: **Successful trajectory.** The ray is reflected within the cap, entering the crystal and reached the APD after several reflections at the wrapping.

9.4 Results

The difficulty is a proper description of each component in SLitrani. Hence, it is possible that the simulated results may vary from real measured values due to some conditions like fingerprints on some surfaces or when a wrapping is so tight that the slice of air in between the wrapping and the crystal disappears somewhere. Influences like these are able to have a high impact on the results. Nevertheless, SLitrani offers insight results which may lead to experimental measurements to understand unknown processes as CMS was able to understand the inhomogeneity of the light yield by varying the light emission along the crystal axis [50].

The simulations are done with the following specifications:

SLitrani	1.4
ROOT	5 – 34 – 00
OS	Ubuntu 16.04 LTS / 64 bit
CPU	Intel Core i5 – 6200U @ 2.4 GHz x 4
RAM	8 GB DDR ₃
GPU	Intel HD Graphics 520 Skylake GT2
	GeForce 940M

Table 33: **Computer specifications.** The GPU is supported by an open source nouveau display driver. The ROOT version 5 – 34 – 00 is the latest stable version SLitrani can be used with.

To determine results which do not change with the number of photons or their sample number, a transmission efficiency is studied. The fiber is placed at the geometrical world origin which is $x = y = z = 0$ and at an angle of $\theta = 0^\circ$. This means the fiber is pointing directly towards the center of the crystal and is 17 mm away from its surface. Since the simulation is based on a Monte-Carlo process, the number of photons is increased and different sample numbers are examined. A sample is defined as a randomly generated set of photons.

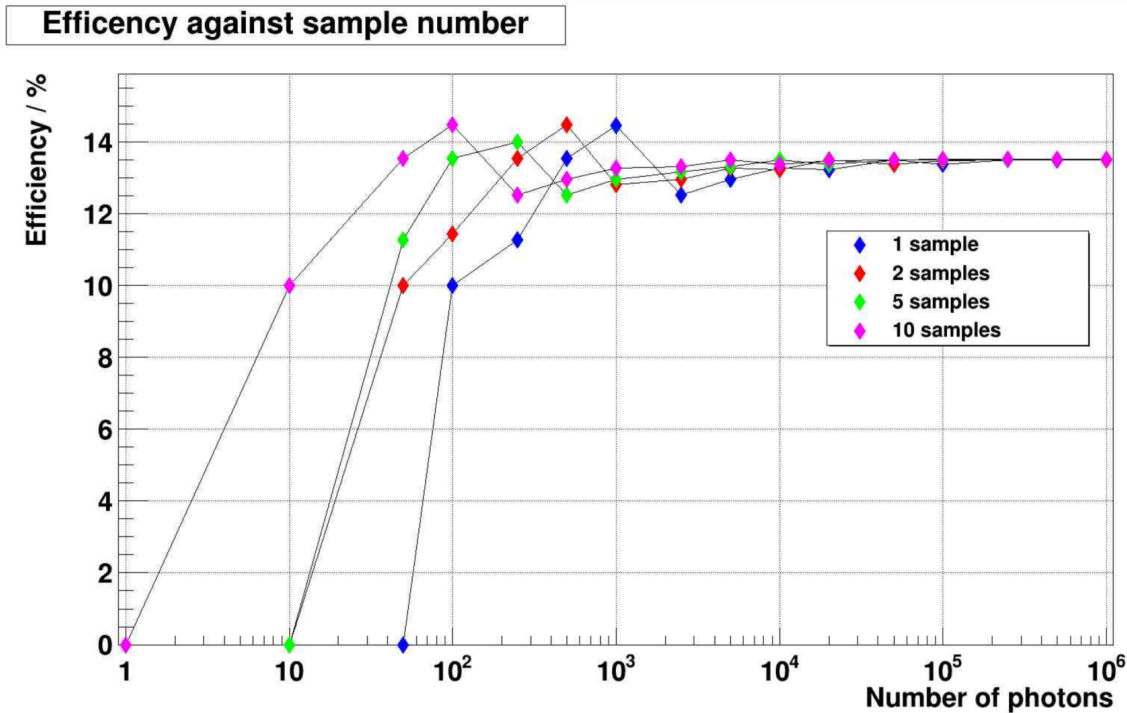


Figure 195: **Efficiency dependency on number of photons.** Since SLitrani is a Monte Carlo simulation, it depends on the number of samples and its number of photons. Each efficiency value is connected with an individual error which is always below $\sim 0.001\%$.

The efficiency depends on the number of photons (see fig. 195) respectively their statistical fluctuations. To get a compromise between stability and calculation time, one sample with a photon number of 50,000 is chosen.

9.4.1 Setup

The asset of the cap, to inject light into the crystal, is tested by positioning the fiber at several coordinates at in 29 positions in total. Though the cap is axial-symmetric, it is not feasible to study only the one half because the APDs are not located at the center of the backface (see fig. 196). At specifically selected positions, all angles ϑ between -180° and $+180^\circ$ are studied in increment steps of 1° , making ϑ as the *dependent parameter* inside SLitrani in most of the cases. The angle varies in the z-dimension due to the orientation of the slice in regard to the crystal and APD mounting inside a slice. In the experiment, the fiber can be placed in principle everywhere but since the cables as well as the light fibers will be aligned in the direction of the beam, the possibilities to place the fiber can be reduced to a two dimensional problem: x and z . The dimension x represents the distance between fiber and crystal while the dimension z is the dimension along the beam direction.

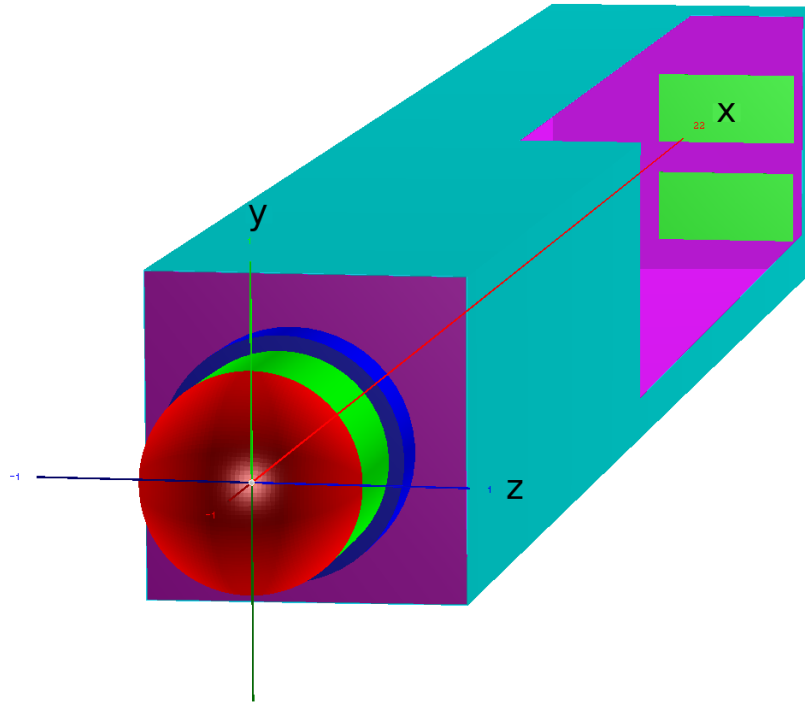


Figure 196: **Orientation of APDs, crystal and simulation axis.** The crystals will be mounted inside the slice such that the long side of the APDs will follow the beam direction. Thus, the angle region for the position studies varies in the z dimension (*blue*). To depict this geometrical orientation, the whole object is cut partially to show how the APDs are aligned in regard to the crystal and the propagation axis x .

The colors are assigned to specific components: Red is the sphere of the cap, green is the tube of the cap, blue is the edging of it, the wrapping is in cyan and the crystal is in magenta while the glue is in green. The APDs are hidden behind.

The drilling or opening in the cap for the light fiber is ignored because the light fiber will be attached such that there will be almost no gap. At each position, the most efficient angle is determined and studied in detail afterwards. A position study of an angle range of 360° requires a run time of ~ 22 minutes.

9.4.2 Angle study at origin

At first, to achieve a rough understanding how the injected light behaves inside the setup and finally to see how much is detected, the efficiency is studied against the angle of the fiber. Therefore, the light injection is analyzed such that the fiber is rotated by 360° (see fig. 197). At each of the 361 angles, one sample of photons is produced and for each angle the corresponding efficiency is recorded.

Figure 197: *360° angle scan at $x=y=z=0$.* The total efficiency is measured in each step. The fiber is rotated in 360 1°-steps and the most efficient angle is -106° at the origin.

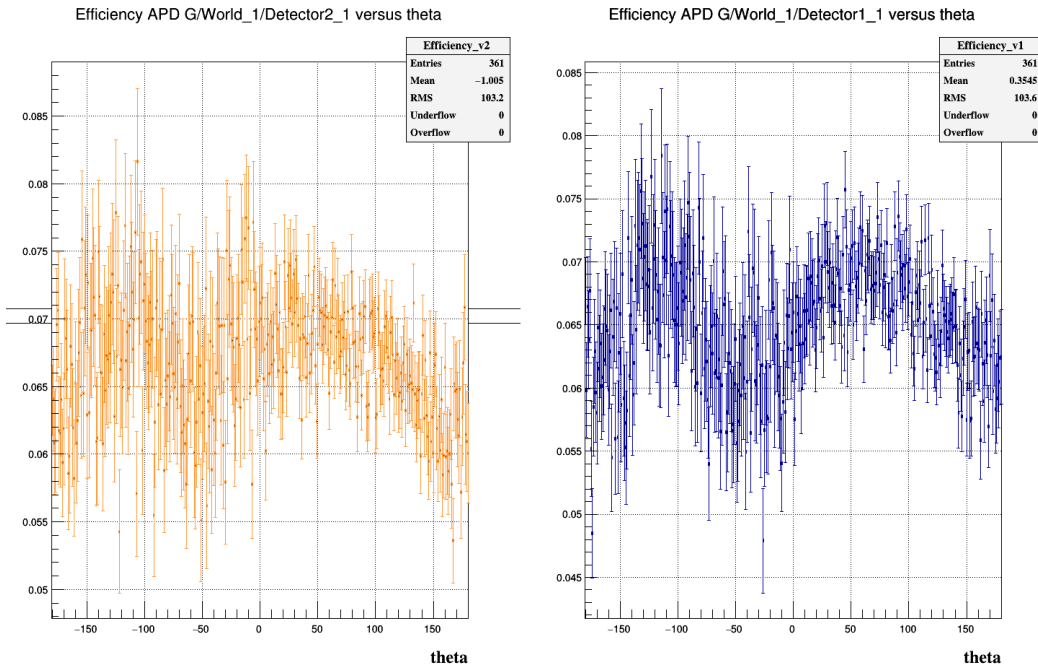
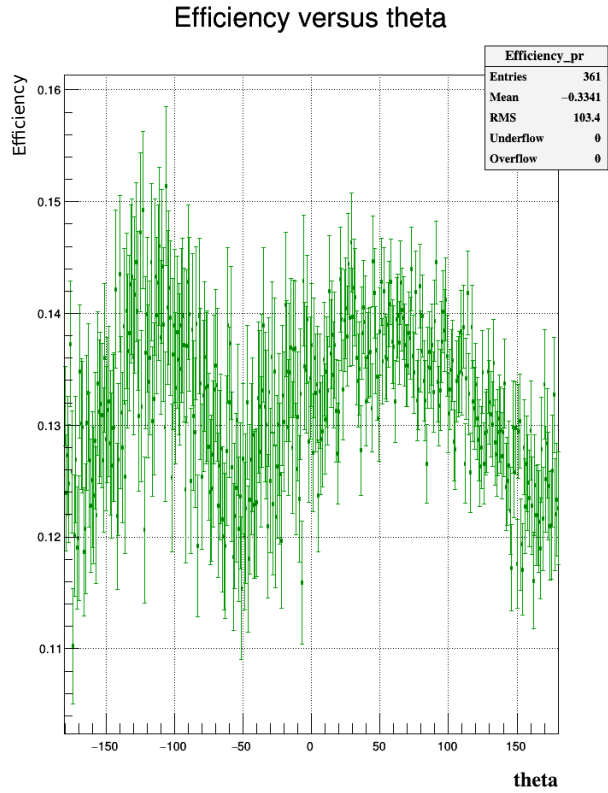


Figure 198: *360° angle scan of both APDs at $x=y=z=0$.* Both APDs correlate with each other but show also independent detection properties nevertheless.

The total efficiency (fig. 197) is based on the single efficiencies of both APDs (fig. 198). Due to their specific positions at the rear of the crystal, each APD detects a different amount of light but, yet, both are highly correlated. The highest total efficiency is almost 16 % at an angle of -106° and can be assigned half to each individual APD. The efficiency is almost good on the opposite side at about $90 - 100^\circ$ and rather worse at the other angles.

9.4.3 Angle study at specific coordinates

In addition to the study of the light injection at the origin, many further coordinates are investigated as well to obtain a general comprehension of the light propagation inside the cap. Therefore, these investigations are performed at 29 coordinates in total and the most efficient angle at each coordinate is recorded (see fig. 199). All angles at each coordinate are analyzed with the help of 100,000 photons by using 10 samples of 10,000 photons (see fig. 195).

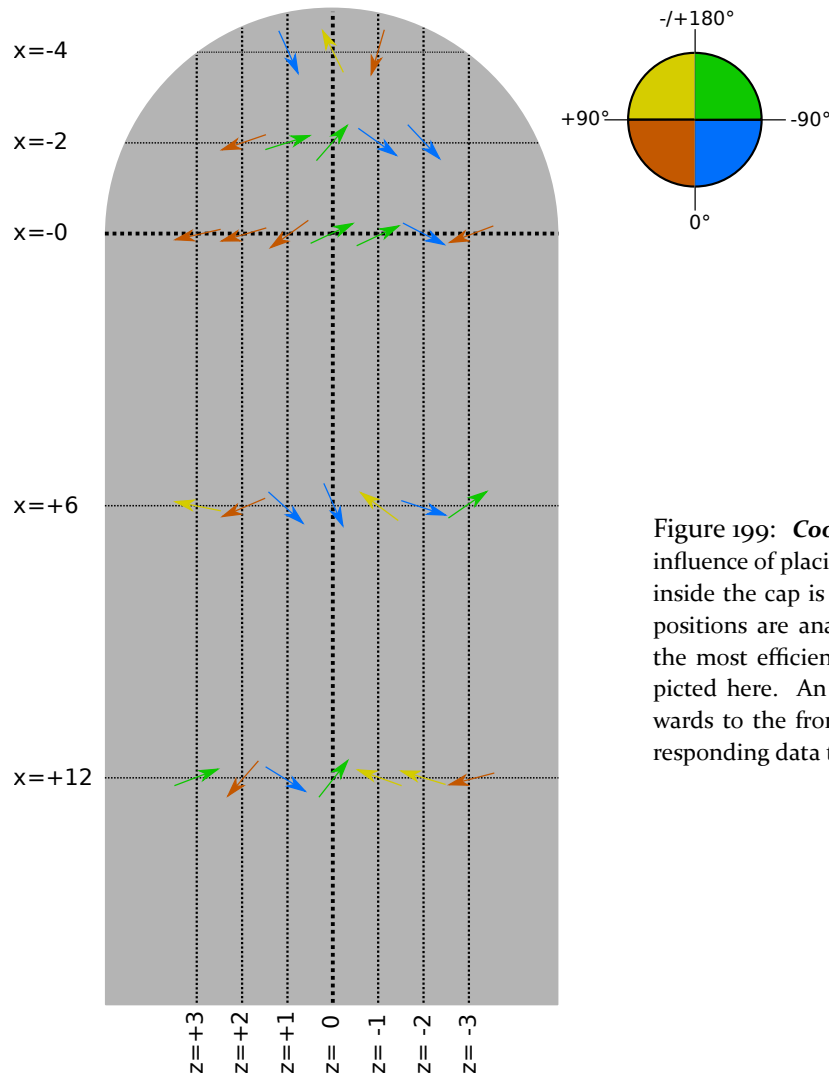


Figure 199: **Coordinate and angle study.** The influence of placing the fiber at various positions inside the cap is studied. Therefore, in total 29 positions are analyzed and at each coordinate, the most efficient angle is determined and depicted here. An angle of 0° points directly towards to the frontface of the crystal. The corresponding data table can be seen on .

The efficiencies at the different coordinates show hardly an unambiguous preference. The most efficient angles vary from coordinate to coordinate without following a clear priority. The angles pointing back to the spherical part of the cap are least efficient (see). Furthermore, in the greatest part of the angle region, the fiber is not aiming straightly towards the APDs. This can be related to the circumstance that the photons are reflected several times until reaching an APD. The fact that a photon undergoes about 10 – 12 interactions along its trajectory underlines this assumption (see *Number of interaction points along trajectory* on page 185). Next, the angles in fig. 199 are depicted with their efficiency in fig. 200:

9.4.4 Efficiency map

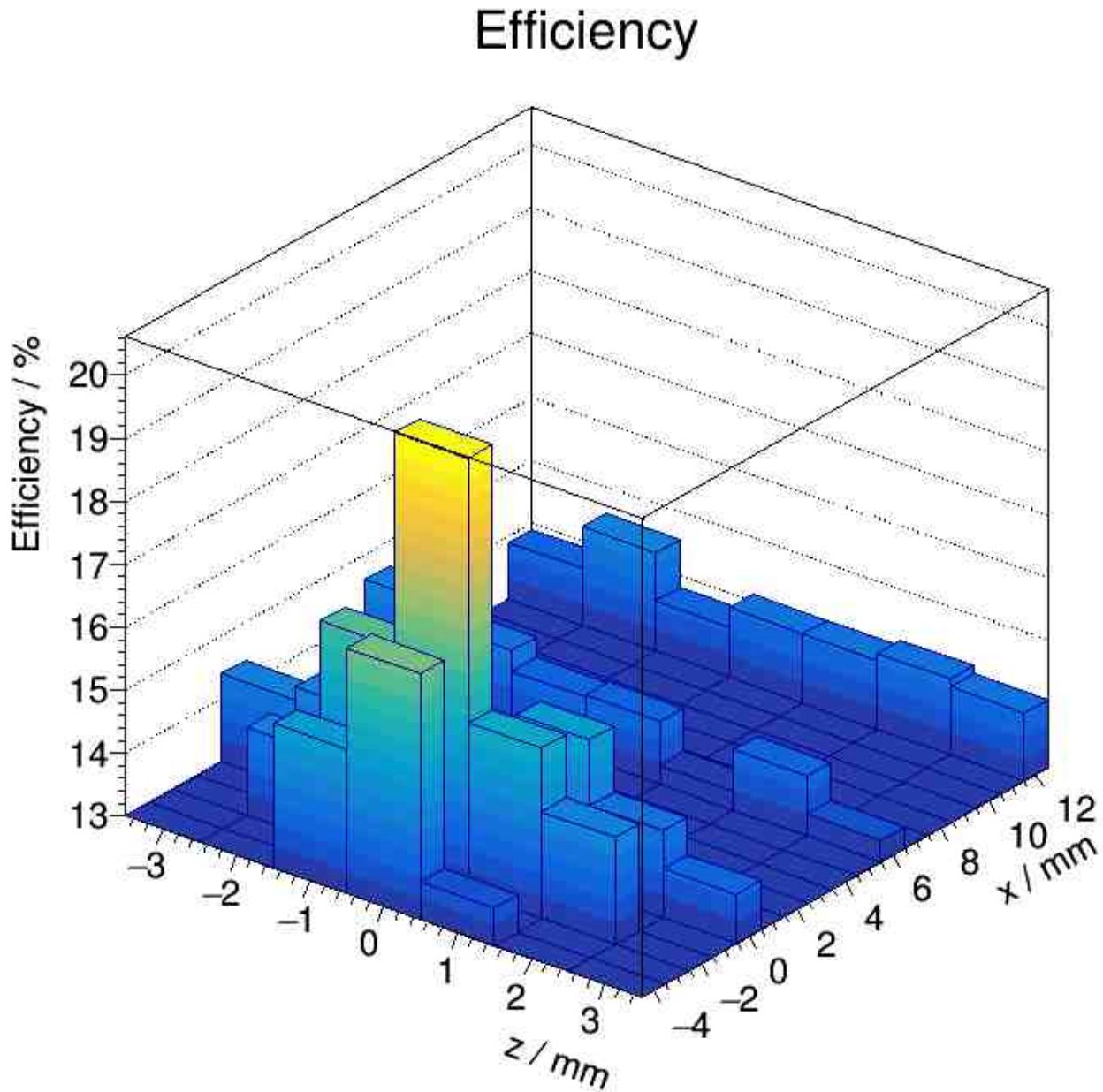


Figure 200: *Efficiency map*. This map shows that the efficiency is clearly the highest, when the fiber is located in the upper side of the cap. The highest value is 19.9 % at $x = -2$ mm and $z = 0$.

The map visualizes the efficiency of the most efficient angles at each coordinate and reveals how much it varies among the analyzed coordinates. While the values at $x = 6$ mm and $x = 12$ mm are relative homogeneous, they are quite different in the top region with the spherical part of the cap. When the light is injected from the upper part of the cap, the more light reaches the APDs. As the most efficient angles at the coordinates $x = -2$, $x = -4$ show in fig. 199, the amount of detected light is higher when it is reflected by the cap at the beginning. All efficiencies are subject to an error of 0.00116 %.

9.4.5 Elapsed time

Since the velocity of a photon depends on the medium it is traversing, the required total time to be detected by an APD is assumed to vary among the coordinates of generation:

Elapsed time

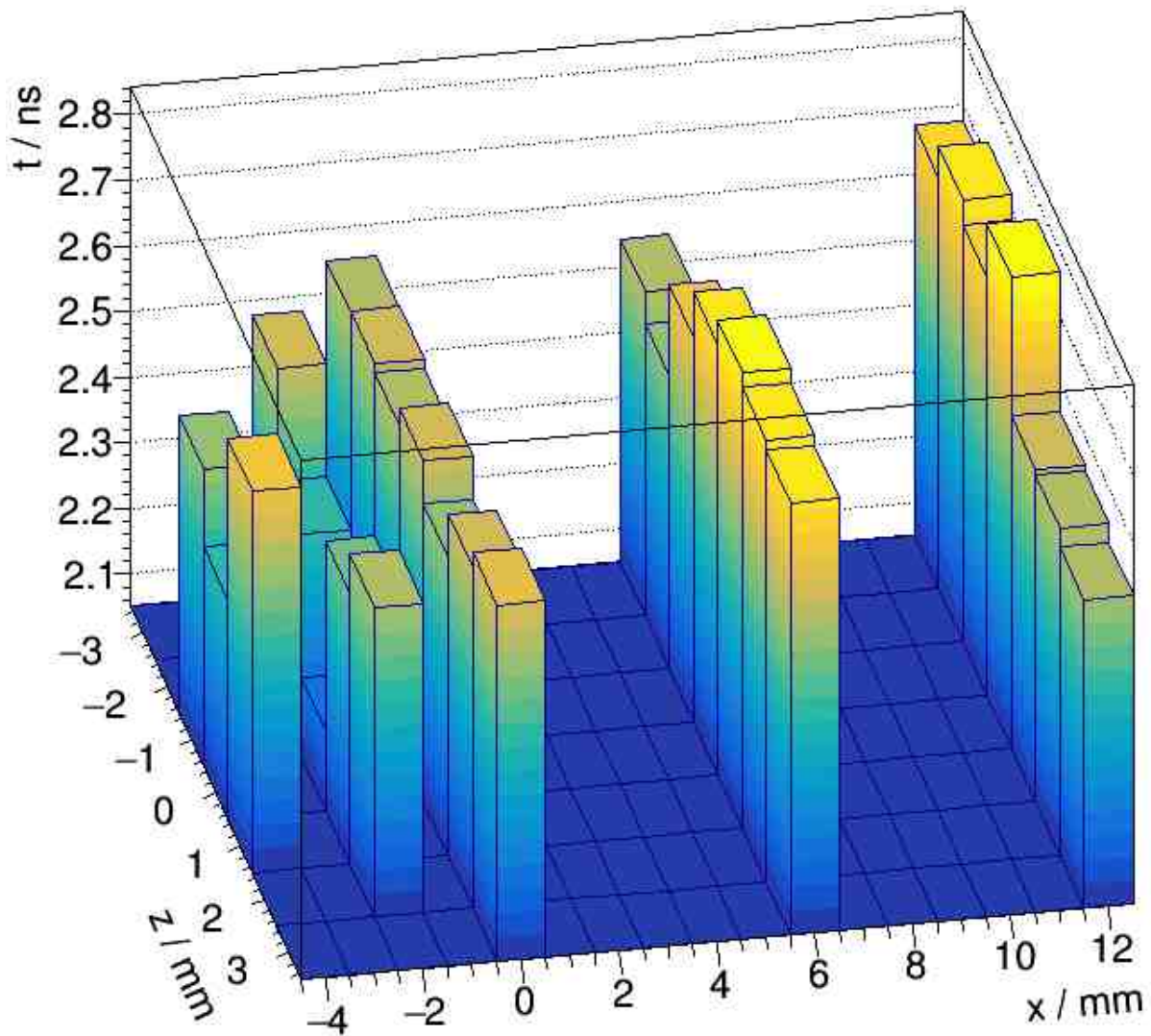


Figure 201: **Time elapsed until detection.** The photons need different time lengths until reaching the APDs and getting eliminated. Remarkable is, that photons generated closer to the crystal, need more time than photons created further away from it.

The necessary time from generation to elimination appears to be the higher the closer the source of generation is to the crystal. This time is up to 20 % higher compared to the top positions where the elapsed time is lower. A look at the according distance shows a correlation between elapsed time and distance (see fig. 202).

9.4.6 Elapsed distance

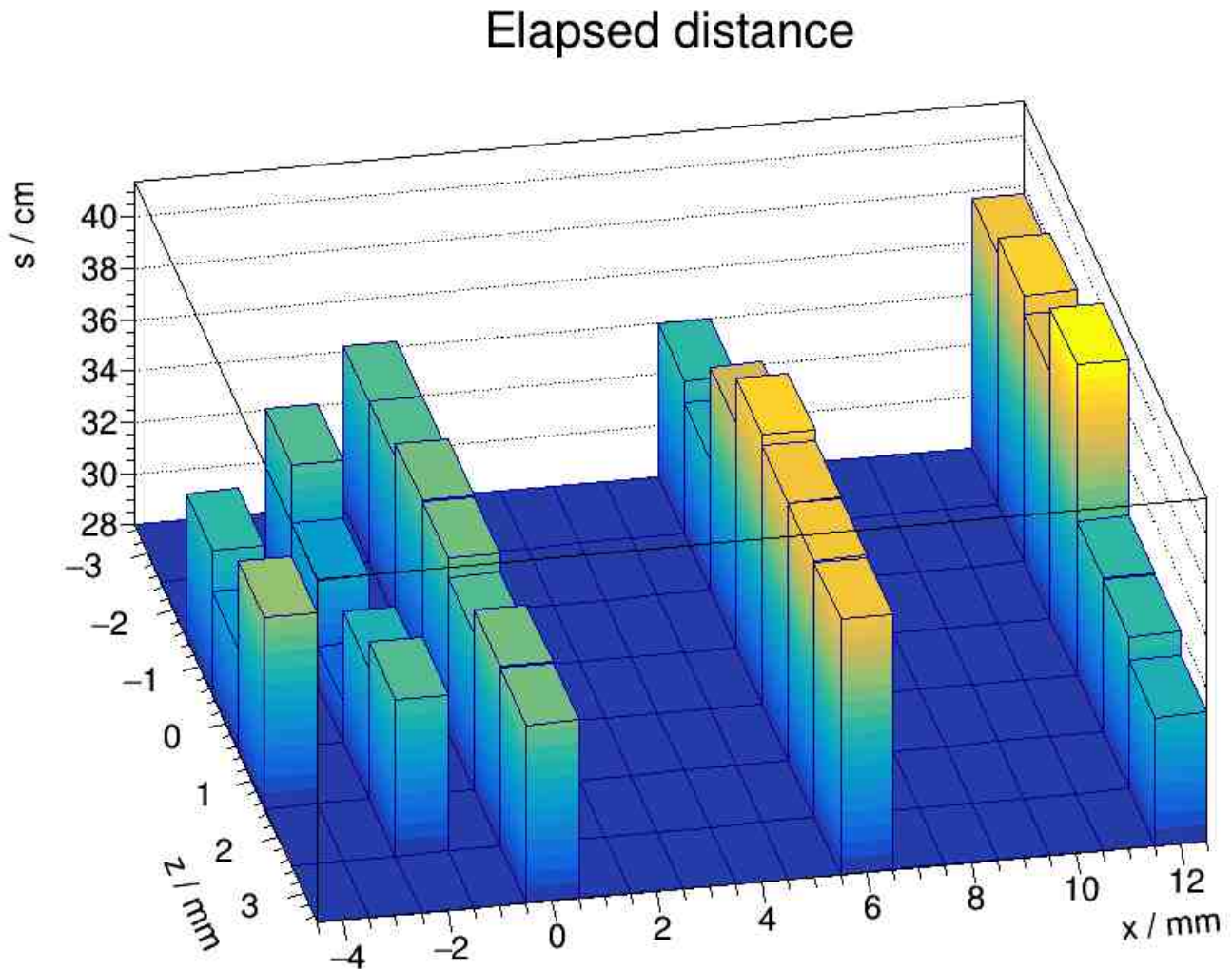


Figure 202: *Elapsed distance until detection*. The map shows for each coordinate the light's travelled distance, from generation to elimination. It yields a similar pattern as the elapsed time map (see 201).

By comparing the path lengths of the photons due to the different start coordinates (see fig. 202), it appears that the trajectory from generation until elimination is not straight at all. Hence, the path lengths vary accordingly. For example, the set of the path lengths at the coordinates at $x = 12$ mm can be divided into a half providing a large distance to travel and into a half of a rather small distance. Also is there a large difference between $z = 0$ mm and $z = 1$ mm.

The length of a crystal is 20 cm and the cap has a length of about 2.4 cm, but the minimum travelled distance is about 28 cm. Hence, the photons have to undergo several reflections. The number of interactions, seen from the origin along the trajectory, is calculated with ~ 9 but connected with a large rms of ± 7.8 (see fig. 203). The elapsed mean time is 2.57 ± 1.848 ns (see fig. 201) with an elapsed mean distance of 34.81 ± 24.86 cm (see fig. 202).

Number of points along trajectory

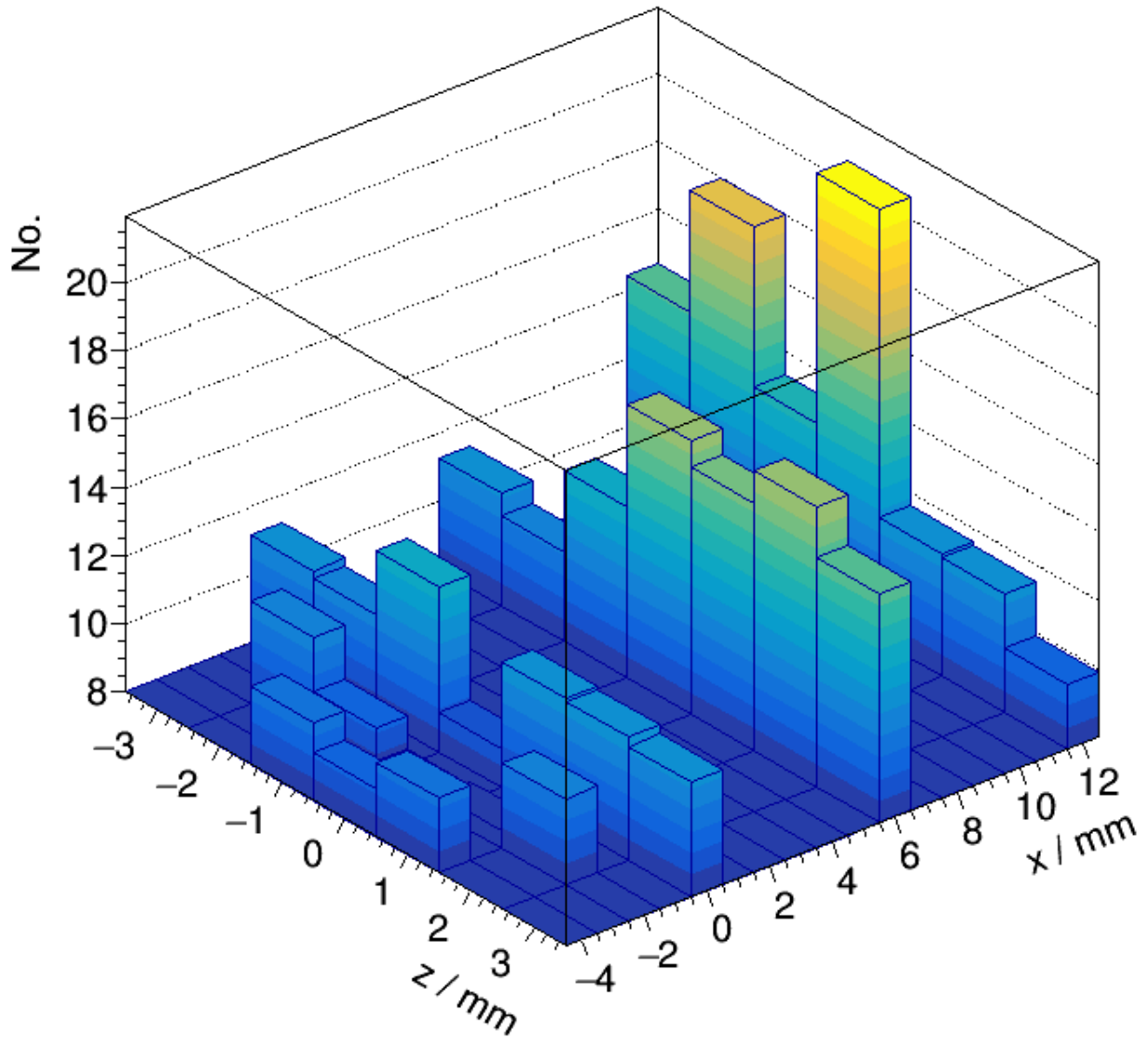


Figure 203: *Number of interaction points along trajectory.* The trajectories of the photons provide different number of points. This number varies strongly among the generation points.

The photons, generated at large x , have to undergo more interactions along their trajectory (see fig. 203). Together with the high elapsed distance and time, this in sum, is likely related to the circumstance that these photons are reflected more often. According to fig. 200, the efficiency is highly correlated with the number of interactions.

In the following, characteristic values for the number of photons are listed for specific material transitions, generated at the coordinates $x = -2$ and $x = 12$. The row designations (left) indicate the material the photons originate from and the column designations (top) represent the material the photons travel to or get reflected by.

Absorbed by the wrapping

	$BaSO_4$	VM2000
PbWO ₄		978
Air	3	2395

Table 34: *Absorption by wrapping at $x=-2$.*

	$BaSO_4$	VM2000
PbWO ₄		753
Air	5	2752

Table 35: *Absorption by wrapping at $x=12$.*

In regard to the wrapping which is able to absorb photons, there is not a significant difference between both spawning points, $x = -2$ and $x = 12$. Only a few more photons get absorbed by the wrapping, at $x = 12$.

Reflected by the wrapping

	$BaSO_4$	VM2000
PbWO ₄		16275
Air	194519	374949

Table 36: *Reflection by wrapping at $x=-2$.*

	$BaSO_4$	VM2000
PbWO ₄		16219
Air	1324310	40844

Table 37: *Reflection by wrapping at $x=12$.*

In case of reflections caused by the wrapping, there is a great imbalance when considering the transitions air↔cap and air↔wrapping between both coordinates. In case of $x = -2$, only a fraction of photons of about 15 %, compared to coordinate $x = 12$, is reflected by the cap. In addition, about 9x more photons are reflected by the wrapping. Furthermore, none photon is reflected by the cap and enters the crystal directly without passing the air. In general, the number of reflections exceeds the number of photons often, thus, some photons must be reflected multiple times. Since the number of reflections by the cap is much higher in case of $x = 12$, this leads to the assumption that a great part of the light does not even enter the crystal. Hence, the number of photons reflected by the wrapping is lower accordingly. The question still remains open, why the number of photons, reflected at the transition crystal↔wrapping, is quite the same for both coordinates.

Transitions between the materials

	Air	PbWO ₄	Plastic	Glue
Glue	4069			
Silicon	324	23441		16
Plastic	2950			
PbWO ₄	125863			
Air		36595	95038	4003

Table 38: *Transitions at $x=-2$.*

	Air	PbWO ₄	Plastic	Glue
Glue	2758			
Silicon	711	14819		39
Plastic	13632			
PbWO ₄	115601			
Air		37934	95015	2661

Table 39: *Transitions at $x=12$.*

Especially the fact, that at $x = 12$ roughly 5 times more photons leave or rather re-enter the fiber than at $x = -2$, gives a hint not to locate the fiber too close to the crystal. Furthermore, slightly more than only the half of photons enter the APDs in case of a light emission from $x = 12$. However, this is already known due to the low efficiency generated there.

Reflections by the materials

	<i>Air</i>	<i>PbWO₄</i>	<i>Plastic</i>	<i>Glue</i>
Glue	176			
Silicon	288	2931		14
Plastic	382			
PbWO ₄	23353			
Air		180879	4962	317

	<i>Air</i>	<i>PbWO₄</i>	<i>Plastic</i>	<i>Glue</i>
Glue	145			
Silicon	664	2000		16
Plastic	1864			
PbWO ₄	44163			
Air		366498	4985	564

Table 40: *Reflection at $x=-2$.*

Table 41: *Reflections at $x=12$.*

Concerning the reflections, the occurring differences between both coordinates are similar to those at the wrappings. At $x = 12$, way more photons are reflected by the fiber, when coming from the outside. Additionally, more photons are also reflected by the air when passing the crystal. The same is valid in case of the APDs.

9.4.8 Correlations between the propagation quantities

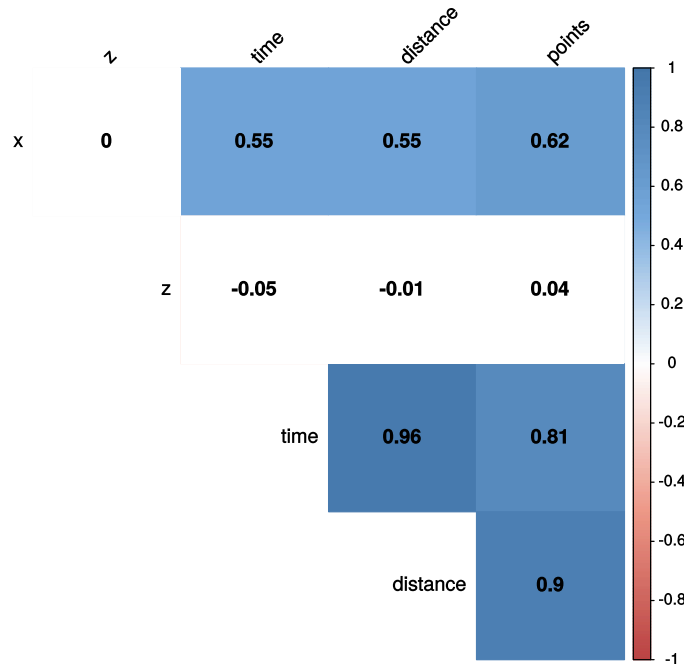


Figure 204: *Correlation plot of the propagation quantities.* Points refer to the number of interactions. The significance level is 5 %.

In the previous plots (fig. 200 - fig. 203), it seems that the one side of the cap ($-z$) shows generally different properties than ($+z$) does, e.g., the number of interaction points. However, there is no correlation between the z -coordinate and those quantities. Nevertheless, strong correlations are present between *time*, *distance* and *number of points*. Hence, as the former tables (table 34 - table 41) already underpin this, the assumption, that photons generated close to the crystal, require more time due to more reflections and longer travel paths, seems valid. However, the corresponding correlations are not as high as expected.

9.4.9 APD ratio during rotation

Since the APDs are independent of each other, they will detect a different amount of light though they are meant to deliver the same signal. To analyze their exact difference, the angle of the fiber will be the single running parameter as SLitrani enables only one at the same time. Furthermore, the fiber is placed at the origin.

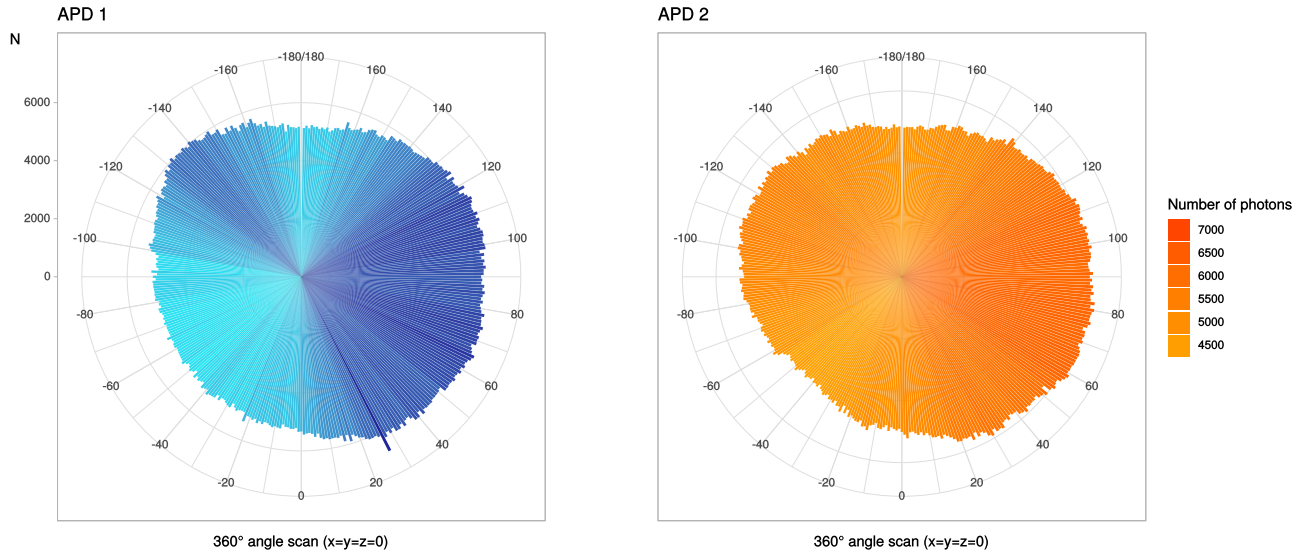
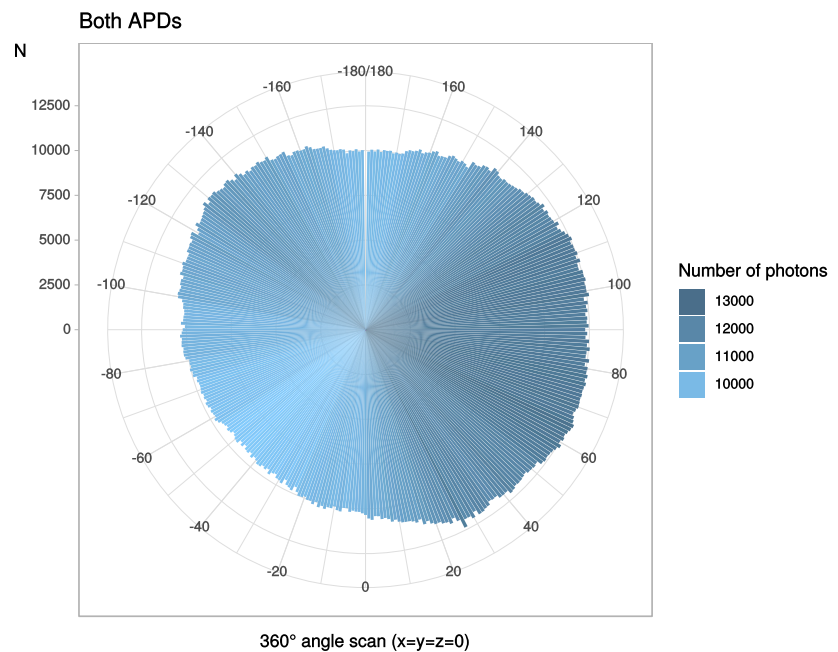


Figure 205: **APD ratio in dependency on the angle of the fiber.** The amount of light is represented by the length of the radius. APD₁ (*left*) detects, at certain angles, slightly more light than APD₂ does (*right*).

The APDs show a highly correlated behaviour with respect to the angle of the fiber. Furthermore, the APDs provide in general a better detection efficiency when the fiber is aligned between +180° and 0° and a worse one in the range from 0° to -90°, where the APDs are in direct line-of-sight.

Figure 206: **Light injection in dependency on the angle in total for both APDs.** The angle range from 0° to 180° is more efficient than the one from -180° to 0°.



9.4.10 APD ratio during x translation

The fiber is shifted along x , with fixed $y = z = 0$ and $\theta = 0^\circ$. It has to be mentioned, that here, $x = 0$ is equal to $x = -4$. Hence, to compare it with the other results, the x -values have to be added with 4 or subtracted by 4, respectively. This circumstance is due to the recording of the running parameter inside SLitrani.

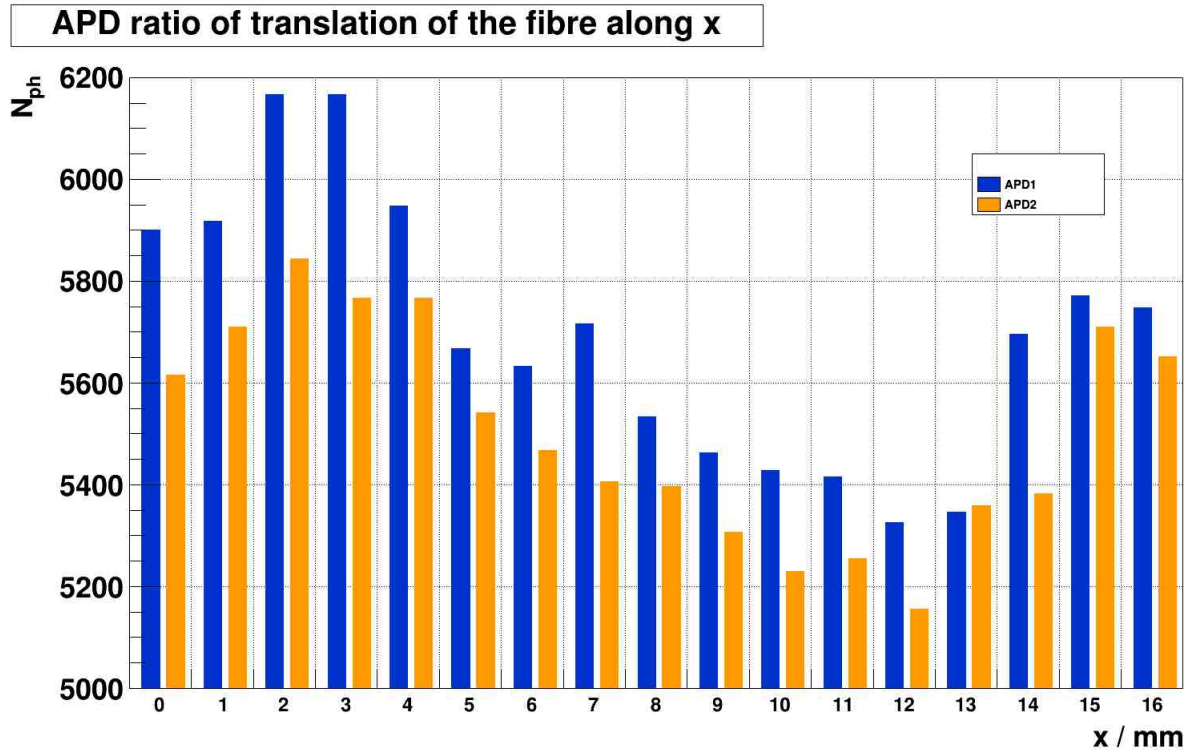


Figure 207: *Detected number of photons at different x-positions of the fiber.* The detected light varies when moving the fiber along x . Noteworthy is that the amount of detected light is the highest when the fiber is the most distant away from the crystal and decreases when placed closer. Very close to the crystal, it increases rapidly. The independent axis, the number of photons, begins at a detected amount of photos of 5,000. The difference between the highest and the lowest amount of detected photons is about 16 %.

The detected amount of light is the highest at or near the origin and decreases continuously from there on. The more it reaches the crystal, the detected amount of light increases again. The general NUF⁷⁸-behaviour of the crystals might be the reason because of their tapered parallelepipedal geometry (see fig. 209).

When the fiber is located at the origin, the maximum radius of the light cone impinging the crystal is then ~ 12 mm. Hence, a part of the emitted light will be reflected by cap. This changes when the fiber reaches $x = 3$, then the light cone will not cover any part of the cap anymore.

Furthermore, APD1, which is rather positioned centrally, collects nearly always more light than APD2 does. However, the differences are not very large.

⁷⁸Non-UniFormity

9.4.11 Type scan

The type of the crystal in previous studies was always one of type 6 since it represents an average of all crystal types (see fig. 208). To gather an overview of the influence of the corresponding geometries, the light injection of all types is measured at fixed parameters, $x = y = z = \theta = 0$:

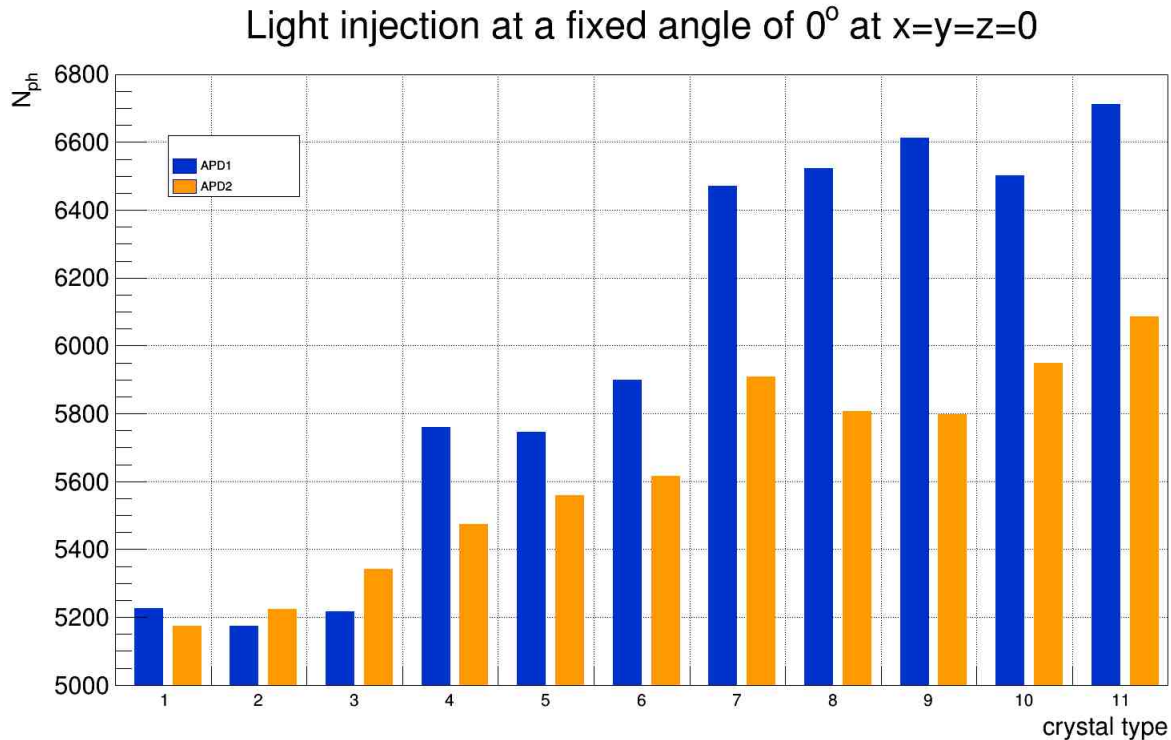


Figure 208: **Light injection at the origin across all crystal types.** From 1 to 11, the crystals are tapered more and more and the results show that the amount of detected light strongly depends on the crystal type.

A crystal of a type 6 represents also the average in terms of detected amount of light. APD₁ collects nearly always more light, except for the crystal types 2 and 3. Hence, in case of APD₂, the detected light increases quite constantly with the crystal type number.

However, the detection of light in case of APD₁ can be divided into three regions: 1 to 3, 4 to 6 and 7 to 11. Above all, the geometries vary in their angles: The tapering angles α , β and γ are the largest at the crystal type 1 and decrease towards higher type numbers (see fig. 209). As it can be seen in fig. 210, all angles decrease with the number of the crystal type. Linking this to fig. 208, it turns out that the smaller the tapering angle, the greater the efficiency.

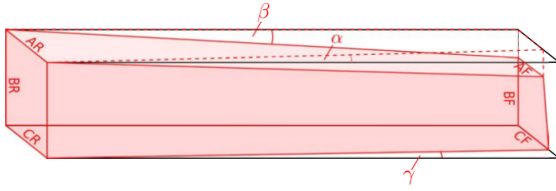


Figure 209: *Angle definition of the crystal [38].* The angle α refers to the side AR-AF, the angle β refers to the side BR-BF and γ refers to the side CR-CF.

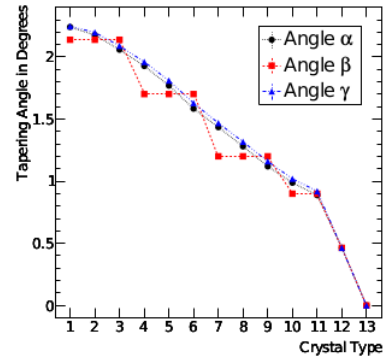


Figure 210: *Angle dependency on the crystal type [38].* The higher the crystal type the lower the angles. Crystal 12 and 13 represent crystals of the forward end-cap and backward end-cap.

9.4.12 Position impact

The position of the incident light on the entrance window of the APDs will also change with the position of the fiber. When shifting along x , and holding $y = z = 0$ constant, the detected light will vary accordingly to the most efficient angle:

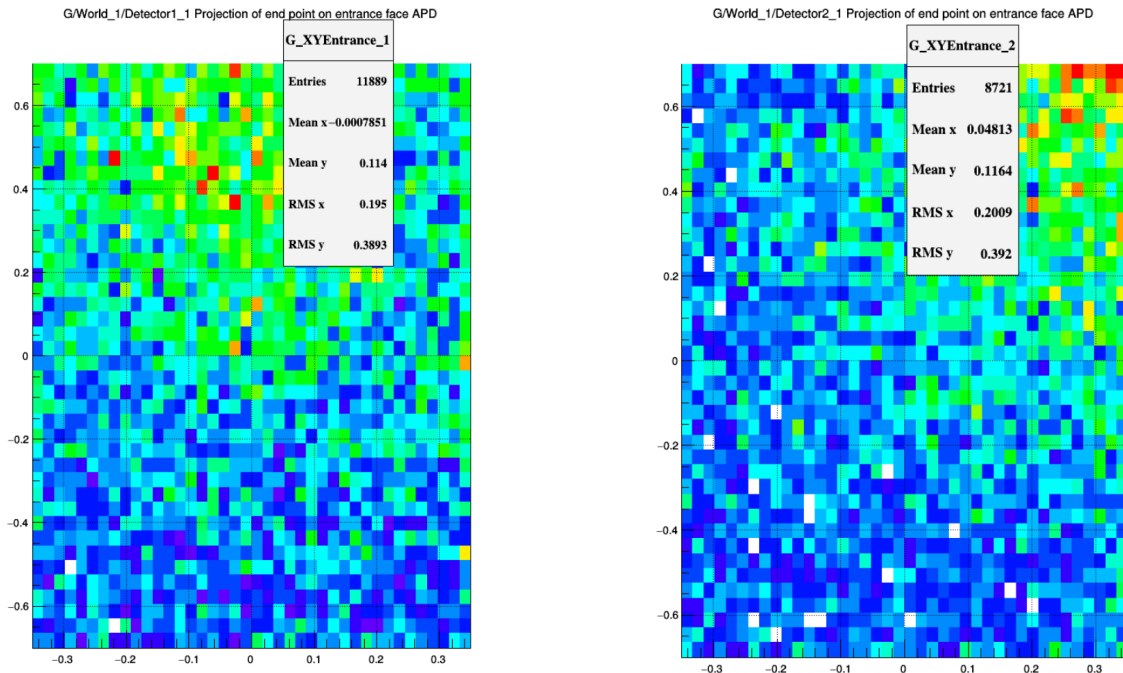


Figure 211: *Light impinging the entrance window of the APDs at $x=-4$ and at $\theta = 171^\circ$.* APD₁ detected 9124 photons and APD₂ 8721.

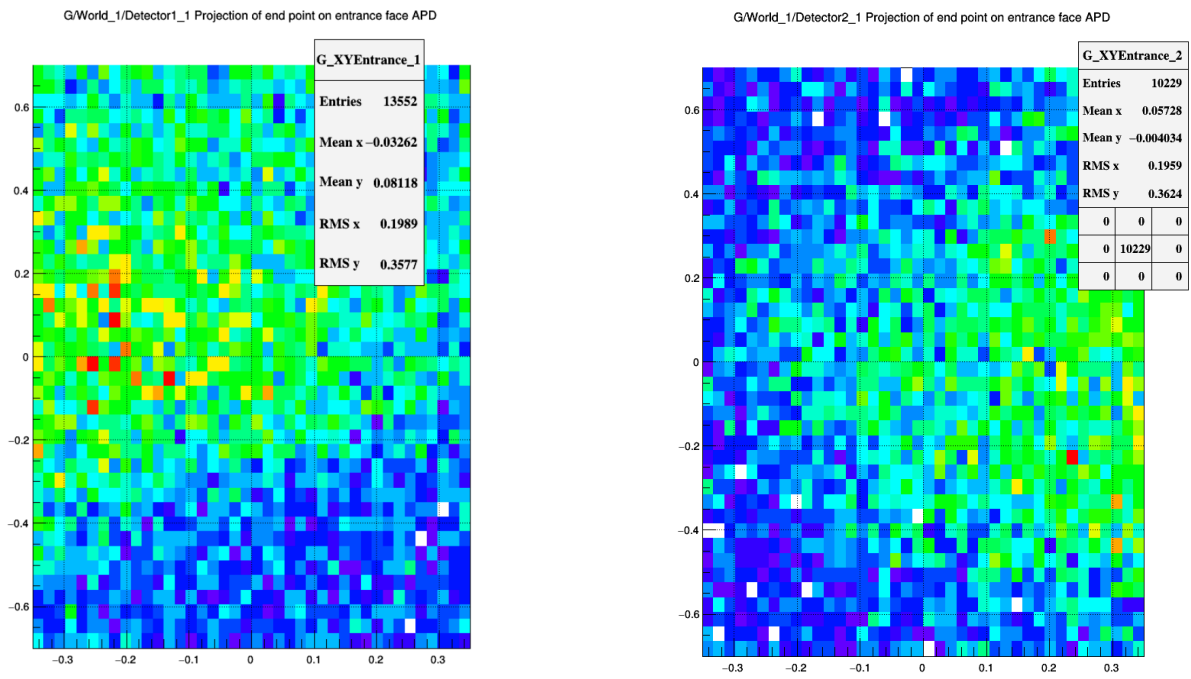


Figure 212: *Light impinging the entrance window of the APDs at $x=-2$ and at $\theta = -134^\circ$. APD₁ detected 10438 photons and APD₂ 7929.*

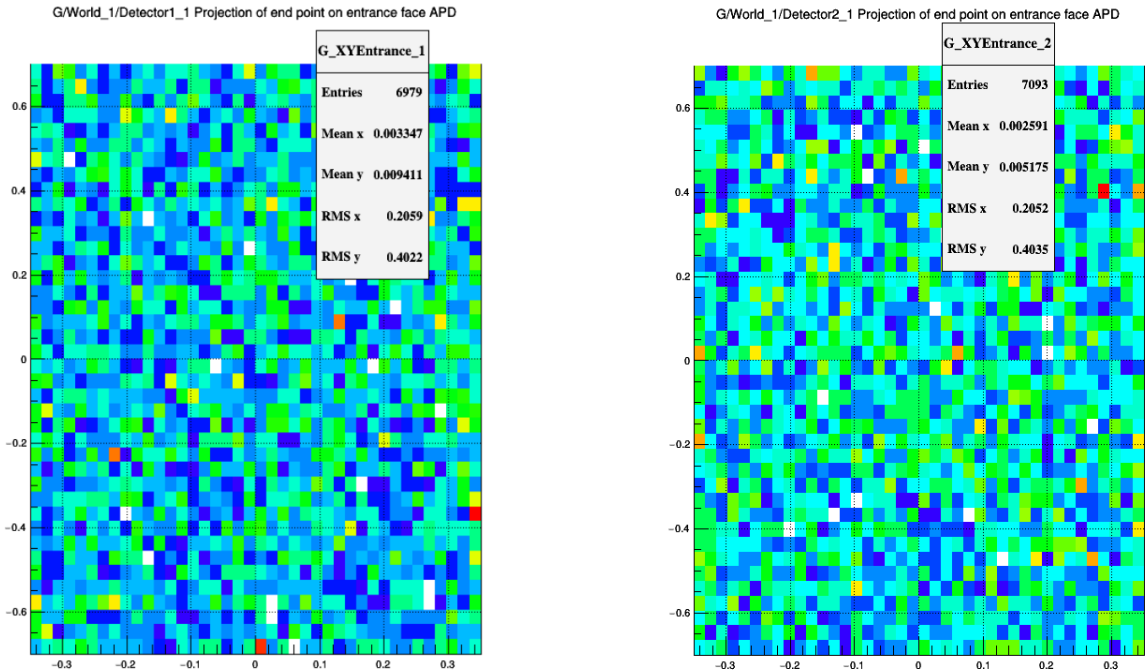


Figure 213: *Light impinging the entrance window of the APDs at $x=0$ and at $\theta = -106^\circ$. APD₁ detected 5227 photons and APD₂ 5352.*

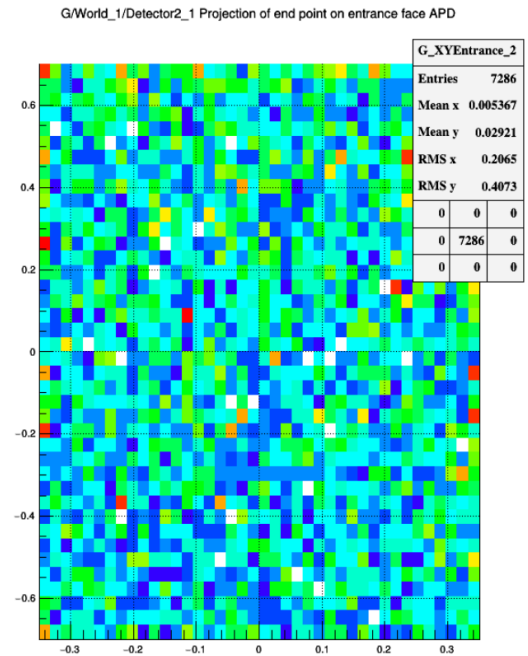
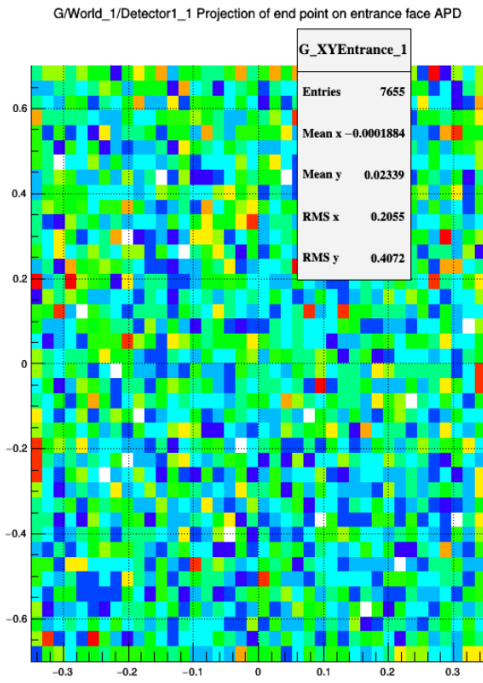


Figure 214: *Light impinging the entrance window of the APDs at $x=6$ and at $\theta = -106^\circ$. APD₁ detected 5740 photons and APD₂ 5510.*

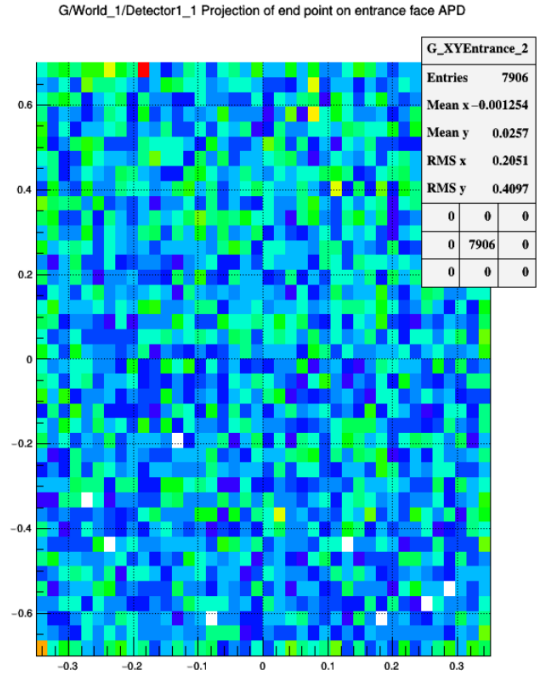
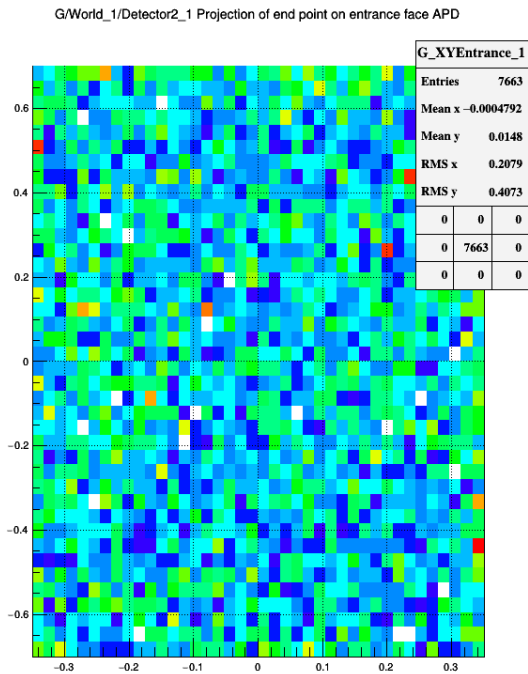


Figure 215: *Light impinging the entrance window of the APDs at $x=12$ and at $\theta = 167^\circ$. APD₁ detected 5854 photons and APD₂ 5694.*

It has to be noted, that a photon is considered as detected when it leads to a release of 5 electrons. Out of this reason, there is a discrepancy between the number of entries, indicated in the top right in each plot (fig. 211 - fig. 215), and the ultimately measured photons. The latter are given as numbers in the figure descriptions. The position of impact varies notably with the fiber placement, especially when it is placed in the spherical part of the cap.

10 Conclusion and outlook

An irradiation of the crystals can lead to considerable changes in their properties. The most significant consequence will be a loss of transmission causing varying signals over time. Without any irradiation, the crystals will recover slowly with time, for example, in the forward region it would require an annealing time of 400 hours at $T = -25\text{ }^{\circ}\text{C}$ after a radiation dose of 30 Gy (see fig. 35). As of this writing, researches are performed to allow an online recovery to enable an annealing of the crystals without a temporary shutdown of the experiment.

Monitoring ensures to be aware of any changes in regard to the scintillation behaviour, mainly caused by irradiation. Therefore, a light pulser will provide a defined light signal which is close to the emission signal of PbWO_4 (see fig. 182). Because of that, the blue LED of the light pulser has a wavelength of $447 \pm 8.5\text{ nm}$ while the main emission wavelength of PbWO_4 is 420 nm. Since the light pulser will be located outside of the EMC, its light has to be guided into the crystals by using light fibers. Finally, to inject this light properly, an appropriate coupling device is necessary. The overall goal is to transmit as much light as possible from the light pulser to the photo detector, finally. The first proposal is designed by IHEP and is a simple cap (see fig. 164). It is made of polyamide by a 3D printer. This coupling device was analyzed in detail in this work, experimentally in the lab as well as with the help of a simulation in SLitrani.

The experimental setup comprises as main components a PANDA-crystal, type 6, wrapped in VM2000, a PMT and a readout system (see fig. 169). The measurement objects are stored in a climate chamber at a fixed temperature of $18\text{ }^{\circ}\text{C}$. To get started, some materials for the coatings were investigated. For this reason, a radioactive source, Cs-137, was placed at the upper edge of the crystal as well as at the lower edge. The coating is foreseen to increase the reflectivity of the cap (see fig. 172). In addition, the type of application is studied as well and it has been shown that neither the material nor the method to apply provides a significant difference. Some are present but within the measurement uncertainty. For example, the obtained light yield without a cap is about $21.5\text{ phe}^-/\text{MeV}$ and with a cap roughly $22.3\text{ phe}^-/\text{MeV}$. The latter is almost the same for a sprayed, brushed or plunged coating. To ensure that these measurements are not subject to an inaccurate application, a cap with aluminum and a cap with barium were covered industrially. While the latter is slightly worse than the manually coated ones, the former is slightly better. The cap with the highest measured light yield is one equipped with a reflector foil. In any case, all different materials are within the measurement uncertainty. It is also examined how the cap is affected by an irradiation of γ 's with 30 Gy (see fig. 173). Finally, neither the application method nor the irradiation affects the measured light yield significantly.

Next, to gather knowledge about the dependency of the light injection on position and angle, respectively (see fig. 176), five arbitrary positions were chosen and studied in detail. The amount of detected light is subject to the position of the fiber together with the angle relative to the crystal and it is the highest the closer the fiber is located to the crystal and pointing towards it. The measurements were taken at two different coupling depths (8 mm and 12 mm) and at two different crystals. The light pulser used for this purpose is a different light pulser than the one which will be used in the experiment. Therefore, to obtain a reference, a study with the second light pulser was performed as well by shifting the fiber along the distance perpendicular to the crystal. When the fiber makes nearly contact with the crystal, at a coupling depth of 22 mm, an energy of about 1.05 GeV can be injected. At a coupling depth of 12 mm, it is 0.66 GeV (see fig. 185).

Another aspect is the polishing of the fiber. For a rough comprehension, two batches of fibers, each consisting of three fibers, were made and compared to each other. The one batch has only one polished end face and the other one has two. The fibers with one polished side were arranged such that the unpolished surface was emitting the light towards the crystal. Two of each batch are rather similar to each other while two fibers show

deviant results but in opposite directions: The unpolished fiber provides the highest measured signal and the unpolished one the lowest signal (see fig. 186). For an unambiguous conclusion, further studies could be conducted with a higher number of fibers as well as with varying polishing levels. Other design studies for the coupling device are performed at the moment as well. The idea of an Ulbricht sphere did not show promising results, also not combined with a very thick light fiber with a diameter of 0.2 cm inside of it [84]. An ongoing research uses a prism to inject the light. However, the use of additional fibers will likely lead to the demanded amount of injected light (in the order of 10 GeV) but this simple approach provides the drawback of further mechanical requirements due to the little space inside the EMC.

The previously discussed cap was studied with the help of a photomultiplier but the EMC uses two APDs per crystal as photodetectors. To achieve a more detailed knowledge of the coupling capability of the cap in general, it is built from scratch and simulated in SLitrani together with the entire setup (see fig. 196). This means, the simulation includes the fiber, the cap and its coating, the crystal and its wrapping as well as the APDs and the glue to attach it to the crystal. The geometries were defined with the help of the TGeo class in CERN ROOT and linked to optical parameters in SLitrani. Instead of using barium sulfate for the coating, the well implemented aluminum properties in SLitrani were used instead as the reflectivity properties are almost the same. Furthermore, since SLitrani does not provide the definition of a coating, it was realized as a revetment. The wrapping has a thickness of 63.5 μm and the world medium is air. In between the wrapping and the crystal is a thin slice of air of 100 μm .

Because SLitrani is a Monte Carlo simulation, the dependency on the number of photons per sample and the number of samples itself on the efficiency was studied first. The calculated efficiency remains quite constantly when a total number of photons of 100,000 is used. When using 10 samples, a number of 10,000 photons shows the same results (see fig. 195). Subsequently, to get a rough understanding of the light injection process, the fiber is located at the origin (where the cap goes into its spherical part) and rotated in 1° steps in a 360° circle. This turned out that the light injection does clearly depend on the angle of the fiber (see fig. 197). Furthermore, it shows that not the straightest alignment of the fiber towards the APDs provides the best results. Instead, when the fiber points to the opposite side of the APDs, the amount of injected light is higher. This might be due to reflections when the light propagates through the crystal. However, the simulation can hardly model the lab conditions, for example, the polishing properties of the fiber, where the loss of light is stronger in regard to the angle and coupling depth of the fiber. Hence, the results show a difference between the maximum and minimum efficiency of about 5 %.

In the next step, several positions inside the cap were chosen to place the light source. The calculation effort for each coordinate is quite large and to map the efficiency of the cap, 29 specific coordinates were chosen to represent the general properties of the cap. These 29 coordinates are divided into 5 sets with a different x-value and into 7 sets with a different z-value (see fig. 199 and fig. 200). All these coordinates were studied with respect to a 360° angle rotation of the fiber and the most efficient angle of each coordinate has been studied separately in detail. However, this analysis reveals that the light injection or propagation properties change significantly from coordinate to coordinate. Hence, the results are difficult to realize technically. One key insight is that the spherical part provides a higher efficiency and the closer the fiber is located at the crystal, the lower the efficiency is. This seems to be connected to the corresponding number of interactions in regard to the generation coordinate (see fig. 203). While the one half of the cap seems to provide in average a higher efficiency than the other one does, a correlation study among all investigated quantities could not underline this effect (see fig. 204). Another aspect is how the injected light splits between the two APDs. When shifting the fiber towards the crystal with fixed parameters $z = y = 0 = \theta$, APD₁ collects nearly always more light than APD₂ does (see fig. 207). In addition, all different crystal types were investigated as well. Therefore, the fiber was located at the origin, $z = x = y = 0 = \theta$, and the geometries of the different crystals were swapped in and out. This revealed that the light injection varies continuously along the crystal type number. While the crystal type 1, which is the most centered one inside the slice and thus, located closest at the interaction point, provides the lowest efficiency, the crystal type 11 shows the highest efficiency (see fig. 208). This can likely be explained by the NUF-behaviour of the crystals due to their tapering angles (see fig. 210).

Part 4

Appendix

11 Background

11.1 Crystal geometries

Type	Volume (cm^3)	AF (mm)	BF (mm)	CF (mm)	AR (mm)	BR (mm)	CR (mm)	Quantity / Slice	
								Left	Right
1	126.86	21.21	21.28	21.27	29.04	28.75	29.12	40	40
2	126.56	21.18	21.28	21.39	28.78	28.75	29.07	40	40
3	125.79	21.17	21.28	21.51	28.36	28.75	28.81	40	40
4	120.85	21.17	21.28	21.60	27.90	27.22	28.45	40	40
5	119.69	21.17	21.28	21.69	27.35	27.22	28.01	40	40
6	118.35	21.19	21.28	21.78	26.72	27.22	27.47	40	40
7	112.9	21.22	21.28	21.86	26.23	25.47	26.99	40	40
8	111.75	21.23	21.28	21.91	25.70	25.47	26.51	20	20
9	110.52	21.23	21.28	21.95	25.14	25.47	26.00	20	20
10	107.01	21.25	21.28	22.00	24.70	24.42	25.56	20	20
11	106.25	21.25	21.28	22.02	24.35	24.42	25.23	15	15

Table 42: *Geometries of the different types of crystals* [154]. The crystals are produced in eleven different geometries. The front height is always of the same size of 21.28 mm.

12 Matching

12.1 APD Parameters

12.1.1 Share of wafers in data points

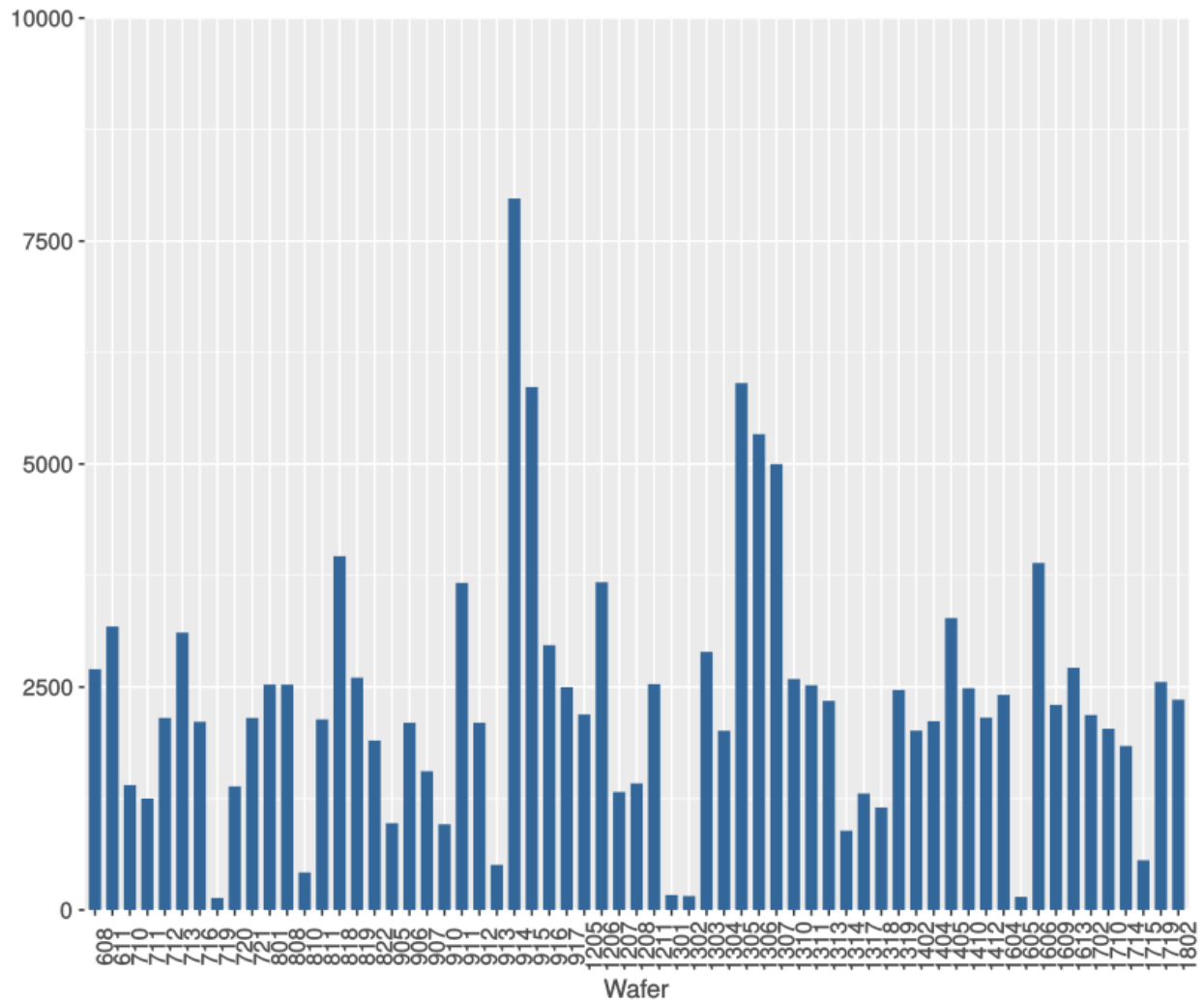


Figure 216: *Share of Wafers relative to the total number of data points.* To satisfy a simple visualization, the wafers are grouped.

12.1.2 APD 711006317

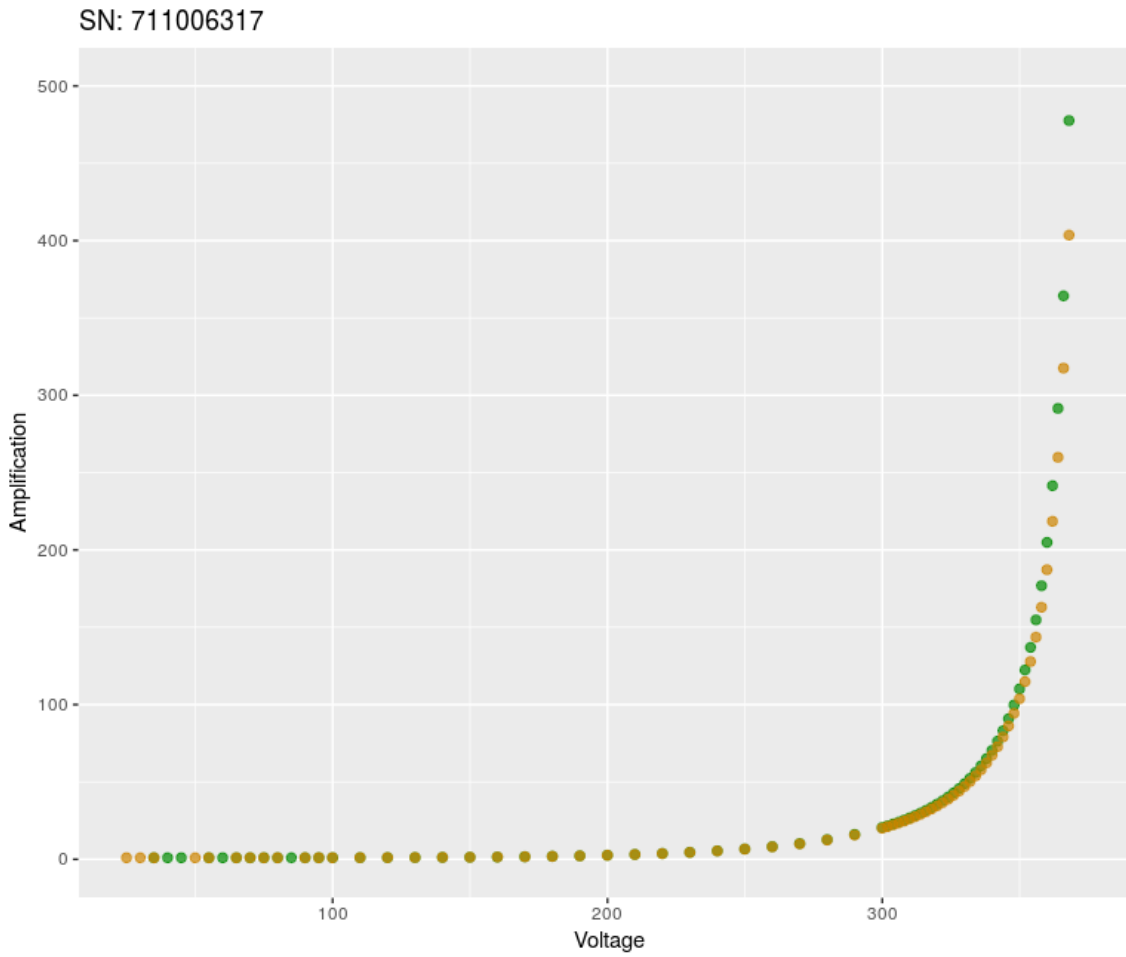


Figure 217: *APD 711006317* curve. Both irradiated (*green*) and non-irradiated (*orange*) data sets are depicted.

12.1.3 Linear mixed model

Mixed models study the sources of variation and correlation which emerge in grouped data like in hierarchical structures. The response variable Y , which is the amplification gain M in this context here, is modelled as a function of one or more predictor variables X [87], here the voltage V :

$$Y = X\beta + Z\gamma + \varepsilon$$

$$\gamma \sim \mathcal{N}(0, G) \text{ with } G = \text{var}(\gamma) = E\left((\gamma - \mu)^2\right) \text{ and } \varepsilon \sim \mathcal{N}(0, \sigma^2)$$

Y	response variable		$E(y) = X\beta$
β	fixed effects	fixed and unknown	
γ	random effects	random and unknown	$E(\gamma) = 0$
ε	error	unobserved and unknown	$E(\varepsilon) = 0$
X	fixed effects design matrix	fixed and known	
Z	random effects design matrix	fixed and known	

The design matrix X represents the so-called fixed effects. Effects which are random and uncontrollable enter the model, too, and are represented by the design matrix Z . These random parameters γ affect the response variable without being part of the fixed effect terms. To categorize, which effects are fixed and which are random, depends mainly on the goal. A handy example is the idea of a drug experiment: A pool of test persons is divided into a group getting drugs and into a group getting placebos. The separation makes the groups being *fixed* while the corresponding individuals will be *random*.

Fixed and random effects can be separated such that fixed effects are representing the APD pool in general while random effects represent parts of it like the single APDs which properties are able to vary across the APD pool.

A mixed models requires several assumptions: The residuals are centered around 0 with variance σ^2 [88]. Hence, the residuals must be normally distributed, must not be systematic and have to be homoscedastic, thus: $\text{Var}(\varepsilon_i) = \sigma^2 < \infty$. The latter requires the variance of the data to be approximately equal across the range of the predicted values. Furthermore, the errors are not assumed to be correlated: $\text{Cov}(\varepsilon_i, \varepsilon_j) = 0$. All these assumptions are known as “the Gauß-Markow assumptions”. The fixed effects $\hat{\beta}$ are estimated via BLUE⁷⁹ and the random effects $\hat{\gamma}$ via BLUP⁸⁰ [140]. The BLUE of $X\beta$ is

$$(X\beta) = X (X^T V^{-1} X)^{-1} X^T V^{-1} y \quad (4.1)$$

$$V = ZGZ^T + R \text{ with } R = \sigma I$$

Furthermore, the BLUP of $\hat{\gamma}$ is:

$$\hat{\gamma} = GZ^T V^{-1} (y - X\hat{\beta}) \quad (4.2)$$

which are both solutions of the HMME⁸¹:

$$\begin{bmatrix} X^T R^{-1} X & X^T R^{-1} Z \\ Z^T R^{-1} X & G^{-1} + Z^T R^{-1} Z \end{bmatrix} \begin{bmatrix} \hat{\beta} \\ \hat{\gamma} \end{bmatrix} = \begin{bmatrix} X^T R^{-1} y \\ Z^T R^{-1} y \end{bmatrix} \quad (4.3)$$

The linear mixed model is realized by using the lmer⁸² model within the lme4[43] package, available in R. Due to diode-to-diode differences within the diode measurements, the corresponding mixed model is unbalanced.

⁷⁹Best linear unbiased estimator

⁸⁰Best linear unbiased prediction

⁸¹Henderson’s mixed model equations

⁸²Linear Mixed-Effects Models

The estimated parameters $\hat{\beta}$, $\hat{\gamma}$ can be calculated by MLE⁸³ or REML⁸⁴. The $I(X, i)$ polynomials of lme4, where i is the polynomial degree, are correlated and lead to several problems, overall in regard to numerical stabilities. This is important when a model shall be regressed against higher polynomials. Using $poly(X, i)$ introduces **orthogonal polynomials**, $p_i \perp p_j$ with $i \neq j$.

12.1.4 Influence of single APDs

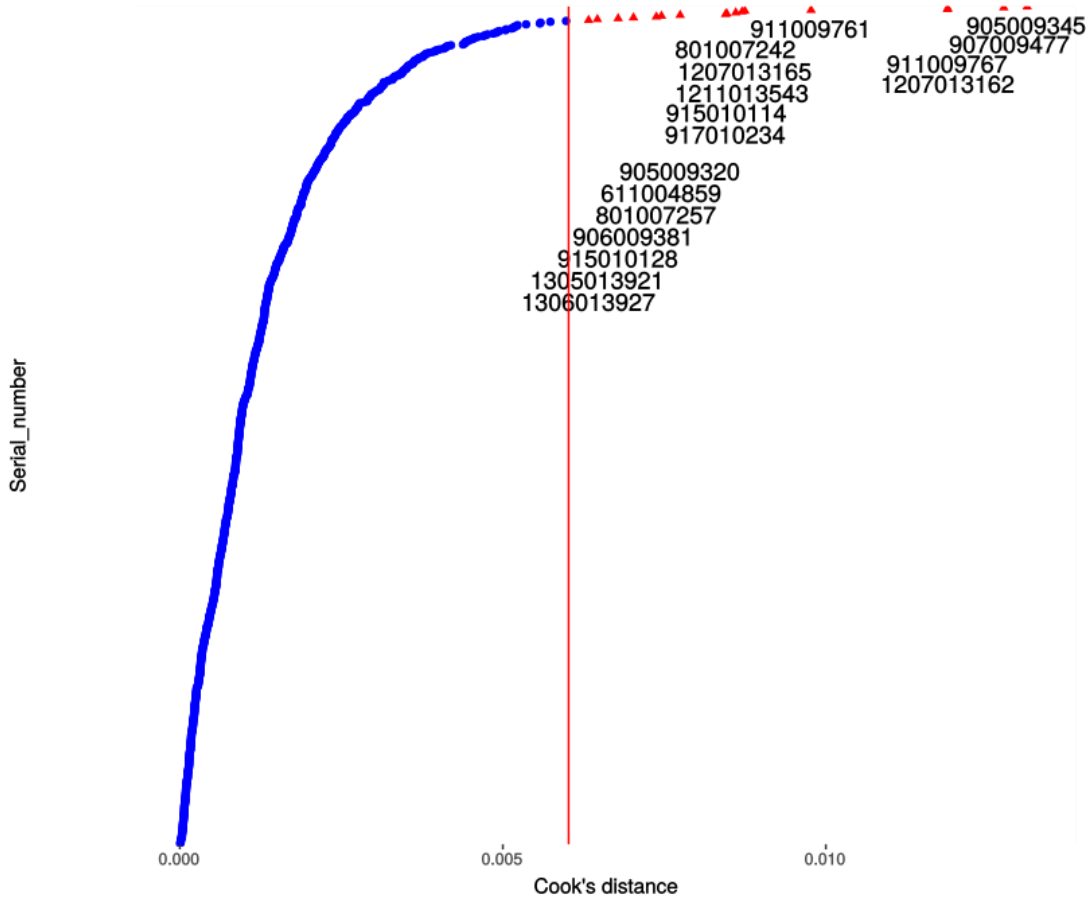


Figure 218: *Cook's distance of the APDs with respect to the mixed model regression.* 17 single irradiated APDs influence the model. Removing these APDs is not really expedient as each new model provides new influential APDs again.

⁸³Maximum Likelihood Estimation

⁸⁴Restricted (Residual) Maximum Likelihood Estimation

12.1.5 Residual plot of the lots

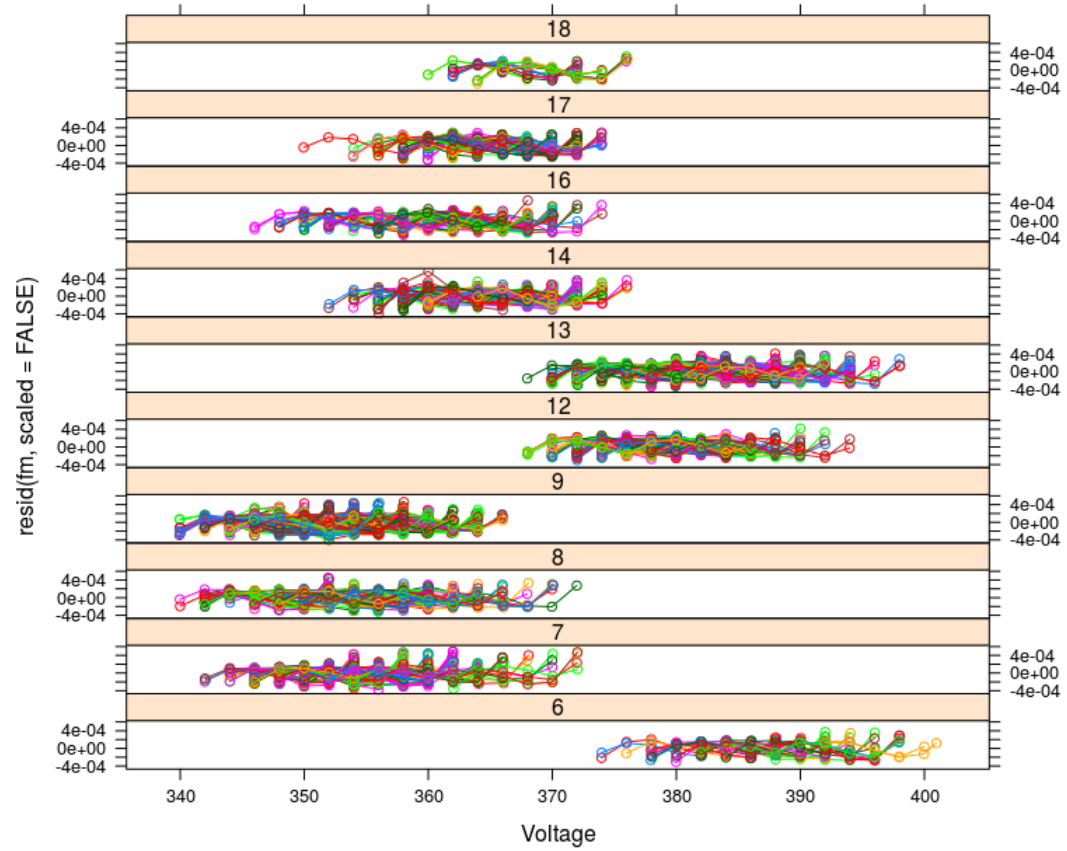


Figure 219: *Residuals of the lots over the voltage range.*

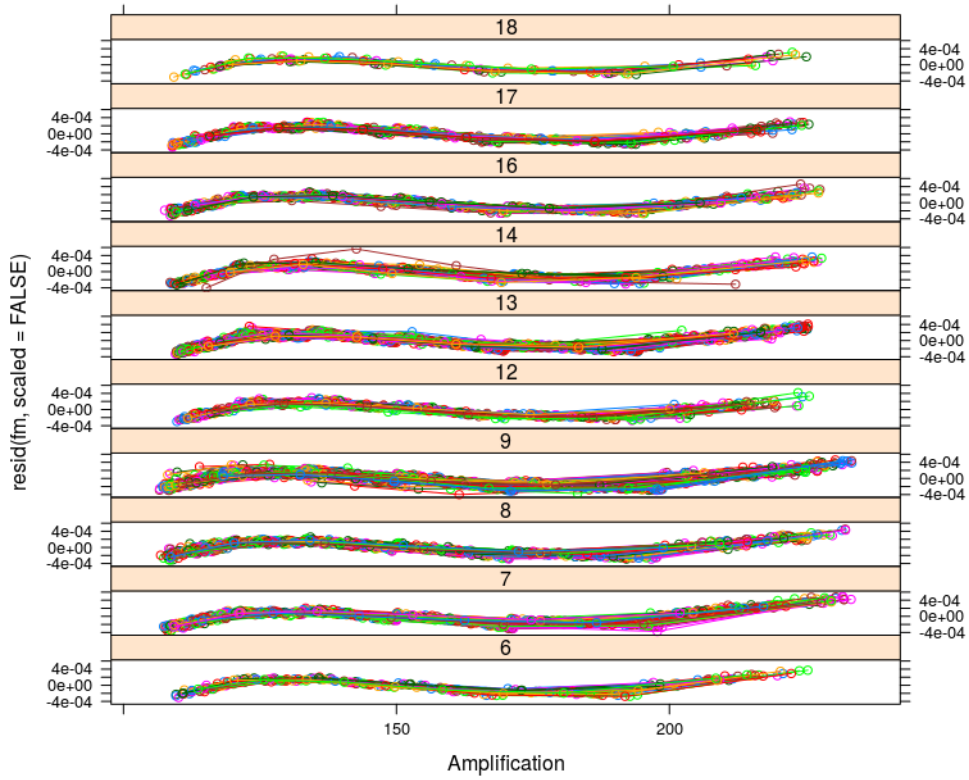


Figure 220: *Residuals of the lots over the amplification range.*

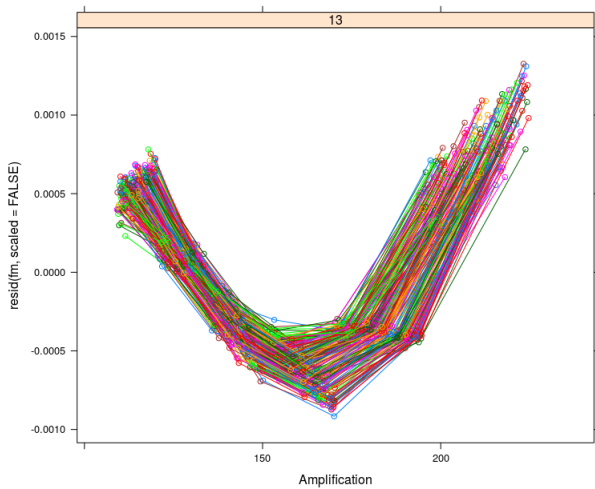


Figure 221: *Residuals of the lot 13 - polynomial of a mixed model with 2nd order.*

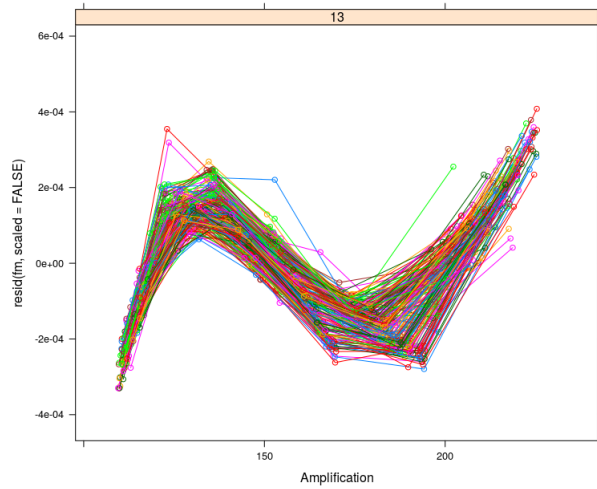


Figure 222: *Residuals of the lot 13 - polynomial of a mixed model with 3rd order.*

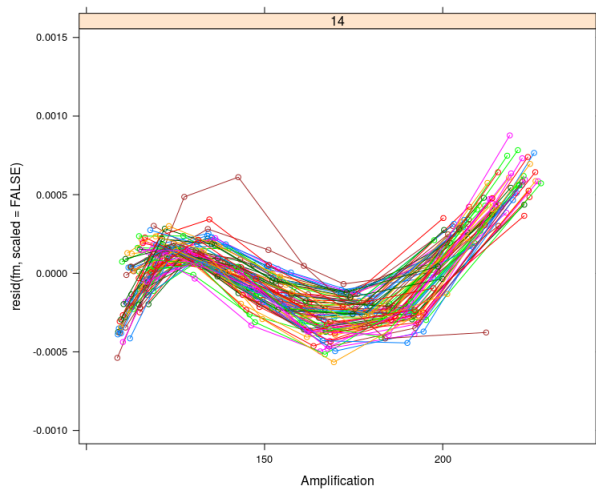


Figure 223: *Residuals of the lot 14 - polynomial of a mixed model with 2nd order.*

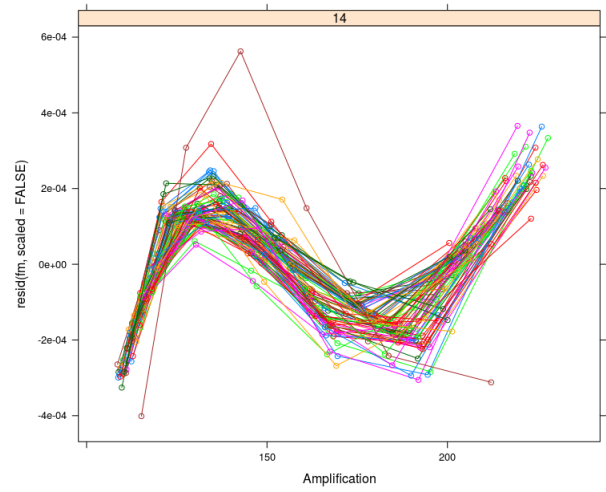


Figure 224: *Residuals of the lot 14 - polynomial of a mixed model with 3rd order.*

12.1.6 Q-point

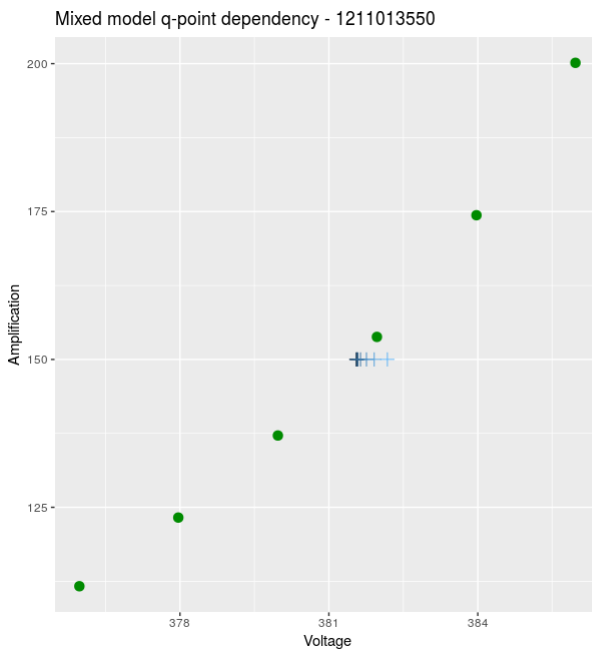


Figure 225: *Q-point of irradiated APD 1211013550 - mixed model.*

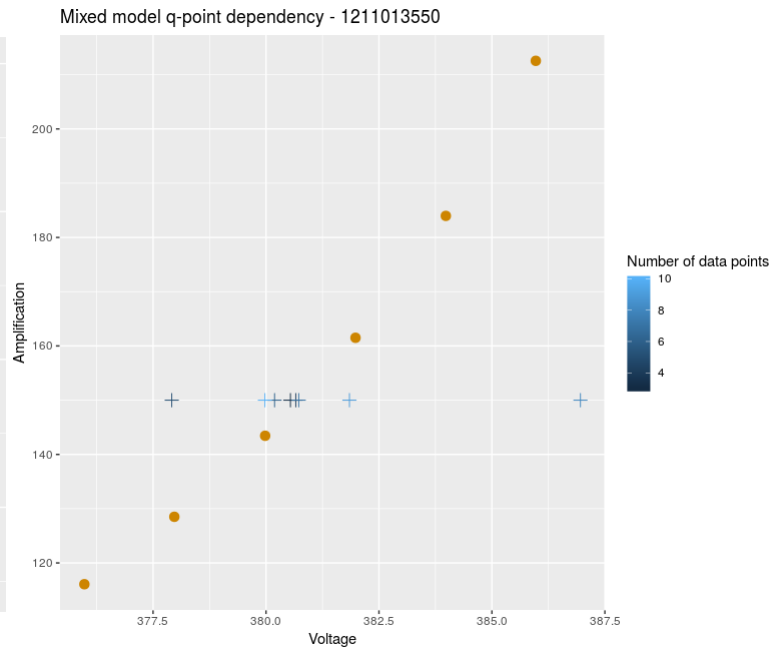


Figure 226: *Q-point of non-irradiated APD 1211013550 - mixed model.*

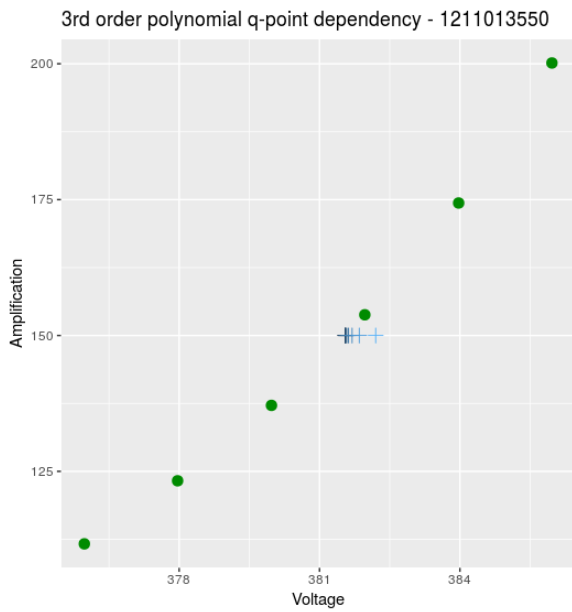


Figure 227: *Q-point of irradiated APD 1211013550 - polynomial 3rd order.*

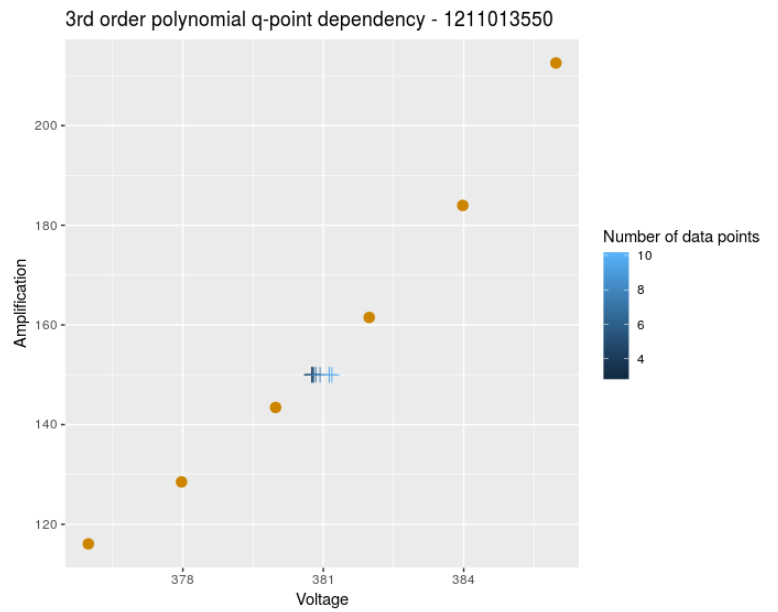


Figure 228: *Q-point of non-irradiated APD 1211013550 - polynomial 3rd order.*

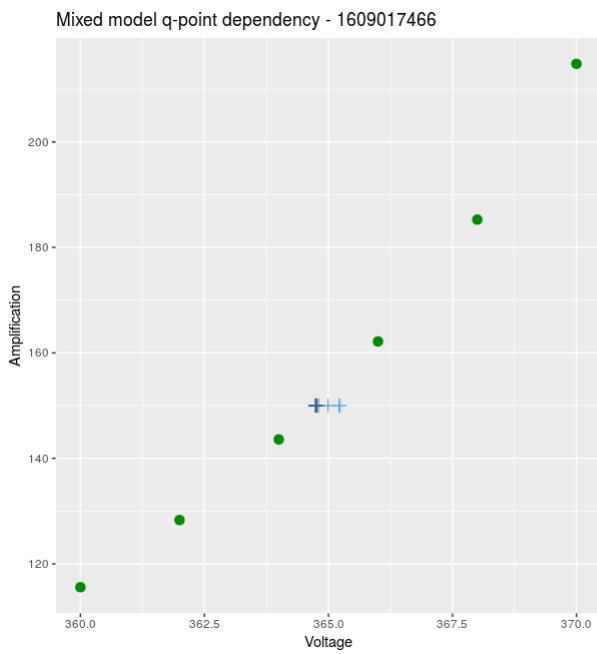


Figure 229: *Q-point of irradiated APD 1609017466 - mixed model.*

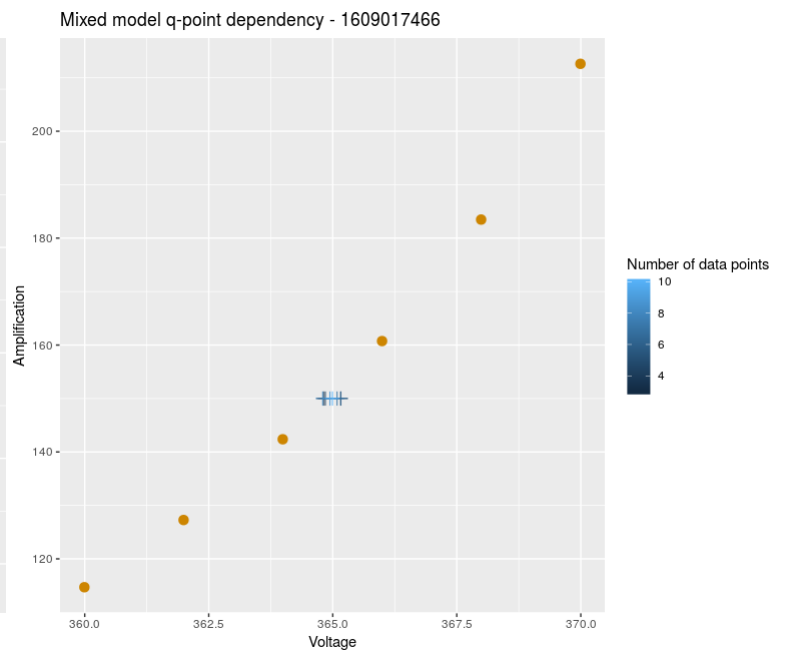


Figure 230: *Q-point of non-irradiated APD 1609017466 - mixed model.*

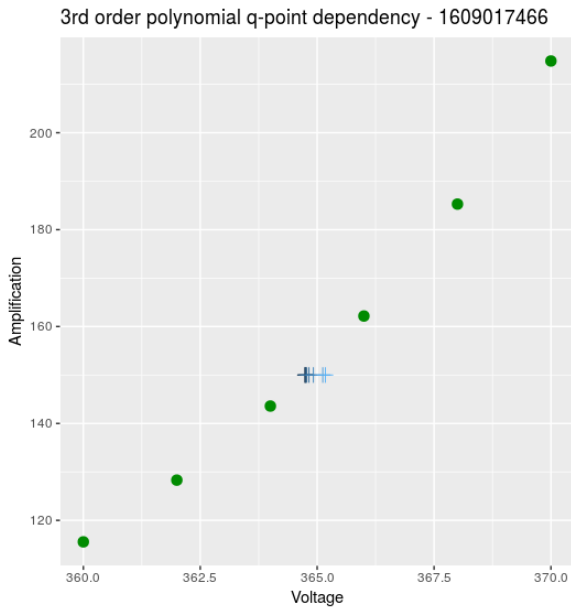


Figure 231: *Q-point of irradiated APD 1609017466 - polynomial 3rd order.*

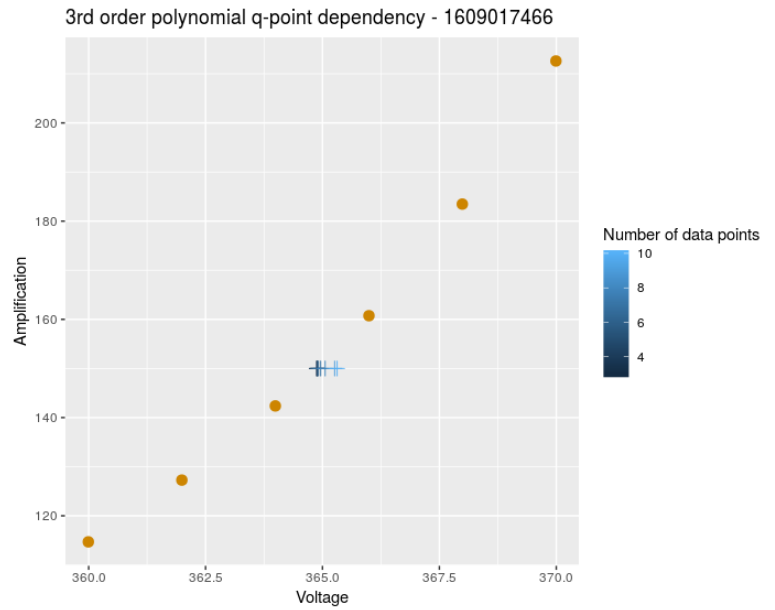


Figure 232: *Q-point of irradiated APD 1609017466 - polynomial 3rd order.*

It seems that, for the APDs 711006317 and 1211013550, the regular polynomial model is more robust against the number of data points. The mixed model is quite sensitive in case of the non-irradiated data. This might be related to the corresponding data set as it provides more outliers than the irradiated data set does.

12.1.7 Breakdown voltage

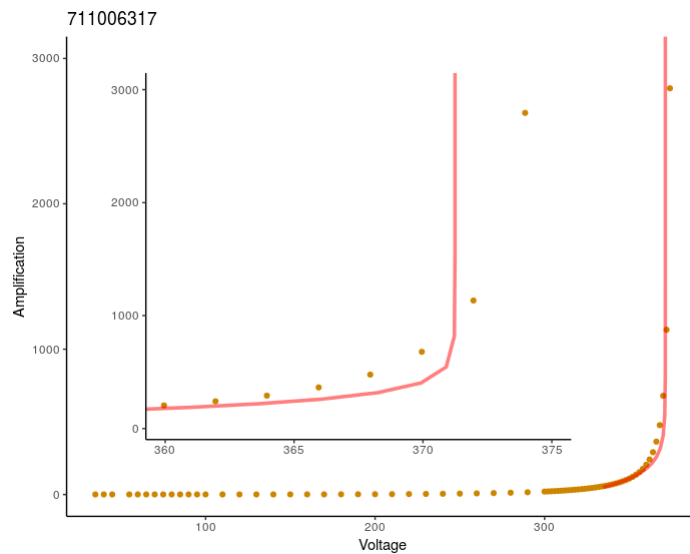


Figure 233: *Fitted breakthrough voltage - 711006317 - not irradiated.*

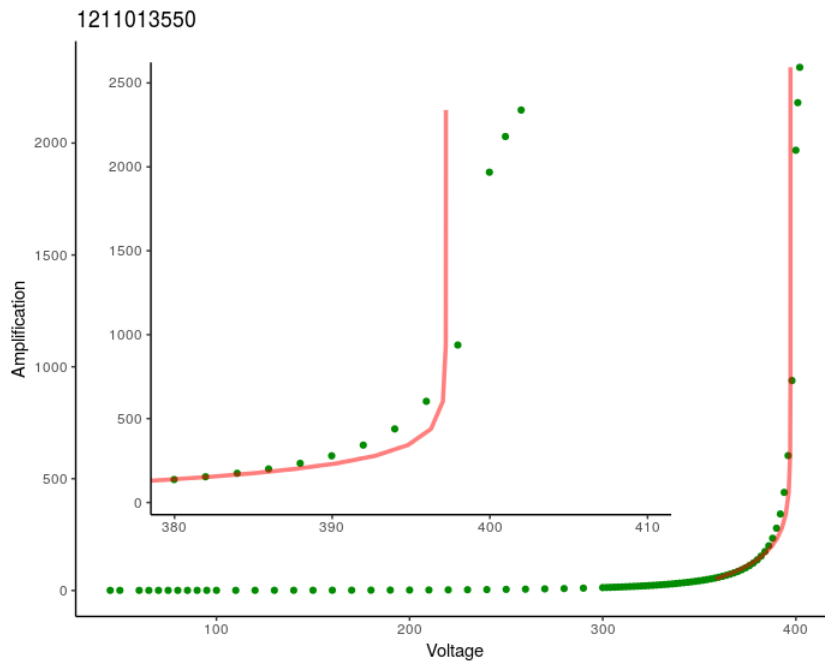


Figure 234: *Fitted breakthrough voltage -1211013550 - irradiated.*

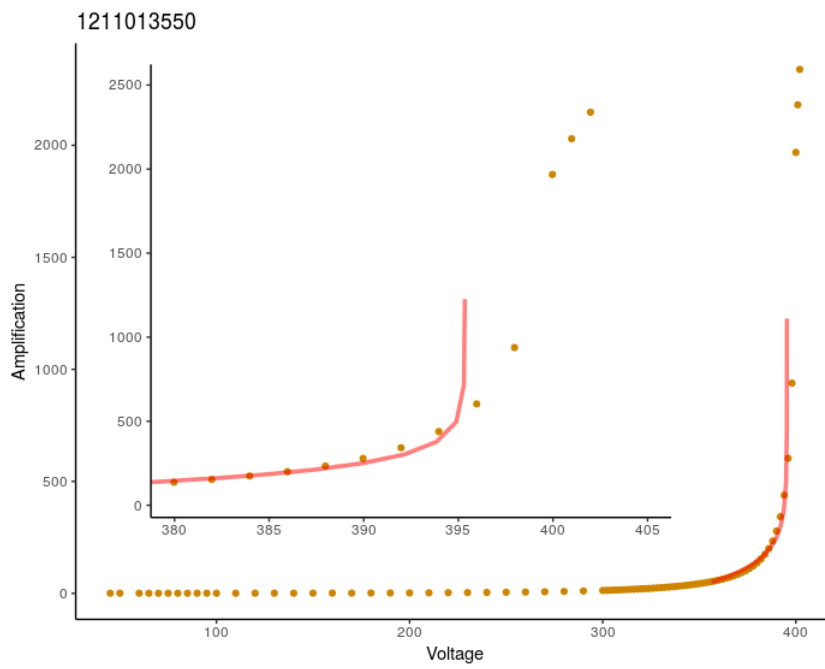


Figure 235: *Fitted breakthrough voltage -1211013550 - not irradiated.*

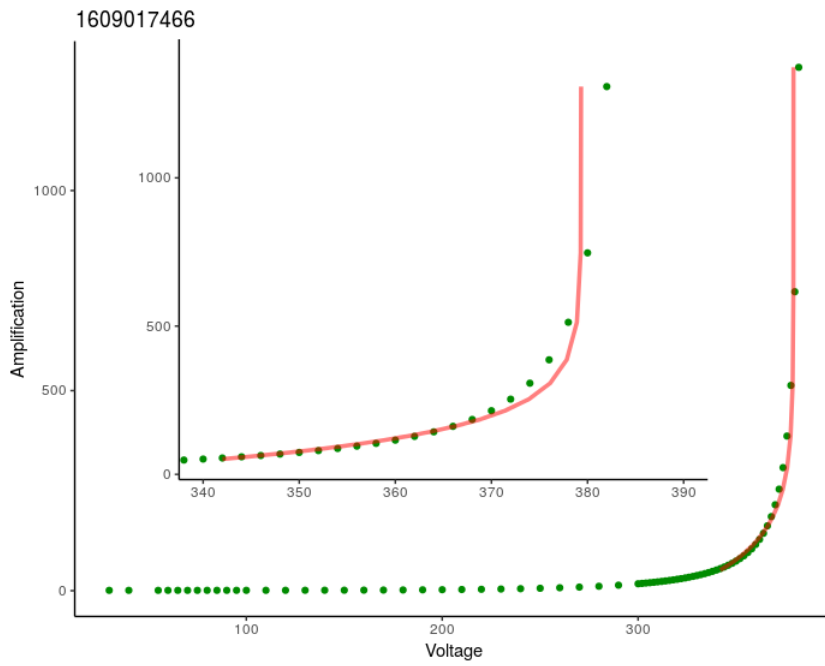


Figure 236: *Fitted breakthrough voltage -1609017466 - irradiated.*

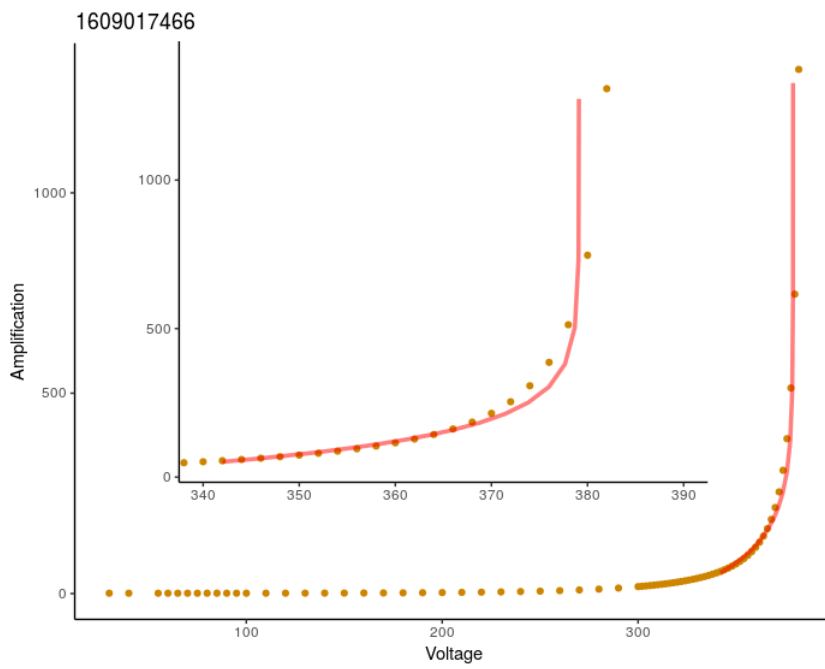


Figure 237: *Fitted breakthrough voltage -1609017466 - not irradiated.*

12.1.8 Parameters against lots

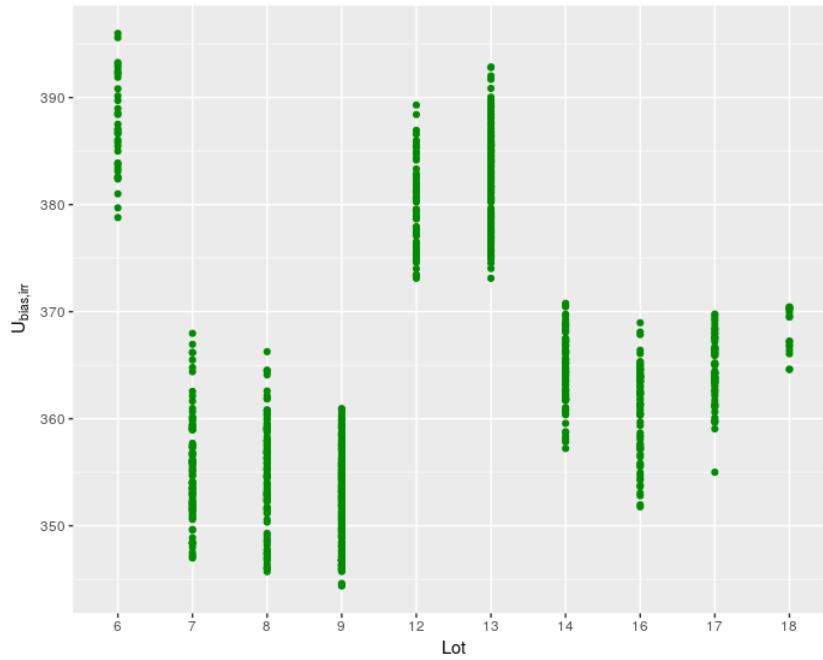


Figure 238: *Bias voltages of the irradiated APDs per lot.*

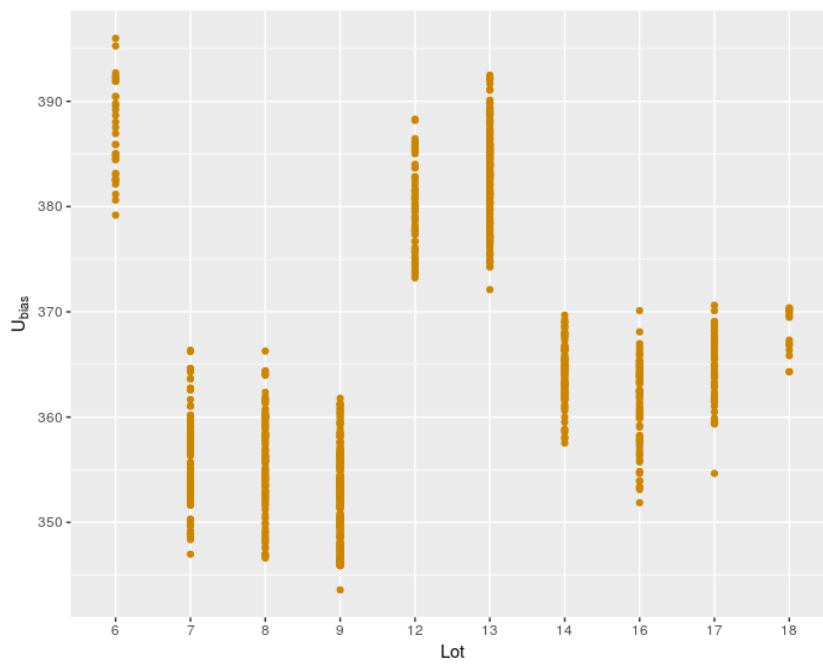


Figure 239: *Bias voltages of the non-irradiated APDs per lot.*

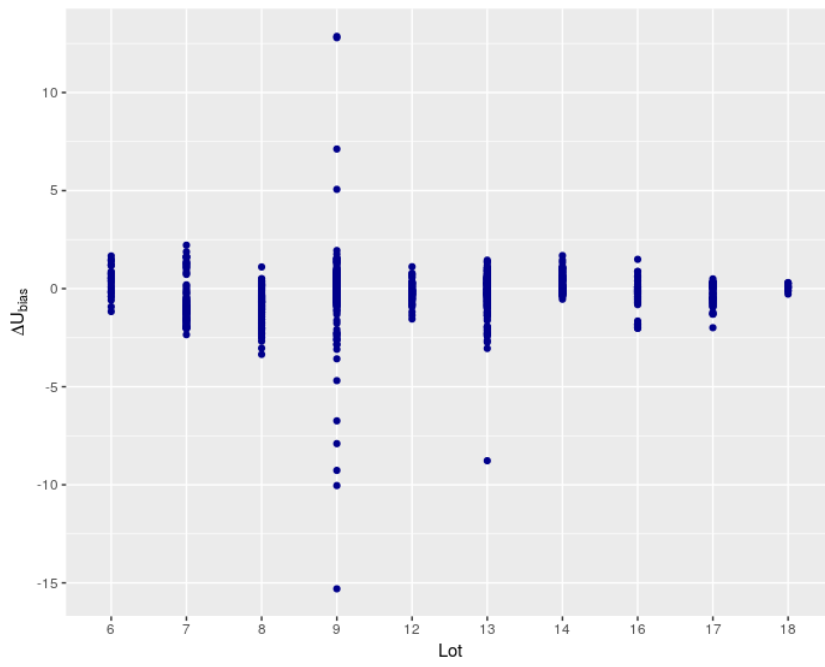


Figure 240: *Change of the bias voltages per lot.*

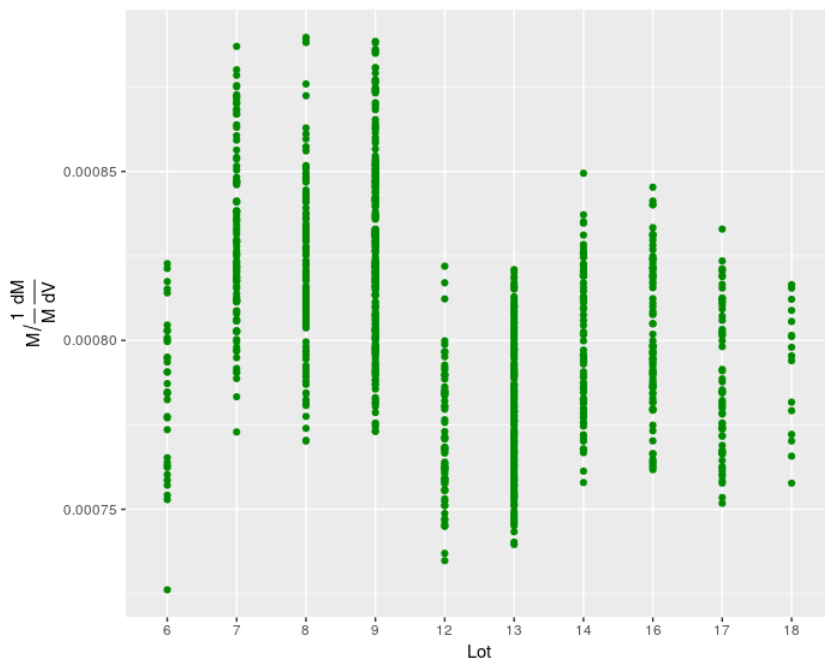


Figure 241: *Slope of the irradiated APDs per lots.*

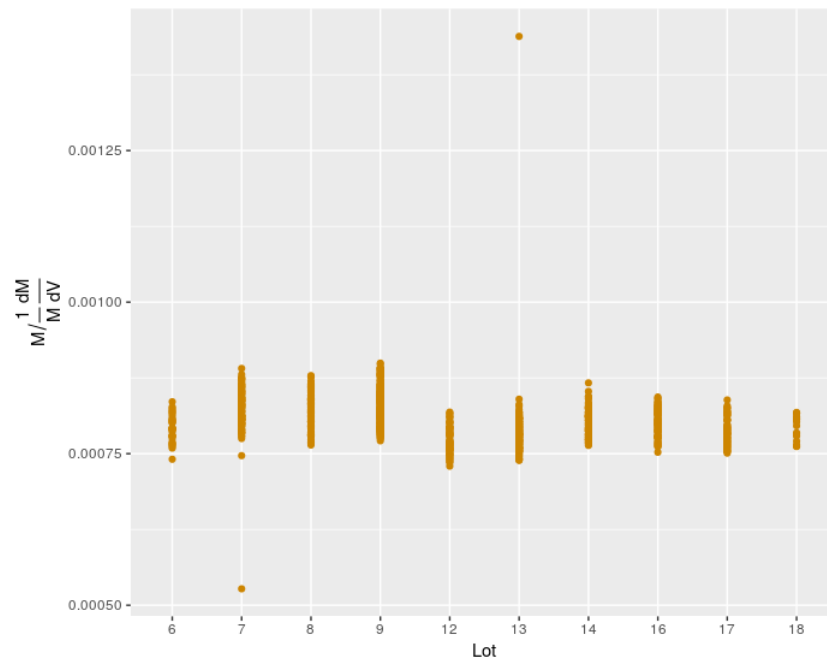


Figure 242: *Slope of the non-irradiated APDs per lots.*

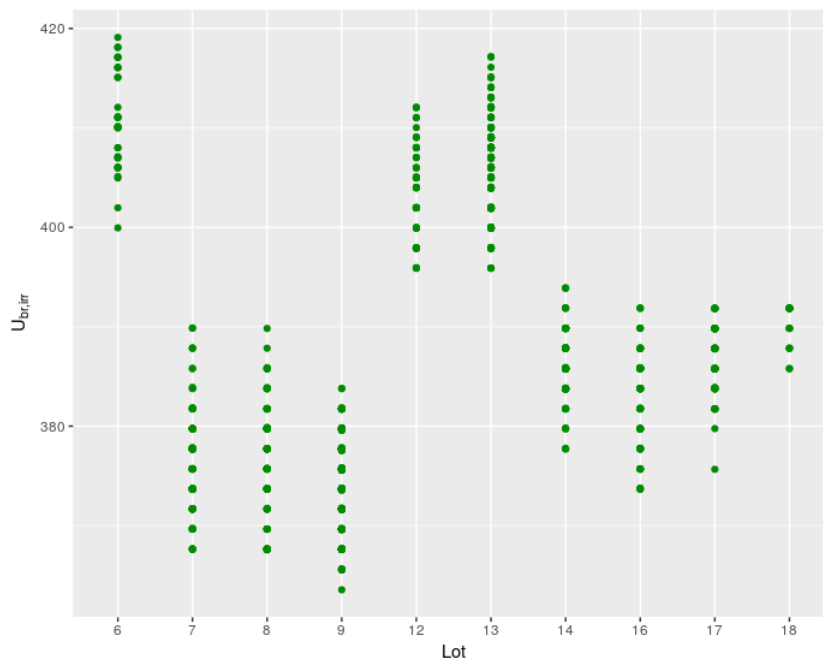


Figure 243: *Breakdown voltages of the irradiated APDs per lot.*

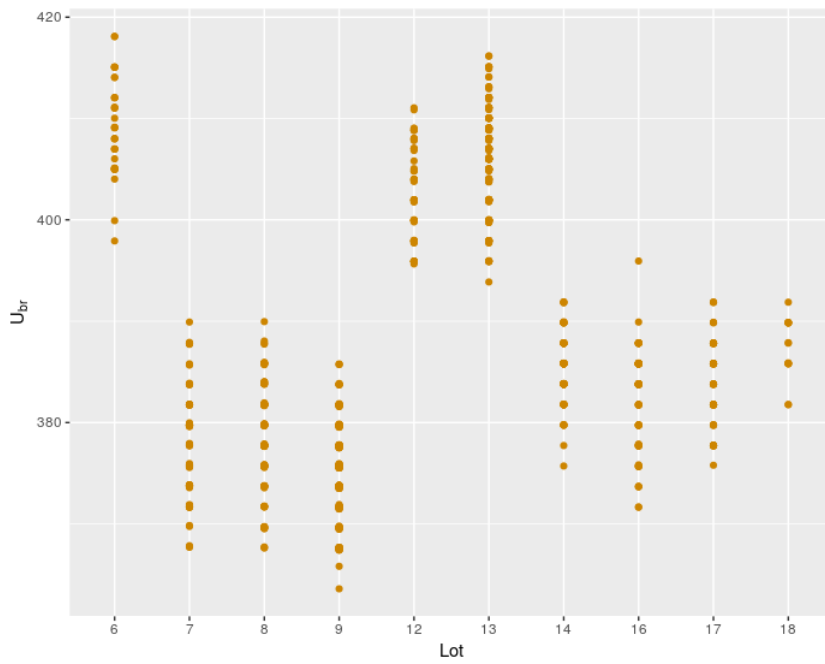


Figure 244: *Breakdown voltages of the non-irradiated APDs per lot.*

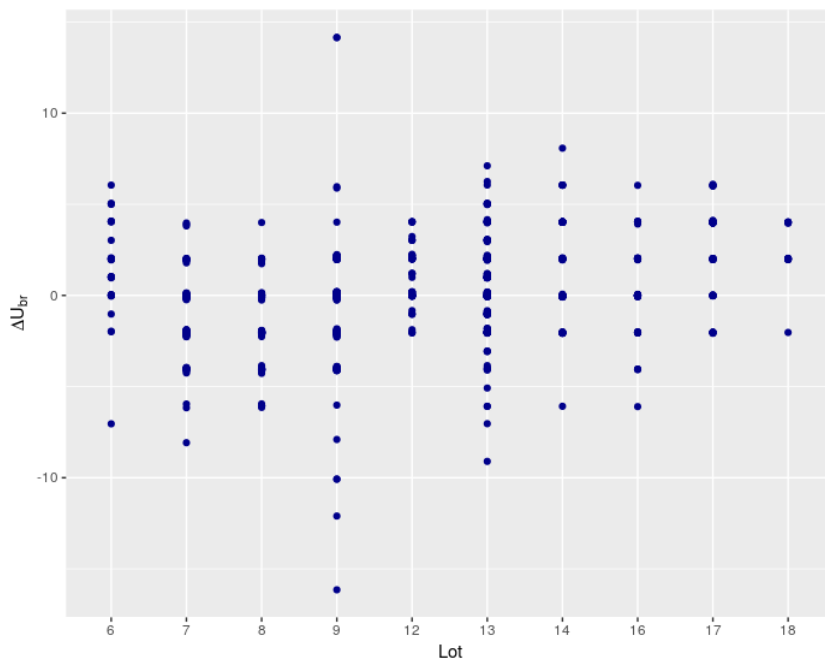


Figure 245: *Change of the breakdown voltages of the APDs per lot.*

12.1.9 Temperature

Though the temperature of the APDs is fixed at a temperature of $-25\text{ }^{\circ}\text{C}$ later in the experiment, the temperature behaviour of the APDs is checked and reveals a linear change of the bias voltage with the temperature:

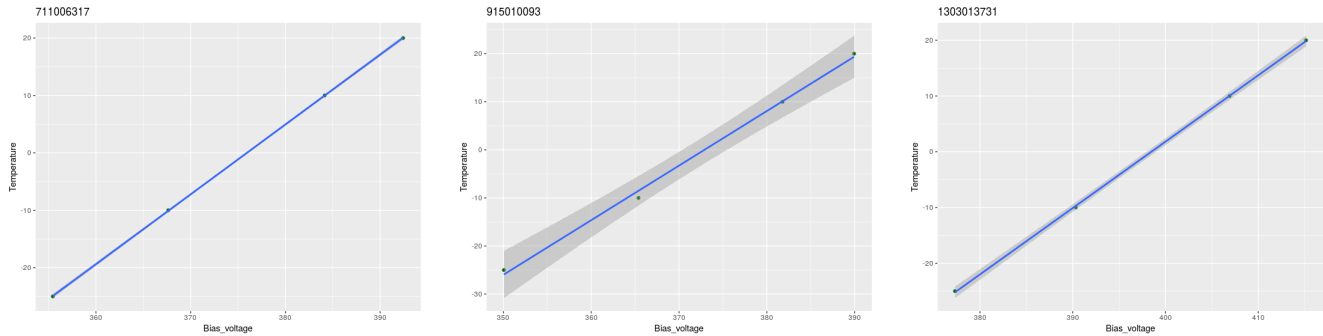


Figure 246: *The change of the bias voltage due to temperature changes.* A confidence interval of 95 % is applied.

The APD pool behaves very similar:

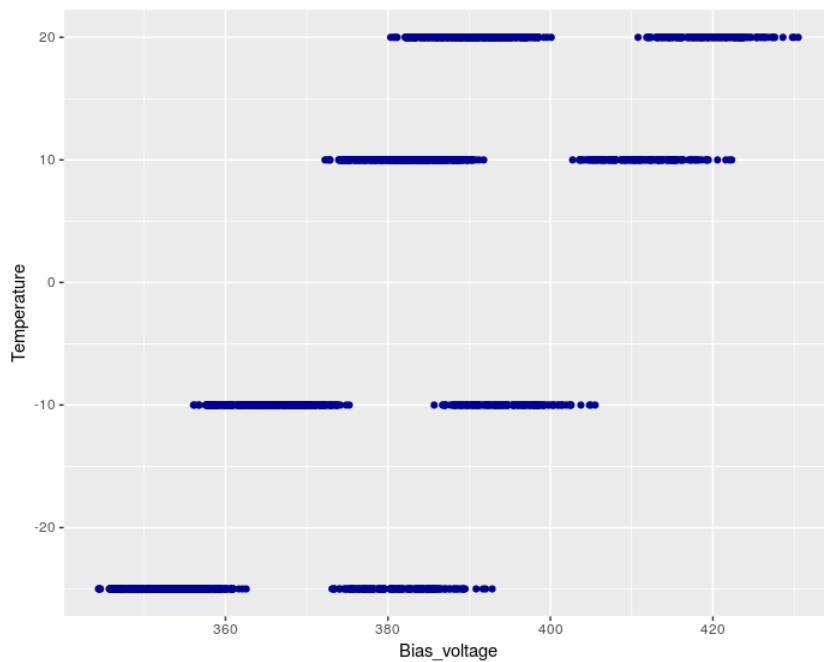
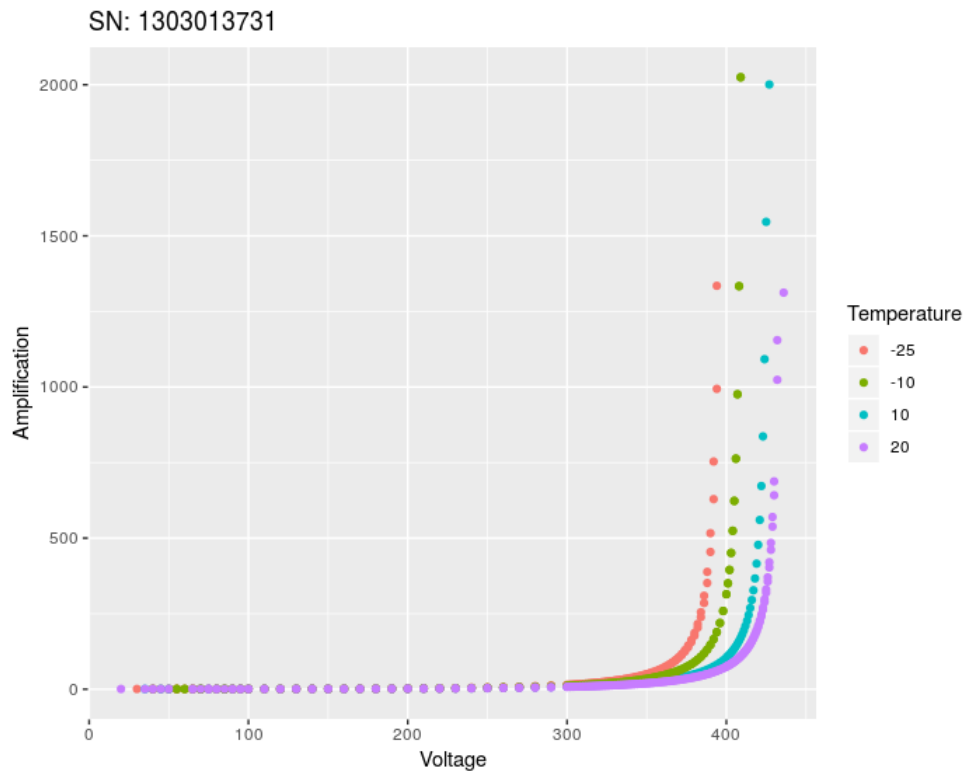


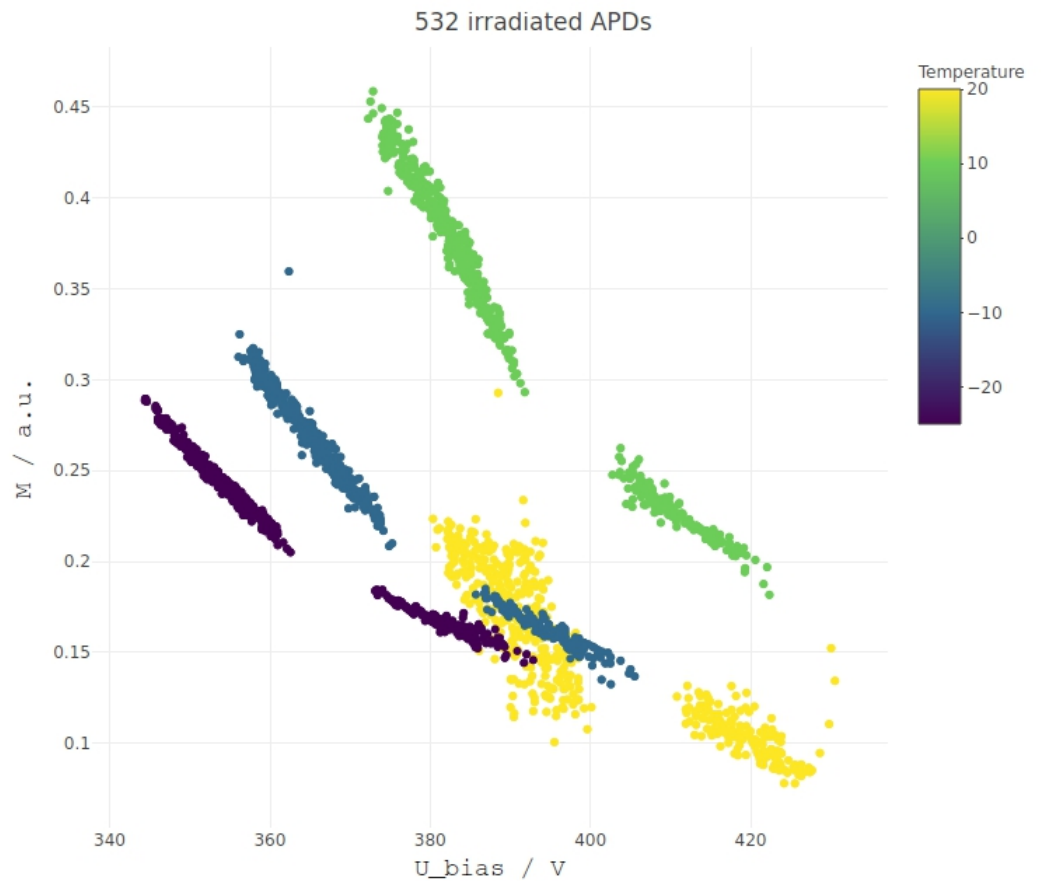
Figure 247: *The change of the bias voltage of 532 APDs due to temperature changes.* Only 532 APDs in total provide data for all four temperatures. It is not considered, whether these APDs are part of those 1,000 APDs which are analyzed here in this work to be able to take into account as most as possible APDs.

Figure 248: *APD 13103013731-irradiated*. The $M - V$ curves of the single APD show that temperature changes cause a constant shift in the x axis.



In fig. 249, the parameter space of the 532 irradiated APDs in fig. 247 is depicted:

Figure 249: *Temperature behaviour*. Some data could not be fitted with a polynomial of a third degree (for example, the data at $T = 20^\circ\text{C}$), therefore, to make a comparison possible, the APDs are fitted with the mixed model. These APDs are 532 arbitrary ones for which data at different temperatures exist. Here, the slopes are not normalized by the amplification gain of 150.



12.2 Assignment & Matching

12.2.1 Similarity measure

Figure 250: **Outlier across lots.** The Mahalanobis distance as a function of the lots. Here, the similarities between the APDs are measured with the entire pool as a reference which yields exactly 600 APDs to be within 3 standard deviations.

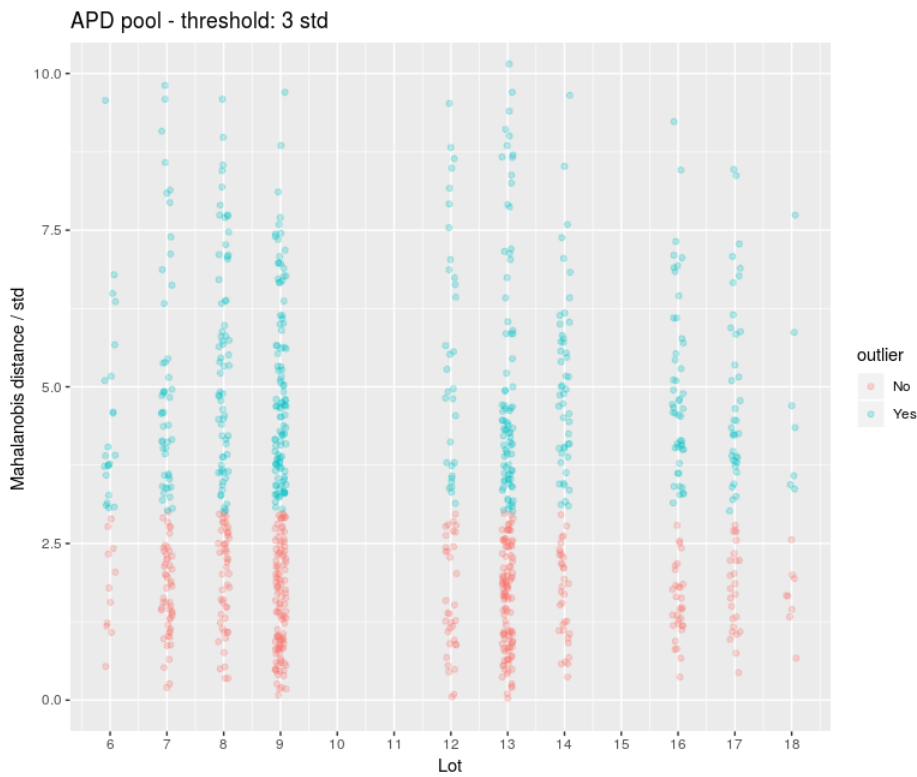
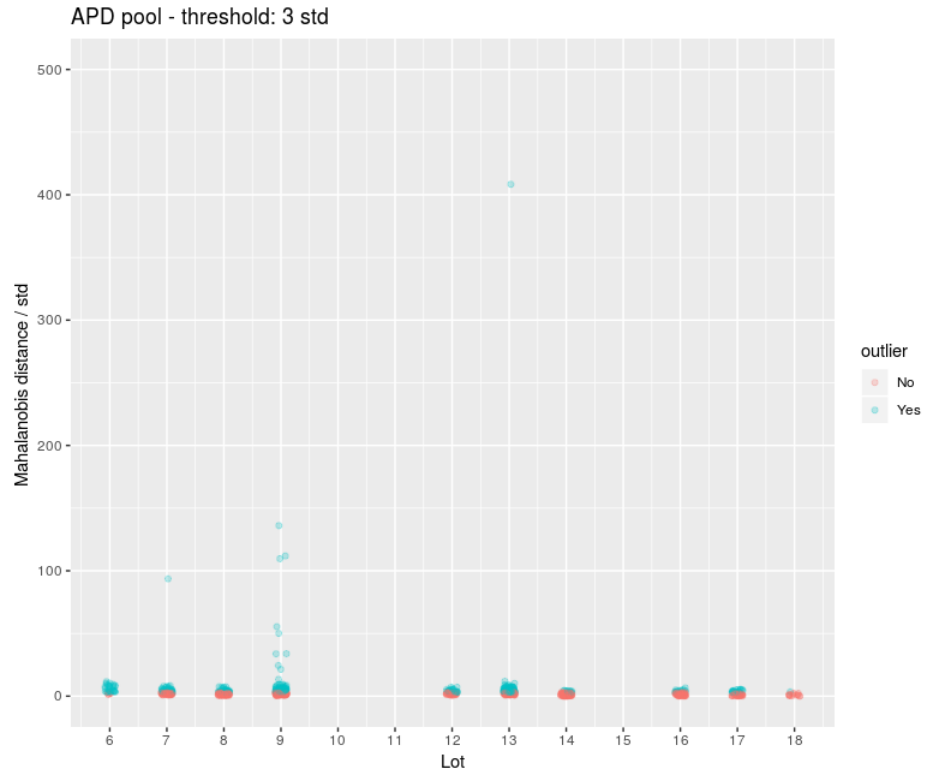


Figure 251: **Outlier per lots.** The similarities are measured within the lots and not within the entire pool now. This means, the similarities of the APDs are checked if they can statistically be treated as part of the lot they belong to. Now, only 471 APDs are within 3 standard deviations.

12.2.2 Influence of irradiation

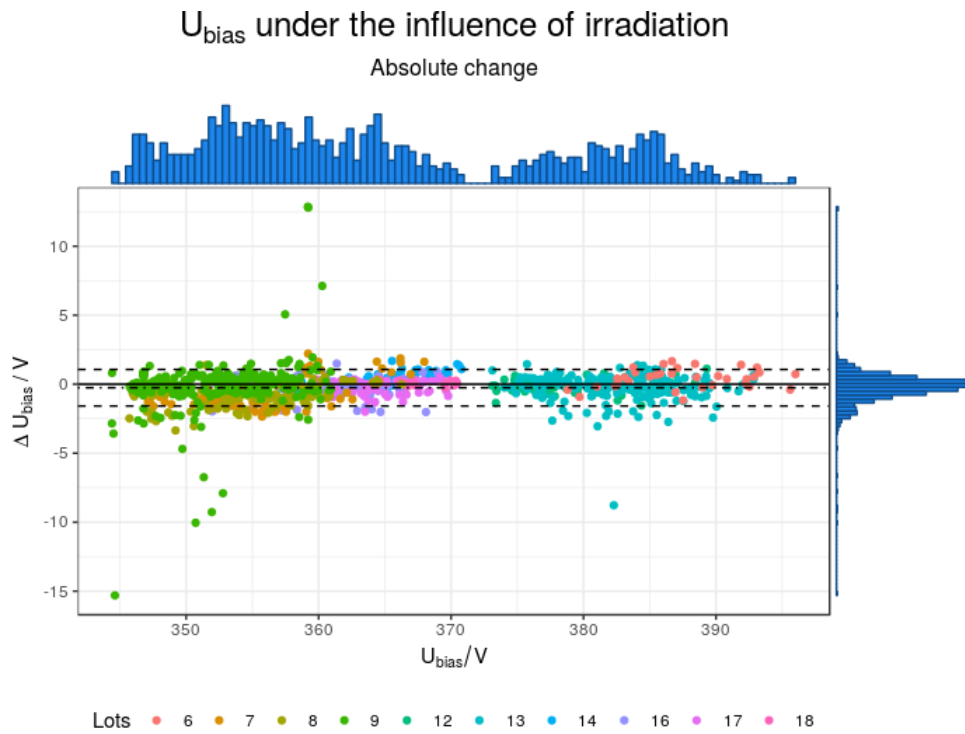


Figure 252: *Absolute change of U_{bias} under the influence of irradiation.* Absolute change in Volt. The lines mark a deviation of 1 std.

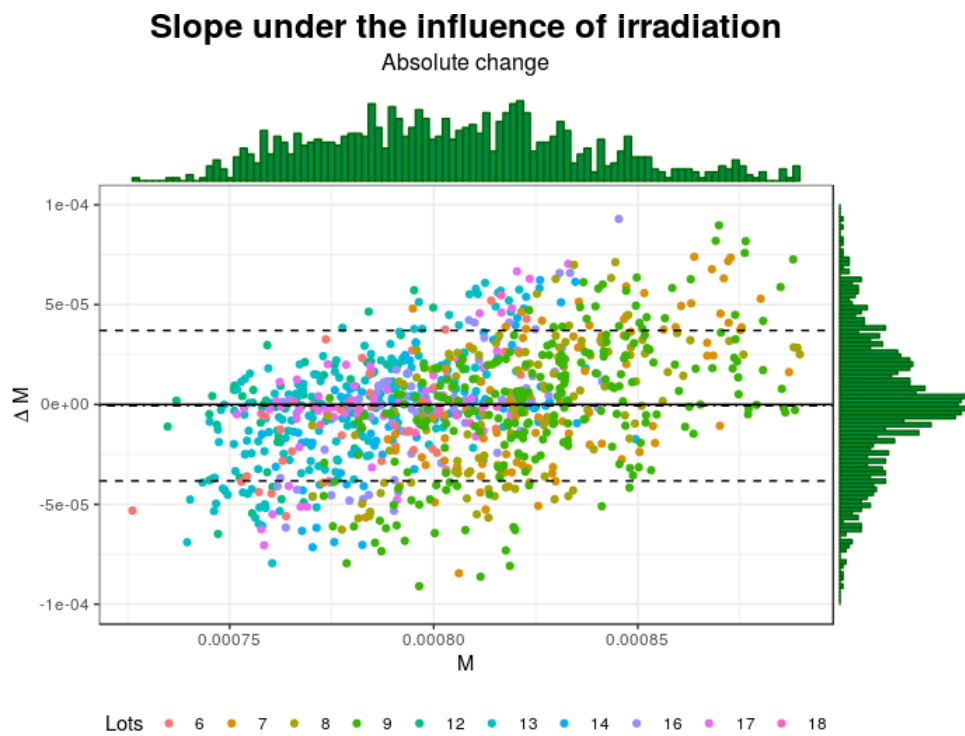


Figure 253: *Absolute change of dM under the influence of irradiation.* Absolute change in $1/M (dM/dV)$. The lines mark a deviation of 1 std.

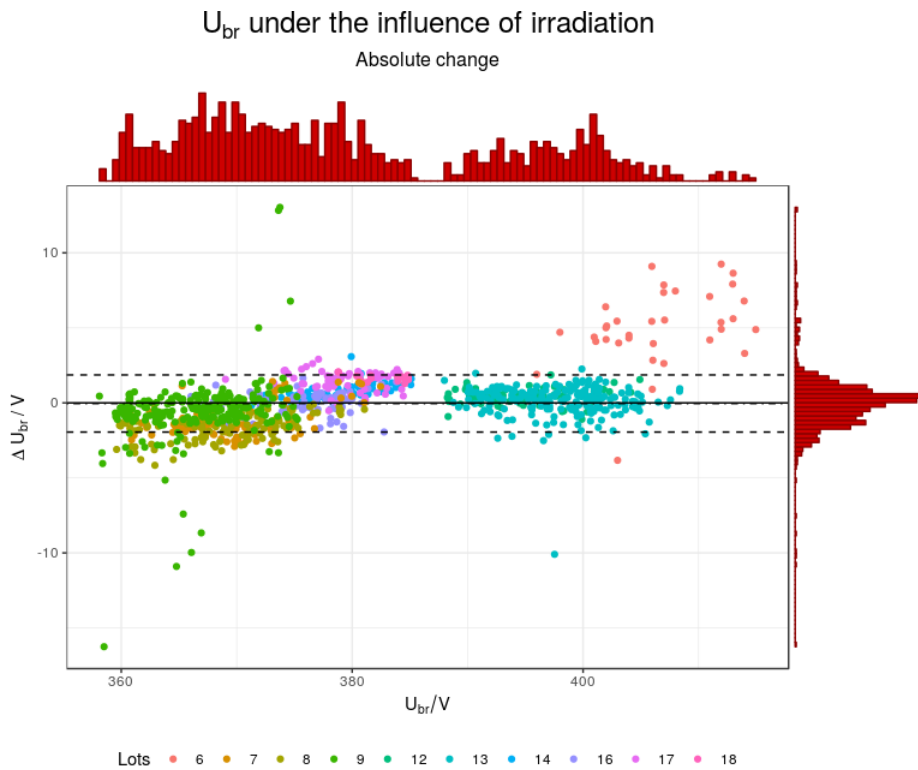


Figure 254: *Absolute change of U_{br} under the influence of irradiation.* The lines mark a change of 1 std.

12.3 Graph theory

A graph G is a structure such that a set of objects is represented together with connections between them. Systems which can be described by graphs are called a **network** [90]. A graph G is a two-element pair and defined as following: $(V, E) : V = X \cup Y \wedge E \subseteq X \times Y$ with V as a set of vertices and E as a set of edges where E and V are disjoint. The vertices, also called nodes, are connected to each other by the edges. Two vertices are adjacent or neighbouring if they are endpoints of the same edge. Hence, an edge is incident with the vertices when it connects them.

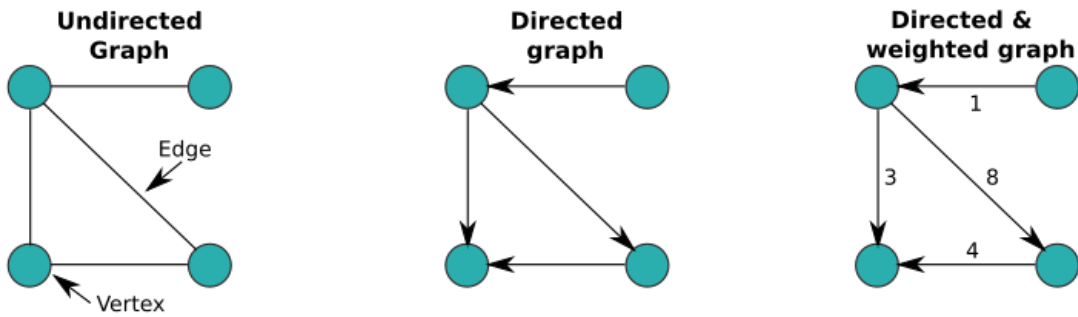


Figure 255: *Graphs.* Weighted graphs can also be undirected

An undirected graph $G = (V, E)$ is a two-element unsorted pair: (V, E) and a directed graph $G = (V, E)$ is a two-element sorted pair: $\{V, E\}$. In addition, edges can be **weighted** and be assigned with a real number. Edge-weighted graphs can be directed or undirected. Given the vertices A and B with $A \neq B$, then the distance from vertex A to vertex B is called an edge ab , or also path ab . The number of edges that leave or end in a vertex is called the **degree** of a vertex.

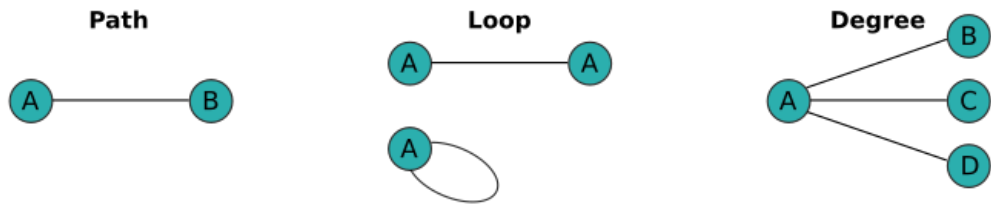


Figure 256: **Vertices**. The degree of a vertex is given by the number of its incident edges

A **path** consists of a sequence of edges, where vertices are different and in which each edge occurs only once. A closed path, i.e., where start and end vertices are identical, is called a cycle. A graph, where each vertex is connected with each other vertex is a connected graph.

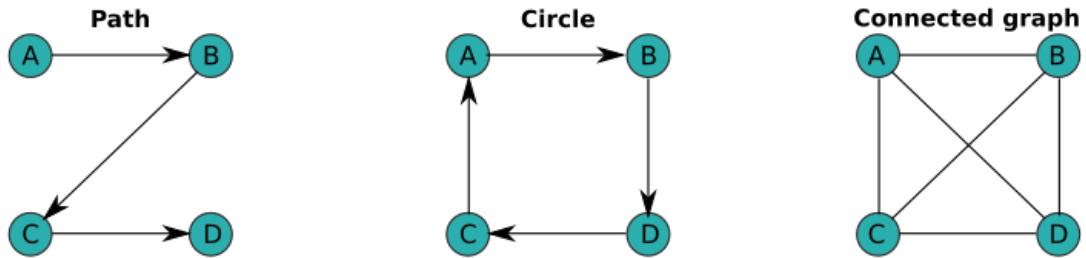


Figure 257: **Walks**. A circle is a closed path.

A path is an **alternating path** with respect to M when its edges are alternating between M and G . If the first and last edges of an alternating path are not edges of a matching, then this path is an **augmenting path** in M . Hence, the first and last vertex of an alternating path have to be exposed. By swapping the matched and not matched edges of the augmenting path, the matching can be enlarged. A graph without any cycle is called a **tree** [39]. If this tree provides a vertex from where all other vertices can be reached then this vertex is called a root. A graph with disjoint trees is a **forest**.

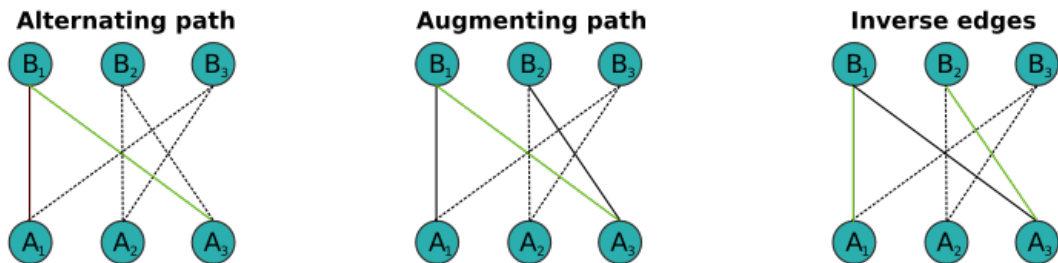


Figure 258: **Paths**. A search along alternating paths for an augmenting path often tends to exchange the edges which are in M . This will increase the matching M by one edge.

A graph $G = (V, E)$ is called p -partite, $p \geq 2$ and $p \in \mathbb{N}$, when $V(G)$ can be divided into p disjoint sets of edges V_1, \dots, V_p . Such sets are called partitions of the graph. Within such a set, the vertices must not be connected. A set of vertices U of G is called a vertex cover of G if all edges of G are incident to at least one vertex of U . If no other vertex cover U^* of G exists with $|U^*| < |U|$, then U is the minimum (edge) vertex cover of G . A vertex v is covered if $v \in U$.

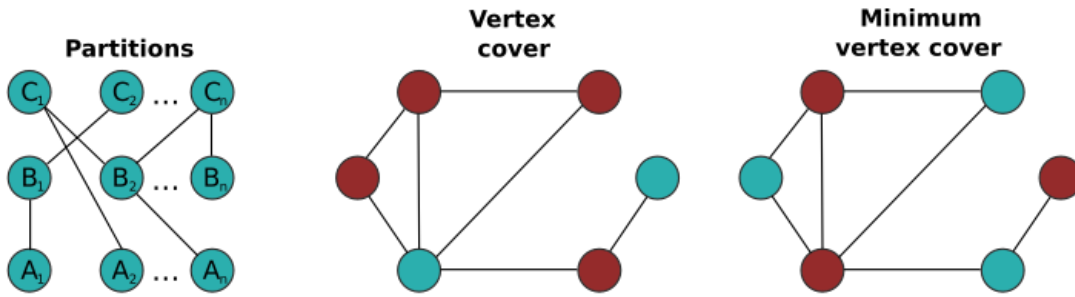


Figure 259: **Partitions and cover.** A minimum vertex cover colors not more vertices as necessary.

A matching M in G is a set of pairwise non-adjacent edges and means that no two edges share the same vertex. There are different types of a matching: The maximal matching, where the matching cannot be augmented such that there is an edge $e \in E \setminus M$, the maximum matching which represents the highest possible number of edges and the perfect matching providing a matching without any free vertices and edges. Then it is $2 \cdot |M| = |V|$.

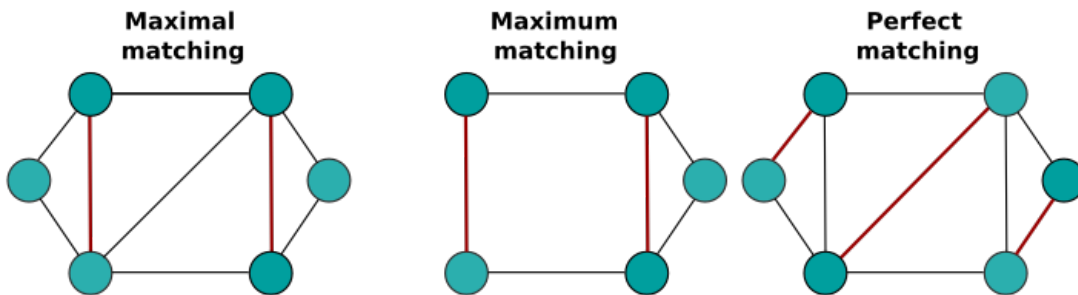


Figure 260: **Matchings.** A perfect matching can only exist at an even number of vertices.

12.4 Adjustment to a single set

The concept of “The Hungarian Algorithm with a Single Input Set” [48] is realized by modifying a framework for the regular Hungarian method from [159]. In principle, the idea is to mirror some steps of the initial implementation as following:

1. Find arbitrary, maximal matching - *same*
2. When augmenting a path, edges will also be added to a second matching M'
3. Check root tree for augmented path - *same*
4. Enlarge matching through exchanging the edges, stop when $M \cup M'$ is perfect

This “mirrored matching” can be sketched and looks like:

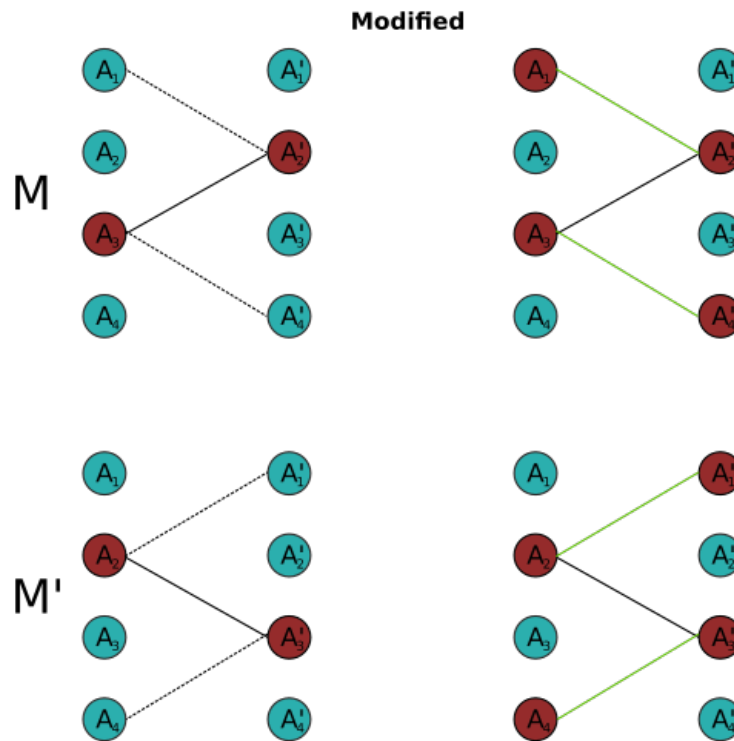


Figure 261: *Adjustment to a single set*. M represents the regular matching and M' contains the mirrored edges which enter M' each time an edge is added to M .

Considering only one of both matchings, either M or M' , then there is in principle no difference to the initial implementation as the underlying procedure is on its own basically the same. The unmodified algorithm terminates when the number of edges in M is half the number of vertices of G . To apply it on a single set, the single set A will be copied and labelled as A' . Both sets represent the same objects. The adjustment to a single set input requires that each time an edge (a_i, a'_j) is added to M , a second one, (a'_j, a_i) , will be added to M' (see fig. 261). This second edge can be seen as a “mirrored” edge. It turned out that this approach cannot extend the Hungarian method to be able to handle unipartite sets as it leads to several issues: For example, the algorithm assigns $A1 \leftrightarrow A'2$ and $A3 \leftrightarrow A'4$ in M , then also $A2 \leftrightarrow A'1$ and $A4 \leftrightarrow A'3$ in M' . The algorithm has to end because there are no other exposed vertices left. As consequence, this procedure cannot check whether there are better assignments available as it quits when $V/2$ iterations are reached. In case it will not finish before V iterations are performed, then either M is the same as M' or, more likely, many vertices cannot be coloured correctly or marked as an exposed vertex because they are already part of one of both matchings. Furthermore, depending on the searching method, here it is BFS, it can happen that self-loops will be generated (see fig. 262):

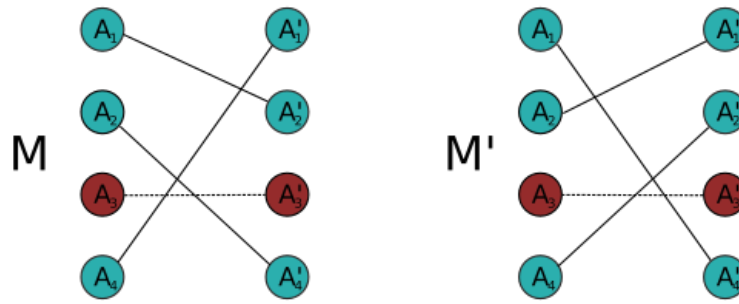


Figure 262: **Self loop.** A problem occurs that when the graph is not bipartite. Then, self loops can be constructed. This issue is not solved by the *Adjustment to a single set* as it does not uses mirrored edges. For example, the edge (a_3, a'_3) is allowed in a bipartite graph and the mirrored edge (a'_3, a_3) will not prevent this problematic scenario.

A workaround is to force the algorithm to terminate, for example, after $V/2$ iterations but then the constructed tree cannot take into account all APDs and will quit with a certain amount of remaining un-assigned APDs. But in most cases, e.g., when V iterations have to be performed, it will never terminate as it will run into an odd-length cycle which does not happen in a bipartite graph as its absence is fundamental there. Finally, this concept leads to the problem that either the algorithm does not terminate, it will assign APDs twice, generate self-loops or it will end at a local optimum. In the end, the basic idea violates the requirement of the Hungarian method with respect to the need of bipartite sets and, thus, it is not possible to be applied on an unipartite graph.

12.5 Results

12.5.1 Distance scan

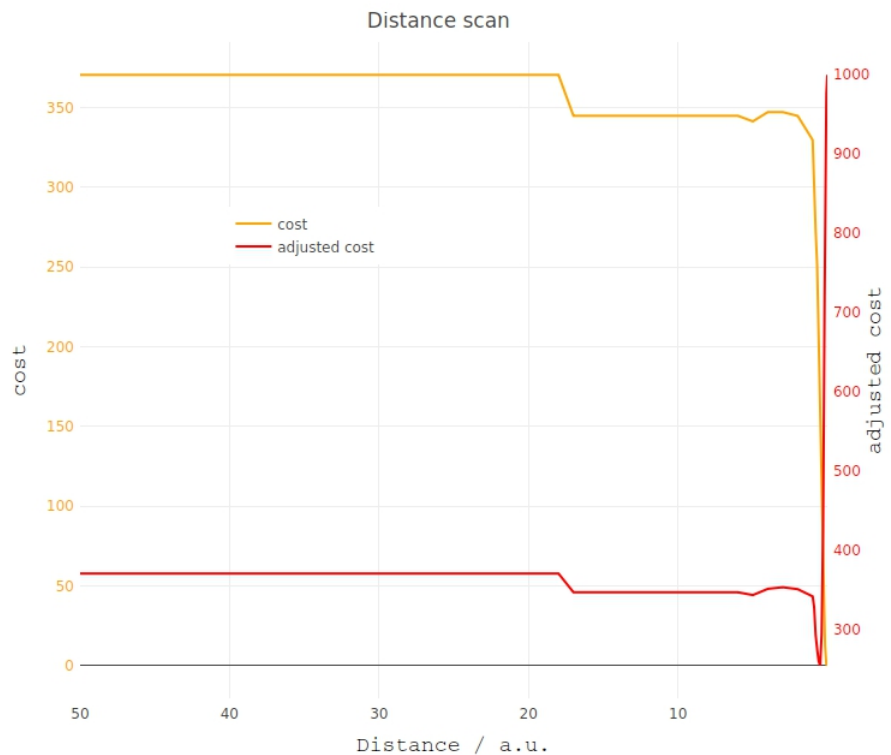


Figure 263: **Full distance - cost against adjusted cost.**

Figure 264: *Distance in the range from 5 to 0 - cost against adjusted cost.*

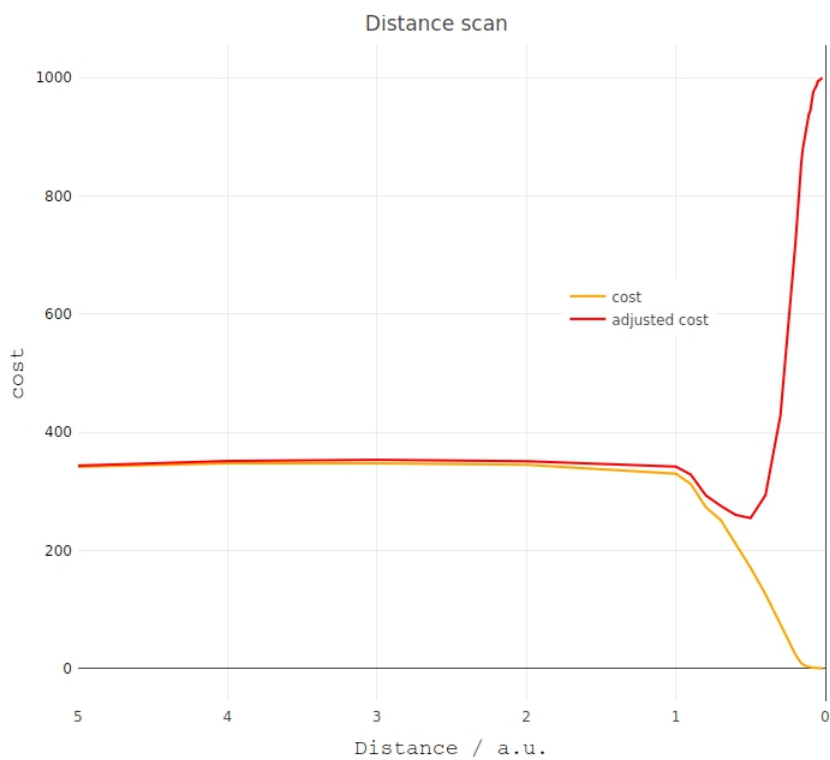
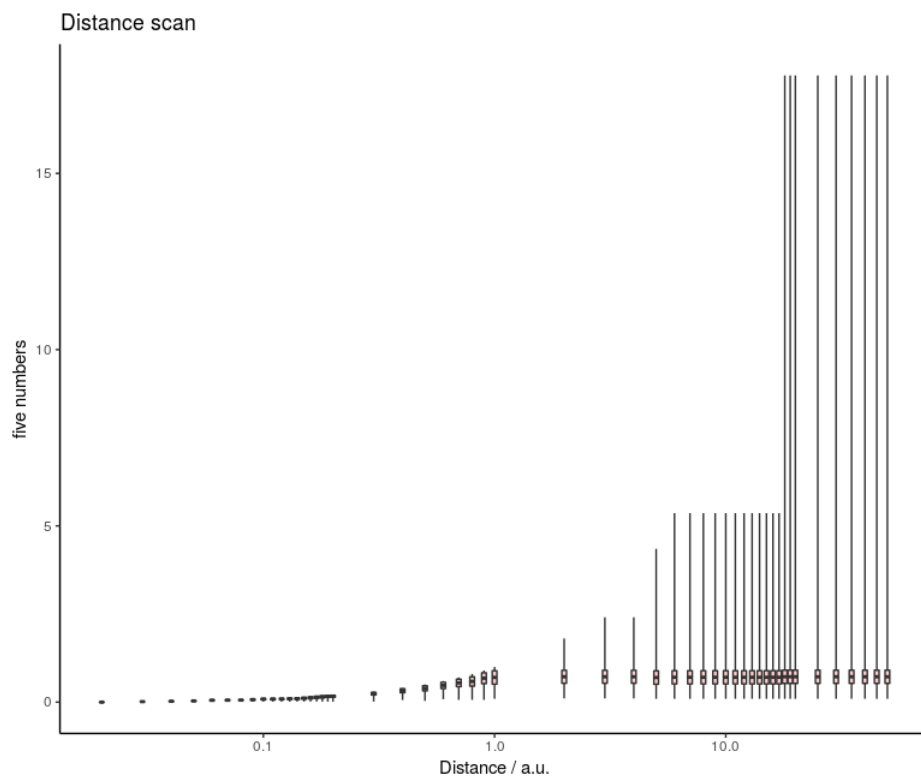


Figure 265: *Five numbers in the full distance range.*



Voltage difference between the pairings:

Constrictions: $d < 0.5$

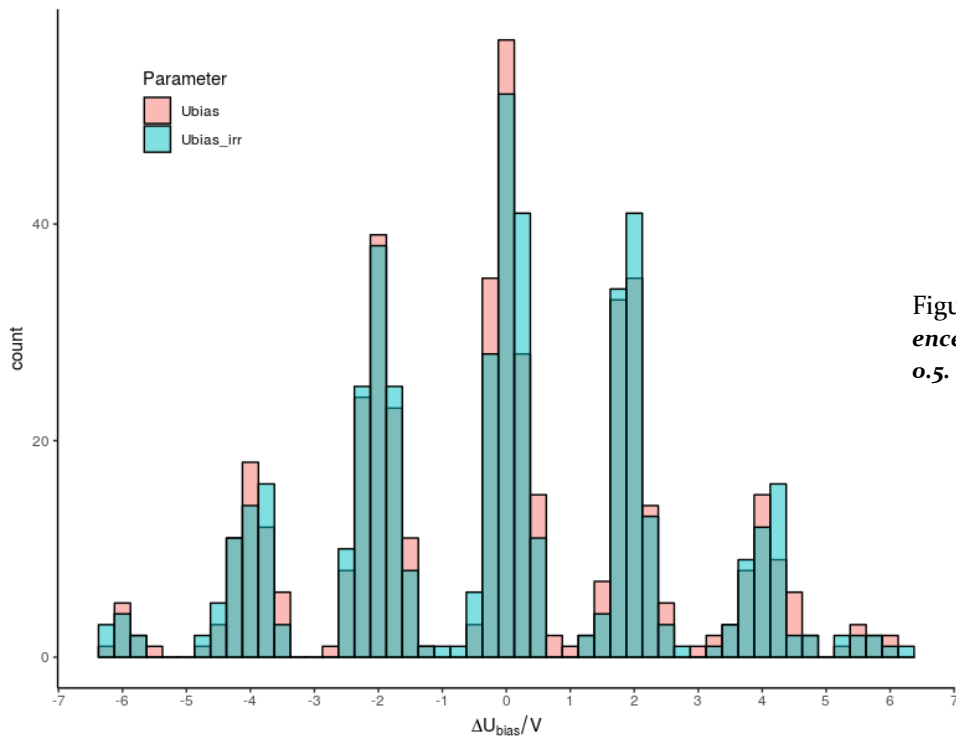


Figure 266: Voltage differences at a distance limit of 0.5.

Slope difference between the pairings:

Constrictions: $d < 0.5$

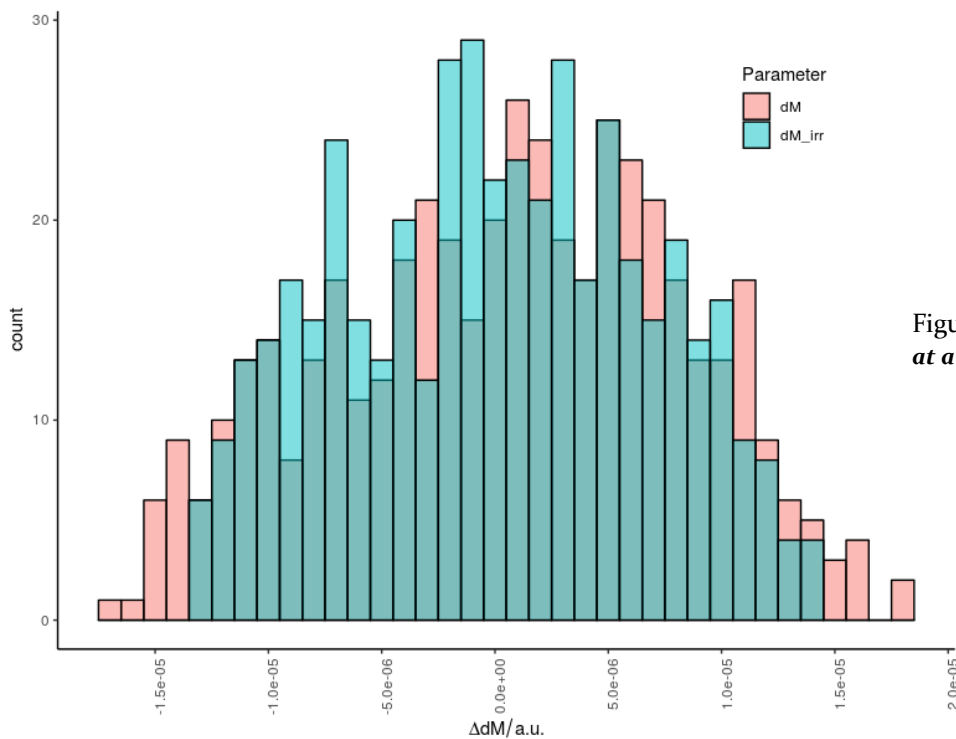


Figure 267: Slope differences at a distance limit of 0.5.

Voltage difference between the pairings:

Constrictions: $d < 0.3$

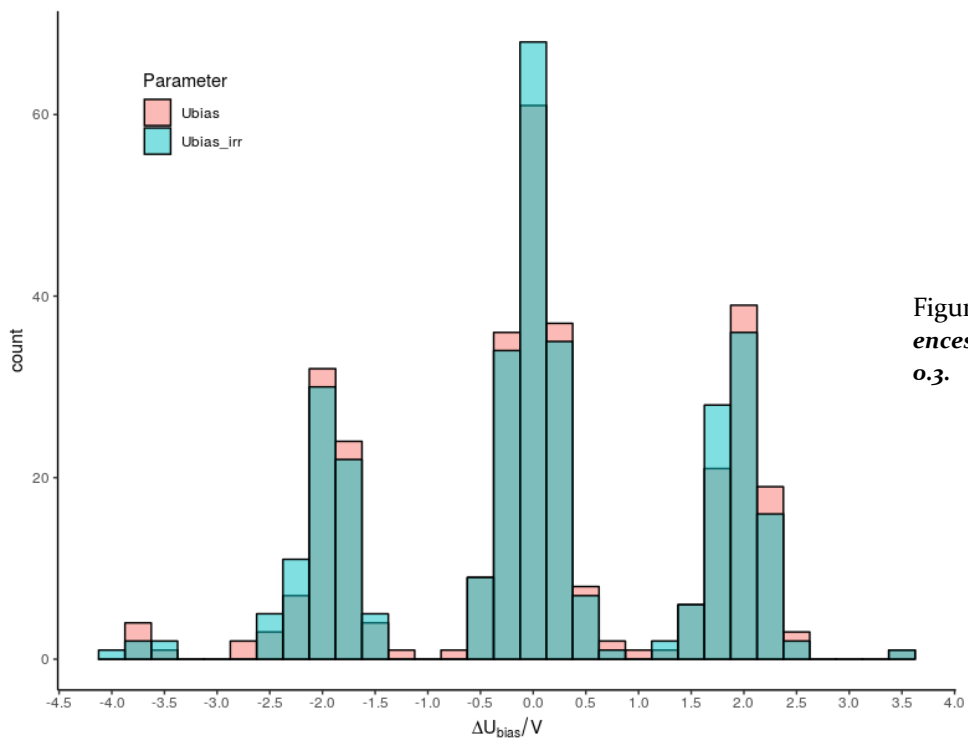


Figure 268: Voltage differences at a distance limit of 0.3.

Slope difference between the pairings:

Constrictions: $d < 0.3$

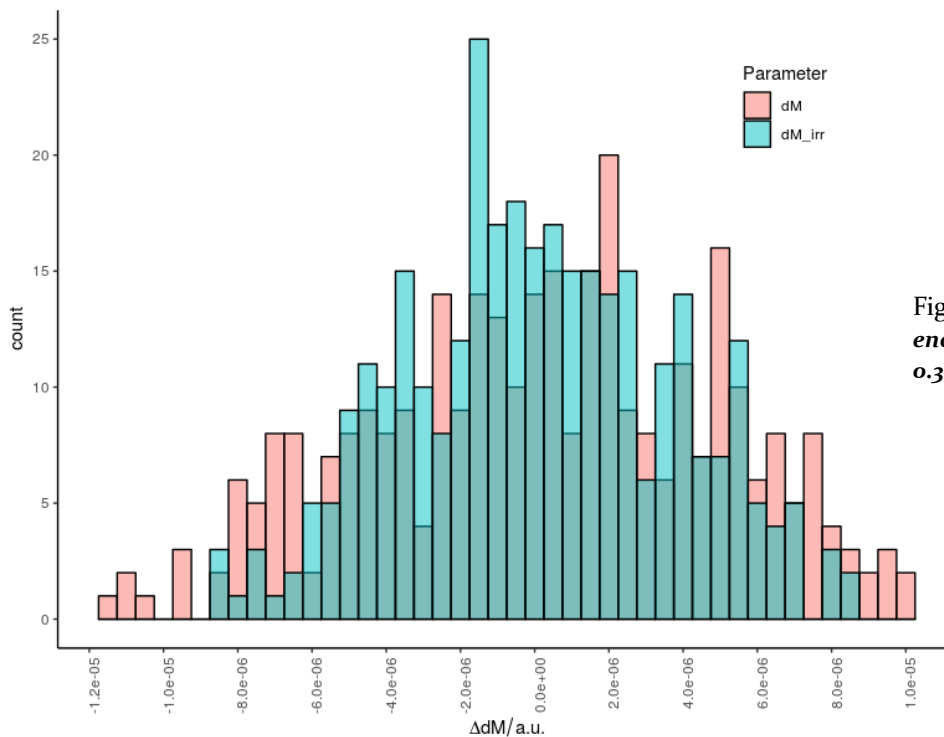


Figure 269: Slope differences at a distance limit of 0.3.

Voltage difference between the pairings:

Constrictions: $d < 0.1$

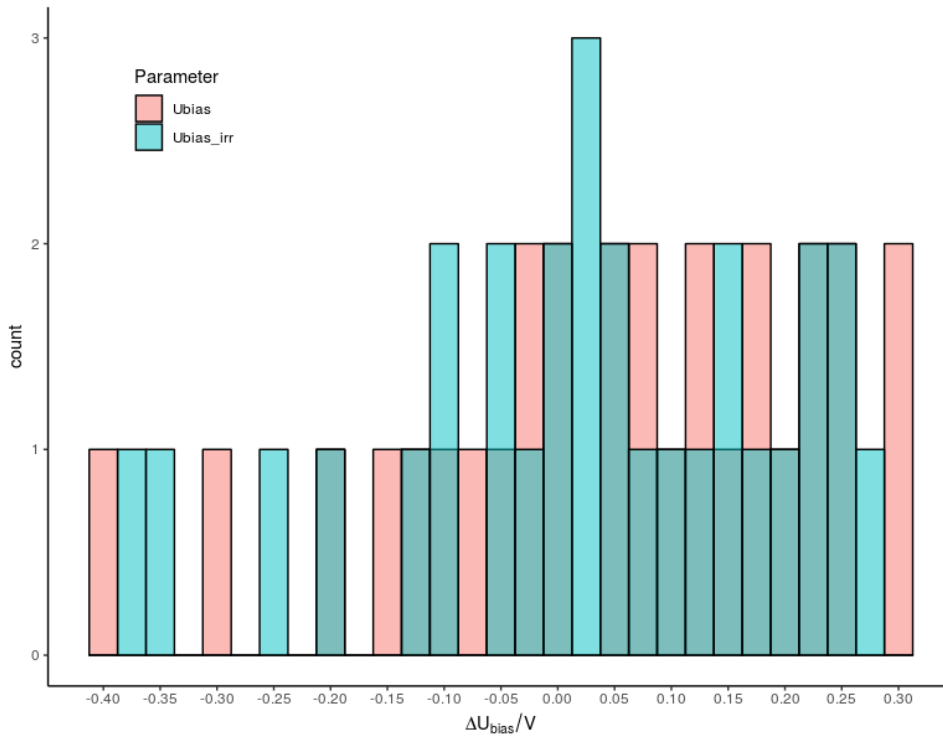


Figure 270: *Voltage differences at a distance limit of 0.1.*

Slope difference between the pairings:

Constrictions: $d < 0.1$

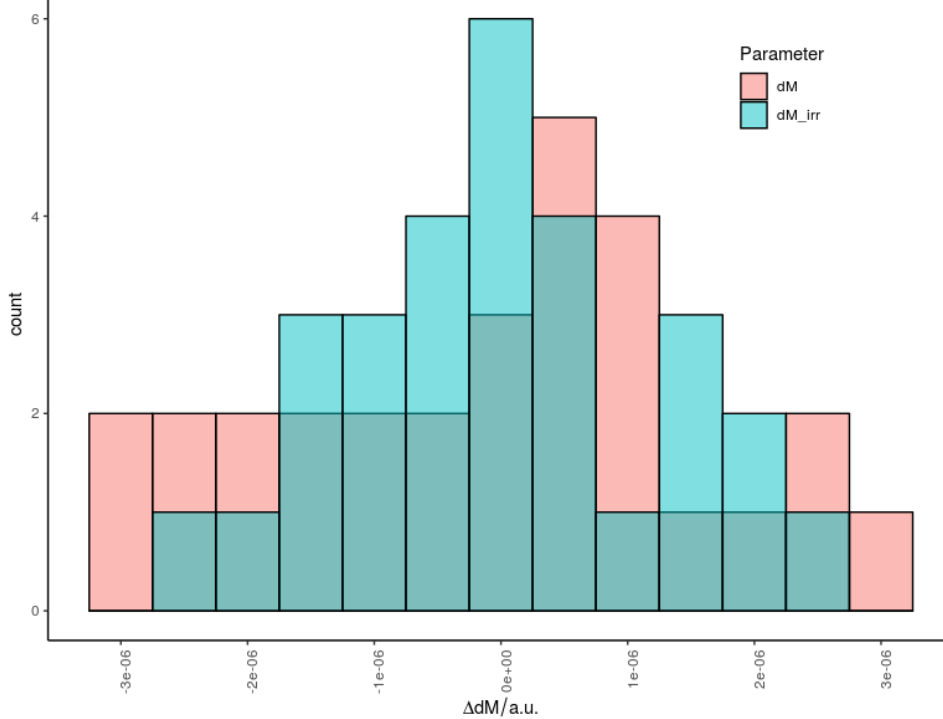


Figure 271: *Slope differences at a distance limit of 0.1.*

12.5.2 Voltage scan

Here, a fixed voltage limit of $U_{\text{bias,irr}} = 0.1 \text{ V}$ is applied to the irradiated values and another voltage limit to the non-irradiated values which varies in the following. Thus, in total two thresholds are set.

Figure 272: *Number of vertices against costs for varying non-irradiated voltage limits.*

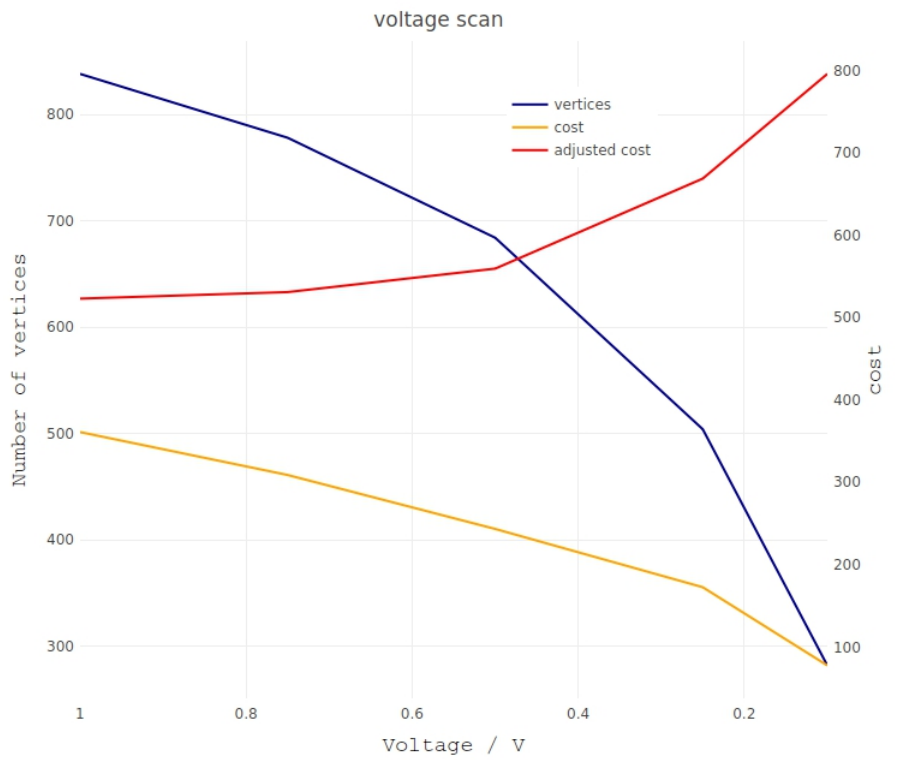


Figure 273: *Number of edges against costs for varying non-irradiated voltage limits.*

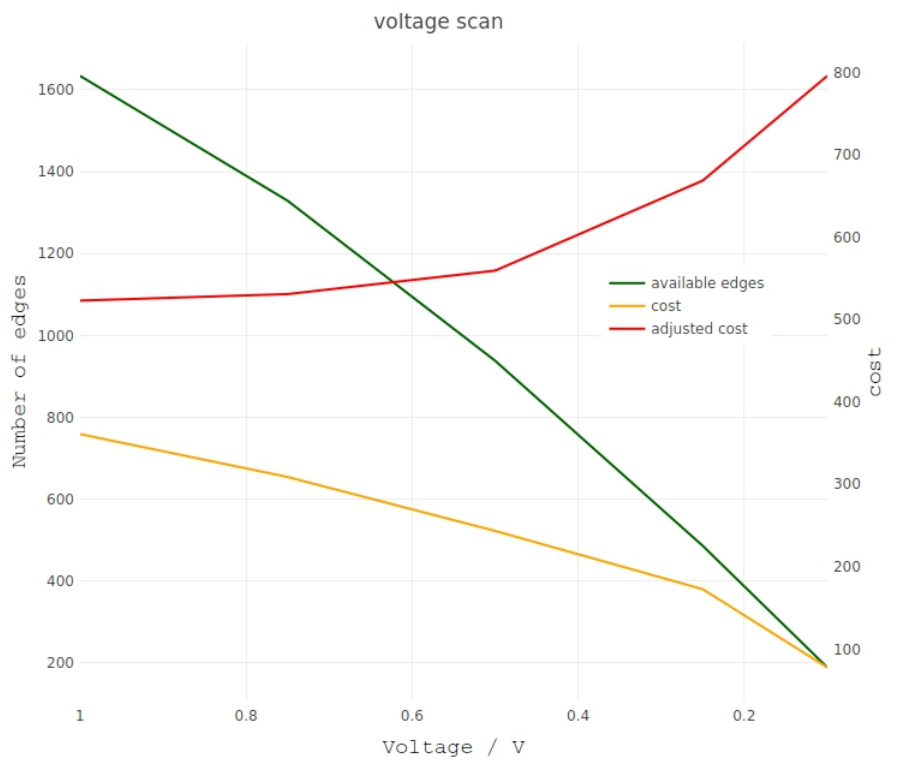


Figure 274: *Number of vertices against edges for varying non-irradiated voltage limits.*

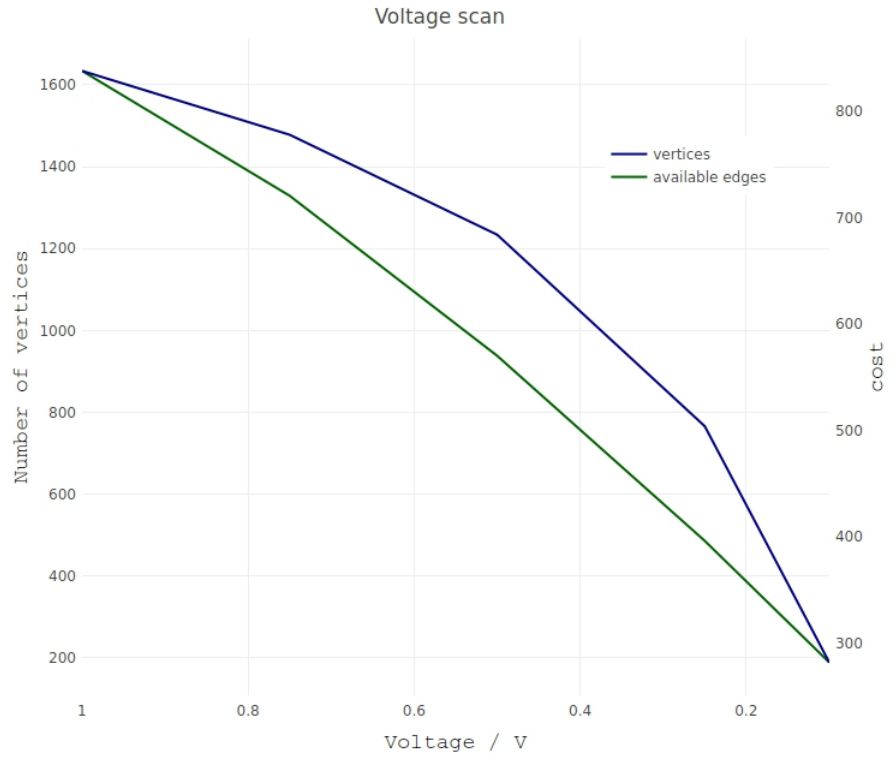
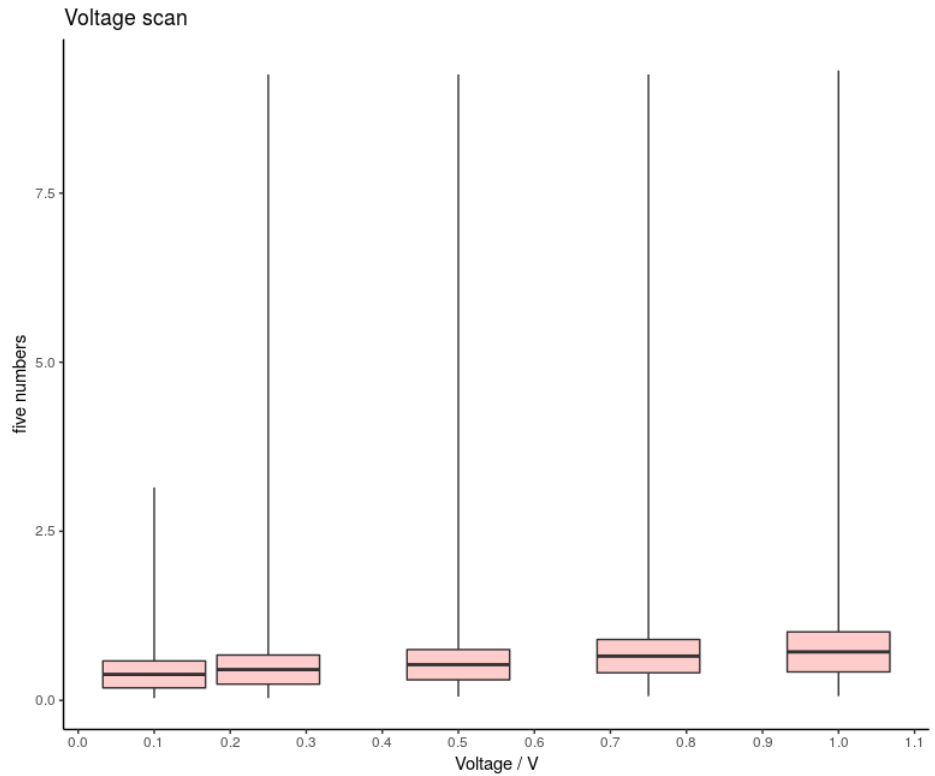


Figure 275: *Five numbers for two voltage thresholds in parallel.*



The additional voltage limit for the non-irradiated does not provide an optimum as a higher limit only reduces the number of successfully assigned APDs.

12.5.3 Reduced graph

When the network is reduced due to the introduction of constraints applied to the edges, the edge table has to be modified accordingly. A reduction removes all edges which do not meet these constraints. This means, some vertices of the network might not be involved at all. To realize this, there are two ways possible: Either the distances which exceed the threshold will be assigned with an infinite weight and their resulting pairings will be simply taken out of the matching or these edges will not be considered at all. Thus, they will not enter the algorithm which is operating only on a subnetwork then:

$$\begin{array}{r}
 \text{origin vertices: } 0 \mid 1 \mid 2 \mid 3 \mid 4 \mid 5 \mid 6 \mid \dots \mid 1000 \\
 \text{order} \quad \quad \quad \mathbf{0} \mid \mathbf{1} \mid \mathbf{2} \mid \mathbf{3} \mid \mathbf{4} \mid \mathbf{5} \mid \mathbf{6} \mid \dots \mid \mathbf{1000} \\
 \downarrow \\
 \text{origin vertices } 0 \mid 2 \mid 4 \mid 5 \mid 6 \mid \dots \mid 998 \\
 \text{new order} \quad \quad \mathbf{0} \mid \mathbf{1} \mid \mathbf{2} \mid \mathbf{3} \mid \mathbf{4} \mid \dots \mid \mathbf{984}
 \end{array}$$

16 APDs are removed here and thus, the adjacency matrix has to be modified similarly. In the end, the origin data set and the connected structures are shrunk and spanned like a blossom. This approach enables the algorithm to operate only on the subset instead of just removing bad pairs afterwards. In this context, when an odd number of APDs is encountered, then a dummy APD is introduced which provides only one single edge which is incident to the previous last APD. In case the matching contains this APD, the affected pair will be removed from the output. An odd number prevents the algorithm to achieve a perfect matching which is a prerequisite to terminate.

APD		0	1	2	3	4		APD		0	1	3	4		APD		0	1	3	4	
		0	1	2	3	4				0	1	3	4				0	1	2	3	
0	0	d_{00}	d_{01}	x	d_{03}	d_{04}		0	0	d_{00}	d_{01}	d_{03}	d_{04}		0	0	d_{00}	d_{01}	d_{03}	d_{04}	
1	1	d_{10}	d_{11}	x	d_{13}	d_{14}	\Rightarrow	1	1	d_{10}	d_{11}	d_{13}	d_{14}	\Rightarrow	1	1	d_{10}	d_{11}	d_{13}	d_{14}	
2	2	x	x	x	x	x		3	3	d_{30}	d_{31}	d_{33}	d_{34}		3	2	d_{30}	d_{31}	d_{33}	d_{34}	
3	3	d_{30}	d_{31}	x	d_{33}	d_{34}		4	4	d_{40}	d_{41}	d_{43}	d_{44}		4	3	d_{40}	d_{41}	d_{43}	d_{44}	
4	4	d_{40}	d_{41}	x	d_{43}	d_{44}															

As mentioned on page 123, the matching will be limited by taking out the bad pairings after the algorithm's operation. In the following, only those edges of the basic graph are considered which are **below a value of 1**. In fig. 276, the corresponding network is visualized:



Figure 276: **Edges of the sub-network with edges below a value of 1.** Only 30297 edges are drawn which fulfill a distance threshold of less than 1. This limit reduces the number of available vertices respectively APDs by a number of 12. With a density of 0.062, this is a so-called sparse graph.

This matching contains 988 vertices and 30297 edges. Hence, some vertices are neglected due to the lack of providing edges below a value of 1. The network diameter⁸⁵ is 11, the graph density is 0.062 and the average cluster coefficient is 0.624. The average degree is 61.330, the average cluster coefficient is 0.624 and the modularity is 0.54 with a number of communities of 14.

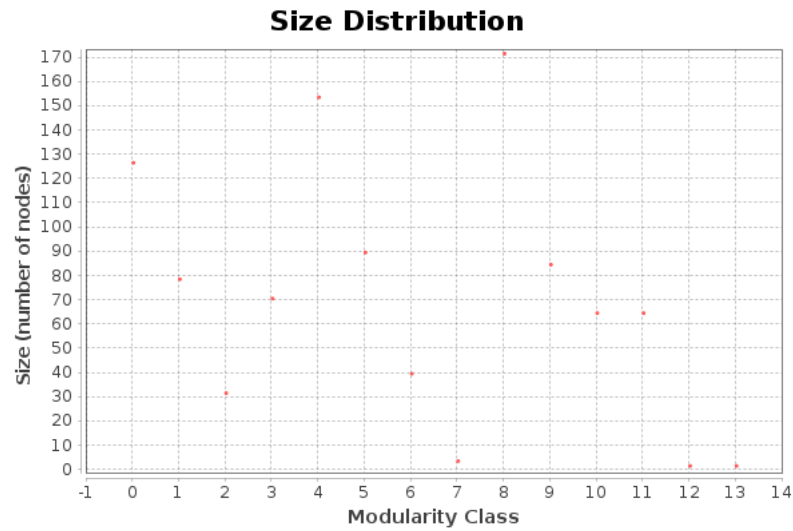


Figure 277: *Modularity of the reduced graph.* The modularity is calculated with 0.54 and only three communities (7, 12, 13) provide very few vertices.



Figure 278: *Colored communities of the reduced graph.* 14 communities were identified though only 10 lots are present.

⁸⁵Distance between the two most distant vertices

12.6 List of APDs

Serial_numbers:

Lot 6							
608004648	608004649	608004650	608004651	608004652	608004653	608004654	608004655
608004657	608004659	608004661	608004663	608004664	608004665	608004666	608004667
611004841	611004842	611004843	611004844	611004845	611004847	611004848	611004849
611004851	611004852	611004853	611004854	611004855	611004856	611004857	611004858
611004859	611004860						

Lot 7							
710006246	710006247	710006255	710006256	710006258	710006261	710006265	710006267
710006269	710006270	711006316	711006317	711006319	711006320	711006321	711006324
711006325	711006327	711006328	712006333	712006335	712006336	712006337	712006338
712006340	712006341	712006342	712006374	712006375	712006377	712006380	712006384
712006385	712006386	712006387	713006388	713006389	713006390	713006391	713006392
713006394	713006436	713006437	713006438	713006439	713006440	713006441	713006442
713006445	713006446	713006449	713006450	713006451	713006453	713006454	713006456
713006457	716006612	716006613	716006614	716006616	716006617	716006618	716006620
716006622	716006623	716006626	716006628	716006630	716006634	716006635	716006636
716006637	719006851	720006853	720006855	720006856	720006857	720006859	720006860
720006861	720006862	720006863	720006865	720006866	721006962	721006964	721006965
721006966	721006967	721006968	721006969	721006971	721006974	721006975	721006976
721006977	721006980	721006982	721006984	721006985			

Lot 8							
801007242	801007243	801007244	801007245	801007246	801007248	801007249	801007250
801007251	801007252	801007253	801007254	801007256	801007257	801007258	801007259
801007260	801007262	801007263	808007770	808007771	808007772	808007775	808007776
808007777	808007778	808007779	808007780	808007781	808007782	808007783	808007784
808007786	808007788	808007789	808007790	808007791	810007991	810007992	810007993
811007994	811007995	811007996	811007997	811007999	811008000	811008001	811008002
811008003	811008004	811008005	811008006	811008007	811008008	811008009	818008561
818008562	818008563	818008564	818008565	818008566	818008567	818008568	818008570
818008571	818008572	818008575	818008576	818008577	818008580	818008581	818008627
818008628	818008630	818008631	818008634	818008635	818008636	818008637	818008638
818008639	818008640	818008641	818008642	819008644	819008645	819008647	819008648
819008649	819008650	819008652	819008653	819008654	819008655	819008656	819008658
819008659	819008660	819008661	819008662	819008663	819008665	819008667	819008669
822008900	822008903	822008906	822008908	822008909	822008911	822008913	822008914
822008915	822008917	822008918	822008919	822008920	822008921	905009317	905009318
905009320	905009337	905009345	906009371	906009372	906009373	906009374	

Lot 9							
905009317	905009318	905009320	905009337	905009345	906009371	906009372	906009373
906009374	906009375	906009376	906009377	906009378	906009379	906009381	906009383
906009384	906009386	906009388	906009389	906009390	907009465	907009466	907009467
907009469	907009470	907009471	907009472	907009474	907009475	907009477	907009484
907009485	910009746	910009747	910009748	910009749	910009752	910009754	910009755
911009757	911009760	911009761	911009762	911009763	911009764	911009766	911009767
911009768	911009769	911009770	911009771	911009772	911009773	911009775	911009777
911009778	911009780	911009781	911009783	911009784	911009785	911009790	911009791
911009792	911009802	911009804	911009806	912009890	912009892	912009894	912009895
912009897	912009898	912009899	912009902	912009903	912009905	912009909	912009910
912009912	912009913	912009915	913009917	913009918	913009985	913009987	914009988
914009989	914009991	914009992	914009993	914009996	914009997	914009999	914010002
914010004	914010006	914010007	914010008	914010010	914010011	914010012	914010013
914010014	914010015	914010016	914010018	914010019	914010020	914010021	914010022
914010023	914010024	914010025	914010026	914010027	914010028	914010029	914010030
914010031	914010032	914010033	914010034	914010035	914010036	914010037	914010038
914010039	914010040	914010041	914010043	914010046	914010048	914010049	914010055
914010057	914010058	914010059	914010060	914010063	914010064	914010065	914010066
914010067	915010068	915010070	915010072	915010073	915010074	915010075	915010076
915010077	915010078	915010082	915010083	915010087	915010088	915010089	915010091
915010093	915010094	915010096	915010097	915010098	915010099	915010100	915010101
915010102	915010103	915010108	915010109	915010110	915010112	915010113	915010114
915010115	915010117	915010118	915010119	915010120	915010122	915010123	915010124
915010125	915010126	915010127	915010128	915010134	915010138	916010139	916010140
916010141	916010142	916010143	916010144	916010185	916010186	916010187	916010188
916010189	916010192	916010194	916010195	916010196	916010197	916010198	916010200
916010202	916010203	916010204	916010205	917010228	917010229	917010230	917010233
917010234	917010235	917010236	917010237	917010238	917010239	917010240	917010241
917010242	917010243	917010244	917010245	917010246	917010247	917010248	

Lot 12							
1205013067	1205013069	1205013070	1205013071	1205013072	1205013073	1205013074	1205013075
1205013076	1205013077	1205013078	1205013080	1205013081	1205013082	1206013088	1206013089
1206013090	1206013091	1206013092	1206013093	1206013094	1206013095	1206013096	1206013097
1206013101	1206013102	1206013103	1206013106	1206013148	1206013150	1206013151	1206013152
1206013153	1206013155	1206013156	1206013157	1206013158	1207013160	1207013161	1207013162
1207013163	1207013164	1207013165	1207013167	1207013168	1208013279	1208013280	1208013283
1208013284	1208013287	1208013289	1208013299	1208013300	1208013303	1211013537	1211013538
1211013539	1211013540	1211013541	1211013542	1211013543	1211013544	1211013545	1211013546
1211013547	1211013549	1211013550	1211013551	1211013552			

Lot 13							
1301013557	1302013716	1303013718	1303013719	1303013720	1303013721	1303013722	1303013723
1303013724	1303013725	1303013726	1303013727	1303013728	1303013729	1303013730	1303013731
1303013732	1303013733	1303013734	1303013735	1304013760	1304013762	1304013763	1304013764
1304013766	1304013767	1304013772	1304013773	1304013774	1304013778	1304013779	1304013783
1305013870	1305013873	1305013874	1305013875	1305013876	1305013877	1305013879	1305013880
1305013881	1305013883	1305013884	1305013885	1305013886	1305013891	1305013893	1305013894
1305013896	1305013897	1305013898	1305013899	1305013900	1305013901	1305013902	1305013903
1305013904	1305013906	1305013907	1305013908	1305013910	1305013911	1305013912	1305013914
1305013917	1305013919	1305013921	1306013926	1306013927	1306013930	1306013936	1306013937
1306013938	1306013981	1306013982	1306013983	1306013984	1306013985	1306013986	1306013987
1306013988	1306013989	1306013990	1306013992	1306013993	1306013994	1306013995	1306013996
1306013997	1306013998	1306014001	1307014023	1307014026	1307014027	1307014029	1307014030
1307014031	1307014032	1307014033	1307014034	1307014035	1307014036	1307014037	1307014038
1307014039	1307014041	1307014043	1307014044	1307014046	1307014048	1307014049	1307014050
1307014051	1307014052	1307014053	1307014054	1307014056	1307014057	1307014058	1307014059
1307014063	1310014243	1310014245	1310014247	1310014248	1310014249	1310014250	1310014251
1310014252	1310014253	1310014254	1310014256	1310014257	1310014258	1310014259	1310014260
1310014261	1311014350	1311014352	1311014353	1311014354	1311014355	1311014356	1311014360
1311014361	1311014362	1311014363	1311014365	1311014366	1311014370	1311014372	1311014373
1313014497	1313014500	1313014501	1313014502	1313014503	1313014504	1313014506	1313014507
1313014511	1313014512	1313014514	1313014517	1313014518	1313014523	1314014595	1314014596
1314014597	1314014598	1314014600	1317014833	1317014835	1317014839	1317014840	1317014841
1317014842	1317014843	1317014844	1318014845	1318014847	1318014848	1318014850	1318014851
1318014853	1318014855	1319014968	1319014969	1319014971	1319014976	1319014977	1319014978
1319014979	1319014980	1319014981	1319014982	1319014984	1319014985	1319014986	1319014987
1319014988							

Lot 14							
1402015190	1402015191	1402015193	1402015194	1402015195	1402015196	1402015197	1402015198
1402015199	1402015201	1402015202	1402015203	1402015204	1402015209	1404015382	1404015383
1404015384	1404015385	1404015386	1404015387	1404015388	1404015389	1404015390	1404015391
1404015392	1404015393	1404015395	1404015396	1404015397	1405015398	1405015399	1405015400
1405015401	1405015402	1405015403	1405015405	1405015406	1405015407	1405015408	1405015409
1405015410	1405015411	1405015412	1405015413	1405015414	1405015415	1405015416	1405015417
1405015418	1405015419	1405015420	1405015422	1410015815	1410015817	1410015818	1410015819
1410015820	1410015822	1410015824	1410015825	1410015826	1410015827	1410015828	1410015829
1410015830	1410015831	1410015832	1410015833	1410015835	1412015997	1412015999	1412016000
1412016001	1412016002	1412016003	1412016004	1412016006	1412016007	1412016009	1412016011
1412016012	1412016013	1412016014	1412016016				

Lot 16							
1604017006	1604017008	1604017009	1604017010	1604017011	1604017012	1604017013	1604017014
1604017015	1604017017	1604017019	1604017020	1604017021	1604017022	1604017023	1604017025
1604017026	1605017143	1606017145	1606017146	1606017147	1606017148	1606017151	1606017152
1606017154	1606017155	1606017156	1606017159	1606017161	1606017162	1606017185	1606017186
1606017187	1606017189	1606017191	1606017192	1606017193	1606017194	1606017195	1606017196
1606017197	1606017199	1606017200	1606017201	1606017202	1606017205	1609017454	1609017458
1609017461	1609017462	1609017463	1609017464	1609017465	1609017466	1609017467	1609017468
1609017470	1609017471	1609017472	1609017473	1609017474	1609017480	1613017768	1613017769
1613017770	1613017771	1613017772	1613017773	1613017774	1613017775	1613017776	1613017777
1613017778	1613017779	1613017780	1613017781	1613017782	1613017783	1613017784	1613017786
1613017787	1613017788						

Lot 17							
1702018488	1702018490	1702018492	1702018494	1702018496	1702018497	1702018498	1702018499
1702018501	1702018502	1702018503	1702018504	1702018505	1702018506	1702018508	1710019156
1710019158	1710019159	1710019160	1710019161	1710019162	1710019163	1710019165	1710019166
1710019167	1710019168	1710019169	1710019170	1710019173	1714019466	1714019467	1714019468
1714019469	1714019471	1714019472	1714019473	1714019474	1714019475	1714019477	1714019478
1714019479	1714019480	1715019497	1715019498	1715019500	1715019501	1719019828	1719019830
1719019831	1719019832	1719019833	1719019834	1719019835	1719019836	1719019837	1719019838
1719019839	1719019840	1719019841	1719019842	1719019843	1719019845	1719019846	1719019848

Lot 18							
1802020116	1802020118	1802020119	1802020120	1802020121	1802020122	1802020123	1802020124
1802020125	1802020126	1802020127	1802020130	1802020131	1802020132	1802020133	1802020135

Light injection

A close-to-final subunit of the ECAL, the Proto120 was tested at MAMI⁸⁶, mainly from 11.12.2015 to 14.12.2015. Major goal was to study the response of a prototype of 80 crystals to photons. The specific aim of this beamtime was to test some electronic upgrades like a slow control, a new network cable as well as, for the first time, a $5 \cdot 5$ matrix of crystals. Furthermore, the crystals were equipped with light fibers to make use of a light pulser system. Such a system is necessary to keep track of the optical transmissions of the scintillation crystals. These have to be measured to ensure an ongoing monitoring of the damages and spontaneous or also stimulated recoveries of the crystals.

Basically, a calibration of the \bar{P} ANDA EMC will be done with the help of muons and ultimately via $\bar{p}p \rightarrow \pi^0\pi^0\pi^0$ and $\bar{p}p \rightarrow \pi^0\pi^0\eta$. For analysis purposes, the prototype is calibrated via muons, simulated results and the light pulser.

13 Beam time with Proto120 in Main

Proto 120

13.1 Mainzer Mikrotron

Tests are performed at the MAMI facility in Mainz, Germany. It comprises several sections like, for example, A1 housing the electron-scattering setup and A2 providing a real photon beam. The special feature of MAMI is that it delivers a continuous wave electron beam resulting in currents of 100 μ A. Thus, a duty factor⁸⁷ of nearly

⁸⁶Mainzer Mikrotron

⁸⁷the time quotient of beam is switched on to beam is switched off.

100 % can be obtained [91]. This has been achieved by constructing MAMI as a racetrack microtron. MAMI consists of four racetracks, RTM1, RTM2, RTM3 and HDSM⁸⁸.

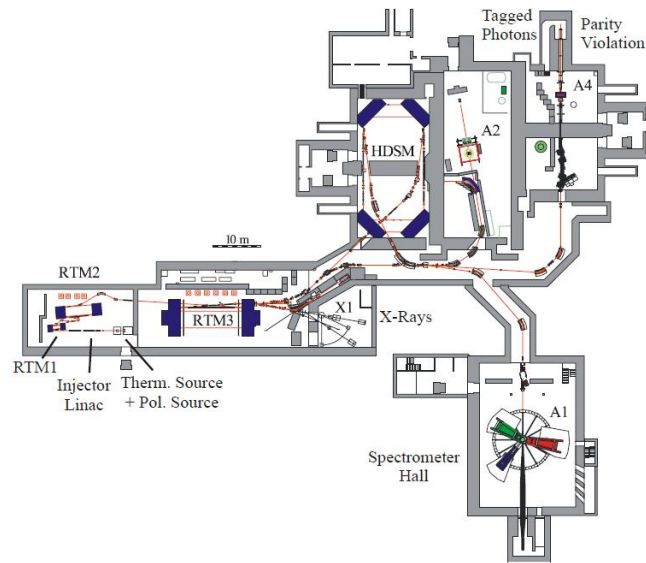


Figure 279: *MAMI facility* [168]. The RTM₁ and RTM₂ form MAMI-A, RTM₃ is the backbone of MAMI-B and HDSM is MAMI-C.

The electrons are initially produced by a thermal source and then accelerated electromagnetically in a linear accelerator. Afterwards they will run through a cascade of microtrons many times which are using up to four 90° bending magnets. RTM₁ and RTM₂ form MAMI-A, RTM₃ is MAMI-B and the HDSM is MAMI-C.

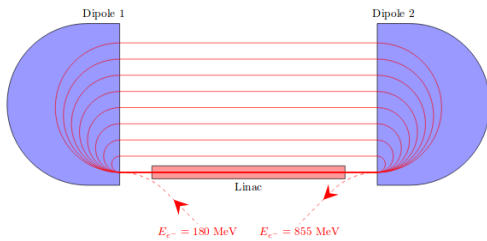


Figure 280: *MAMI-B* [141]. RTM₃ is the backbone of MAMI-B.

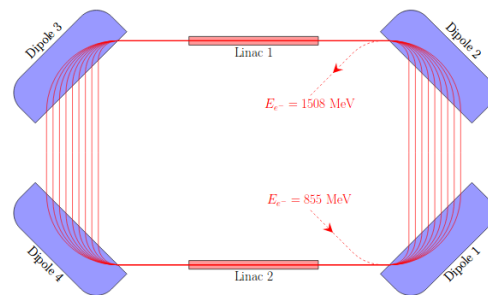


Figure 281: *MAMI-C* [141]. The HDSM was the solution to overcome the circumstance of larger magnets.

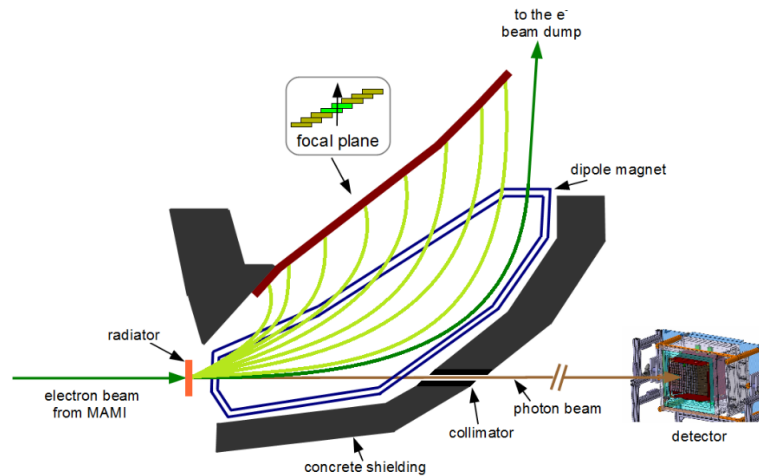
Finally, each endpoint energy is given by the physical size of the magnets. In case of RTM₁ it is 14.86 MeV, RTM₂ provides 180.1 MeV, RTM₃ 855 MeV and the HDSM up to 1.5 GeV/c. The electrons will be extracted and guided to different experiments. The Proto120 was tested at the A2 stage where Crystal Ball is located.

⁸⁸Harmonic Double Sided Microtron

13.1.1 A2

The A2 facility is providing structures to enable physics investigations with the help of real photons. These photons are generated by producing Bremsstrahlung (see 29) through electrons scattering at atoms of a radiator: $eZ \rightarrow e'\gamma Z$. The energy E_γ of a photon is determined by how much it is influenced by the Coulomb field of an atom. Due to the small cross section of Bremsstrahlung, not all electrons will undergo this interaction process. The number of photons expected with an energy E_γ can be approximated with $N(E_\gamma) \propto 1/E_\gamma$.

Figure 282: *Glasgow Tagger*. The electrons are tagged due to the deflection by a magnet. On this basis, their energy can be determined by using the specific scintillator they imping on.



To ensure that as many electrons as possible radiate, a large dipole magnet of 4.4 T deflects the electrons and guides them into the Glasgow Tagger or beam dump. Their bending radius R can be calculated by $R = E/ecB$. The tagger consists of 352 EJ-200 plastic scintillators arranged in the focal plane. Hence, the electrons will hit them perpendicularly. These scintillators overlap a bit with each other (see fig. 282) to enable coincidence signals. They are 2.4 cm wide and 2 mm thin. Electrons impinging on these scintillators will generate a signal in the attached R1635 PMTs from Hamamatsu. The position or rather the specific scintillator represents the energy of the corresponding photon according to $E' = E_0 - E_\gamma$. The more energy electrons lose due to the radiator respectively the higher E_γ is the more they will be deflected by the magnet. A very important aspect is to achieve a reliable coincidence between the tagged electron and the corresponding photon. To ensure that photons only follow a straight forward direction, a collimator is placed between radiator and target. The collimator is of copper with a diameter of 1.5 mm and was placed 2.5 m next to the radiator. The Proto120 was mounted into a $xy\theta$ table placed 15.5 m away from the radiator in downstream direction.

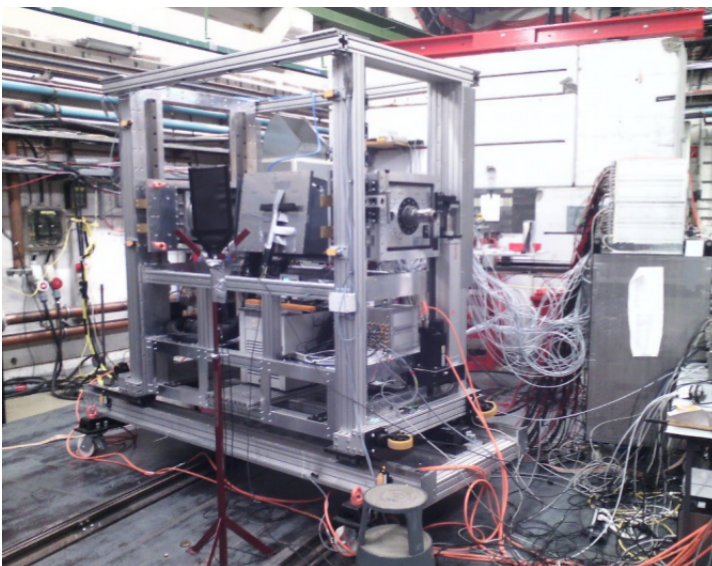


Figure 283: *Proto120*. The Proto120 inside the $xy\theta$ -table. The spot of the photon beam is positioned with the help of a laser. CAD drawings provide projected positions to align the photon beam correctly with the Proto120.

13.1.2 Readout

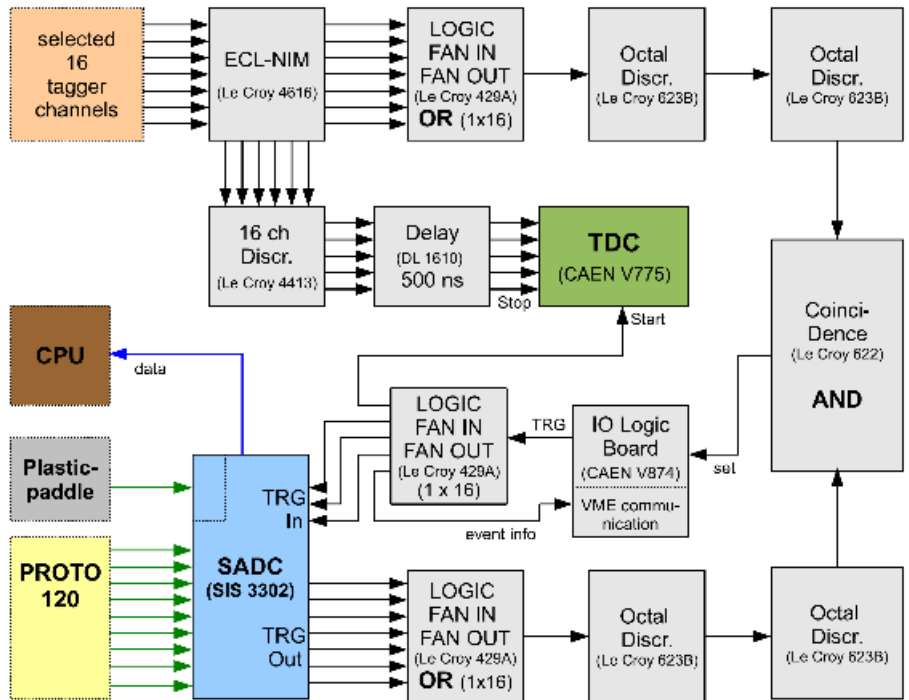
By using coincidence checks, monoenergetic photons only were selected. 16 tagger channels in total were used, beginning at 56.36 MeV and ending at 766.76 MeV.

TDC channel	Tagger channel	Energy / MeV	TDC channel	Tagger channel	Energy / MeV
0	350	56.355 ± 2.741	8	208	406.304 ± 2.724
1	340	80.124 ± 2.788	9	195	438.129 ± 2.653
2	330	104.078 ± 2.829	10	185	462.34 ± 2.638
3	320	128.2 ± 2.862	11	125	599.907 ± 2.262
4	307	159.784 ± 2.858	12	105	641.732 ± 2.12
5	294	191.582 ± 2.844	13	85	681.167 ± 2.043
6	275	238.339 ± 2.775	14	50	743.916 ± 1.721
7	220	376.649 ± 2.749	15	36	766.775 ± 1.688

Table 43: *Tagger energy channels*. In total, 16 different energy channels were used to study the Proto120.

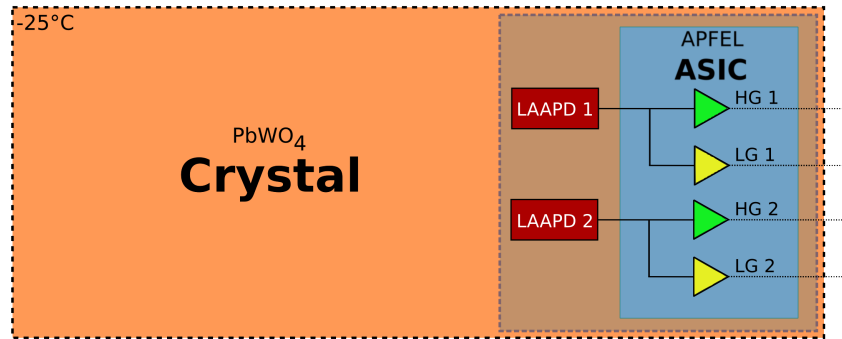
All the tagger channels are assigned with an OR and connected with all channels of the PROTO120 through a coincidence setup with an AND. The time signal was delayed by 500 ns and used as a stop signal.

Figure 284: *Readout diagram of the beam time at MAMI [146]*. Events will be recorded when one channel of the Proto120 exceeds a certain threshold and is in coincidence with one channel of the Tagger. The TDC has a resolution of about 550 ps at a range of 140 ns and a 8-bit resolution.



The detected light is converted into an electric charge and amplified via two gains by the APFEL, the high gain and the low gain. The first is more important because the higher gain is necessary to utilize low signals down to 10 MeV. The APFEL will then extract both signals to the buffer board and from there, these differential signals will be routed to SIS 3302 SADCs via RJ45 Ethernet coax cables.

Figure 285: **Gain read-out.** Two signals per APD are recorded.



In the following an overview of the Proto120 and the cable routing among all used components:

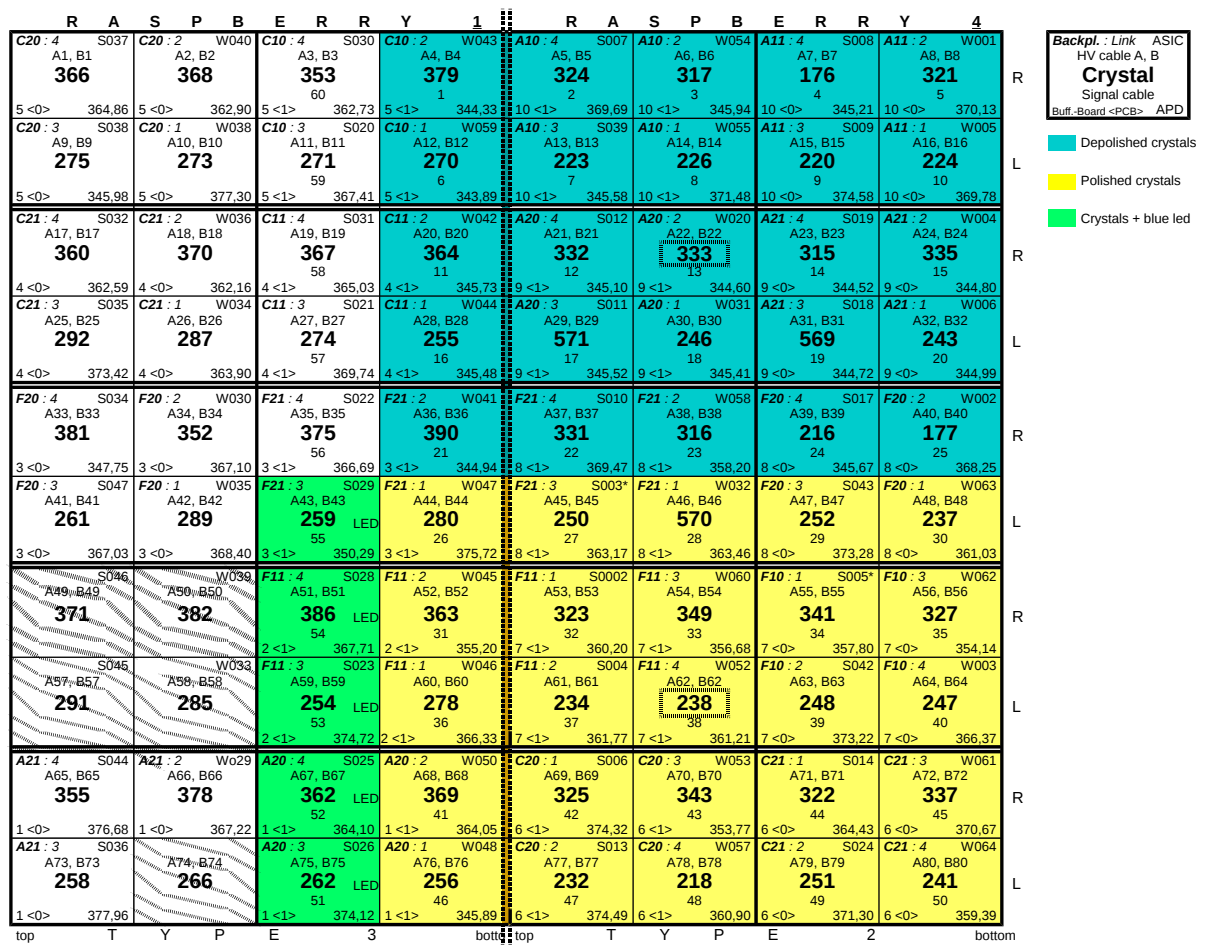


Figure 286: **Routing map of Proto120.** The numbers bottom right indicate the applied high voltage to operate the APDs.

The crystals were read out by two APDs via four signals in total which were amplified afterwards by the APFEL ASIC. The complete readout chain of the Proto120 is given in fig. 287:

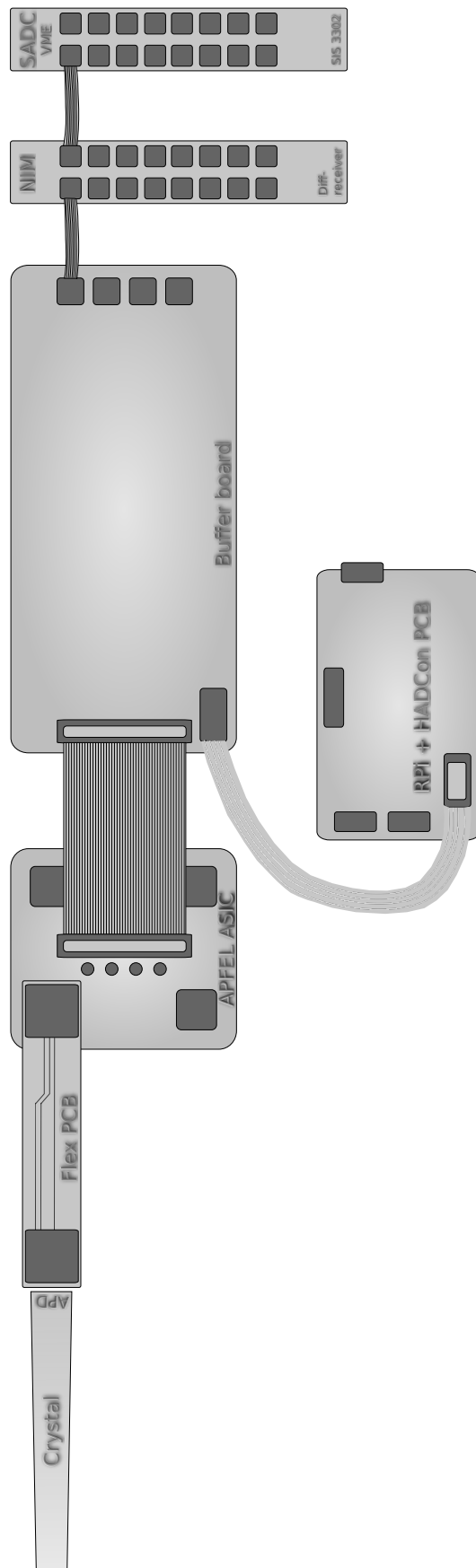


Figure 287: **Proto120 readout.** The APD signals are transmitted via the Flex PCB and pre-amplified by the APFEL ASIC. The buffer board converts the signal into RJ45 which is further transmitted and finally digitized by SADCs and stored. All crystals of type 3 were controlled by the Raspberry Pi 1 and all crystals of the type 2 were controlled by the Raspberry Pi 4. Groups of eight crystals are each read out via a separate buffer board and backplanes supply groups of four crystals with high voltage.

13.1.3 Setup

The Proto120 is the successor prototype to the Proto60 [38, 104, 156]. Major modifications are the use of the APFEL ASIC instead of the Basel preamp and two APDs instead of one. Detailed information can be found in [148, 27].

The subsequently discussed beamtime was performed to test mainly electronic components newly introduced. This includes the use of ASIC flex-PCBs v6, a newly designed cooling plate, spacers and an intermediate plate. Also a slow-control was implemented.

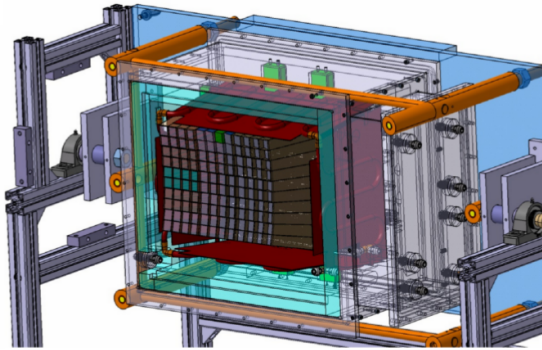


Figure 288: *Proto120*. The Proto120 together with the $xy\theta$ -table.

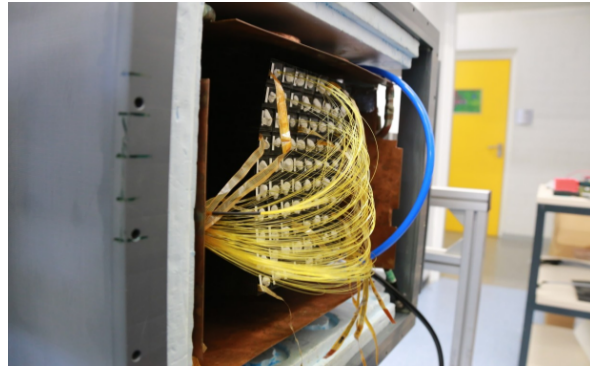


Figure 289: *Proto 120 fibers*. Each crystal is equipped with a fiber to receive light from the Bochum light pulser.

The Proto120 contained two modules with 40 type I crystals and 40 type II crystals. Type III crystals were not used, thus, the Proto120 comprised only 80 crystals in total. Overall, the main component was a $5 \cdot 5$ crystal matrix made of depolished crystals together with a 5×5 crystal matrix of polished crystals. Each crystal was equipped with monitoring light fibers by making use of a reflective front stopper to attach them. Furthermore, the crystals were wrapped with the reflective foil VM2000 of $63.5 \mu\text{m}$. Hence, 40 crystals (20 left and 20 right types) are placed into a carbon alveole with a thickness of $200 \mu\text{m}$. All crystals are aligned to the center of the front side of the Proto120.

The Proto120 has two distinctive temperature regions, the so-called warm region and the so-called cold or cooled region ($T = -25 \text{ }^\circ\text{C}$). Everything is housed within a pvc box and sealed with silicon. The cold side is stuffed with several pipes which are flooded by a mixture of water and ethanol, driven by a chiller.

Two APDs are applied to one high voltage which is the mean of both individual high voltages necessary for a gain of 150. These data are provided by the PSL Darmstadt.

13.2 Results

Several runs were performed:

- Central hit on the 5×5 depolished matrix (140 minutes)
- Cable test (30 minutes)
- light pulser (10 minutes)
- Cosmic (7 days)
- Quartz (60 minutes)

The cosmic run took place the week right after the beam time. The cosmic were measured such that they traversed the Proto120 vertically. Hence, coincidences including 1 up to 5 crystals occurred.

13.2.1 Data acquisition

The sampling frequency of the SADC was set to 50 Mhz. The trace length comprises 500 samples and the time interval between these is 20 ns. Thus, one trace represents 10 μ s. These are transferred further to a CPU via a VME bus. Only triggered traces respectively events were stored which fulfilled a logical OR among the tagger and the Proto120. The SADCs were equipped with an internal leading edge threshold in the software. Signals fulfilling this marked the start signal. The tagger information were converted to analogue NIM signals, delayed and used as a stop signal for the TDC which provides a time gate of 140 ns at a resolution of 8 bit, ultimately providing a time resolution of 550 ps.

Though the crystal matrix comprised 25 crystals, the low gains were only read out from the inner 3×3 matrix.

13.2.2 Feature Extraction

To make use of the raw traces, features like energy, noise and time have to be extracted properly. Before getting started with defining how to gather these, the events have to be discriminated unambiguously to separate clear signals and background. The first aspect to consider is the tagger multiplicity. Only events are processed further which are not assigned with a multiplicity > 1 .

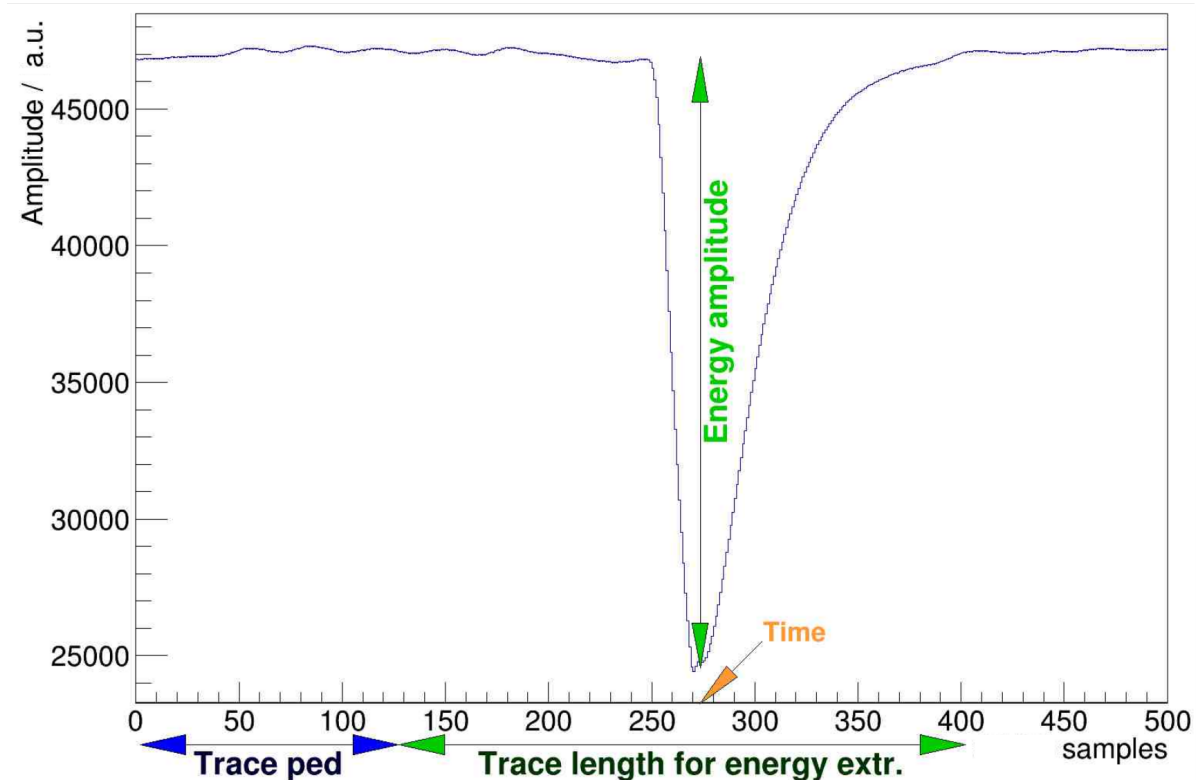


Figure 290: **Raw trace.** Baseline, energy and time information.

The first value to obtain is the baseline. It is achieved by taking the arithmetic mean of the first 130 samples. On this basis, the energy can be calculated by using the amplitude which represents the difference between baseline and peak. For that, the samples 130 to 400 are taken into account. The time information is determined by the peak position.

The last parameter is the noise. It is extracted after the calibration (see [Noise](#) on page 244) to be represented in a more useful unit of MeV.

13.2.3 Constraints

During the beam time, several issues occurred which made it necessary to switch the beam off and on many times. The breaks in between were meant for diagnostic researches in regard to the electronics and the analysis afterwards turned out that some issues remained. One of the bigger problems was the misalignment of the beam which appears when checking the number of entries in each crystal:

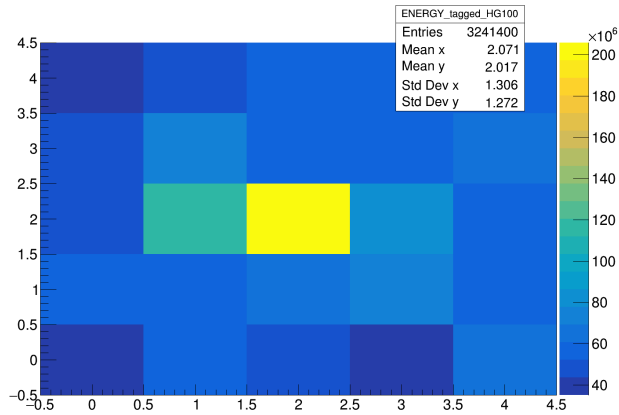


Figure 291: *Tagger channel 1 - HG1.*

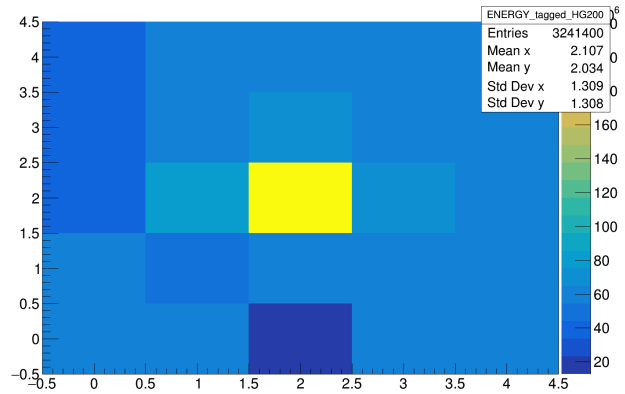


Figure 292: *Tagger channel 1 - HG2.*

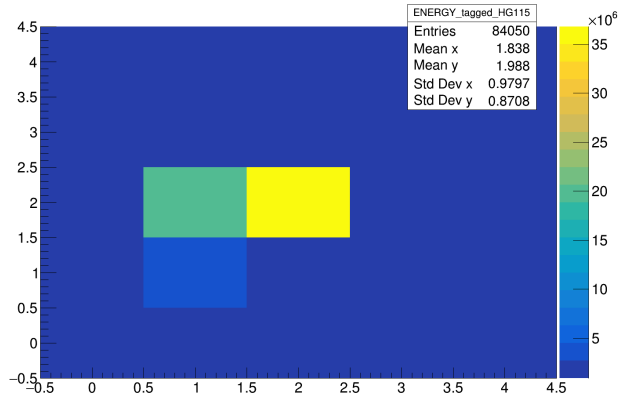


Figure 293: *Tagger channel 16 - HG1.*

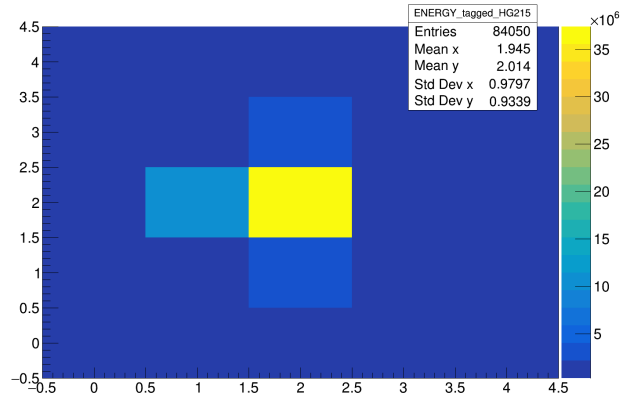


Figure 294: *Tagger channel 16 - HG2.*

A precise alignment to the central crystal would result in a center of gravity at this crystal. Instead, it seems that the beam was slightly shifted to the left crystal. Furthermore, some channels turned out to be dead, since they recorded no signals. To ensure this, the signals were checked from cosmics as well as from a light pulser:

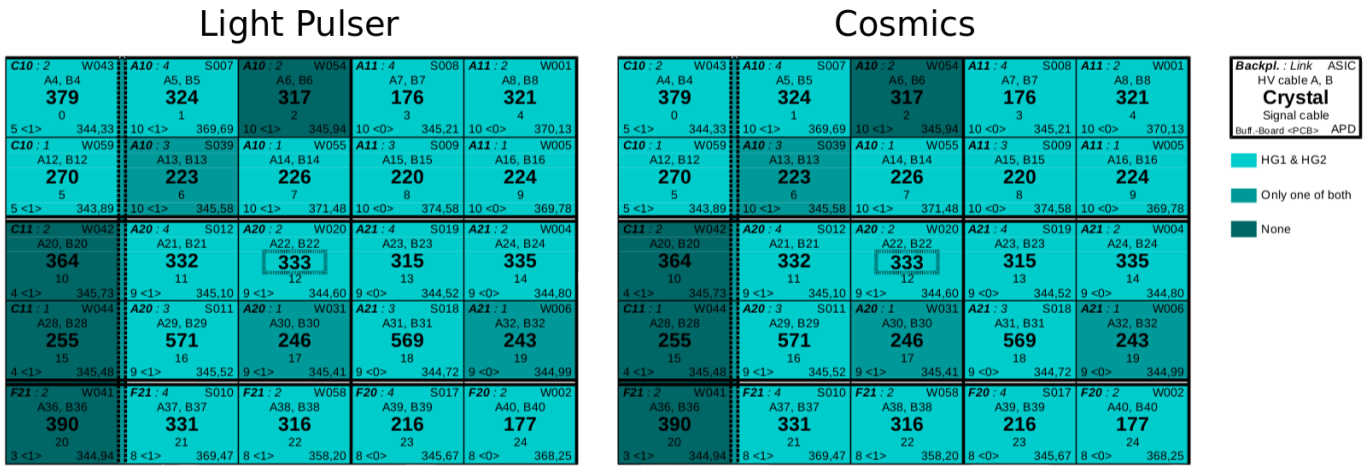


Figure 295: *Crystal readout check*. Some channels cannot be read out.

Beyond that, the arrangement of the crystals in regard to their signal cables turned out to be not correct for some positions. Hence, an extensive reverse investigation is performed to obtain the correct positions of the crystals. This is possible by using coincidence conditions via grouping the crystals into columns (see fig. 296):

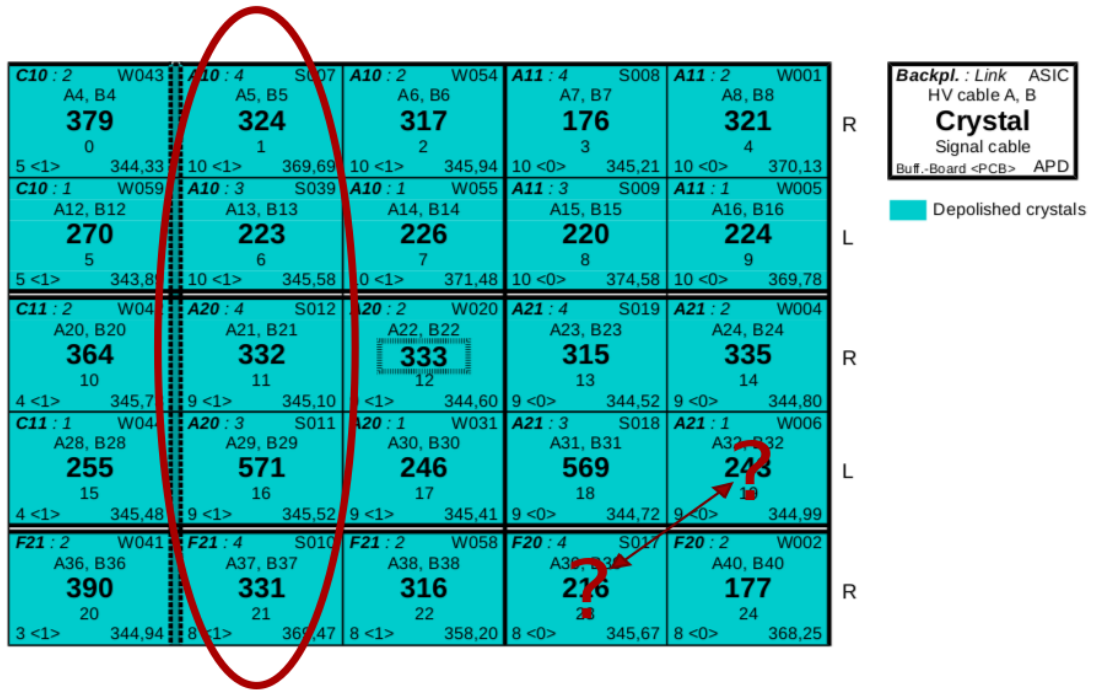


Figure 296: *Cosmic Condition*. The positions of the crystals were swapped and coincidence conditions were put on them.

To get started, the top crystals in each column are treated as fixed crystals. Afterwards, these crystals are studied together with the bottom crystals and both gains are used for that. In the following, all four bottom crystals (21 – 24) are cross-checked with the crystal 7:

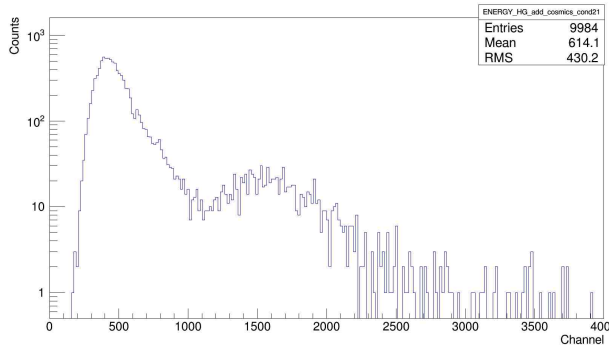


Figure 297: *Crystal 7+21.*

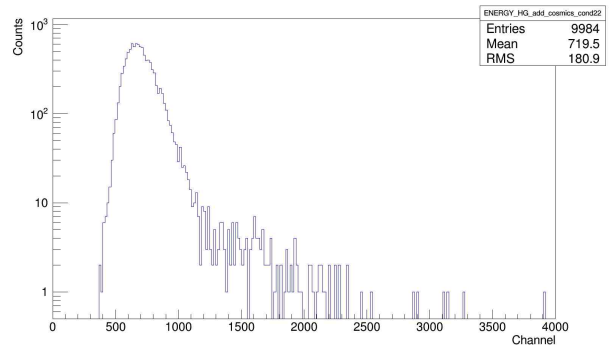


Figure 298: *Crystal 7+22.*

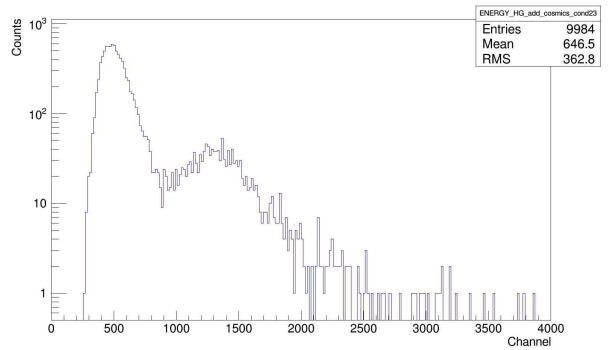


Figure 299: *Crystal 7+23.*

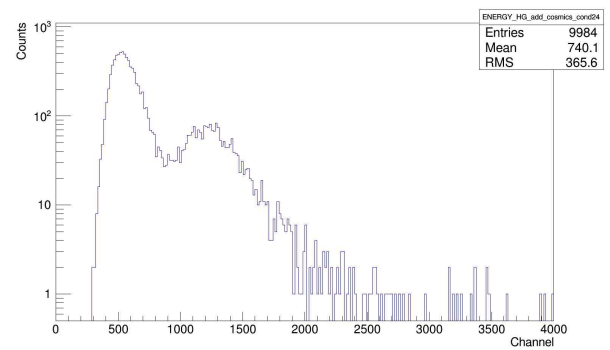


Figure 300: *Crystal 7+24.*

In coincidence with crystal 7, the crystal 24 yields the highest amplitude (see fig. 300). This procedure is continued with the other crystals as well. To verify the assumptions, the crystals in the middle row will be added. Row 2 and 4 are not taken into account since the crystals in there seem to be at their correct positions. Next, all combinations are studied and the global arrangement with the highest amplitudes in each case is chosen as the true matrix. Thus, it will be the initial matrix from here on.

Three crystals in condition:

Crystal 1:

Crystal:	Entries:	Amplitude:
21	13193	3
22	13193	0
23	13193	60
24	13193	25

Crystal:	Entries:	Amplitude:	Crystal:	Entries:	Amplitude:	Amplitude:	Amplitude:	Amplitude:	Amplitude:	Amplitude:	Amplitude:	Amplitude:	Amplitude:	Amplitude:	Amplitude:	Amplitude:
11	3893	6	1	2825	7	16	73	210	105	105	105	105	105	105	105	105
11	33377	35	1	26654	38	73	80	210	105	105	105	105	105	105	105	105
11	6808	70	1	7158	80	210	210	210	210	210	210	210	210	210	210	210
11	25324	35	1	20834	45	105	105	105	105	105	105	105	105	105	105	105

Crystal 3:

Crystal:	Entries:	Amplitude:
21	20948	35
22	20948	25
23	20948	3
24	20948	30

Crystal:	Entries:	Amplitude:	Crystal:	Entries:	Amplitude:	Amplitude:	Amplitude:	Amplitude:	Amplitude:	Amplitude:	Amplitude:	Amplitude:	Amplitude:	Amplitude:	Amplitude:	Amplitude:
13	5601	60	3	4516	40	135	135	135	135	135	135	135	135	135	135	135
13	44134	40	3	27723	30	95	95	95	95	95	95	95	95	95	95	95
13	8150	3	3	5237	7	13	13	13	13	13	13	13	13	13	13	13
13	34444	30	3	23806	25	85	85	85	85	85	85	85	85	85	85	85

Crystal 4:

Crystal:	Entries:	Amplitude:
21	7209	20
22	7209	55
23	7209	1
24	7209	3

Crystal:	Entries:	Amplitude:	Crystal:	Entries:	Amplitude:	Amplitude:	Amplitude:	Amplitude:	Amplitude:	Amplitude:	Amplitude:	Amplitude:	Amplitude:	Amplitude:	Amplitude:	Amplitude:
14	4306	25	4	2252	35	80	80	80	80	80	80	80	80	80	80	80
14	36163	100	4	10415	80	235	235	235	235	235	235	235	235	235	235	235
14	6393	17	4	1261	5	23	23	23	23	23	23	23	23	23	23	23
14	28102	30	4	6168	25	58	58	58	58	58	58	58	58	58	58	58

Crystal 7:

Crystal:	Entries:	Amplitude:
21	9984	25
22	9984	4
23	9984	40
24	9984	80

Crystal:	Entries:	Amplitude:	Crystal:	Entries:	Amplitude:	Amplitude:	Amplitude:	Amplitude:	Amplitude:	Amplitude:	Amplitude:	Amplitude:	Amplitude:	Amplitude:	Amplitude:	Amplitude:
12	3449	11	7	3829	40	76	76	76	76	76	76	76	76	76	76	76
12	21283	25	7	17770	40	69	69	69	69	69	69	69	69	69	69	69
12	5284	25	7	4661	60	125	125	125	125	125	125	125	125	125	125	125
12	17241	50	7	15546	100	230	230	230	230	230	230	230	230	230	230	230

Matrix:

0	1	2	3	4
5	6	7	8	9
10	11	12	13	14
15	16	17	18	19
20	21	22	23	24
	23	24	21	22

Figure 301: **Crystal arrangement analysis.** The crystals are investigated by using cosmic coincidences. Next, several combinations of positions are studied and compared to each other.

13.2.4 Cosmic single calibration

The calibration is performed by using cosmics and coincidences within the crystal columns. At first, the raw peaks are gathered without any condition. These are obtained by applying Landau fits onto the raw data:

1060	1120		1350	1059	1209	982		1200	1226
1278	1292	960	2050	970	1321		1198	1150	1220
	1900	1900	2087	1323		1200	1920	1140	1217
	1165		1500	2054		1143	1378	1450	
	1297	825	1099	960		1499	1387	1212	1231

Table 44: *Cosmic raw peaks.*

In the next step, coincidences are set such that only those events of an APD are selected when the second APD registered events above the cosmic peak. This ensures a suppression of background signals.

1072	1119		895.8	1061	1218	987.9		993	1215
1289	1303	962	1863	928.9	1350		1186	1075	1182
	1607	1599	2246	1339		993	1924	1205	1248
	1191		1223	2215		1175	1437	1299	
	1299	673	1101	785.9		1507	1393	1212	1265

Table 45: *Cosmic coincidence peaks.*

The values in table 45 are used to calibrate the crystals. In contrast to previous works which utilized the mean of both APDs, this is the very first calibration based on single APDs. This means, though each crystal is equipped with two APDs, the crystal matrix is treated such as it would exist twice: Once for high gain 1 and once for high gain 2.

Next, two calibrations are applicable: A relative calibration where all channels are calibrated with regard to the central channel or an absolute calibration where all channels are calibrated independent from each other relating to an “external” reference. The decision is made for an absolute calibration utilizing the mean energy deposit of cosmics traversing a crystal. Assuming cosmic muons to be at relativistic speeds at ground level, they can be treated as MIPs. Therefore, they will deposit 2 MeV/(g/cm²) in average. The mean stopping power of a crystal is given as 27.526 MeV/cm [147].

Then, the crystals are individually calibrated with this mean energy loss of cosmics.

13.2.5 Noise

There are two different common methods to determine noise: RMS⁸⁹ and standard deviation which are basically the same when the mean is zero (this is valid when a DC component is not present). In case of using the standard deviation (AC) the mean is equal to zero which is not the case when using RMS (AC+DC) [149]. Thus, the major difference is the division by N instead of $N - 1$. Given measurements of a value x with n observations, it is:

$$x_{\text{RMS}} = \sqrt{\frac{1}{n}(x_1^2 + x_2^2 + \dots + x_n^2)} \quad (4.4)$$

$$x_{\text{Std}} = \sqrt{\frac{\sum (x_i - \bar{x})^2}{N - 1}} \quad (4.5)$$

⁸⁹Root mean square

In principle, the standard deviation is a measure of the variation in the observations and the RMS is a sort of an average of them. The noise input is assumed to be Gaussian. Hence, in the following, the noise is defined as $N = 3 \cdot x_{\text{RMS}}$. The noise is an important aspect to determine precisely the energy of particles since signals are subject to variations:

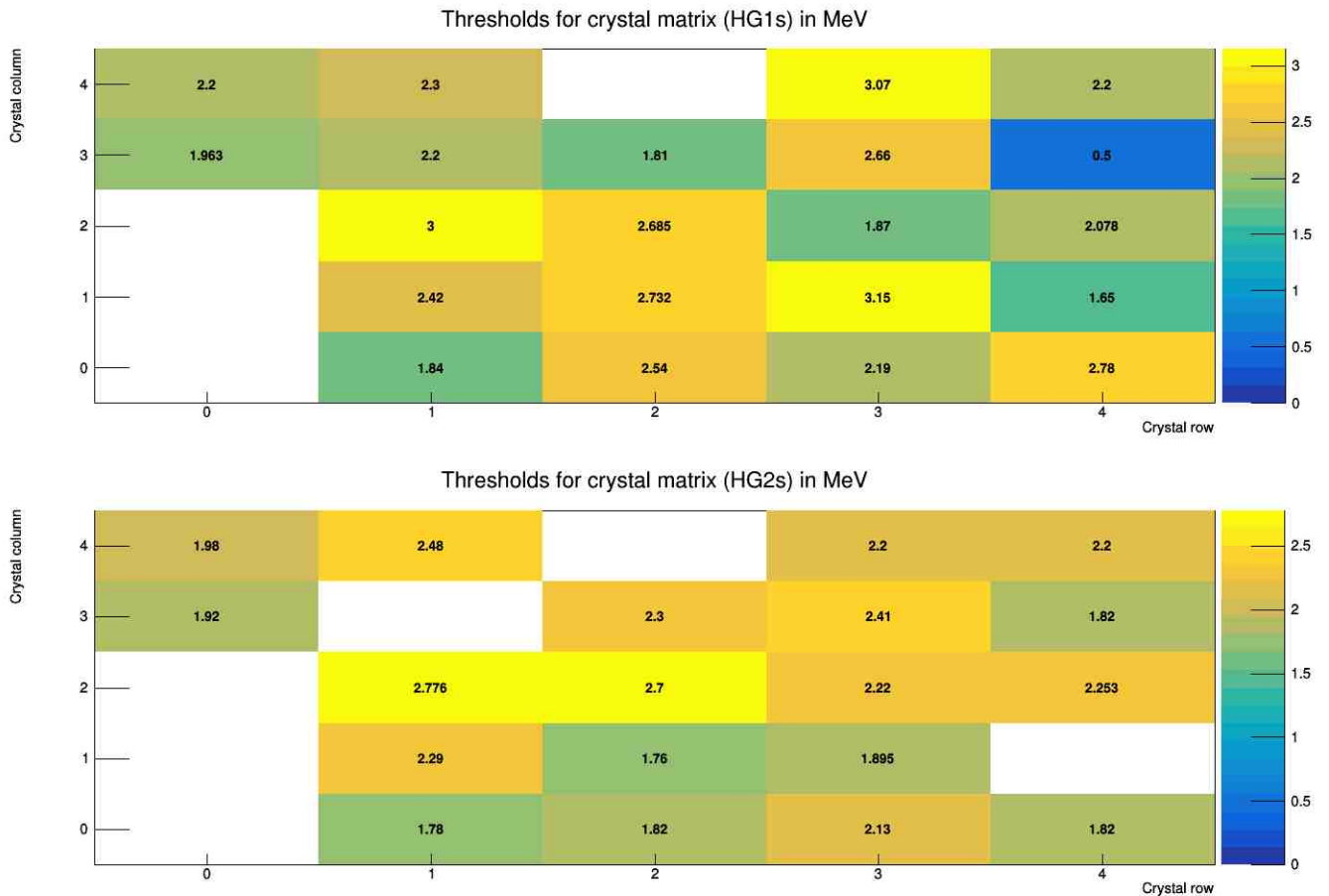


Figure 302: *Individual noise of each channel*. All channels are below 3 MeV.

13.2.6 Linearity

As already mentioned in Electromagnetic Calorimeter on page 24, the linearity of a detector is one of the most important aspects. A linear calorimeter will deliver a constant response for given energies. The relationship between measured signal and deposited energy is extremely significant in order to draw reliable conclusions about the observed particle. In the following in fig. 303, the measured linearity of the Proto120 is depicted for the selected tagger energies:

Energy linearity for HG1

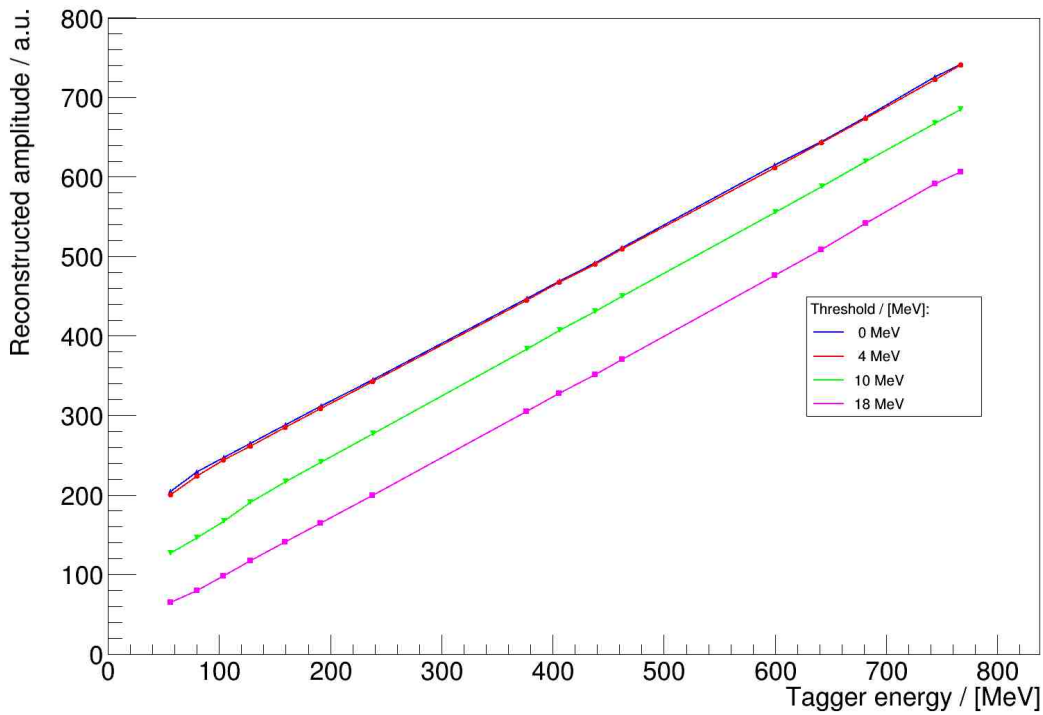


Figure 303: *Energy linearity of the Proto120 using one readout channel.* Since only the linearity among the tagger channels is of interest here, the energy itself is not referred to an absolute reference.

Some thresholds are applied on the readout channels to study the amount of deviation they will cause. A threshold of 4 MeV does very hardly change the reconstruction of energy. Higher thresholds will subtract energies and complicate the reconstruction of the correct corresponding energy.

Energy linearity for both APDs

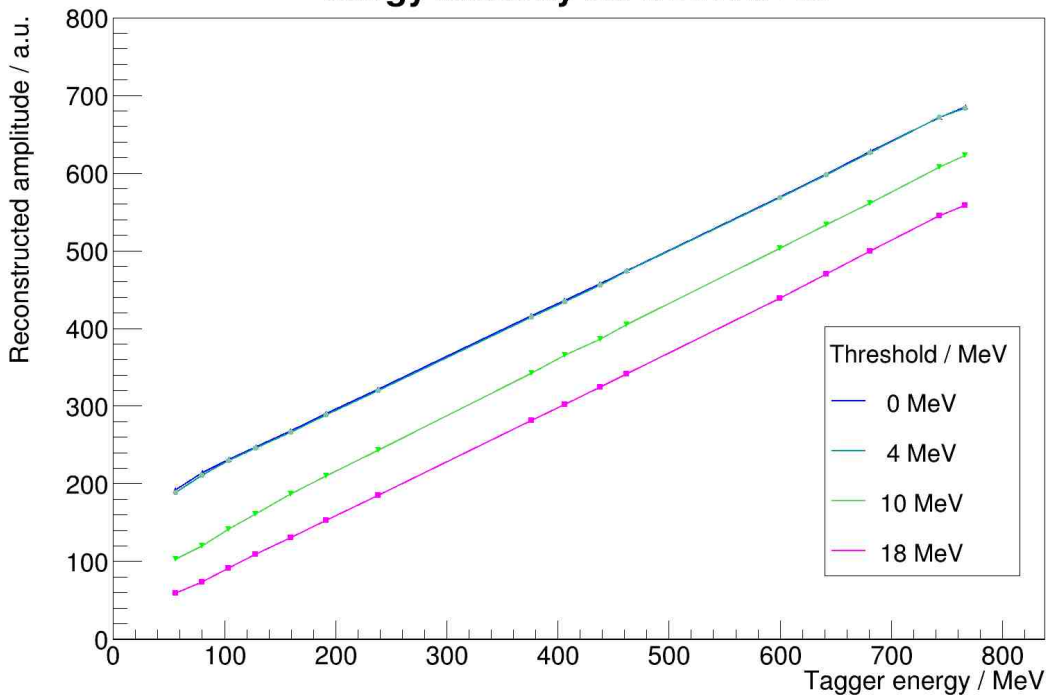


Figure 304: *Energy linearity of the Proto120 using both readout channels.* The linearity is also given when the second channel is taken into account in addition.

13.2.7 Readout cable

Due to routing constraints within the slice, a new differential readout cable is produced by Bedea and checked. The attenuation between the regular CAT6 cable and the new Bedea cable is $E_{\text{Bedea}}/E_{\text{cat6}} \sim 64\% = -2 \text{ dB}$ and it is within the specs. Furthermore, it can also be restored by modifying the line driver.

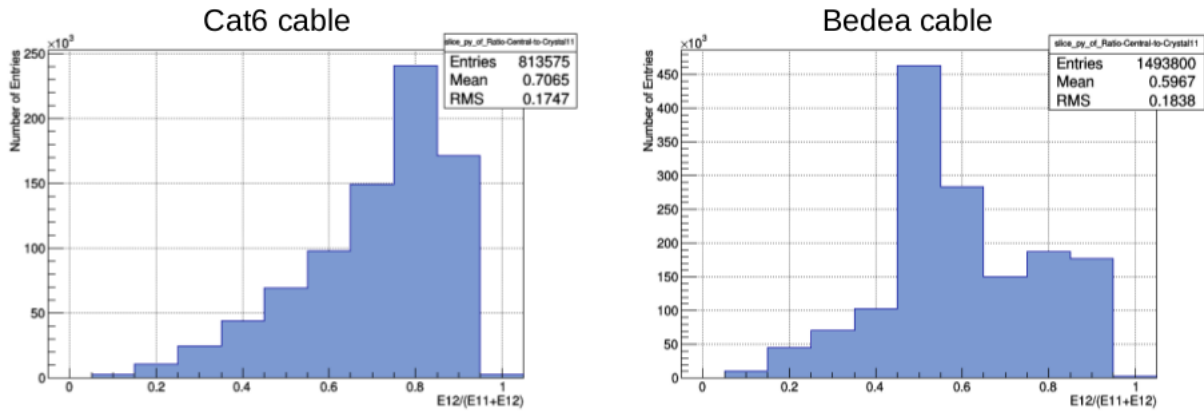


Figure 305: *Bedea and CAT6 cable comparison* [76]. Only the central crystal is applied with the Bedea cable. Hence, a ratio $E_{12}/(E_{11} + E_{12})$ between crystal 11 and 12 is used for both cables to get a better comparison.

13.2.8 Light pulser fiber coupling

A calibration utilizing the light pulser reveals that the obtained calibration factors differ more than by performing a calibration via cosmics.

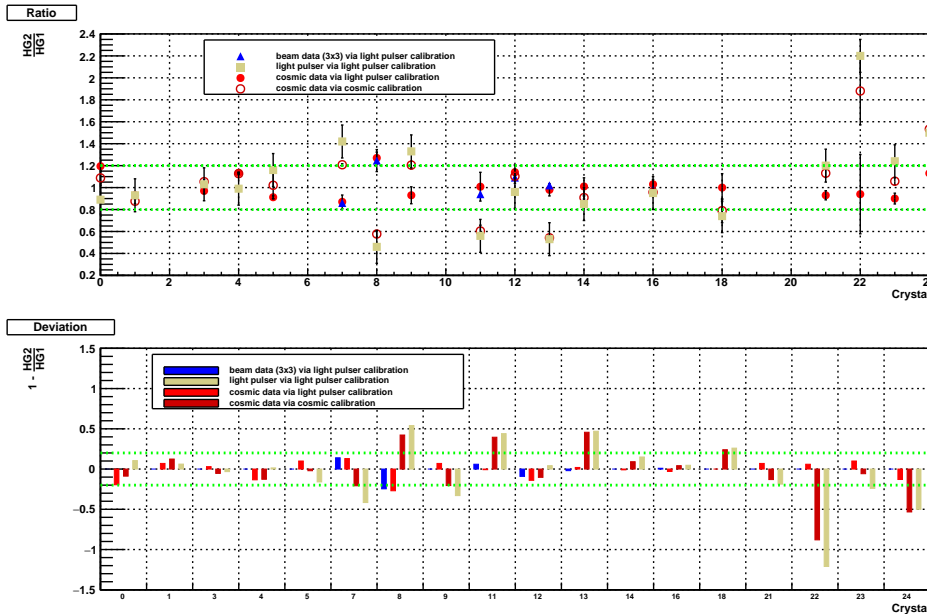


Figure 306: *APD ratio of different signal productions*. To study the ratio between the APD gains, these are calibrated according to different signal production mechanism: Each with the light pulser and to validate the data compared with cosmic calibration via cosmics.

The green lines mark an arbitrary region around the APD gain ratio of 1. It appears that a calibration via beam data is the most satisfying. But due to the obvious differences between the calibration results when using the light pulser, the light injection into the crystals is investigated in detail (see on page 161).

14 Light coupling

14.1 Filters

Filter	Coupling depth / mm	Voltage / kV	Current / mA	Time / min
/	5	1.823	1.499	10
8	5	1.822	1.502	10
7	5	1.822	1.502	10
6	5	1.822	1.502	10
5	5	1.822	1.502	10
4	5	1.822	1.502	10
4	7.5	2.174	1.502	10
3	7.5	2.173	1.797	10
3	7.5	2.395	1.996	10
2	7.5	2.395	1.996	10

Table 46: *Measurement settings when using the filters.* The fiber is attached to position (1), thus, at top and points directly towards the crystal. Voltage and current refers to the high voltage supply. For the filters 2 and 3, it is necessary to change the coupling depth and high voltage as these filters do not provide enough transmission to keep the settings unmodified. Therefore, filters 4 and 3 are then used as a reference.

14.2 Experimental settings

Position	Coupling depth	Signal / ch.	σ / ch.	Filters	Light yield phe^-
(1)	8 mm	1238	132.4	3	7912.644
(2)	8 mm	1069	115	3	6832.485
(3)	8 mm	2483.2	200.5	4	5774.967
(4)	8 mm	1024.5	123	6	1251.994
(5)	8 mm	871.4	108.7	3 + 4	12952.582

Table 47: *Experimental results for the light coupling using the cap with no coating.* The high voltage is set to 1.806 kV with a current of 1.483 mA.

Position	Coupling depth	Signal / ch.	σ / ch.	Filters	Light yield phe ⁻
(1)	12 mm	1109.3	116	2	12368.6096
(2)	12 mm	866.5	101.7	2	9661.4083
(3)	12 mm	1180.2	126.1	3	7543.2168
(4)	12 mm	1013.1	114.5	3	6475.2016
(5)	12 mm	1857.7	170.2	2	20713.21

Table 48: *Experimental results for the light coupling at 12 mm depth and a cap with no coating.* The high voltage is set to 1.806 kV with a current of 1.483 mA.

Position	Coupling depth	Signal / ch.	σ / ch.	Filters	Light yield phe ⁻
(1)	8 mm	2612.9	159.5	3	16700.28077
(2)	8 mm	2045.8	137.7	3	13075.6762
(3)	8 mm	1795	126.4	4	11453.52028
(4)	8 mm	1886.1	189	6	12054.9579
(5)	8 mm	1297.3	96.7	3 + 4	19283.2

Table 49: *Experimental results for the light coupling at 8 mm depth and a cap with BaSO₄ coating.* The high voltage is set to 1.806 kV with a current of 1.483 mA.

Position	Coupling depth	Signal / ch.	σ / ch.	Filters	Light yield phe ⁻
(1)	12 mm	2028.2	135.75	2	22614.2738
(2)	12 mm	1721.4	121.6	2	19193.47749
(3)	12 mm	2390.2	152.8	3	15276.8996
(4)	12 mm	1928.5	127.4	3	13325.956
(5)	12 mm	2720.6	159.4	2	30344.4805

Table 50: *Experimental results for the light coupling at 12 mm depth and a cap with BaSO₄ coating.* The high voltage is set to 1.806 kV with a current of 1.483 mA.

14.3 Slitrani settings

14.3.1 Geometrical and optical properties

The parameters are given without units as they are prescribed inside the physics of SLitrani.

Air	
n	1.0003
ρ	0.001239
La	10000
	isotropic

Table 51: *Optical properties of air.* The world medium is air.

14.3.2 Fiber

Fiber					
<i>Geometric</i>	properties		<i>Optical</i>	properties	
Medium	plastic		Emission	sinuscosinus	
r_{\min}	0		t_{\max}	35	°
r_{\max}	0.1	cm	Emission axis	x	
z	0.2	cm	Emission spectrum	/	
ϕ_{start}	-180	°	fixed source	false	
ϕ_{end}	+180	°	source	/	
μ	1		emission face	true	
			direction face	x	
			λ	464.8	nm

Table 52: *Geometrical and optical properties of the fiber.* The properties of the fiber are taken from the manufacturer's datasheet (see).

14.3.3 Cap

Cap_{sphere}			Cap_{tube}		
<i>Geometrical properties</i>			<i>Geometrical properties</i>		
Medium	BaSO ₄		Medium	BaSO ₄	
r_{\min}	0.5	cm	r_{\min}	0.5	cm
r_{\max}	0.7	cm	r_{\max}	0.7	cm
θ_{\min}	0	°	z	1.7	cm
θ_{\max}	180	°			
ϕ_{\min}	+90	°			
ϕ_{\max}	-90	°			

Table 53: **Geometrical properties of the cap.** The cap consists of four single pieces of which three form the tube part. Together they represent the Cap_{tube} above.

BaSO₄	
<i>Optical properties</i>	
Proportion of diffused photons	0.01
n_{real}	~ 0.65
n_{complex}	~ 5.6
μ	1
Supplementary absorption	0.01
θ_{\max} of diffused photons	90°
type of source	isotropic

Table 54: **Optical properties of the coating.** The reflective properties of barium sulfate are very similar to those of aluminum which is used in the simulation. The proportion of diffused photons indicates the amount of photons which are diffused instead of reflected. Supplementary absorption is used for revetments and adds an additional part of absorption. The maximum angle for diffused photons is θ_{\max} . The difference between diffusion and reflection is that diffusion is not limited to a plane to reflect the photons.

Real part of refraction index | Pure aluminium

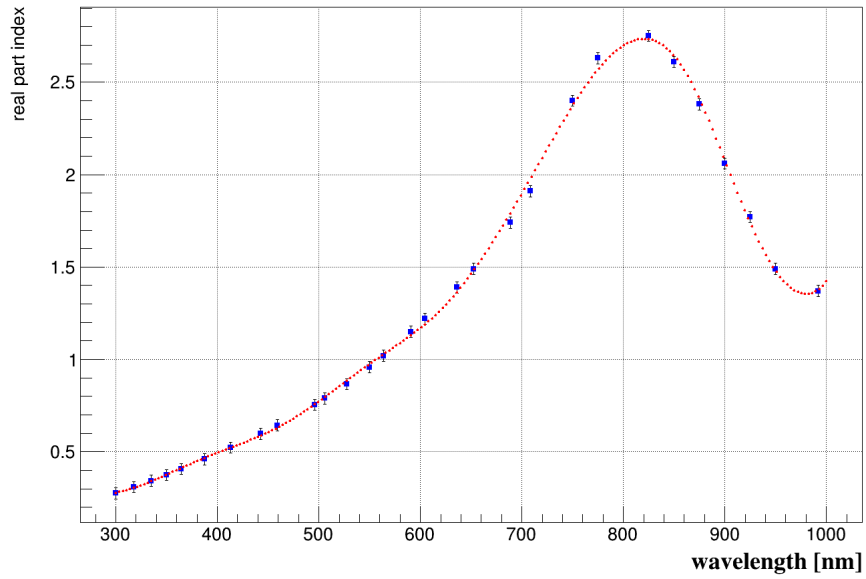


Figure 307: *Real part of the refraction index of aluminum.*

Im. part of refraction index | Pure aluminium

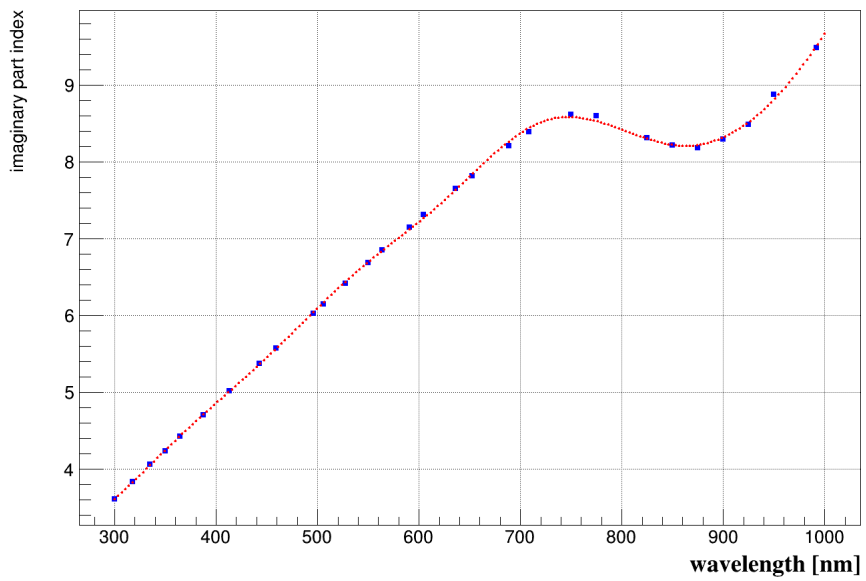


Figure 308: *Imaginary part of refraction index of aluminum.*

14.3.4 Crystal

Crystal		
<i>Geometrical</i>		
Medium	PbWO ₄	
z	20	cm
<i>Optical</i>		
X_0	0.893	
λ_γ	19.5	
R	2	
μ	1	
r	1.0003	
ρ	0.001239	
	anisotropic	
	IsUniAxialNegBirefr	

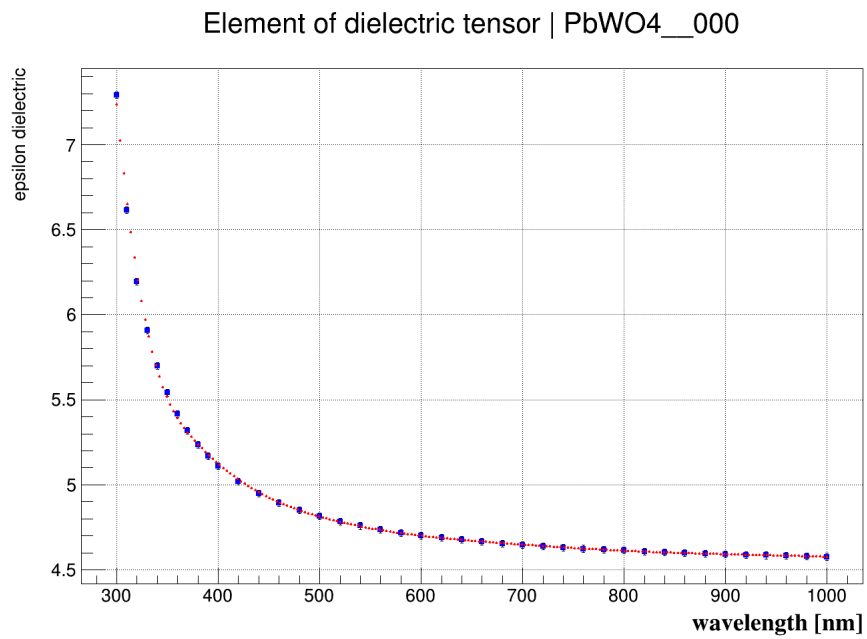


Figure 309: *Dielectric tensor of PbWO₄.*

Absorption Length | PbWO₄

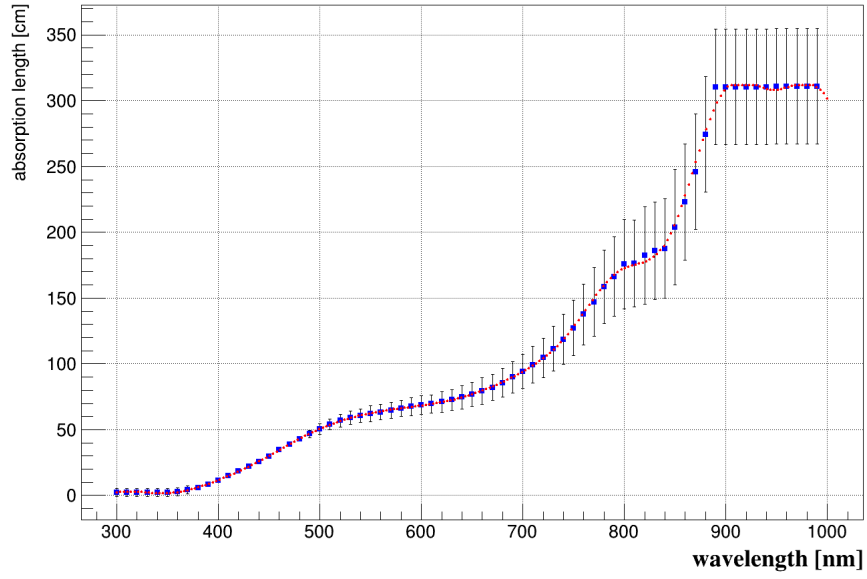


Figure 310: *Absorption length of PbWO₄.*

Emission Spectrum | Lead tungstate PbWO₄ doped with lanthane

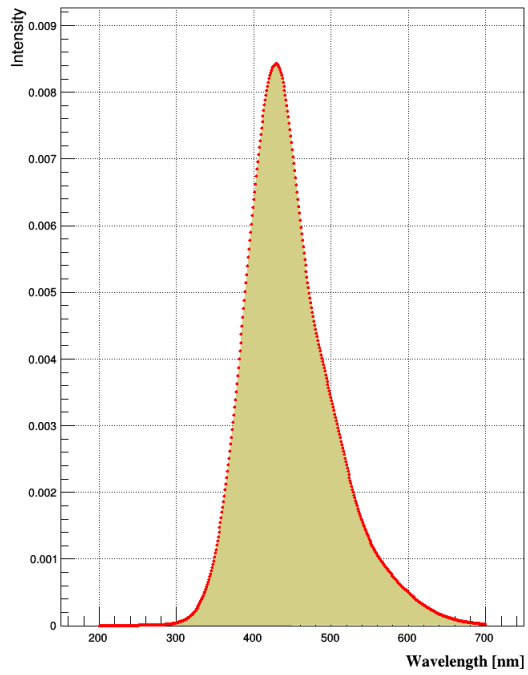


Figure 311: *Emission spectrum of PbWO₄.*

14.3.5 Wrapping

Wrapping

Medium	DF ₂₀₀₀ MA	
z	$20 + 2 * 63.5 \cdot 10^{-4} + 2 * 100 \cdot 10^{-4}$	cm

Real part of refractive index | VM2000

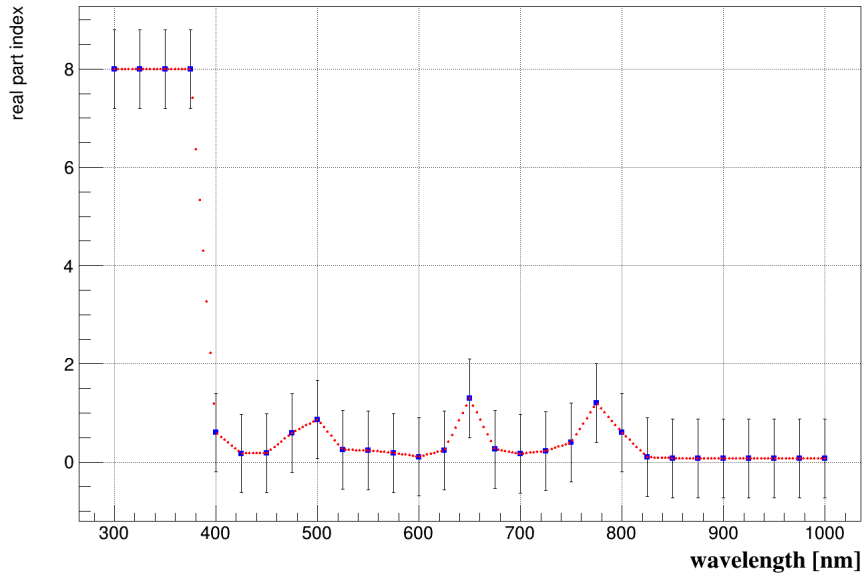


Figure 312: *Real part of VM2000.*

Im. part of refractive index | VM2000

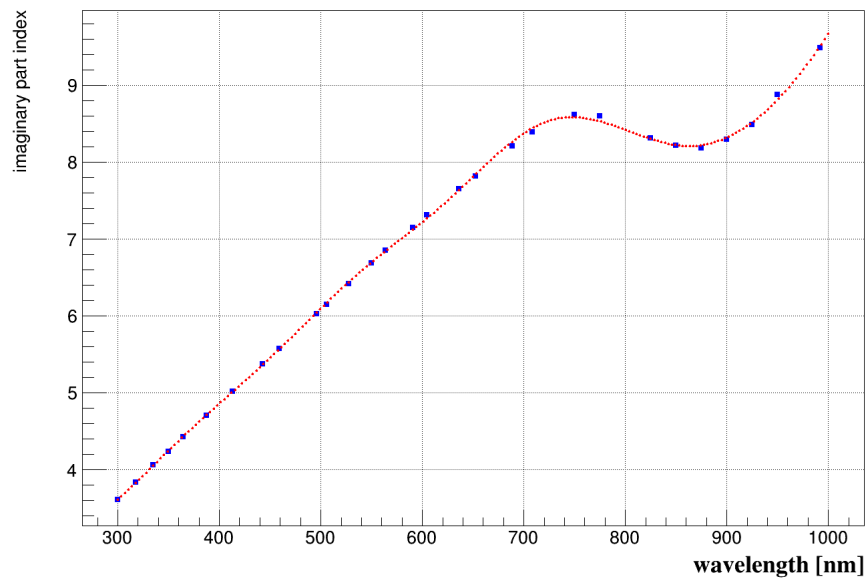


Figure 313: *Imaginary part of VM2000.*

14.3.6 Glue

Glue		
Medium	Dow Corning 3145 Silicone Adhesive Clear	
x	0.0005	cm
y	1.4 + 0.01	cm
z	0.7 + 0.01	cm

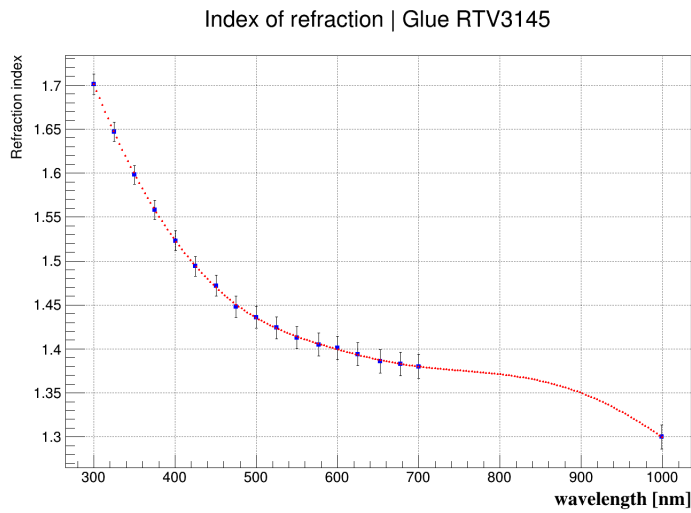


Figure 314: *Refraction index of the glue.*

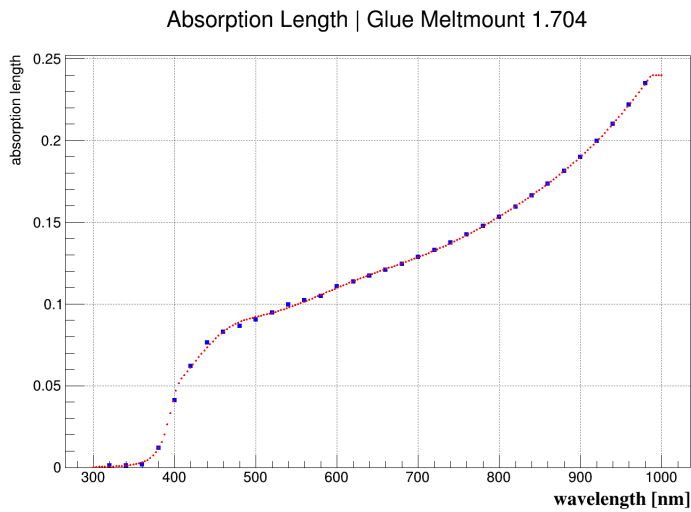


Figure 315: *Absorption length of the glue.*

14.3.7 Silicon

Silicon		
ρ	2.33	g/cm ³
sensible	true	
μ	1.0	

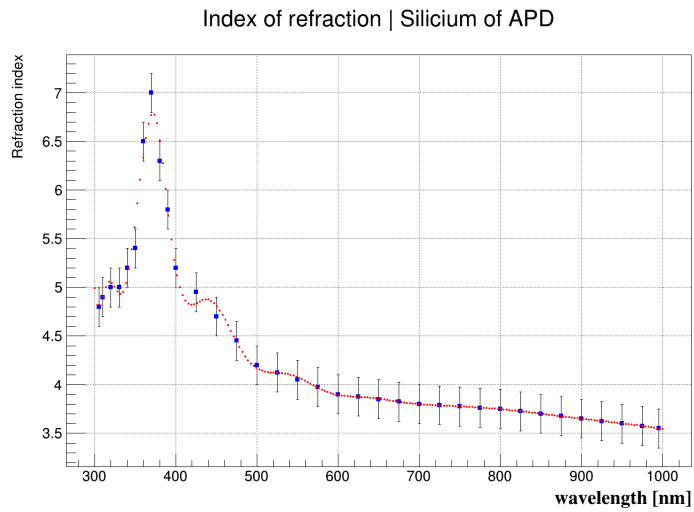


Figure 316: *Refraction index of silicium.*

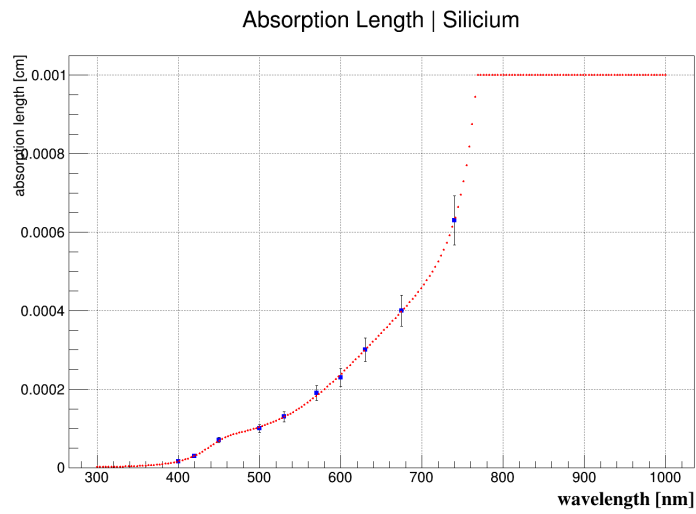


Figure 317: *Absorption length of silicium.*

14.3.8 APD

APD		
Medium	Silizium	
x	1.4	cm
y	0.7	cm
z	0.02	cm

Gain profile of APD or PIN | APD used in CMS

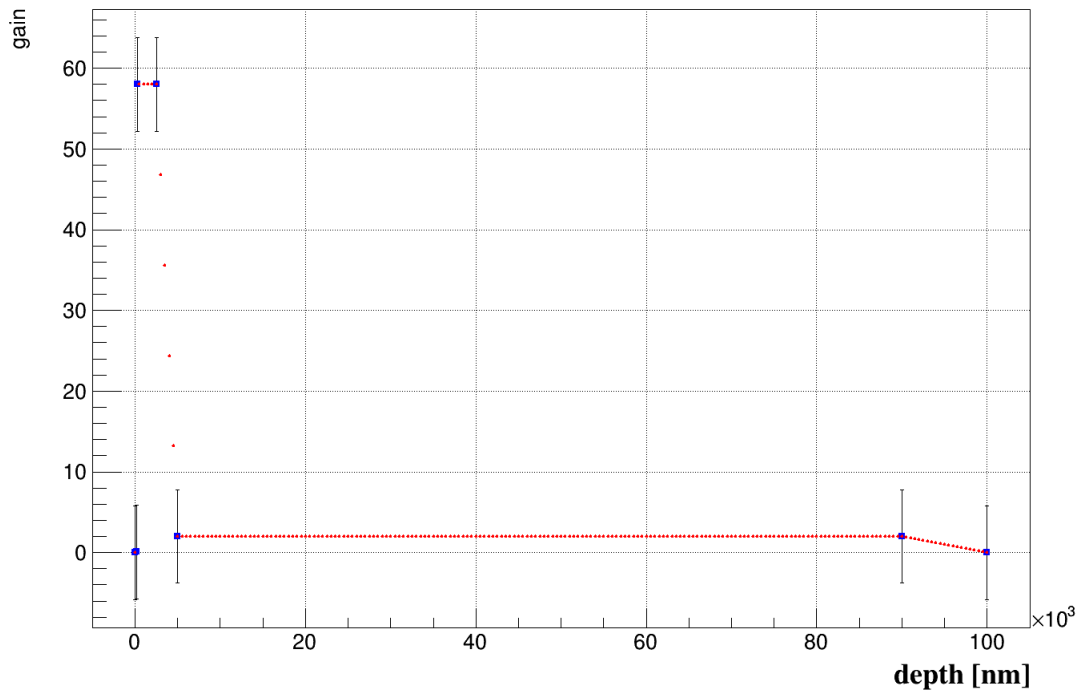


Figure 318: *Slitrani gain profile of the APD*. The maximum gain value is 60 in SLitrani.

14.3.9 Best angles

		z	+3	+2	+1	0	-1	-2	-3
	x								
Efficiency	-4				15.3 %	16.9 %	14.3 %		
Angle					-8°	171°	+7°		
Efficiency	-2		14.39 %	16.5 %	19.9 %	15.7 %	14.7 %		
Angle			+81°	-100°	-134°	-49°	-43°		
Efficiency	0	14.4 %	14.6 %	14.6 %	13.9 %	15.4 %	14.37 %	13.78 %	
Angle		+82°	+84°	+61°	-106°	-106°	-57°	75°	
Efficiency	6	14.6 %	14 %	13.97 %	14 %	13.28 %	13.96 %	14.25 %	
Angle		111°	78°	-67°	-42°	+131°	-67°	-112°	
Efficiency	12	13.9 %	14.56 %	13.8 %	14.1 %	14.1 %	14.2 %	14.08 %	
Angle		-109°	40°	-70°	167°	+120°	118°	86°	

Table 55: *Results of the light simulation of the cap.* The table shows the most efficient angle within a 360° angle scan at certain positions. The x-axis indicates the direction to the crystal. The efficiencies provide an error of 0.0016 %.

15 Data sheets

Type No. S11048(X2)

Doc. No. K30-B70077

2. Ratings and Characteristics

2-1. General Ratings

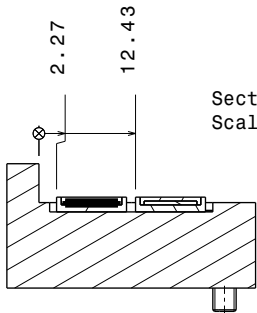
Parameter	Rating	Unit
Window material	Epoxy resin	--
Active area	14.0x6.8	mm
Package	Ceramic	--

2-2. Absolute Maximum Ratings

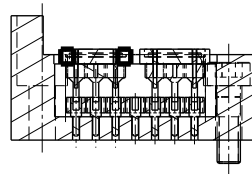
Parameter	Symbol	Value	Unit	Remark
Operating Temperature	Topr	-20 ~ +60	°C	Non-Condensing
Storage Temperature	Tstg	-20 ~ +80	°C	Non-Condensing

2-2. Electrical and Optical Characteristics (Ta=25°C)

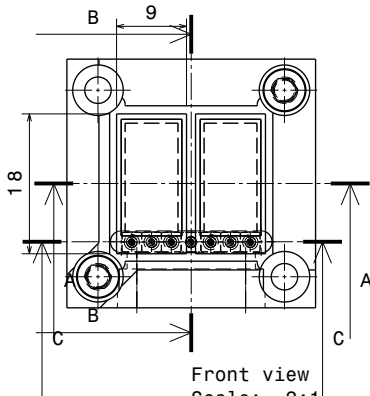
Parameter	Symbol	Condition	Min.	Typ.	Max.	Unit
Spectral Response range	λ	M=50	--	320 to 1000	--	nm
Peak sensitivity wavelength	λ_p	M=50	--	580	--	nm
Quantum Efficiency	QE	$\lambda=420\text{nm}$, M=1	--	70	--	%
Breakdown Voltage	VBR	IR=100 μ A	--	400	500	V
Dark Current	ID	M=50	--	10	80	nA
Cutoff Frequency	fc	M=50, RL=50 Ω	--	11	--	MHz
Terminal Capacitance	Ct	M=50, f=100kHz	--	270	--	pF
Excess Noise Figure	x	M=50, $\lambda=420\text{nm}$	--	0.2	--	--
Gain	M	$\lambda=420\text{nm}$	--	50	--	--



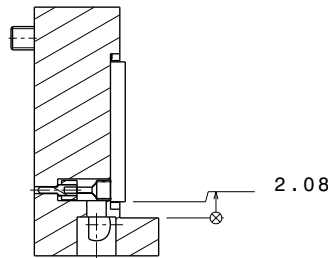
Section view A-A
Scale: 2:1



Section view C-C
Scale: 2:1



Front view
Scale: 2:1



Section view B-B
Scale: 2:1

DIESE ZEICHNUNG WURDE AUF
THIS DRAWING WAS DRAW ON
CAD
GEZEICHNET, ALLE VERÄNDERUNGEN
MÜSSEN AM COMPUTER ERFOLGEN.
ALL MODIFICATIONS MUST BE DONE
ON COMPUTER
STAND VOM: 19.12.17. T.W.
REVISION STATE

SOWEIT NICHT ANDERS ANGEGEBEN
ALLE SCHRAUBEN NACH ISO 4762
ALLE STIFTE NACH ISO 8735
UNLESS OTHERWISE NOTED
ALL SCREWS IN ISO 4762
ALL BOLTS IN ISO 8735

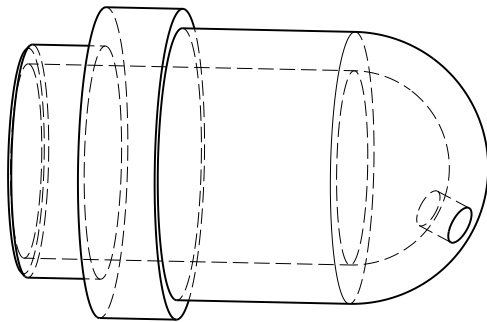
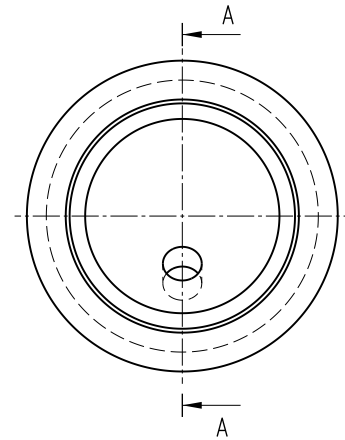
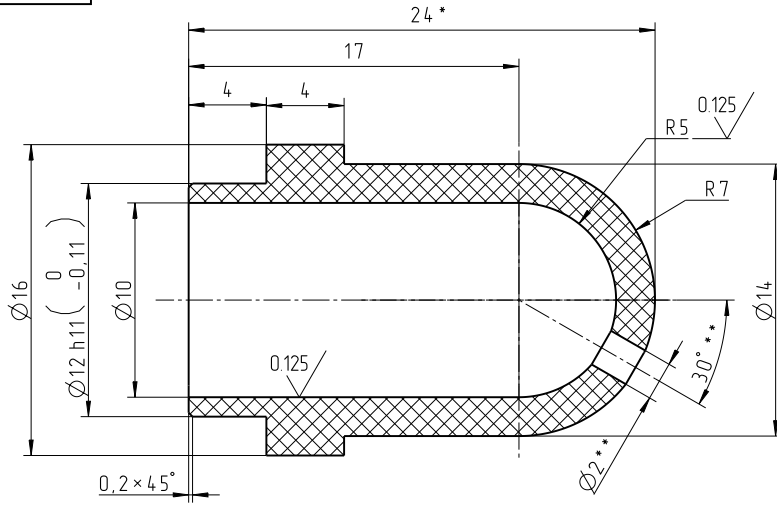
ALLE SCHRAUBEN UND MUTTERN
MIT SCHNORRSCHIBE GESICHERT
ALL SCREWS SECURED BY TOOTHED
WASHERS FORM "S" Fa. SCHNORR

	BL. NR.
ZUS BLAETTER	200
ASSY. SHEET	
DETAIL BLAETTER	300 - 304
DETAIL SHEET	
BRENSCH.-BL.	--
TEMPL. SHEET	

JUSTUS-LIEBIG- UNIVERSITÄT GIESSEN FACHBEREICH 07			Mass-Staff Scale	SH.VIEW												
<table border="1"> <tr> <th>2013</th> <th>Datum Date</th> <th>Name</th> </tr> <tr> <td>Entw. Des.</td> <td>19.01.</td> <td>WASEM</td> </tr> <tr> <td>Gez. Drawn</td> <td>19.01.</td> <td>WASEM</td> </tr> <tr> <td>Gepr. Check.</td> <td>00.00</td> <td>Name</td> </tr> </table>			2013	Datum Date	Name	Entw. Des.	19.01.	WASEM	Gez. Drawn	19.01.	WASEM	Gepr. Check.	00.00	Name	<p>Für diese Zeichnung behalten wir uns alle Rechte vor, auf für den Fall der Patenterteilung oder Gebrauchsmustereintragung. We reserve all rights for this drawing even in case of patent, grant and registration of other industrial property rights. © JUSTUS-LIEBIG UNIVERSITÄT GIESSEN</p>	
2013	Datum Date	Name														
Entw. Des.	19.01.	WASEM														
Gez. Drawn	19.01.	WASEM														
Gepr. Check.	00.00	Name														
			BEW_KOPF													
			--													
ANSPRECHPARTNER PHYSIK: Dr. R. NOVOTY			13K_004_020_12													
			200													
			xx Bl.													


94-00-00-60*6

32/√1√1



Isometric view[2]
Scale: 5:1

- ** Location of the hole with diameter 2 mm is defined by the customer. Hole machining have to be made by the customer.
- ISO 2768-mK
- ISO 13715 $L^{-0.1} l^{-0.1}$
- * Dimensions for reference.
- Material: plastic. Color: white. Material for reflector production is defined by the customer.

				9409-00-00-15				
CHNG	SHEET	N DOCUM	SIGN	DATE	Reflector Type N1	LIT	WEIGHT	SCALE
DRAWN		Kvashina E.		09/11/16			0,002	5:1
CHKR		Ferapontov V.				SHEET	SHEETS 1	
M.CONTR.						 INSTITUTE FOR HIGH ENERGY PHYSICS Russia Protvino		
S.CONTR.					see it.5 TR			
APPD		Levin A.			Format A3			

FIRST APPLICATION 9409-00-00-00
 NOTE N
 SIGN AND DATE
 COPY N
 CHANGE N
 SIGN AND DATE
 N. ORIG.

Optran® UV, Optran® WF

Silica / silica fiber

Superior performance and fiber optic properties from UV to IR wavelengths: CeramOptec®'s Optran® UV / WF fibers are available in a range of core diameters and assemblies, tailored to your specific application needs.

Wavelength

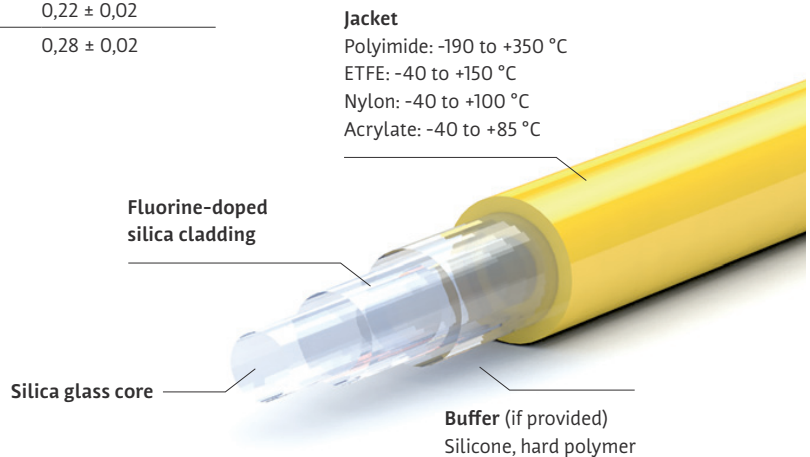
Optran® UV	190–1200 nm
Optran® WF	300–2400 nm

Numerical aperture (NA)

Low	0,12 ± 0,02
Standard	0,22 ± 0,02
High	0,28 ± 0,02

Advantages

- Pure synthetic, fused silica glass core
- High resistance against laser damage
- Step-index profile
- Special jackets available for high temperatures, high vacuum and harsh chemicals
- Very low NA expansion
- Biocompatible material
- Sterilisable using ETO and other methods



Technical data

Wavelength / spectral range	Optran® UV: 190 – 1200 nm Optran® WF: 300–2400 nm
Numerical aperture (NA)	0,12 ± 0,02 0,22 ± 0,02 0,28 ± 0,02 or customised
Operating temperature	-190 to +350 °C
Core diameter	Available from 25 to 2000 µm
Standard core / cladding ratios	1:1,04 1:1,06 1:1,1 1:1,15 1:1,2 1:1,25 1:1,4 or customised
OH content	Optran® UV: high (> 700 ppm) Optran® WF: low (< 1 ppm) Fibers with OH contents < 0,25 and < 0,1 ppm are available upon request
Standard proof test	100 kpsi (nylon, ETFE, acrylate jacket) 70 kpsi (polyimide jacket)
Minimum bending radius	50 × cladding diameter (short-term mechanical stress) 150 × core diameter (during use with high laser power)
Product code	See reverse side

Headquarter

CeramOptec® GmbH, Siemensstr. 44, 53121 Bonn, Germany
Sales / Development, Brühler Straße 30, 53119 Bonn, Germany
 Phone: +49.228.979 670, Fax: +49.228.979 6799
sales@ceramoptec.com, www.ceramoptec.com

Production sites

CeramOptec® GmbH Brühler Straße 30, 53119 Bonn, Germany
 CeramOptec® SIA Domes iela 1a, 5316 Livani, Latvia



Daylighting Film DF2000MA

Description

3M™ Daylighting Film DF2000MA is a polymeric film providing specular reflection with greater than 99% luminous reflectivity. This metal-free, non-corroding and non-conducting film is well-suited for daylighting applications. It has a pressure-sensitive adhesive for a secure bond and a polyethylene liner to protect its reflective surface during installation.

End Uses

Film DF2000MA may be used for a variety of commercial and residential applications.

Unsuitable End Uses for This Film

- Exposure to:
 - Sunlight radiation wavelengths less than 380 nm
 - Abrasive conditions, which may scratch the film
- Graphics and signs; contact 3M Graphics Market Center at 1-800-374-6772 for alternatives

Product Characteristics

Optical Characteristics

Characteristic	Value	Test
Luminous Reflectivity	> 99%	ASTM E1164-02/ E308-01
Color a* b*	-2 < a* < 2 -2 < b* < 2	ASTM E1164-02/ E308-01
Bandwidth, 90% Reflectivity (0 to 80° angle of incidence)	400 to 775 nm	3M
Wavelengths Transmitted (0 to 80° angle of incidence)	> 775 nm	3M

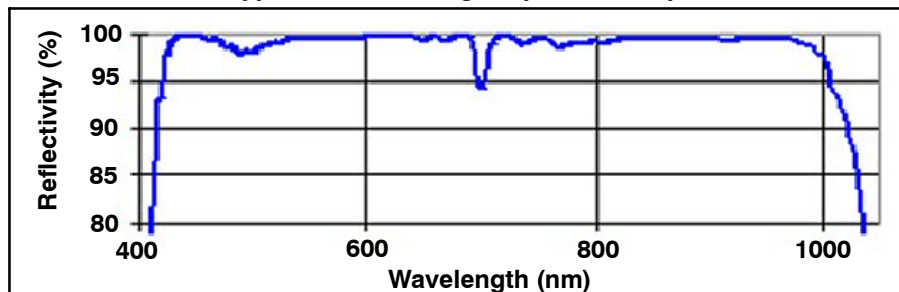
Optical Characteristics (continued)

Characteristic	Value	Test
Wavelengths Absorbed	< 400 nm	3M
Usage Angle	0 to 90 degrees	3M

Physical Characteristics

Characteristic	Value	Test
Film	Polymeric film	-
Liner, Adhesive	Paper	-
Liner, Protective	Polyethylene	-
Adhesive	Pressure-sensitive	-
Width Film and Liners Adhesive	51 inches (130 cm) > 49 inches (125 cm)	-
Total Thickness (nominal) Film Adhesive Liner, Adhesive Liner, Protective	8.1 mils (206 μm) 2.6 mils (66 μm) 1.5 mils (38 μm) 2.9 mils (74 μm) 1.1 mils (28 μm)	3M
Total Density (film, adhesive and liners)	20 ft ² /lb (4 m ² /kg)	3M
Tensile Strength (film)	> 35 lb/in (6.2 kg/cm)	ASTM D-882
Elongation at Break (film)	> 60%	ASTM D-882
Modulus (film)	> 550 lb/in ² (39 kg/cm ²)	ASTM D-882
Heat Shrinkage (film)	< 1% at 302°F (150°C), 15 minutes	ASTM D-1204-02

Typical Normal Angle Spectral Response



**Fast Time Response, 51 mm (2 Inch) Diameter,
12-Stage, Bialkali Photocathode Head-on Type**

GENERAL

Parameter		Description / Value	Unit
Spectral Response	R1828-01	300 to 650	nm
	R2059	160 to 650	nm
Wavelength of Maximum Response		420	nm
Photocathode	Material	Bialkali	—
	Minimum Effective Area	φ46	mm
Window Material	R1828-01	Borosilicate glass	—
	R2059	Synthetic silica glass	—
Dynode	Structure	Linear focused	—
	Number of Stages	12	—
Operating Ambient Temperature		-30 to +50	°C
Storage Temperature		-30 to +50	°C
Base		20-pin glass base	—
Suitable Socket		E678-20B (supplied)	—

MAXIMUM RATINGS (Absolute Maximum Values)

Parameter		Value	Unit
Supply Voltage	Between Anode and Cathode	3000	V
	Between Anode and Last Dynode	400	V
Average Anode Current		0.2	mA

CHARACTERISTICS (at 25 °C)

Parameter		Min.	Typ.	Max.	Unit
Cathode Sensitivity	Luminous (2856 K)	60	90	—	μA/lm
	Radiant at 420 nm	—	85	—	mA/W
	Blue Sensitivity Index (CS 5-58)	—	10.5	—	—
Anode Sensitivity	Luminous (2856 K)	200	1800	—	A/lm
	Radiant at 420 nm	—	1.7 × 10 ⁶	—	A/W
Gain		—	2.0 × 10 ⁷	—	—
Anode Dark Current (after 30 min. storage in darkness)		—	50	400	nA
Time Response	Anode Pulse Rise Time	—	1.3	—	ns
	Electron Transit Time	—	28	—	ns
Pulse Linearity	at 2 % Deviation	—	250	—	mA
	at 5 % Deviation	—	500	—	mA

VOLTAGE DISTRIBUTION RATIO AND SUPPLY VOLTAGE

Electrodes	K	G1	G2 & Dy1	Dy2	Dy3	Dy4	Dy5	Dy6	Dy7	Dy8	Dy9	Dy10	Dy11	Dy12	P
Ratio	1.2	2.8	1.2	1.8	1	1	1	1	1	1	1.5	1.5	3	2.5	

Supply Voltage: 2500 Vdc, K: Cathode, Dy: Dynode, P: Anode, G: Grid

SPECIAL VOLTAGE DISTRIBUTION RATIO FOR PULSE LINEARITY MEASUREMENTS

Electrodes	K	G1	G2 & Dy1	Dy2	Dy3	Dy4	Dy5	Dy6	Dy7	Dy8	Dy9	Dy10	Dy11	Dy12	P
Ratio	1.2	2.8	1.2	1.8	1	1	1.2	1.5	2	2.8	4	5.7	8	5	

Supply Voltage: 2500 Vdc, K: Cathode, Dy: Dynode, P: Anode, G: Grid

References

- [1] Albrecht Gillitzer. Strong Interaction Physics with PANDA. *Meson 2010*, page P. 4, 2010.
- [2] A. Annenkov, E. Auffray, A. Borisevich, M. Korzhik, P. Lecoq, and V. Ligun. Suppression of the radiation damage in lead tungstate scintillation crystal. *Nuclear Instruments and Methods in Physics Research A* 426 486-490, 1999.
- [3] A. A. Annenkov, M.V. Korzhik, and P. Lecoq. Lead tungstate scintillation material. *Nuclear Instruments and Methods in Physics Research A* 490 30-50, 2002.
- [4] Arthur Haas. Einführung in die theoretische Physik mit besonderer Berücksichtigung ihrer modernen Probleme. *Walter de Gruyter & Co.*, 1923.
- [5] Aspencore. <https://www.electronics-tutorials.ws/diode/diode5.gif>. 18.06.18.
- [6] S. Baccaro, L. M. Barone, B. Borgia, F. Castelli, F. Cavallari, I. Dafl. Dafinei. de Notaristefani, M. Diemoz, A. Festinesi, E. Leonardi, E. Longo, M. Montecchi, and G. Organtini. Ordinary and extraordinary complex refractive index of the lead tungstate PWO crystal. *Nuclear Instruments and Methods in Physics Research A* 385, 209-214, 1997.
- [7] Bastian Mathieu, Sebastien Heymann, and Mathieu Jacomy. Gephi: an open source software for exploring and manipulating networks. *International AAAI Conference on Weblogs and Social Media.*, 2009.
- [8] Ben Bolker. <https://bbolker.github.io/mixedmodels-misc/glmmFAQ.html#testing-significance-of-random-effects>. 08.11.2018.
- [9] Ben Bolker. Assessing Convergence for Fitted Models. <https://www.rdocumentation.org/packages/lme4/versions/1.1-17/topics/convergence>, 13.11.2018.
- [10] Bergmann and Schaefer. Lehrbuch Der Experimentalphysik - Band III Optik. *Walter de Gruyter*, page 241.
- [11] J. Beringer et al. Passage of PParticle Through Matter. *Particle Data Group*, page 25, 2013.
- [12] Bertram Kopf. Physics with Antiprotons at PAND. *J. Phys.: Conf. Ser.* 69 012026, 2007.
- [13] A. Borisevich, A. Fed, A. Fedorov., Hofstaetter, M. Korzhik.and K. Meyer, O. Missevitch, and R. Novotny. Lead tungstate scintillation crystal with increased light yield for the PANDA electromagnetic calorimeter. *Nuclear Instruments and Methods in Physics Research A* 537 (2005) 101-104, 2005.
- [14] A. E. Borisevich, V. I. Dormenev, M. V. Korzhik, O.V. Misevich, and A. A. Fedorov. Lead Tungstate Scintillation Crystals with Improved Light Yield for Experimental High-Energy Physics. *ISSN 0020-4412, Instruments and Experimental Techniques, 2006, Vol. 49, No. 2, pp. 199-202, Pleiades Publishing, Inc, 2005.*
- [15] M. Bosetti, C. Furetta, C. Leroy, S. Pensotti, P.G. Rancoita, M. Rattaggi, M. Redaelli, M. Rizzatti, A. Seidman, and G. Terzi. Effects on charge collection and structure of n-type silicon detectors irradiated with large fluences of fast neutrons. *Nuclear Instruments and Methods in Physics Research A* 343 435-440, 1994.
- [16] Brandon M. Greenwell. Inverse Estimation/Calibration Functions. <https://github.com/bgreenwell/investr>, 2016.
- [17] Bundesministerium für Bildung und Forschung. https://static1.bmbfcluster.de/5/4/8/4_cb57bb50968c33b/5484meg_4141928c73c2343.jpg. 14.06.2017.
- [18] S. Burachas, M. Ippolitov, V. Manko, S. Nikulin, A. Vasiliev, A. Apanasenko, A. Vasiliev, A. Uzunian, and G. Tamulaitis. Temperature dependence of radiation hardness of lead tungstate (PWO) scintillation crystals. *Elsevier*, 2009.

- [19] M. P. Bussa. On Behalf Of tThe Panda Collaboration. *Czechoslovak Journal of Physics, Vol. 55, Suppl. A*, 2005.
- [20] M. Böhm, A.E. Borisevich, G.Yu. Drobychev, A. Hofstaetter, O.V. Kondratiev, MV. Korzhik, M. Luh, B.K. Meyer, J.P. Peigneux, and A. Scharmann. Influence of Mo Impurity on The Spectroscopic And Scintillation Properties PbWO₄ Crystals. *LAPP-EXP-*, 1999.
- [21] P. Bühler. Studying hadrons in matter with PANDA. *Hyperfine Interact 209:105–110*, 2012.
- [22] D. Calvo et al. Hybrid pixel detector in the PANDA experiment. *Proceedings Of Science*, 2009.
- [23] Changling Huang, Christopher C. Lowman, Brandon E. Osborne, Gabrielle M. Salib, Ari Rapkin Blenkhorn, Jonathan S. Graf, Samuel Khuvis, Matthias K. Gobbert, Tyler Simon, and David Mountain. Performance Studies of the Blossom V Algorithm.
- [24] Chemming Hu. https://people.eecs.berkeley.edu/~hu/Chenming-Hu_chi.pdf. *University of California, Berkely*, 2009.
- [25] Christian Joachim Schmidt. GSI Darmstadt.
- [26] Christof Motzko. Analyse des Zeralls Psi(2S) -> KsKsPioPiogamma und Entwicklung eines Lichtpulser-systems für das PANDA EMC. *Ruhr-Universität Bochum*, 2012.
- [27] Christoph Rosenbaum. Optimization of the Front-End electronics of the PANDA Barrel EMC. *Uni Glessen*, 2016.
- [28] Christopher Lukas Hahn. Measurements on the radiation hardness of the high voltage subdistribution prototype of the Electromagnetic Calorimeter for the PANDA Experiment. *Master Thesis*, 2017.
- [29] Claude Leroy and Pier-Giorgio Rancoita. Radiation interaction in Matter and Detection. *World Scientific Publishing Co. Pte. Ltd*, 2009.
- [30] Colin J Morningstar and Mike Peardon. The glueball spectrum from an anisotropic lattice study. *arXiv:hep-lat/9901004v2* ; Image from <https://www.andrew.cmu.edu/user/cmorning/glueballs.html>, 1999.
- [31] CMS Collaboration. The Electromagnetic Calorimeter Technical Design Report. *CERN/LHCC 97–33, CMS TDR 4*, 1997.
- [32] PANDA Collaboration. Technical Progress Report for: PANDA. Strong Interaction Studies with Antiprotons.
- [33] PANDA Collaboration. Technical Design Report for the: PANDA Micro Vertex Detector. 2011.
- [34] PANDA Collaboration. The Cluster-Jet Target Developments for the Pellet Target, modified. *Technical Design Report for the PANDA Internal Targets*, 2014.
- [35] ConvertUnits.com. page <https://www.convertunits.com/molarmass/PbWO4>, 26.01.2018.
- [36] Crystal Clear Collaboration. <https://crystalclear.web.cern.ch>. 25.09.2018.
- [37] Crystaltechno Ltd. <http://www.crystaltechno.com/Img/Al.gif>. 15.09.2018.
- [38] Daniel Andreas Bremer. Measurements and Simulations on Position Dependencies in the Response of Single PWO Crystals and a Prototype for the PANDA EMC. 2013.
- [39] David Guichard. An Introduction to Combinatorics and Graph Theory. *Creative Commons, 543 Howard Street, 5th Floor, San Francisco, California, 94105, USA*, 2018.

- [40] K. Deiters, M. Diemoz, N. Godinovic, Q. Ingram, E. LonE. Longo. Montecchi, Y. Musienko, S. Nicol, B. Patel, D. Renke, S. Reucroft, R. Rusack, T. Sakhelashvili, A. Singovski, I. Soric, J. Swain, and P. Vikas. Investigation of the avalanche photodiodes for the CMS electromagnetic calorimeter operated at high gain. *Elsevier, Nuclear Instruments and Methods in Physics Research A* 461 574–576, 2001.
- [41] A. Dolinskii. Collector Ring project at FAIR. <https://www.researchgate.net/publication/280491941>, 2015.
- [42] A. Dolinskii, K. Knie, C. Dimopoulou, V. Gostishchev, S. Litvinov, F. Nolden, and M. Steck. Antiproton complex at the FAIR project. *Nuclear Instruments and Methods in Physics Research - Section A - Accelerators Spectrometers Detectors and Associated Equipment*, 2011.
- [43] Douglas Bates, Martin Maechler, Ben Bolker, Steven Walker, Rune Christensen, Henrik Singmann, Bin Dai, Fabian Scheipl, Gabor Grothendieck, and Peter Green. Linear Mixed-Effects Models using 'Eigen' and S4. <https://github.com/lme4/lme4/> <http://lme4.r-forge.r-project.org/>.
- [44] Eric Hart. Antiproton Physics at GSI - The GSI Project. 2015.
- [45] W. Erni et al. Technical Design Report for the PANDA Straw Tube Tracker. 2012.
- [46] Excelitas Technologies. Avalanche photodiode : A User Guide. 13.06.2018.
- [47] Fan Yang, Rihua Mao, Liyuan Zhang, and Ren yuan. A Study on Radiation Damage in PWO-II Crystals. *IEEE Transactions on Nuclear Science* , Vol. 60, No. 3, 2013.
- [48] Fatemeh Rajabi Alni and Alireza Bagheri. The Hungarian Algorithm with a Single Input Set. *Advanced Studies in Biology*, Vol. 4, No. 1, page 27 – 35, 2012.
- [49] Francis Halzen and Alan D. Martin. Quarks & Leptons: An Introductory Course in Modern Particle Physics. *John Wiley & Sons, Inc*, 1984.
- [50] Francois-Xavier Gentit. Litrani: a general purpose Monte-Carlo program simulating light propagation in isotropic or anisotropic media. *Nuclear Instruments and Methods in Physics Research A* 486 35–39, 2002.
- [51] Frank Herbert Attix. Introduction to Radiological Physics And Radiation Dosimetry. *WILEY-VCH Verlag GmbH & Co. KGaA*, page 130.
- [52] François-Xavier Gentit. Optics inside anisotropic media. *DSM/DAPNIA. CEA Saclay 91191 Gif-sur-Yvette*.
- [53] A. Fyodorov, M. KorM. Korzhik. Missevitch, V. Pavlenko., V. Kachanov, A. Singovsky, A.N. Annenkov, A. Ligun, J.P. Peigneux, J.P. Vialle, J.L. Faure, and F. Binon. Progress in PbWO₄ scintillating crystal. *Radiation Measurements*, Vol. 26, No. 1, pp. 107-115, 1996.
- [54] Gafur Gulyamov, Nosir Yusupjanovich Sharibaev, and Ulugbek Inoyatillaevich Erkaboev. The Temperature Dependence of the Density of States in Semiconductors. *World Journal of Condensed Matter Physics*, 3, 216-220, 2013.
- [55] Gang Li and Xiaoyan Wang. Prediction Accuracy Measures for a Nonlinear Model and for Right-Censored Time-to-Event Data. *arXiv:1611.03063v1*, 2016.
- [56] Gass S.I. and Fu M.C. Symmetric Primal-Dual Problems. *Encyclopedia of Operations Research and Management Science, Springer, Boston*, 2013.
- [57] A. Gelman and J. Hill. Data analysis using regression and multilevel/hierarchical models. *Cambridge University Press*, page 46, 2006.
- [58] Georg Schepers. Technical Assessment Group PID Status Report. *Talk*, 2006.
- [59] Gerrit Eichner. Lineare Modelle mit R: Regression und Varianzanalyse, Lecture. *Mathematisches Institut, Justus-Liebig-Universität Gießen*, 2017.

- [60] Gerrit Eichner. personal communication. 2018.
- [61] Gesellschaft für Schwerionenphysik Darmstadt. https://www.gsi.de/work/beschleunigerbetrieb/beschleuniger/ionenquellen/sources/ion_sources.htm. 06.01.2018.
- [62] Gesellschaft für Schwerionenphysik Darmstadt. https://panda.gsi.de/oldwww/framework/content/detector/img/panda_beamtarget.jpg. 06.11.2017.
- [63] Gesellschaft für Schwerionenphysik Darmstadt. https://panda.gsi.de/oldwww/framework/content/detector/img/panda_STT_E_cut_2.jpg. 09.11.2017.
- [64] Gesellschaft für Schwerionenphysik Darmstadt. http://web-docs.gsi.de/rdzhigad/data/gallery/panda/dirc_1200x1200.png. 12.11.2017.
- [65] Gesellschaft für Schwerionenphysik Darmstadt. https://www.gsi.de/fileadmin/_processed_/8/8/csm_PandaDetector_oa32377bf8.png. *modified*, 23.10.2017.
- [66] P. Gianotti et al. The Straw Tube Trackers of the PANDA Experiment. <https://arxiv.org/pdf/1307.4537.pdf>.
- [67] J Gott, III and R. et al. A Map of the Universe. *The Astrophysical Journal* 624 (2), 2005.
- [68] L. Groening and L. Dahl. A Dedicated 70 MeV Proton Linac For The Antiproton Physics Program of The Future Facility For Antiproton And Ion Research (FAIR) at Darmstadt. *Proceedings of LINAC 2004, Lübeck, Germany*, page 42, 2004.
- [69] L. Groening, S. Mickat, and R. Brodhage. Upgrade of The Unilac For FAIR. *Proceedings of IPAC 2015, Richmond, VA, USA*, pages 1281 -- 1283, 2015.
- [70] L. et al Groening. Status of The Fair 70 MeV Proton Linac. *Proceedings of LINAC2012, Tel-Aviv, Israel*, 2012.
- [71] L. Groening et al. Upgrade of The Unilac For FAIR. *IPAC2015, Richmond, VA, USA*, 2015.
- [72] F. Grum and G. W. Luckey. Optical Sphere Paint and a Working Standard of Reflectance. *Applied Optics*, 1968.
- [73] H. H. Gutbrod, I. Augustin, H. Eickhoff, K.-D. Groß, W. F. Henning, D. Krämer, and G. Walter. FAIR Baseline Technical Report (Executive Summary). 2006.
- [74] Günther Rosner. Reise ins Innerste der Materie. *Wissenschaft für alle, GSI Darmstadt*, 2012.
- [75] Hamamatsu. Si APD, MPPC. *Handbook*, 26.02.2019.
- [76] Hans Georg Zaunick. Update on Barrel EMC Developments and Planning of Barrel Slice Assembly. *PANDA Collaboration meeting*, 08.06.2016.
- [77] Harold N. Gabow and Robert E. Tarjan. FaFast Scaling Algorithms for General Graph-Matching Problems. *Journal of the Association for Computing Machinery*, Vol. 38, No 4, 1991.
- [78] Harold W. Kuhn. The Hungarian Method for the assignment problem. *Naval Research Logistics Quarterly*, 1955.
- [79] Hirayama. Lecture Note on Photon interactions and Cross Sections. *International Conference on the Monte Carlo*, 2000.
- [80] Johannes Gutenberg Universität Mainz Institut für Kernphysik. <http://www.kernphysik.uni-mainz.de/1177.php>. 06.07.2018.
- [81] Jack Edmons. Paths, Trees And Flowers. *Canadian Mathematical Society*, 1965.

- [82] Jerzy Smyrski. Overview of the PANDA experiment. *TIPP 2011 - Technology and Instrumentation in Particle Physics*, 2011.
- [83] Johan Messchendorp. The PANDA Experiment at FAIR - Subatomic Physics with Antiprotons. 2016.
- [84] Johannes Bilk and Markus Moritz. 2018.
- [85] John C Nash, Ravi Varadhan, and Gabor Grothendieck. Expanded Replacement and Extension of the 'optim' Function. *CRAN*, 30.09.2018.
- [86] José Pinheiro, Douglas Bates, Saikat DebRoy, Deepayan Sarkar, EISPACK authors, Siem Heisterkamp, Bert Van Willigen, and R-core. Linear and Nonlinear Mixed Effects Models. *CRAN*, 2018-04-07 12:20:47 UTC.
- [87] José Pinheiro and Douglas M. Bates. Mixed-Effects Models in S and S-Plus. *Springer*, 2000.
- [88] Julian J. Faraway. Extending the linear model with R - Generalized linear, mixed effects and nonparametric regression models. *CRC Press*, 2016.
- [89] Julian Rieke. The high performance PANDA detector. *International Workshop on Antiproton Physics and Technology at FAIR*, 2015.
- [90] Juraj Stacho. Lecture notes, Introduction to Operations Research. *Columbia University, New York*, 2014.
- [91] Kai Ingo Mengel. Ansprechverhalten von PbWO₄ Szintillationskristallen auf monochromatische Photonen im Bereich zwischen 50 und 790 MeV. *Justus Liebig Universität Gießen*, 1997.
- [92] M. Kavatsyuk, H. Löhner, J. G. Messchendorp, H. Moeini, and G. Tambave. Trigger-Less Readout of the PANDA Electromagnetic Calorimeter. *DPG HK 34.1*, 2012.
- [93] Ken Suzuki. SiPM photosensors and fast timing readout for the Barrel Time-of-Flight detector in PANDA. *DIRC2017*, 2017.
- [94] Ken Suzuki et al. Technical Design Report for the PANDA Barrel Time-of-Flight. 2016.
- [95] Klaus Peters. Open and hidden charm physics with PANDA. *Talk, Beijing*, 2004.
- [96] EUGENE L. LAWLER. Combinatorial Optimization: Networks and Matroids. *Holt, Rinehart, and Winston*.
- [97] P. Lecoq, I. Dafinei, E. Auffray, M. Schneegans, M.V. Korzhik, O.V. Missevitch, V.B. Pavlenko, A.A. Fedorov, A.N. Annenkov, V.L. Kostylev, and V.D. Ligun. Lead tungstate (PbWO) scintillators for LHC EM calorimetry. *Nuclear Instruments and Methods in Physics Research A 365 291-79X*, 1995.
- [98] R. Maier. THE HIGH-ENERGY STORAGE RING (HESR). 2011.
- [99] Marco Delmastro. Experimental particle physics. *European School of Instrumentation in Particle & Astroparticle Physics*, 2014.
- [100] Maria Patsyuk. R & D for the PANDA Barrel DIRC. *Dubna Conference*, 2012.
- [101] Marin A. Pilloud and Joseph T. Hefner. Biological Distance Analysis - Forensic and Bioarchaeological Perspectives. *Elsevier Inc.*, 2016.
- [102] Mark Chen. Scintillation and Light Sensitive Detectors. *Queen's University*.
- [103] Markus Friedl. The CMS Silicon Strip Tracker and its Electronic Readout. 2001.
- [104] Markus Moritz. Measurements and improvements of the response of the PANDA-EMC prototype PROTO 60 to high energetic particles and photons in accelerator experiments. 2013.

- [105] Martin A. Green. Intrinsic concentration, effective densities of states, and effective mass in silicon. *Journal of Applied Physics* 67, 2944 (1990); doi: 10.1063/1.345414, 1989.
- [106] Matthew Shepherd, Jozef J, Dudek, and Ryan Mitchell. Searching for the rules that govern hadron construction. *Nature* 534 | Review, 2016.
- [107] J. Matthews. A Heitler model of extensive air showers. *Astroparticle Physics* 22, 387–397, 2005.
- [108] Michael Düren et al. The PANDA time-of-propagation disc DIRC. *JINST* 4 P12013, 2009.
- [109] Milan N. Wagner, Sören Fleischer, Jifeng Hu, Ye Hua, Wolfgang Kühn, Sören Lange, Yutie Liang, and Björn Spruck. Concepts for Pre-Assembly Data Acquisition for the PANDA Experiment. 52 *International Winter Meeting on Nuclear Physics - Bormio*, 2014.
- [110] Miles V. Klein and Thomas E. Furtak. *Optik. Springer-Lehrbuch*, 1986.
- [111] National Institute of Standards and Technology. <https://physics.nist.gov/PhysRefData/Xcom/html/xcom1.html>. 26.01.2018.
- [112] Naveen Kumar, Christina Mastrangelo, and Doug Montgomery. Hierarchical Modeling Using Generalized Linear Models. *wileyonlinelibrary.com*, DOI: 10.1002/qre.1176, 2011.
- [113] M. Nikl, P. Boháček, E. Mihóková, M. Martini, F. Meinardi, A. Vedda, P. Fabeni, G. P. Pazzi, M. Kobayashi, M. Ishii, and Y. Usuki. Influence of doping on the emission and scintillation characteristics of PbWO₄ single crystals. *Journal of Applied Physics* 87, 4243, 2000.
- [114] Nina Hall. FACILITY FOR ANTIPROTON AND ION RESEARCH. 2013.
- [115] F. Nolden, K. Beckert, P. Beller, U. Blell, C. Dimopoulou, A. Dolinskii, U. Laier, G. Moritz, C. Mühle, I. Nesmiyan, C. Peschke, and M. Steck. THE COLLECTOR RING CR OF THE FAIR PROJECT. 2006.
- [116] Nora Pitz. Strahlenhärte-tests mit Neutronen an Large Area APDs für das elektromagnetische Kalorimeter des PANDA-Detektors. *Johan Wolfgang Goethe Universität Frankfurt*, 2008.
- [117] R W Novotny and the PANDA collaboration. The Electromagnetic Calorimetry of the PANDA Detector at FAIR. *Journal of Physics: Conference Series* 404 (2012) 012063, 2012.
- [118] Oliver Boine-Frankenheim et al. FAIR beam parameters and intensity limits. 2015.
- [119] OptoPolymer. *München*.
- [120] K. P. O'Donnell and X. Chen. Temperature dependence of semiconductor band gaps. *Applied Physics Letters* 58 (25, page 2924, Juli, 1991.
- [121] Particle data group. Passage of particles through matter. *PDG*, 2005.
- [122] Particle data group. <http://pdg.lbl.gov/2016/AtomicNuclearProperties/index.html>. 30.12.2017.
- [123] Paul Lecoq, Alexander Gektin, and Mikhail Korzhik. Inorganic Scintillators for Detector Systems: Physical Principals and Crystal Engineering. *Springer*.
- [124] Peter Wieczorek. ASIC Development for APD readout of the PANDA EMC. *PANDA Meeting*, 2006.
- [125] Peter Wieczorek. Entwicklung eines ladungsempfindlichen Vorverstärkers zur Auslese von Lawinenfotodioden. *Johann Wolfgang Goethe – Universität*, 2008.
- [126] Peter Wieczorek and Holger Flemming. Low Noise Preamplifier ASIC for the PANDA -Experiment. *TWEPP 2011 Topical Workshop on Electronics for Particle Physics, Contribution ID 18*, 2011.

- [127] Qiang Wang, Dapeng Jin, Andreas Koop, Wolfgang Kühn, Jens Sören Lang, Yutie Liang, Ming Liu, Zhen-an Liu, David Münchow, Björn Spruck, and Hao Xu. PANDA EMC Trigger and Data Acquisition Algorithms Development. *XLVIII International Winter Meeting on Nuclear Physics, BORMIO2010*, 2010.
- [128] Rainer W. Novotny. Fast and Compact Lead Tungstate Based Electromagnetic Calorimeter for the PANDA Detector at GSI. *IEEE Transactions on Nuclear Science* 51(6):3076 - 3080, 2005.
- [129] Rainer Willi Novotny, Valera Dormenev, Till Kuske, and Markus Moritz. High-quality PWO crystals for the PANDA-EMC. *Journal of Physics Conference Series*, 2011.
- [130] Rense Nieuwenhuis, Ben Pelzer, and Manfred te Grotenhuis. Tools for Detecting Influential Data in Mixed Effects Models. <https://cran.r-project.org/web/packages/influence.ME/influence.ME.pdf>, 13.11.2018.
- [131] Richard Wigmans. Calorimetry - Energy Measurement in Particle Physics. *Oxford Science Publications*, 2000.
- [132] Rihua Mao, Liyuan Zhang, and Ren-Yuan Zhu. Optical and Scintillation Properties of Inorganic Scintillators in High Energy Physics. *IEEE Nuclear Science Symposium Conference Record*, 2007.
- [133] Roger Rusack, William Gilbert, and Rick Egeland. <http://www.hep.umn.edu/us-cms/ecal/>. 14.12.2018.
- [134] Rohit Saraf, C. Shivakumara, Sukanti Behera, H. Nagabhushana, and N. Dhananjaya. Facile synthesis of PbWO₄: Applications in photoluminescence and photocatalytic degradation of organic dyes under visible light. *ELSEVIER: Spectrochimica Acta Part A: Molecular and Biomolecular Spectroscopy* 136 (2015) 348–355, 2015.
- [135] RPubS. https://rstudio-pubs-static.s3.amazonaws.com/33653_57fc7b8e5d484c909b615d8633coid51.html. 12.11.2018.
- [136] Samir Khuller. Design and Analysis of Algorithms: Course Notes. *Department of Computer Science, University of Maryland*, 1994.
- [137] C. Schwarz. The PANDA detector at FAIR. *PACS PACS* 29.20.Dh · 29.30.Ep · 29.30.Kv.
- [138] Schwarz et al. The Barrel DIRC of PANDA. *IOP*, doi:10.1088/1748-0221/7/02/C02008, 2011.
- [139] P.A. Semenov for the PANDA collaboration. PANDA electromagnetic calorimeters. *Nuclear Instruments and Methods in Physics Research A* 598 (2009) 224–228, 2009.
- [140] Shayle R. Searle. The Matrix Handling of BLUE and BLUP in the Mixed Linear Model*. *Elsevier Science Inc.*, 1997.
- [141] Simon Gardner. Polarisation observables in neutral pion photoproduction with MAMI. *University of Glasgow*, 2016.
- [142] Simone Bianco. Tracking and vertex reconstruction with the PANDA Micro-Vertex-Detector. page 45, 2013.
- [143] S.L.Miller. Avalanche breakdown in germanium. *Phys. Rev.* 99, 1955.
- [144] Spektrum. Doppelbrechung. *Spektrum Akademischer Verlag, Heidelberg*, 1998.
- [145] Stan Wagon. Blossom Algorithm. *MathWorld--A Wolfram Web Resource, created by Eric W. Weisstein*. <http://mathworld.wolfram.com/BlossomAlgorithm.html>, 21.01.2019.
- [146] Stefan Diehl. Optimization of the Influence of Longitudinal and Lateral Non-Uniformity on the Performance of an Electromagnetic Calorimeter. *Justus Liebig Universität Gießen*, 2015.
- [147] Stefan Diehl. private conversation. 2015-2016.

- [148] Stefan Diehl, Rainer Willi Novotny, Benjamin Wohlfahrt, and Reinhard Beck. Readout concepts for the suppression of the slow component of BaF₂ for the upgrade of the TAPS spectrometer at ELSA. *Journal of Physics Conference Series* 587 012044, 2015.
- [149] Steven Smith. Digital Signal Processing: A Practical Guide for Engineers and Scientists. Newnes, page 14, 2003.
- [150] Susan Garner Garille and Saul I. Gasss. Stigler's Diet Problem Revisited. *Operations Research* 49(1):1-13. <https://doi.org/10.1287/opre.49.1.1.11187>, 2001.
- [151] Sven Menke. Messung der starken Kopplungskonstanten α_s und der hadronischen Spektralfunktionen in τ -Zerfällen.
- [152] S. M. Sze. Physics of Semiconductor Devices. Wiley-Interscience, page 683, 2007.
- [153] The electronic structure of oxygen related defects in PbWO₄ and CaMoO₄ crystals. Yonas B. Abraham and N. A. W. Holzwarth and R. T. Williams and G. Eric Matthews and Alan R. Tackett. 2001.
- [154] The PANDA Collaboration. Technical Design Report for PANDA Electromagnetic Calorimeter (EMC). 2008.
- [155] Thomas Kirn. Pilotuntersuchungen zu einem elektromagnetischen Kalorimeter aus PbWO₄-Kristallen. *Rheinisch-Westfälische technische Hochschule Aachen*, 1999.
- [156] Tobias Eißner. The new PWO Crystal Generation and Concepts for the Performance Optimisation of the PANDA EMC. 2013.
- [157] Tobias Triffterer. APD Validierungsstatus. *Ruhr*, 2017.
- [158] E. Tomasi Gustafsson. Antiproton Physics with PANDA at FAIR.
- [159] Topcoder. Hungarian algorithm. <https://www.topcoder.com/community/competitive-programming/tutorials/assignment-problem-and-hungarian-algorithm/>, 26.12.2018.
- [160] Trevor Hastie, Robert Tibshirani, and Jerome Friedman. The Elements of Statistical Learning - Data Mining, Inference and prediction. Springer, 2001.
- [161] Ulrich Wiedner. Future Prospects for Hadron Physics at PANDA. *Prog. Part. Nucl.Phys.* 66:477-518,2011, 2011.
- [162] Y. P. Varshni. Temperature Dependence of the Energy Gap in Semiconductors. *Physica* 34, 149-154, 1967.
- [163] W.N. Venables and B.D. Ripley. Statistics and Computing. *Modern Applied Statistics with S*, page 218, 2002.
- [164] Venkatesh S Kaushik. Electromagnetic Showers and Shower Detectors. *Dept of High Energy Physics, University of Texas at Arlington*, 2002.
- [165] Vladimir Kolmogorov. Blossom V: A new implementation of a minimum cost perfect matching algorithm. *Mathematical Programming Computation (MPC)*, July 2009.
- [166] P. Wieczorek and H. Flemming. Low noise preamplifier ASIC for the PANDA EMC. 2008.
- [167] P. Wieczorek and H. Flemming. Low noise preamplifier ASIC for the PANDA experiment. *JINST*, 6, C12055, 2011.
- [168] Wikimedia. https://upload.wikimedia.org/wikipedia/commons/o/ob/Floorplan_of_the_MAMI_facility.jpg. 30.09.2018.

- [169] Wikipedia Commons. https://upload.wikimedia.org/wikipedia/commons/thumb/e/e9/Ordinary_extraordinary_ray_in_birefringence.png/800px-Ordinary_extraordinary_ray_in_birefringence.png. 19.09.2018.
- [170] William W. Moses. Current trends in scintillator detectors and materials. *Nuclear Instruments and Methods in Physics Research A* 487 123–128, 2002.
- [171] A. Wilms, B. Lewandowski, and K Peters. Development of Large Area APDs for the PANDA-EMC.
- [172] Wolfgang Niessner. Elektronen-Energieverlust-Spektroskopie an Gruppe-III-Nitriden und Übergangsmetall-Oxiden. page 48, 2000.
- [173] Yu. A. Hizhnyi and S.G. Nedilko. Investigation of the luminescent properties of pure and defect lead tungstate crystals by electronic structure calculations. *ournal of Luminescence* 102–103 688–693, 2003.

15.1 Figures

List of Figures

1	<i>The modernized universal ion linear accelerator (Unilac).</i>	5
2	<i>The new proton linear accelerator (p-linac).</i>	5
3	<i>Extraction parameters of the main accelerator SIS100</i>	6
4	<i>Extraction parameters of the main accelerator SIS100</i>	6
5	<i>Production of antiprotons</i>	7
6	<i>Cooler ring</i>	8
7	<i>High energy storage ring</i>	9
8	<i>Observable hadrons at HESR</i>	11
9	<i>Charmonium states</i>	13
10	<i>Glueball spectrum</i>	14
11	<i>Hadrons in nuclear matter</i>	15
12	<i>PANDA detector</i>	17
13	<i>Target Spectrometer</i>	18
14	<i>Target system</i>	19
15	<i>Micro Vertex Detector</i>	20
16	<i>Straw Tube Tracker</i>	20
17	<i>Time-of-Flight</i>	21
18	<i>DIRC Detector</i>	21
19	<i>The Muon Tracker</i>	22
20	<i>Tracking & particle identification</i>	23
21	<i>Interactions of particles with matter</i>	25
22	<i>Mass attenuation and photon cross section of PbWO₄</i>	28
23	<i>Scheme of an electromagnetic shower</i>	30
24	<i>Longitudinal and lateral development of an electromagnetic shower</i>	31
25	<i>Shower development in iron, neon and lead tungstate.</i>	32
26	<i>Scintillation process</i>	33
27	<i>Band structure of doped inorganic scintillators and stages of the scintillation mechanism.</i>	34
28	<i>Loss of π^0 against the energy threshold</i>	35
29	<i>Overview of the barrel part of the electromagnetic calorimeter</i>	36
30	<i>Types of different crystal geometries in longitudinal direction of the EMC</i>	37
31	<i>Crystal geometry</i>	38
32	<i>Crystal geometry</i>	38
33	<i>Crystal geometry</i>	38
34	<i>Crystal structure of PbWO₄</i>	39
35	<i>Radiation damage</i>	41
36	<i>Temperature dependency of PbWO₄</i>	41
37	<i>Electronic band structure of semiconductors</i>	42
38	<i>pn junction</i>	43
39	<i>Schematic construction and mechanism of an Avalanche Photodiode</i>	44
40	<i>APD Quantum efficiency</i>	45
41	<i>Diode curve</i>	46
42	<i>APDs of CMS and PANDA in comparison</i>	47
43	<i>Diode I-V curves of irradiated APDs</i>	48
44	<i>Preamplifier and shaper APFEL ASIC.</i>	50
45	<i>Readout of the APFEL ASIC.</i>	50
46	<i>Readout chain of the EMC</i>	51
47	<i>Scheme of the complete process</i>	52
48	<i>Screening Flow Chart</i>	54

49	<i>Hierarchical structure of the Avalanche Photodiodes</i>	55
50	<i>Share of Lots relative to the pool of observations</i>	55
51	<i>Deviations in amplification and voltage observations</i>	56
52	<i>Amplification in dependency of Voltage and Lot</i>	57
53	<i>Number of observations per APD</i>	57
54	<i>Determining the bias voltage</i>	59
55	<i>Miller fit for irradiated APD 711006317</i>	62
56	<i>Miller fit zoomed</i>	62
57	χ^2_{red} <i>of the Miller fit</i>	63
58	<i>Nonlinear least square fit</i>	64
59	<i>Logarithmic transformation of APD 711006317</i>	66
60	<i>Double logarithmic transformation of APD 711006317</i>	66
61	<i>Double logarithmic transformation of the irradiated APD pool</i>	68
62	<i>Double logarithmic transformation of the not irradiated APD pool</i>	68
63	<i>Global fit for the transformed irradiated APD pool</i>	70
64	<i>Global global fit for the transformed not irradiated APD pool</i>	70
65	<i>Reconstructed global fit for the irradiated APD pool</i>	70
66	<i>Reconstructed global fit for the not irradiated APD pool</i>	70
67	<i>Individual linear mixed model fits</i>	71
68	<i>Individual linear mixed model fits</i>	72
69	<i>Residual plot - zoomed</i>	73
70	<i>Residual plot</i>	74
71	<i>qq-plot</i>	76
72	<i>Residual plot - zoomed</i>	76
73	<i>Residuals of the lots</i>	77
74	<i>Random coefficients of the mixed model</i>	78
75	<i>Q-point against amount of data points for mixed model</i>	79
76	<i>Q-point against amount of non-irradiated data points for mixed model</i>	79
77	<i>Q-point against amount of data points for polynomial</i>	79
78	<i>Q-point against amount of non-irradiated data points for polynomial</i>	79
79	<i>Change of bias voltage between mixed model and 3rd order orthogonal polynomial</i>	80
80	<i>Change of bias voltage between mixed model and 3rd order raw polynomial</i>	81
81	<i>Change of bias voltage between 3rd order raw and orthogonal polynomial</i>	81
82	<i>breakdown voltage fit of APD 711006317 at T=-25°C.</i>	83
83	<i>breakdown voltage fit of APD 711006317 at T=20°C.</i>	83
84	<i>Distributions of the bias voltages of the pool.</i>	84
85	<i>Distributions of the slopes of the pool.</i>	85
86	<i>Distributions of the breakdown voltages of the pool.</i>	86
87	<i>Distributions of the breakdown voltage of the pool through the max values.</i>	87
88	<i>Distribution of the breakdown voltage of the pool given by Hamamatsu.</i>	88
89	<i>Distribution of the fitted breakdown voltages of the pool.</i>	89
90	<i>Differences between Hamamatsu data and the fit.</i>	90
91	<i>Distances between bias voltage and breakdown voltage via max voltage values.</i>	91
92	<i>Distances between bias voltage and breakdown voltage at M=500.</i>	92
93	<i>Distances between the fitted bias and breakdown voltages.</i>	93
94	<i>The change of the bias voltage due to irradiation</i>	94
95	<i>The change of the slopes due to irradiation</i>	95
96	<i>The change of the breakdown voltages due to irradiation</i>	96
97	<i>Correlations among all parameters</i>	100
98	<i>Parameter space.</i>	101
99	<i>Parameter space - zoomed.</i>	101

100	<i>Parameter space - irradiated.</i>	101
101	<i>Parameter space - not irradiated.</i>	101
102	<i>Change of the parameter space.</i>	102
103	<i>Parameter space - similarity measurement.</i>	103
104	<i>Outlier identification for irradiated data with a threshold of 0 std.</i>	105
105	<i>Outlier identification for not irradiated data with a threshold of 0 std.</i>	105
106	<i>Outlier identification for irradiated data with a threshold of 1 std.</i>	105
107	<i>Outlier identification for not irradiated data with a threshold of 1 std.</i>	105
108	<i>Outlier identification for irradiated data with a threshold of 3 std.</i>	106
109	<i>Outlier identification for not irradiated data with a threshold of 3 std.</i>	106
110	<i>Outlier identification for irradiated data with a threshold of 10 std.</i>	106
111	<i>Outlier identification for not irradiated data with a threshold of 10 std.</i>	106
112	<i>Greedy algorithm</i>	107
113	<i>Greedy algorithm - enhancement</i>	108
114	<i>Blossom shrinkage and expansion</i>	109
115	<i>Sequence.</i>	112
116	<i>Edges of the basic matching.</i>	113
117	<i>Distribution of the pairings</i>	114
118	<i>Distribution of the pairings for the greedy algorithm</i>	115
119	<i>Influence of the APD pool on the single distances</i>	116
120	<i>Comparison between the metrics for the 1st slice</i>	117
121	<i>Voltage differences among the pairings of the 1st slice</i>	118
122	<i>Voltage differences among the pairings from greedy algorithm</i>	119
123	<i>Voltage differences among the pairings from blossom algorithm</i>	120
124	<i>Slope differences among the pairings of the 1st slice</i>	121
125	<i>Slope differences among the pairings of the greedy algorithm</i>	122
126	<i>Slope differences among the pairings of the Blossom algorithm</i>	123
127	<i>Parameter space - sphere.</i>	124
128	<i>The number of vertices in dependency on the number of edges</i>	126
129	<i>The costs in dependency on the number of vertices</i>	127
130	<i>The costs in dependency on the number of edges</i>	128
131	<i>The costs in dependency on the number of edges- range from 1 to 0</i>	129
132	<i>Five numbers in the range of {0,5} of the distance scan</i>	130
133	<i>Matching at a distance limit of 0.5.</i>	131
134	<i>Voltage and slope differences at a distance limit of 0.5.</i>	132
135	<i>Slope differences at a distance limit of 0.5.</i>	133
136	<i>Visualized network with a distance limit of 0.5.</i>	134
137	<i>Comparison of the matching with a distance limit of 1 between Blossom and Greedy</i>	135
138	<i>Comparison of the voltage difference between Blossom and Greedy at a distance limit of 0.5</i>	135
139	<i>Comparison of the voltaslopege difference between Blossom and Greedy at a distance limit of 0.5</i>	136
140	<i>Comparison of the matching with a distance limit of 1 between Blossom and Greedy</i>	137
141	<i>Comparison of the voltage difference between Blossom and Greedy at a distance limit of 1</i>	137
142	<i>Comparison of the slope difference between Blossom and Greedy at a distance limit of 1</i>	138
143	<i>Vertices and edges slope</i>	138
144	<i>Slope limits against cost and adjusted cost</i>	139
145	<i>Costs against slope limit</i>	140
146	<i>Five numbers of the slope scan in the range of $\{1 \cdot 10^{-10}, 1 \cdot 10^{-7}\}$</i>	141
147	<i>Matching of the optimal slope limit</i>	142
148	<i>Slope differences at the slope optimum</i>	143
149	<i>Voltage differences at the slope optimum</i>	144
150	<i>Number of vertices and costs against voltage limit</i>	145

151	<i>Voltage limits against cost and adjusted cost</i>	146
152	<i>The number of vertices against the number of edges in dependency on the voltage limit</i>	147
153	<i>Cost and edges against voltage limit</i>	148
154	<i>Five numbers in the voltage limit range of 0 – 100 V</i>	149
155	<i>Matching at a voltage limit of 100 mV.</i>	150
156	<i>Voltage differences at a voltage limit of 100 mV.</i>	151
157	<i>Slope differences at a voltage limit of 100 mV.</i>	152
158	<i>Visualized network with a voltage limit of 100 mV.</i>	152
159	<i>High voltage supply to operate eight APDs.</i>	154
160	<i>Multi matching.</i>	154
161	<i>Maximum voltage difference of the 8-APD cluster via Mahalanobis distance.</i>	155
162	<i>Maximum voltage difference of the 8-APD cluster by assigning the quartets via irradiated bias voltages.</i>	156
163	<i>Maximum voltage difference within the APD clusters via voltage assignment only</i>	157
164	<i>Basic fiber coupling device</i>	161
165	<i>Wrapped crystal without cap</i>	162
166	<i>Wrapped crystal with cap</i>	162
167	<i>Crystal types 7 to 1 in beam direction.</i>	162
168	<i>Crystal types 1 to 11 in beam direction</i>	162
169	<i>Readout chain of the light yield setup</i>	163
170	<i>Stability study over cooling time</i>	164
171	<i>Repeatability study</i>	165
172	<i>Comparison of overall light yield for various materials and coatings</i>	166
173	<i>Influence of irradiation on light yield for several application methods</i>	167
174	<i>Novosibirsk light pulser system</i>	168
175	<i>Transmission of the filters of the Novosibirsk light pulser system</i>	169
176	<i>Cap-fiber coupling</i>	169
177	<i>Lab setup</i>	169
178	<i>Tip insertion</i>	170
179	<i>Light injection dependency on position and angle of the fiber entry.</i>	170
180	<i>Bochum light pulser</i>	171
181	<i>Driver</i>	171
182	<i>Polishing influence on light injection</i>	171
183	<i>Spectrum of radioactive sources</i>	172
184	<i>Calibration via radioactive sources</i>	172
185	<i>Intensity in dependency of the coupling depth</i>	173
186	<i>Influence of polishing the fiber end</i>	173
187	<i>Birefringence</i>	175
188	<i>Scheme of ray propagation inside a fiber</i>	175
189	<i>Reflectivity of barium sulfate</i>	176
190	<i>Reflectivity of aluminum</i>	176
191	<i>Reflection within the cap</i>	177
192	<i>Absorbed beam</i>	177
193	<i>Backscattering of the beam</i>	177
194	<i>Successfull trajectory</i>	177
195	<i>Efficiency dependency on number of photons</i>	178
196	<i>Orientation of APDs, crystal and simulation axis</i>	179
197	<i>360° angle scan at x=y=z=0</i>	180
198	<i>360° angle scan of both APDs at x=y=z=0</i>	180
199	<i>Coordinate and angle study</i>	181
200	<i>Efficiency map</i>	182

201	<i>Time elapsed until detection</i>	183
202	<i>Elapsed distance until detection</i>	184
203	<i>Number of interaction points along trajectory</i>	185
204	<i>Correlation plot of the propagation quantities</i>	187
205	<i>APD ratio in dependency on the angle of the fiber</i>	188
206	<i>Light injection in dependency on the angle in total for both APDs</i>	188
207	<i>Detected number of photons at different x-positions of the fiber</i>	189
208	<i>Light injection at the origin across all crystal types</i>	190
209	<i>Angle definition of the crystal</i>	191
210	<i>Angle dependency on the crystal type</i>	191
211	<i>Light impinging the entrance window of the APDs at $x=-4$ and at $\theta = 171^\circ$.</i>	191
212	<i>Light impinging the entrance window of the APDs at $x=-2$ and at $\theta = -134^\circ$.</i>	192
213	<i>Light impinging the entrance window of the APDs at $x=0$ and at $\theta = -106^\circ$.</i>	192
214	<i>Light impinging the entrance window of the APDs at $x=6$ and at $\theta = -42^\circ$.</i>	193
215	<i>Light impinging the entrance window of the APDs at $x=12$ and at $\theta = 167^\circ$.</i>	193
216	<i>Share of Wafers relative to the total number of data points</i>	197
217	<i>APD 711006317 curve</i>	198
218	<i>Cook's distance of the APDs with respect to the mixed model regression</i>	200
219	<i>Residuals of the lots over the voltage range</i>	201
220	<i>Residuals of the lots over the amplification range</i>	202
221	<i>Residuals of the lot 13 - polynomial of a mixed model with 2nd order.</i>	202
222	<i>Residuals of the lot 13 - polynomial of a mixed model with 3rd order.</i>	202
223	<i>Residuals of the lot 14 - polynomial of a mixed model with 2nd order.</i>	203
224	<i>Residuals of the lot 14 - polynomial of a mixed model with 3rd order.</i>	203
225	<i>Q-point of irradiated APD 1211013550 - mixed model.</i>	203
226	<i>Q-point of non-irradiated APD 1211013550 - mixed model.</i>	203
227	<i>Q-point of irradiated APD 1211013550 - polynomial 3rd order.</i>	204
228	<i>Q-point of non-irradiated APD 1211013550 - polynomial 3rd order.</i>	204
229	<i>Q-point of irradiated APD 1609017466 - mixed model.</i>	204
230	<i>Q-point of non-irradiated APD 1609017466 - mixed model</i>	204
231	<i>Q-point of irradiated APD 1609017466 - polynomial 3rd order.</i>	205
232	<i>Q-point of irradiated APD 1609017466 - polynomial 3rd order.</i>	205
233	<i>Fitted breakthrough voltage - 711006317 - not irradiated.</i>	205
234	<i>Fitted breakthrough voltage -1211013550 - irradiated</i>	206
235	<i>Fitted breakthrough voltage -1211013550 - not irradiated</i>	206
236	<i>Fitted breakthrough voltage -1609017466 - irradiated</i>	207
237	<i>Fitted breakthrough voltage -1609017466 - not irradiated</i>	207
238	<i>Bias voltages of the irradiated APDs per lot.</i>	208
239	<i>Bias voltages of the non-irradiated APDs per lot.</i>	208
240	<i>Change of the bias voltages per lot.</i>	209
241	<i>Slope of the irradiated APDs per lots</i>	209
242	<i>Slope of the non-irradiated APDs per lots</i>	210
243	<i>Breakdown voltages of the irradiated APDs per lot.</i>	210
244	<i>Breakdown voltages of the non-irradiated APDs per lot.</i>	211
245	<i>Change of the breakdown voltages of the APDs per lot.</i>	211
246	<i>The change of the bias voltage due to temperature changes.</i>	212
247	<i>The change of the bias voltage of 532 APDs due to temperature changes.</i>	212
248	<i>APD 13103013731 - irradiated.</i>	213
249	<i>Temperature behaviour</i>	213
250	<i>Outlier across lots</i>	214
251	<i>Outlier per lots</i>	214

252	<i>Absolute change of U_{bias} under the influence of irradiation</i>	215
253	<i>Absolute change of dM under the influence of irradiation</i>	215
254	<i>Absolute change of U_{br} under the influence of irradiation</i>	216
255	<i>Graphs</i>	216
256	<i>Vertices</i>	217
257	<i>Walks</i>	217
258	<i>Paths</i>	217
259	<i>Partitions and covers</i>	218
260	<i>Matchings</i>	218
261	<i>Adjustment to a single set</i>	219
262	<i>Self loop</i>	220
263	<i>Full distance - cost against adjusted cost</i>	220
264	<i>Distance in the range from 5 to 0 - cost against adjusted cost</i>	221
265	<i>Five numbers in the full distance range</i>	221
266	<i>Voltage differences at a distance limit of 0.5.</i>	222
267	<i>Slope differences at a distance limit of 0.5.</i>	222
268	<i>Voltage differences at a distance limit of 0.3.</i>	223
269	<i>Slope differences at a distance limit of 0.3.</i>	223
270	<i>Voltage differences at a distance limit of 0.1.</i>	224
271	<i>Slope differences at a distance limit of 0.1.</i>	224
272	<i>Number of vertices against costs for varying non-irradiated voltage limits.</i>	225
273	<i>Number of edges against costs for varying non-irradiated voltage limits.</i>	225
274	<i>Number of vertices against edges for varying non-irradiated voltage limits.</i>	226
275	<i>Five numbers for two voltage thresholds in parallel.</i>	226
276	<i>Edges of the subnetwork with edges below a value of 1</i>	227
277	<i>Modularity of the reduced graph.</i>	228
278	<i>Colored communities of the reduced graph.</i>	228
279	<i>MAMI facility</i>	233
280	<i>MAMI-B</i>	233
281	<i>MAMI-C</i>	233
282	<i>Glasgow Tagger</i>	234
283	<i>Proto120</i>	234
284	<i>Calibration via radioactive sources</i>	235
285	<i>Gain readout</i>	236
286	<i>Routing map of Proto120</i>	236
287	<i>Proto120 readout</i>	237
288	<i>Proto120</i>	238
289	<i>Proto120 fibers.</i>	238
290	<i>Raw trace of crystal 12</i>	239
291	<i>Tagger channel 1 - HG1</i>	240
292	<i>Tagger channel 1 - HG2</i>	240
293	<i>Tagger channel 16 - HG1.</i>	240
294	<i>Tagger channel 16 - HG2</i>	240
295	<i>Crystal readout check</i>	241
296	<i>Cosmic Condition</i>	241
297	<i>Crystal 7+21</i>	242
298	<i>Crystal 7+22</i>	242
299	<i>Crystal 7+23.</i>	242
300	<i>Crystal 7+24</i>	242
301	<i>Calibration via radioactive sources</i>	243
302	<i>Individual noise of each channel.</i>	245

303	<i>Energy linearity of the Proto120 using one readout channel.</i>	246
304	<i>Energy linearity of the Proto120 using both readout channels.</i>	246
305	<i>Bedeac and CAT6 cable comparison</i>	247
306	<i>APD ratio of different signal productions.</i>	247
307	<i>Real part of the refraction index of aluminum</i>	252
308	<i>Imaginary part of refraction index of aluminum</i>	252
309	<i>Dielectric tensor of PbWO₄</i>	253
310	<i>Absorption length of PbWO₄</i>	254
311	<i>Emission spectrum of PbWO₄.</i>	254
312	<i>Real part of VM2000</i>	255
313	<i>Imaginary part of VM2000</i>	255
314	<i>Refraction index of the glue</i>	256
315	<i>Absorption length of the glue</i>	256
316	<i>Refraction index of silicium</i>	257
317	<i>Absorption length of silicium</i>	257
318	<i>Slitrani gain profile of the APD</i>	258

Danksagung

Da ich diese Arbeit thematisch nicht im Goto-Stil, also weitgehend linear geschrieben habe, stellt diese Seite jene dar, auf die ich so lange hingearbeitet habe. Auch wenn sie im Verlauf immer weiter von mir rückte. Nun ist es soweit und diese Zeilen stellen die letzten Meter des Ariadnefadens dar, dem ich über mehrere Jahre hinweg gefolgt bin. Da solch eine Arbeit stets auch mit dem Umfeld verknüpft ist, in der sie entsteht, möchte ich hiermit allen danken, die daran mitgewirkt haben:

Zunächst Kai, der mir quasi durch Bereitstellen des Fadens es überhaupt ermöglichte, mich diesem Unterfangen gerüstet stellen zu können. Auch als der Faden knapp wurde, hast Du ihn erweitert und so dafür gesorgt, dass ich den Stier überhaupt erreichen konnte. Ohne Dich wäre ein wichtiges Kapitel in meinem Leben nicht möglich gewesen, dafür vielen Dank!

Mit dem Faden ist es natürlich nicht getan, denn er musste ja schließlich auch ausgelegt werden. Hierbei konnte ich vor allem auf Eric, Hans und Gerrit zählen. Eric, Du hattest immer ein Ohr offen für mich, selbst dann, wenn es gerade eigentlich nicht passte. Das rechne ich Dir hoch an. Entsprechend auch das Beantworten überabzählbarer Fragen, zu denen zum Beispiel jene zur Klassifizierung der Delta-Resonanzen gehört. Aber auch für jegliche, weitere Unterstützung habe ich Dir zu danken und ich vermisse die morgendlichen Diskussionen, pünktlich um 7 Uhr beginnend, jetzt schon. Das beinahe instantane Korrigieren der vielen Seiten kann ich gar nicht versuchen zu begleichen. Aber wenn doch, lass es mich wissen! Hans, wie auch Eric, warst auch Du mir stets eine große Hilfe und immer verfügbar, wenn ich nicht weiter wusste. Vor allem bezüglich allem, was mit Programmieren zu tun hat, warst Du ein sehr hilfreicher Haltepunkt und hattest on-the-fly stets parat, was meinen eigenen Zeilen fehlte. Ohne Dich hätte so manches merklich länger gedauert. Gerrit habe ich insofern zu danken, als dass Du mir eine neue Welt gezeigt hast, nämlich die der Statistik. Ich habe durch Dich viel gelernt, gerade, was das statistische Programmieren anbelangt aber auch diverse Modelle, Vorgehensweisen und Gedankengänge drumherum. Letztlich kann ich sagen, dass ein bedeutender Teil dieser Arbeit ohne Dich lange nicht so detailliert und kompetent möglich gewesen wäre. Die angenehmen Gespräche und den guten Tee darf ich hier natürlich auf keinen Fall vergessen. Eric, Hans und Gerrit: Ohne Euch Drei wäre das tiefe und weitläufige Labyrinth nicht so beleuchtet und sicherlich noch größer gewesen.

Für alle technischen Belange und jegliche Laboraufbauten waren mir zudem Valera, Markus und René eine unverzichtbare Hilfe. Beim Zähmen der Ausleseelektronik, sowie bei allen mechanischen und elektronischen Belangen konnte ich mich immer an Euch wenden. Stefan, Markus und Christof danke ich zudem für die Unterstützung beim Proto120 und zu ROOT. Die letzte Strahlzeit mit dem Proto120 in Mainz werde ich nicht vergessen. Der Mangel an Schlaf konnte mit Pizza zwar kompensiert werden aber in Zukunft werde ich doch Orte mit Sonneneinstrahlung >0 vorziehen. Und Kabel werden nacheinander verlegt. Für die Hilfe bei jeglichen Verwaltungsaspekten und Formalitäten habe ich insbesondere Anita zu danken, da Du mir stets den Rücken freihieltst und Dinge im Hintergrund in Bewegung setztest, deren Existenz ich nicht mal wusste.

Von der inhaltlichen Unterstützung abgesehen habe ich natürlich im übergeordneten Rahmen der gesamten Arbeitsgruppe im Allgemeinen zu danken. Ich habe die Zeit bei Euch sehr genossen und danke Euch für die immer sehr angenehme Atmosphäre, bei der der Mensch nie zu kurz kam. Die Grundsatzdiskussionen mit meinem ehemaligen Bürokollegen Till werden in Zukunft hoffentlich an anderer Stelle weitergeführt. Dir und Christopher, sowie Wihan, Lukas, Marvin und Matthias danke ich insbesondere für die tolle Zeit als Bürogemeinschaft. Die Zeit zum nächsten Nerf-Gefecht könnt Ihr derweil ja mit Training überbrücken, damit Eure Büroseite nicht nur von weißen Fahnen bestimmt wird. Spätestens dann, wenn auch Ihr Euch an der Stelle befindet, wo ich gerade stehe. Nun ist es aber erstmal Zeit, die Flügel auszubreiten.

Der Aufwand und Umfang einer solchen Arbeit erstreckt sich aber natürlich auch auf das private Umfeld. Hier gebührt Anneka mein unschätzbare Dank. Du warst mir immer eine große Hilfe und nur durch Deine Unterstützung, im Kleinen wie im Großen, konnte ich letztlich die Kraft und Energie aufbringen, um diesen Weg zu gehen. Du hast mich in den letzten Jahren in allerlei Abschnitten und Phasen begleitet und dafür gesorgt, dass alles funktioniert, wenn ich den Fokus mal wieder zu scharf gestellt habe. Zum Beispiel, die diversen Male, als ich vergaß Nahrung zu mir zu nehmen und Du dann mit den vielen, kleinen Präsenten morgens dafür gesorgt hast, dass ich gut durch die Strapazen des Tages komme. Deine Teilhabe an den etlichen Gedankenspielen, Erklärungen, Modellen usw. hat mir auch sehr viel geholfen. Ohne Dich hätte ich zum Beispiel wichtige Schritte in den graphentheoretischen Algorithmen wohl nie verstanden und adaptieren können. In diesem Sinne tut es

mir übrigens leid, dass Du quasi direkt/indirekt an der Entstehung von nicht nur einer Doktorarbeit mitwirken musstest. Diese hat mich zwar enorm weitergebracht und meinen Horizont nicht nur einmal und nicht nur in einer Richtung erweitert, aber die weitaus wichtigere Erkenntnis, die ich machen durfte, ist jene, als Du in mein Leben eingetreten bist. Das überwiegt alles andere und ich wiederhole diese seitdem Tag für Tag. Nicht nur, weil ich vergesslich bin, sondern weil es sich immer mehr und mehr bestätigt.

Auch meiner Familie habe ich sehr viel zu verdanken. Der Dank erstreckt sich hier nicht nur auf die letzten Jahre, sondern auf Eure Unterstützung über mein gesamtes Leben hinweg. Auf Euch konnte ich immer zählen, wenn es eng wurde und ohne Euch wäre es manche Male sicherlich mehr als schwierig gewesen. Näher darauf eingehen würde der Rahmen hier schnell nicht mehr fassen können aber Ihr wisst ja selber, dass ich ohne Euch nicht eine Feder an meine Flügel hätte setzen können. Aber es soll dennoch nicht unerwähnt sein: Mutter, für das vielfache Korrekturlesen und auch Vater, für die unzähligen Situationen, in denen es mehr als Worte bedurfte, kann ich Euch gar nicht genug danken. Laura, Dir danke ich für die eine von den wenigen Auszeiten in Berlin. Das sollten wir bei Gelegenheit wiederholen, mit Ausnahme des einen Abends, wo wir faktisch fünf Stunden lang bis morgens einfach nur auf einem Gelände ohne sonstige Aussicht beziehungsweise könnte man schon ohne jeden Grund sagen, rumstanden. Du weißt, was ich meine.

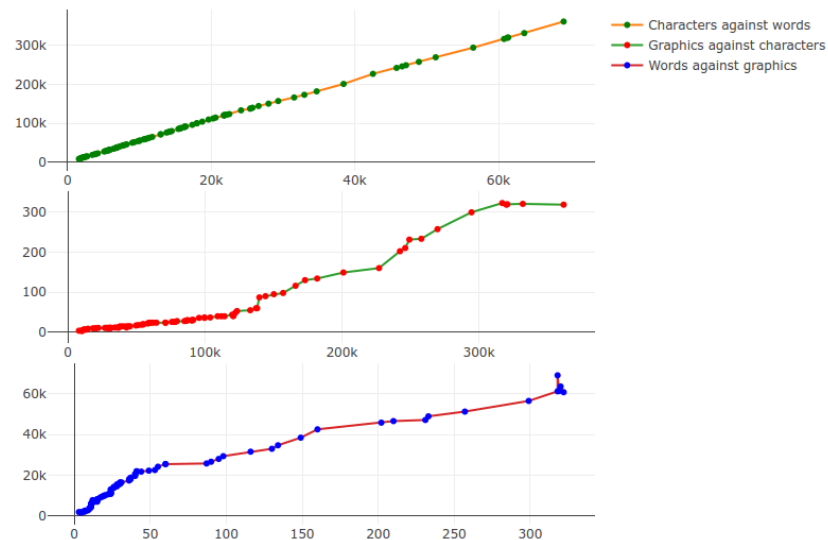
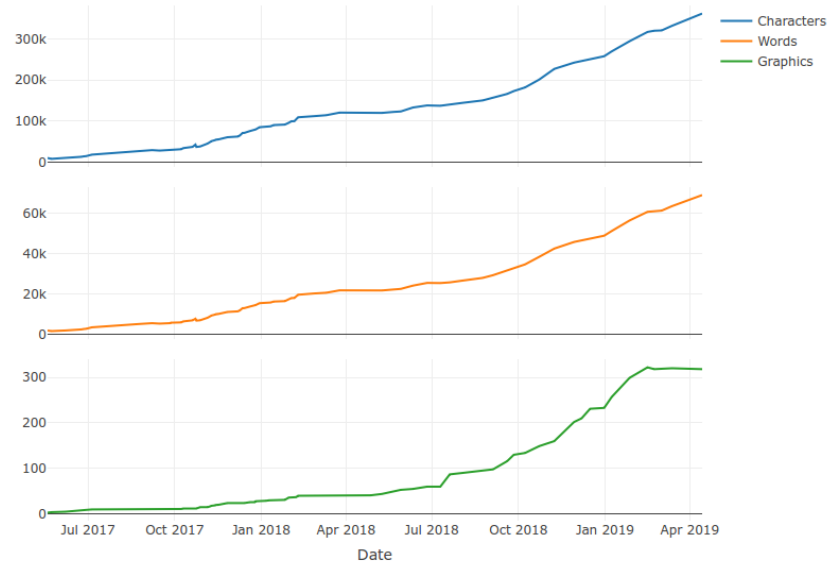
Ansonsten muss ich mich bei meinen Sportgruppen entschuldigen, dass wir uns die letzten Jahre kaum gesehen haben. Das wird sich hoffentlich bald wieder ändern. Auch wenn die Arbeit faktisch durch meinen Geist erfolgte, so habe ich aber auch meinem Körper zu danken, als dass er die Mühen am Schreibtisch so wacker durchhielt. Beiden ist die gegenseitige Hilfe beim kontinuierlichen Verschieben der Grenzen jeweils hoch anzurechnen. Ich danke auch meinem Laptop, der nach wie vor fehlerfrei funktioniert und nicht einmal Anlass zur Beunruhigung lieferte.

Zuguterletzt habe ich auch sehr vielen unbekanntem Menschen aus dem virtuellen Schwarm zu danken, die mir bei sehr speziellen und komplizierten Anliegen geholfen haben. Vor allem Anonymous, einer der frühesten Begleiter von ROOT, habe ich dafür zu danken, dass die längst nicht mehr aktuellen SLitrani- und ROOT-Bibliotheken und dem passenden Compiler harmonisierten. Auch DeltaIV vielen Dank für die sehr umfangreichen Konversationen bezüglich statistischer Modellierungen.

All jene, die ich hier nicht namentlich erwähnt habe, aber trotzdem in irgendeiner Form an dieser Arbeit mitgewirkt haben, auch Euch gebührt mein Dank!

Behavioural analysis of my own person

The fact that a document has been written for several years is, of course, an ideal occasion to analyse yourself. For this reason, I have documented my own behaviour from the first to the last lines with the help of a total of 93 data points. In this process I recorded the number of letters, words and graphics. Ultimately, I wanted to know whether I was behaving exponentially in the temporal development - how it felt to be a basic human characteristic - or whether the curves would provide other characteristics. Also whether you can identify various situations (beginning of a new chapter, corrections, summer/winter time, etc.) or not.



The number of graphics used is exponential, while letters and words are more linear. This can be explained by the fact that my ability to work was quite constant, but in the last chapter comparatively many graphics were used. This is actually the case, as you can see in the graphic "Graphics against words". Otherwise, the ratio of letters to words is very linear, so I wanted to investigate whether one tends towards long or short words in the progression. The characters are counted without spaces.

Statement of authorship / Selbstständigkeitserklärung

I declare that I have completed this dissertation single-handedly without the unauthorized help of a second party and only with the assistance acknowledged therein. I have appropriately acknowledged and cited all text passages that are derived verbatim from or are based on the content of published work of others, and all information relating to verbal communications. I consent to the use of an anti-plagiarism software to check my thesis. I have abided by the principles of good scientific conduct laid down in the charter of the Justus Liebig University Giessen „*Satzung der Justus-Liebig-Universität Gießen zur Sicherung guter wissenschaftlicher Praxis*“ in carrying out the investigations described in the dissertation.

Ich erkläre: Ich habe die vorgelegte Dissertation selbstständig und ohne unerlaubte fremde Hilfe und nur mit den Hilfen angefertigt, die ich in der Dissertation angegeben habe. Alle Textstellen, die wörtlich oder sinngemäß aus veröffentlichten Schriften entnommen sind, und alle Angaben, die auf mündlichen Auskünften beruhen, sind als solche kenntlich gemacht. Ich stimme einer evtl. Überprüfung meiner Dissertation durch eine Antiplagiat-Software zu. Bei den von mir durchgeführten und in der Dissertation erwähnten Untersuchungen habe ich die Grundsätze guter wissenschaftlicher Praxis, wie sie in der „*Satzung der Justus-Liebig-Universität Gießen zur Sicherung guter wissenschaftlicher Praxis*“ niedergelegt sind, eingehalten.

Date, Datum

Signature, Unterschrift